PhD-FSTC-2019-36
The Faculty of Sciences, Technology and Communication

DISSERTATION

Defence held on 09/05/2019 in Esch-sur-Alzette

to obtain the degree of

DOCTEUR DE L'UNIVERSITÉ DU LUXEMBOURG

EN PHYSIQUE

by

Max Hilaire WOLTER
Born on 29 May 1989 in Esch-sur-Alzette (Luxembourg)

OPTICAL INVESTIGATION OF VOLTAGE LOSSES IN HIGH-EFFICIENCY CU(IN,GA)SE_2 THIN-FILM SOLAR CELLS

Dissertation defence committee

Dr. Susanne Siebentritt, dissertation supervisor
Professor, Université du Luxembourg

Dr. Thomas Kirchartz
Professor, Forschungszentrum Jülich GmbH

Dr. Jan Lagerwall, Chairman
Professor, Université du Luxembourg

Dr. Stephan Bücheler
Empa – Swiss Federal Laboratories for Materials Science and Technology

Dr. Phillip Dale, Vice Chairman
Associate Professor, Université du Luxembourg

Contents

Abstract **1**

1 Introduction **3**

2 Background **7**
2.1 Semiconductor basics . . . 7
2.1.1 Electron and hole concentrations . . . 8
2.1.2 The pn junction . . . 10
2.2 The chalcopyrite Cu(In,Ga)Se_2 . . . 13
2.2.1 Crystal structure and properties . . . 13
2.2.2 Intrinsic point defects . . . 15
2.3 The Cu(In,Ga)Se_2 solar cell . . . 18
2.3.1 Device structure . . . 18
2.3.2 Working principle and device characterization . . . 20
2.4 Fundamental losses in Cu(In,Ga)Se_2 solar cells . . . 22
2.5 Recombination losses in Cu(In,Ga)Se_2 solar cells . . . 26
2.5.1 Radiative recombination . . . 27
2.5.2 Non-radiative recombination . . . 28
2.5.3 Influence of recombination on V_{OC} . . . 30
2.6 Cu(In,Ga)Se_2 solar cells: recent advances . . . 31
2.6.1 A brief history of Cu(In,Ga)Se_2 solar cells . . . 31
2.6.2 The double gallium gradient . . . 32
2.6.3 The alkali post-deposition treatment . . . 33
2.7 Photoluminescence spectroscopy . . . 37
2.7.1 Absorption and generation . . . 37
2.7.2 Radiative recombination processes . . . 39
2.7.3 Band-to-band recombination . . . 41
2.7.4 Photoluminescence in compensated semiconductors . . . 43

3 Experimental details **47**
3.1 Photoluminescence setup . . . 47
3.1.1 Spectral calibration . . . 49
3.1.2 Intensity calibration . . . 50
3.2 Spatially-resolved photoluminescence setup . . . 51
3.3 Sample overview . . . 53

4 Thin-film interference in Cu(In,Ga)Se_2 **57**
4.1 Origin of near band edge photoluminescence . . . 58
4.2 Thin-film interference . . . 63
4.2.1 Influence of surface roughness on interference . . . 65
4.2.2 Influence of absorber thickness on interference . . . 67
4.3 Angle-resolved photoluminescence . . . 67
4.3.1 Limitations of angle-resolved photoluminescence . . . 70

4.3.2 ARPL as a tool to detect interference fringes . . . 72
4.4 Scattering surface layer . . . 73
4.4.1 Deposition process . . . 74
4.4.2 Working principle . . . 75
4.4.3 Influence on the photoluminescence signal . . . 76
4.4.4 Effectiveness at room temperature . . . 77
4.4.5 Effectiveness at low temperatures . . . 78
4.5 Summary . . . 79

5 Near band edge photoluminescence 81
5.1 Extraction of optoelectronic properties . . . 82
5.1.1 Extracting the quasi-Fermi level splitting . . . 82
5.1.2 Extracting the Urbach energy . . . 84
5.1.3 Pitfalls and good practice . . . 85
5.2 Influence of alkali atoms on the quasi-Fermi level splitting . . . 89
5.2.1 Case of low-temperature absorbers . . . 89
5.2.2 Case of high-temperature absorbers . . . 91
5.3 Influence of the alkali PDT on the band tails . . . 94
5.3.1 Influence on the Urbach energy determined by PL . . . 95
5.3.2 Comparison to other methods . . . 98
5.4 Influence of the alkali PDT on absorber homogeneity . . . 99
5.4.1 Case of high-temperature absorbers . . . 100
5.4.2 Case of low-temperature absorbers . . . 102
5.4.3 Comparison to older records . . . 103
5.5 Summary . . . 105

6 Investigation of photoluminescence at low temperatures 107
6.1 Deep-level defects . . . 108
6.2 Electrostatic potential fluctuations . . . 110
6.2.1 Revisiting interference effects . . . 110
6.2.2 Case of high-temperature absorbers . . . 112
6.2.3 Case of low-temperature absorbers . . . 120
6.2.4 Comparison to other studies . . . 123
6.3 Summary . . . 124

7 What limits the voltage in Cu(In,Ga)Se_2 solar cells? 127
7.1 Cu(In,Ga)Se_2 solar cells: State of the Art . . . 128
7.1.1 Revisiting band tails . . . 128
7.1.2 External radiative efficiency . . . 130
7.1.3 Quantified voltage losses . . . 134
7.1.4 Summary . . . 137
7.2 Influence of alkali elements on the optoelectronic quality of CIGS . . . 138
7.2.1 Influence of NaF . . . 138
7.2.2 Influence of sodium and RbF . . . 139
7.2.3 Summary . . . 141
7.3 Voltage losses in Cu(In,Ga)Se_2: open questions . . . 142
7.3.1 Potential fluctuations . . . 142
7.3.2 Deep-level defects . . . 143
7.3.3 Structural defects . . . 144
7.3.4 Lack of photon recycling . . . 145

8 Summary **147**

9 Outlook **151**

A Appendix of Chapter 2 **153**
A.1 The solar spectrum . . . 153
A.2 Optical and collection losses . . . 154
A.3 Electrical resistance losses . . . 156
A.4 Alkali literature overview . . . 156
A.5 Collection of doping changes in CIGS from literature . . . 160

B Appendix of Chapter 3 **161**
B.1 Sample structure and solar cells . . . 161
B.2 Determination of band gap energies . . . 166

C Appendix of Chapter 4 **169**
C.1 Exfoliation experiment on a bare Cu(In,Ga)Se_2 absorber . . . 169
C.2 Excitation-dependent PL on exfoliated Cu(In,Ga)Se_2 . . . 169
C.3 Cu(In,Ga)Se_2 penetration depth for varying excitation energies . . . 170
C.4 ARPL on bare H0 and CdS-covered L1 samples . . . 171
C.5 Additional reflectance spectra . . . 174
C.6 Excitation-dependent PL on sample L1 . . . 175
C.7 Scanning electron microscope scan . . . 175
C.8 Reflectance of absorbers covered by polystyrene . . . 176
C.9 Polystyrene reflectance and transmittance . . . 177
C.10 ARPL in the cryostat . . . 177
C.11 ARPL on PS-covered CIGS absorbers . . . 178
C.12 Low-energy signal at low T and large angles . . . 179

D Appendix of Chapter 5 **181**
D.1 Effect of various parameters on the PL spectrum . . . 181
D.2 Effect of temperature on the extraction of $\alpha(E)$ . . . 182
D.3 Temporal evolution of $\Delta\mu$ for samples L1, L2, and L3 . . . 183
D.4 Quasi-Fermi level splitting of samples LN1, LN2, and LN3 . . . 184
D.5 Collection of spatially-resolved PL spectra . . . 186
D.6 Temporal evolution of $\Delta\mu$ for samples H1 and H2 . . . 187
D.7 Absorption coefficient spectra for various samples . . . 188
D.8 Other techniques for the extraction of E_U . . . 189
D.9 External quantum efficiency of H1 and H2 . . . 191
D.10 Spatially-resolved μ-PL on absorber H1 . . . 191
D.11 Spatially-resolved μ-PL on absorber H2 . . . 193
D.12 Spatially-resolved μ-PL on absorber L1 . . . 194
D.13 Influence of excitation density on absorber H1 . . . 194

E Appendix of Chapter 6 **197**
E.1 Spectral calibration function for the InAs detector . . . 197
E.2 Spectral calibration of absorbers H2's PL spectrum . . . 198
E.3 Comparison: extended vs. conventional setup . . . 199
E.4 Influence of excitation density on the PL spectrum at 10 K . . . 200
E.5 PL spectra of samples H1, L1, L2, measured with the InAs detector . . . 201
E.6 Low-temperature PL of HS, H1, and L2 . . . 201
E.7 PL of H1 at 12.5 K and 20 K . . . 203

E.8 PL of H2 at 80 K under different excitation densities . . . 204
E.9 PL of H1 and H2 at 140 K . . . 204
E.10 PL spectra of L1 and L3 at different temperatures . . . 205

F Appendix of Chapter 7 **207**
F.1 Absorption coefficient of $CuInSe_2$ absorber . . . 207
F.2 Band tails in the Shockley-Queisser model . . . 207
F.3 Details of the SCAPS simulation . . . 210
F.4 Extracting Q_{ext}^{lum} from EQE . . . 212
F.5 Internal radiative efficiency . . . 214
F.6 Method to quantify voltage losses . . . 216
F.7 Influence of doping on $\Delta\mu$ . . . 218

Acknowledgements **221**

Scientific contributions **223**

Bibliography **247**

Abstract

The increases in power conversion efficiencies up to 23.35 % in thin-film Cu(In,Ga)Se_2 (CIGS) solar cells in recent years can mainly be ascribed to the alkali post-deposition treatment (PDT). The latter consists of an additional treatment step after absorber growth where alkali elements, such as sodium (Na) or rubidium (Rb), are injected into the absorber. While the beneficial effects of the alkali PDT, attributed partly to a reduction of voltage losses, are undeniable, it is not yet entirely clear what underlying mechanisms are responsible. To clarify the specific influence of the alkali PDT on the voltage of the CIGS solar cells, photoluminescence (PL) spectroscopy experiments were conducted on state-of-the-art CIGS absorbers having undergone different alkali PDTs. Photoluminescence allows the investigation of possible voltage losses on the absorbers through the analysis of optoelectronic quantities such as the absorption coefficient, the quasi-Fermi level splitting, electronic defects, and potential fluctuations.

Mainly due to a smooth surface and a band gap minimum inside the bulk, the PL spectra of state-of-the-art CIGS absorbers are distorted by interference fringes. To remove the interference fringes at room temperature, an experimental method, which revolves around the measurement of PL under varying angles, is developed in this thesis. In addition, to enable PL experiments even at low temperatures, an auxiliary polystyrene-based scattering layer is conceptualized and deposited on the surface of the absorbers.

With the influence of the interference fringes under control, the quasi-Fermi level splitting $\Delta\mu$ can be measured on bare and CdS-covered absorbers. The results reveal an improvement of $\Delta\mu$ in absorbers that contain Na with an additional increase being recorded in absorbers that also contain Rb. The improvement of $\Delta\mu$ is present in both bare and CdS-covered absorbers, indicating that the beneficial effect of the alkali PDT is not only occurring on the surface but also inside the bulk.

To identify possible origins of the $\Delta\mu$ increase, various PL-based experiments were performed. At room temperature, spatially-resolved PL measurements on the microscopic scale do not reveal any optoelectronic inhomogeneities in state-of-the-art CIGS absorbers. Defect spectroscopy at low temperatures also does not reveal the presence of deep-level trap states. Through temperature- and excitation-dependent PL experiments, a reduction of electrostatic potential fluctuations is observed in absorbers that contain Na with a stronger reduction witnessed in absorbers that contain Rb as well. The extraction of the absorption coefficient through PL measurements at room temperature reveals a reduction of band tails with alkali PDT that empirically correlates to the measured increase in $\Delta\mu$. This correlation might indicate that the band tails, through non-radiative recombination, may be the origin of the performance-limiting voltage losses.

In combination with reports from literature, it is suggested that the beneficial effect of the light alkali PDT (Na) is mainly a doping effect i.e. an increase in the $\Delta\mu$ through an increase in the hole carrier concentration. The beneficial effect of the heavier alkali PDT (Rb) is attributed partly to a surface effect but mainly to a grain boundary effect, either through a reduction in band bending or a reduction of non-radiative recombination through tail states.

Finally, the various voltage losses in state-of-the-art CIGS solar cells are compared to the best crystalline silicon device, revealing almost identical losses. This shows that the alkali PDT enables the fabrication of high-efficiency CIGS solar cells that show, in terms of voltage, identical performance. To bridge the gap between CIGS and the even better performing GaAs, the results of this thesis suggest that grain boundaries are crucial in this endeavour.

1 Introduction

"[...] the most systemic threat to humankind remains climate change [...]". These were the words uttered by Secretary-General António Guterres during the United Nations press conference on climate change in March 2018 [1]. Later the same year, the Intergovernmental Panel on Climate Change (IPCC) published a special report on the necessity of limiting the Global Warming to 1.5° C that would require unprecedented changes in all aspects of societal life [2]. These changes consist, among others, of a reduction of the global CO_2 emission by 45 % from 2010 levels by 2030 along with an increase of 85 % of renewable energy contribution to the global electricity by 2050 [2]. With the current total primary energy supply provided almost entirely (i.e. above 80 %) by fossil fuels [3] combined with an ever increasing population [4] and energy demand [5], the need for renewable energies is more prevalent than ever.

Photovoltaic (PV) solar energy has the potential to act as the main foot board in the current energy crisis as it exhibits high power conversion efficiencies and a never-ending fuel supply. From the readily available PV technologies, the thin-film Cu(In,Ga)Se_2 (CIGS) solar cells show a huge potential due to high material savings, a low CO_2 footprint, and long-term stability [6]. In addition, due to the ability to manufacture the solar cells onto flexible substrates, CIGS is set to find a large applicability in fast-emerging market sectors such as building-integrated photolvoltaics (BIPV) and building-applied photovoltaics (BAPV). With the recent precedent-setting intention of the European Commission that renewable energies provide 32 % of the total energy in the European Union by 2030 [7] and the fact that 40 % of the EU's final energy demand is coming from buildings, it is clear why preparing CIGS for BIPV and BAPV is a strategy worth pursuing.

With 23.35 % [8], Cu(In,Ga)Se_2 currently exhibits the highest power conversion efficiencies among all stable thin-film PV technologies [9], [10]. In an effort to increase the efficiency, in 2015, the "Sharc25"[1] project was launched by the European Commission and spearheaded by the PV research groups of ZSW[2] and Empa[3] [11]. Both ZSW and Empa are big players in the CIGS community with ZSW having held the world record for CIGS efficiency several times in recent years [10] and with Empa being the current world record holder for the highest efficiency of any flexible solar cell (20.4 % CIGS) [12]. The main aim of the Sharc25 project was to bring together global experts in various analysis techniques to study the current limitations of the best CIGS devices and to find strategies to improve upon them. Among the eleven participating institutions, the Laboratory for Photovoltaics from the University of Luxembourg contributed to the project by investigating the optoelectronic properties of the state-of-the CIGS absorbers provided by ZSW and Empa. This thesis describes and elaborates on the insights that could be achieved in the framework of the Sharc25 project.

The strong increase in power conversion efficiency from 20.3 % [13] in 2011 to the current record efficiency 23.35 % [8] (early April 2019) is mainly due to the beneficial effects of the alkali post-deposition treatment (PDT). The alkali PDT consists of an additional treatment step after the growth of the CIGS absorber where alkali elements are deposited onto the surface of the

[1] Sharc25 stands for "Super high efficiency Cu(In,Ga)Se_2 thin-film solar cells approaching 25 %" [11].
[2] Center for Solar Energy and Hydrogen Research Baden-Württemberg, Stuttgart, Germany.
[3] Swiss Federal Laboratories for Materials Science and Technology, Dübendorf, Switzerland.

absorber. Under elevated temperatures, the alkali atoms are able to diffuse into the absorber. While the concept of the alkali PDT was introduced back in 2004 by Rudmann *et al.* [14], first depositions were only made with the light alkali element sodium (Na). It was not until the switch to heavier alkali elements, such as potassium (K) [12], rubidium (Rb) [15], and caesium (Cs) [16] was made and the process improved, that the increases in efficiency mentioned above were made possible.

The beneficial effects of the alkali elements on the CIGS solar cells are clear: an improvement of the solar cell parameters that define the power conversion efficiency. These are: the short-circuit current density j_{SC}, the open-circuit voltage V_{OC}, and the fill factor FF. However, what is not yet entirely clear is how exactly the alkali elements affect the different parameters. Thus, in the framework of the Sharc25 project, several CIGS absorbers and solar cells were prepared and treated with various alkali PDTs by ZSW and Empa and sent to the different partners for analysis. The samples sent to the Laboratory for Photovoltaics were to be analysed through photoluminescence (PL) spectroscopy. The latter is a powerful tool to investigate the optoelectronic properties of the absorbers and thus does not require finished solar cell devices. As such, it is possible to investigate the influence of the alkali PDT already in the absorbers. Photoluminescence is based on the principle of charge carrier excitation via external illumination and the subsequent collection of the absorber's emitted radiation. The optoelectronic properties that can thus be analysed are dictated by the recombination processes inside the absorber which ultimately define the voltage losses.

Hence, the general aim of this thesis is to investigate the influence of the alkali post-deposition treatment on the optoelectronic properties of state-of-the-art CIGS absorbers, and thus on the voltage losses in the corresponding solar cells. In the following, the structure and content of the thesis are presented.

Beyond this introduction chapter, the thesis starts with chapter 2 that houses the background information and literature review. The chapter starts by introducing the semiconductors basics such as electron and hole concentrations as well as the pn junction. Afterwards, the chalcopyrite Cu(In,Ga)Se_2 along with its crystal structure and intrinsic point defects is discussed. A defect model is introduced that allows for the possible presence of a deep-level defect which could lead to significant voltage losses. After the description of the CIGS absorber, the full solar cell structure is described along with the working principle of solar cells. Single-junction solar cells are only able to use approximately one third of the sun's irradiated power and are thus fundamentally limited. These fundamental limitations are briefly introduced before describing the various recombination losses, and thus potential causes for voltage losses, that can occur inside CIGS solar cells. Afterwards, the history of CIGS with its milestones is briefly elucidated. Since the alkali PDT is a very important milestone in the history of CIGS and since it is also part of the main topic of this thesis, a very broad and general literature review of observed and known effects is given. The chapter is concluded with the theoretical principle behind photoluminescence spectroscopy.

The chapter 3 describes the experimental setups that are used to perform the photoluminescence measurements in this thesis. In addition, the chapter also houses the details about the various samples that are measured in this thesis.

Chapter 4 deals with the principle of interference effects in thin-film CIGS absorbers. When measuring photoluminescence on CIGS absorbers at room temperature, a broad peak is expected. However, this is not the case in state-of-the-art CIGS absorbers where a distorted spectrum is recorded instead. Thus, the origins of these interference effects are investigated. Consequently, two methods, that have been developed specifically for the removal of interference fringes from the measured spectra under various experimental conditions, are presented.

Chapter 5 contains the main PL measurements that are done at room temperatures. From the measured PL spectra of the various CIGS absorbers, the quasi-Fermi level splitting can be

extracted. The quasi-Fermi level splitting is an upper limit for the open-circuit voltage in solar cell devices and thus directly reflects the voltage losses. Through a comparison between various samples, present under the form of bare and CdS-covered absorbers, first conclusions about the effect of the alkali PDT can be drawn. But not only the quasi-Fermi level splitting, also the band tails can be extracted from room-temperature PL measurements. Band tails represent states within the band gap of CIGS that promote harmful recombination processes. By investigating their reaction to the application of various alkali PDTs, more insight on the recombination processes can be gained. Finally, the chapter ends with spatially-resolved photoluminescence scans on the micrometer scale to examine absorber inhomogeneities which can, incidentally, also cause voltage losses.

In chapter 6, the photoluminescence measured at low temperatures is explored. Conducting PL experiments at low temperatures allows for the detection and analysis of possible deep-level defects and electrostatic potential fluctuations. Both are possible causes for voltage losses in CIGS solar cells.

In the final results-related chapter 7, the CIGS absorbers and their corresponding finished solar cell devices are compared to other PV technologies such as gallium arsenide and crystalline silicon. The various voltage losses are extracted from external quantum efficiency measurements and compared to the best available devices. Following this, a tentative suggestion for the influence of the alkali post-deposition treatment on the voltage losses in state-of-the-art CIGS absorbers and solar cells is provided. The chapter is concluded by briefly discussing several remaining open questions.

Chapter 8 summarizes the main results and insights of the thesis and the following chapter 9 offers an outlook.

Beyond the chapters that are listed above, the thesis offers a large appendix that contains a variety of supporting information. However, the main part of the thesis is written such that the appendix is not needed to understand the results and follow the suggested interpretations.

2 Background

In this chapter the basics about semiconductors, $Cu(In,Ga)Se_2$ thin-film solar cells, and photoluminescence spectroscopy are introduced. The chapter is split into seven sections with the first section briefly reviewing semiconductor basics where expressions for electron and hole concentrations are established and where the pn junction, upon which the working principle of solar cells is built, is explained.

The second section introduces the chalcopyrite material $Cu(In,Ga)Se_2$ by illustrating and describing its crystal structure and properties. The section ends with a brief discussion about intrinsic point defects. The discussion is complemented with recent data and results from literature as well as the introduction of a defect model that describes the influence of impurities on doping and recombination activity.

The third section explains why and how $Cu(In,Ga)Se_2$ works as a solar cell by describing the general solar cell structure along with standard characterization methods that are used to determine its power conversion efficiency.

The fourth section deals with fundamental losses in single-junction solar cells and introduces the Shockley-Queisser model. This model uses very basic thermodynamic assumptions to derive expressions that enable the determination of a theoretical threshold for the power conversion efficiency of any solar cell.

The fifth section builds upon the prior section by describing the various recombination losses that can occur in the real $Cu(In,Ga)Se_2$ solar cell device. These recombination losses reduce the performance of the solar cells and are, alongside other losses, responsible for not reaching the efficiencies set by the theoretical Shockley-Queisser model.

The sixth section provides a summary of the state-of-the-art properties of $Cu(In,Ga)Se_2$ solar cells. The section starts with a brief history before introducing two very important milestones in the development of $Cu(In,Ga)Se_2$ in detail: the graded band gap and the alkali post-deposition treatment.

The chapter ends with the introduction of the measurement technique based on photoluminescence spectroscopy that is used extensively in this thesis to characterize the optoelectronic properties of $Cu(In,Ga)Se_2$ absorbers by analysing its recombination activity.

2.1 Semiconductor basics

Semiconductors are materials whose electrical conductivity can vary between that of metals and insulators. This is possible because they possess a band structure that exhibits a forbidden occupation zone, i.e. an energetic band gap. At zero point kelvin, the low-energy states below the band gap are entirely occupied by electrons which inhibits any charge transport. The high-energy states above the band gap are then unoccupied. In the terminology of semiconductors, the highest occupied low-energy band is called valence band while the lowest unoccupied high-energy band is called conduction band. By increasing the temperature, it is possible to excite electrons from the valence band across the energetic band gap into the conduction band. The resulting unoccupied states in the valence band are then called holes and can, as is the case for the excited electrons in the conduction band, contribute to charge transport. In the following, important key concepts and expressions of semiconductors are introduced. If not otherwise stated, the information has been adapted from standard textbooks such as [17]–[19].

2.1.1 Electron and hole concentrations

The concentration of electrons in the conduction band is given by the conduction band density of states and the Fermi-Dirac distribution function. In the case of a non-degenerate semiconductor and in thermal equilibrium, the electron concentration amounts to

$$n_0 = N_C \exp\left(-\frac{E_C - E_F}{k_B T}\right), \tag{2.1}$$

where N_C is the effective density of states of the conduction band, E_C the conduction band edge energy and E_F the Fermi energy. The information of the conduction band structure, through the electron effective mass, is entirely contained within N_C. Similarly, the concentration of holes in the valence band is given by

$$p_0 = N_V \exp\left(-\frac{E_F - E_V}{k_B T}\right), \tag{2.2}$$

where N_V is the effective density of states in the valence band and E_V the valence band edge energy.

Both equations (2.1) and (2.2) are only valid if the Boltzmann approximation can be applied to the Fermi-Dirac distribution i.e. if the Fermi energy is more than $3k_B T$ away from either of the band edges. This is indeed the case when considering an intrinsic semiconductor (i.e. without impurities) where the concentration of thermally excited electrons and holes is exactly equal. In this case the intrinsic Fermi level $E_{F,i} = E_F$ is exactly in the middle of the band gap. The concentration of either electrons or holes is then denoted as intrinsic carrier concentration $n_i = n_0 = p_0$. Taking the product of equations (2.1) and (2.2) yields

$$n_0 \cdot p_0 = n_i^2 = N_C N_V \exp\left(-\frac{E_C - E_V}{k_B T}\right) \tag{2.3}$$

or

$$n_i = \sqrt{N_C N_V} \exp\left(\frac{-E_g}{2k_B T}\right) \tag{2.4}$$

where $E_g = E_C - E_V$ is the band gap energy. From equation (2.4), it is clear that the intrinsic carrier concentration is independent of the Fermi level and varies strongly with temperature.

The concentration of excited charge carriers is directly proportional to the electrical characteristics of the semiconductor material. For multiple application purposes, having a large carrier concentration is often desired. In the case of an intrinsic semiconductor, the charge carrier concentration can only effectively be changed by varying the temperature which is why the usefulness of intrinsic semiconductors is limited.

Consequently, most devices that are based on semiconductors use an extrinsic semiconductor material where small and controlled amounts of impurities or other defects are added. These impurity atoms act as dopants and provide additional charge carriers. This is done by adding to the semiconductor a material that has a different amount of valence electrons than the host material. A prominent example is the addition of phosphorus to a silicon lattice. Phosphorus has five valence electrons while silicon only has four. Thus, when added, only four valence electrons of phosphorus engage in a covalent bond with the four valence electrons of the neighbouring silicon, leaving the fifth valence electron loosely bound to the impurity atom. With this impurity atom in place, only a small amount of thermal energy is necessary to ionize the atom (rendering it positively charged) by exciting the remaining valence electron into the conduction band. In an energy diagram, the energy of the impurity atom is thus slightly below the conduction band. In the aforementioned case, the phosphorus atom donates an electron

to the conduction band and is thus called donor atom. If mostly donor atoms are added to a semiconductor material, the semiconductor is said to be n-type doped.

Similarly, by adding an impurity atom with less valence electrons than the host lattice (boron doping in silicon e.g.), electrons from the valence band are easily excited into the hole of the so-called acceptor atom (rendering it negatively charged). A material doped with predominantly acceptor atoms is then said to be p-type doped. The role of donors and acceptors must not necessarily be played by impurities but can also be fulfilled by other defects (cf. section 2.2.2).

The difference between n-type and p-type doping is the concentration of the free charge carriers. In a p-type doped material, there are considerably more holes than electrons. The holes are then denoted as majority charge carriers while the electrons are denoted as minority charge carriers. In n-type doped material, it is the other way around. Varying the charge carrier concentration also changes the Fermi energy in thermal equilibrium. Generally, the Fermi level moves towards the band with the highest charge carrier concentration. In the case of a p-doped semiconductor, the Fermi level position is closer to the valence than to the conduction band (and vice versa for an n-type semiconductor). The concentration of holes p_0 is greatly increased due to the presence of acceptor defects while the concentration of electrons n_0 is greatly reduced. If a considerable density of acceptors N_A is added and is almost completely ionized at room temperature, then $p_0 \approx N_A$ and $n_0 = n_i^2/N_A$. Compared to the intrinsic case, the conductivity is greatly increased but it is mainly dominated by holes as they are the majority charge carriers. It is important to note that the relation $n_0 \cdot p_0 = n_i^2$ still holds true for the extrinsic semiconductor in thermal equilibrium (however, now the individual equilibrium electron n_0 and hole p_0 concentrations differ from the intrinsic ones).

In thermal equilibrium, for both intrinsic and extrinsic semiconductors, the charge carrier concentration can be described by a single Fermi level or Fermi energy. This is shown as an example in Fig. 2.1A where a simplified energy band diagram of a p-type doped semiconductor is illustrated. At room temperature, the acceptor atoms are almost all ionized due to electrons (blue circles) being thermally excited from the valence band into the acceptor states, leaving behind holes (hollow red circles). Some electrons are even excited directly from the valence

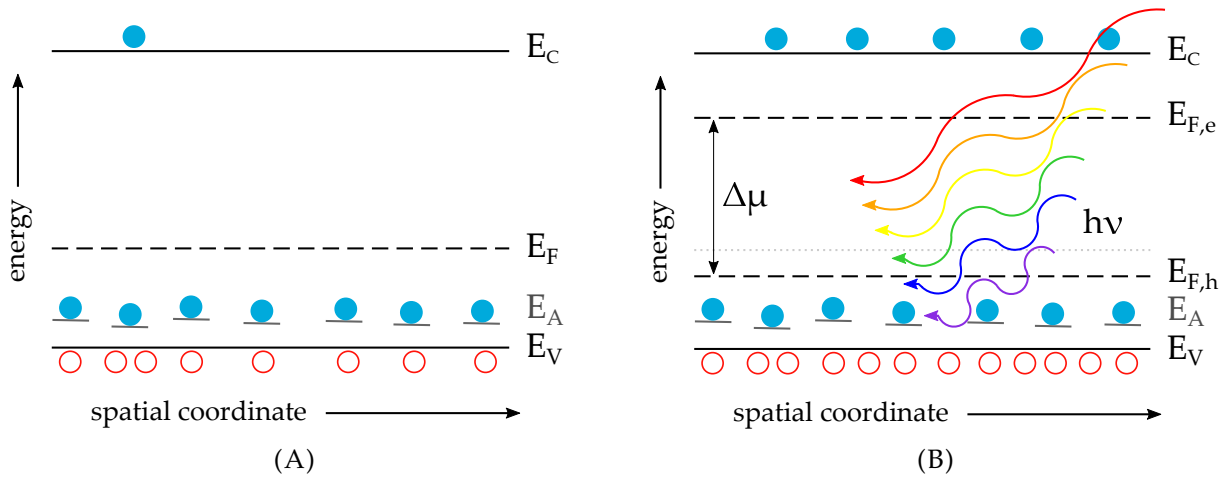

FIGURE 2.1: **(A)** Simplified energy band diagram of a p-type doped semiconductor in thermal equilibrium at room temperature. The discrete acceptor states with energy E_A are completely ionized leading to a larger concentration of holes (hollow red circles) in the valence band than electrons (blue circles) in the conduction band. **(B)** Perturbing the semiconductor via external radiation of energy $h\nu$ leads to an identical increase of electrons and holes and subsequently a splitting of the quasi-Fermi levels ($\Delta\mu$).

band into the conduction band (some 10 orders of magnitude or more less than holes). Due to the higher concentration of holes in the system, the Fermi level E_F is below mid band gap.

In the case of non-equilibrium, e.g. by exposing the system to light of energy $h\nu > E_g$, as shown in Fig. 2.1B, the concentrations of electrons n and holes p are equally increased above their equilibrium concentrations. The newly excited electrons Δn and holes Δp thermalise relatively quickly with the lattice and assume a state of quasi-thermal equilibrium. The excited charge carrier concentrations $n = \Delta n + n_0$ and $p = \Delta p + p_0$ are then larger than the equilibrium carrier concentrations such that $n \cdot p > n_i^2$, which is not achieved by doping alone. The exact procedure of charge carrier excitation via external radiation is discussed in detail in section 2.7.1.

While a single Fermi level is able to describe the carrier distributions in thermal equilibrium, this is not possible any more in quasi-thermal equilibrium. Due to the equal amount of generated electrons Δn and holes Δp, the Fermi level splits up into an electron quasi-Fermi level $E_{F,e}$ and a hole quasi-Fermi level $E_{F,h}$. The distribution of electrons in the conduction band is then entirely described by $E_{F,e}$ while the distribution of holes in the valence band is described by $E_{F,h}$. The electron density in the conduction band is given by

$$n = N_C \exp\left(-\frac{E_C - E_{F,e}}{k_B T}\right). \tag{2.5}$$

Similarly, the hole density in the valence band is given by

$$p = N_V \exp\left(-\frac{E_{F,h} - E_V}{k_B T}\right). \tag{2.6}$$

Considering equation (2.3), it follows

$$n \cdot p = n_i^2 \exp\left(\frac{E_{F,e} - E_{F,h}}{k_B T}\right) \tag{2.7}$$

where $E_{F,e} - E_{F,h} = \Delta\mu$ is labelled as the quasi-Fermi level splitting (QFLS). It describes the maximal extractable energy and is thus is a very important parameter in photoluminescence spectroscopy of semiconductors and for the use of semiconductors in a solar cell.

2.1.2 The pn junction

Very useful for device fabrication are the so-called pn junctions. A pn junction is formed by bringing an n-type semiconductor into contact with a p-type semiconductor. In the most basic case, the semiconductors brought into contact are of the same material and the pn junction will then be a homojunction.

Fig. 2.2A shows a simplified energy band diagram of an n-type (left) and p-type (right) semiconductor before they are joined together. At room temperature and in thermal equilibrium, the electron density in the conduction band in the n-type material is much larger than in the p-type material and vice-versa for the holes in the valence band. In a Gedankenexperiment, upon contact of both semiconductors, electrons diffuse from the n-type side to the p-type side because of a strong concentration gradient. Similarly, holes diffuse from the p-type side to the n-type side. This is possible because the excited charge carriers in the bands can move around rather freely, and their behaviour can in many cases be described by classical gas theory. After diffusion, both Fermi levels in the n-type and p-type side equilibrate to a single Fermi level. While the electrons and holes in the bands are able to diffuse to the other side, the ionized impurity atoms are stuck in the crystal lattice. The resulting accumulation of positive charges in the n-type side and negative charges in p-type gives rise to an electrostatic potential between

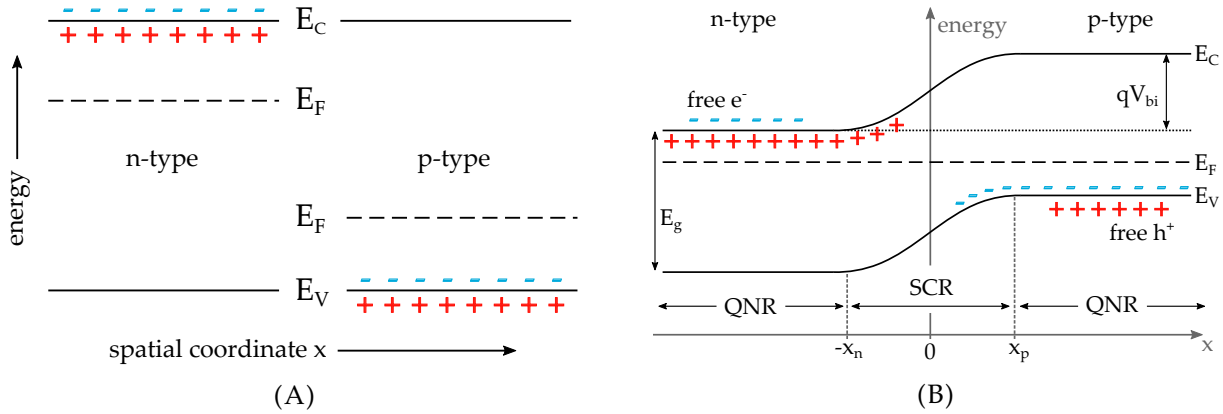

FIGURE 2.2: **(A)** Simplified energy band diagram of an n-type (left) and p-type (right) semiconductor. The illustration focusses mainly on charges: the red crosses represent positively charged entities i.e. holes and ionized donors while the blue bars represent negatively charged entities i.e. electrons and ionized acceptors. **(B)** Energy band diagram of the a pn junction in equilibrium, created by joining together both semiconductors from (A). The bands are deformed due to the formation of a built-in potential V_{bi} as a consequence of an electric field from the positively charged n-type side to the negatively charged p-type side.

both sides. Around the junction interface, an electric field from the positive to the negative side is formed. Since the region around the junction is devoid of any free carriers, it is called depletion region or space-charge region (SCR). As a consequence of the electric field, a "built-in" potential V_{bi} is formed and leads to a bending of the conduction and valence bands as depicted in Fig. 2.2B. In the energy representation, the built-in potential creates a potential barrier qV_{bi} that prevents electrons from crossing over from the n-type side to the p-type and vice-versa for the holes.

In thermal equilibrium, the Fermi level across the pn junction is constant and no driving force exists. Consequently, no current flows and the majority of the electrons are present in the quasi-neutral region (QNR) in the n-type side and the majority of holes are present in the QNR in the p-type side. Applying an external disturbance to the system, for example in the form of an applied bias, will break the equilibrium. Depending on the polarity of the applied bias V_a, the band bending and space-charge region width W are changed. In general, it can be shown that the width W of the space-charge region is given by

$$W = |-x_n| + |x_p| = \sqrt{\frac{2\epsilon\epsilon_0}{q}\left(\frac{1}{N_A} + \frac{1}{N_D}\right)(V_{bi} - V_a)} \tag{2.8}$$

where ϵ represents the dielectric constant of the material, ϵ_0 the dielectric constant in vacuum, N_A the density of acceptors, N_D the density of donors and V_a an applied external bias voltage.

By applying a negative voltage to the n-type side and a positive voltage to the p-type side, an additional electric field is created that acts in the opposite direction as the "built-in" electric field. The consequence of this positive applied bias $V_a > 0$ is a reduction of the potential barrier across the depletion region as depicted in Fig. 2.3A. The application of the forward bias leads to a splitting of the Fermi levels such that electrons coming from the n-type region move into p-type region where they recombine as minority carriers having travelled a distance equal to their diffusion length L_n. Similarly, holes move from the p-type side to the n-type side and recombine there. Hence, under forward bias, a net current flows across the SCR. Additionally, from eq. (2.8), it can be seen that the application of a forward bias leads to an decrease of the SCR width.

Similarly, the pn junction can also be operated in reverse bias by applying a positive voltage

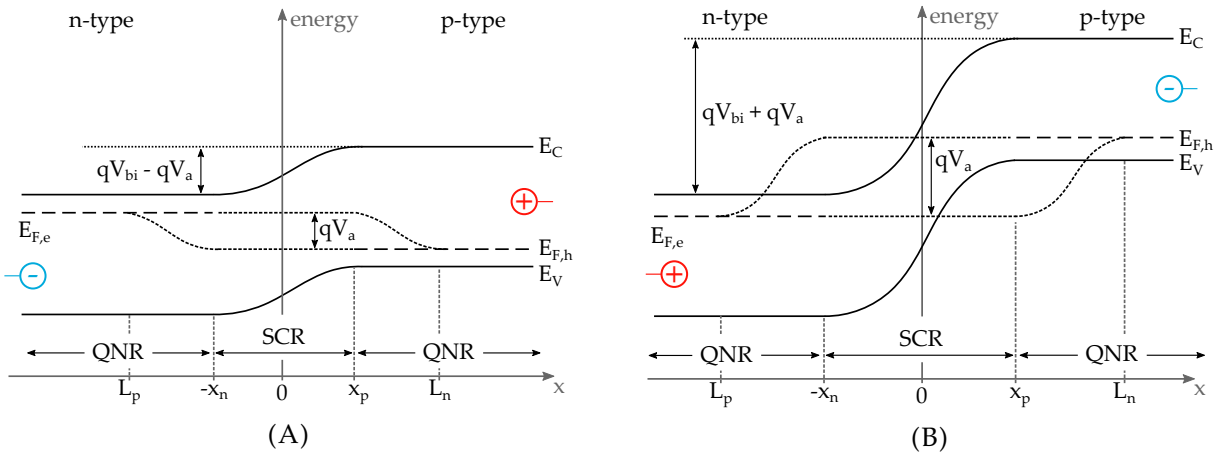

FIGURE 2.3: **(A)** Energy band diagram of a pn junction under forward bias $V_a > 0$. Applying a negative voltage to the n-type side and a positive voltage to the p-type side leads to the formation of an electric field in the opposite direction as the electric field in the SCR. As a result, the potential barrier is decreased which leads to a splitting of the Fermi level. **(B)** Energy band diagram of a pn junction under reverse bias $V_a < 0$. Applying a positive voltage to the n-type side and a negative voltage to the p-type side leads to the formation of an electric field in the same direction as the electric field in the SCR. As a result, the potential barrier is increased which leads to a splitting of the Fermi level.

to the n-type side and a negative voltage to the p-type side as is shown in Fig 2.3B. As a consequence of the negative applied bias $V_a < 0$, an electric field in the same direction to that in the SCR is formed which leads to an even larger potential barrier and a splitting of the Fermi levels. Due to polarity of the reverse bias, electrons are injected into the p-type side but are not transported as the p-type side consists entirely of holes. However, due to thermal radiation, some electrons are excited into the conduction band and may still move towards the n-type side (if they are generated within a diffusion length of the SCR). As a consequence, a small current flows across the junction. Due to the fact that electrons must first have been generated, this current is often labelled as generation current. The same principle, but vice versa, is valid for holes. According to eq. (2.8), under reverse bias $V_a < 0$, the SCR width is increased.

From the semiconductor transport equations, the total net current across the junction can be determined. The derivation can be reviewed in the relevant literature e.g. refs. [18]–[20]. The total net current density is mathematically described by

$$j = j_0 \left[\exp\left(\frac{qV_a}{Ak_BT} \right) - 1 \right], \tag{2.9}$$

which is also known as the Shockley diode equation [21]. The diode ideality factor A describes how close the device is to an ideal diode and can take on values between 1 (ideal diode) and 2. The diode ideality factor is described in section 2.5.3. The quantity j_0 is labelled as saturation current density and is the current density that flows across the pn junction under reverse bias (i.e. the generation current density mentioned above).

From Fig 2.3, it can be seen that the quasi-Fermi level splitting is given by the applied external potential

$$E_{F,e} - E_{F,h} = \pm qV_a. \tag{2.10}$$

This relation is of high importance for the comparison between optical and electrical properties of photovoltaic devices and will be revisited in later sections.

2.2 The chalcopyrite Cu(In,Ga)Se_2

An example of a p-type doped semiconductor is the chalcopyrite Cu(In,Ga)Se_2 (CIGS). It is a direct band gap semiconductor which is able to create excited electron-hole pairs by absorbing photons and thus constitutes the main part of CIGS based solar cells. In the first part of this section, the crystal structure and basic electronic properties of CIGS are introduced. In the second part, the potential impurities that define the performance of CIGS as a solar cell are briefly discussed.

2.2.1 Crystal structure and properties

A chalcopyrite is a material that crystallizes in the tetragonal structure. In the case of Cu(In,Ga)Se_2, the crystal is made up of I-III-VI_2 group elements i.e. copper (group I), indium and gallium (group III) and selenium (group VI). CIGS is a solid solution of the ternary chalcopyrite compounds $CuInSe_2$ and $CuGaSe_2$ and shares thus many of their properties.

The tetragonal structure of CIGS can be derived from the sphalerite structure which is closely related to the diamond structure. Fig. 2.4A shows the sphalerite structure in the case of zinc selenide (ZnSe) i.e. a face-centered cubic structure with a diatomic basis. From the sphalerite structure, replacing the group II elements (Zn) by half a group I element (Cu) and half a group III element (In or Ga) and stacking both unit cells on top each other, one ends up with the CIGS chalcopyrite superlattice as shown in Fig. 2.4B. In this constellation, each copper and group III element atom has four nearest selenium neighbour atoms to which they are tetragonally bound. The indium and gallium atoms are randomly distributed among the group III element sites resulting in the possibility that two neighbouring CIGS unit cells can differ significantly from each other, giving thus rise to alloy fluctuations in the macroscopic crystal. The lattice constants a and c depend on the bond length between the different atoms. For the ternary $CuInSe_2$, a is approximately of the length of 5.85 Å while c is approximately of the length of 11.73 Å [23]. In $CuGaSe_2$, the interatomic distances are slightly smaller such that a measures approximately 5.60 Å with c being approximately 11.01 Å [24]. For the solid solution CIGS, the lattice constants lie somewhere in between the ternary ones. From the values, it can be seen

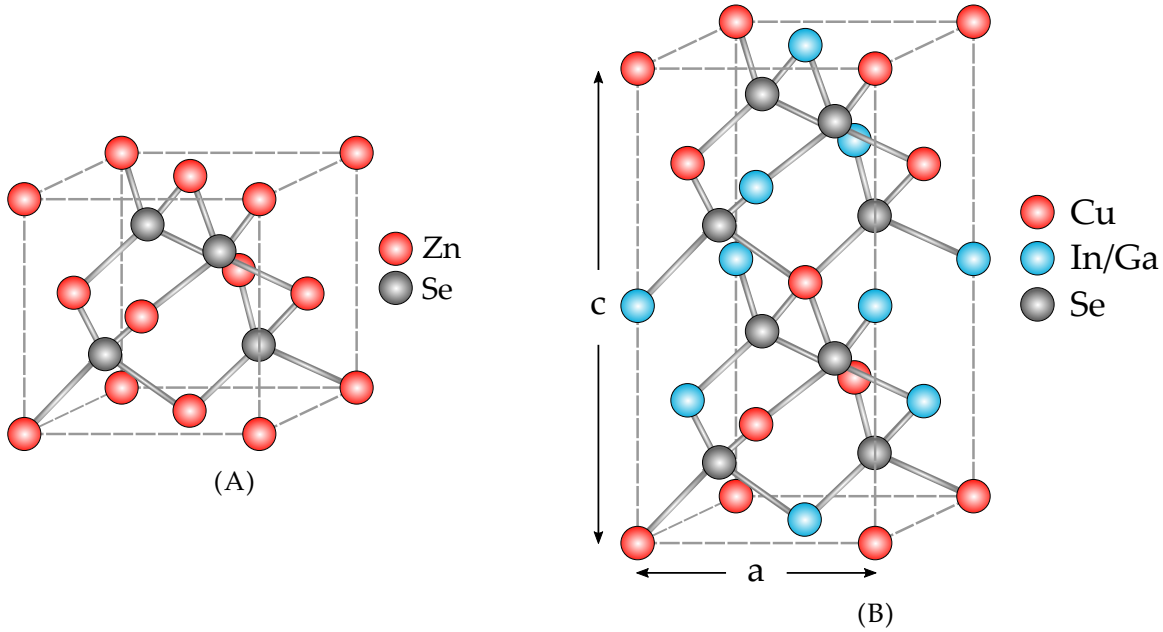

FIGURE 2.4: **(A)** Sphalerite structure in the case of the zinc selenide (ZnSe) crystal. **(B)** Chalcopyrite structure formed by stacking two sphalerite structures on top of each other. Adapted from ref. [22].

that the ratio of c/a is not exactly equal 2 which means that the tetragonal structure is slightly distorted. This tetragonal distortion results from the different bond lengths between Cu-Se and In/Ga-Se [25].

One remarkable property of CIGS is that it crystallizes in the chalcopyrite α-phase, i.e. the tetragonal structure depicted in Fig. 2.4B, for a wide range of off-stoichiometric compositions. Deviations from stoichiometry (i.e. ratio of Cu:In/Ga:Se = 1:1:2) are usually expressed by the copper to copper-III element ratio [Cu]/([Ga]+[In]) (CGI). While CIGS crystals grown under Cu-rich conditions (CGI > 1) exhibit a superior crystal quality, expressed e.g. through higher charge carrier mobilities and lifetimes, they make for a poor solar cell material [26]. In contrast, while CIGS crystals grown under Cu-poor conditions (CGI < 1) exhibit a slightly poorer crystal quality, they are currently the absorber of choice in CIGS based thin film solar cells with the highest efficiencies [9]. A detailed phase diagram of $CuInSe_2$ can be found in ref. [27].

Another important property of the CIGS solid solution is that the gallium and indium atom concentrations can be exchanged at will. Their share in the overall CIGS composition is usually expressed in the form of the [Ga]/([Ga]+[In]) (GGI) ratio. For a GGI of 0, the ternary $CuInSe_2$ is formed and for a GGI of 1, the ternary $GuGaSe_2$ is formed. Since the band gap energies E_g of $CuInSe_2$ and $CuGaSe_2$ are about 1.004 eV and 1.663 eV [28] respectively, CIGS can exhibit any band gap in between both ternaries, depending on the GGI ratio. This property is crucial for the energy conversion of the CIGS solar cell device as the band gap energy determines the portion of the solar spectrum that is absorbed and used (see section 2.4). Recently, Carron *et al.* [28] performed ellipsometry, reflectance and transmittance measurements on CIGS absorbers with varying CGI and GGI ratios and found the following empirical expression to describe the band gap energy evolution with GGI ratio

$$E_g = 1.004\,(1 - \mathrm{GGI})\,\mathrm{eV} + 1.663\,\mathrm{GGI}\,\mathrm{eV} - 0.033\,\mathrm{GGI}\,(1 - \mathrm{GGI})\,\mathrm{eV}. \tag{2.11}$$

It is worth mentioning that expression (2.11) is slightly different from similar empirical expressions in literature [30], [31], which themselves, are also slightly different from each other. The determination of expression (2.11) depends on the measurement techniques and the compositions of the samples used[1]. The increase in band gap energy with increasing gallium content

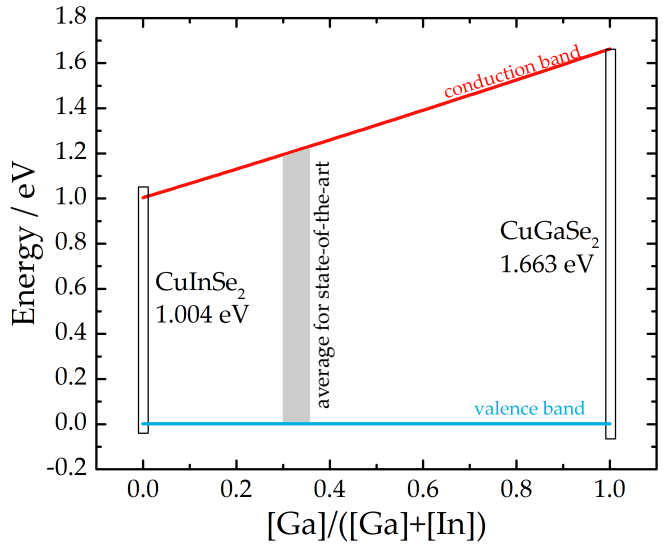

FIGURE 2.5: Evolution of conduction band minimum (CBM) and valence band maximum (VBM) with GGI ratio in CIGS. Also indicated are the band gap energies of the ternaries. The evolution of the VBM energy is approximately constant (within experimental error) [29]. The CBM energy is calculated based on the band gap energy from eq. (2.11). The grey tinted box represents the GGI range of highly efficiency CIGS solar cells.

[1]Some samples that are investigated in this thesis were grown under similar conditions as the samples used in the study of Carron *et al.* [28] which is why expression (2.11) is preferred to the expressions given in literature.

from $CuInSe_2$ to $CuGaSe_2$ is, in a first approximation, entirely due to an increase of the conduction band minimum [29]. The band gap energies of CIGS for varying GGI ratios are depicted in Fig. 2.5.

The exact content of gallium and indium has huge ramifications for the properties of the material which is why, for clarification purposes, the solid solution is often presented under the chemical formula $Cu(In_{x-1}Ga_x)Se_2$ where x denotes the GGI ratio. The best solar cell devices based on CIGS exhibit a CGI ratio of around 0.90-0.93 and a GGI of around 0.30-0.35[2] [12], [15]. Additionally, while silicon-based record efficiency devices are based on single crystal material, CIGS-based solar cells show higher efficiencies as polycrystalline material [9].

2.2.2 Intrinsic point defects

When growing crystals, even in the case of single crystalline material, the laws of thermodynamics dictate that the presence of impurities is unavoidable. This is especially true if the crystals consists of several elements, as is the case for CIGS. In semiconductor crystals, impurity or defect concentrations are largely responsible for their performance as they heavily influence properties such as conductivity and charge carrier mobility and lifetime [32]. More specifically, for example, shallow defects act as donor or acceptor states and thus regulate the doping of the crystal. In CIGS, these dopants are of intrinsic nature which means that the semiconductor is doped even without the addition of impurities. While defects may contribute in a benign way to the performance of the semiconducting crystals (as is usually the case for shallow defects) and thus constitute an indispensable part of the semiconductor architecture, they can also be malign. An example of malign defects are deep defects, i.e. impurities energetically positioned deep within the band gap, that induce non-radiative recombination of charge carriers which severely limits the optoelectronic properties of the semiconductor (see section 2.5).

In polycrystalline CIGS, the most prominent defects are grain boundaries and intrinsic point defects (dislocations can also appear in polycrystalline material but will not be considered

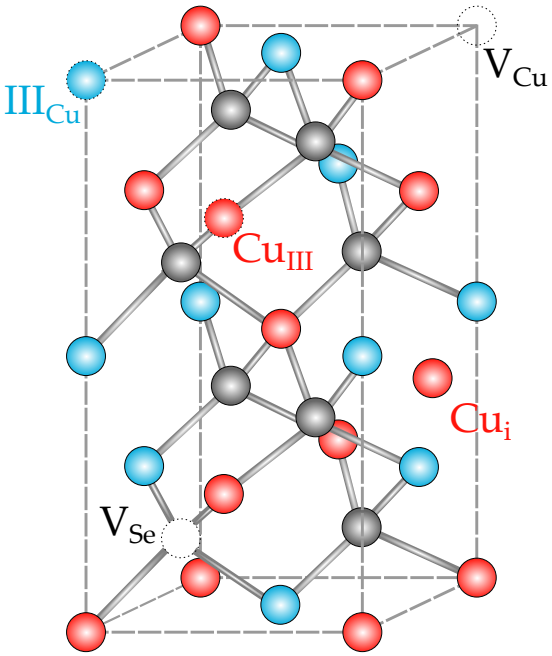

FIGURE 2.6: Cu(In,Ga)Se_2 unit cell with selected intrinsic point defects in contrast to the perfect unit cell shown in Fig. 2.4B. Intrinsic point defects can be categorized in three groups: vacancies (e.g. V_{Cu}, V_{Se}), interstitials (e.g. Cu_i) and antisites (e.g. III_{Cu}, Cu_{III}).

[2] As will be shown in section 2.6.2, the values given for the GGI are averaged over the whole thickness of the CIGS absorber. The state-of-the-art CIGS solar cells exhibit a considerable gallium gradient and thus the GGI varies with the depth of the absorber.

here). Grain boundaries are a natural product of polycrystalline material and may affect recombination of charge carriers as well as the electronic structure of the valence and conduction bands. Grain boundaries are briefly discussed in section 7.3.3. Due to its large tolerance towards off-stoichiometric composition, it is possible to form a large variety of different intrinsic point defects in CIGS. They can be placed in three different categories with some examples illustrated in Fig. 2.6. Atoms missing from their original lattice site lead to vacancy defects. As an example, if the CIGS semiconductor is grown under Cu-poor conditions, it is possible that some copper lattice sites are empty, thus creating copper vacancies V_{Cu}. In contrast, if a lot of copper atoms are present, they may sit in between lattice sites where usually no atom is positioned. These defects are called interstitials and an example would be the copper interstitial Cu_i. Finally, it could also be that some atoms displace other atoms from their original sites by taking their place in the crystal lattice. These defects are called antisites and an example would be the copper-on-element III antisite Cu_{III}.

The existence of point defects can be estimated from theoretical calculations and measured experimentally by various defect spectroscopy techniques. While an in-depth description of point defects in CIGS lies outside the scope of this thesis, a brief summary of the current knowledge is given below.

The theoretical calculations are usually based on density functional theory (DFT) which is a modelling method used to investigate many-body systems. While first calculations date back to the 1990s, nowadays DFT are combined with hybdrid functions (see also: HSE approach [33]) that are currently assumed to yield the most reliable results. Recent theoretical studies were mainly done on $CuInSe_2$ and can be found in refs. [34]–[40]. While these theoretical studies predict a certain amount of intrinsic point defects in $CuInSe_2$ (the number varies with the study), in the more complex $Cu(In,Ga)Se_2$, a slightly larger amount of point defects are theoretically possible [41].

Given the large amount of theoretical studies, their predicted results overlap surprisingly well. However, the point defects predicted by theory largely outnumber the defects seen in experiments. Recently, a considerable effort was undertaken by Spindler to carefully compare the results from the different theoretical studies with experimental photoluminescence data measured in an in-house setup and from literature. In the course of his doctoral studies [41], Spindler came up with a new defect model for the solid solution CIGS and its ternaries. To date, the model is extended to also include contributions from capacitance and transport measurements (e.g. Hall, admittance spectroscopy) and structural measurements (e.g. neutron and X-ray diffraction, positron annihilation). While the interested reader is referred to this extensive study [42], a simplified representation of the defect model is shown in Fig. 2.7 and described in the following.

The defect model predicts a shallow donor D1 in $CuInSe_2$ and $CuGaSe_2$ some 10 to 12 meV below the conduction band minimum (CBM). This donor induces a donor-acceptor-pair recombination process with the shallow acceptor A1 that has experimentally been observed in photoluminescence studies, even in CIGS [43]–[45]. The donor D1 is attributed to the copper interstitial Cu_i in $CuGaSe_2$ while it can possibly have two origins in $CuInSe_2$: the copper interstitial Cu_i under Cu-rich conditions and the In_{Cu} antisite under Cu-poor conditions. The shallow acceptor A1, 40 meV and 60 meV above the valence band maximum in $CuInSe_2$ and $CuGaSe_2$ respectively, is attributed to the copper vacancy V_{Cu} that is abundant under Cu-poor conditions.

The second shallow acceptor A2 is attributed to the Cu_{III} antisite and has experimentally been observed in both $CuInSe_2$ (60 meV above the VBM) and $CuGaSe_2$ (100 meV above the VBM) by photoluminescence under the form of a donor-acceptor-pair transition involving the

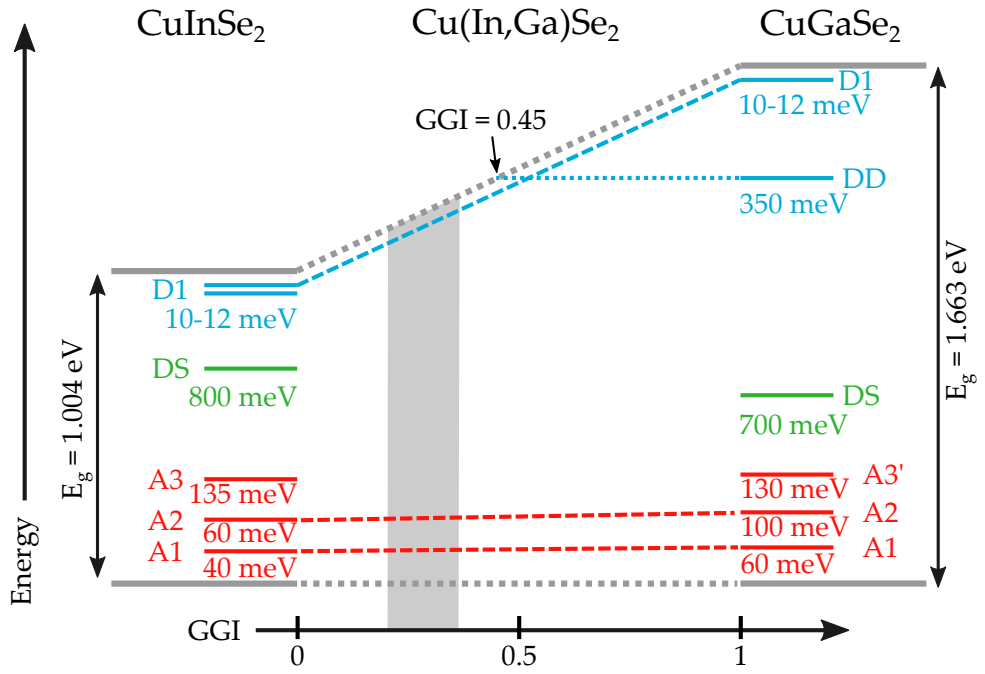

FIGURE 2.7: Simplified representation of the defect model of Cu(In,Ga)Se$_2$ and its ternaries CuInSe$_2$ and CuGaSe$_2$ as suggested by Spindler [41], [42]. The horizontal grey lines depict the valence and conduction bands of the ternaries. The model accounts for three shallow acceptors A1, A2, and A3/A3' and one shallow donor D1 in the ternaries. Additionally, the model also accounts for the possibility of a deep defect DS across the whole composition range and a deep donor DD in high gallium CIGS and pure CuGaSe$_2$. The dashed red and blue lines interpolate the experimentally confirmed presence of donor and acceptor defects into the CIGS solid solution. The grey tinted area delimits the GGI ratios that are relevant for high-efficiency CIGS based solar cells.

donor D1 [43]. Since the defect transition was observed in both ternaries, it was assumed that it would also be present in the solid solution. Recently, this has been confirmed by Babbe *et al.* [46].

A third acceptor could also be seen in the ternaries by experimental means. However, it seems as if the defect is of different origin in both materials. In CuGaSe$_2$, the A3' defect was first observed by spatially-resolved cathodoluminescence spectroscopy [47]. Later, the same defect transition was observed by spatially-resolved photoluminescence for a particular CuGaSe$_2$ composition [48]. In CuInSe$_2$, the third acceptor A3 was only observed recently and is still under investigation at the time of writing [46], [49]. However, in all cases, the third acceptor can only be seen in a few select samples with specific elemental compositions. It is thus likely that transitions involving this defect are never dominant.

Furthermore, a deep defect DS is predicted inside the band in both ternaries and is potentially attributed to the Cu$_{\text{III}}$ antisite in the (-1/-2) double-charged state [38]. In pure CuInSe$_2$ and low gallium CIGS, a defect transition could be observed in photoluminescence at about 800 meV above the VBM under Cu-rich conditions [41], [46] and very faintly under Cu-poor conditions [42]. Similarly, in pure CuGaSe$_2$ and high gallium CIGS, a defect transition in photoluminescence was observed at about 700 meV above the VBM in Cu-rich conditions only [41]. In literature, a comparable defect transition in photoluminescence in the Cu-poor solid solution CIGS was only ever found by Mansfield *et al.* [50]. However, there exist additional records of a possible deep transition in Cu-poor CIGS (for a wide variety of GGI ratios) but only when the transient photocapacitance measurement technique is involved, see e.g. [51]–[54]. Thus, while a deep defect is present in Cu-poor CIGS, its atomistic attribution is not yet fully clear and needs further investigation.

Finally, in high gallium CIGS and pure $CuGaSe_2$, a deep donor DD is predicted. This defect is attributed to the Ga_{Cu} antisite and was experimentally measured to be located 350 meV below the CBM [41], [55]. While it is assumed that this deep defect is one of the causes of the poor performance of $CuGaSe_2$ based solar cells, the deep defect becomes shallow for a GGI below 0.45 such that it resonates with the conduction band and becomes irrelevant for CIGS solar cells with low gallium content [41].

Summing up, according to the defect model, the defects that have been confirmed to be present in Cu-rich and Cu-poor CIGS, with average GGIs of around 30 %, are (see grey tinted area in Fig. 2.7):

- the copper interstitial Cu_i or In_{Cu} antisite as a shallow donor
- the copper vacancy V_{Cu} as a first shallow acceptor
- the Cu_{III} antisite as a second shallow acceptor
- and a deep defect approximately 0.8 eV above the valence band maximum.

The shallow impurities are assumed to be beneficial for the performance of CIGS as a solar cell as they define the doping concentration and the p-type nature of the absorber. The CIGS absorbers and solar cells investigated in this thesis are all of Cu-poor composition. Due to the copper deficiency, the defect model thus only deems the presence of the shallow In_{Cu} donor and V_{Cu} acceptor likely.

As deep defects limit the performance of CIGS solar cell devices (cf. section 2.5), they are undesired. The investigation of the presence of the deep defect from the defect model above in state-of-the-art CIGS absorbers is investigated through photoluminescence in this thesis (cf. section 6.1).

2.3 The Cu(In,Ga)Se_2 solar cell

The p-type Cu(In,Ga)Se_2 absorber alone does not constitute a solar cell. For photovoltaic applications, the separation and collection of excited charge carriers is necessary. Typically, this is done by forming a pn junction (i.e. through the addition of an n-type material) and the connection of electrical contacts to the device. In the following, the CIGS based solar cell along with selected device characterization methods are introduced.

2.3.1 Device structure

While, in its simplest form, a CIGS solar cell can be built from a pn junction and electrical contacts only, the real devices exhibit a more sophisticated material stack. Fig. 2.8A shows a typical thin film CIGS solar cell stack.

The starting block of the CIGS solar cell is the substrate. Soda-lime glass (SLG) is in most cases the substrate of choice as it is low-cost, has a similar thermal expansion coefficient as the CIGS absorber [25] and withstands temperatures around 550° C [56]. Additionally, SLG as a substrate improves the performance of the solar cell devices due to incorporation of sodium and potassium during the absorber growth [57]–[59]. Due to the thin nature of the CIGS absorber, it is also possible to build flexible solar cells. In the case of flexible solar cells, the rigid SLG is substituted by flexible polyimide foil. However, since polyimide foils cannot withstand as high temperatures as SLG, they are used in growth processes at lower temperatures [12], [60].

The electrode at the back of the solar cell (i.e. the back contact) is made of molybdenum and deposited onto the SLG by direct-current sputtering. Mo is a low-cost material with a low

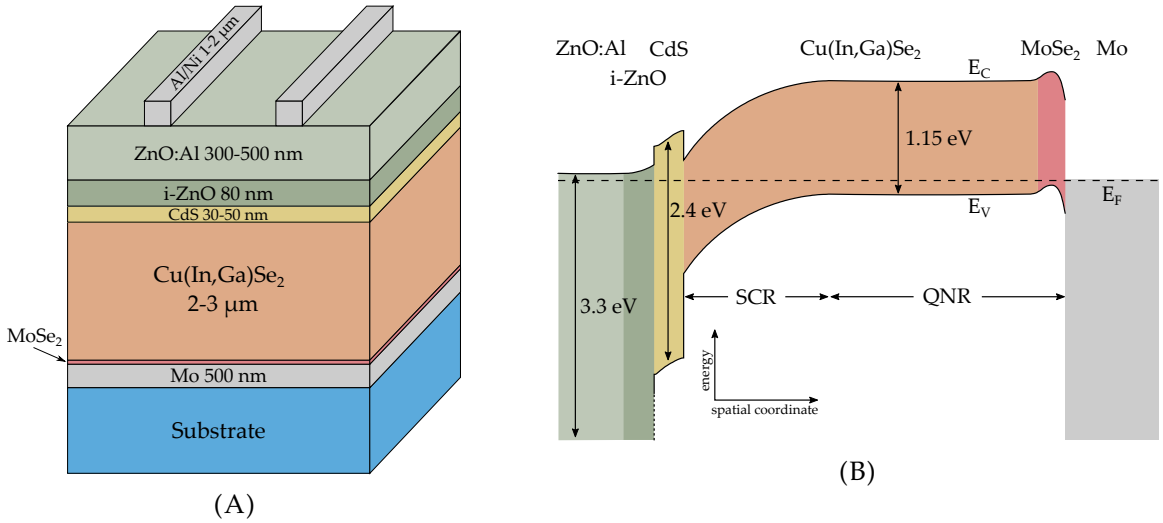

FIGURE 2.8: **(A)** Schematic representation of a typical thin film Cu(In,Ga)Se$_2$ based solar cell stack. While the layer thicknesses are also indicated, the scheme is not to scale. Adapted from [61]. **(B)** Energy band diagram corresponding to the solar cell stack in thermal equilibrium. Indicated are the Fermi level, the band gap energies of the different layers as well as the space-charge region and quasi-neutral region widths. Adapted from ref. [60].

sheet resistance [25], a high melting point and low diffusivity into the other parts of the cell stack [56]. During the deposition of the CIGS layer, a molybdenum diselenide layer is formed on top of the Mo [62], [63]. The very thin $MoSe_2$ layer has a slightly larger band gap energy than CIGS and thus ensures that the CIGS/$MoSe_2$/Mo back contact is of quasi-ohmic nature [64], [65].

The deposition of the Cu(In,Ga)Se$_2$ absorber layer can be done via various methods. The samples investigated in this thesis (cf. section 3.3) were prepared via thermal co-evaporation using elemental copper, indium, gallium and selenium sources under high vacuum. A description of this process can be found in ref. [25]. Other methods include deposition via sputtering, electro-deposition or printing. A summary of CIGS deposition methods and their technological status can be found in refs. [66], [67]. While the basic crystallographic properties of CIGS were mentioned in section 2.2, the more recent advances which led to the current state of the art are discussed in section 2.6.

After the growth of CIGS, a thin cadmium sulfide (CdS) buffer layer is deposited via chemical bath deposition (CBD). The CdS layer is usually n-type doped and has a band gap energy of 2.4 eV. This large band gap leads to a favourable band alignment at the CdS/CIGS interface which leads to reduced interface recombination [68], [69]. Additionally, the CdS layer protects the CIGS layer from air exposure[3], and prevents sputtering damage from the subsequent zinc oxide deposition. While CdS is still the material of choice for the buffer layer, it carries some disadvantages including its low band gap energy (leading to parasitic absorption of solar radiation) and its elemental toxicity. The optimization of alternative buffer layers is the subject of current research and very promising results have so far been achieved by using a zinc oxysulfide Zn(O,S) buffer layer [71]. A summary about current buffer layer research can be found in refs. [67], [72].

Since the sunlight needs to reach the CIGS layer to be absorbed, transparent conductive oxides are chosen as front contact and consist of two layers (usually called window layer). A thin intrinsic zinc oxide (i-ZnO) layer is deposited first onto the CdS buffer layer. This layer

[3] As the chemical bath deposition is done in air, the CIGS absorber is exposed to oxygen for short durations during the manufacturing process. Air exposure leads to the swift degradation of the CIGS surface. It has been shown that the CdS layer passivates the surface and prevents the oxidation of the surface [70].

is highly resistive and is used to passivate spots that are not covered up by the buffer layer and thus prevents current leakage [73]. The actual conductive contact, in the form of n-type aluminium doped zinc oxide (ZnO:Al), is deposited on top of the resistive layer. While the heavy doping ensures a high conductivity, it also leads to parasitic free carrier absorption in the visible and near-infrared radiation range [67]. Both constituents of the window layer are deposited via radio-frequency magnetron sputtering and exhibit a band gap energy of approximately 3.3 eV [74]. As is the case for the buffer layer, current research focusses on the search of alternative window layers. At the time of writing, the best CIGS based solar cells are fabricated either by substituting the first i-ZnO window layer by a zinc magnesium oxide (Zn,Mg)O layer [15], [71], or by substituting both i-ZnO and ZnO:Al layers by a single boron doped zinc oxide ZnO:B layer [16]. A summary about alternative window layers can be found in ref. [73].

The current collection from the solar cell is improved by depositing a supporting metallic grid structure consisting of aluminium and nickel on top of the window layers. Furthermore, to reduce reflection losses of the solar light from the surface, an anti-reflection coating (ARC) in the form of a magnesium fluoride layer (MgF_2, not shown in Fig. 2.8A) is deposited on top of the solar cell structure.

Due to the different materials used, the pn junction of a CIGS based solar cell is a heterojunction. The junction is formed between the p-type CIGS and both n-type ZnO:Al and CdS layers. The energy band diagram, along with the space-charge region and quasi-neutral region, is shown in Fig. 2.8B for the case of thermal equilibrium. Due to the low doping concentration N_A in CIGS compared to N_D of the doped window layer [56], as per eq. (2.8), the space-charge region almost fully extends into the CIGS absorber.

2.3.2 Working principle and device characterization

The working principle of the $Cu(In,Ga)Se_2$ solar cells is that photons from an irradiation source enter the structure through the window layer and are absorbed in the CIGS layer. The absorbed photons create electron-hole pairs that are separated by the electric field in the space-charge region. The electrons are swept to the window layer while the holes are swept into the quasi-neutral region of the absorber. By connecting the front contact and the back contact to a load, the electrons from the window layer pass through the load, expend their potential energy that they received following the absorption of the photon and subsequent elevation from the valence into the conduction band, and are re-emitted into the absorber from the back, ultimately recombining with the holes. The solar cell is thus based on the photoelectric effect where electrons absorb energy from photons and then transform this electrochemical energy into electrical energy.

While Fig. 2.8B shows the real band diagram of a CIGS based solar cell, the dependence of the electric current to an applied bias voltage is best explained in the case of an ideal pn homojunction such as in Fig. 2.2B.

In the absence of illumination, i.e. in the dark, the current density j_d that can be drawn from the diode is given by the Shockley equation (2.9). Under illumination, as described above for the case of CIGS, electrons and holes are created inside the absorber. If the electrons are created within a distance below or equal their diffusion length in the p-type CIGS, they can reach the SCR and flow from the p-type side to the n-type side. This leads to the creation of an additional photocurrent density j_{ph} flowing in the opposite direction of the diode current density j_d. The total current density is then

$$j = j_d - j_{ph} = j_0 \left[\exp\left(\frac{qV_a}{Ak_BT} \right) - 1 \right] - j_{ph}. \tag{2.12}$$

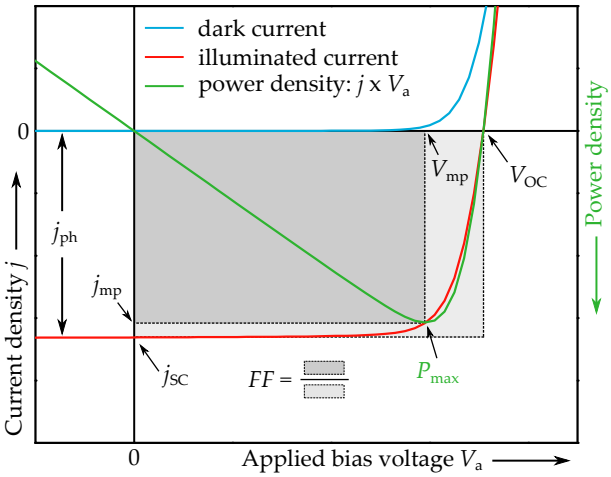

FIGURE 2.9: Current-voltage JV measurement curves of a solar cell in the dark (blue) and under illumination (red). The green curve represents the power density that can be drawn from the solar cell (right-hand side axis). Also indicated are the most important parameters for solar cell characterization.

Equation (2.12) describes the changes to the current density under a varying applied voltage bias in the dark ($j_{ph} = 0$) or under illumination ($j_{ph} \neq 0$) and is visually represented by the so-called current-voltage (JV) measurement curve in Fig. 2.9. Under illumination and under reverse bias, the current density across the pn junction is entirely described by the photocurrent density j_{ph}. Due to the illumination, the Fermi level is split inside the QNR and experiences, due to the potential difference at the junction, a strong gradient. When no external bias is applied (electrical contacts still connected but no load), the pn junction is short-circuited and the quasi-Fermi level gradient at the junction is maximal, leading to a maximal current density across the junction. The photocurrent density is then the so-called short-circuit current density j_{SC} which is an important parameter in solar cell characterization. Applying an increasing forward bias voltage to the pn junction leads a reduction of the potential barrier and thus to a reduced quasi-Fermi level gradient at the junction. Thus, a reduced photocurrent density flows across the junction and is extracted from the device. Increasing the forward bias voltage further leads to a situation where the potential barrier has been reduced to such an extent that the quasi-Fermi levels are flat. The quasi-Fermi level splitting is thus identical across the pn junction and no current density flows. The device is said to operate in open-circuit mode and the corresponding open-circuit voltage V_{OC} can be derived from eq. (2.12) by setting $j = 0$:

$$V_{OC} = \frac{Ak_BT}{q} \ln\left(\frac{j_{ph}}{j_0} + 1\right). \tag{2.13}$$

Similar to the short-circuit current density, the open-circuit voltage V_{OC} is an important characterization parameter for solar cells. Eq. (2.13) reveals that the V_{OC} depends on the saturation current density j_0 that was introduced in section 2.1.2. Increasing the applied bias voltage beyond the open-circuit voltage leads to an exponential increase of the diode current density j_d according to eq. (2.12), which then eventually dominates the current-voltage characteristics of the device. It is worth mentioning that in Fig. 2.9 the sign convention is such that the photocurrent density is assumed to be negative since it flows in the opposite direction to the dark diode current density. Usually, as in many textbooks (see e.g. [75]), the sign convention is inverted such that the photocurrent density is positive. In the following, the sign convention as represented in Fig. 2.9 is kept on being used.

The most crucial parameter for the solar cell performance is the power density that is generated by the device. The power density can be extracted by evaluating the product of the current density and voltage. As shown by the green curve in Fig. 2.9, the power density exhibits a maximum P_{max} (in absolute values) at the current density j_{mp} and voltage V_{mp} maximal power points. The maximal power point introduces another figure of merit, namely the fill

factor (FF). The fill factor is defined as

$$FF = \frac{j_{mp} V_{mp}}{j_{SC} V_{OC}}, \tag{2.14}$$

and is a measure of the "squareness" of the current-voltage curve. Closely linked to the output power density of the solar cell is the power conversion efficiency η. As its name suggests, the efficiency is the ratio between the power that can be drawn from the solar cell and the power that flows into the cell. In terms of the figures of merit that were introduced earlier, the efficiency can be written as

$$\eta = \frac{P_{max}}{P_{in}} = \frac{j_{mp} V_{mp}}{P_{in}} = \frac{FF\, j_{SC}\, V_{OC}}{P_{in}}. \tag{2.15}$$

Thus the solar cell power conversion efficiency depends on the fill factor FF, short-circuit current density j_{SC} and open-circuit voltage V_{OC} which are all parameters that can directly be evaluated by measuring a current-voltage curve. Eq. (2.15) also indicates that the efficiency depends on the illumination power which is why, in order to compare the efficiency between different solar cells, standard testing conditions have been established. The measurements of the current-voltage curves are typically done by using the so-called AM1.5 solar spectrum as incident illumination. This spectrum represents the solar spectrum incident onto the Earth under an angle of 48.2° between the Sun's position in the sky and the Earth's zenith. The AM1.5 spectrum carries a power density P_{in} of $1000\,W/m^2$. More details about the AM1.5 spectrum are provided in appendix A.1.

It is mandatory to mention that equation (2.12) describes the current density behaviour in an ideal solar cell (for $A = 1$). In reality, however, solar cells are never ideal and some loss parameters need to be introduced in the mathematical description. A more accurate description of real solar cells is provided by eq. (A.3) in appendix A.3.

In addition to current-voltage curves that provide the performance defining parameters, the quantum efficiency (QE) of the solar cell device can be measured to investigate optical and collection losses. The quantum efficiency describes the ratio between incident photons of varying energies and subsequent collected electrons. In the ideal case, every photon that is incident on the solar cell and has a larger energy than the band gap energy is absorbed by the CIGS and creates an electron-hole pair. Each pair is then successfully separated and the electrons are all collected by the contacts. This means that a perfect QE curve is a rectangular curve with value 1 for energies above the band gap of the CIGS and below the band gap of the buffer and window layers. In reality, however, the measured QE curves look considerably different as the photons are partially reflected and absorbed before reaching the CIGS absorber. In addition, from all the charge carriers that are created by the photons, not all are collected by the electrical contacts. An example of a measured external quantum efficiency (EQE - i.e. measured "outside" the cell) curve is shown in Fig. A.2 and a more in-depth description can be found in section A.2.

2.4 Fundamental losses in Cu(In,Ga)Se_2 solar cells

While the total irradiance of the AM1.5 spectrum amounts to $1000\,W/m^2$, it is not possible for the solar cell to convert all this power into energy. In fact, at most only one third of the total irradiance can be used in single-junction Cu(In,Ga)Se_2 based solar cells. This is due to some fundamental limiting mechanisms or losses.

The maximal power conversion efficiency of single-junction solar cells can be calculated using the Shockley-Queisser (SQ) model [76]. Originally proposed in 1961, the model is based on the following assumptions.

- The solar cell behaves like an ideal grey body with a step-like absorption i.e. only photons with energies that equal the solar cell band gap or above are absorbed.
- Each absorbed photon leads to the creation of exactly one electron-hole pair. Additionally, each excited charge carrier is collected by the electrical contacts.
- The performance of the solar cell is fundamentally limited by the principle of detailed balance.

The principle of detailed balance states that in steady state, a system that absorbs a certain photon flux density also emits the same photon flux density [77]. The principle of detailed balance is equivalent to Kirchhoff's law that states that a body in thermal equilibrium with its surrounding environment absorbs and emits thermal radiation at the same rate and spectral dependence [78]. When a solar cell is homogeneously illuminated by an additional irradiation source such as e.g. the sun, the principle of detailed balance also applies when the solar cell is operated under open circuit. In this case, the emitted photon flux density can be described by Planck's generalized law (cf. eq. (2.53) in section 2.7.3).

While Shockley and Queisser used the irradiation of a black body at a temperature of 6000 K in their model to calculate the maximal efficiency of single junction solar cells [76], the AM1.5 solar spectrum is used in recent calculations (see e.g. refs. [79], [80]). In the following, the key concepts of the model are introduced and explained.

The attractiveness of the Shockley-Queisser model is partly based on the relative simplicity of the assumptions mentioned above and partly on the fact that only one material-specific quantity, the band gap energy E_g, is needed as input parameter. The calculation of the maximal power conversion efficiency is based on eq. (2.15) and the total power density P_{in} from the AM1.5 spectrum (i.e. 1000 W/m^2 - see section A.1). As per the models assumption above, the short-circuit current density j_{SC}^{SQ} results from the collection of all absorbed photons from the solar irradiation only. Since the solar radiation is a spectral quantity, the short-circuit current density is calculated through integration:

$$j_{SC}^{SQ} = q \int_{E_g}^{\infty} \Phi_{sun}(E)\, dE, \tag{2.16}$$

where $\Phi_{sun}(E)$ is the AM1.5 spectrum expressed as a spectral photon flux density[4]. The open-circuit voltage in the SQ limit V_{OC}^{SQ} can be calculated by using eq. (2.13) i.e.

$$V_{OC}^{SQ} = \frac{k_B T}{q} \ln\left(\frac{j_{SC}^{SQ}}{j_0^{SQ}} + 1\right). \tag{2.17}$$

where $A = 1$, $j_{ph} = j_{SC}^{SQ}$, and the saturation current density in the SQ limit j_0^{SQ} are inserted. As was introduced in section 2.1.2, the latter describes a thermal generation current density inside the device. Following the principle of detailed balance, the thermal generation must eventually also lead to recombination. As such, j_0 can also be viewed as the consequence of the unavoidable radiative recombination that results from the thermal generation of electron-hole

[4]The AM1.5 solar spectrum in Fig. A.1 is displayed as spectral irradiance in units of $W\,m^{-2}\,nm^{-1}$. Transforming the spectral irradiance into energy space and dividing by the photon energy, one finds the spectral photon flux density $\Phi_{sun}(E)$ of the sun in units of photons $m^{-2}\,s^{-1}\,eV^{-1}$.

pairs. Assuming the solar cell to be a grey body with a temperature of 300 K, the recombination current density in the SQ limit, similarly to j_{SC}^{SQ}, can be calculated through

$$j_0^{SQ} = q \int_{E_g}^{\infty} \Phi_0(E, T = 300\,\mathrm{K})\,\mathrm{d}E, \tag{2.18}$$

where $\Phi_0(E, T)$ is the emitted thermal photon flux density given by Planck's law:

$$\Phi_0(E, T) = \frac{2E^2}{h^3c^2} \frac{1}{\exp\left(\frac{E}{k_B T}\right) - 1} \epsilon_{out}, \tag{2.19}$$

The thermal photon flux density Φ_0 is emitted into the solid angle $\mathrm{d}\Omega$ while obeying Lambert's cosine law. This angular dependence is represented as the so-called étendue

$$\mathrm{d}\epsilon_{out} = \cos\theta\,\mathrm{d}\Omega. \tag{2.20}$$

It is usually assumed that the back of the solar cell consists of a perfect reflector and thus the thermal radiation is only emitted into one hemisphere as depicted in Fig. 2.10A. Integrating the étendue over a single hemisphere leads to

$$\epsilon_{out} = \int_0^{2\pi} \mathrm{d}\varphi \int_0^{\pi/2} \cos\theta \sin\theta\,\mathrm{d}\theta = \pi \tag{2.21}$$

Thus, the saturation current density is

$$j_0^{SQ} = \frac{2\pi q}{h^3c^2} \int_{E_g}^{\infty} \frac{E^2}{\exp\left(\frac{E}{k_B T}\right) - 1} \mathrm{d}E. \tag{2.22}$$

Inserting the calculated j_{SC}^{SQ} and j_0^{SQ} into the Shockley equation (2.12) allows to calculate the current density j of the solar cell for varying applied voltages V_a. From these values, the solar cell power output can be calculated via $P_{out} = j \cdot V_a$. By computing the maximal power points j_{mp} and V_{mp} through

$$\frac{\mathrm{d}\,(j \cdot V_a)}{\mathrm{d}V_a} = 0, \tag{2.23}$$

the maximal power output $P_{max} = j_{mp} \cdot V_{mp}$ can be extracted. Inserting P_{max} and $P_{in} = 1000\,\mathrm{W/m^2}$ into eq. (2.15) then yields the maximal single-junction solar cell efficiency η^{SQ} in the Shockley-Queisser limit. Fig. 2.10B shows η^{SQ} for various band gap energies.

Incidentally, P_{max} also enables the calculation of the SQ fill factor FF^{SQ} via eq. (2.14). Alternatively, although not envisioned by Shockley and Queisser, the fill factor can also be calculated from the empirical expression [81]

$$FF^{SQ} = \frac{v_{OC} - \ln(v_{OC} + 0.72)}{v_{OC} + 1}, \tag{2.24}$$

where v_{OC} is the normalized voltage $qV_{OC}/k_B T$.

Fig. 2.10B shows that a single-junction solar cell with a band gap of 1.14 eV should be able to reach a power conversion efficiency of 33.5 %. The fact that only one third of the total incident irradiance can be used by the solar cell is due to three unavoidable limiting mechanisms and three intrinsic loss mechanisms. All six performance-reducing mechanisms are depicted in Fig. 2.11 showing a simplified situation of a solar cell under illumination. The greek letters label the unavoidable limiting mechanisms while the latin letters label the intrinsic loss

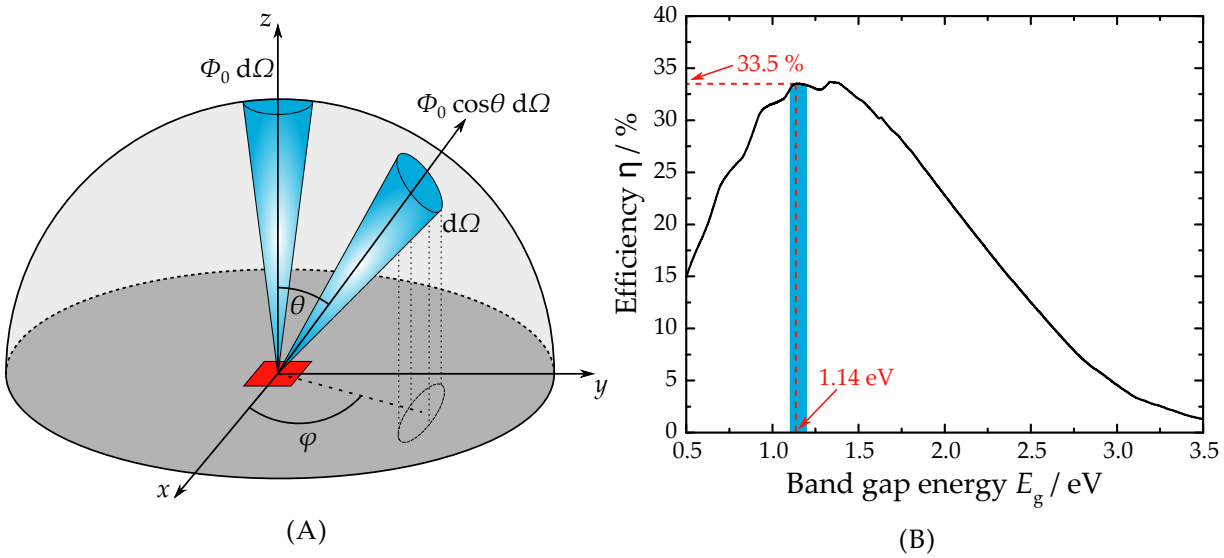

FIGURE 2.10: **(A)** As per Kirchhoff's law, the solar cell (depicted as red square) emits thermal radiation (blue cones) into its surrounding. The thermal photon current density Φ_0 is emitted into a solid angle $d\Omega$ and obeys Lambert's cosine law. Usually this angle dependence is expressed by the so-called étendue $d\epsilon = \cos\theta d\Omega$ where θ is the angle between the surface normal and the direction of Φ_0. The azimuthal angle is given as φ. **(B)** Power conversion efficiency η for single-junction solar cells plotted against band gap energy E_g in the SQ model. The blue bar represents the technologically relevant 1.1 - 1.2 eV band gap range for Cu(In,Ga)Se$_2$, within which the maximal efficiency reads 33.5 % for a band gap energy of 1.14 eV.

mechanisms.

The first unavoidable performance limit is the so-called Carnot loss [82]. In analogy to a Carnot engine, a solar cell can be seen as a heat engine at temperature T_{cell} and in contact with its thermal environment. The absorption of a photon from the sun, i.e. a hot reservoir at T_{sun}, leads to an exchange of entropy which then, due to the large difference in temperature, leads to a reduction in energy that cannot be converted to work by the solar cell [83]. The second limiting mechanism is due to the principle of detailed balance: the solar cell absorbs black body radiation both from the sun (at approx. 6000 K) and from the surrounding environment (at approx. 300 K). However, the emitted photon flux density from the solar cell is given by Planck's generalized law (cf. section 2.7.3). For both the absorbed and emitted photon flux densities to be equal, the photon flux density described by Planck's generalized law needs to carry less energy. The third limiting mechanism is the so-called fill factor loss. It is due to the fact that the solar cell is operated at the maximal power point voltage V_{mp} that, contrary to open-circuit or short-circuit conditions, represents an irreversible state where not all generated charge carriers are collected [84].

The first instrinsic loss is due to a mismatch of the incident ϵ_{in} and emitted ϵ_{out} light étendues and can also be seen as an exchange of entropy [85]. More specifically, the incident light from the sun is contained within a very narrow solid angle and thus can be thought of as having a small entropy. The emitted light, however, is emitted into the whole hemisphere and the involved entropy is considerably larger. The loss term related to this étendue mismatch is labelled as Boltzmann loss term [82]. The second loss term is due to thermalisation. If the absorbed photons carry an energy larger than the band gap energy, the charge carriers will be excited to higher energy states. Quickly thereafter, they will thermalise with the lattice, creating phonons, and thus occupy minimum energy states at the band edges. This excess kinetic energy that is used to create phonons is lost and cannot be used by the solar cell to create electrical work. Finally, the third and last loss process is due to non-absorption of photons with

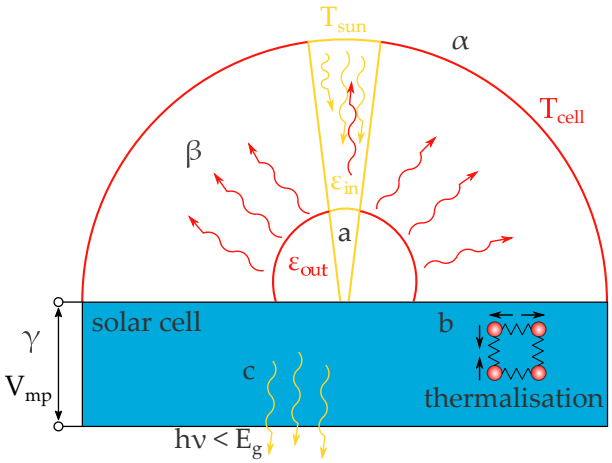

FIGURE 2.11: Simplified depiction of fundamental limitations and losses in a solar cell under illumination. The different performance-limiting mechanisms are indicated by letters and are as follows: α**)** Carnot loss, β**)** detailed balance, γ**)** fill factor loss, **a)** Boltzmann loss, **b)** thermalization loss, **c)** non-absorption loss.

energies lower than the band gap energy. These non-absorbed photons are either transmitted through the back of the solar cell (depicted in Fig. 2.11) or, in the case of a perfect back reflector, reflected and transmitted through the surface.

While it is not possible to avoid the fundamental limiting mechanisms labelled by the greek letters in Fig. 2.11, the remaining three loss mechanisms can be mitigated. The Boltzmann loss can be avoided by either using concentration lenses to increase the incidence angle (see e.g. [86]) or by creating an appropriate solar cell surface architecture such that the emission angle equals the absorption angle (see e.g. [87]). The loss due to non-absorption and thermalisation can be mitigated by using a combination of multijunction (see e.g. [88], [89]) and hot carrier solar cells (see e.g. [90], [91]).

2.5 Recombination losses in Cu(In,Ga)Se_2 solar cells

While the power conversion efficiency given by the Shockley-Queisser model represents the upper limit for the case of an ideal single-junction solar cell, the real measured efficiencies lie considerably below even the 30 % efficiency mark. Only GaAs based solar cells have been able to come relatively close with their current record efficiency of 28.8 % [9]. At the time of writing, the record efficiency for CIGS is at 23.35 % [8], some 10 % absolute lower than the theoretical limit. While the preceding section introduced the general fundamental limits to solar cells, this section will introduce performance-limiting recombination losses that mainly affect the open-circuit voltage V_{OC} and fill factor FF. There exist also other performance-limiting losses such as optical and collection losses mainly affecting the short-circuit current density j_{SC} and series as well as shunt resistance losses mainly affecting FF. Since this thesis focusses on recombination losses, the optical and collection as well as resistance losses are not discussed here but are briefly introduced in appendices A.2 and A.3 respectively.

As mentioned in section 2.4, in the ideal solar cell device the only recombination mechanism is occurring through radiative recombination where excited charge carriers recombine and emit photons. In real solar cell devices, however, additional recombination mechanisms can take place, such as non-radiative recombination and Auger recombination. The latter is a recombination mechanism where charge carriers, upon recombination, do not emit photons but transfer their energy to a third carrier which then expends this energy in a series of collisions with the crystal lattice. As such, Auger recombination is strongly dependent on the doping concentration of the solar cell. Auger recombination is said to play no role in CIGS based solar cells with

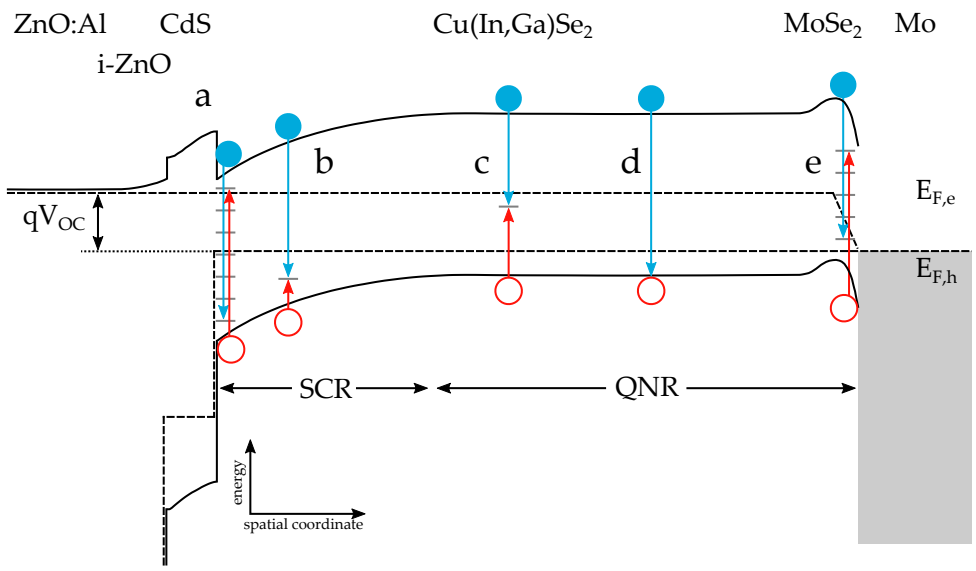

FIGURE 2.12: Schematic energy band diagram of a CIGS solar cell under illumination and operated under open-circuit conditions. Illustrated are the different recombination regions where electrons (blue full circles) can recombine with holes (red hollow circles): **a)** interface recombination, **b)** SCR recombination, **c)** deep-level defect recombination, **d)** radiative recombination **e)** back interface recombination. Defect states are represented by short grey horizontal bars. Due to the solar cell being operated under open-circuit conditions, the band bending at the CdS/CIGS interface is reduced (cf. 2.8B). Adapted from refs. [41], [49].

doping concentrations of less than 10^{17} cm^{-3} [56]. Similar to Auger recombination, during non-radiative recombination, the recombining charge carriers also do not emit photons but expend their energy through the creation of phonons.

Thus, in CIGS based solar cells, the recombination mechanisms are either of radiative or of non-radiative nature. While radiative recombination takes place almost exclusively in the quasi-neutral region of the absorber, non-radiative recombination is likely to take place either where both types of charge carriers are present in similar concentrations alongside defects (such as e.g. in the space-charge region) or where there are deep-level defect states. The different regions of recombination are schematically shown in Fig. 2.12 for the case of an illuminated CIGS solar cell and will briefly be described in the following. For a more detailed description about all recombination process, the interested reader is guided towards ref. [56].

2.5.1 Radiative recombination

The radiative recombination as depicted in Fig. 2.12 **d)** is the unavoidable recombination between electrons in the conduction band and holes in the valence band that follows from the principle of detailed balance. The radiative recombination rate R_{rad}, expressed in units of cm^{-3} s^{-1}, is proportional to the charge carrier densities that are present in the bands. In equilibrium, the radiative recombination rate R^0_{rad} is given by

$$R^0_{\mathrm{rad}} = B n_0 p_0 = B n_{\mathrm{i}}^2, \tag{2.25}$$

where B is a material specific radiative recombination coefficient [92]. During illumination, the radiative recombination rate is governed by the total charge carrier densities $n = \Delta n + n_0$ and $p = \Delta p + p_0$, where Δn and Δp are the newly excited charge carrier densities. The net radiative recombination rate R_{rad} is then

$$R_{\mathrm{rad}} = B\left(np - n_0 p_0\right) = B n_{\mathrm{i}}^2 \left[\exp\left(\Delta\mu / k_{\mathrm{B}} T\right) - 1\right], \tag{2.26}$$

where the latter equality is reached by considering eq. (2.7). In the case of low carrier injection (e.g. during standard solar cell operation) and p-type CIGS, the relations between the charge carrier densities are such that $p \approx p_0$ and $p_0 \gg n_0$. As a result, the net radiative recombination rate

$$R_{\text{rad}} = Bp_0\Delta n = \frac{\Delta n}{\tau_{\text{rad}}} \tag{2.27}$$

is mostly dictated by the density of the minority charge carriers. The so-called lifetime $\tau_{\text{rad}} = 1/Bp_0$ is of utmost importance in solar cells because it dictates how long the carriers remain inside the bands before recombining and thus indicates how long they can take to reach the electrical contacts. Using a p-type acceptor concentration of $N_{\text{A}} = p_0 = 3 \cdot 10^{15}\,\text{cm}^{-3}$ and a radiative recombination coefficient of $B = 1.28 \cdot 10^{-10}\,\text{cm}^3\ \text{s}^{-1}$, CIGS can have a radiative lifetime of $\tau_{\text{rad}} = 2.6\,\mu\text{s}$ [93]. The lifetimes that are measured in real CIGS devices, however, usually lie between several nanoseconds and around 250-300 ns (see e.g. [94]–[97]), i.e. shorter than the microsecond regime. This is due to the fact that the lifetime in real devices is not only dictated by radiative recombination, but also by non-radiative recombination that takes place at a quicker rate.

Here it needs to be reiterated that radiative recombination, if originating from the band-to-band recombination process depicted in Fig. 2.12 **d)**, is *a priori* not harmful for the performance of the solar cell. There are, however, two instances where it can be detrimental. The first instance is the case where photon out-coupling is not ideal i.e. when the photons that are generated following the radiative recombination are not emitted from the solar cell. This issue is discussed in more detail in section 7.3.4 and appendix F.5. The second instance is when the charge carrier collection of the device is poor i.e. when the charge carriers have too low mobilities such that they cannot reach their respective electrical contacts within the radiative lifetime.

Finally, radiative recombination through states below the band edges is also detrimental for the performance of the solar cell, as briefly described in the section 2.5.3 below. Recombination processes through these so-called band tails is an important topic of this thesis and is treated in chapters 5 and 7.

2.5.2 Non-radiative recombination

Non-radiative recombination can occur when electrons and holes recombine over defect states within the band gap [98], [99] (Fig. 2.12 **b)** and **c)**). Additionally, non-radiative recombination can also occur when a multitude of defects states are involved, as is usually the case at the surface of the absorber or at the back contact (Fig. 2.12 **a)** and **e)**). In any case, the net recombination rate R_{RSH} involving a specific trap state can be described by the so-called Shockley-Read-Hall (SRH) equation [100]

$$R_{\text{SRH}} = \frac{np - n_0p_0}{\gamma_{\text{p}}(n + n^*) + \gamma_{\text{n}}(p + p^*)}. \tag{2.28}$$

The quantities n^* and p^* are auxiliary carrier densities that describe their emission from the defect state [56]. The quantities γ_{p} and γ_{n} are place holders and their expression varies depending on the exact region of recombination. The SRH recombination equation declares that both an electron and hole need to be captured by the defect state for non-radiative recombination to occur. In the case of deep-level defect state at an energy E_{T} in the absorber bulk, the auxiliary carrier densities take on the form

$$n^* = N_{\text{C}}\ \exp\left(\frac{E_{\text{T}} - E_{\text{C}}}{k_{\text{B}}T}\right), \qquad p^* = N_{\text{V}}\ \exp\left(\frac{E_{\text{V}} - E_{\text{T}}}{k_{\text{B}}T}\right). \tag{2.29}$$

The auxiliary charge carrier densities follow the principle of detailed balance stating that capture and emission of charge carriers in the defect states must self-balance in thermal equilibrium or steady-state. With the effective density of states of the bands N_C and N_V being proportional to $T^{3/2}$ [18], the following relation can be established

$$n^* \propto T^{3/2} \exp\left(\frac{E_T - E_C}{k_B T}\right), \qquad p^* \propto T^{3/2} \exp\left(\frac{E_V - E_T}{k_B T}\right), \tag{2.30}$$

where the numerator of the exponent can be seen as activation energy. The expressions (2.30) show that the charge carrier emission process from trap states increases exponentially the closer the trap states are to the band edges. This explains why shallow defect states, through a rapid emission and capture of charge carriers from the bands, are significantly less likely to act as non-radiative recombination centers than deep-level defect states.

Eq. (2.28) can be used to extract the charge carrier lifetime that is linked to non-radiative recombination events. In the case of a p-type doped semiconductor with trap states in the middle of the band gap and under low carrier injection, the equilibrium hole carrier density p_0 dominates and eq. (2.28) is simplified to

$$R_{SRH} = \frac{\Delta n}{\gamma_n} \tag{2.31}$$

which is an expression that is similar to the net radiative recombination rate (2.27). If the recombination is taking place within the bulk of the semiconductor (Fig. 2.12 **c)**), the quantity γ_n can be identified as the minimum minority charge carrier lifetime τ_n

$$\gamma_n = \tau_n = \frac{1}{\sigma_n v_{th} N_T}, \tag{2.32}$$

where σ_n is the recombination cross section, v_{th} the electron thermal velocity and N_T the trap density. For a capture cross section of $\sigma_n = 10^{-12}\,\mathrm{cm}^2$, a thermal velocity of $v_{th} = 10^7\,\mathrm{cm/s}$ and a defect density of $N_T = 10^{13}\,\mathrm{cm}^{-3}$, eq. (2.32) yields a lifetime of 10^{-8} s [56] which is two orders of magnitude lower than the radiative lifetime estimated in the preceding section.

At the interfaces, a multitude of defect states are introduced mainly due to discontinuities of the crystal structure (Fig. 2.12 **a)** and **e)**). Recombination via those defect states is usually also taking place within a non-radiative recombination channel and, as such, their recombination rate can be described by eq. (2.28). In this case, the place holder quantities γ_n and γ_p can be expressed as the inverse interface recombination velocities S_n^{-1} and S_p^{-1} respectively. In the case of a p-type doped semiconductor, the interface recombination velocity $S_n = \sigma_n v_n N_{IF}$ of the minority charge carriers is defined by the interface defect density N_{IF} [56]. The recombination rate at the interface at low excitation is then given as

$$R_{SRH,IF} = S_n \Delta n. \tag{2.33}$$

Structural defects such as grain boundaries (GBs) in polycrystalline material can also act as defects and thus constitute potential non-radiative recombination centers. The recombination rate over GBs is then also described by the SRH recombination rate and an expression can be found in [101]. Structural defects are briefly discussed in section 7.3.3.

The total charge carrier lifetime, also called effective lifetime τ_{eff} can be estimated by considering the various recombination channels i:

$$\frac{1}{\tau_{\text{eff}}} = \sum_i \frac{1}{\tau_i} = \frac{1}{\tau_{\text{rad}}} + \frac{1}{\tau_{\text{SRH}}}. \tag{2.34}$$

Equation (2.34) represents a general expression, splitting the contribution to the effective lifetime τ_{eff} into a radiative part τ_{rad} and a non-radiative part τ_{SRH}. Furthermore, the non-radiative lifetime can be split into more, underlying, contributions such as a non-radiative recombination rate stemming from point defects deep within the band gap, or grain boundaries, or defects at the interfaces. Eq. (2.34) also clearly shows that the effective lifetime of the minority charge carriers is limited by the recombination mechanisms with the highest recombination rate. For a good solar cell performance, it is thus key to increase the lifetimes of the limiting recombination processes.

2.5.3 Influence of recombination on V_{OC}

In section 2.3.2, the expression for the open-circuit voltage V_{OC} was introduced, featuring the diode ideality factor A:

$$V_{\text{OC}} = \frac{Ak_{\text{B}}T}{q} \ln\left(\frac{j_{\text{ph}}}{j_0} + 1\right). \tag{2.35}$$

For $A = 1$, the expression for an ideal solar cell is attained (this assumption was used in the Shockley-Queisser model in section 2.4) while a more realistic device exhibits $A > 1$. The ideality factor A can be seen as a measure of recombination. It can be shown that for radiative band-to-band recombination only, $A = 1$, while for recombination via deep defects in the space-charge region, $A = 2$ [80]. Moreover, the saturation current density j_0 can in general be expressed as the result of a temperature-activated process via

$$j_0 = j_{00} \exp\left(\frac{-E_{\text{A}}}{Ak_{\text{B}}T}\right) \tag{2.36}$$

where E_{A} is the activation energy of the process. As such, the expression for the open-circuit voltage can be rewritten as

$$V_{\text{OC}} \approx \frac{E_{\text{A}}}{q} + \frac{Ak_{\text{B}}T}{q} \ln\left(\frac{j_{\text{ph}}}{j_{00}}\right). \tag{2.37}$$

Each non-radiative recombination mechanism leads to the formation of a recombination current density that is characterised by its own saturation current density j_0 and hence activation energy E_{A} [102]. As such, it is possible to identify the dominating recombination mechanism by determining either the ideality factor A or the activation energy E_{A}. The latter quantity is experimentally accessible through temperature-dependent current-voltage measurements. Eq. (2.37) shows that a plot of V_{OC} versus temperature T fitted with a linear function reveals E_{A} as y-axis intercept. It can be shown that if the activation energy is identical to the band gap energy, $E_{\text{A}} = E_{\text{g}}$, the dominating recombination mechanism is occurring within the bulk. If, however, $E_{\text{A}} < E_{\text{g}}$, the dominating recombination mechanism can be found at an interface [103], [104].

Ultimately, any non-radiative recombination mechanism leads to an increase of the saturation current density j_0 and consequently, as is suggested by eq. (2.35), leads to a decrease of V_{OC}. As the fill factor (FF) is dependent on the open-circuit voltage, as expressed in eq. (2.24), a decrease in V_{OC} also negatively affects the FF.

Finally, one last thing needs to be mentioned. So far radiative recombination has been introduced as a non-avoidable transition that does not affect the performance of solar cells in a negative way. This is only the case if the recombination stems from the band-to-band transition and the emitted photons carry an energy that is very close to the band gap energy E_g of the absorber. If the photons, however, carry an energy that is lower than E_g due to a transition involving sub band gap states e.g., the saturation current density j_0 is increased according to eq. (2.22) and thus the V_{OC} is reduced [105], [106]. In CIGS based solar cells, sub band gap states are said to be introduced mainly through band gap fluctuations and electrostatic potential fluctuations [80], both of which are a direct result of alloy disorder and absorber inhomogeneity. Thus, even if only radiative recombination is occurring within the solar cell, a reduction of the effective band gap energy leads to a decrease of the solar cell performance[5]. A more in-depth description of absorber homogeneity is given in section 5.4 and electrostatic potential fluctuations are treated in sections 2.7.4 and 6.2. Radiative recombination through sub band gap states is discussed in detail in sections 5.3 and 7.1.1.

2.6 Cu(In,Ga)Se_2 solar cells: recent advances

This section introduces the state of the art of Cu(In,Ga)Se_2 solar cells. The section starts with a brief introduction and history about CIGS, based mainly on ref. [56], before listing the three most prominent and highest performing CIGS devices. Afterwards two crucial milestones, which are also topic of this thesis and allowed for the state of the art, are introduced.

2.6.1 A brief history of Cu(In,Ga)Se_2 solar cells

The history of I-III-IV_2 solar cells effectively starts in the 1970s with the production of a $CuInSe_2$ solar cell without Ga in the Bell laboratories [107], kicking off the research and development of chalcopyrite solar cells. In the early 1980s, the first milestone was achieved by improving the deposition process via evaporation and finding out that Cu-poor $CuInSe_2$ solar cells performed better than their Cu-rich counterparts. At the end of the 1980s, the chemical bath deposition of a thin CdS layer was introduced and the growth process was improved further. Both these discoveries are considered to be the second milestone in the history of CIGS solar cells. In the early 1990s, as a third milestone, two effects were discovered. These effects are of utmost importance as they effectively form the pillars upon which the high efficiency of nowadays' CIGS solar cells are built.

The first effect was the introduction of Ga into the absorber, creating thus the Cu(In,Ga)Se_2 solid solution solar cell. It was found that Ga leads to an increased band gap energy (see section 2.2.1) and the idea was thus to increase the open-circuit voltage by using an absorber with a larger E_g. The incorporation of Ga was perpetuated by introducing a complicated three-stage co-evaporation process which led to a CIGS absorber with a varying gallium profile and thus a graded band gap [108]. Adjusting and improving the Ga gradient inside the absorber yielded a CIGS record efficiency of 18.7 % on flexible substrates [60] as well as 20.3 % on rigid substrates [13] in 2011.

The second effect that was discovered was that CIGS solar cells grown on sodium-containing glass substrates (such as soda-lime glass) in general showed an improved efficiency. It was found that the sodium (Na) from the substrate diffuses into the absorber during growth at high

[5]Radiative recombination from sub band gap states is not considered in the Shockley-Queisser model which only considers radiative band-to-band recombination processes. This is why, even if the recombination from sub band gap states is of radiative nature, it is still non-ideal.

temperatures, leading to a higher electrical performance [57]. While the exact role of the Na atoms is not yet clear, their effect on the performance of the CIGS solar cell has been recognised and various explanations, listed in the upcoming section 2.6.3, have been proposed. When using a sodium-free substrate, such as flexible polyimide foil, the benefits from a Na incorporation are absent which is why, in 2004, the so-called post-deposition treatment (PDT) was introduced [14]. The PDT consists of an additional step directly after the growth of the absorber where a specific alkali fluoride compound, such as NaF, is deposited onto the surface of the absorber. As such, even without an alkali-containing substrate or during growth at lower temperatures, it is possible to incorporate the alkali atoms into the absorber. After the introduction of the NaF PDT, experiments with heavier alkalis were conducted. As a result, a sequential PDT with both sodium fluoride NaF and potassium fluoride KF in CIGS led to a 20.4 % efficiency on flexible polyimide foil [12] and a solitary KF PDT led to a 21.7 % efficiency on the rigid soda-lime glass substrate [109]. Using even heavier alkali metals, such as rubidium, allowed the creation of CIGS solar cells with efficiencies of 22.6 % [15] and, most recently, of the world record CIGS device with 23.35 % efficiency [8].

The three most prominent CIGS solar cells are thus the following:

- Empa's[6] 20.4 % efficient device grown at low temperatures (i.e. below 500° C) on flexible polyimide foil and treated with a sequential NaF + KF PDT. The solar cells are finished after the deposition of a CdS buffer layer and i-ZnO/ZnO:Al window layers [12], [60].
- ZSW's[7] 22.6 % efficient device grown at high temperature (i.e. above 500° C) on rigid soda-lime glass and treated with a RbF PDT. The solar cells are finished after the deposition of a buffer layer in the form of CdS followed by a resistive window layer (Zn,Mg)O, and finally a doped window layer of ZnO:Al [15], [71].
- Solar Frontier's[8] to-date record 23.35 % efficient device [8]. The details about this specific device are unknown at the time of writing. It is only disclosed that the device does not contain any cadmium. Slightly lower-performing devices made by Solar Frontier are characterized in ref. [16]. These devices are special also because they also contain sulphur i.e. the absorber is actually the compound $Cu(In,Ga)(S,Se)_2$.

The introduction of both the graded band gap and of the post-deposition treatment represent two very important milestones in the history of CIGS but their ramifications are not yet fully understood. It is thus worth to have a closer look at these specific processes.

2.6.2 The double gallium gradient

The double gallium gradient, a standard feature in nowadays' state-of-the-art CIGS solar cells, is characterised by an elevated Ga concentration towards the front and towards the back of the absorber. In between both gradients, a Ga minimum or so-called notch can be found. Fig. 2.13, showing the GGI ratio versus absorber depth on the left-hand y-axis, illustrates a typical double Ga gradient profile. In this particular example, the Ga content at the surface of the CIGS absorber is of 42 % while it is as high as 47 % towards the back of the absorber. The Ga notch is located at 0.3-0.4 μm inside the absorber and exhibits a Ga content of 23 % i.e. considerably lower than towards the surface or back. The right-hand y-axis of Fig. 2.13 shows the resulting band gap energy calculated from the GGI ratio according to eq. (2.11). The increased band gap energy towards the back of the absorber reduces the number of electrons that diffuse towards

[6] Swiss Federal Laboratories for Materials Science and Technology, Dübendorf, Switzerland.
[7] Center for Solar Energy and Hydrogen Research Baden-Württemberg, Stuttgart, Germany.
[8] Solar Frontier, Tokyo, Japan.

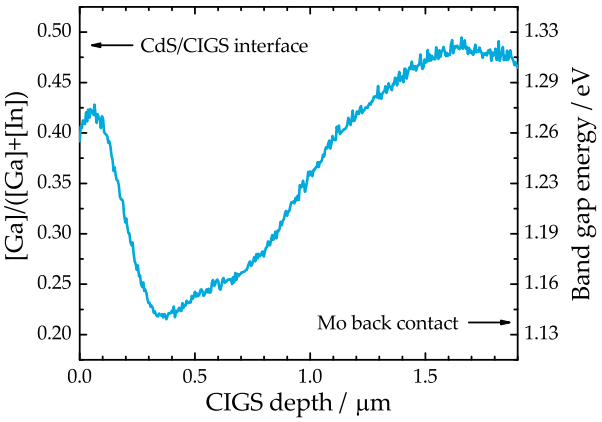

FIGURE 2.13: Example of a double Ga gradient in the form of a graph showing the GGI ratio versus CIGS absorber depth. The band gap energy is calculated from the GGI ratio according to eq. (2.11). The GGI ratio is determined from secondary ion mass spectrometry and is explained in detailed in appendix B.2.

the back contact and recombine at the CIGS/$MoSe_2$/Mo interface [56], [110]. Consequently, as the recombination of electrons is reduced, more electrons can be collected by the contacts, increasing thus the charge carrier collection [111]. Similar to the back contact passivation, the increased band gap towards the front of the CIGS absorber leads to a reduction of charge carrier recombination at the CdS/CIGS interface [112]. Thus, the effects of the double gallium gradient are threefold: an increase in V_{OC} and FF due to back contact and CdS/CIGS interface passivation and an increase in j_{SC} due to an improved charge carrier collection.

It is worth mentioning that a double gallium gradient can potentially also be harmful for the solar cell performance. The steepness of the band gap grading plays an important role; e.g. a too steep front grading may hinder carrier extraction towards the window layer such that non-radiative recombination in the SCR is increased and V_{OC} decreased [60]. Similarly, the position of the band gap notch inside the absorber is crucial [113]. If the band gap notch is too close to the CdS/CIGS interface, recombination is increased. If the band gap notch is too deep inside the absorber, the charge carrier collection is reduced. As a addendum of this brief description, an extensive study about various gallium gradients in CIGS can be found in refs. [71], [113].

2.6.3 The alkali post-deposition treatment

While it was possible to reach power conversion efficiencies of around 20 % with the double graded band gap, the strong efficiency increase in recent years is entirely due to the implementation and optimization of the alkali post-deposition treatment. Figure 2.14 shows a schematic drawing of the PDT procedure as applied in the case of a CIGS absorber. As already mentioned in section 2.6.1, the PDT was developed with the idea to provide the CIGS absorber with the beneficial Na alkali metal even if the absorber is grown on an alkali-free substrate or at low temperatures[9]. In the case of a CIGS absorber growth process on soda-lime glass at high-temperatures, Na naturally diffuses from the glass into the absorber [57] rendering the NaF PDT obsolete (bottom part of Fig. 2.14). Thus, at high-temperature growth, only a solitary alkali fluoride PDT is done. In the case of low-temperature growth or an alkali-free substrate, a sequential PDT is done where NaF is first deposited on the surface of the absorber after the absorber growth (top part of Fig. 2.14). After the first PDT, a second PDT is done where usually a heavier alkali metal such as potassium (K), rubidium (Rb), or caesium (Cs) is used. While the benefits from the alkali PDT are undeniable, it is not yet fully understood how the alkali atoms interact with the CIGS absorber and its adjacent layers. Since the discovery of the beneficial effects of alkali elements on the performance of CIGS solar cells, a huge amount of studies were conducted with some providing conflicting results. In the following, a very broad and

[9] At low temperatures, the Na diffusion from a sodium-containing substrate is reduced compared to growth processes at higher temperatures [115].

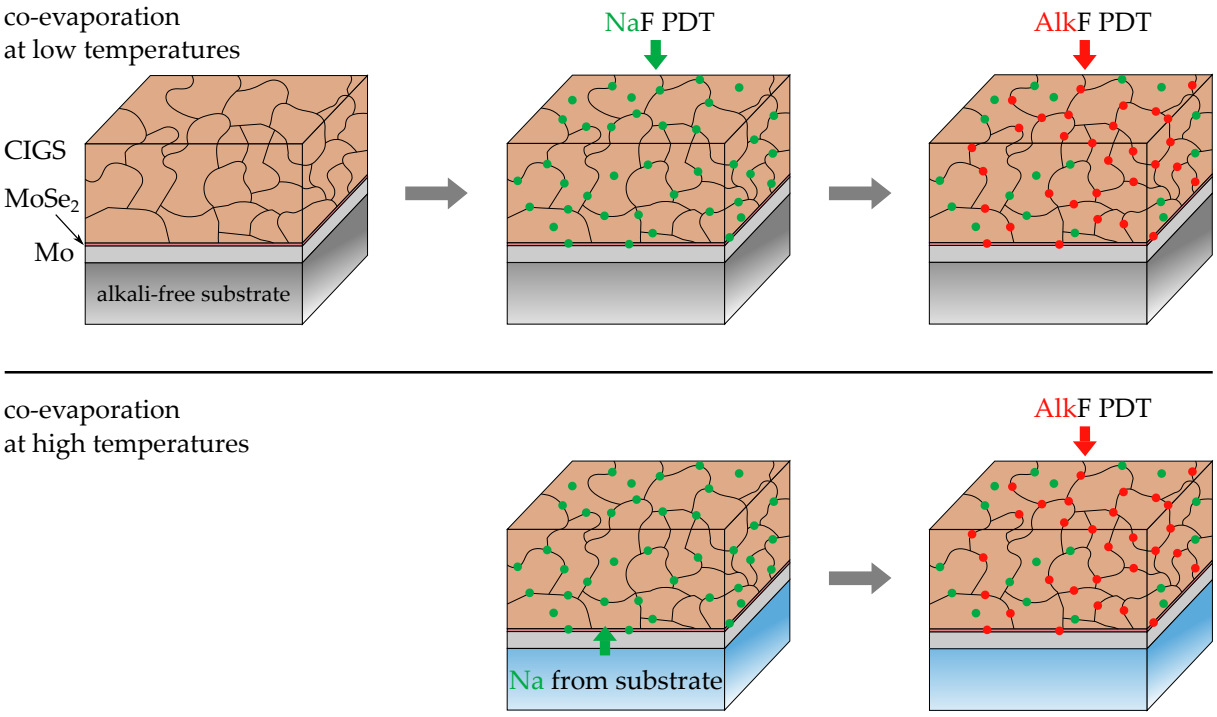

FIGURE 2.14: Schematic drawing of the post-deposition treatment procedure. The top part shows the PDT process done at low temperatures on an alkali-free substrate. Directly after the co-evaporation growth of the polycrystalline CIGS absorber, a first PDT is done where NaF is deposited onto the surface of the absorber. Afterwards, a second PDT is done where another alkali fluoride (AlkF) is deposited onto the surface of the absorber. Usually a heavier alkali metal, such as K, Rb, or Cs, is chosen. Details about the low-temperature process can be found in ref. [12]. The bottom part shows the PDT process at high-temperatures on a standard Na-containing soda-lime glass. Since the Na is diffusing into the absorber during growth, the NaF PDT is obsolete. In this case, only a solitary AlkF PDT is done after absorber growth. More details can be found in ref. [15]. Figure adapted from ref. [114].

general summary of theoretical and experimental results from literature for the different PDTs is given. The summary starts with NaF before treating the KF PDT and finishing with the most recent results about the RbF PDT. It needs to be mentioned that the summary does not claim a complete listing of all effects that have ever been reported.

Numerous atom probe tomography studies have found that, after diffusion into the absorber from either the substrate or after a PDT, Na mainly segregates at the grain boundaries where it exhibits larger concentrations than inside the grains [116]–[122]. Electronically, Na is said to passivate intrinsic point defects through the formation of new point defects. Choi *et al.* and Forest *et al.* suggest a reduction of the compensating In_{Cu} antisite defects due to the formation of Na_{Cu} defects at the grain boundaries [118], [123]. Similarly, Niles *et al.* envisage the possibility of Na_{III} defect formation [124], which is, however, challenged by Oikkonen *et al.* claiming that the formation of Na_{In} e.g. is energetically unfavourable [125]. Kronik *et al.* suggest that Na acts as a catalyst for the creation of O_{Se} defects that would compensate the selenium vacancies V_{Se} at the surface and at the grain boundaries [126]. Theoretical calculation by Wei *et al.* discard the latter explanation by claiming that O_{Se} defects would be deep and thus detrimental to the solar cell performance [127]. Yuan *et al.* suggest that Na promotes the formation of V_{Cu} acceptors that regulate the doping [128]. While the exact nature of the Na involvement is not yet fully clear, most studies agree that Na increases the p-type conductivity. Experimentally, an increase in hole concentration has indeed been confirmed by e.g. Hall [129] and capacitance-voltage [130], [131] measurements in polycrystalline CIGS.

However, the Na atoms do not only act at the grain boundaries but have also been found inside the grains [118], [121], [122]. Thus, even in epitaxial CIGS [132] and $CuInSe_2$ monograin powders [133], the hole concentration is increased after Na doping, indicating that sodium can influence the material even in the absence of grain boundaries. Additionally, a very recent study found that Na also plays an important role in the In/Ga interdiffusion during absorber growth [134], potentially ensuring an improved crystal quality. Ultimately, the main benefit of Na in CIGS is an increase in V_{OC} and fill factor. For more detailed reviews about the incorporation of sodium in CIGS, the interested reader is referred to refs. [135], [136].

As was the case for the NaF PDT, atom probe tomography studies reveal that potassium from the KF PDT tends to aggregate at the grain boundaries as well [137], [138]. Additionally, secondary ion mass spectrometry measurements reveal that the potassium is distributed homogeneously throughout the absorber [12], [139] and quantitative measurements have revealed that its concentration is considerable higher than the concentration of Na [12], [114], [140]. Since both K and Na accumulate at the grain boundaries and since the concentration of K is larger if a KF PDT is applied, it is argued that an ion exchange mechanism is taking place, with the K atoms pushing the Na atoms from the grain boundaries into the grains [12]. This is supported by theoretical calculations [141].

In addition to the ion exchange mechanism, the KF PDT also heavily influences the composition of the CIGS surface. Numerous UV and X-ray photoelectron spectroscopy studies show a strong Cu depletion and K accumulation at the absorber surface [12], [114], [142], [143]. While the In and Se-related signals in these studies are also strong, Ga seems to be present only sparsely at the surface. This special surface composition could be explained by the presence of a so-called "KIS" layer that is predominantly rich in K, In and Se. Recent calculations based on DFT have indeed revealed the favourable formation of a $KInSe_2$ phase on the surface of a pure $CuInSe_2$ absorber [141]. Characterization of the surface via hard X-ray photoelectron spectroscopy and inverse photoemission spectroscopy have revealed a reduced valence band maximum of 0.3 - 0.4 eV and an increased conduction band minimum of 1.0 - 1.1 eV compared to an untreated sample [142], [143]. Thus, the surface layer exhibits a large band gap of 2.52 eV, which is close to the 2.7 eV band gap energy of the $KInSe_2$ compound [143].

In addition to having a wider band gap energy than the bulk CIGS material, the Cu-depleted surface layer also facilitates a more homogeneous CdS coverage during chemical bath deposition compared to an untreated sample (but containing Na from the substrate) [144]. As a consequence, a thinner CdS buffer layer can be deposited without witnessing deteriorations in the V_{OC} that generally accompany thin buffer layers in untreated samples (but containing Na from the substrate) [68]. A thinner CdS buffer layer leads to a reduced parasitic absorption of the solar radiation and thus a larger j_{SC} [12], [130].

In terms of electronic properties, the KF PDT leads to a reduced CdS/absorber interface recombination as determined from temperature-dependent JV measurements on pure Cu-rich $CuInSe_2$ [145]. In Cu-poor CIGS, the KF PDT leads to reduced CdS/absorber interface recombination only when compared to samples treated with NaF only and featuring a thin CdS buffer layer (as mentioned above) [130]. A reduced recombination at the interface would also explain the increase in minority carrier lifetimes that has been measured in time-resolved photoluminescence (TRPL) experiments [146], [147]. However, the TRPL results cannot entirely confirm that the improvement due to the KF PDT only takes place at the interface. It is also possible that the KF PDT influences the bulk of the CIGS absorber itself as well [146]. In this context, a passivation of non-radiative recombination centers at grain boundaries was e.g. proposed by Shin *et al.* [148].

Concerning the influence of the KF PDT on the doping level, various different reports can be found. In the case where the KF PDT is applied to absorbers that do not contain any other alkali elements, an increase in p-type conductivity is observed [130], [139], [149]. In the case where the

KF PDT is applied to absorbers that contain Na, in general an increase in p-type conductivity is observed [146], [150]. However, when applied to absorbers grown at low-temperatures, the sequential NaF + KF appears to lead to a reduction of the bulk p-type conductivity [130].

Thus, as is the case for Na treatment, the underlying mechanisms of the KF PDT are not yet fully understood but their beneficial influence on CIGS solar cell performance, by increasing the j_{SC}, V_{OC} and FF is undeniable.

Attempts of heavier alkali post-deposition treatments, such as RbF and CsF, were done as recently as 2016 and allow the reproducible fabrication of Cu(In,Ga)Se_2 solar cells of 22 % efficiency and above [15], [151]. Although information about the underlying influence is still quite sparse and remains the subject of ongoing investigations, the last years have seen the publication of numerous studies tackling the effect of rubidium on the CIGS absorbers. Electron microscopy and synchrotron nano x-ray fluorescence measurements conducted on CIGS absorber, which received a RbF PDT and were grown on both alkali-free and alkali-containing substrates, reveal the preferential agglomeration of Rb at the grain boundaries and interfaces (front and back) [152], [153]. Highly spatially-resolved atom probe tomography measurements on RbF-treated samples on SLG consolidate these findings [154], [155]. As is the case for the KF PDT, in the case where Na is present prior to the injection of Rb, an ion exchange mechanism occurs where the lighter alkali elements are partly removed from the absorber [154], [156], [157]. Furthermore, various different measurement techniques show that the accumulation of Rb at both the absorber surface and at the grain boundaries is accompanied by an increase in In and Se, as well as a decrease in Cu [140], [153], [156]. As such it is argued, as is the case for the KF PDT, that the Rb engages in the formation of a $RbInSe_2$ phase [158]. The formation of such a phase is deemed favourable in certain conditions by theoretical calculations based on DFT [141] and the presence of a $RbInSe_2$ compound at the CdS/CIGS interface has recently been confirmed experimentally through scanning transmission electron microscopy and energy-dispersive X-ray spectroscopy measurements [159]. While it is argued that the presence of the $RbInSe_2$ leads to a surface passivation effect (similar to $KInSe_2$ described above), Kelvin-probe force microscopy measurements demonstrate that one advantageous feature of the Cu-depleted and Rb-enriched surface is clearly the facilitated formation of the CdS buffer layer compared to untreated samples [160]. Whereas numerous experimental techniques measure the presence of rubidium at the grain boundaries, so far only 3D time-of-flight secondary ion mass spectrometry is able to confirm the presence of significantly reduced concentrations inside the grains [157]. In terms of influence on the doping, the RbF PDT either leads to an increase or a decrease in hole carrier density, depending on the specific growth conditions of the treatment [156], [161].

Thus, from the information about the RbF treatment that is currently available, one can conclude that the Rb behaves similar to the K from the KF PDT i.e. its influence allows for a thinner CdS buffer layer and the Rb alkali atoms accumulate at the grain boundaries and surface. In fact, on the one hand, when comparing the sequential NaF + KF PDT to the NaF + RbF PDT done on CIGS absorbers grown on alkali-free substrates at low temperatures, no clear differences in the solar cell parameters between the KF and RbF PDT were found [140]. On the other hand, however, when comparing CIGS absorbers grown on soda-lime glass at high temperatures, there exist clear differences between the effects of the KF compared to the RbF PDT when comparing the solar cell parameters [15].

Since this thesis deals with voltage losses in CIGS solar cells through recombination mechanisms, the exact influence of the alkali PDT on the V_{OC} (i.e. on the quasi-Fermi level splitting of the absorbers) is crucial. A more extensive literature overview regarding the changes in doping is thus provided in the appendix A.4. The most important insights of this overview have already briefly been mentioned in the paragraphs above.

2.7 Photoluminescence spectroscopy

The experiments in this thesis are conducted through photoluminescence (PL) spectroscopy that is based on exciting electrons from the valence band into the conduction band by illuminating the semiconductor absorbers with an external source. The generated charge carriers may then recombine and, upon emission, reveal various optoelectronic properties of the semiconductor, such as its absorption behaviour or quasi-Fermi level splitting. In the following, the basic principles of photoluminescence spectroscopy are introduced. Many of these principles are considered as basic knowledge and can thus be found in various books. If not stated otherwise, this section closely follows the concepts explained in detail in ref. [20].

2.7.1 Absorption and generation

The first step in photoluminescence experiments is the illumination of the semiconductor and subsequent absorption of the incident photon flux density. The situation is depicted in Fig. 2.15. Assuming a photon flux density $\Phi_{\gamma,\mathrm{inc}}$ to be incident on the semiconductor absorber with a planar surface exhibiting a spectral reflectivity $R(E)$. Of the incident radiation, the portion $\Phi_{\gamma,\mathrm{R}} = R(E) \cdot \Phi_{\gamma,\mathrm{inc}}$ is reflected while the portion

$$\Phi_\gamma(x = 0) = (1 - R(E))\, \Phi_{\gamma,\mathrm{inc}} \tag{2.38}$$

penetrates the material. Upon penetration, the amount of photons that are absorbed depends on the material's probability of absorption. This probability is expressed through the absorption coefficient $\alpha(E)$ that is a spectral material-specific quantity. According to the law of Lambert-Beer, the spatially-dependent photon flux density inside the absorber can be expressed as

$$\Phi_\gamma(x) = \Phi_\gamma(0)\, \mathrm{e}^{-\alpha(E)x} \tag{2.39}$$

$$= (1 - R(E))\, \Phi_{\gamma,\mathrm{inc}}\, \mathrm{e}^{-\alpha(E)x}. \tag{2.40}$$

Upon absorption inside the semiconductor, the photons create electron-hole pairs by exciting the electrons from the valence band into the conduction band. In direct semiconductors, such as Cu(In,Ga)Se_2, this process only obeys the energy and momentum conservation principles between the charge carriers and the absorbed photons. More specifically, a photon with energy $\hbar\omega$ invokes the transition from an initial state of energy E_i into a final state of energy E_f such that $E_\mathrm{f} = \hbar\omega - E_\mathrm{i}$. Assuming the states to be close to the band edges, the final and initial state energies can be seen as the electron and hole energies in their respective bands. With the

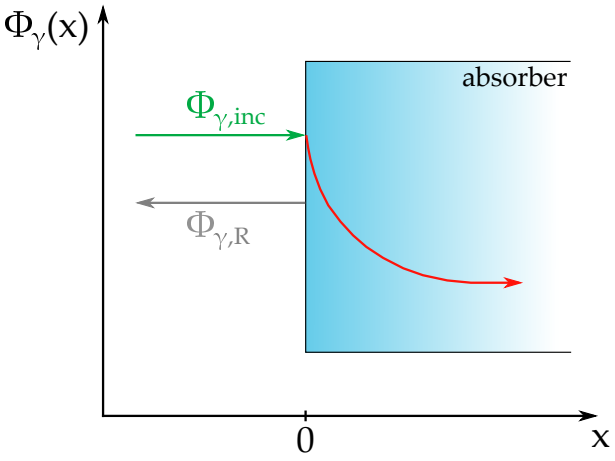

FIGURE 2.15: Spatial dependence of the photon flux density Φ_γ during absorber illumination. Part of the incident photon flux density $\Phi_{\gamma,\mathrm{inc}}$ (green) is reflected as $\Phi_{\gamma,\mathrm{R}}$ (grey) and part is penetrating the absorber at $x = 0$. The penetrating photon flux density is absorbed, following a spatial dependence (red).

parabolic band approximation, the energies can be expressed as

$$E_\mathrm{f} = E_\mathrm{C} + \frac{\hbar^2 k_\mathrm{e}^2}{2m_\mathrm{e}^*}, \qquad E_\mathrm{i} = -E_\mathrm{V} - \frac{\hbar^2 k_\mathrm{h}^2}{2m_\mathrm{h}^*}, \tag{2.41}$$

where $\hbar k_\mathrm{e}$ and $\hbar k_\mathrm{h}$ describe the momenta of the electrons and holes respectively, and m_e^* and m_h^* are the effective electron and hole masses respectively. Thus, via the energy conservation above and the momentum conservation $k_\mathrm{e} = k_\mathrm{h}$ (photon momentum is negligible), it follows

$$\hbar\omega = E_\mathrm{f} + E_\mathrm{i} = E_\mathrm{g} + \frac{\hbar^2 k^2}{2m_\mathrm{r}}, \tag{2.42}$$

where $m_\mathrm{r} = m_\mathrm{e}^* m_\mathrm{h}^* / \left(m_\mathrm{e}^* + m_\mathrm{h}^*\right)$ is the reduced mass. Eq. (2.42) describes the combined energy conservation and shows that the absorbed photon needs to have at least the band gap energy E_g to initiate the excitation of an electron from the valence into the conduction band. Furthermore, eq. (2.42) closely resembles eq. (2.41) such that it is useful to define a so-called combined density of states

$$D_\mathrm{comb}(\hbar\omega) = \frac{\left(2m_\mathrm{r}\right)^{3/2}}{2\pi^2\hbar^3}\sqrt{\hbar\omega - E_\mathrm{g}}, \tag{2.43}$$

as a pendant to the typical density of states of the electrons and holes in the conduction and valence bands respectively. The combined density of states (2.43) is an very important quantity as it describes the states that are available for optical transitions in a direct semiconductor. As such, it is clear that the probability of photon absorption is directly proportional to the states available for transitions i.e.

$$\alpha(\hbar\omega) \propto D_\mathrm{comb}(\hbar\omega) \propto \sqrt{\hbar\omega - E_\mathrm{g}}. \tag{2.44}$$

Thus, in an ideal semiconductor, photons with energies $\hbar\omega < E_\mathrm{g}$ are not absorbed. However, as is discussed throughout many parts in this thesis (see e.g. section 5.3), real semiconductors exhibit states within the band gap that also allow photon absorption for energies lower than the band gap energies. In such cases, the expression for the combined density of states and hence the absorption coefficient needs to be modified accordingly.

Finally, the absorbed photon flux density, under constant illumination conditions, creates a constant generation rate $G_\mathrm{e,h}(x)$ of electron-hole pairs according to

$$G_\mathrm{e,h}(x) = \alpha(E)\,\Phi_\gamma(x) = \alpha(E)\,(1 - R(E))\,\Phi_{\gamma,\mathrm{inc}}\,\mathrm{e}^{-\alpha(E)x}. \tag{2.45}$$

In photoluminescence, the transition from an equilibrium state (dark state) to a steady state following continuous excitation can be divided into three steps illustrated in Fig. 2.16. The initial thermal equilibrium state in the case of a p-type absorber is depicted in Fig. 2.16A. Due to vanishingly small concentration of thermally excited electrons (cf. section 2.1.1) the equilibrium concentration of electrons in the conduction band n_0 is neglected. The concentration of holes in the valence band p_0 is given by eq. (2.2) and the system is described by a single Fermi level $E_\mathrm{F,1}$.

Upon illumination and absorption, electrons are excited from the valence band into the conduction band, leaving behind holes. Approximately 10^{-14} s after generation, the distribution of the $\Delta n = \Delta p$ charge carriers resembles the broad spectral distribution of the absorbed photons. This situation, for the case of low-injection where $\Delta p \ll p_0$, is depicted in Fig. 2.16B. Since no equilibrium has been reached yet, the distribution of the charge carriers cannot be described by any Fermi level.

Finally, the excited charge carriers collide with the crystal lattice and dissipate their kinetic

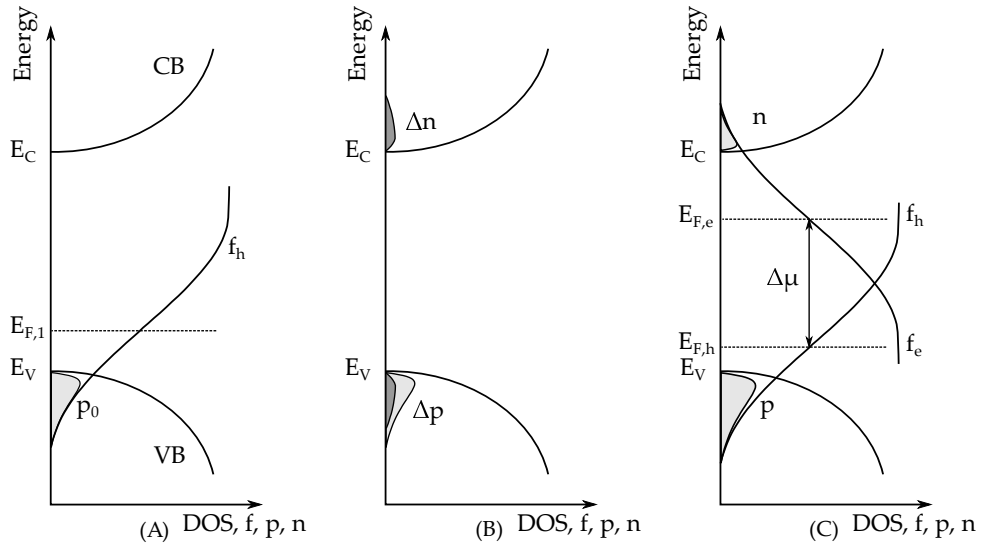

FIGURE 2.16: Energy diagram illustrating the occupation of charge carriers during three distinct steps in the absorption and generation process of a direct p-type semiconductor. The bottom axis describes the density of states DOS, distribution function f, and charge carrier concentrations p and n. **(A)** Thermal equilibrium state where the hole density p_0 is distributed close to the valence band edge. The initial Fermi level $E_{\mathrm{F},1}$ is situated close to the valence band. **(B)** 10^{-14} s after excitation through external illumination, the newly generated charge carrier densities $\Delta n = \Delta p$ are distributed in their respective bands according to the broad photon spectrum. Due to the very short timescale, the system is out-of-equilibrium and the determination of a Fermi level is not possible. **(C)** 10^{-12} s after generation, the charge carriers have relaxed to states of minimal energy. In this quasi-equilibrium, their distribution can be described by Fermi-Dirac statistics which enables the definition of quasi-Fermi levels $E_{\mathrm{F,e}}$ and $E_{\mathrm{F,h}}$ separated by the quasi-Fermi level splitting $\Delta\mu$.

energy through the creation of phonons. As a consequence of this relaxation process, occurring 10^{-12} s after generation, the charge carriers n and p are distributed along the band edges according to eqs. (2.5) and (2.6). This is illustrated in Fig. 2.16C. Due to the very short relaxation times, the system is in a steady state even under continuous illumination. This steady state allows the distribution of charge carriers to be described by Fermi-Dirac statistics through the distribution functions f_{e} and f_{h}. These Fermi-Dirac distribution functions then allow for the definition of the quasi-Fermi levels $E_{\mathrm{F,e}}$ and $E_{\mathrm{F,h}}$ which are separated by the quasi-Fermi level splitting $\Delta\mu$ initially encountered in Fig. 2.1. While the distribution functions describe the occupation of the charge carriers within the bands, they have no meaning within the band gap. In fact, within the band gap, the occupation is entirely governed by the impurity-related capture of electrons and holes (cf. section 2.5.2).

Fig. 2.16 describes the photon absorption and electron-hole pair generation at room temperature. After relaxation of the charge carriers to the band edges, they exist in their excited states for as how long their lifetime allows. Afterwards they participate in recombination processes that are either of radiative or non-radiative nature. At lower temperatures, the charge carriers are relaxing to unoccupied defect states and engage in defect-related transitions.

2.7.2 Radiative recombination processes

In photoluminescence spectroscopy, only the radiative recombination processes are detectable. While there exist multiple impurity-related radiative recombination processes in Cu(In,Ga)Se_2, only a few are relevant for the work done in this thesis and will briefly be described in the following. This section closely follows the concepts laid out in refs. [45], [162].

Of interest are the donor-acceptor-pair (DA), the free-to-bound (FB), and the band-to-band (BB) transitions depicted in Fig. 2.17. While the BB transition is the dominant transition at room temperature (in the absence of large defect concentrations), the defect-assisted transitions DA and FB depend on the temperature of the material and are usually observed at lower temperatures. Furthermore, distinct impurity-related transitions are only observable through PL spectroscopy in Cu-rich CIGS material. In state-of-the-art Cu-poor material, these transitions still occur but are broadened due to the influence of electrostatic potential fluctuations. Defect spectroscopy under the influence of electrostatic potential fluctuations is a relevant topic in this thesis and merits its own section 2.7.4.

After generation, the excited electron and hole charge carriers relax to states of minimal energy. At sufficiently low temperatures, the states of lowest energy are supplied by the defects states that are, in the following, assumed to be single-charged donor and acceptor states. Once the charge carriers occupy these localized states, they can undergo a donor-acceptor-pair transition where the electrons in the neutral donor states recombine with the holes in the neutral acceptor states, emitting photons of energy

$$\hbar\omega = E_\mathrm{g} - E_\mathrm{D} - E_\mathrm{A} + \frac{e^2}{4\pi\epsilon_\mathrm{r}\epsilon_0 r_\mathrm{DA}}. \tag{2.46}$$

Here E_g describes the band gap energy, E_D the donor energy, E_A the acceptor energy, e the elementary charge, ϵ_r the dielectric constant of the CIGS absorber, ϵ_0 the vacuum dielectric constant, and r_DA the spatial distance between involved donor and acceptor impurities within the crystal. The last term on the right-hand side of eq. (2.46) denotes the Coulomb energy that is added to the emitted photons since the DA transition results in a positively charged donor and a negatively charged acceptor. Since the DA transition is occurring over defect states that

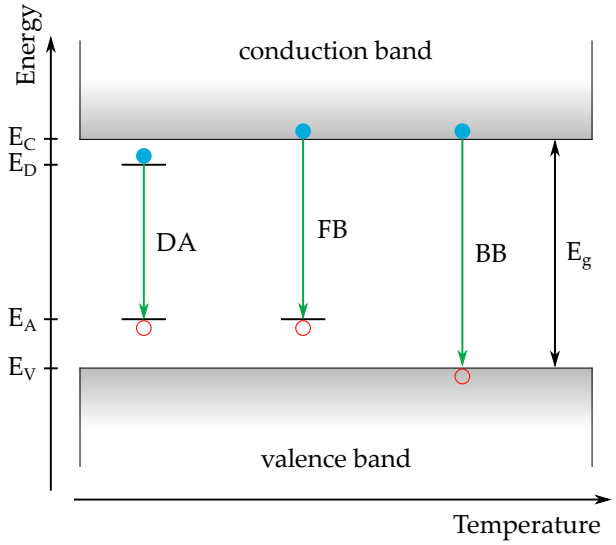

FIGURE 2.17: Schematic illustration of optical transitions in CIGS. Only the transitions relevant for this thesis are depicted. At low temperatures, donor-acceptor (DA) pair transitions are occurring where electrons (blue circles) from donor states of energy E_D recombine with holes (red circles) in acceptor states of energy E_A. At higher temperatures, the shallow donor states are thermally emptied, resulting in free-to-bound (FB) transitions between electrons in conduction band and holes in the deeper acceptor states. Towards room temperature, the acceptor states are also thermally emptied and the resulting band-to-band (BB) transition is occurring between electrons in the conduction band and holes in the valence band.

are spatially separated, the recombining charge carriers participate in a tunnelling step.

DA transitions show a very specific response to varying excitation densities. For example, in the case of an increasing incident photon flux density (corresponds to larger laser powers in PL experiments), more and more charge carriers are generated and occupy the donor and acceptor states. Consequently, the probability of DA transitions occurring between impurities that are spatially less separated is increased. A reduction in r_{DA} in eq. (2.46) leads to larger Coulomb energies and thus to photons of higher energy being emitted. In the measured PL spectra, this occurs as a blueshift of the transition peak. In Cu-rich CIGS absorbers, the blueshift usually ranges between 1 and 5 meV/decade (here "decade" means a change of one order of magnitude in the excitation density).

Depending on the energies of the involved donors E_D and acceptors E_A, DA transitions can also occur between deep-level traps. This is e.g. the case in Cu-rich Cu(In,Ga)Se_2 and $CuInSe_2$ [42], [49] and $CuGaSe_2$ [41], [42] (cf. section 2.2.2). While these deep defect transition still occur through a radiative channel at low temperatures, at room temperature they are mostly occurring non-radiatively and thus present a severe performance-limiting mechanism for the solar cells.

Increasing the temperature of the material leads to thermal quenching of the DA transitions due to one of the occupied impurities being thermally activated i.e. ionized. In stoichiometric CIGS, the shallow donor D1 is usually the impurity that is first ionized [163] (cf. section 2.2.2). Prior to the thermal activation of the shallowest impurity, the DA transition exhibits a blueshift of the order of $k_B T$ with increasing temperatures. After the thermal quenching of the shallowest impurity level is complete, the transition goes over to a free-to-bound transition.

The FB transition, occurring between delocalized electrons in the conduction band and localized holes in the acceptor states[10], shows slightly altered responses to changes in excitation density and temperature. In the case of increasing excitation density, the photons that are emitted following the FB transition do not show any energetic shift. An increase in temperature, by contrast, invokes two mechanisms that alter the energy of the emitted photons. Since the electrons partaking in the FB transition are originating from the conduction band, the temperature-induced band gap shrinkage leads to a slight redshift of the emitted photons. Simultaneously, the increase of the temperature leads to a broadening in the order of $k_B T$ of the Fermi-Dirac distribution of the charge carriers which leads to the electrons occupying higher energy states in the conduction band, ultimately resulting in a blueshift of the emitted photons. The emitted photons can thus show both a redshift and a blueshift with increasing temperatures. However, in both cases the energetic shifts are usually very minor.

Increasing the temperature further towards room temperature leads to the thermal activation of the shallow acceptor state and hence to a thermal quenching of the FB transition. Consequently, the electrons in the conduction can only recombine with the holes in the valence band. This so-called band-to-band transition is of utmost importance in this thesis and therefore merits its own dedicated section.

2.7.3 Band-to-band recombination

The spectral photon flux density that is emitted from the semiconductor absorber following the band-to-band transition can be measured in photoluminescence experiments at room temperature. As it contains optoelectronic properties of the absorber, such as the absorption coefficient and the quasi-Fermi level splitting, its mathematical description needs to be known. In the

[10] FB transitions can also occur between localized electrons on donor states and delocalized holes in the valence band. However, due to the donor in stoichiometric CIGS being considerably shallower than the shallowest acceptor, the latter option is not considered here.

following, the mathematical description is derived in a few simplified steps. This derivation is adapted from refs. [20], [164], where a much more sophisticated and complete derivation can be found.

The band-to-band transition is the result of a spontaneous radiative recombination process involving an upper energy state E_f and a lower energy state E_i. The spontaneous emission rate per volume for a given energy E can be expressed using Fermi's golden rule [20], [92], [165] as

$$r_\mathrm{sp}(E) = |M|^2 \frac{c}{n} D_\gamma(E)\, D_\mathrm{comb}(E)\, [1 - f(E_\mathrm{i})]\, f(E_\mathrm{f}), \tag{2.47}$$

where M is the transition probability matrix, c the vacuum speed of light, n the index of refraction of the absorber, D_γ the density of states of the emitted photons, D_comb the combined density of states of the upper and lower energy levels, $f(E_\mathrm{i})$ the Fermi-Dirac distribution of the lower energy state, and $f(E_\mathrm{f})$ the Fermi-Dirac distribution of the upper energy state. Eq. (2.47) appears intuitive as it contains the probability of unoccupied lower energy states $1 - f(E_\mathrm{i})$ (i.e. holes in the valence band) and of occupied higher energy states $f(E_\mathrm{f})$ (i.e. electrons in the conduction band). The transition probability matrix M contains the allowed rules for the dipole transition and, through the principle of detailed balance, also finds use in the absorption process. It can thus be shown that the absorption coefficient can be expressed as [20]

$$\alpha(E) = |M|^2\, D_\mathrm{comb}(E)\, [f(E_\mathrm{i}) - f(E_\mathrm{f})]\,. \tag{2.48}$$

Eq. (2.48) strongly resembles eq. (2.44) where an occupied valence band $f(E_\mathrm{i}) = 1$ and unoccupied conduction band $f(E_\mathrm{f}) = 0$ was assumed.

Due to the boson nature of the emitted photons, they do not underlie any probability-related restrictions but may only occupy states that are defined by the photon density of the states in the solid angle Ω into which they are emitted. According to [20], [164], the photon density of states is:

$$D_\gamma(E) = \frac{\Omega\, n^3}{4\pi^2 \hbar^3 c^3}\, E^2. \tag{2.49}$$

Finally, by defining a hole quasi-Fermi level $E_\mathrm{F,h}$ for the distribution function $f(E_\mathrm{i})$ and an electron quasi-Fermi level $E_\mathrm{F,e}$ for $f(E_\mathrm{f})$, inserting eqs. (2.48) and (2.49) into eq. (2.47) yields

$$r_\mathrm{sp}(E) = \frac{\Omega\, n^2}{4\pi^3 \hbar^3 c^2}\, \frac{\alpha(E)\, E^2}{\exp\left(\frac{E - \Delta\mu}{k_\mathrm{B} T}\right) - 1} \tag{2.50}$$

Expression (2.50) describes the spontaneous emission rate $r_\mathrm{sp}(E)$ at a specific depth within the absorber. To compute the total spontaneously created photon flux density $\Phi_\mathrm{sp}(E)$, eq. (2.50) is integrated across the whole absorber thickness and yields [164], [166]

$$\Phi_\mathrm{sp}(E) = \frac{\Omega\, n^2}{4\pi^2 \hbar^3 c^2}\, \frac{a(E) E^2}{\exp\left(\frac{E - \Delta\mu}{k_\mathrm{B} T}\right) - 1}. \tag{2.51}$$

where $a(E)$ is the absorptivity of the absorber. While the expression (2.51) is valid in general, it can be adjusted to more specific cases by inserting a specific expression for $a(E)$. There exist numerous models for the absorptivity $a(E)$ with a very general expression being presented in ref. [166]. However, in this thesis, assuming a planar surface and neglecting multiple reflection, the simplified expression

$$a(E) = (1 - R) \left(1 - \mathrm{e}^{-\alpha(E) d}\right), \tag{2.52}$$

where R denotes the surface reflection and d the absorber thickness, is used.

In photoluminescence experiments, only the photon flux density that exits the absorber is detected. Assuming, for simplicity, that only the photons that are emitted towards the surface of the absorber are able to escape. Then, due to the difference in refractive indices between the absorber ($n \approx 3$) and outside ($n \approx 1$), the critical angle beyond which absolute reflection on the surface occurs is small. In appendix F.5, it is derived that the critical solid angle into which the photons need to be emitted in order to be able to escape the absorber amounts to $\Omega \approx \pi/n^2$. Finally, the mathematical expression for the measured photon flux density, resulting from the radiative band-to-band transition, outside the absorber is[11]

$$Y_{\mathrm{PL}}(E) = \frac{1}{4\pi^2\hbar^3c^2} \frac{a(E)E^2}{\exp\left(\frac{E-\Delta\mu}{k_{\mathrm{B}}T}\right) - 1}. \tag{2.53}$$

Due to its strong resemblance to Planck's law of radiation [167], eq. (2.53) is referred to as Planck's generalized law. In fact, it describes the emitted photon flux density as the photon flux density of a black body multiplied at each energy interval by the corresponding absorptivity $a(E)$ and the quasi-Fermi level splitting $\Delta\mu$ of the absorber. As is evident from its derivation, besides the simplifications and assumptions that were used, Planck's generalized law is only valid for absorbers that exhibit flat quasi-Fermi levels. Its validity is discussed on the basis of state-of-the-art Cu-poor CIGS absorbers in section 5.1.

When photoluminescence is measured on CIGS absorbers, the generated electrons and holes cannot be extracted from the material as no electrical contacts exist. Thus, the absorbers are operated under open-circuit conditions. Calibrating the incident illumination to reflect the AM1.5 spectrum, the quasi-Fermi level splitting $\Delta\mu$ represents the upper limit for the open-circuit voltage V_{OC} that can be measured after completing the absorber to a finished solar cell device through eq. (2.10). The extraction of $\Delta\mu$ from the measured PL spectrum Y_{PL} is described in detail in section 5.1.

Moreover, not only are the optoelectronic qualities of the absorber accessed, PL also enables the evaluation of the optical qualities as the emitted photon flux density heavily depends on the spectral absorptivity $a(E)$. In this context, section 5.1 also reveals how, by extracting the absorption coefficient $\alpha(E)$, the density of states within the band gap can be analysed.

2.7.4 Photoluminescence in compensated semiconductors

While Cu-rich CIGS absorbers show a low concentration of donor impurities N_{D}, Cu-poor CIGS absorbers exhibit a similarly large concentration of both donor and acceptor N_{A} impurities [45]. In the latter case, the absorbers are said to be compensated since the electrons from the donor states occupy the holes in the acceptor states. The result of this compensation effect is the appearance of positively-charged donors and negatively-charged acceptors even at the lowest temperatures. This situation is depicted in Fig. 2.18A at low temperatures. The charged impurities are randomly distributed within the crystal and thus exert a randomly fluctuating electrostatic potential [168]. This leads to a distortion of the band edges as illustrated in Fig. 2.18B. In Cu-poor CIGS, the degree of compensation $N_{\mathrm{D}}/N_{\mathrm{A}}$ increases with decreasing CGI ratio [26], [163], [169]. Thus, CIGS absorbers that are poorer in Cu are more compensated than less Cu-poor absorbers. Due to the presence of these electrostatic potential fluctuations, the optical absorption and recombination processes measured in photoluminescence experiments are significantly altered and shall be briefly described in the following. The description is based on the model of Shklovskij and Efros [168] that has been applied in numerous studies such as e.g.

[11] Usually, as is also the case in this thesis, a photon flux density is denoted by the greek letter Φ. However, whenever the photon flux density as expressed through Planck's generalized law (2.53) is used to extract the quasi-Fermi level splitting $\Delta\mu$ (cf. e.g. section 5.1.1), the letter Y is chosen. This applies mostly to chapter 5.

[45], [48], [162].

In Fig. 2.18A, the ionized shallow donors N_D^+ and acceptors N_A^- are depicted as discrete states for illustratory purposes. However, due to their large concentration, the wavefunctions of the energy states overlap and the impurities form a defect band. In the p-type CIGS absorber, the uncompensated acceptor concentration is given by the difference between the total acceptor concentration and the compensated acceptor concentration i.e. $N_A^0 = N_A - N_A^-$ (with $N_A^- = N_D^+ = N_D$). At low temperatures, these neutral acceptors remain unionized. Increasing the temperature towards room temperature leads to their ionization such that the hole carrier concentration is given as $p_0 = N_A - N_D$.

While Fig. 2.18A shows the random distribution of ionized and neutral impurity states, Fig. 2.18B shows a more accurate depiction of reality. Due to the shallowness of the donor impurities ($E_C - E_D \approx 10 - 12$ meV, cf. section 2.2.2), the donor impurity band merges with the conduction band. Thus, even at very low temperatures, the free-to-bound transition is observed instead of the donor-acceptor-pair transition. The FB transition occurs between electrons occupying localized states of minimal energy in the potential valleys of the conduction band and holes in localized valleys of the acceptor band. Due to the tunnelling steps that are accompanying the FB transition, the emitted photons show a much broader energy distribution than in conventional DA or FB transitions. As a consequence, the measured PL spectra show a broad low-energy tail while the peak maximum is limited by the largest energy difference between potential valleys. The high-energy slope of the PL spectrum is dictated through thermal broadening and the density of states. Moreover, since the average transition energy is lower, the PL spectra show a redshift in compensated absorbers compared to their uncompensated counterparts.

In addition to the broader PL spectrum, the FB transition occurring in the presence of electrostatic potential fluctuations also shows a completely different response to changes in the excitation density and temperature compared to the uncompensated case described in section

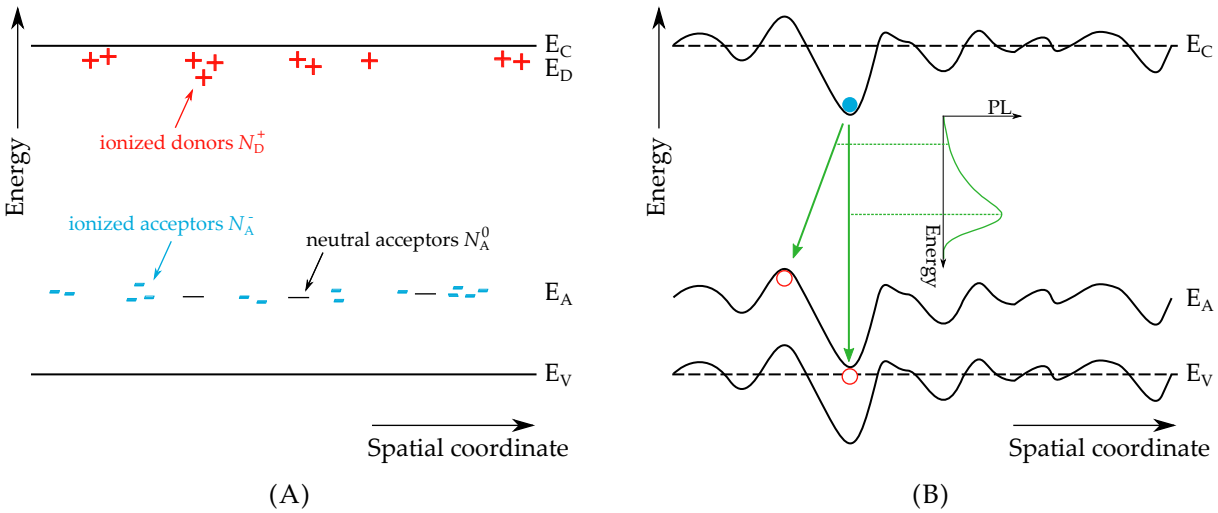

FIGURE 2.18: Schematic illustration of the energy band diagram of Cu-poor CIGS at low temperatures. **(A)** The absorber exhibits a random distribution of ionized donors N_D^+ and acceptors N_A^- that exert a Coulomb force on the charge carriers inside the bands. **(B)** As a consequence of the Coulomb force, the conduction and valence bands are modulated. The radiative FB transition between electrons (blue circles) in the conduction band and holes (red circles) in the acceptor band is asymmetrically broadened since various low-energy transitions are possible.

2.7.2. Increasing the excitation density leads to the creation of free electron and hole charge carriers. These charge carriers both neutralize the ionized impurities and screen them. This leads to a decrease of the electrostatic potential and thus to a blueshift of the measured PL emission. Contrary to conventional FB transitions where no energetic shift of the emitted photons is observed, in the presence of electrostatic potential fluctuations, the blueshift can range from 10 to 30 meV/dec [169]–[171].

Increasing the temperature provides the electrons inside the conduction band and holes inside the acceptor band with additional thermal energy. Consequently, the charge carriers become more mobile and may overcome the potential barriers between valleys such that they populate even the deepest potential valleys. As a result, a redshift of the emitted PL is observed. Increasing the temperature further leads to either an increased number of thermally excited charge carriers that screen the ionized impurities or a thermal quenching of the acceptor band. In the first case, a blueshift of the emitted PL is expected as the electrostatic potential fluctuations are reduced. In the second case, the FB transition is quenched and the band-to-band transition is observed.

Depending on the amplitude of the electrostatic potential fluctuations, it is possible that they still persists even at room temperature. Since modulated band edges promote radiative recombination through states that lie below the unmodulated band edges, electrostatic potential fluctuations leads to sub band gap absorption and emission. As was explained in section 2.5, radiative emission from states below the band edges is detrimental for the performance of the solar cell. It is thus important to quantify the amplitude of the fluctuations. There exist several methods to do so and a summary is given in ref. [48].

Unfortunately, the samples that are investigated in this thesis behave slightly differently than what is usually reported in literature such as e.g. refs. [45], [48]. As a result, the typical model and quantification methods for the fluctuation amplitude can only conditionally be used. Consequently, the model of Shklovskij and Efros [168] is adapted to account for the observations that are made in this thesis. The measurements, results, and interpretations are given in section 6.2 and the influence of electrostatic potential fluctuations on the quasi-Fermi level splitting and open-circuit voltage in state-of-the-art CIGS solar cells is ultimately discussed throughout chapter 7.

Finally, while this section argued that the electrostatic potential fluctuations are due to a inhomogeneous distribution of charge impurities, they can also be caused by band bending at the grain boundaries [172].

3 Experimental details

This chapter houses the experimental details of the measurements that were performed in the framework of this thesis. The first section 3.1 introduces the standard setup for photoluminescence experiments and explains its individual components. In addition, the concepts of spectral and intensity calibration are introduced. The second section 3.2 describes the experimental setup that was used to measure spatially-resolved photoluminescence on a microscopic scale. Finally, the third section 3.3 provides a detailed overview of the different samples that were investigated in this thesis.

3.1 Photoluminescence setup

Photoluminescence (PL) is based on the principle of illuminating a sample (in this case a semiconductor) by an external radiation source of sufficient energy and subsequent collection of the sample's emitted radiation. Thus, fundamentally, an experimental photoluminescence setup only requires an external illumination source, a sample, and a detector. For more detailed measurements and more variety, a more sophisticated setup is needed. The home-built experimental setup used for almost all experiments (bar the spatially-resolved PL ones - see section 3.2) was designed by Dr. Conrad Spindler and is schematically depicted in Fig. 3.1. A very detailed description of the experimental setup can be found in ref. [41].

The setup houses two sources of external radiation: an argon ion laser emitting monochromatic green light with a wavelength of 514.5 nm (2.41 eV) and a diode laser emitting monochromatic red light with a wavelength of 660 nm (1.88 eV). For the majority of the photoluminescence measurements conducted in this thesis, the diode laser was used. After exiting the laser, the laser beam passes through a series of optical filters. These filters consists of various bandpass and laserline filters and serve to remove unwanted wavelengths in the laser's spectrum. Beyond the optical filters, a filter wheel is installed that contains neutral density filters with optical densities ranging from OD0 to OD4. The neutral density filters attenuate the laser beam and are thus used, along with varying the laser output power on its console, to regulate the excitation flux density that is ultimately reaching the sample position. The setup has the capacity to optionally flip a convex lens into the laser beam path. This lens, with a focal length of 150 mm, narrows the laser spot down to a diameter of approximately 80 μm at the sample position, increasing thus the excitation density. Without the lens, the diode laser beam has a diameter of 2.6 mm while the Ar-ion laser beam has a diameter of 2.2 mm at the sample position. Before reaching the sample, the laser beam passes through an aperture in the off-axis parabolic mirror (OAP1).

The sample to be measured is usually fixed to a xyz-stage and illuminated perpendicular to its surface. The stage is used to shift the position of the sample relative to the incident laser beam and thus illuminate and measure from different spots on the sample (used e.g. in section 5.2.2). A cryostat, into which the sample is inserted, can be fixed onto the xyz-stage. By connecting the cryostat to a cryogenic liquid (helium) container, the temperature of the sample can be reduced which enables the measurement of photoluminescence down to low temperatures. PL measurements at low temperatures using the cryostat are discussed entirely within chapter 6. The xyz-stage can be removed completely and an alternative sample holder

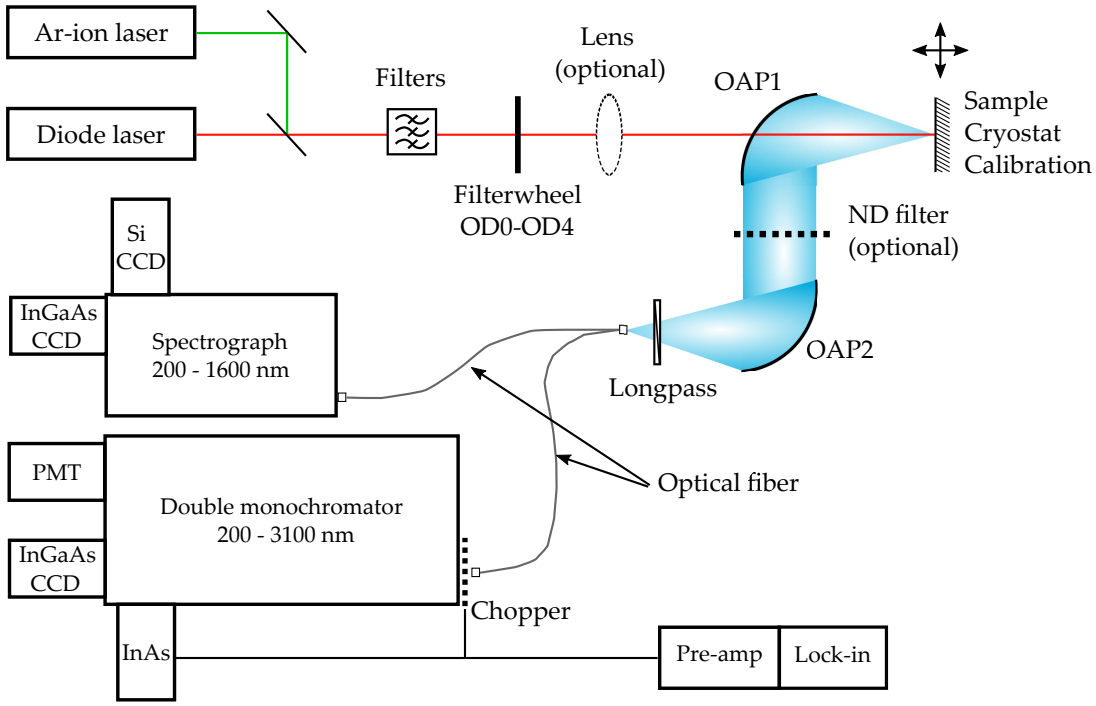

FIGURE 3.1: Schematic illustration of the experimental setup used for photoluminescence measurements. The various components are described in the main text. Adapted from ref. [41].

put in place. For the case of angle-resolved photoluminescence e.g., the sample holder depicted in Fig. 4.9 of section 4.3 is installed.

The collection of the emitted photoluminescence is done, in a first instance, by the off-axis parabolic mirror (OAP1) through which the laser beam passes to reach the sample position. This parabolic mirror exhibits a focal length of 101.6 mm which is twice as long as its diameter of 50.8 mm. These dimensions are chosen to reach a high angular aperture (i.e. 2, which is the ratio between focal length and diameter) enabling a high collection efficiency. While it is possible to reach higher collection efficiencies by increasing the angular aperture, this would require a smaller focal length which limits the space available for sample (or cryostat) placement. The off-axis parabolic mirror is coated with aluminium and exhibits a flat reflectance profile over a wide spectral range which leads to a minimization of chromatic aberration errors. From the OAP1, the photoluminescence is collimated into a second, nearly identical off-axis parabolic mirror (OAP2). In between both mirrors, neutral density filters can be placed to attenuate the photoluminescence signal and avoid detector saturation if necessary. In contrast to OAP1, the second mirror OAP2 has a focal length of 152.6 mm. This length is chosen because the optical fiber, into the photoluminescence is focussed, has a numerical aperture of 0.22 and thus only ideally accepts light within an aperture half-angle of 12.7°. Thus, if the same OAP1 mirror would be used in place of the OAP2, the light would be focussed into a half-angle of 14° and would lead to a non-ideal signal transmission due to total reflection losses within the fiber. With the OAP2, the focussed half-angle amounts to 9.5° and no signal is lost during the coupling-in. Before entering into the optical fiber, however, the photoluminescence light passes through a longpass filter that removes unwanted rogue signals, such as the reflection of the laser light from the sample surface.

Through the optical multi-mode fiber, the photoluminescence reaches into the spectrograph (monochromator) where it is directed onto a grating. With a grating density of 100 lines/mm, the photoluminescence is dispersed into its spectral components and directed either onto a Si-CCD (200 - 1100 nm) or onto an InGaAs-array detector (800 - 1600 nm). Using a the

100 lines/mm grating and a multi-model fiber of 550 μm inner core diameter enables a wavelength resolution of the photoluminescence spectrum down to 15 nm. Using a thinner multimode fiber of 200 μm diameter enables a higher resolution of 6 nm but a weaker overall signal.

In addition to the components that were just described, the experimental setup is also equipped with a double monochromator that houses, amongst a photomultiplier tube (PMT) and an InGaAs array (both not used in this thesis), an InAs photovoltaic diode detector. The InAs detector enables the measurement of photoluminescence spectra carrying wavelengths of up to 3100 nm (0.4 eV). Due to its high specific detectivity in the near- and mid-infrared, the background noise originating from thermal black body radiation of the surrounding environment causes large unwanted signals. The InAs detector is thus embedded within a container surrounded by hollow walls. These hollow walls can be filled with liquid nitrogen to shield the detector from the surrounding radiation. In addition, the background noise is further reduced by modulating the photoluminescence signal through a chopper (frequency of 175 Hz) and using a lock-in amplifier to deconvolute the modulated signal. The InAs detector is only used in section 6.1 of this thesis. More information about the double monochromator and the InAs detector can be found in ref. [41].

3.1.1 Spectral calibration

The principle of spectral calibration is described in the following by focussing, for illustrative purposes, on the spectrograph housing the Si and InGaAs detectors in Fig. 3.1.

Upon the dispersion into its spectral components through the grating inside the spectrograph, the photoluminescence is directed into a CCD camera (i.e. the Si or InGaAs detector). These cameras consists of arrays of pixels that are attributed to specific wavelengths. Upon absorption on one such pixel, a signal is recorded by the camera and put out in units of "counts". The recorded raw photoluminescence spectrum carries an naturally larger overall signal due to a non-negligible contribution from surrounding thermal radiation. In the case where this thermal radiation is not too severe, a background measurement is done where a shutter in front of the camera is closed. This background is then subtracted from the measured raw data.

The necessity for a spectral calibration is twofold: to account for optical losses of the emitted and collected photoluminescence (reflection losses of the off-axis parabolic mirrors, transmission losses of the neutral density or longpass filters, transmission losses within the fiber, sensitivity of the detectors, water absorption in air), and to provide the measured raw spectrum with physical units. The measurement of the spectral calibration function CF is initiated by placing a spectralon diffusor at the sample position in Fig. 3.1. A spectralon diffusor is a surface that exhibits a flat reflection curve close to unity across a broad spectral range and has a Lambertian emission profile. Onto the spectralon diffusor, a calibrated halogen lamp is guided and its reflected spectrum is recorded. From the halogen lamp spectrum $\Phi_{\text{Hal.}}$ that is known (i.e. that is provided by the manufacturer and shows how the "real" spectrum of the lamp should look like) and the measured lamp spectrum in the experimental setup $\Phi_{\text{meas.}}$, the calibration function can be computed:

$$CF = \Phi_{\text{Hal.}}/\Phi_{\text{meas.}}. \tag{3.1}$$

To receive the spectrally calibrated sample spectrum $\Phi_{\text{cal.}}$, it suffices to multiply the measured PL spectrum Φ_{sample} by the calibration function:

$$\Phi_{\text{cal.}} = CF \cdot \Phi_{\text{sample}}. \tag{3.2}$$

A visual example of the halogen lamp spectrum, as provided by the manufacturer and as measured by the setup, as well as the spectral calibration function can be seen in appendix E.1 (albeit for the case of the InAs detector).

The halogen lamp spectrum provided by the manufacturer $\Phi_{\text{Hal.}}$ is in units of [photons $\text{cm}^{-2}\ \text{s}^{-1}\ \text{nm}^{-1}$] while the halogen lamp spectrum measured in the setup $\Phi_{\text{meas.}}$ is in units of [counts]. Following the above steps for the spectral calibration leads to the calibrated sample spectrum $\Phi_{\text{cal.}}$ receiving the same units as the halogen lamp spectrum provided by the manufacturer i.e. [photons $\text{cm}^{-2}\ \text{s}^{-1}\ \text{nm}^{-1}$]. Under this form, the calibrated sample spectrum is displayed in wavelength space. However, for convenience purposes, as photoluminescence spectroscopy in this thesis is done on semiconductors where the band gap energy and defect transitions are expressed in eV, the calibrated sample spectrum is transformed into energy space. Generally, this is done via a Jacobian transformation [173] i.e. assuming a spectrum $\Phi(\lambda)$ in λ-space and converting it to E-space requires the operation

$$\Phi(\lambda)\,\mathrm{d}\lambda = \Phi(E)\,\mathrm{d}E \quad \Leftrightarrow \quad \Phi(E) = \Phi(\lambda)\,\mathrm{d}\lambda/\mathrm{d}E. \tag{3.3}$$

In terms of the y- and x-axis of the calibrated sample spectrum $\Phi_{\text{cal.}}$, the Jacobian transformation translates to

$$y\ \left[\text{photons}\,\text{cm}^{-2}\,\text{s}^{-1}\,\text{nm}^{-1}\right] \longmapsto y \cdot \frac{x^2}{hc}\ \left[\text{photons}\,\text{cm}^{-2}\,\text{s}^{-1}\,\text{eV}^{-1}\right]$$
$$x\ [\text{nm}] \longmapsto \frac{hc}{x}\ [\text{eV}]\,,$$

where $hc \approx 1240\,\text{eV}\cdot\text{nm}$ is used as a facilitated unit conversion measure for the product of Planck's constant h and the speed of light c. Almost all photoluminescence spectra shown in this thesis are expressed in units [photons $\text{cm}^{-2}\ \text{s}^{-1}\ \text{eV}^{-1}$] and represent thus a photon flux density in energy space. Only the spectra shown in section 6.1 are represented in wavelength space for the reasons outlined in appendix E.1.

3.1.2 Intensity calibration

While the spectral calibration gives physical units to the measured sample spectra, the values are relative to the experimental conditions under which the measurements were conducted. In this case, the photon flux density of the sample PL spectrum has no meaning in terms of absolute values. Consequently, whenever a PL spectrum is not calibrated for intensity, its y-axis units are displayed as [arb. u.] even though a photon flux density is spectrally displayed. This is the case for many spectra that are presented in this thesis. When conducting PL experiments where different samples are analysed one after the other without changing the experimental setup, the non-intensity calibrated PL spectra can still be used to compare between the photon flux densities of the different samples. However, after altering the experimental setup and repeating the experiments, the y values of the measured PL spectra cannot be compared to the recorded spectra prior to the change in the setup. To still be able to compare the photon flux density of the measured PL spectra between different samples after changes in the experimental setup, the spectra will need to be calibrated for intensity.

The principle of intensity calibration is based on the measurement of a known quantity. More specifically, the photon flux density of the excitation laser is measured with external instruments and later compared to its value when measured in the spectrograph and CCD camera (i.e. the same way a sample would be measured). To compute the photon flux density of the laser, its radius must be known. The laser beam shape is measured by placing a camera with a CMOS (complementary metal-oxide semiconductor) sensor at the sample position in Fig. 3.1. From the Gaussian beam shape, the radius ρ is determined (the radius is usually defined at the position where the maximum intensity of the laser beam is reduced by a factor of $1/\text{e}^2$). Furthermore, the power density that the laser beam carries is required. The power at the sample

position can be measured by placing a photodiode power sensor (labelled "powermeter" in the following) in the beam path. Thus, the photon flux density Φ_{laser} of the laser beam that arrives at the sample position can be calculated through

$$\Phi_{\text{laser}} = \frac{2P\lambda}{\pi\rho^2 hc}, \tag{3.4}$$

where the factor 2 accounts for the fact that the powermeter measures the total power P of the laser beam. However, the quantity of interest is not the total power of the laser but the maximum power. In the case of a Gaussian beam, the ratio between maximum and total power is just this factor 2. Moreover, in eq. (3.4), λ describes the wavelength of the laser beam and thus its energy. For the diode laser ($\lambda = 660\,\text{nm}$), the beam radius amounts to $\rho \approx 1.3\,\text{mm}$, while for the Ar-ion laser ($\lambda = 514.5\,\text{nm}$), the beam radius amounts to $\rho \approx 1.1\,\text{mm}$.

While eq. (3.4) describes the photon flux density that is incident on the sample position, it does not represent the photon flux density that is measured by the cameras in the spectrograph. To measure this, the laser beam needs to be incident on a reflective surface at the sample position and coupled into the spectrograph the same way the PL from a sample would. While it would appear trivial to use a mirror to reflect the laser beam back into the setup, this would not represent the collection of the emitted PL. The collection of the emitted PL is best represented by having the laser beam reflect of a lambertian surface. Thus, as is the case for the spectral calibration, the spectralon diffusor is installed at the sample position and the reflected light is coupled into the spectrograph and directed onto the Si CCD. While, in theory, the laser light is monochromatic, its spectrum is broadened by the fiber and spectrograph. Hence, the recorded laser light spectrum is integrated to reveal a measured photon flux density. To receive the intensity calibration factor, the photon flux density measured with the powermeter and calculated via eq. (3.4) at the sample position is divided by the measured photon flux density in the Si CCD. Finally, by multiplying the measured sample spectrum by this intensity calibration factor, the real emitted photon flux density is recorded.

While the above description allows one to compute the exact emitted photon flux density from the sample, in intensity-calibrated measurements the incident laser beam is usually set to a photon flux density that reflects the AM1.5 spectrum. The photons that are absorbed by the sample depend on the band gap energy E_g. Thus, in the case that the band gap energy of the material to be measured is known, the AM1.5 spectrum is integrated over the values above E_g which yields the desired Φ_{laser}. Via eq. (3.4), the total power of the AM1.5 spectrum can be calculated for the desired photon flux density. Finally, the laser output power is varied such that the power that is read on the powermeter equals the power that corresponds to the AM1.5 spectrum.

Intensity-calibrated PL measurement are presented in section 5.2 and 7.1.2 of this thesis.

3.2 Spatially-resolved photoluminescence setup

The home-built experimental setup in which the spatially-resolved photoluminescence (μ-PL) experiments are conducted is depicted in Fig. 3.2. The setup was designed by Dr. Levent Gütay and Dr. Jes K. Larsen and is based on the confocal approach i.e. the excitation and collection is occurring through the same focussing lens. A detailed description of the experimental setup can be found in ref. [48].

As an external excitation source, the Ar-ion laser is used. Through a flippable mirror, the beam path can be changed from the one in Fig. 3.1 such that, instead of going into the conventional PL setup described in section 3.1, the laser beam is redirected towards a lens. This lens focusses the laser beam down a single-mode fiber which directs the laser beam into the

μ-PL setup that is contained within a black box (and can thus be operated independently of other measurement activities in the laboratory room). A single-mode fiber is used as it exhibits a low dispersion and thus yields a "clean" laser spot upon out-coupling. From the fiber, the laser beam is directed towards a series of lenses that significantly expand the size of the beam. Via a beam splitter, the laser beam is deviated towards a microscope lens, exhibiting a numerical aperture of 0.65, and focussed down onto the sample. This high value is the reason why the beam is expanded prior to reaching the microscope as it allows to take full advantage of the lens' resolution capabilities. With a wavelength of 514.5 nm, the diameter of the laser beam on the sample can be estimated to be approximately 1 μm which indicates the maximum resolution of the μ-PL setup. The microscope lens is attached to a motorized piezoelectric table that allows lateral spatial steps with a resolution of 1 nm (i.e. much smaller than the size of the laser beam on the sample). The total scan area that can be covered by the table amounts up to $80 \cdot 80\,\mu m^2$. In addition, the piezoelectric table also has a vertical degree of freedom such that the focus of the laser beam (and consequently the collection of the emitted PL) can be optimized.

Due to the extremely small excitation and collection spot size of 1 μm, the generated charge carriers can easily diffuse out of the focus (as diffusion lengths in good CIGS absorber can be of a few microns - see e.g. [174]). As a consequence, the emitted PL that is ultimately collected by the microscope lens is reduced even if the excitation density is relatively high due to the small excitation area. To facilitate placement in front of the microscope lens, the sample is attached to a xyz-stage.

After emission from the sample, the PL is collected by the microscope lens, directed through the beam splitter and a longpass filter and ultimately focussed into an optical fiber. From the fiber, the PL is directed into the spectrograph that is also used, and was described, in the conventional PL setup in section 3.1.

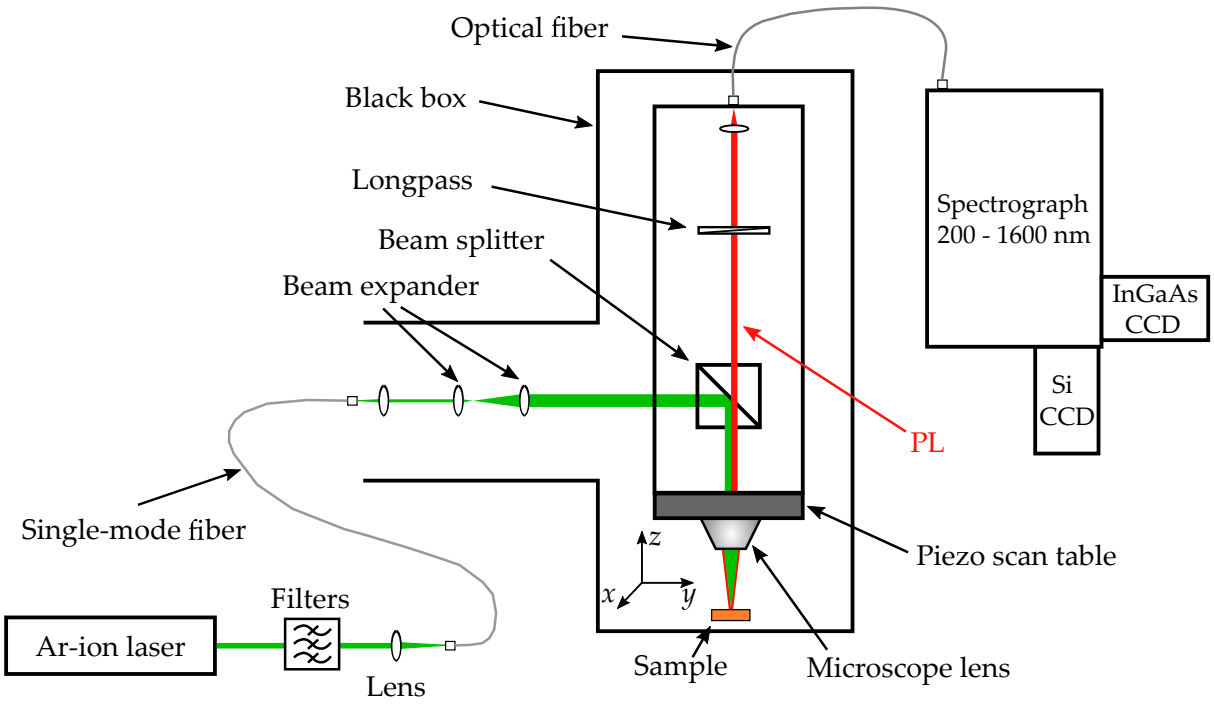

FIGURE 3.2: Schematic illustration of the experimental setup used for spatially-resolved photoluminescence with micrometer resolution. The various components are described in the main text. Adapted from ref. [48].

Spatially-resolved μ-PL measurements are presented in section 5.4, where more information about the individual measurements is provided.

3.3 Sample overview

The vast majority of Cu(In,Ga)Se_2 samples investigated in this thesis were grown and prepared in the framework of the Sharc25 project (cf. chapter 1). Their main properties are listed in Table 3.1. Information about the typical solar cell structure and the alkali post-deposition process are provided in section 2.3.1 and 2.6.3 respectively.

Two samples sets were prepared by project partner ZSW and are labelled "H1" and "H2". These samples were grown at elevated temperatures (i.e. above 500° C) on Mo-coated soda-lime glass and are therefore labelled "high-temperature samples" throughout the thesis. The exact details of the growth process are unknown but published details of similar processes can be found in refs. [15], [71]. Sample set H1 received a RbF PDT after growth while H2 remained untreated. Since both sample sets were grown on an alkali-containing substrate, they both contain Na atoms. The sample sets were prepared under three different forms:

- Bare CIGS absorbers exhibiting the structure: SLG/Mo/CIGS.
- CdS-covered CIGS absorbers exhibiting the structure: SLG/Mo/CIGS/CdS.
- Finished solar cell devices exhibiting the structure: SLG/Mo/CIGS/CdS/(Zn,Mg)O/ZnO:Al/Grids.

The samples were prepared individually i.e. the substrate strips underwent the same growth process (positioned next to each other) but were then processed differently as listed above. The dimensions and shape of the absorbers and solar cells are depicted in appendix B.1. Due to the special design of the high-temperature strips, up to 10 solar cells are grown onto a substrate strip. Thus, the measured solar cell parameters in Table 3.2 represent average values over all solar cells. The individual results are presented in Table B.1 of appendix B.1.

There are other high-temperature samples that are (sparsely) investigated in this thesis and are briefly described in the following. More specifically, these samples are only used in investigations related to interference fringes in chapter 4 and its related appendix C and thus do not require a more detailed specification. The CdS-covered "HS" absorber (with RbF PDT) possesses a rough surface and thus exhibits weak interference fringes. The sample "H0", available as both bare and CdS-covered absorbers (RbF PDT) shows strong interference fringes and was used in the beginning of the PhD project to investigate the influence of interference effects. The sample "HT" (with KF PDT) also shows strong interference effects and was used to test various methods to reduce interference fringes through the deposition of an auxiliary surface layer.

Six sample sets were prepared by project partner Empa and are labelled "L1", "L2", "L3", "LN1", "LN2", and "LN3". These samples were grown at lower temperatures (i.e. below 500° C) and are therefore labelled "low-temperature samples" throughout the thesis. The low-temperature sample sets prepared by Empa differ from the high-temperature sample sets prepared by ZSW in that a silicon oxide (SiOx) barrier layer was deposited onto the substrate. This barrier hinders the in-diffusion of alkali elements into the absorbers such that only the alkali elements that are added through the post-deposition treatment are present. They exact PDT allocation to the different samples can be reviewed in Table 3.1. The sample sets were prepared under three different forms:

- Bare CIGS absorbers exhibiting the structure: SLG/SiOx/Mo/CIGS.

- CdS-covered CIGS absorbers exhibiting the structure: SLG/SiOx/Mo/CIGS/CdS.
- Finished solar cell devices exhibiting the structure: SLG/SiOx/Mo/CIGS/CdS/i-ZnO/ZnO:Al/Grids.

The samples were prepared individually but instead on being grown on different strips, they were grown on the same strip and after growth (and PDT) broken into different pieces and processed further. The dimensions and shape of the absorbers and solar cells are depicted in B.1. Table 3.2 represents average values measured over six neighbouring solar cells. The solar cell parameters of the individual solar cells can be found in Tables B.2 and B.3 of appendix B.1.

Two other samples prepared by Empa are investigated in this thesis: the low-temperature sample LS and the $CuInSe_2$ sample. Both samples are present only under the form of a CdS-covered CIGS absorber. These absorbers are not investigated thoroughly but are only included in a few experiments.

The sample LS is present under the form of a SLG/SiOx/Mo/CIGS/CdS absorber and was originally prepared for a collaboration which resulted in the published study [93]. The corresponding solar cell was finished after depositing an i:ZnO/ZnO:Al window layer on top. The sample was treated with a sequential NaF + RbF PDT after growth. More information about the sample can be found in ref. [93].

Similar to the LS sample, the $CuInSe_2$ sample also stems from a collaboration with Empa. It is included in chapter 7 where it serves as an useful pendant to the CIGS samples. The sample is present under the form of a CdS-covered absorber and was grown on a Mo-coated soda-lime glass (contains thus Na from the substrate). After growth, a RbF PDT was applied. Moreover, even though the sample is labelled as the ternary $CuInSe_2$, it exhibits a significant gallium gradient towards the back contact. Details about similar samples are published and can be found in ref. [111].

At specific points throughout the thesis, additional samples are measured and mentioned. However, these samples then only have a specific purpose and are elaborated when being discussed. The important core samples of this thesis are all describe above and summarized in Tables 3.1 and 3.2.

TABLE 3.1: Important properties of the samples that prominently feature in this thesis. The values represent averages across several solar cells. Indicated are the post-deposition treatment (PDT), the compositional [Ga]/[Ga]+[In] (GGI) ratio, the [Cu]/[Ga]+[In] CGI ratio, the thickness, and the band gap energy. The method for the determination of the band gap energy is described in appendix B.2. The measurements of these parameters were done by the project partners ZSW and Empa.

Sample	PDT	GGI	CGI	Thickness / μm	Band gap / eV
H1	RbF	0.31	0.92	2.80	1.077
H2	None	0.31	0.93	2.20	1.083
L1	NaF + RbF	0.35	0.86	1.90	1.147
L2	NaF	0.34	0.87	1.85	1.148
L3	None	0.33	0.87	2.00	1.142
LN1	NaF + RbF	0.33	0.89	2.07	1.124
LN2	NaF	0.34	0.90	1.86	1.137
LN3	None	0.35	0.87	2.12	1.146
LS	NaF + RbF	0.41	0.94	3.05	1.129
$CuInSe_2$	NaF + RbF	-	0.96	2.9	1.000

TABLE 3.2: Solar cell parameters of the samples that prominently feature in this thesis. The values represent averages across several solar cells. Indicated are the post-deposition treatment (PDT), the short-circuit current density j_{SC}, the open-circuit voltage V_{OC}, the fill factor FF, and the power conversion efficiency η. All samples are without anti-reflective coating. The measurements of these parameters were done after growth by the project partners who prepared them.

Sample	PDT	j_{SC} / mA cm^{-2}	V_{OC} / V	FF / %	η / %
H1	RbF	36.4	0.707	77.6	20.0
H2	None	35.6	0.690	77.9	19.1
L1	NaF + RbF	33.1	0.708	77.3	18.2
L2	NaF	30.9	0.685	78.0	16.5
L3	None	31.4	0.581	72.9	13.3
LN1	NaF + RbF	32.9	0.705	76.9	17.8
LN2	NaF	31.8	0.689	75.5	16.5
LN3	None	31.0	0.568	66.4	11.7
LS	NaF + RbF	35.8	0.716	75.8	19.2
$CuInSe_2$	NaF + RbF	41.8	0.611	72.1	18.4

4 Thin-film interference in $Cu(In,Ga)Se_2$

Measuring the photoluminescence (PL) of a copper-poor $Cu(In,Ga)Se_2$ semiconductor absorber at room temperature should yield a single broad asymmetric peak in the photon flux density spectrum [26]. This peak describes the near band edge photoluminescent transition between electrons and holes and provides information about important quantities such as the quasi-Fermi level splitting, the effective band gap energy or the absorption coefficient. An example of a measured PL spectrum on a state-of-the-art CIGS absorber is shown in Fig. 4.1. The dashed blue curve illustrates the expected broad PL peak while the red curve shows the real, measured signal. As is evident, the measured signal does not consist of a single broad peak but exhibits a multiple-peak or shoulder structure. One reason for the occurrence of these features may be the presence of additional phases in the material, as is the case for zinc selenide ZnSe in the kesterite $Cu_2ZnSnSe_2$ absorber [175]. However, as is shown by the reflectance spectrum measured on the same absorber and displayed in green in Fig. 4.1, the features in the PL spectrum are more likely to be due to interference effects as reflectance minima and PL maxima line up reasonably well. The interference fringes superimpose onto the measured PL spectrum and distort it, limiting the information that can be gained from photoluminescence spectroscopy.

In some cases, the occurrence of interference effects can be used to gain valuable insight into the properties of the material. For example, in epitaxial ZnSe layers, the interferences fringes can be used to determine the thickness and surface quality [176]. In anodic oxide films such as Al_2O_3, the interference fringes are used to monitor film growth [177] as well as investigate film porosity [178]. However, in other cases, as was described above, the occurrence of interference fringes is rather harmful towards the insight that can be drawn from the measurements (see also e.g. [179]–[181]). This is especially true in thin-film absorbers that are used for photovoltaic applications where the occurrence of interference effects is still largely ignored by the community. While a misinterpretation of measured PL spectra due to interference effects in $Cu_2ZnSnSe_4$ was recently confirmed [182], [183], there exist other published measurement

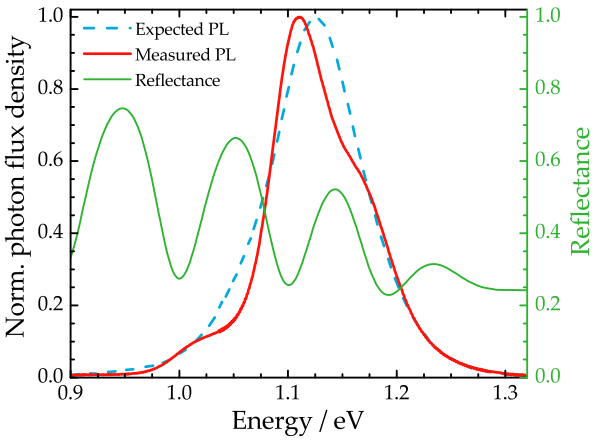

FIGURE 4.1: Photoluminescence spectrum of a CIGS absorber plotted as photon flux density in function of photon energy. Normally, for Cu-poor material, one expects a broad peak (dashed blue curve) but PL measurements reveal a slightly distorted structure (red curve). The reflectance spectrum measured on the same samples shows huge variations that are due to multiple-beam interference. The thus-induced reflectance minima line up reasonably well with the PL maxima, indicating that the distorted PL structure is due to interference effects.

results that show strong hints towards the presence of interference effects without even considering the possibility of their existence [147], [184], [185]. The latter examples clearly show that interference effects are a major problem as they can hinder the correct interpretation of measured luminescence spectra.

It is important to mention that the occurrence of interference effects is not only limited to chalcopyrites but can be observed in a wide variety of other thin-film semiconductor materials such as SiO_2 [186], a-Si [186], ZnSe [187], AlGaN/GaN [188], or ZnO/ZnMgO [189]. Additionally, experimentally, the interference fringes are not only observed in the PL spectra, but also in other luminescence-based spectroscopy techniques such as UV-vis, electroreflectance [190], electroluminescence [177], or cathodoluminescence [186].

This chapter focusses on the thin-film interference effects that are observable in Cu(In,Ga)Se_2 thin films. To understand why interference fringes are observable in the first place, the origin of the photoluminescence within the CIGS absorber has to be identified. The first section 4.1 investigates the influence of the graded band gap on the radiative recombination activity of charge carriers by performing an exfoliation experiment where the photoluminescence is measured under different sample configurations and orientations. This section is largely based on ref. [191].

Section 4.2 describes the theoretical aspect of the interference effects. Since the CIGS absorber with its surface and varying gallium content constitutes a very complicated structure, a simplistic approach is taken to understand the core experimental parameters that influence the interference effects.

Based on the findings and elucidations of the preceding section, section 4.3 introduces an experimental concept with which it is possible to reduce the interference fringes observable in room-temperature PL spectra. This concept consists of measuring the PL for varying angles and constitutes a powerful tool to quickly test for the presence of interference effects during measurements. The concept was conceived and experimentally developped within the framework of this thesis. This section is largely based on ref. [192].

The final section 4.4 of the chapter introduces a scattering layer that can be deposited onto the surface of the absorber. The scattering layer severely reduces the interference effects which enables photoluminescence studies even at low temperatures in a cryostat. The section presents the scattering layer deposition method of choice as well as its influence on the PL spectra of the samples itself. The contents of this section are to be published in ref. [193].

4.1 Origin of near band edge photoluminescence

The concept of the double gallium gradient and consequently the graded band gap structure in Cu(In,Ga)Se_2 was introduced in section 2.6.2 where a typical GGI profile was shown. In this context, Fig. 4.2 shows the same GGI profile (blue curve) as well as the GGI profile of a CIGS absorber grown in a high-temperature co-evaporation process (red curve). The graph serves to highlight the general differences between the GGI profiles for both types of samples. The sample grown in the low-temperature co-evaporation process shows a much stronger front gradient but a weaker back gradient all the while being considerably thinner. The sample grown in the high-temperature co-evaporation process, in contrast, shows a very weak front gradient but a very strong back gradient that reaches GGI values of up to 0.65. It is crucial to note that both types of samples show a GGI or band gap minimum at the surface and inside the bulk (as illustrated by the gray dashed lines). In photoluminescence spectroscopy experiments, the electron charge carriers are excited into the conduction band after illumination. Prior to undergoing a radiative recombination process, the excited charge carriers diffuse along the

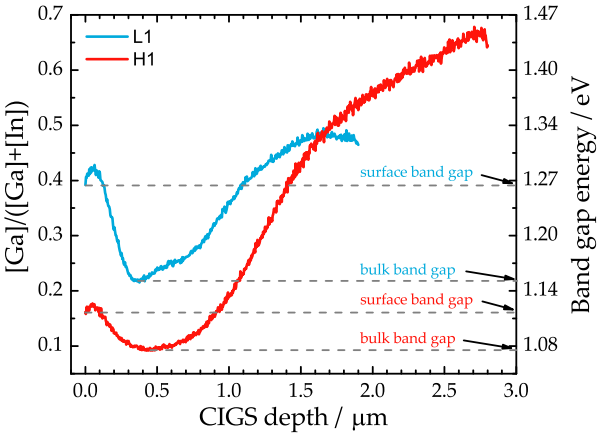

FIGURE 4.2: GGI profile and band gap energies E_g of two distinct CIGS absorbers in dependence of their thickness. The blue curve shows the GGI profile and E_g of sample L1 that has been grown in a low-temperature co-evaporation process. The red curve shows the GGI profile and E_g of the H1 sample grown in a high-temperature co-evaporation process. The graph serves to highlight the differences in band gap gradients between both types of samples. Measurements done by Dr. Romain Carron from Empa.

graded band gap structure to a state of minimum energy. Since the graded band gap structure suggests that there are two different band gap minima, it is *a priori* not clear from which one the charge carriers recombine radiatively.

Given the different locations of the band gap minimum within the absorber, it is possible to probe the energy of the emitted photon flux density in the photoluminescence measurements by illuminating the CIGS absorbers either from the front side or from the back side. *A priori* it can be assumed that a frontal excitation leads to a recombination from the surface band gap minimum while a back-side excitation leads to a diffusion and subsequent recombination of the charge carriers from the band gap minimum inside the bulk. Since the CIGS absorbers are grown on the molybdenum metal back contact, it is not possible to simply illuminate the samples from the back because the laser light does not reach the absorber. To circumvent the Mo layer, the samples will need to be exfoliated from the Mo-coated substrate glass first. The whole exfoliation process along with the PL measurements in the different configurations is summarized in Fig. 4.3 for the case of a sample stack consisting of a CdS-covered CIGS absorber grown on a Mo-coated SLG substrate. The sample chosen for this experiment was the HS sample (see section 3.3). Unfortunately, the exact GGI profile is not available but it is assumed that it follows the same trend as the one of sample H1 shown in Fig. 4.2. This particular sample was chosen as it does not exhibit interference fringes in its room-temperature PL spectrum (see section 4.2.1 for more information). The exfoliation process is split into three distinct steps. In the first step, Fig. 4.3 (a), the PL is measured in the normal (N) configuration where the sample is illuminated from the front. In a second step, Fig. 4.3 (b), the exfoliation process is prepared by glueing a glass substrate onto the surface of the CIGS absorber. The glue that is used is a two-component transparent epoxy glue that was shown to not contribute any significant PL signal in the relevant energy range. In order to monitor the influence of the glass and glue on the absorber and to have a reference measurement prior to the exfoliation, the PL is measured through the glass and glue in the (G) configuration. In the last step, Fig. 4.3 (c), the absorber is mechanically detached from the Mo-coated substrate enabling the PL measurement from the back side of the absorber i.e. in the (ExB) configuration. In addition, to investigate the influence of the exfoliation process itself, the PL is again measured through the glass in the (ExG) configuration.

The results of the exfoliation study are shown in Fig. 4.4 where the PL spectra measured in the different configurations are shown in a semi-logarithmic representation to facilitate comparison. The black curve shows the PL spectrum of the CIGS absorber measured in the normal (N) configuration and serves as a reference spectrum as this is the usual configuration for PL experiments. The red curve shows the PL spectrum that was measured in the (G) configuration after glueing the glass substrate onto the surface of the absorber. Compared to the PL spectrum

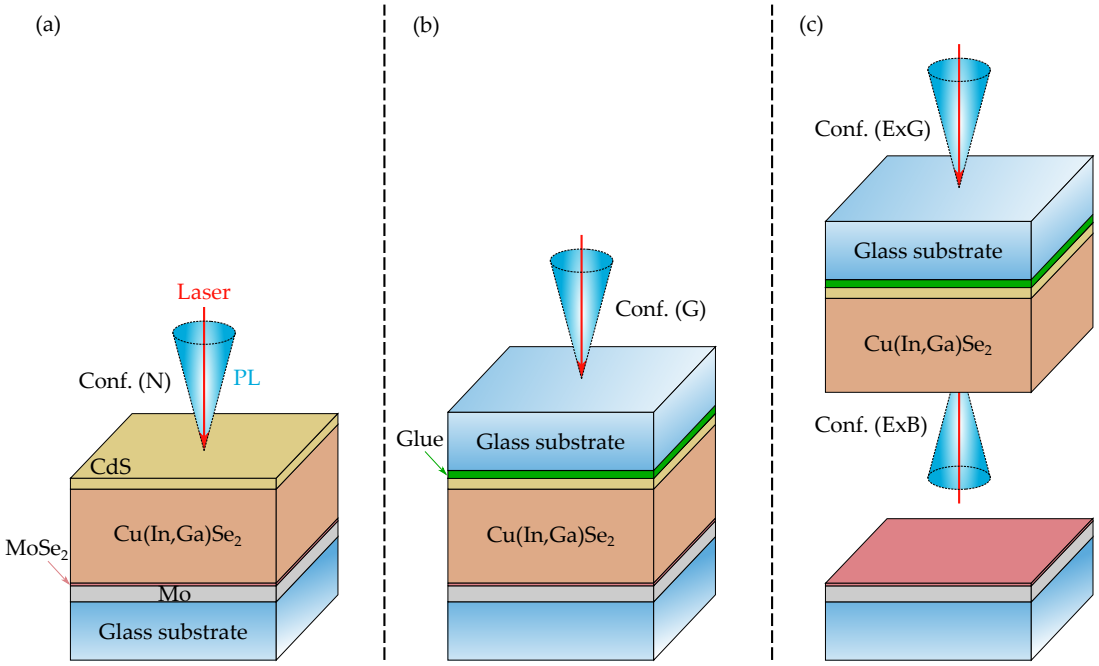

FIGURE 4.3: Schematic illustration of the exfoliation process and its accompanying photoluminescence measurements on a CdS-covered CIGS absorber grown on a Mo-coated soda-lime glass substrate. **(a)** PL (blue cone - representing here only the fraction of the PL as collected by the detector) measured in the normal configuration (N) as a result of laser illumination (red arrow) from the front side. **(b)** Deposition of a glass substrate onto the surface of the absorber using a two-component epoxy glue and subsequent PL measurement through the glass substrate and glue (G). **(c)** Detachment of the absorber from the original substrate through exfoliation and PL measurements from the back side (ExB) and from the front side (ExG). Figure adapted from ref. [191].

measured in (N), the spectrum in (G) shows a clear decrease in the photon flux density. This is due to the fact the laser light is partially scattered and partially absorbed by both the glass substrate and the glue before reaching the CIGS absorber. Likewise, the emitted luminescent light is also partially scattered and absorbed before being collected by the detector. Aside from the difference in photon flux density in both configurations, the measured PL spectra are identical. Thus, the glueing process itself does not induce any change, be it structural or optoelectronic, in the absorber and the location of radiative recombination remains the same. After the exfoliation of the absorber from its original substrate, the subsequent PL measurement in the (ExB) configuration reveals the existence of two peaks in the PL spectrum. The peak at high energies is centered around the transition energy of 1.31 eV and will be discussed further below. The peak at low energies represents the main radiative transition in this measurement configuration. Comparing this transition energy to the transition energies observed in the (N) and (G) configurations reveals a red-shift of approximately 14 meV. Since the excitation of the absorber is done entirely from the back side, the low-energy peak in the (ExB) configuration can only be due to a radiative recombination from the band gap minimum inside the bulk. As such, the energy difference of 14 meV in the transitions observed in the (N) and (ExB) configurations may suggest a different recombination location inside the absorber. However, the PL spectrum measured in the (ExG) configuration shows a peak with a transition energy identical to the low-energy transition in the (ExB) configuration. Thus, the transition energy in the (ExG) configuration also shows the same red-shift of 14 meV compared to the transition energy in the (G) configuration. Since the excitation profiles in the (G) and (ExG) configuration are identical, the radiative recombination has to be occurring from the same band gap minimum. Furthermore,

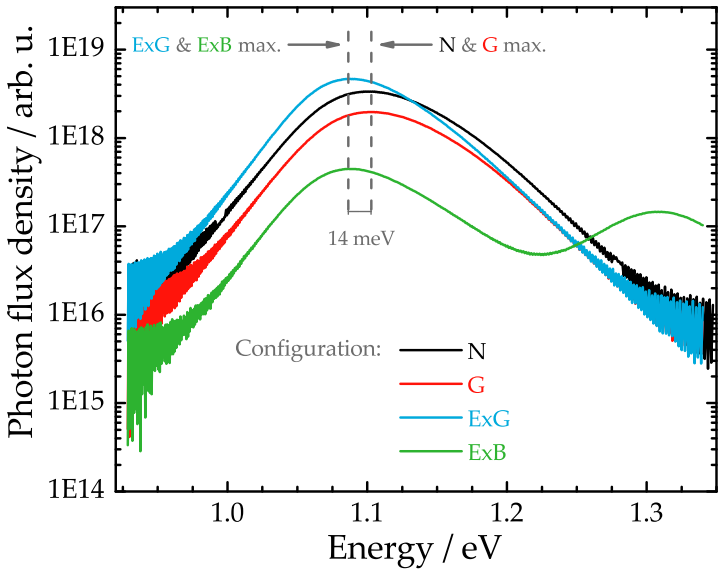

FIGURE 4.4: Semi-logarithmic representation of the PL spectra measured at the different stages during the exfoliation process described in Fig. 4.3 on the HS sample covered by a CdS buffer layer. The black curve shows the PL measured in the normal (N) configuration. The red curve shows the PL measured after the glass substrate was glued to the surface of the absorber in the (G) configuration. The blue and green curves show the PL spectra measured after exfoliation from the front through the glass (ExG) and from the back (ExB), respectively. Both PL spectra measured after exfoliation show a transition energy that is red-shifted by 14 meV compared to the transition energy measured before the sample detachment. The PL spectrum measured in the (ExB) configuration shows an additional radiative transition at around 1.31 eV. Figure adapted from ref. [191].

since the low-energy transitions in the (ExB) and (ExG) configurations are identical, the recombination in all four configurations has to originate from the band gap minimum located inside the bulk and not from the surface.

Since the radiative recombination in all four configurations (except for the high-energy transition in (ExB)) is originating from the same band gap minimum, the clearly observable red-shift of 14 meV before and after exfoliation has to be of a different origin. To investigate this red-shift, part of the experiments in Fig. 4.3 are repeated on the H1 sample. The sample is first measured in the normal (N) configuration, then cut into two pieces which are then exfoliated. However, one piece of the sample is detached only 3 hours after the glueing process while the second piece is detached 96 hours after the glueing process. After the exfoliation of each piece, the PL is measured in the (ExG) configuration and compared to the reference (N) measured spectrum. The results are shown in Fig. 4.5. The sample piece that was exfoliated after only 3 hours shows a red-shift of 29 meV (blue curve) while the sample piece that was exfoliated after 96 hours shows a clearly reduced red-shift of 10 meV (green curve) when compared to the reference signal (red curve). The same experiment was repeated on the bare H1 absorber where exfoliating the absorber from the substrate after only 6 hours yielded a red-shift of 18 meV, while the exfoliation after a curation time of the glue of 168 hours led to a reduced red-shift of 10 meV. The details about this experiment are provided in appendix C.1.

These experiments show that the red-shift is linked to the circumstances of the exfoliation process, more specifically to structural changes to the CIGS absorber crystal. Due to the lattice mismatch between CIGS and Mo, the CIGS crystal structure is expected to be slightly strained. During the detachment, the CIGS is removed from the back contact and its structure is able to relax. The different energy red-shifts suggest that the more time the glue has to harden, the weaker the strain release after detachment and the smaller the red-shift. Similarly, the less

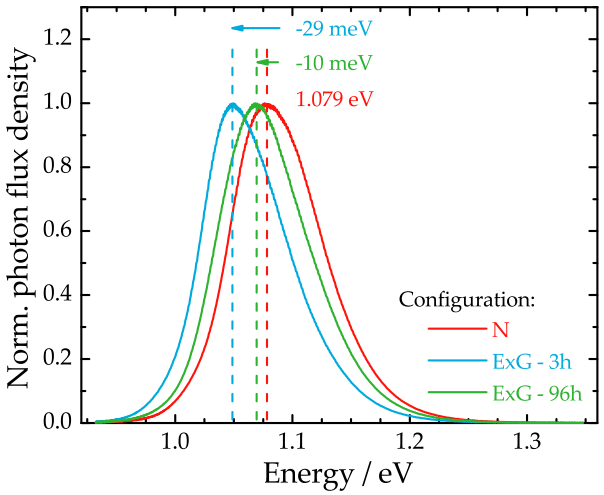

FIGURE 4.5: PL spectra measured on the CdS-covered H1 absorber. The red curve shows the PL spectrum measured in the normal configuration (N) prior to exfoliation. The blue curve shows the PL spectrum measured in the (ExG) configuration on the exfoliated absorber piece after a glue curation duration of 3 hours while the green curve shows the respective spectrum after a curation time of 96 hours. Figure adapted from ref. [191].

time the glue has to harden, i.e. the softer it is, the stronger the strain release and the larger the energy red-shift. As such, the observed red-shift after exfoliation is potentially due to a band gap energy reduction that is a direct result of a strain release within the crystal structure of CIGS. Since the CIGS solid solution with its varying Ga content constitutes an extremely complex structure, it is not straightforward to theoretically predict the band gap change that follows any kind of structural change and it is difficult to relate with a certain amount of strain release. X-ray diffraction measurements are able to provide more insight into these suggested structural changes and were attempted. However, the presence of the glue layer leads to a broad peak (due to the glue's amorphous structure) that overlays the CIGS features in the XRD diffractogram such that a meaningful interpretation was not possible.

Finally it has to be mentioned that the red-shift could potentially also be due to inhomogeneities between the different absorber pieces that were analysed in the exfoliation experiments. However, as is shown in section 5.2.2, sample H1 is spatially homogeneous with its main radiative transition energy exhibiting a standard deviation of 3 meV across the whole absorber length. Since the magnitude of this standard deviation is considerably less than any red-shift observed after absorber detachment, the possibility that the change in emission energy is due to absorber inhomogeneities can be excluded.

Looking at the PL spectra displayed in Fig. 4.4, one can see that the photon flux density measured in the (ExG) configuration is highest. This increase in the photon flux density after exfoliation can be explained by the reduced band gap energy. Comparing the PL spectra of configurations (G) and (ExG), it is evident that their high-energy slopes are identical. According to section D.1, this means that their quasi-Fermi level splittings are also identical. The same quasi-Fermi level splitting in a lower band gap material directly translate into a larger density of excited charge carriers which then translates into a larger radiative efficiency which is exactly what is observed here.

In the previous description of Fig. 4.4, the additional energetic transition at 1.31 eV observable in the (ExB) configuration has already been mentioned. Looking at the GGI profiles in Fig. 4.2 suggests that this high-energy transition is likely to be occurring from somewhere at the back of the absorber. This is reinforced by the fact that the transition is only observable when illuminating the absorber from the back side. The reduced photon flux density originating from the band gap minimum inside the bulk in the (ExB) configuration can be explained by this additional radiative recombination at the back since only charge carriers that have not yet recombined at the back can diffuse into the bulk. However, for the charge carriers to recombine at the back in the first place, there has to be some transport barrier otherwise the charge carriers would all be expected to diffuse into the band gap minimum. Scanning electron

microscope cross-section investigations have revealed that CIGS absorber that are grown following the three-stage process (i.e. exhibiting the graded band gap structure) are likely to exhibit smaller grains close to the back contact (see e.g. [194], [195]). It is thus likely that the increased amount of grain boundaries at the back of the absorber effectively leads to transport barriers for the excited charge carriers, limiting their diffusion properties. As a consequence, only the charge carriers that are either able to overcome these barriers or which are excited further inside the bulk are able to diffuse into the band gap minimum. This interpretation is reinforced by PL measurements with varying laser powers shown in the Appendix C.2. Finally, the increased density of grain boundaries at the back of the absorber would also lead to an increased non-radiative recombination rate which explains the overall smaller photon flux density of the PL spectrum measured in the (ExB) configuration.

Thus, the exfoliation experiments clearly show that the photoluminescence in state-of-the-art absorbers is originating from the band gap minimum inside the bulk. This interpretation is underlined by similar results from literature where e.g. Neumann *et al.* measured PL on consecutively etched absorbers [196] and Haarstrich *et al.* measured depth-dependent cathodoluminescence on CIGS [197].

4.2 Thin-film interference

The occurrence of interference effects in thin films is not a novel concept and is treated in every standard optics textbook (see e.g. [198], [199]) and is used in many applications (such as anti-reflection coatings). In a thin film, interference effects are observable because light beams are entering the film from outside, are reflected multiple times from the partially reflective surfaces inside the film and upon exiting, create an interference pattern. This multiple-beam interference pattern is characterised by a particular pattern of alternating high and low intensity which is a consequence of constructive and destructive superposition of the coherent light wavefunctions. The conditions for constructive and destructive superposition depend on the difference in optical path and thus the phase difference that the individual light beams accumulate on their way through the thin film. In the simplest case, the intensity of the interfering light outside the film I_{out} is proportional to the Airy function [198]

$$I_{\text{out}} \propto \frac{1}{1 + \mathcal{F} \sin^2\left(\frac{\Delta}{2}\right)}, \tag{4.1}$$

where $\mathcal{F}$ is the so-called coefficient of finesse that describes the sharpness of the interference fringes. The quantity Δ represents the phase difference between two successive beams and its value dictates whether the interference is constructive (large I_{out}) or destructive (small I_{out}). Under its most simple form, the phase difference is given as [198]

$$\Delta = \frac{4\pi}{\lambda_0} n\, d \cos\theta, \tag{4.2}$$

where λ_0 is the vacuum wavelength of the light, n is the refractive index of the thin film, d is the film thickness and θ is the specular reflection angle inside the film. The multiple-beam interference, sometimes also called Fabry-Perot interference, is typically observed in the reflectance spectra of thin films and, as such, can be seen as the green curve in Fig. 4.1 for the case of a state-of-the-art CIGS absorber. During the description of Fig. 4.1 it was already mentioned that the interference fringes in the reflectance spectrum match the interference fringes in the photoluminescence spectrum reasonably well. However, the agreement is not perfect as the interference pattern in the PL spectrum is not only due to multiple-beam interference (MBI)

but also due to wide-angle interference (WAI) [181]. Wide-angle interference only occurs when the light is emitted from a narrow location inside the film[1]. Since, as was shown in the previous section 4.1, the luminescence in double graded CIGS absorbers is originating from the localized band gap minimum inside the bulk, the interference pattern in CIGS is assumed to have both MBI and WAI contributions. As a graphical example, Fig. 4.6 illustrates the emitted luminescence from the band gap minimum and two possible paths it can take through the absorber and will serve as a basis for the following discussion.

For interference effects to occur in the photoluminescence spectra of CIGS, several conditions have to be met [181]. Upon originating from the band gap minimum inside the bulk, the light is emitted into a solid angle of 4π. Since the energy of the emitted photons is determined by the band gap minimum, the probability of re-absorption (and re-emission) on their way through the absorber is relatively low. As such, the emission centre at the band gap minimum constitutes a coherent light source and is one of the main reasons why interference effects are likely to be seen in state-of-the-art band gap graded CIGS absorbers. After their emission, the photons are partially reflected from the surface- and back contact interfaces. Especially for the case of MBI, the reflectivity at the interfaces must be sufficiently high. Additionally, in order for specular reflection to take place, the surface and interface roughness must be relatively small. More specifically, the surface roughness, being very sensitive to the particular absorber growth conditions, plays an important role in the occurrence of interference effects (see section 4.2.1

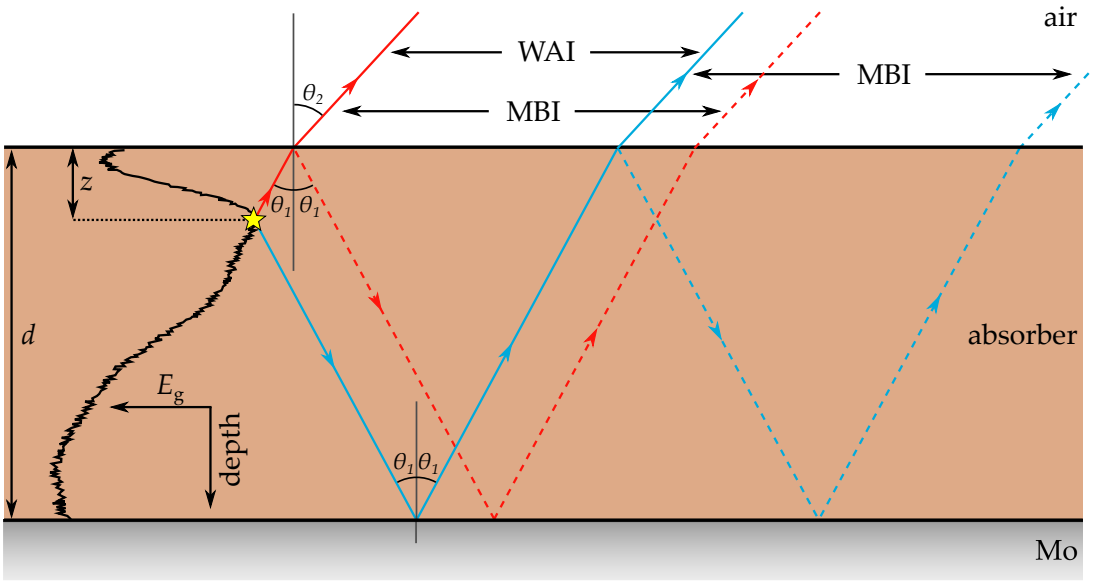

FIGURE 4.6: Schematic illustration of the path that the photoluminescence, emitted from within the CIGS absorber of thickness d, can take. For simplicity, only two light rays are shown and the $MoSe_2$, as well as a potential CdS layer, are omitted. After originating from the band gap minimum, located at a distance z inside the absorber, the coherent light rays can go either towards the surface (red lines) or towards the back contact (blue lines). In addition, the light rays are partially reflected at the layer interfaces under the reflection angle θ_1. Upon exiting the absorber under the angle θ_2 the rays interfere depending on the path they have taken i.e. depending on the phase difference they have accumulated. In this situation, light rays of the same color undergo a multiple-beam interference (MBI) while light rays of a different color undergo a wide-angle interference (WAI).

[1]Reflectance spectra are measured by illuminating the thin film with an external light source and then measuring a ratio between reflected and reference light intensities. As such, the measured light is always originating from the external source, and never from a light-emitting process inside the film. As a consequence, wide-angle interference cannot be seen in typical reflectance or transmittance spectra.

for more details). Finally, the thickness of the absorber also plays an important role as it determines the spectral distance between the interference fringes. For a film thickness of 2 - 3 μm, as is typical in state-of-the-art CIGS, the interference fringes are such that they heavily influence broad spectral signals (cf. Fig. 4.1). The influence of the absorber thickness on the interference fringes in PL spectra is described in section 4.2.2.

Thus, the occurrence of interference in thin-film CIGS can be attributed to four causes: weak re-absorption of the emitted PL throughout the absorber, high reflection from the internal interfaces, a smooth surface, and an absorber thickness that is of the same order of magnitude as the emitted PL wavelength.

Due to the simultaneous contribution of MBI and WAI to the overall interference pattern, as well as the depth-dependent structural nature (GGI gradient) of CIGS affecting its dielectric properties, modelling the interference fringes is not a straightforward task. For the less complicated structure of homogeneous SiO_2 and amorphous Si films, Holm *et al.* derived a model describing the interference function based on the spontaneous emission of randomly oriented electric dipoles inside the absorber [186]. Recently, Larsen *et al.* have modified this model for the case of $CuZnSnS_4$ and $Cu(In,Ga)Se_2$ thin-films by including the roughness of the interfaces [181]. Using this model to describe the experimentally measured interference fringes requires the exact knowledge of various properties of the thin absorber film such as the dielectric functions, surface roughness, and exact PL emission depth which necessitates tremendous experimental work. This is why, in the following, the most important part of the model, i.e. the phase difference between the waves, is discussed qualitatively. Both MBI and WAI contribute to slightly different phase differences [181], [186] (adapted to the situation in Fig. 4.6) according to

$$\Delta_{\mathrm{MBI}} = \frac{4\pi}{\lambda_0}\, n_{\mathrm{CIGS}}\, d \cos\theta_1 \tag{4.3}$$

$$\Delta_{\mathrm{WAI}} = \frac{4\pi}{\lambda_0}\, n_{\mathrm{CIGS}}\, (d - z) \cos\theta_1. \tag{4.4}$$

As can be seen, the MBI contribution to the phase difference (4.3) is equal to eq. (4.2). The WAI contribution is of a similar form, but the phase difference has a slightly spatially-dependent offset in $d - z$ due to the localised emission centers in the absorber. Both MBI and WAI contribute to the observed interference fringes in the PL spectrum with the MBI creating the oscillating fringes as observed in the reflectance spectra and the WAI superposing a beating pattern [186]. Depending on the distribution width of the emission centres within the absorber, either one of the MBI and WAI can be the dominating contribution. For example, the photoluminescence in typical epitaxial thin-film ZnSe is expected to originate from a wide distribution of radiative recombination centers. Consequently, the observed interference fringes are due to MBI and have successfully been modelled by a modified Airy function by Weber *et al.* [176]. In fact, according to Larsen *et al.*, the WAI is only of importance if the emission originates from centers that are distributed within a width of less than 80 nm [181].

4.2.1 Influence of surface roughness on interference

As was already mentioned, the internal specular reflection plays an important role for the observation of interference fringes as the light beams have to travel several times through the absorber to accrue varying phase differences that lead to the alternating constructive and destructive interference pattern. If the internal reflection would not be specular but instead diffuse, the coherence between the different light beams would vanish and the interference fringes would smear out. Specular reflection with a fixed reflection angle θ_1 occurs at smooth interfaces while diffuse reflection, with a distribution of reflection angles, occurs at rougher interfaces.

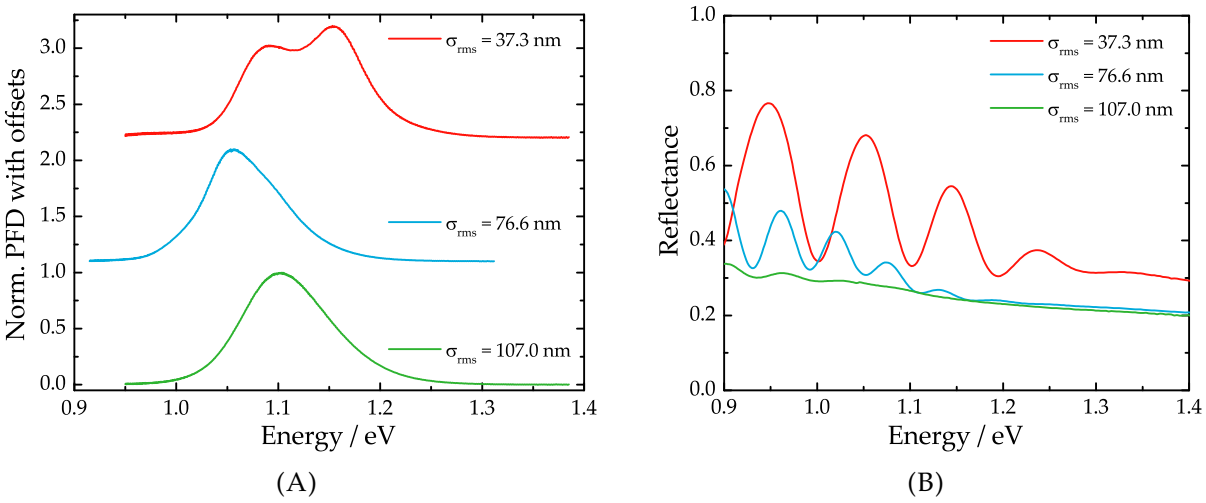

FIGURE 4.7: **(A)** Normalized PL spectra (labelled PFD - photon flux density) of samples L1 (red curve), H1 (blue curve) and HS (green curve) with offsets for improved visualization purposes. Also indicated are their respective surface roughness σ_{rms} as measured by atomic force microscopy (measured by Dr. Yves Fleming from the Luxembourg Institute of Science of Technology). **(B)** Respective reflectance spectra, plotted over the same spectral range as the PL spectra. Both PL and reflectance measurements were done on the CdS-covered CIGS absorbers.

Typically the Mo/MoSe$_2$/CIGS interface in state-of-the-art absorber is always considered to be relatively smooth such that the internal reflection depends mainly on the surface roughness. Depending on the growth conditions, it is possible to form CIGS absorber with smooth or rough surfaces. Fig. 4.7A shows the room-temperature PL spectra measured on three absorbers exhibiting a considerably different surface roughness. Connectedly, Fig. 4.7B shows their respective reflectance spectra. Also indicated are the surface roughness in the form of the root-mean-square distribution σ_{rms} as measured by atomic force microscopy (AFM). Sample L1 (red curve) shows a very smooth surface with $\sigma_{\text{rms}} = 37.3\,\text{nm}$ and exhibits huge interference fringes that lead to the formation of two distinct peaks in the PL spectrum. Sample H1 (blue curve), with a surface roughness of $\sigma_{\text{rms}} = 76.6\,\text{nm}$ shows a reduced interference pattern but the PL spectrum is still distorted. Sample HS (green curve), due to its surface roughness of $\sigma_{\text{rms}} = 107.0\,\text{nm}$, exhibits almost no interference fringes in the spectral range of interest and, as a consequence, its PL spectrum shows a single broad peak. The latter value of 107 nm is in close agreement with the value of 120 nm that the model of Larsen *et al.* predicts for a significant reduction of interference effects [181]. It needs to be mentioned that the three samples exhibit different band gap minimum energies which is why the PL emission energy as well as the energetic onset of interference fringes in the reflectance spectra is not identical between the samples.

As a conclusion of these results, it can be argued that the surface roughness indeed plays an important role for the occurrence of interference effects. Consequently, to remove the interference fringes from the measured spectra, one could think of purposefully growing absorbers with rough surfaces. However, the surface roughness is not directly controllable and rather a by-product of the state-of-the-art co-evaporation process that leads to highly-efficient CIGS solar cell devices. If the surface roughness is to be increased, this has to be done artificially, for example by depositing an supplementary scattering layer on the surface (see section 4.4).

4.2.2 Influence of absorber thickness on interference

The occurrence of interference effects in thin films is mainly due to the fact that the film thickness is of the same order of magnitude as the wavelength of the interacting or emitted light. The effect of the film thickness on the phase difference and interference pattern can be seen in equations (4.1)-(4.4). Increasing the film thickness leads to a reduced spectral inter-fringe distance as well as a reduced interference amplitude. This effect is shown in Fig. 4.8 where the PL spectrum of the 2 μm thin L1 absorber (red curve) is compared to the spectrum of a 4 μm thick CdS-covered CIGS sample (blue curve). In contrast, decreasing the film thickness leads to an increase in the interference amplitude as well as the inter-fringe distance. As such, one could think of growing thinner CIGS absorbers where the inter-fringe spacing is so large as to not affect the measured PL peak. Similarly, in thicker CIGS absorbers the interference fringes would have amplitudes that are too small to distort the PL spectrum. According to Larsen *et al.*, for interference effects to not play a role in the PL of CIGS, the absorber would need to be either thinner than 500 nm or thicker than 10 μm [181]. While ultra-thin CIGS absorber are currently a relevant research topic (see e.g. [200], [201]), thicker CIGS are of no technology-relevant importance. In any case, neither ultra-thin nor thick CIGS absorbers are considered state of the art and thus the current growing process cannot be adapted to change the absorber thickness.

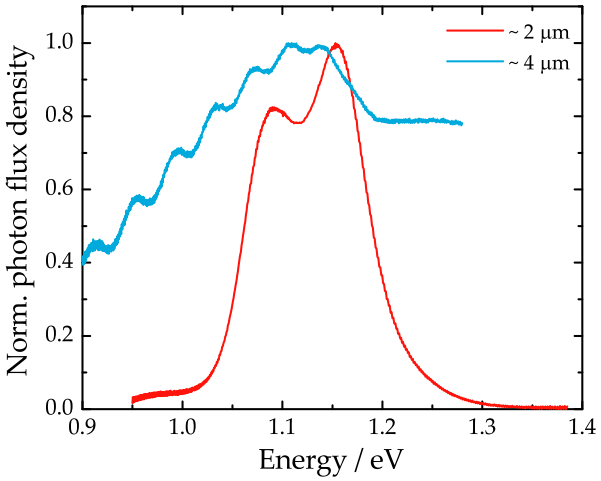

FIGURE 4.8: Normalised PL spectra of the 2 μm thin L1 CIGS (red curve) and of a 4 μm thick CIGS sample (blue curve). Both absorbers are covered by a CdS layer. The thick absorber was grown specifically for this thickness comparison by simply extending the co-evaporation growth duration. As such, the CIGS absorber is of unknown quality but its PL spectrum suggests it to be mediocre as its shape is completely different from a single broad peak that is characteristic for Cu-poor CIGS.

4.3 Angle-resolved photoluminescence

Equations (4.3)-(4.4) describe the dependence of the phase difference on the beam path through the absorber via the internal reflection angle θ_1. As a result, light beams that are reflected under different angles θ_1 will contribute to different phase differences and ultimately lead to a spectrally shifted interference pattern. In angle-resolved photoluminescence (ARPL) spectroscopy, it is possible to measure these different interference patterns by measuring the photoluminescence of the sample for varying entrance and detection angles Θ. By making use of these shifts, it is possible to remove the influence of the interference fringes from the PL spectra. The experimental setup for ARPL measurements at room temperature is schematically illustrated in Fig. 4.9 and its working principle is explained in the following.

The ARPL setup consists of a motorized rotary disc platform onto which a sample holder is fixed. The sample is pinched into the sample holder such that the sample surface lies exactly on the rotation axis of the rotary disc platform. This ensures that the incident laser spot on the sample surface remains stationary even at large angles Θ. In the standard configuration, the laser is irradiating the sample along the surface normal with the emitted PL being collected

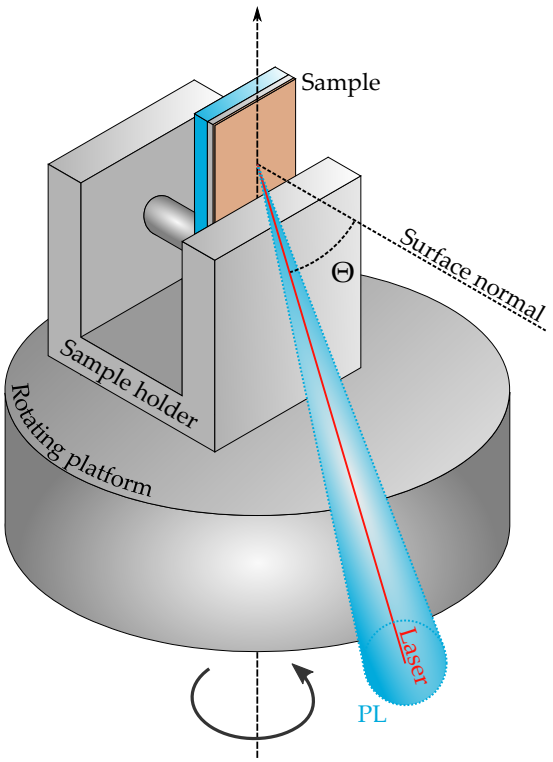

FIGURE 4.9: Schematic illustration of the sample setup for angle-resolved photoluminescence measurements. The sample is pinched by a holder that is fixed to a rotary disc platform such that the sample surface lies exactly on the platform's rotation axis. By varying the rotation angle Θ, it is possible to measure the PL (blue cone) that results from the laser excitation (red line) for different directions compared to the surface normal (black dashed line).

along the same path. In this standard configuration, only PL photons that are hitting the internal surface under very small angles θ_1 (cf. Fig. 4.6) are able to be collected by the stationary detector outside the sample. After tilting the sample by an angle Θ, the previously measured photons are unable to reach the detector and only photons that hit the internal surface at a larger angle $\theta_1' > \theta_1$ are collected. Since varying the internal angles θ_1 directly translates to collecting photons with different phase differences, the interference fringes are shifted in the measured PL spectra.

In this context, Fig. 4.10A shows the PL spectra measured on the CdS-covered H0 CIGS absorber (see section 3.3 for details) for a multitude of angles Θ, ranging from 0° to 75° in steps of 5°. The shifts of the interference fringes with the varying angles can very clearly be seen in the semi-logarithmic representation of the PL spectra. Also observable is a steady decrease of the photon flux density with increasing angles. This decrease can be attributed to two reasons. Firstly, since the PL detector is stationary, increasing the tilting angle leads to the detection of a reduced fraction of emitted photons. In section 2.4, it was assumed that the electromagnetic radiation emitted from the sample surface obeys Lambert's cosine law. As such, the decrease of the photon flux density with increasing angles Θ should be proportional to $\cos(\Theta)$. Secondly, the rotation of the sample leads to an elliptic distortion of the otherwise circular laser spot on the surface. Thus, the incident photon flux density from the laser also decreases by a factor $\cos(\Theta)$ for larger angles. Integrating the different PL spectra and plotting the integrated photon flux density against the rotation angle yields the graph shown in Fig. 4.10B. While there are some slight discrepancies for intermediate angles, the integrated photon flux density (red dots) follows the decrease dictated by $\cos^2(\Theta)$ (blue dashed line) reasonably well. The exact cause for the discrepancy at intermediate angles is not fully known but it is speculated that the CIGS surface does not perfectly behave like a Lambertian surface.

From Fig. 4.10A it is evident that measuring the PL for increasing angles leads to the interference fringes gradually spectrally shifting from a minimum into a maximum. By adding the different spectra, as a consequence, one would expect that the interference fringes cancel out. Before doing so, however, the PL spectra first need to be scaled. Since the photon flux

density decreases with increasing Θ according to $\cos^2(\Theta)$, the individual spectra can be scaled by multiplying them by $\cos^{-2}(\Theta)$. This scaling process results in the PL spectra all having a similar photon flux density as shown in Fig. 4.10C. By adding up all the scaled PL spectra and dividing the resulting spectrum by the total number of spectra, one finds the interference-free spectrum (blue curve) shown in Fig. 4.10D. By comparing the interference-free PL spectrum to the interference-riddled spectrum measured at 0° (red curve), it can be seen that the interference fringes at low energies have completely vanished. Additionally, the comparison also reveals that the high-energy slope is identical in both spectra. This latter result is of utmost importance because it clearly states that the high-energy slope is not affected by interference effects and can also be evaluated without removing them from the PL. The reason for the unaffected high-energy slope is briefly explained in section 4.3.2.

The underlying idea of removing the interference fringes from the PL spectra by measuring

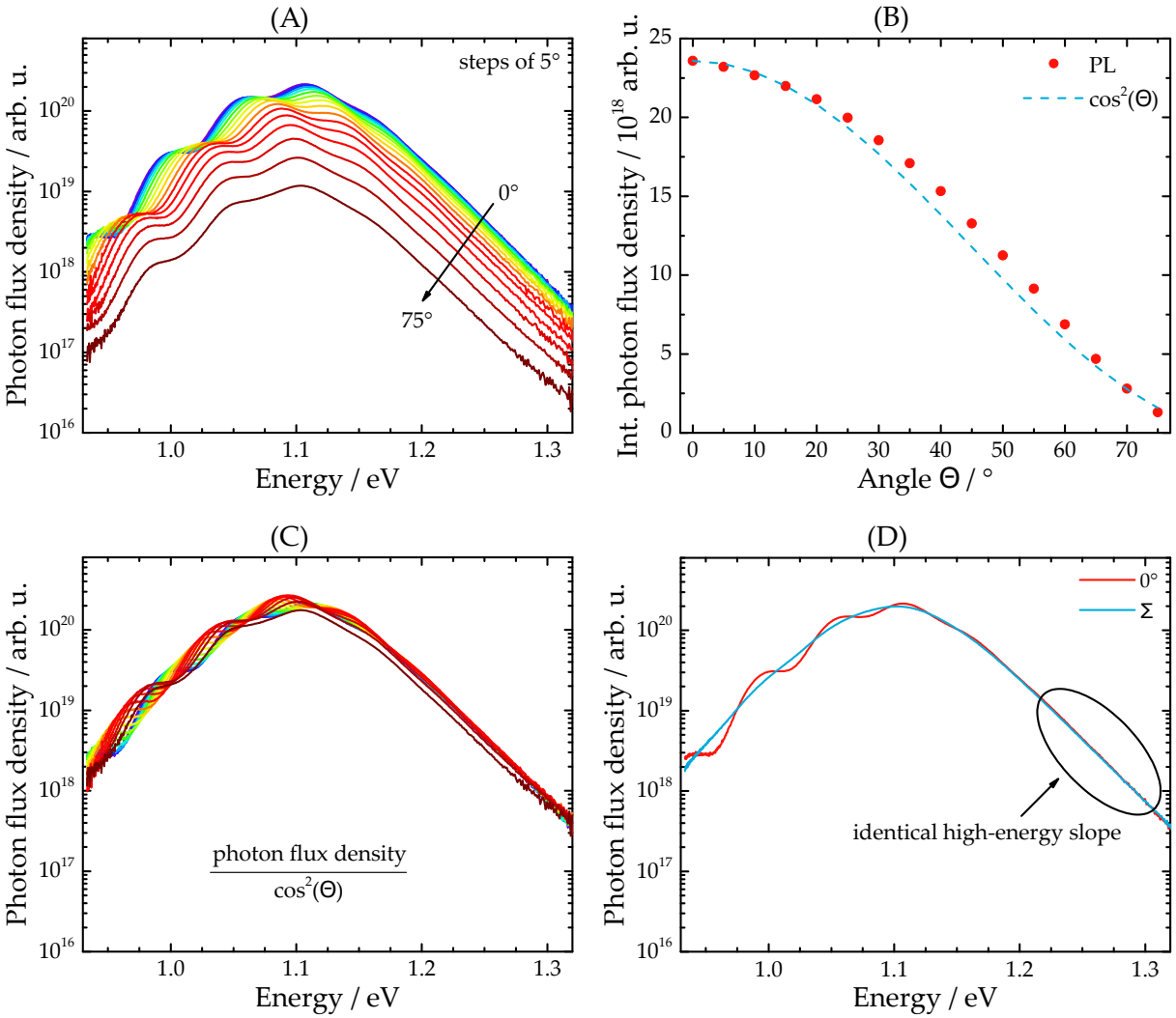

FIGURE 4.10: **(A)** PL spectra measured under varying excitation/detection angles Θ, from 0° to 75° in steps of 5°. The measurements are done on the CdS-covered absorber of the H0 sample. **(B)** Integrated photon flux density of the PL spectra (red dots) plotted against the tilting angles. The decrease in photon flux density closely follows a $\cos^2(\Theta)$-dependence (blue dashed line). **(C)** Multiplying the various PL spectra by $\cos^{-2}(\Theta)$ leads to the curves being scaled to a similar common photon flux density. **(D)** Comparison between the PL spectrum measured at 0° (red curve) and the interference-free PL spectrum (blue curve) that results from summing and averaging over all scaled PL spectra.

ARPL is based on measuring the various photons that have accumulated different phases. In Fig. 4.10, the PL at a total of 16 different angles was measured. To measure all the possible contributions, it would theoretically be necessary to measure every angle between 0° and 90°. However, this is experimentally not feasibly, especially for the case of very large angles approaching and including 90°. The fact that an interference-free PL spectrum can still be extracted from ARPL measurements can be explained by the very small contribution of the photons to the total phase difference at large angles. At very large angles, the optical path of the photons through the absorber is so large that the coherence between the light waves is diminished. This can be seen in Fig. 4.10A where the interference fringes in the 75° PL spectrum are less severe than in the 0° spectrum.

The interference-free PL spectrum is extracted by summing up and averaging over all the PL spectra measured at different angles such that the fringe maxima shift into the minima and cancel each other out. *A priori* one would think that it would suffice to measure the PL only at two distinct angles, where the minima and maxima of the fringes are shifted *exactly* into each other. However, this would only be possible if the spectral distance between the interference fringes were constant over the energy range of interest (which is quite wide since the PL peak is several 100 meV broad). This is not the case in state-of-the-art CIGS absorbers mainly due to the fact that the elementary composition throughout the thickness is not identical (e.g. double gallium gradient) such that the dielectric constants, and hence the refractive index, will vary throughout the thin film and are thus strongly wavelength-dependent. Thus, measuring the PL at a multitude of angles is mandatory to remove interference fringes through ARPL.

Finally, it is worth mentioning that the CdS buffer layer does not hinder the principle of removing interference fringes through ARPL in any significant way. Since the CdS constitutes an alien layer with different dielectric properties than the absorber, the internal reflection angles inside the absorber are influenced by its presence. However, the results in Fig. 4.10 suggest that as long as the CdS layer is homogeneous, it does not hinder the correction for interference fringes. While Fig. 4.10 showed the ARPL principle for the CdS-covered H0 sample, Fig. C.4 in the Appendix C.4 shows the respective graphs for the bare H0 absorber for the sake of completeness.

4.3.1 Limitations of angle-resolved photoluminescence

While ARPL enables to remove the interference fringes from the H0 sample, the exact same cannot be said for other samples, such as the sample L1. In this context, Fig. 4.11A shows the PL spectra measured on the CdS-covered L1 sample for angles 0°-80° in steps of 10°. In Fig. 4.11B the individual spectra are summed up and averaged over, yielding the supposedly interference-free PL spectrum (blue curve). However, the low-energy slope of the PL peak still shows some bumps indicating that the interference fringes were not completely removed. This raises the question: why is it possible to remove interference fringes in the H0 sample, but not in the L1 sample? A glance at their measured reflectance spectra, shown in Fig. C.6 in the Appendix C.5 reveals that the MBI contribution to the interference fringes is quite similar in both sets of samples. The working principle of ARPL is based on a complete dominance of either MBI or WAI over the combined interference pattern. As such, failing to completely remove interference fringes through ARPL indicates that sample L1 might exhibit a non-significant contribution from WAI. As already mentioned in section 4.2, the contribution from WAI is stronger for very narrowly distributed luminescence centers. Looking at the band gap gradients in Fig. 4.2 (no GGI profile is available for sample H0 but its profile is assumed to be very similar to the one from H1), the band gap notch region in the L1 sample is indeed narrower which would

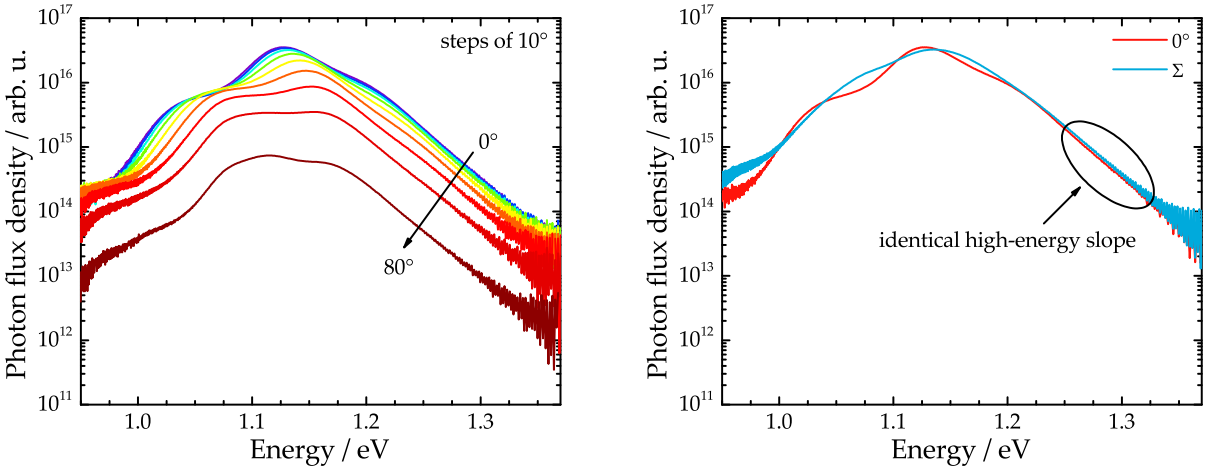

FIGURE 4.11: **(A)** PL spectra measured under varying excitation/detection angles Θ, from 0° to 80° in steps of 10°. The measurements are done on the CdS-covered absorber of the L1 sample. **(B)** Comparison between the PL spectrum measured at 0° (red curve) and the PL spectrum (blue curve) that results from summing and averaging over all scaled PL spectra. The slight bumps on the low-energy slope indicate that the interference fringes are not completely removed. The complete set of graphs for the ARPL measurements on this particular sample are shown in Fig. C.5 in the appendix C.4.

directly translate to a narrower luminescence center distribution. As such, the WAI might indeed be stronger in the L1 sample, explaining why it is not possible to remove the interference fringes through ARPL as two different interference-inducing mechanisms with different phases act simultaneously.

This failing showcases the biggest deficiency of removing interference through ARPL: it does not work without fail. For some samples the method works well, for some other samples, it does not. While the reason is not yet entirely certain, a possible explanation would be that two competing interference-inducing mechanisms, MBI and WAI, lead to two different interference phases which cannot be cancelled with the same method. For the sake of completeness, Fig. 4.12A shows the PL spectrum of a pure $CuInSe_2$ sample (red curve) that also shows significant interference fringes. In this case, since the emission centers in $CuInSe_2$ are not originating from a narrow band gap minimum inside the bulk but from a wide distribution of recombination centers close to the surface, no WAI contribution is expected. As a consequence, the interference fringes can perfectly be removed through ARPL, as is shown by the blue PL spectrum in Fig. 4.12A. In the case of a sample where the measured PL spectrum does not exhibit any interference fringes, measuring ARPL results in spectra that show a decreasing photon flux density but are otherwise identical. One such example is shown in Fig. 4.12B where ARPL was measured on the CdS-covered CIGS absorber of sample HS.

The second deficiency is rather minor: it is only possible to remove interference fringes if the shape of the PL spectra does not change with varying excitation flux densities. For example, the shape of the PL spectra of state-of-the-art CIGS absorbers is always identical for varying excitation flux densities when measured at room temperature (see e.g. Fig. C.7 in the appendix C.6). For these samples, the setup depicted in Fig. 4.9 is ideal. However, when measuring the same samples at low temperatures, the PL spectra show a strong energetic red- and blue-shift with varying excitation flux densities. Thus, measuring the PL under different excitation/detection angles will not only shift the interference fringes but also the spectra themselves which makes the interference removal through the spectra summation impossible. The second deficiency is

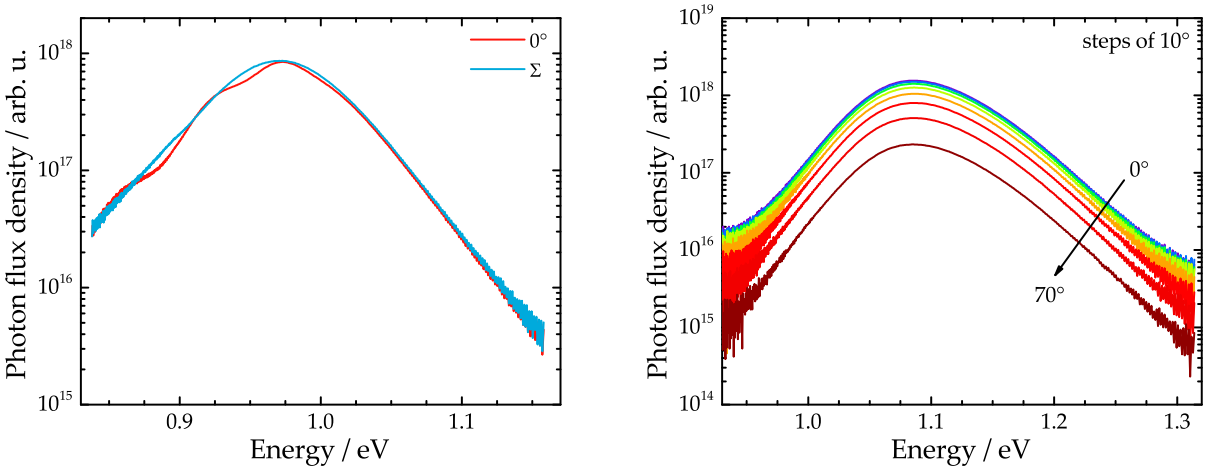

FIGURE 4.12: **(A)** Comparison between the PL spectrum measured at 0° (red curve) and the PL spectrum (blue curve) that results from summing and averaging over all scaled PL spectra. The measurements are done on the CdS-covered absorber of a pure in-house $CuInSe_2$ sample provided by Dr. Finn Babbe. In this case, it is possible to completely remove the interference fringes through ARPL. **(B)** PL spectra measured under varying excitation/detection angles Θ, from 0° to 70° in steps of 10° on the CdS-covered absorber of the HS sample. Since the HS sample originally does not show any interference fringes at room temperature (cf. Fig. 4.7), measuring ARPL only results in a decrease of the photon flux density with increasing rotation angles.

minor because it is possible to use a different setup at low temperatures: instead of tilting the sample and thus varying both excitation and detection angles, only the detector can be rotated around the sample. This way, the circular laser spot on the sample surface will not be distorted, leading to a constant excitation flux density throughout the ARPL measurement while still being able to detect photons with different accumulated phases (see Fig. C.12 in C.10 for a schematic illustration).

Even though it is not possible to completely remove the interference fringes from the low-energy slope in the L1 sample, Fig. 4.11B again shows that the high-energy slope of the PL peak is unaffected by the interference fringes.

4.3.2 ARPL as a tool to detect interference fringes

As was already mentioned in the conclusion of the study by Larsen *et al.*, a straightforward method to verify the presence of interference effects is to measure the PL at two different angles [181]. In this context, Fig. 4.13A shows the PL spectra measured at the angles 0° (red curve) and 30° (blue curve) of the sample L1 (cf. Fig. 4.11A). By taking the ratio of both PL spectra, it is possible to visualise the shift of the interference fringes, as shown by the green curve. The interference fringe pattern in the PL ratio closely resembles the MBI pattern that can be seen in the reflectance spectrum (yellow curve). However, both patterns are not exactly identical as they exhibit a slightly different period (i.e. spectral energy distance between maxima and minima). These discrepancies in the period might be explained by the fact that the reflectance spectrum is only susceptible to the MBI contribution, while the PL spectra possess both MBI and WAI contributions.

In any case, if the ratio of two PL spectra measured at different angles shows interference fringes, it can safely be concluded that the respective PL spectra are also distorted by interference effects. If the PL spectra do not exhibit any interference fringes, then the ratio is constant.

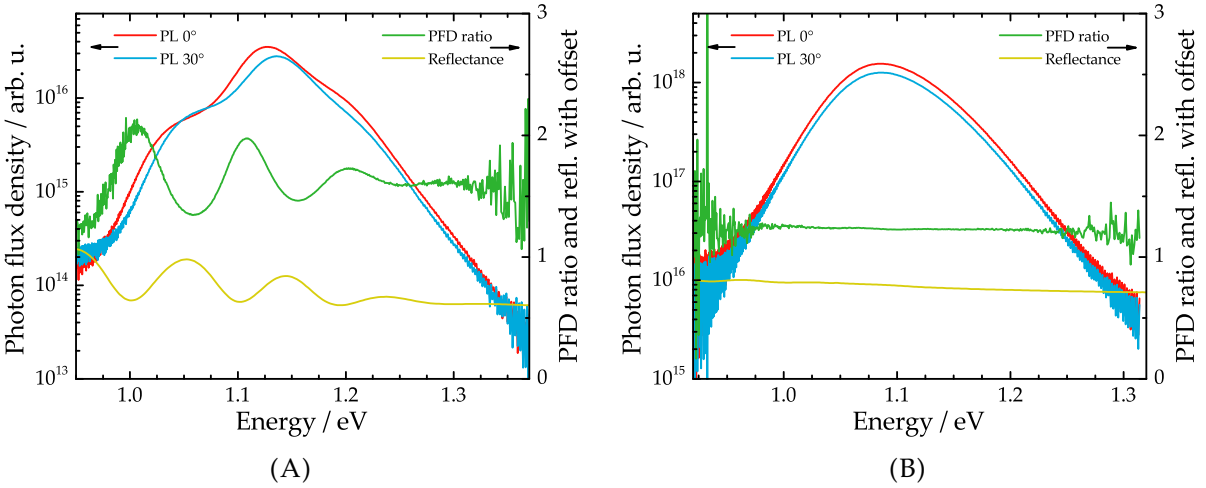

FIGURE 4.13: **(A)** PL spectra measured at 0° (red curve) and 30° (blue curve) on the CdS-covered L1 sample, displayed on the left-hand-side axis. The right-hand-side axis shows the ratio between both PL spectra (as photon flux density PFD - green curve) as well as the corresponding reflectance spectrum with offsets for improved visibility. **(B)** PL spectra measured at 0° (red curve) and 30° (blue curve) on the CdS-covered HS sample, displayed on the left-hand-side axis. The right-hand-side axis shows the ratio between both PL spectra (as photon flux density PFD - green curve) as well as the corresponding reflectance spectrum with offsets for improved visibility.

This is shown, in the form of sample HS, in Fig. 4.13B. Instead of measuring the PL at different angles to verify for interference fringes, a quick reflectance measurement is sometimes sufficient. However, if the amplitude of the interference fringes in the reflectance is sufficiently low, the interference effects will not be observable in the PL spectrum (this can be seen in Fig. 4.7 where the reflectance spectrum of sample HS shows weak fringes but which are not observable in the corresponding PL spectrum). Thus, the verification via ARPL should be the preferred choice.

Furthermore, the PL ratio and reflectance spectrum in Fig. 4.13A also clearly demonstrate that the interference fringes do not affect the high-energy slope of the PL spectra. The reason being that the photons that are emitted with these large energies, in contrast to lower-energy photons, are partially re-absorbed on their way through the absorber. These high-energy photons are thus absorbed before being multiply reflected from the internal surfaces and their contribution to the interference effects is vanishingly small.

4.4 Scattering surface layer

While it is possible to completely remove the interference fringes from photoluminescence spectra through angle-resolved photoluminescence, the method shows constraints when used on absorbers where both multiple beam and wide angle interference contribute to the overall interference pattern. Furthermore, the method can only be applied on thin-film absorbers at room temperature where a change in excitation density does not lead to a change of the spectral PL shape. Thus, to remove interference fringes from CIGS absorbers where the ARPL method fails or when measured at low temperatures, a new approach must be found.

As was shown in section 4.2.1, increasing the absorber surface roughness leads to a decrease of the interference fringes because the emitted photons are scattered in different directions. Since purposefully growing CIGS absorber with rougher surfaces while still conserving their high-quality optoelectronic properties is not possible, the rough surface must be deposited in the form of an auxiliary surface layer. Ideally, the deposition of this layer should be done at

room temperature (to avoid any temperature-activated diffusion processes into the absorber material) and should not damage the absorber surface. Additionally, the thickness of the layer needs to be of the same order of magnitude as the wavelength of the emitted photons. Finally, when measuring photoluminescence, the surface layer needs to consist of a material that is as neutral as possible to both the incident excitation photons as well as the emitted luminescence. Considering these necessary conditions, polystyrene latex beads offer themselves as a suitable material. A single polystyrene bead has a diameter of 1.1 μm and consists mainly of 69 % water and 30 % polymer while suspended in an aqueous solution[2].

4.4.1 Deposition process

The deposition process consists of depositing the polystyrene (PS) beads onto the absorber surface at room temperature via pipetting and is schematically illustrated in Fig. 4.14. The process is inspired by similar processes reported in literature [203], [204]. The deposition is initiated by inserting the absorber into a container with a volume of approximately 2700 mm^3 and submerging it in water (Fig. 4.14A). A ramp (made of glass) is inserted next to the sample. Then a polystyrene bead solution is prepared. The idea of this solution is to dilute the commercially acquired polystyrene suspension such that they can be floated on top of the water surface and

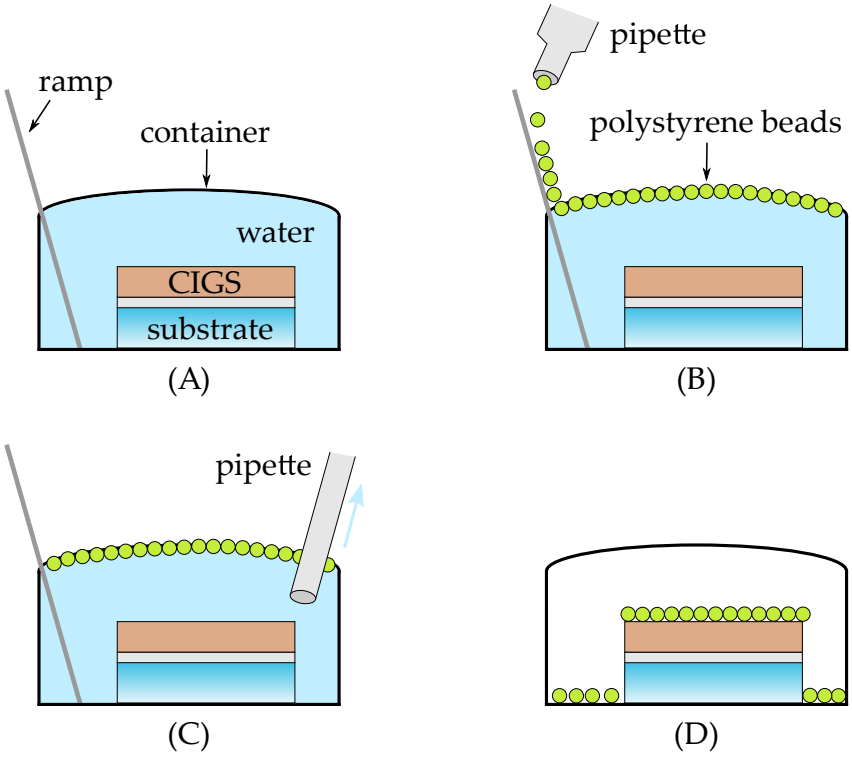

FIGURE 4.14: Schematic illustration of the polystyrene beads deposition process. **(A)** Deposition process is prepared by submerging the absorber (displayed as a SLG/Mo/CIGS stack for simplicity) into water inside a container. **(B)** The diluted polystyrene beads solution is introduced by carefully pipetting the solution along a ramp onto the water. **(C)** Due to their packing order, they beads agglomerate on the water surface and form an homogeneous monolayer. With a pipette, the water is slowly drained such that the monolayer of polystyrene beads is "falling" onto the sample surface. **(D)** With the water gone, the sample and polystyrene can dry in air.

[2]The polystyrene latex beads used in this work can be commercially acquired from the company Merck [202] in different sizes. While several tests were conducted with beads of 0.6 and 3 μm diameter, the 1.1 μm variant delivered the most consistent results.

create a polystyrene monolayer. Thus, preparing the diluted solution depends on the dimensions of the container and on the packing density of the beads i.e. their size. In the case of PS beads with a diameter of 1.1 μm, 10.2 μL of PS bead solution is diluted with 210.5 μL of ethanol C_2H_5OH and 180.3 μL of deionized water H_2O. Before introducing the prepared diluted solution onto the water, the solution is agitated inside an ultra-sonic bath to ensure a uniform suspension. After preparing and agitating the solution, the polystyrene beads can be carefully pipetted onto the ramp such that they are gently led onto the water surface, creating a homogeneous monolayer of agglomerated polymer beads (Fig. 4.14B). After letting the layer rest for a while (several minutes), another pipette is introduced inside the water and the water is carefully and slowly drained (Fig. 4.14C). During the drainage, the beads are lowered with the water level until they are eventually deposited onto the absorber surface where they create a monolayer of 1.1 μm thickness (Fig. 4.14D). Finally, the sample is taken out of the container and is left in air to dry. This constitutes a single deposition process that can be repeated to deposit additional PS layers until a desired thickness if reached.

The PS beads are not tightly fixed onto the absorber surface but can easily be removed by washing the sample with deionized water. As a consequence, great care has to be exercised when handling the samples because even the slightest touch can remove the beads from the surface. Additionally, when not taking care during the submersion process shown in Fig. 4.14A, the deposited PS layer might come off, nullifying the whole deposition up to that point. Furthermore, it is not possible to exclude that no beads are partially removed from the surface during any point of the deposition process.

4.4.2 Working principle

The idea of depositing polystyrene beads on the absorber surface is to create an artificial surface roughness that increases the scattering of the emitted photoluminescence. As such, a monolayer of PS is *a priori* not sufficient to create the degree of scattering that is high enough to weaken the interference fringes. Fig. 4.15A shows the reflectance spectra measured on sample HT (cf. section 3.3) after each additional PS deposition process. The results show that the thicker the deposited PS layer, the weaker the interference fringes in the reflectance spectra.

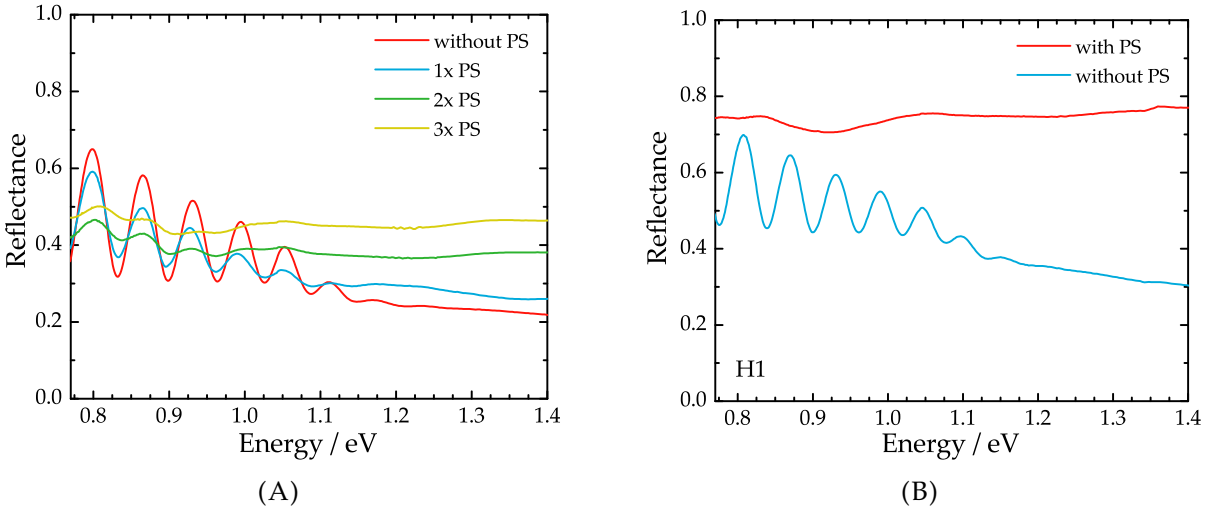

FIGURE 4.15: **(A)** Reflectance spectra measured on the sample HT before the deposition of any PS layer (red curve), after a single deposition process (blue curve), after two processes (green curve), and after three PS deposition processes (yellow curve). **(B)** Reflectance spectra measured on the sample H1 after a ten-time repeated PS deposition process (red curve) and without any PS at all (blue curve).

In addition, as seen at higher energies, the reflectance increases after each deposition process which shows that the PS beads purposefully act as a scattering medium, encouraging a diffuse reflection. As a consequence, a thick-enough PS layer appears white and grainy to the eye.

Looking at a scanning electron microscope scan of the absorber surface after the deposition of three PS layers in Fig. C.8 in the appendix C.7 reveals that the PS beads actually do not form a homogeneous layer but that there are island with a considerable amount of beads and that there are holes where no PS beads are found. Such an inhomogeneous bead distribution certainly contributes to a higher degree of scattering and is thus beneficial for the reduction of interference fringes. Thus, it is interesting to know how many layers must be deposited at a minimum to ensure an adequate suppression of interference fringes in the reflectance spectra. After the conduction of several tests, the conclusion was found that repeating the deposition ten times leads to satisfactory results based on reflectance spectra only. As an example, Fig. 4.15B shows the comparison of the reflectance spectra of the H1 sample without PS beads and with a layer that resulted from a ten-times repeated deposition process. The thick PS layer in this case leads to a complete removal of interference fringes from the reflectance spectrum.

It can be argued that the ten-time PS deposition might be exaggerated. However, while some absorbers show a rougher intrinsic surface by default and do not necessitate such a thick PS layer, other samples do need a thick-enough scattering surface layer. To keep the measurement conditions the same for all investigated samples, the PS bead deposition was done simultaneously on all samples shown in Fig. 4.15B and Figs. C.9 and C.10 in appendix C.8.

4.4.3 Influence on the photoluminescence signal

The reflectance measurements indicate that the deposition of various polystyrene layers leads to the removal of interference fringes. While this result is certainly encouraging, it does not prove that the interference fringes are also suppressed in the PL spectra. In addition, it might well be that the PS layers act as either a blocking and/or absorbing medium for the incoming laser which would reduce its usefulness in standard PL experiments. The latter assumptions are investigated by depositing a macroscopically thick PS layer on a piece of conventional microscope slide glass and measuring the transmittance and reflectance spectra. The result of this investigation is shown in Fig. C.11 in appendix C.9. From the reflectance R and transmittance T spectra, the absorbtance $A = 1 - R - T$ spectrum can be extracted and is shown as the green curve in Fig. 4.16A. The first thing to notice is that the photons emitted by the laser with a wavelength of 660 nm are not absorbed by the polystyrene beads. With this laser being the one that is used to conduct the PL experiments on all the samples that received a PS deposition in this work, this result confirms that the PS beads are neutral to the incident excitation radiation. In the near-infra-red, there is a slight absorption of wavelengths ranging from 1000 nm to 1600 nm which is typically the energy of the photons that are potentially emitted from state-of-the-art CIGS absorbers in PL experiments. However, since the absorptance is only very weak in that range, it will only lead to a slight decrease of the measured photon flux density. Beyond 1600 nm, the absorptance shows a similar spectral behaviour as measured by Hudak *et al.* (blue dotted curve)[205]. In the ultraviolet region, a strong and sudden increase of the absorptance is registered. Comparing the measured data to the results from Cho *et al.* (yellow dotted curve) [206] reveals a similar yet slightly different behaviour. While the measurements from Cho *et al.* where done on a pure sample of polystyrene, the measurements in this work were done on a thick polystyrene layer deposited on glass. As such, a partial absorption from the glass is also expected which might explain the discrepancies at large photon energies.

Based on the results from these photospectrometric measurements, the PS layer does not act as an absorbing medium. Extending these tests to the photoluminescence measurements, Fig. 4.16B shows the PL spectrum of the CdS-covered H1 sample with several layers of PS beads

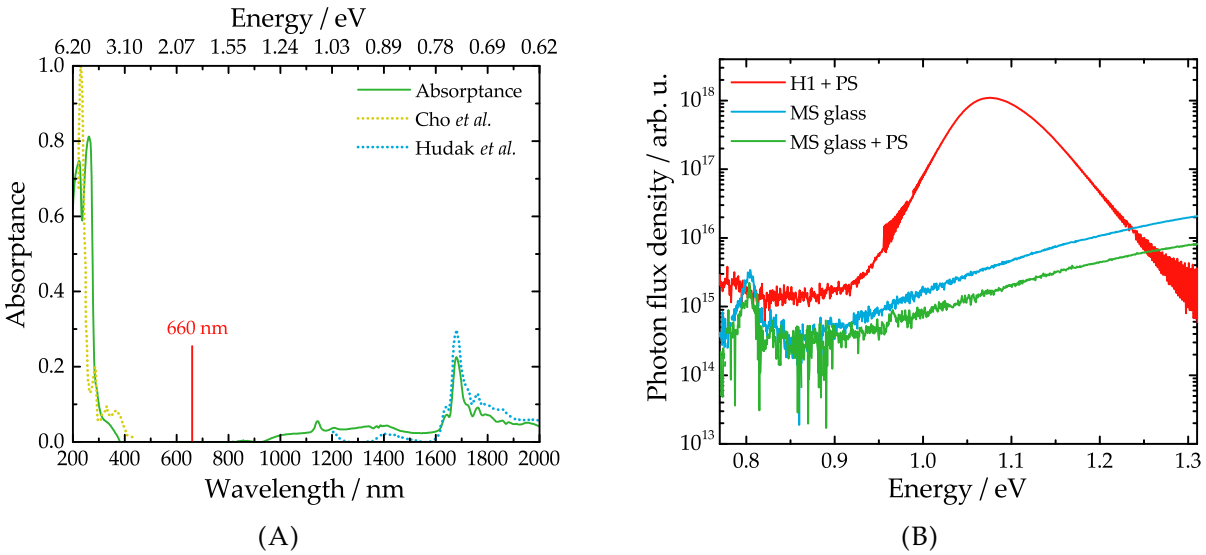

FIGURE 4.16: **(A)** Absorptance spectrum of a macroscopically thick PS layer deposited on a microscope slide glass (green curve). To verify the validity of the photospectrometric measurement, the absorptance of polystyrene as measured by Cho *et al.* (yellow dotted curve) [206] and Hudak *et al.* (blue dotted curve) [205] is displayed. Also shown is the 660 nm wavelength of the excitation laser used in PL experiments. **(B)** PL spectra measured on the CdS-covered H1 absorber upon which several layers of PS were deposited (red curve). Also displayed are the PL spectra measured on a bare microscope slide glass (MS glass - blue curve) and on an identical glass piece but covered by the same amount of PS layers as for the H1 sample (green curve).

(red curve) at room temperature. Also shown are the PL spectra of a microscope slide glass with the same amount of PS beads (green curve) and a bare microscope slide glass (blue curve). The PL spectrum of the H1 sample shows a clear broad peak that is not distorted by any interference fringes. While the PL peak itself does not exhibit any additional alien signals, a small background signal can be detected at energies below and including 0.9 eV. While it is possible that this weak background signal stems from the polystyrene, the signal strength of the measured PL peaks is usually orders of magnitude larger such that the background signal should not hinder the extraction of information from typical PL measurements. The PL spectrum of the microscope slide glass with and without PS shows a nearly identical shape but a clear difference in photon flux density. The reduced photon flux density in the case of the glass covered with PS beads is due to the scattering of the incoming radiation as well as of the emitted photoluminescence off the beads, leading to the detection of a reduced signal.

4.4.4 Effectiveness at room temperature

The deposition of polystyrene beads on the surface of the absorber suppresses the interference fringes in the measured PL spectra, as can be clearly seen in Fig. 4.17. In this context, Fig. 4.17A shows the PL spectra measured on the CdS-covered L2 absorber with and without PS at room temperature. Removing the interference fringes from the PL spectra leads to a significantly different shape. Typically one would expect such a shape from a band-to-band transition in Cu-poor CIGS absorbers at room temperature. Comparing both spectra also shows again how the high-energy slope is not affected by interference effects while the low-energy slope clearly is.

To verify whether the interference fringes are really removed, the sample is put into a cryostat which enables the measurement of the PL at different temperatures and angles. While the original function of the cryostat is to investigate the temperature-dependent optoelectronic

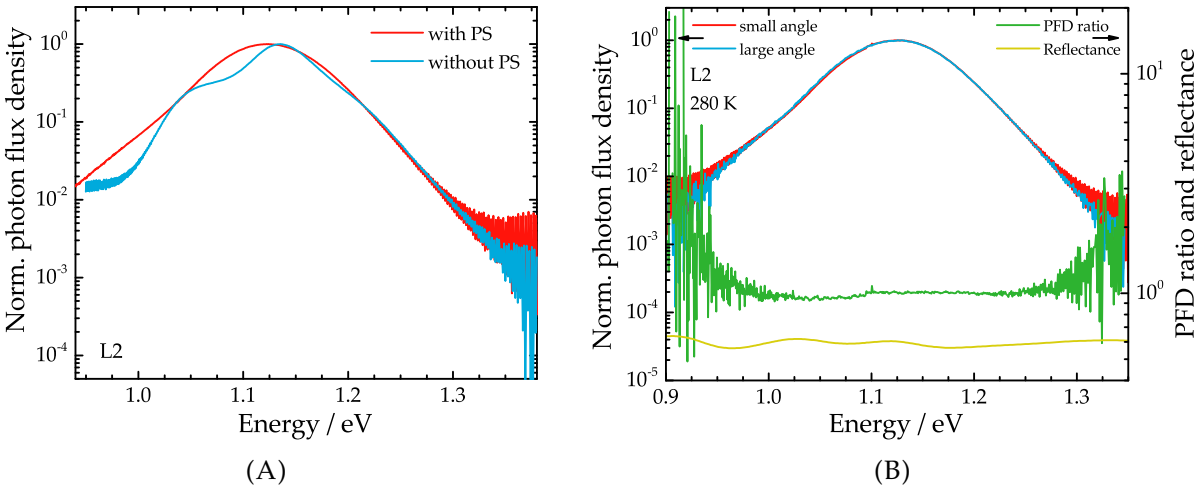

FIGURE 4.17: **(A)** Normalized PL spectra measured on the CdS-covered L2 absorber after a ten-times repeated PS deposition process (red curve) and after the beads were washed away from the surface with deionized water (blue curve). **(B)** Normalized PL spectra measured at a small (red curve) and large (blue curve) detection angle on the CdS- and PS-covered L2 sample at 280 K. The ratio between both spectra (as photon flux density PFD - green curve) shows no fringes whatsoever. For the sake of completeness, the corresponding reflectance spectrum is also dislayed (yellow curve).

properties of the sample, it can be slightly modified such that the sample can be measured at different detection angles. As such, the low-temperature setup can be used as a slightly modified ARPL setup where the excitation angle is fixed and only the detection angle is changed. A schematic illustration of the angle-resolved PL measurement inside the cryostat is given in Fig. C.12 in appendix C.10. Measuring the sample at two different angles at 280 K and extracting the ratio between both spectra results in the green curve in Fig. 4.17B. From the photon flux density (PDF) ratio, it can clearly be seen that there are no more interference fringes present in the PL spectra of the L2 sample after an adequate PS layer deposition, confirming thus that PS beads are indeed able to remove the interference fringes. As a consequence, it is possible to evaluate the optoelectronic properties that can be extracted from the low-energy slope of the PL spectrum at room temperature, such as the band tails (see section 5.1).

In Fig. C.13A in the appendix C.11 the interference-free PL spectrum of the PS-covered L2 sample is compared to the spectrum that results from ARPL at room temperature. The comparison confirms that in this sample the removal of interference fringes through ARPL is not possible.

4.4.5 Effectiveness at low temperatures

With the ability to completely remove the interference fringes distorting the PL spectra at temperatures close to and including room temperature verified, the next step is to investigate the effectiveness of the polystyrene layer at lower temperatures. The abovementioned setup is used to decrease the temperature to a value where the PL spectrum is very broad such that any interference influence or distortion can readily be observed.

Fig. 4.18A shows the same measurements as shown in Fig. 4.17B but at a temperature of 140 K. The PL spectrum measured at a small detection angle (red curve) exhibits two main peaks at around 1.0 eV and 1.1 eV and a rather moderate low-energy slope. *A priori* there is no indication of any interference fringes. The corresponding PL spectrum measured at a large collection angle (blue curve) shows the same two peaks as measured under the small angle while there seems to be an additional signal at low energies. Looking at the photon flux density ratio of both spectra (green curve), this low-energy signal leads to a rather broad bump. The

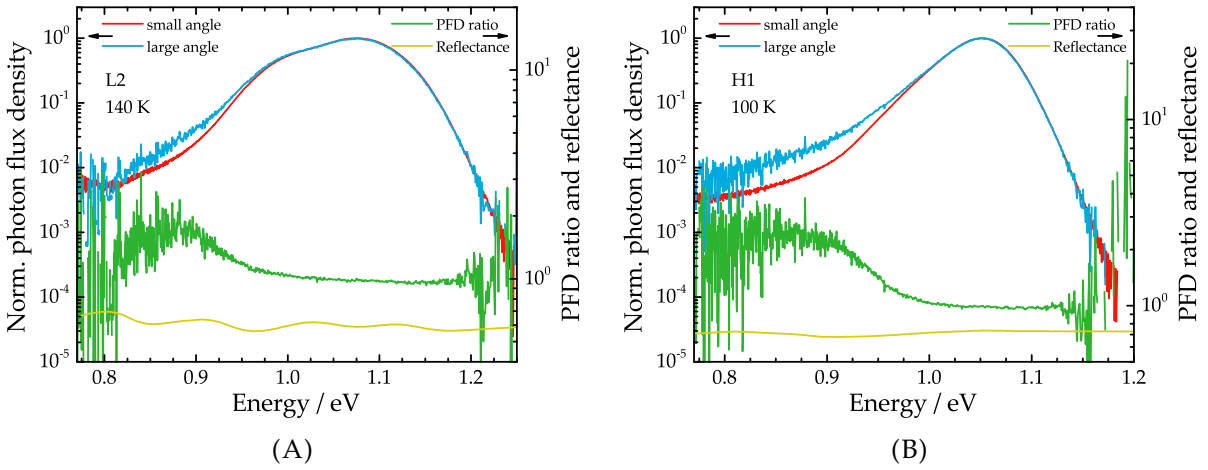

FIGURE 4.18: **(A)** Normalized PL spectra measured at a small (red curve) and large (blue curve) detection angle on the CdS- and PS-covered L2 sample at 140 K. The ratio between both spectra (as photon flux density PFD - green curve) shows no fringes that have a similar period to the weak fringes in the corresponding reflectance spectrum (yellow curve). The nature of the PL signal at low energies and the resulting bump in the PFD ratio is discussed in the main text. **(B)** Normalized PL spectra measured at a small (red curve) and large (blue curve) detection angle on the CdS- and PS-covered H1 sample at 100 K. Both the ratio between both spectra (as photon flux density PFD - green curve) and the reflectance spectrum (yellow curve) show no interference fringes. The occurrence of the PL signal at low energies and the resulting broad bump in the PFD ratio is discussed in the main text.

bump is much broader than a typical interference fringe period in the corresponding reflectance spectrum (yellow curve). Thus, the low-energy signal is unlikely to be due to interference effects but might be induced by the polystyrene beads themselves. A similar signal at low energies can be seen in the PL spectrum measured under a large angle on the H1 sample at 100 K shown in Fig. 4.18B. Again, the ratio between the PL spectra measured at different angles reveals a broad bump at energies where the corresponding reflectance spectrum is nearly flat.

As the low-energy bump is clearly spectrally much broader than an interference fringe period, it is unlikely that it is connected to interference effects. A brief discussion about possible origins is given in appendix C.12. Here it is only noted that the bump only appears when measuring the PL under a large angle and at low temperatures. Since in typical measurements this configuration is not used, it can safely be assumed that the PS layer also removes interferences fringes at lower temperatures. It is worth mentioning that, in the appendix C.11, Fig. C.14 shows how the PL spectra look like when no PS layer is deposited and that the interference-verification through ARPL works in this setup. The discussion about interference fringes affecting the PL spectra at low temperatures is continued in section 6.2.1.

Finally it needs to be mentioned that, although the polystyrene layer is not excited by the laser photon flux densities used in this work, the incident laser and emitted photons are still scattered. This leads to a strong reduction of the photoluminescence measurement signal. In addition, since the exact degree of scattering is unknown, intensity calibrated PL experiments cannot be conducted on absorbers that are covered by a PS layer.

4.5 Summary

The double-graded Ga profile in the CIGS absorbers leads to the presence of two band gap minima: one at the absorber surface and one inside the bulk. By conducting photoluminescence experiments on exfoliated CIGS absorbers under different configurations, it was shown in this

thesis that the band-to-band transition at room temperature in state-of-the-art CIGS originates only from the band gap minimum inside the bulk.

A consequence of the emission of photons from the global absorber band gap minimum is a considerably increased possibility of interference fringes occurring in the measured PL spectra as the emitted photons are only weakly re-absorbed on their way through the absorber. However, the double graded band gap is not the only reason for the occurrence of interference fringes. In addition, a relatively smooth absorber surface, a high reflection from the interfaces of the film, and an absorber thickness that is of the same order of magnitude as the emitted PL wavelength, which are all hallmarks of state-of-the-art CIGS absorbers, are also responsible for the presence of interference fringes.

The interference pattern that can be observed in the measured PL spectra is highly dependent on the phase, and consequently the optical path, of the emitted photons. Thus, in the framework of this thesis, a method was developed that revolves around measuring PL under varying angles which enables the collection of photons with different phases. A shift in phase leads to a shift of the observed interference pattern. By measuring the PL for a range of different angles, summing the spectra and averaging the resulting spectrum, it was shown that it is possible to extract an interference-free PL spectrum. However, this method of removing the interference distortion is only possible in some samples but not in others. A possible explanation could be that in the samples where ARPL removes the interference fringes, the interference pattern is dominated by multiple-beam interference. In contrast, in the samples where the ARPL is unable to completely remove the fringes, the pattern possibly exhibits a non-negligible contribution from both MBI and wide-angle interference. In any case, it was shown that the interference fringes, although very harmful for determining the low-energy slope, do not affect the high-energy slope of the PL spectra. Consequently, the high-energy slope can be evaluated without correcting for interference effects in state-of-the-art CIGS absorbers.

To remove the interference fringes completely from the PL spectra without using any theoretical models, an auxiliary surface layer was conceptualized in the framework of this thesis. This layer consists of polystyrene beads, deposited in a pipetting process onto the absorber surface, and acts as a scattering layer, effectively and artificially increasing the surface roughness. The spectral absorptance behaviour of the PS beads was measured and it was concluded that the laser excitation, which is used in PL experiments, is not exciting the polystyrene and thus is not creating any alien signals that prevent information extraction. PL measurements at different angles and at different temperatures have shown that the PS layer, if thick enough for certain absorbers, is indeed able to remove the interference fringes from the PL spectra, enabling the study of the low-energy slope and of the temperature-dependence of the photoluminescence spectra in state-of-the-art CIGS absorbers.

5 Near band edge photoluminescence

In the previous chapter 4, the general shape of the photoluminescence emission of state-of-the-art Cu-poor Cu(In,Ga)Se_2 was introduced. Experimental results showed that the radiative band-to-band recombination originates from the band gap minimum inside the bulk of the absorber and that interference effects do not influence the measured PL spectrum at high energies. These findings are crucial because they directly lead to a better understanding of the results that will be presented in this chapter. At room temperature, the near band edge photoluminescence is measured as a broad spectral peak that can be described by Planck's generalized law (2.53) that was derived in section 2.7.3. From the measured PL spectrum and Planck's generalized law, several important optoelectronic quantities of the thin-film absorber such as the quasi-Fermi level splitting (QFLS), the effective band gap energy, the sub band gap absorption coefficient, and the radiative efficiency can be extracted. In this chapter, the focus lies on the extraction of the quasi-Fermi level splitting and the characterization of the band tails (via the absorption coefficient) of CIGS absorbers that received various post-deposition treatments (PDT) after growth. A summary of the various known effects of alkali atoms on the thin-film CIGS absorbers was given in section 2.6.3. With the underlying mechanisms and exact causes of these effects not yet entirely clear, the aim is to investigate the influence of the alkalis on the optoelectronic properties of the absorbers and contribute to a more complete understanding.

The first section 5.1 introduces the method for the extraction of the quasi-Fermi level splitting and the absorption coefficient from the measured PL spectra in a step-by-step fashion. Each step of the extraction method is presented and discussed in detail. The section is concluded with a brief discussion about similar methods in literature and the advantages/disadvantages of the method of choice in this thesis.

Based on the extraction method of the first section, section 5.2 presents the measured QFLS $\Delta\mu$ of CIGS thin film absorbers that underwent various PDTs. The results suggest that the alkali PDT does not only improve the interface between the CdS and CIGS, but also the bulk properties of the CIGS absorber itself. The results of this section have already been published in ref. [191].

Section 5.3 investigates the influence of the alkali atoms on the band tails of the CIGS absorber through the absorption coefficient. The results show that the band tails are reduced with heavier alkali PDT, proving thus that the alkalis largely affect the bulk properties of the CIGS absorbers. Additional measurements based on external quantum efficiency and photocurrent spectroscopy on the corresponding finished solar cell devices show an identical trend and consolidate the results. The results of this section are to be published in ref. [207].

With the findings from the previous two sections indicating an increase in bulk absorber quality by applying the alkali PDT, the next step is to look for the specific causes of this improvement. An absorber quality that directlys translate into the QFLS and band tails is its homogeneity. Section 5.4 thus investigates the influence of the alkali PDTs on the absorber homogeneity via spatially-resolved photoluminescence with micrometer resolution. The results show that state-of-the-art CIGS absorbers are very homogeneous on a microscopic scale, independently of the alkali PDTs used.

5.1 Extraction of optoelectronic properties

For the characterization and description of the radiative band-to-band recombination in state-of-the-art Cu-poor CIGS thin-film absorbers around room temperature, Planck's generalized law of radiation is essential. While the law was already derived and its validity discussed in section 2.7.3, its main points are briefly repeated below. Planck's generalized law describes the photoluminescence emitted from the absorber in terms of the photon flux density [164]

$$Y_{\mathrm{PL}} = \frac{1}{4\pi^2\hbar^3c^2}\frac{a(E)E^2}{\exp\left(\frac{E-\Delta\mu}{k_{\mathrm{B}}T}\right)-1}, \tag{5.1}$$

and is only valid if the emitting semiconductor exhibits homogeneous material properties and flat quasi-Fermi levels [162], [164]. In state-of-the-art Cu-poor CIGS where the sample composition is not constant (double gallium gradient through the whole absorber thickness - see section 2.6.2; copper deficit at the surface - see section 2.6.3), the optical material properties are certainly not homogeneous. However, as was already introduced in section 2.6.2 and experimentally shown in section 4.1, following illumination, the excited charge carriers diffuse into the bulk band gap minimum and recombine from there. Under steady state illumination, which is fulfilled when measuring PL under excitations close to AM1.5 conditions, the radiative emission is thus entirely governed by the recombination centres in the band gap minimum. Thus, the electron quasi-Fermi level is only determined by the occupation of states in and around the conduction band minimum in the bulk (as the gallium concentration only influences the conduction band - cf. section 2.2.1) where a much smaller compositional variety than in the rest of the semiconductor is present. In contrast, the valence band only shows a very weak elemental composition dependence and due to the high mobilities of the charge carriers, the hole quasi-Fermi level can be considered flat. Thus, with both electron and hole quasi-Fermi levels being flat, Planck's generalized law is valid and can be applied.

Both the absorptivity $a(E)$ and the quasi-Fermi level splitting $\Delta\mu$, incidentally playing a central role in the characterization of CIGS absorbers, dictate the course of Planck's generalized law. While the QFLS is a quantity that depends on the illumination conditions, the absorptivity is a highly spectrally-dependent quantity. Conventionally, the absorptivity is accessed through spectrophotometric measurements [166] that require the absorbers to be exfoliated from their substrate, influencing thus the material properties (cf. section 4.1). Other methods revolve around the measurements of optical constants via ellipsometry [28], [31]. Thus, in order to access the absorptivity, a huge effort is necessary. However, by considering some simple assumptions, it is also possible to access the absorptivity via Planck's generalized law describing the photoluminescence spectrum. The method of extraction for both the QFLS $\Delta\mu$ and the absorptivity $a(E)$, based on the previous works of [162], [166], [208], [209], is presented in the following.

5.1.1 Extracting the quasi-Fermi level splitting

The extraction method is visualised with the help of sample H1 which was covered by several polystyrene (PS) layers to remove the interference fringes. In Fig. 5.1A, the radiative band-to-band recombination at room temperature is plotted as spectral photon flux density Y_{PL}. Generally, the photon density flux is expressed in photons $\mathrm{cm}^{-2}\ \mathrm{s}^{-1}\ \mathrm{eV}^{-1}$ but in this case the photon flux density is expressed in arbitrary units. This is because the PS layers prevent the intensity-calibrated PL measurement and thus the PL signal is not calibrated to yield the exact number of photons. Theoretically, the PL spectrum can be described by Planck's generalized law (5.1) if the absorptivity $a(E)$ is known. However, as this is usually not the case, the spectrum under

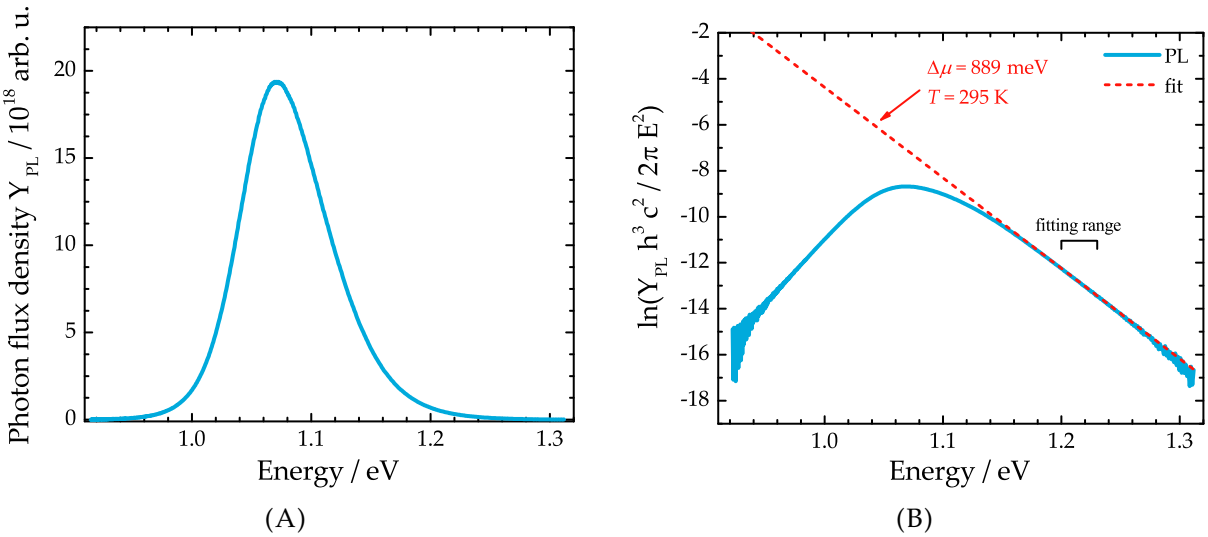

FIGURE 5.1: **(A)** PL spectrum of sample H1 that is covered by several PS layers to remove the interference fringes. The spectrum shows the radiative band-to-band transition at room temperature in terms of photon flux density. As the spectrum is not intensity-calibrated, the units are set to arbitrary. Furthermore, the y-values were divided by a numerical factor of 10^{18} for improved visualization purposes. **(B)** PL spectrum after approximation and transformation according to eq. (5.2). The high-energy slope of the PL spectrum can be fitted to yield the electron temperature T and the quasi-Fermi level splitting $\Delta\mu$. The fitting range and results of the fit (red dashed line) are shown.

this form yields only limited information. By applying some approximations to Planck's generalized law, the spectrum can be brought into another form from which more information can be extracted: in state-of-the-art Cu-poor CIGS absorbers, $\Delta\mu$ is always several 100 meV below the spectral emission energy such that $E - \Delta\mu \gg k_B T$ and the Bose-Einstein term can be approximated by a Boltzmann term. In addition, on the high-energy wing of the PL spectrum at sufficiently high energies (typically >0.1 eV above the band gap energy), the absorptivity $a(E)$ can approximated to be unity [162], [208]. With these approximations in mind, eq. (5.1) can be rearranged into the following expression:

$$\ln\left(\frac{Y_{PL}\, h^3 c^2}{2\pi E^2}\right) = -\frac{E - \Delta\mu}{k_B T}. \tag{5.2}$$

Applying this transformation to the measured PL spectrum results in the spectrum shown in Fig. 5.1B. The high-energy wing of the spectrum, where $a(E) \approx 1$ was assumed, shows a linear progression and can be fitted to yield the electron temperature T and the quasi-Fermi level splitting $\Delta\mu$ according to eq. (5.2). Using this method, the fitting range is of crucial importance. It cannot be set at too low energies since then the approximation $a(E) \approx 1$ is not valid but it also cannot be set at too high energies since then the background signal of the measurement influences the linear fit. In the present example, the fit results in a temperature of 295 K and a quasi-Fermi level splitting $\Delta\mu$ of 889 meV. The $\Delta\mu$ value in this case is too high for an absorber that shows a radiative transition centered around 1.1 eV and can be explained by the fact that the measured PL spectrum is not calibrated for intensity[1]. The temperature of 295 K is very close to the room temperature of the optics laboratory where the measurements were taken.

The method described above concludes the extraction of the quasi-Fermi level splitting $\Delta\mu$.

[1]Usually, when intending to determine the quasi-Fermi level splitting, the PL spectra are measured under intensity calibration such that absolute values can be extracted. However, in this example, the interference fringes are removed from the spectra for visualization purposes, making intensity-calibrated measurements very difficult. An example of an intensity-calibrated PL spectrum is given in Fig. 5.4.

If the aim of a measurement is to determine $\Delta\mu$ and compare it to the open-circuit voltage V_{OC} of the finished solar cell device (for this case the PL spectra need to be intensity-calibrated), the data evaluation can be stopped here. Finally it needs to be mentioned that the PL spectrum is influenced by multiple variables such as the band gap energy, the quasi-Fermi level splitting of the absorber, or the temperature and each of these variables has a distinct effect on the spectrum. For the sake of completeness, their effects are briefly shown in Appendix D.1

5.1.2 Extracting the Urbach energy

After extracting the temperature T and the quasi-Fermi level splitting $\Delta\mu$ from the measured photon flux density Y_{PL} spectrum, the absorptivity $a(E)$ can be calculated according to a rearranged form of Planck's generalized law [162], [209]:

$$a(E) = Y_{PL}(E)\,\frac{4\pi^2\hbar^3c^2}{E^2}\left[\exp\left(\frac{E-\Delta\mu}{k_BT}\right)-1\right]. \tag{5.3}$$

For sample H1, the calculated absorptivity spectrum is shown in Fig. 5.2A. Also indicated is the fitting range that was used to extract the temperature and QFLS in Fig. 5.1B, clearly showing that $a(E) \approx 1$ was a valid assumption in this case. The data shows that the absorptivity spectrum deviates considerably from a Heaviside step function that is assumed when calculating solar cell parameters in the Shockley-Queisser limit (cf. section 2.4). The real $a(E)$ spectrum resembles a smeared-out step function due to the fact that there are states that extend into the band gap and hence promote the absorption of photons with lower energies. These states are usually referred to as band tails and are discussed in section 5.3.

The absorptivity $a(E)$ is closely linked to the absorption coefficient $\alpha(E)$ via Lambert-Beer's law [20]

$$a(E) = (1-R)\left(1-e^{-\alpha(E)d}\right), \tag{5.4}$$

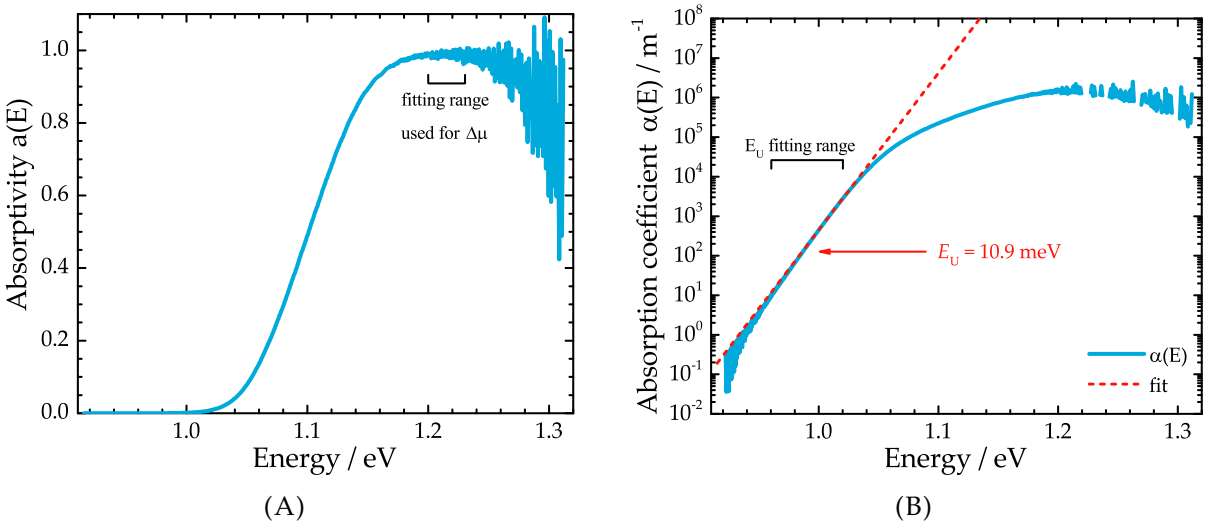

FIGURE 5.2: **(A)** Absorptivity spectrum of sample H1 derived from the measured PL spectrum according to eq. (5.3). Also shown is the fitting range that was used in Fig. 5.1B to extract the temperature and the QFLS. **(B)** Semi-logarithmic representation of the absorption coefficient spectrum in arbitrary units derived from the absorptivity spectrum according to eq. (5.5). The absorption coefficient can be fitted (red dashed line) at low energies, as indicated by the fitting range, according to eq. (5.6) to yield the Urbach energy E_U.

where R describes the reflectivity of the absorber surface and d the absorber thickness. Expression (5.4) was already introduced in section 2.7.3 and is a very strong approximation since it assumes a planar surface and neglects the occurrence of multiple reflection. The validity of this approximation is discussed in section 5.1.3. From eq. (5.4), by neglecting the surface reflectivity, i.e. $R \approx 0$, and knowing the exact thickness d of the absorber, the absorption coefficient $\alpha(E)$ can be derived [162], [209]:

$$\alpha(E) = -\frac{\ln(1 - a(E))}{d}. \tag{5.5}$$

The extracted absorption coefficient $\alpha(E)$ for sample H1 is shown in Fig. 5.2B in semi-logarithmic representation. The graph shows that the absorption coefficient can reliably be measured for several orders of magnitude below the band gap energy (that is 1.077 eV for sample H1 - see table 3.1 in section 3.3). As was already shown by Rey *et al.* [166], PL offers a considerably higher dynamic range for the detection of $\alpha(E)$ than other methods such as spectrophotometry or photothermal deflection spectroscopy[2]. Furthermore, the absorption coefficient shows an exponential behaviour at low energies. The absorption coefficient, as is the case for the absorptivity $a(E)$, reflects the density of states that reach into the band gap [20], [92]. If the density of states exhibit an exponential decrease from the band edges towards the midgap, the band tails can be described as Urbach tails [210] and the absorption coefficient can be modelled according to [211]

$$\alpha(E) = \alpha_0 \exp\left(-\frac{E_0 - E}{E_U}\right), \tag{5.6}$$

where α_0 and E_0 are material-specific parameters. The so-called Urbach energy E_U describes the behaviour of $\alpha(E)$ below the band gap and, as such, is a characteristic parameter that reflects the band tails: the larger E_U, the more the band tails extend into the band gap. For the sample H1, a fit according to eq. (5.6) yields an Urbach energy E_U of 10.9 meV. As was the case for the extraction of the QFLS, the fitting range needs to be selected with care. It cannot be set too close to the band gap energy where $\alpha(E)$ does not show an Urbach behaviour and it cannot be set at too low energies where the background signal of the PL measurement influences the fit. To ensure a good fitting quality by avoiding the fit to extend over several orders of magnitude, the natural logarithm of $\alpha(E)$ and the corresponding altered eq. (5.6) is typically taken for the fitting process. An in-depth description and discussion of band tails is given in section 5.3.

5.1.3 Pitfalls and good practice

The assumption $a(E) \approx 1$ in eq. (5.2) and the expression for the absorptivity in eq. (5.4) are very strong approximations that do not necessarily represent the complicated material properties and recombination physics in CIGS absorbers. Recently, Rey *et al.* published an extensive study where they analysed the influence of various expression for the absorptivity $a(E)$ on the determination of the quasi-Fermi level splitting $\Delta\mu$ and the Urbach energy E_U [166]. The study reveals that the assumption $a(E) \approx 1$ is only rarely valid and that the absorptivity needs to be described by a more sophisticated expression than eq. (5.4) which requires more sample-specific parameters, such as the index of refraction or the spectral reflectance. However, the study also reveals that the deviations, when using simple approximations such as $a(E) \approx 1$ and eq. (5.4), are small in high-quality absorbers and can easily be spotted. For example, using an inadequate expression for the absorptivity yields an increased temperature during the fitting process. As such, the temperature in eq. (5.2) is a crucial parameter and can be used to

[2]Conversely, at energies above the band gap, PL proves to be an inadequate technique to extact the absorption coefficient as only states of minimum energy emit light (for excitation densities close to and slightly above AM1.5 conditions). This is why the $\alpha(E)$ at high energies in Fig. 5.2B is so choppy.

verify the validity of the simplified approach, and, very conveniently, even force the approach to become correct.

As an example, the fitting procedure of the high-energy slope of the rearranged PL spectrum in Fig. 5.1B using eq. (5.2) yields an electron temperature of 295 K. This electron temperature, being close to the ambient room temperature, is assumed to be equal to the lattice temperature of the semiconductor due to the strong electron-phonon coupling [212]. One needs to be careful when determining the temperature from the measured PL spectra as the lattice temperature depends on the excitation conditions, i.e. the larger the excitation photon flux density that is incident on the CIGS absorbers, the higher the temperature. However, for illumination conditions close to AM1.5, the lattice temperature was measured to not deviate from the room temperature with a thermal camera [49]. Thus, the fitted temperature of 295 K for the H1 sample in Fig. 5.1B agrees well with the room temperature, and thus, the simplified approach of eq. (5.2) is accurate, rendering the necessity for a more sophisticated expression for the absorptivity obsolete.

While the fitting procedure for sample H1 yields a realistic temperature, the same cannot be said for other samples. In this context, Fig. 5.3A shows the rearranged PL spectrum of the CIGS absorber L1 covered with PS layers. Also visualized in the graph are two fits that both yield a different $\Delta\mu$ and T. The PL spectrum is measured under very similar excitation conditions as for the H1 sample in Fig. 5.1B (since both absorbers were covered with a similar amount of PS layers, it is not possible to know the exact excitation conditions but they can be assumed to be very similar). However, when fitting the high-energy slope of the PL spectrum, a temperature of 333 K and a QFLS of 825 meV are extracted (green dashed line). *A priori*, there is no reason why the lattice temperature of the H1 absorber should be different to the one of the L1 absorber when both are measured under the same conditions. By fixing the temperature to a more realistic value of 296 K, a QFLS of 874 meV can be extracted (red dashed line). Both fits were done following the Levenberg-Marquardt algorithm [213] and yield a comparable coefficient of determination R^2: 0.914 for the fit where the temperature was left as a free parameter, and 0.900 where the temperature was fixed to 296 K. While the overall quality of both fits is not optimal, in the fitting range that was forcefully selected to be quite narrow (at as high as possible energies but not too close to the background noise), the fits are are deemed acceptable.

The discrepancy in the extracted temperatures is due to the fact that the approximation $a(E) \approx 1$ in eq. (5.2) is not entirely accurate in the case of sample L1. As was mentioned before and described in detail in [166], the inadequacy of an expression for the absorptivity is directly reflected in the fitted temperature. The discrepancy also shows in the absorptivity spectra in Fig. 5.3B that are derived following eq. (5.3) while using both sets of $\Delta\mu$ and T from Fig. 5.3A. Both spectra differ significantly in that the absorptivity spectrum that results from a fitted temperature of 333 K (green curve) shows a shape that one would expect and which is similar to the absorptivity spectrum of sample H1 in Fig. 5.2A. Contrastingly, the absorptivity resulting from the fit with the fixed temperature of 296 K (red curve) shows a deteriorated shape. From the fitting range, it can also be seen that the absorptivity is not unity in the energy range where the original fit was placed. Thus, it can be concluded that the approximation $a(E) \approx 1$ at large energies is not as accurate for the sample L1 than for the sample H1. The discrepancy between both samples must be originating from a distinct difference between both absorbers.

This difference is found in the double band gap grading. In this context, Fig. 4.2 demonstrates that the band gap minimum, from which the photon flux density is emitted, is spatially considerably larger for the H1 sample than for the L1 sample. This means that the photons are more likely to be absorbed on their way through the H1 absorber than in the L1 absorber. Thus, an absorptivity below unity even for high photons energies seems plausible in the case

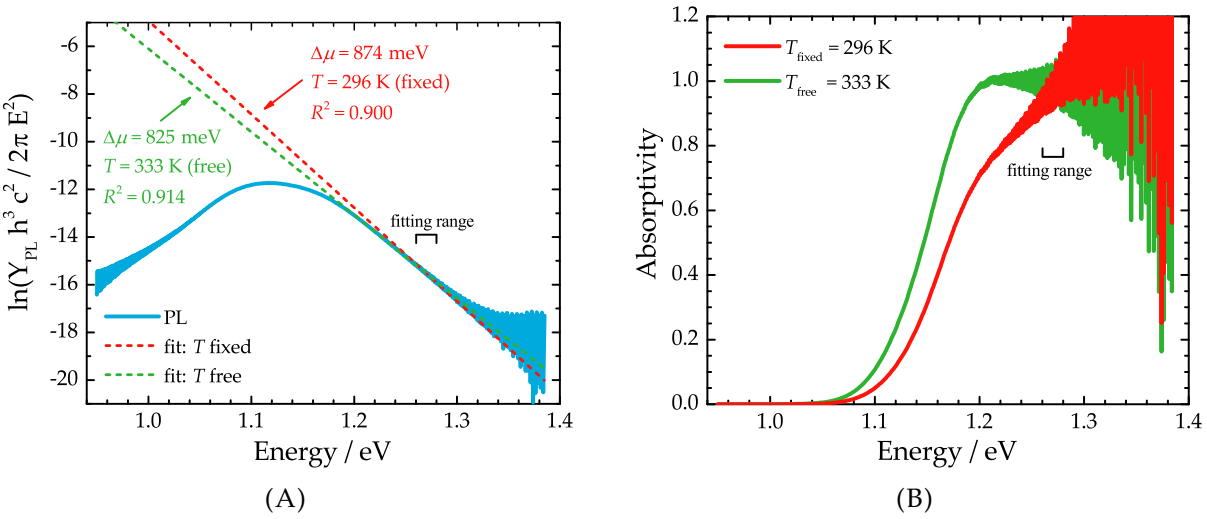

FIGURE 5.3: **(A)** Rearranged PL spectrum of sample L1. The high-energy slope within the selected range was fitted by leaving the temperature as a free parameter (green dashed line) and by fixing the temperature to 296 K (red dashed line). The results of the fits, i.e. quasi-Fermi level splitting $\Delta\mu$, temperature T and coefficient of determination R^2 are indicated. **(B)** Corresponding derived absorptivity spectra for the fit where the temperature was left as a free parameter (green curve) and for the fit where the temperature was fixed to 296 K (red curve). Also shown is the fitting range that was used for the PL spectra.

of the L1 sample. Considering this insight, coupled with the fact that both H1 and L1 absorbers were measured under the same conditions and the recent findings of Rey *et al.* [166], two conclusions can be drawn. On the one hand, the temperature that is extracted from the fitting process should ideally equate the room temperature (when using low-enough excitation densities that prevent heating effects). If the fitted temperature is larger than the room temperature, the approximation $a(E) \approx 1$ is not valid. On the other hand, by fixing the temperature to the measured room temperature, the approximation $a(E) \approx 1$ can be forced and the extracted quantities such as QFLS $\Delta\mu$, absorptivity $a(E)$, and absorption coefficient $\alpha(E)$ are accurate.

For the sake of completeness, appendix D.2 shows the impact of the temperature on the derived absorption coefficient spectra and the subsequent Urbach energy extraction, underlining once more the necessity for the correct determination of this crucial fitting parameter.

It needs to be mentioned that there exists an alternative model in literature that uses a slightly different form of Planck's generalized law by envisioning a multitude of models for the absorption coefficient [214]. With the absorption coefficient and thus the absorptivity spectrum being modelled, it is possible to fit the whole PL spectrum and not just the high-energy slope. While the model yields quasi-Fermi level splittings that agree well with corresponding open-circuit voltages, the fitted temperatures can reach up to 380 K which seems rather unrealistic. Additionally, due to the usage of multiple numerical models, the fitting routine is rather computational-heavy which reduces its usefulness in certain scenarios (e.g. when extracting $\Delta\mu$ for spatially-resolved PL on the microscopic scale - see section 5.4).

Discarding this alternative model and keeping in mind the insights about the absorptivity and temperature as discussed above, a "good practice" approach can be established for the extraction of the quasi-Fermi level splitting and ultimately the derivation of the absorption coefficient spectrum. With the temperature being such a crucial fitting parameter, the PL spectra should be measured such that the fitting procedure is as unambiguous as possible. This can

be done by measuring the PL over a broad spectral range allowing the detection of the high-energy slope for several orders of magnitude to higher energies which enables the fitting at the highest possible energies, enabling the approximation $a(E) \approx 1$ to become more accurate. As an example, Fig. 5.4 shows the intensity-calibrated PL spectrum of sample LS, measured using both the InGaAs and Si arrays as detectors in the experiment. Fitting the PL curve in the selected range and fixing the temperature to 296 K (red curve) results in a coefficient of determination of 0.999 using the Levenberg-Marquardt algorithm. This proves that extending to the high-energy slope to higher energy yields excellent results. One might argue that the fitting range could potentially be set to even higher energies but it is also imperative to avoid the background noise that sets in at some point (in this case, the PL curve starts bending upwards at already 1.35 eV due to the background). Due to the lack of polystyrene layers, the PL spectrum exhibits significant interference fringes that distort the low-energy slope. Thus, the spectrum cannot be used to derive the absorptivity and consequently the absorption coefficient spectra. However, as was discussed and shown in sections 4.3 and 4.4, the high-energy slope is not influenced by the interferences effects. Thus, the quasi-Fermi level splitting can safely be extracted and if the PL spectrum is measured in absolute photon flux density units, the $\Delta\mu$ can be compared to the open-circuit voltage V_{OC} (the latter quantity being 716 mV in this case - see Table 3.2 in section 3.3).

The above example shows that it is possible to receive excellent fitting results even if the temperature needs to be fixed to 296 K. However, it needs to be mentioned that the goodness of the fit is only excellent if the emitted photon flux density is high, i.e. in absorbers that are of a certain quality. In absorbers that show a lower quality, it is not possible to measure the high-energy slope over several orders of magnitude. In this case, the temperature still needs to be fixed to 296 K but the quality of the fit will suffer.

The "good practice" approach consists thus of measuring the photoluminescence over a broad spectral range such that the fitting can be done at sufficiently high energies on the high-energy slope. Additionally, the temperature of the fit is to be fixed at the ambient laboratory temperature (e.g. 296 K) during the experiment which can be measured by a conventional room thermometer (if the samples are measured at conditions close to or below AM1.5 excitation densities). The good practice approach is used, whenever applicable, to all the measured PL spectra in this thesis.

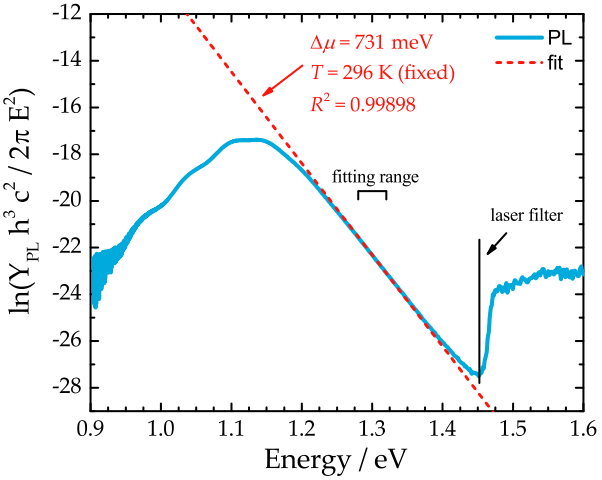

FIGURE 5.4: Rearranged intensity-calibrated PL spectrum of sample LS (CdS-covered CIGS absorber) measured over a broad spectral range. The high-energy slope is fitted in the selected range, yielding the red dashed line and the $\Delta\mu$, T, and R^2 as indicated in the graph. During the measurement, a long pass filter of 850 nm ($\approx$ 1.46 eV) was used. Figure adapted from ref. [93].

5.2 Influence of alkali atoms on the quasi-Fermi level splitting

A summary of the various effects of alkali atoms on the thin-film CIGS absorbers, that are known so far from literature, was given in section 2.6.3. While most experiments in literature concentrate on the surface properties of the absorbers, little information is available about how the bulk properties are affected. Photoluminescence measurements on state-of-the-art CIGS absorbers are sensitive to the bulk properties as the emitted photons are originating from the band gap minimum inside the bulk. Thus, variations in the bulk properties are expected to affect shape, energetic transitions, quasi-Fermi level splitting as well as the absorption properties of the emitted PL. Variations in the surface properties, however, only affect the total emitted photon flux density (and consequently the quasi-Fermi level splitting).

In the following, the quasi-Fermi level splitting, extracted from intensity-calibrated PL measurements done on Cu-poor CIGS absorbers having undergone different post-deposition treatments, is presented. Each sample that received a PDT is measured as bare absorber and as absorber covered by a CdS buffer layer. In addition, the measurements are conducted on absorbers that were grown in a low-temperature co-evaporation process and on absorbers grown in a high-temperature co-evaporation process. Finally, the extracted QFLS values are compared to the open-circuit voltage V_{OC} of the corresponding finished solar cell devices. The results are discussed and compared to the relevant findings in literature. Here it needs to be mentioned that the findings in literature do not necessarily apply to state-of-the-art absorbers which are treated in the following.

5.2.1 Case of low-temperature absorbers

The measured quasi-Fermi level splittings $\Delta\mu$ of samples L1, L2, and L3 are summarized in the bar plot in Fig. 5.5. The blue bars represent the QFLS measured on the bare absorbers, the red bars represent the QFLS measured on the CdS-covered absorbers and the white bars represent the open-circuit voltage as measured on the corresponding finished solar cell devices (six neighbouring cells in each case). The sample layout and distribution can be found in appendix B.1. The PL was measured on several spots on the samples to account for any macroscopic inhomogeneities. A statistical analysis reveals a standard deviation of the extracted QFLS of approximately 2 meV for the CdS-covered absorbers and up to 6 meV for the bare absorbers. Considering uncertainties from the fitting procedure, the calibration factor, the excitation density[3], and the QFLS standard deviation, an estimated error in $\Delta\mu$ of ± 10 meV and ± 15 meV is attributed to the CdS-covered and bare absorbers respectively. The error attributed to the V_{OC} equals the standard deviation of the measured values across six neighbouring solar cells. Finally, as the $\Delta\mu$ and V_{OC} depend on the band gap energy of the absorber, it needs to be mentioned that all three samples show minimum band gap energies that lie within 6 meV of each other (see table 3.1 in section 3.3). As such, the influence of the band gap energy on the measured values is completely negligible.

First of all, the analysis of the QFLS measured on the CdS-covered absorbers in Fig. 5.5 reveals an increase for heavier alkali PDTs: the absorber treated with only NaF shows a considerably higher $\Delta\mu$ than the non-treated sample, only then to show a lower $\Delta\mu$ than the NaF + RbF sequentially-treated absorber. For absorbers with a similar band gap energy, an increase in the quasi-Fermi level splitting can directly be attributed to an increase of radiatively-recombining charge carriers and thus a decrease of non-radiative recombination. Thus, from the CdS-covered absorbers it can be concluded that the post-deposition treatment with heavier alkali atoms leads a reduced non-radiative recombination rate.

[3] The excitation density was set to mirror the photon flux density of the AM1.5 spectrum for a band gap energy of 1.1 eV.

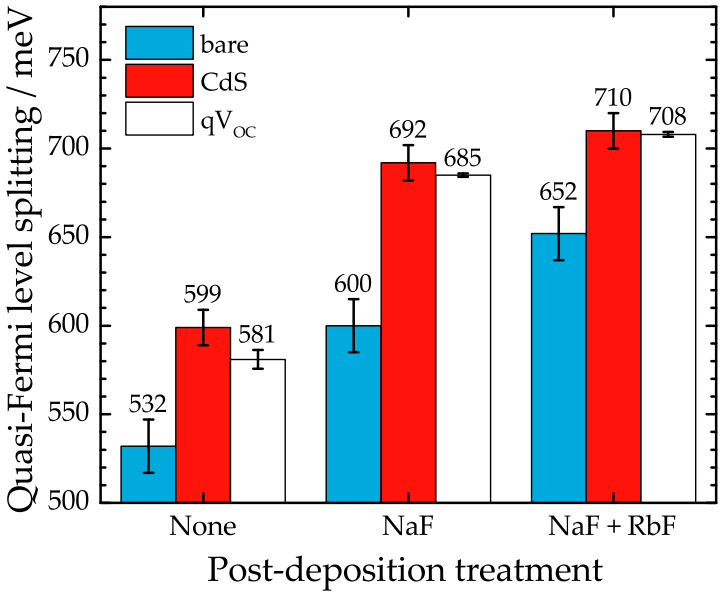

FIGURE 5.5: Bar plot showing the quasi-Fermi level splitting of bare (blue bars) and CdS-covered (red bars) CIGS absorbers having undergone different post-deposition treatments. For comparison, the qV_{OC} (white bars) as measured on the finished solar cell devices is also shown. The values represent average values. Also included are error bars that were estimated according to the reasoning outlined in the main text. The non-treated sample corresponds to sample L3, the NaF treated sample corresponds to sample L2 and the NaF + RbF treated sample corresponds to sample L1. Figure adapated from ref. [191].

Next, the V_{OC} of the corresponding finished solar cell devices is compared to the measured QFLS of the CdS-covered absorbers. It can be seen that the V_{OC} follows the same trend as the $\Delta\mu$: an increase in solar cells whose absorbers were treated with a heavier alkali PDT after growth. From these results, it can be concluded that the beneficial effects from the alkali atoms are independent of the window layer deposition i.e. the band bending that is caused by the n-doped ZnO during solar cell fabrication. As the QFLS represents an upper limit for the V_{OC}, a quantitative comparison describes the loss in V_{OC} resulting from the CIGS/CdS absorber to the finished solar cell device fabrication step. This difference amounts to 2 meV for the NaF + RbF treated sample, 7 meV for the NaF-only treated sample, and 18 meV for the non-treated sample. While a difference of 2 meV and 7 meV is too small to be considered as a real loss in V_{OC} for the NaF + RbF and NaF-only treated cells, the difference of 18 meV in the non-treated cell is very likely to indicate a real loss during solar cell finishing. Looking at the error bars, one might think that the measured $\Delta\mu$ could potentially also be inferior to the V_{OC}. While this is a possibility, it needs to be kept in mind that the PL measurements were done on adjacent absorber pieces. As such, if these pieces were fabricated into solar cells, they might show lower V_{OC} values that do not conflict with the error bars. Given these uncertainties (that are not dared to be included in the error bars), the above interpretation of the measured values is assumed correct.

Finally, from the blue bars in Fig. 5.5, it can be seen that the measured QFLS of the bare absorbers is considerably lower than the QFLS of the CdS-covered absorbers. This increase of non-radiative recombination is due to the surface degradation in air over time [70]. Independent of the surface degradation, the measured QFLS of the bare absorbers also shows an increase if the sample was treated with heavier alkali atoms. This result suggests that the alkali PDT already improves the absorber and its surface, even before any CdS deposition. At first, one might suggest that the increase in $\Delta\mu$ is entirely due to an improvement of the CIGS surface and that the measured low values are only due to degradation in air (meaning that they would be as high as the CdS values if no surface degradation would take place). Effects of

the RbF PDT on the absorber surface were already reported in literature [140] (see also section 2.6.3) indicating why an improvement of the CIGS surface with RbF seems plausible. However, evidence for a similar effect for the NaF-only PDT is lacking. In fact, Na was found to have a negligible effect on surface passivation [215]. Furthermore, knowing that Rb atoms also segregate at the grain boundaries in the bulk material [154], the possibility of the alkali atoms only affecting the CIGS surface and not the bulk can be discarded. Thus, the above reasoning leads to the conclusion that the alkali PDT does not only improve the CIGS absorber surface but also the bulk material itself by reducing the non-radiative recombination.

The measurements shown in Fig. 5.5 were done after letting the samples (both bare and CdS-covered) rest for several weeks under atmospheric conditions, allowing ample diffusion of atmospheric components through the surface. The main idea was to have a sample set where the bare absorbers were stable over several days as the phenomenon of surface degradation in air was already well-known. However, first, but not so extensive, measurements were already done earlier (shortly after sample preparation) and additional measurements were done later, across several months. The whole temporal evolution of the measured quasi-Fermi level splitting is shown in the Appendix D.3. The results of these measurements show that the CdS layer is indeed a very good passivator as it conserves the optoelectronic properties, expressed as $\Delta\mu$, over months. Additionally, the NaF + RbF PDT potentially also leads to some kind of surface passivation layer but which is quickly broken under laser illumination. While the results are interesting, they do not affect the interpretation of the results in Fig. 5.5 and are just mentioned for the sake of completeness.

The experiments were repeated on a second set of samples LN1, LN2, and LN3. However, these samples were originally grown for different purposes and show stronger variations in their compositions, most notably in their gallium gradient. The results of the measurements are shown in Appendix D.4. Due to the absorber showing stronger discrepancies, the results are to be viewed with caution but a similar trend as in Fig. 5.5 can be recognized.

5.2.2 Case of high-temperature absorbers

The samples H1 and H2 grown at high temperatures are present in a different shape than the low-temperature samples (see Appendix B.1 for details). Due to the non-negligible inhomogeneity in the measured solar cell parameters across the 10 solar cells that are situated next to each other on a sample strip, it was decided to also measure the quasi-Fermi level splitting spatially-dependent on spots that would correspond to a solar cell if the absorber were to be finished into solar cell devices. The results of these macroscopic spatially-resolved PL measurements are shown in Fig. 5.6A. The measured $\Delta\mu$ of the CdS-covered absorbers H1 (full red circles) and H2 (full blue circles) shows a steady decline from cell number 2 to cell number 10 for both samples (albeit to a reduced degree in sample H1). A similar trend is observed for the bare H1 absorber (hollow red circles) and for the bare H2 absorber (hollow blue circles). Since a decrease of the quasi-Fermi level splitting is generally due to an increase in non-radiative recombination in the material, the observed trend might suggest a strong spatial inhomogeneity such that cells on left-hand side are of a higher quality than cells on the right-hand side.

However, a reduction of the QFLS could also be due to a reduction in band gap energy E_g (cf. section D.1). This can be verified by computing the QFLS deficit $E_g - \Delta\mu$ which is a quantity that is independent of changes in the band gap energy and reflects the real trend in absorber quality. Since the reliable determination of the band gap energy for every cell takes a considerable amount of effort, the PL transition energy E_{PL}, which scales with the band gap energy, can be taken as a substitute. In this context, the energetic QFLS deficit $E_{PL} - \Delta\mu$ is shown in Fig.

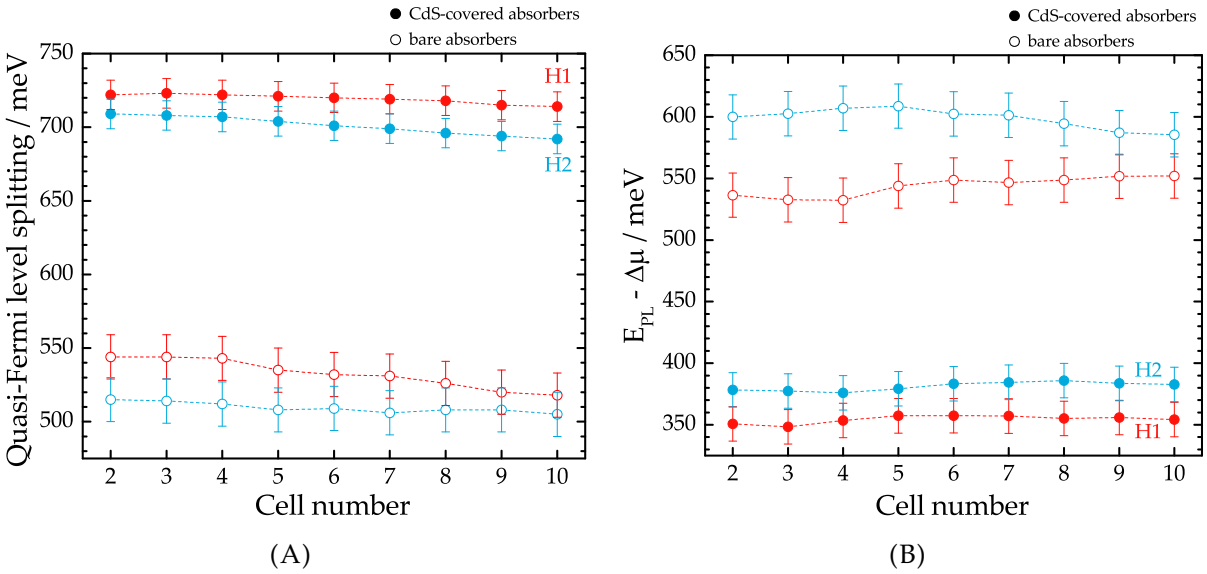

FIGURE 5.6: Spatial dependence of the quasi-Fermi level splitting **(A)** and energetic QFLS deficit $E_{PL} - \Delta\mu$ **(B)** of samples H1 (red circles) and H2 (blue circles). The CdS-covered absorber values are visualized as full circles while the bare absorbers are represented as hollow circles. The individual spectra were measured on 9 side-by-side cells and can be viewed in Appendix D.5. A precise drawing of the sample structure, including cell allocation and placement, can be found in Appendix B.1. Cell number 1 was not measured as it was already separated from the strip and used for other measurements prior.

5.6B. In this representation, the QFLS deficit is relatively constant across the whole sample for the CdS-covered absorbers H1 and H2. Thus, one can conclude that the spatially varying QFLS is primarily due to a spatial dependence of the band gap energy in the samples. The energetic QFLS deficit for the bare absorbers shows a more irregular trend that cannot be explained by spatial variations in the band gap energy alone. The variations in QFLS in the bare absorbers could be explained by real spatial differences in the absorber quality or by a reduced fitting quality due to very low PL signals. The latter explanation is assumed to be more likely.

A similar determination of the V_{OC} deficit (i.e. $E_g - V_{OC}$) on the corresponding solar cells is not possible since the band gap energies of the individual solar cells are not available. As such, to represent the data in bar plot similar to the one shown in the previous section, the average $\Delta\mu$ across all absorber cells is taken and shown in Fig. 5.7. For clarification, the reader is reminded that the non-treated absorber in this case was grown on soda-lime glass at high temperatures, meaning that Na is present in the sample and thus did not require a NaF PDT. The measured $\Delta\mu$ for the CdS-covered absorbers (red bars) shows an increase if the sample was treated with RbF after growth. The same trend can be seen in both the V_{OC} of the solar cell devices (white bars) and the QFLS of the bare absorbers (blue bars). Contrary to the sample set L1, L2, and L3, where the band gap energy between the samples was almost identical, sample H1 shows a slightly reduced band gap energy compared to sample H2 (see Table 3.1 section 3.3). This difference in band gap energies is not accounted for in Fig. 5.7. However, since the measured $\Delta\mu$ and V_{OC} are larger for sample H1 than for sample H2 in any case, the consideration of the band gap energies would only increase the gap between both samples and would not change the interpretation of the results.

Looking at the measured $\Delta\mu$ of the bare absorbers H1 and H2 reveals much lower values than in bare absorbers L2 and L3 (where similar alkalis are present in the absorbers). The measurements shown in Fig. 5.7 on the bare high-temperature absorbers were done just a few days prior to the measurements on the low-temperature sample set, indicating that the lower

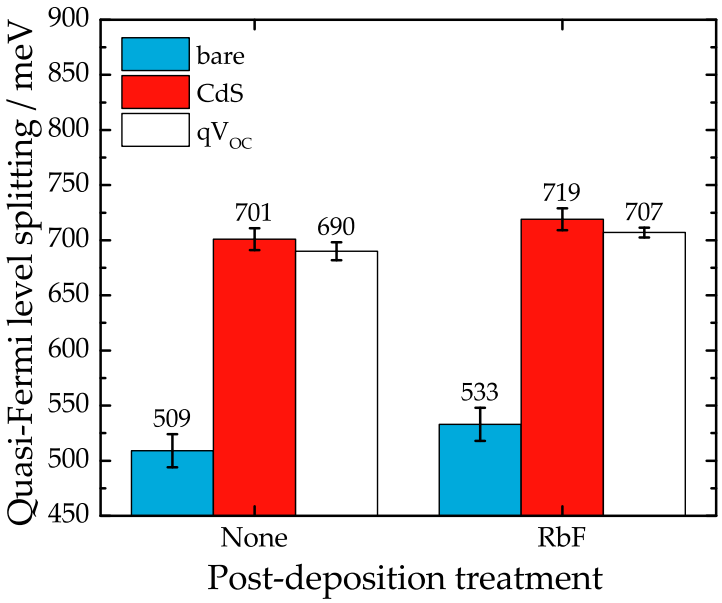

FIGURE 5.7: Bar plot showing the quasi-Fermi level splitting of bare (blue bars) and CdS-covered (red bars) CIGS absorbers having undergone different post-deposition treatments. For comparison, the qV_{OC} (white bars) as measured on the finished solar cell devices are also shown. The values represents average values. The non-treated sample corresponds to sample H2, while the RbF treated sample corresponds to sample H1.

$\Delta\mu$ cannot be due to a longer exposure to air. However, as can be seen in Fig. 4.7, the high-temperature absorber show a significantly rougher surface. A rougher surface leads to a larger total surface area which enters into contact with air and thus leads to a swifter degradation. The lower $\Delta\mu$ in the bare high-temperature absorbers can thus be attributed to a stronger degree of surface degradation. More information about measurement timing and differences between high-temperature and low-temperature sample sets are given in Appendix D.6.

Before concluding, one last important thing needs to be mentioned: the measured PL spectra on both the high- and low-temperature absorbers were all evaluated without taking into consideration the surface reflectance of the samples. The reason is that the V_{OC} of the solar cells was also measured the same way and, most importantly, without the presence of an anti-reflective coating. However, changes in the reflectance of the sample surface, i.e. bare, CdS-covered, and with a ZnO window layer surfaces, surely influence the photon flux density of the incident illumination that is absorbed by the CIGS absorber. In order to investigate these influences, the reflectance is measured in spectrophotometric experiments and reveals only very tiny changes between the various PDTs and samples. These changes lead to quasi-Fermi level splitting differences of 1 - 3 meV which are dwarfed by other measurements uncertainties that are reflected in the error bars.

Finally, as a conclusion of the intensity-calibrated photoluminesence measurements and comparison of the quasi-Fermi level splitting $\Delta\mu$ and open-circuit voltage V_{OC} of different samples, the results suggest that the high-temperature samples respond to the alkali PDT in the same way as the low-temperature sample set. That is an improvement of the absorber surface with heavier alkalis (as already reported in literature) as well as an improvement of the bulk material due to a reduced non-radiative recombination (new insight).

5.3 Influence of the alkali PDT on the band tails

The results from the previous section 5.2 suggest that the alkali atoms, which are incorporated into the absorber during the post-deposition treatment, do not only improve the absorber's surface but also its bulk properties. While these results yield important information, they are not able to entirely clarify the exact nature of the improvements. To provide additional insight, the influence of the alkali atoms on the absorption properties is investigated. As was introduced in section 5.1.2, the Urbach energy E_U can act as a descriptive quantity of the band tails i.e. absorption coefficients that extent exponentially into the band gap. In fact, an exponential decrease of the absorption coefficient is a common occurrence in a multitude of semiconductor materials such as e.g. kesterite ($CuZnSn(S_xSe_{1-x})_4$) [216], gallium arsenide (GaAs) [217], [218], crystalline silicon (c-Si) [219], amorphous silicon (a-Si:H) [220], cadmium telluride (CdTe) [221], metal and organometal halide perovskites ($MAPbI_3$, $CH_3NH_3PbI_3$) [222], [223], and lead sulfide (PbS) [224]. The fact that an exponential behaviour of the absorption coefficient can be observed in a multitude of materials suggests a common underlying origin. Theoretical calculations by John *et al.* reveal that Urbach tails are caused by disorder that leads to deviations from the perfect crystal lattice [225]. This disorder can be present under different forms and the case of CIGS is explained below. There exist additional models that describe a different, non-linear-exponential behaviour of the absorption coefficient below the band gap energy. A summary of the various models can be found in [214] but will not be considered here as the observed behaviour is clearly one of Urbach type.

In CIGS, band tails can originate from potential fluctuations that affect the conduction and valence band edges [92]. These potential fluctuations can be present under two forms in CIGS: band gap fluctuations and electrostatic potential fluctuations.

Band gap fluctuations arise from compositional inhomogeneities within the absorber [105]. As the gallium content dictates the band gap energy of the absorber, local variations in the GGI ratio will induce local variations in the band gap energy. But not only gallium is responsible for the band gap energies, also copper has shown to influence the positions of the conduction and valence bands [226]. Furthermore, non-stoichiometry can lead to strain-induced fluctuations of the crystal lattice, which in turn, lead to fluctuations of the band edges [106].

While the concept of electrostatic potential fluctuations was introduced in section 2.7.4, some main points are briefly picked up here again. In Cu-poor CIGS absorbers, the concentrations of donor and acceptor impurities are similar. This leads to a compensation effect where the electrons from the donor atoms are trapped by the acceptor atoms. Thus, the dopant atoms are ionized and produce a Coulomb potential. Consequently, an ionized acceptor exerts an attractive force on the holes in the valence band and a repulsive force on the electrons in the conduction band (and vice-versa for the ionized donors). Since donor and acceptor impurities are not distributed equally within the absorber, the exerted Coulomb force that distorts the edges of the conduction and valence bands is stronger in some locations than in others. The ionized impurities can be present within the grains, such as e.g. in the form of shallow acceptors and donors, or at the grain boundaries. The presence of ionized impurities at the grain boundaries, which have been confirmed by several studies [227]–[229], cause band bending that can technically also be classified as potential fluctuations. Thus, as was the case for band gap fluctuations (where GGI and CGI variations play a role), electrostatic potential fluctuations can also be due to a disordered distribution of impurities/defects, as well as due to band bending at the grain boundaries.

The potential fluctuations influence both the valence and conduction band, causing the joint density of states to extend into the band gap. In the case of electrostatic potential fluctuations, the band gap energy remains locally constant. However, through tunnelling processes,

spatially-separated states may also participate in recombination processes (cf. Fig. 2.18 in section 2.7.4). The absorption coefficient is proportional to the joint density of states (cf. refs. [20], [92] and section 2.7.1), explaining why the band tails are observable in the absorption spectra in the first place. The effect of band tails on the performance of solar cells are various. On the one hand, states below the band gap lead to the absorption of photons with lower energies, increasing thus the portion of the AM1.5 spectrum that is absorbed and is contributing to a larger short-circuit current j_{SC} (this is shown in Fig. A.2 in appendix A.2). On the other hand, the principle of detailed balance imposes that the absorptivity equals the emissivity, meaning that states below the band gap that absorb light will also emit light. This additional channel of recombination, albeit of radiative nature, leads to an increase of the saturation current density j_0 and ultimately to a decrease in open-circuit voltage V_{OC} (cf. eq. (2.13) in section 2.3.2). The implications of potential fluctuations on solar cell performance have been laid out in various studies [105], [106], [230], [231]. It was found that the losses in V_{OC} that are occurring in CIGS solar cells can potentially entirely be explained by strong potential fluctuations that effectively lead to a reduction of the band gap energy. In addition, in the case of strong potential fluctuations, some states reach deep into the band gap where they can act as non-radiative recombination centers and thus reduce the V_{OC} even further [216].

So far, there exists no general consensus regarding the strength of the potential fluctuations in state-of-the-art CIGS absorbers. From the behaviour of the absorption coefficient below the band gap energy, it is not possible to distinguish between band gap and electrostatic potential fluctuations. However, the Urbach energy can be used to investigate qualitative differences between absorbers and thus conclude whether the alkali PDT has an influence on the detrimental density of states reaching into the band gap.

5.3.1 Influence on the Urbach energy determined by PL

In the following, the Urbach energy is extracted for the CdS-covered CIGS absorbers having undergone various alkali post-deposition treatments. As the sub band gap absorption coefficient is derived from the low-energy slope of the photoluminescence spectra, the samples are covered by several polystyrene (PS) layers to remove the interference fringes. Due to the presence of these layers, which are not identical for every sample (a non-avoidable result of the deposition process - see section 4.4.1), it is not possible to identify the exact photon flux density that is incident on the sample surface. Fortunately, the photon flux density, and consequently the emitted photoluminescence yield, have no influence on the absorption coefficient as long as the shape of the measured PL spectra is not influenced [166]. A possible culprit for spectra distortion in state-of-the-art CIGS is the temperature increase that comes along with too high excitation densities. To verify that no heating effects are taking place, the PL spectra are measured for multiple excitation densities. A comparison of the high-energy slope of the spectra between the different excitation densities does not reveal any changes apart from an expected reduction of the signal-to-noise ratio. Thus, under the excitation densities used in these experiments, it can safely be concluded that the temperature remains constant at room temperature. The absorption spectra presented in this section and in the appendix D.7 are the ones that were recorded under the highest selected excitation density to reduce the signal-to-noise ratio as much as possible.

Fig. 5.8A shows the absorption coefficient spectra of samples H1 (red curve) and H2 (blue curve) in semi-logarithmic representation. The fitting range that is displayed acts as an example. In this specific case, the Urbach energy E_U that is extracted from the fit (dashed line) reveals a lower value of 10.8 meV for the H1 absorber compared to 12.1 meV for the H2 absorber. This

result suggests that the band tails are weaker in the absorber that received a RbF PDT than in the absorber that did not.

The same trend is seen in the absorbers that are grown in a low-temperature process. Fig. 5.8B shows the absorption coefficient spectra of samples L1 (red curve), L2 (blue curve), and L3 (green curve). Again, the extracted Urbach energies for the displayed examplary fitting range are lower for absorbers that were treated with heavier alkali atoms. Comparing the Urbach energies of the low-temperature samples to the high-temperature ones, it is clear that samples H1 and H2 exhibit weaker band tails than samples L1, L2, and L3. This discrepancy can be attributed to the different elemental compositions of the absorbers. For example, it is well-known that a low CGI ratio promotes compensation and consequently stronger potential fluctuations [163], [171]. Looking at the measured elemental composition of the samples at hand (see table 3.1 in section 3.3), the high-temperature absorbers indeed exhibit a higher CGI than the low-temperature absorbers.

For both sample sets in Fig. 5.8, the Urbach energies are extracted from the visualized fitting ranges. The fitting ranges are selected such that they are at sufficiently low energies to not be influenced by the band-to-band absorption but not too low to avoid the higher noise contribution to the signal. To investigate the influence of various fitting ranges on the extracted Urbach energies, the samples are all measured over a broad spectral range (the spectra in Fig. 5.8 show a narrow spectral range) and for various excitation densities (to reduce the signal-to-noise ratio at low energies and allow for a more precise fit). The absorption coefficient spectra measured over a broad range and the extracted Urbach energies for sample L1 for three different fitting ranges are shown in Fig. D.7A in the appendix D.7. While the extracted Urbach energies show a very weak dependence on the improved signal-to-noise ratio (as most of the fitting is done away from the low signals anyway), the fitting ranges have a much stronger influence on the extracted Urbach energies in the case of the low-temperature absorbers (almost no influence in the case of the high-temperature absorbers). To account for the influence of the fitting range,

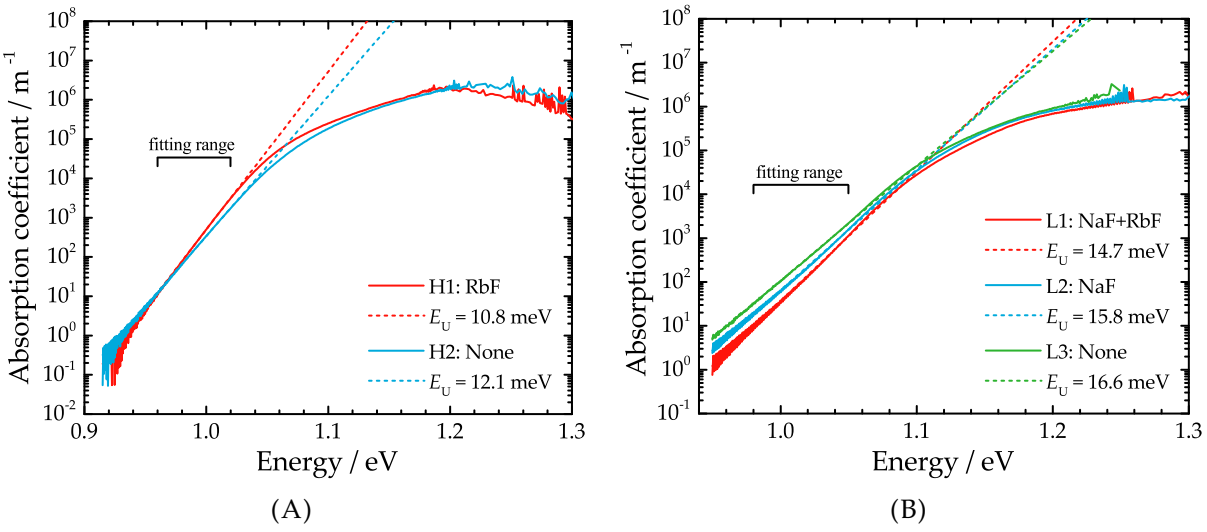

FIGURE 5.8: **(A)** Absorption coefficient spectra derived from PL measurements on the PS- and CdS-covered H1 (red curve) and H2 (blue curve) absorbers in semi-logarithmic representation. The dashed lines represent the fit according to eq. (5.6) in the indicated fitting range. The Urbach energies E_U extracted from the fit are shown in the bottom-right corner. **(B)** Absorption coefficient spectra derived from PL measurements on the PS- and CdS-covered L1 (red curve), L2 (blue curve), and L3 (green curve) absorbers in semi-logarithmic representation. Extracted Urbach energies from the fits (dashed lines) are displayed in the bottom-right corner.

the extracted Urbach energy is averaged over several fitting ranges (cf. Fig. D.7A and Fig. D.8 in appendix D.7).

Since the absorbers grown in the different processes exhibit different elemental compositions, a comparison of the high-temperature and the low-temperature samples in the representation of Fig. 5.8 is futile. A better frame for comparison, providing also a direct link to the losses in optoelectronic quality, is the graph in Fig. 5.9 where the energetic quasi-Fermi level splitting deficit $E_{PL} - \Delta\mu$ is shown in dependence of the extracted Urbach energy. As a reminder, E_{PL} represents the energy of the PL peak maximum and can be seen as a substitute for the band gap energy. The values for the QFLS $\Delta\mu$ are taken from the previous section 5.2. Along the samples shown in Fig. 5.8 and discussed above, additional samples are included and are motivated in the following (available solar cell parameters for the samples can be found in Table 3.2 of section 3.3). The error bars that are attributed to the different data points consist of an estimated uncertainty of 15 meV for $E_{PL} - \Delta\mu$ and a standard deviation for E_U computed from the extracted values for different fitting ranges (and different excitation densities where the improved signal-to-noise leads to slightly better fits) as described in appendix D.7.

The inclusion of samples LN1 and LN2 (green dots) into the graph is straightforward as their quasi-Fermi level splitting was already investigated in appendix D.4. The absorption coefficient spectra of both PS- and CdS-covered absorbers are given in Fig. D.7B in appendix D.7. Sample LN3 is not included because the absorption coefficient spectrum exhibited a significant bump at low energies, leading to an unreliable extraction of the Urbach energy. While the origin of this bump is not entirely clear, it is very likely that the polystyrene deposition process did not yield the same results as for the other samples and failed to completely remove the interference fringes in this case.

The orange data point in Fig. 5.9 represents the PS- and CdS-covered absorber LS. This

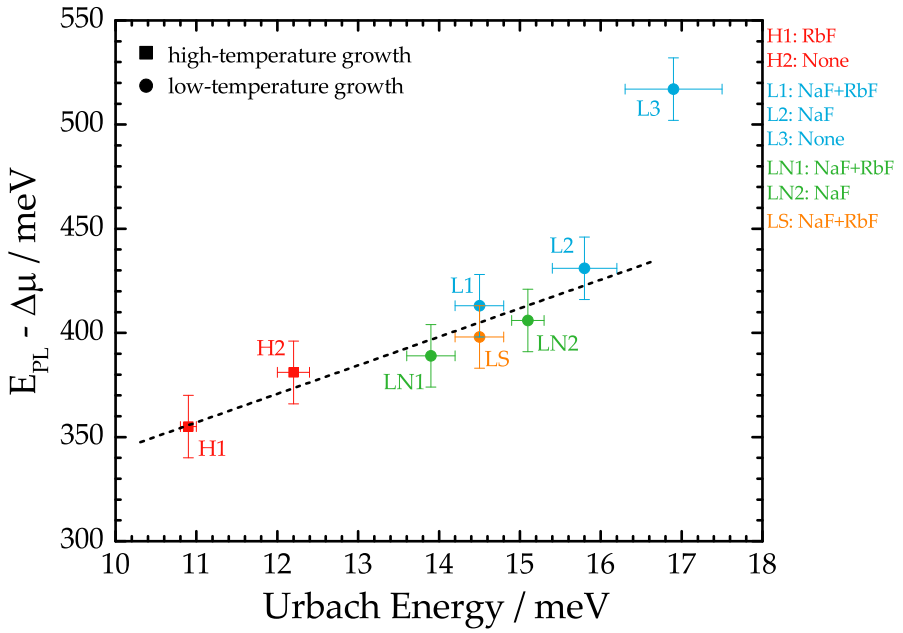

FIGURE 5.9: Energetic quasi-Fermi level splitting deficit $E_{PL} - \Delta\mu$ in dependence of the Urbach energy E_U for absorbers grown under high temperatures (squares) and under low temperatures (circles). The color code refers to samples that were grown under the same conditions but received different post-deposition treatments. The sample names are indicated next to the corresponding data points. The allocation of error bars is explained in the main text. The black dashed line is a guide to the eye that visualizes the correlation between $E_{PL} - \Delta\mu$ and E_U.

absorber is included because its corresponding finished solar cell devices yield the highest efficiencies of all the samples grown in a low-temperature process in this thesis. Its absorption coefficient spectrum for a given excitation density is shown in Fig. D.8 in appendix D.7.

Apart from sample L3, which shows a very large energetic QFLS deficit, the other samples show a very clear and precise trend. This trend is represented by the black dashed line and reveals a correlation between optoelectronic losses and the Urbach energy for state-of-the-art CIGS absorbers[4]. This result is very important and reveals two major conclusions. Firstly, the alkali post-deposition treatment greatly affects the bulk properties of the CIGS absorbers. This is in good agreement with the findings from the previous section 5.2 where an effect on the surface and bulk properties was found. Secondly, it can be argued that whatever causes the band tails also causes the $\Delta\mu$ losses and consequently the V_{OC} losses. An attribution of the band tails and the reduction of their detrimental effect with alkali PDT to a specific mechanism is not possible based solely on the present data. However, this discussion is very important and will be re-addressed in the later section 7.2.

Finally it needs to be mentioned that the representation of the energetic QFLS deficit $E_{PL} - \Delta\mu$ in Fig. 5.9 is not the real QFLS deficit $E_g - \Delta\mu$ but a substitute quantity that was chosen because the measurements were all performed on the CIGS absorbers where the band gap energies are not exactly known. Thus, for a similar representation but in the form of the QFLS deficit $E_g - \Delta\mu$, one would expect a slight shift of all data points towards larger y-values albeit the conclusion discussed above would be identical.

5.3.2 Comparison to other methods

In section 5.1.2, it was mentioned that photoluminescence measurements allow for the detection of the absorption coefficient over a dynamic range of several orders of magnitude. Since the extraction of the Urbach energies is done at low energies, photoluminescence is more suited to this task than other techniques. Nonetheless, it is useful to verify if the trend that is observed in Fig. 5.8, i.e. the reduction of band tails with heavier alkali PDT, can be replicated with other techniques.

One such technique is photocurrent spectroscopy (PCS) where the generated electron current due to photon absorption of different energies can be measured. In this case, the samples are illuminated by a continuous-wave polychromatic light source and the extracted photocurrent is normalized to the flux of incident photons. More details can be found in reference [232]. Since a current needs to be extracted, the PCS measurements have to be done on the solar cells and not on the absorbers. Fig. 5.10A shows the natural logarithm of the normalized photocurrent for the L1, L2, and L3 solar cells. The fitting range was fixed from a lower limit of 1.05 eV, where the background signal is not yet affecting the spectrum, to an upper limit of 1.10 eV that can still be deemed sub band gap (the band gap energies for these solar cells are around 1.14 eV - see section 3.3). The fits (dashed lines) reveal a decrease in the Urbach energy E_U for samples treated with alkali PDT. Thus, PCS measurements reveal the same trend as PL measurements.

A very similar technique that can be used to investigate the absorption edge is external quantum efficiency (EQE). In this context, Fig. D.9A in appendix D.8 shows the natural logarithm of the EQE for the same L1, L2, and L3 solar cells. For the same fitting range as in the PCS measurements, the same trend of reduced E_U with alkali PDT can be seen. The EQE measurements are included, even though the technique is very similar to PCS, because they were done in another laboratory (Empa) under different conditions.

[4] A similar trend in the V_{OC} deficit across different PV technologies was also discovered by De Wolf *et al.* [223]. The representation of the V_{OC} deficit is not chosen in Fig. 5.9 but will be picked up in the later section 7.1.1.

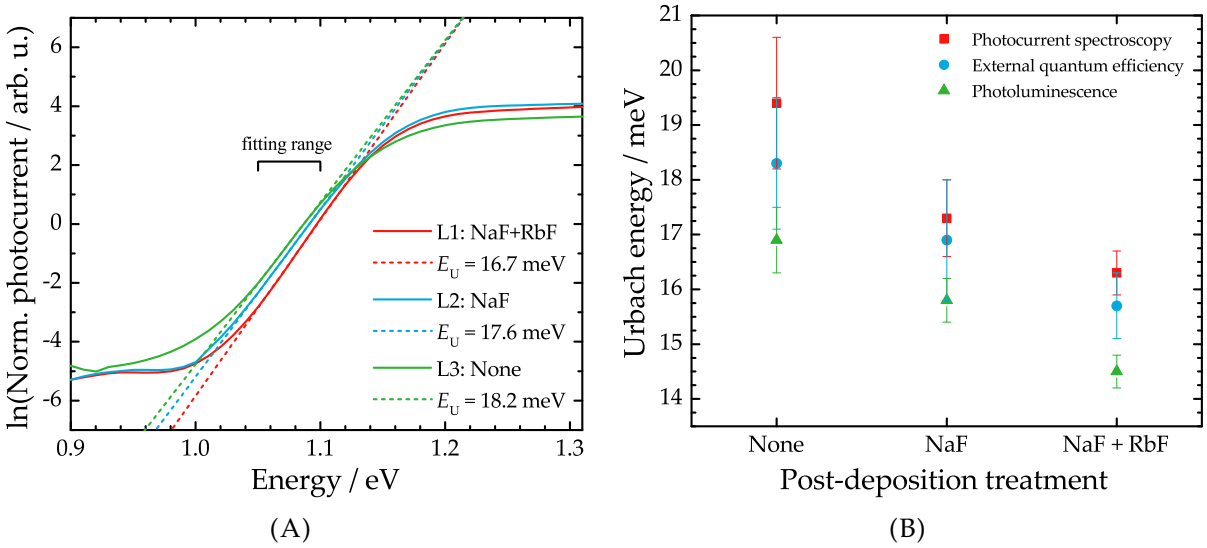

FIGURE 5.10: **(A)** Natural logarithm of the spectral photocurrent measured by photocurrent spectroscopy on the solar cells L1 (red curve), L2 (blue curve), and L3 (green curve). The fits of eq. (5.6) between 1.05 eV and 1.10 eV are represented by the dashed lines. The Urbach energies extracted from the fits are displayed in the bottom-right corner. The PCS measurement were conducted by Dr. Emilie Bourgeois from the University of Hasselt. **(B)** Comparison of the extracted Urbach values for the low-temperature samples in dependence of the PDT they received after growth. The non-treated sample corresponds to sample L3, the NaF-treated sample corresponds to sample L2, and the NaF+RbF-treated sample corresponds to sample L1. The red squares, blue dots, and green triangles correspond to the Urbach energies measured from PCS, EQE, and PL respectively. The error bars are explained in the main text.

The comparison of the Urbach energies obtained from the different techniques is shown in Fig. 5.10B where the results from PCS are represented by the red squares, from EQE by the blue dots, and from PL by the green triangles. The plotted data points all represent average values. In the case of PCS, the Urbach energy was extracted from 2 solar cells on sample L1, from 3 solar cells on sample L2, and from 3 solar cells on sample L3. In the case of EQE, the Urbach energy was extracted from 2 solar cells on sample L1, from 2 solar cells on sample L2, and from 3 solar cells on sample L3. The error bars in Fig. 5.10B represent standard deviations evaluated from the values measured across the different cells. The Urbach energies from PL are taken from Fig. 5.9. Despite discrepancies in the absolute values of E_U (possible explanations are discussed in appendix D.8), Fig. 5.10B reveals the same trend: no matter the measurement technique, the band tails are reduced when the absorbers are treated with heavier alkali atoms.

On the high-temperature absorbers H1 and H2, only external quantum efficiency measurements were done. The respective extraction of the Urbach energy is shown in appendix D.9 and shows the same trend as for the PL measurements.

5.4 Influence of the alkali PDT on absorber homogeneity

The measurements of the quasi-Fermi level splitting in section 5.2 suggest that the alkali atoms, which are incorporated into the CIGS absorbers after growth, improve the absorber surface and bulk. In the previous section 5.3, the bulk improvement is confirmed with the alkali PDT causing a reduced density of states that extend into the band gap. It was argued that the band tails are caused by potential fluctuations which can be of various origin. As the measurements were done on a macroscopic scale, however, only spatially averaged effects of alkali atoms

are observed. Consequently, smaller spatial inhomogeneities that can cause band tails, such as locally non-uniform alloy disorder or defect densities, go unnoticed. To remedy this issue, microscopically-sensitive measurement techniques can be employed. One example of such a technique is spatially-resolved photoluminescence spectroscopy with micrometer resolution, in the following labelled as μ-PL. This latter technique has found many applications in the study of CIGS absorbers such as the investigation of band gap fluctuations [233]–[236], the detection of defects [46], [48], [236], [237], or local variations in the quasi-Fermi level splitting $\Delta\mu$ [209], [233], [238]–[240]. The latter is very important as the spatial distribution of $\Delta\mu$ acts as a homogeneity indicator of the absorber since it is influenced by spatial variations of elemental compositions (doping concentrations, band gap fluctuations), transport properties, and recombination activity.

In the following, μ-PL is used at room temperature to investigate the spatial distribution of the radiative recombination in state-of-the-art CIGS. The measurement and characterization principle is briefly introduced with the concrete example of the H1 absorber. Afterwards, the same measurements on the L1 absorber are showcased. Finally, the results are summarized and compared to similar studies in literature. The absorbers measured in the μ-PL experiments are all covered by a CdS layer to ensure high emitted signals. Furthermore, the samples do not feature polystyrene layers[5].

5.4.1 Case of high-temperature absorbers

The experimental setup along with its confocal optics, described in detail in section 3.2, allow for the excitation and collection of PL from an approximately 1 μm spot size. With the sample being stationary, the optics are scanned across the sample such that maps of $41 \cdot 41\,\mu\text{m}^2$ are measured. For each micrometer of the map, a PL spectrum is measured, resulting in a total of 1681 recorded spectra. Each spectrum can then be analysed and evaluated at will. In this context, Fig. 5.11A shows the integrated photon flux density in a $41 \cdot 41\,\mu\text{m}^2$ spatial scan of sample H1. Each pixel represents the integrated photon flux density of the corresponding PL spectrum that was measured at that specific location. The photon flux density is represented in arbitrary units as intensity-calibration in not possible in the current form of the μ-PL setup. Due to the minuscule spot size of the excitation radiation, the incident photon flux density on the surface of the H1 absorber in this case amounted to approximately $4 \cdot 10^{24}\,\text{m}^{-2}\,\text{s}^{-1}$ i.e. roughly 1500 suns.

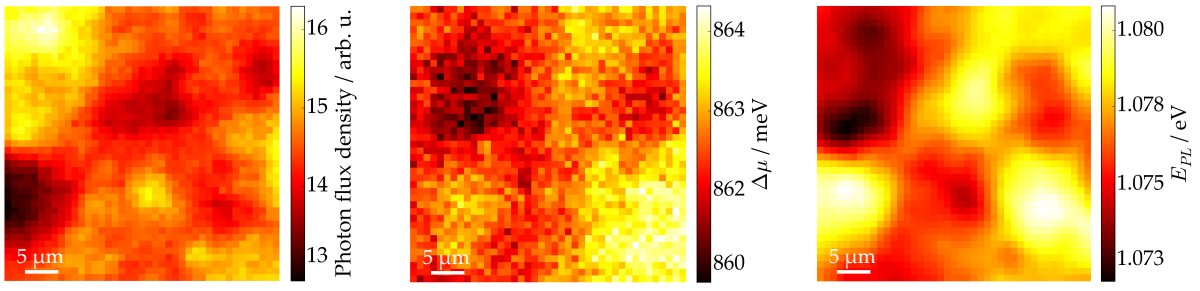

FIGURE 5.11: Spatially-resolved $41 \cdot 41\,\mu\text{m}^2$ photoluminescence maps of sample H1 where each pixel represents the **(A)** integrated photon flux density Y_{PL}, **(B)** quasi-Fermi level splitting $\Delta\mu$, and **(C)** the transition energy E_{PL} of the corresponding measured spectrum.

[5]The main reason being that the measurements were conducted before the discovery of the effects of the polystyrene layer. As such, the influence of a laser spot with micrometer resolution on the PS beads of similar dimension is not yet fully investigated but is the subject of future research.

In addition to the integrated photon flux density, from each recorded spectrum of the map, the quasi-Fermi level splitting $\Delta\mu$ can be extracted and displayed in a spatial arrangement as shown in Fig. 5.11B. While the extraction method of $\Delta\mu$ follows the same principles as laid out in section 5.1.1, it is not as straightforward and a few issues, such as the temperature, need to be considered. In this context, the extraction of $\Delta\mu$ from a random spot of the recorded H1 map in Fig. 5.11 is showcased in appendix D.10. This example details the importance of fixing the temperature to a value that provides a good fit to the data. Under the experimental conditions mentioned above, a fixed temperature of 310 K was chosen.

With the quasi-Fermi level splitting $\Delta\mu$ acting as an indicator for absorber homogeneity, Fig. 5.11B can be statistically evaluated to yield descriptive quantities such as the mean $\Delta\mu_{\text{mean}}$ and the standard deviation $\sigma_{\Delta\mu}$. In this context, Fig. 5.12 shows the statistical distribution of $\Delta\mu_{i,j} - \Delta\mu_{\text{mean}}$ where $\Delta\mu_{i,j}$ is the quasi-Fermi level splitting of spot (i,j) of the 2-dimensional scan. For this specific scan of absorber H1, the standard deviation amounts to 0.88 meV. Additionally, the largest difference between the $\Delta\mu$ of two spots on the spatial map is as low as 5 meV (see Fig. D.13A and D.12 in appendix D.10). Both these values show that the H1 CIGS absorber is very homogeneous on a microscopic scale.

Even though the spread of the quasi-Fermi level splitting in absorber H1 is very tiny, it is still worth investigating. Since the temperature can be considered constant across the absorber, only changes in the radiative recombination rate or in the band gap energy can lead to spatial variations in $\Delta\mu$. As the band gap energy is not accessible, the energy E_{PL} of the main PL transition is used as a substitute and is shown in Fig. 5.11C. To identify the cause for the variations in $\Delta\mu$, the degree of correlation between the different maps can be investigated. The cross-correlation coefficient $C_c(M_A, M_B)$ between two maps or matrices M_A and M_B is defined as [48]

$$C_c(M_A, M_B) = \frac{1}{n} \sum_{i,j} \frac{\left(M_A(i,j) - \overline{M_A(i,j)}\right)\left(M_B(i,j) - \overline{M_B(i,j)}\right)}{\sigma(M_A(i,j))\,\sigma(M_B(i,j))}, \tag{5.7}$$

where n is the total number of spots or pixels of a map, $M_{A/B}(i,j)$ is the matrix containing the relevant data, $\overline{M_{A/B}(i,j)}$ is the mean value of the matrix, and $\sigma(M_{A/B}(i,j))$ is the standard deviation of the matrix. The closer the cross-correlation coefficient to the value 1, the higher the degree of correlation between two maps (and the closer to -1, the higher the degree of anti-correlation). Conversely, if the coefficient ranges between -0.3 and 0.3, the involved maps are said to be uncorrelated [241]. In the case of the H1 sample, the cross-correlation coefficient between $\Delta\mu$ and the photon flux density Y_{PL} yields $C_c(\Delta\mu, Y_{\text{PL}}) = -0,09$ while the correlation between $\Delta\mu$ and E_{PL} reads $C_c(\Delta\mu, E_{\text{PL}}) = 0.69$. From these values it can be concluded that

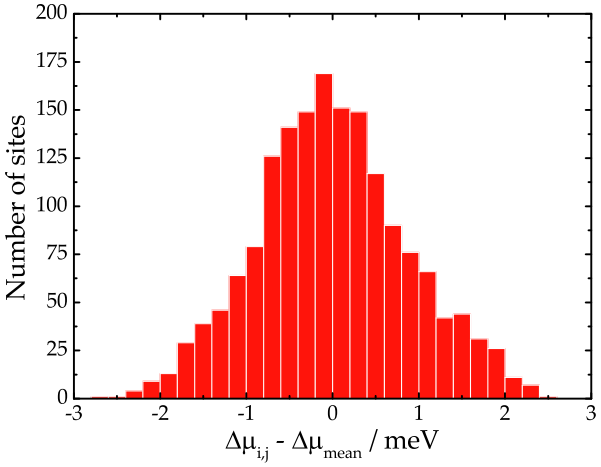

FIGURE 5.12: Statistical distribution of the quasi-Fermi level splitting for each pixel $\Delta\mu_{i,j}$ offset by the mean value $\Delta\mu_{\text{mean}}$.

the variations in $\Delta\mu$ are largely due to variations in the band gap energy and not due to inhomogeneities that cause fluctuations in the radiative and non-radiative recombination rate. Fig. D.13B in appendix D.10 shows the PL spectra with the lowest and highest extracted $\Delta\mu$, clearly demonstrating the dominating influence of the band gap energy in this case. Finally it can be concluded that the variations, whether in quasi-Fermi level splitting, photon flux density or band gap energy, are overall vanishingly small.

For the H2 absorber, the spread of the quasi-Fermi level splitting for a similar measurement (same scan size but twice as much incident excitation density than for sample H1) is also vanishingly small: $\sigma_{\Delta\mu} = 1.18\,\text{meV}$. The corresponding maps are shown in Fig. D.14 in the appendix D.11. Interestingly, the cross-correlation coefficient between $\Delta\mu$ and photon flux density $C_c(\Delta\mu, Y_{PL})$ reads 0.87 while it is only amounting to $C_c(\Delta\mu, E_{PL}) = -0.16$ between $\Delta\mu$ and the transition energy. Thus, in the case of the sample H2, the variation in $\Delta\mu$ is largely due to local microscopic regions exhibiting increased and reduced non-radiative recombination rates. However, in both H1 and H2 samples, the local variations of all involved quantities are too low to allow for any meaningful conclusion regarding the effects of the alkali post-deposition treatments.

To ensure that the findings shown above reflect the real behaviour of the high-temperature CIGS absorbers and are not the result of peculiar or unusual spots, the spatially-resolved scans were measured on three different locations across the sample. While all the data are not displayed here, the maps show exactly the same behaviour as mentioned above for the H1 and the H2 absorber.

5.4.2 Case of low-temperature absorbers

As was the case for the high-temperature absorbers, $41 \cdot 41\,\mu\text{m}^2$ scans were also done on the low-temperature absorbers L1, L2, and L3, where four different scans were measured across each absorber. As an example, the recorded maps of one scan on sample L1 under an excitation photon flux density of approximately $10^{25}\,\text{m}^{-2}\,\text{s}^{-1}$ (approx. 4000 suns) are displayed in Fig. 5.13. It is immediately evident that the photon flux density (Fig. 5.13A) is strongly correlated to the quasi-Fermi level splitting (Fig. 5.13B), while the transition energy (Fig. 5.13C) shows a different spatial variation. In terms of the cross-correlation coefficient, the numbers read $C_c(\Delta\mu, Y_{PL}) = 0.88$ and $C_c(\Delta\mu, E_{PL}) = 0.34$, proving thus that the spatial fluctuations in $\Delta\mu$ are predominantly due to the locally distributed regions of larger and smaller rates of non-radiative recombination. This behaviour is shared between all maps of all low-temperature absorbers.

It needs to be mentioned that the transition energy E_{PL} in the case of the low-temperature absorbers does not relate to the band gap energy as smoothly as for the high-temperature absorbers. This is due to the fact that the main PL peak of the low-temperature absorbers is heavily distorted by interference effects. As such, the transition energy is extracted from one of several peaks (cf. Fig. D.15 in appendix D.12) where it is not entirely clear whether a shift is due to an actual change in the band gap energy or a shift in the interference fringes. However, due to the extremely strong correlation between the photon flux density and the quasi-Fermi level splitting, spatial variations in the band gap energy do not play a role.

The distribution of the quasi-Fermi level splitting in Fig. 5.13D indicates a much stronger spread than for the high-temperature absorbers. The standard deviation for this particular scan e.g. amounts to $\sigma_{\Delta\mu} = 3.33\,\text{meV}$ while the largest difference in $\Delta\mu$ between two spots is as high as 29 meV (cf. Fig. D.15 in appendix D.12). While both high-temperature absorbers show a similar spread of $\Delta\mu$, the low-temperature absorbers show more variability in that regard. Across all maps for the different absorbers, the average $\Delta\mu$ spread amounts to approximately 3.41 meV for L1, to approximately 1.44 meV for L2, and to approximately 4.11 meV for L3. These values

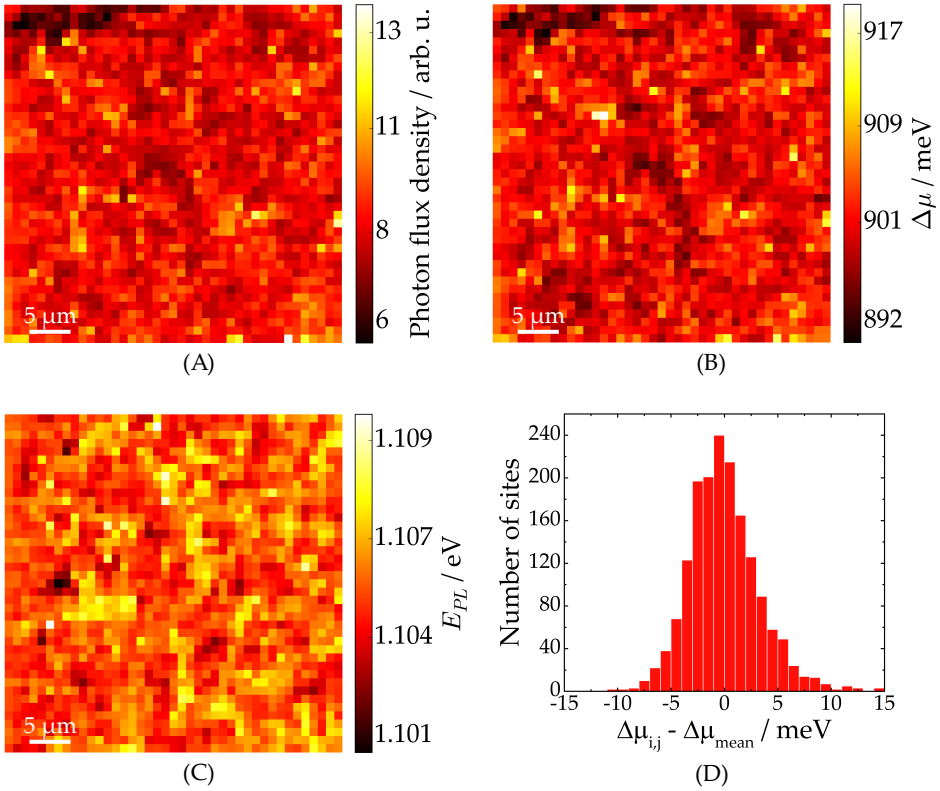

FIGURE 5.13: Spatially-resolved $41 \cdot 41\ \mu m^2$ photoluminescence maps of sample L1 where each pixel represents the **(A)** photon flux density, **(B)** quasi-Fermi level splitting $\Delta\mu$, and **(C)** the transition energy E_{PL} of the corresponding measured spectrum. **(D)** Statistical distribution of the quasi-Fermi level splitting for each pixel $\Delta\mu_{i,j}$ offset by the mean value $\Delta\mu_{mean}$.

are overall too low and too similar to conclude upon a trend (even if the low-temperature absorbers show a stronger deviation between each other than the high-temperature ones).

5.4.3 Comparison to older records

The spatially-resolved quasi-Fermi level splittings extracted from the multiple photoluminescence scans of the absorbers H1, H2, L1, L2, and L3 are summarized in Fig. 5.14. This bar plot shows the standard deviation of $\Delta\mu$, acting as a measure of homogeneity, in dependence of the post-deposition treatment that the samples received. The indicated values represent averages over the different scans (three for the high-temperature absorbers and four for the low-temperature ones) while the error bars represent the standard deviation from these scans.

The $\Delta\mu$ spread in the high-temperature absorbers (red bars) is nearly identical, discarding thus a potential effect of the PDT on the absorber homogeneity. In addition, the spatial variation of $\Delta\mu$ is so low on this microscopic scale that no further analysis can be done. Conversely to the high-temperature absorbers, the low-temperature ones (blue bars) show a stronger variation between the different post-deposition treatments. The extracted spatial variations in $\Delta\mu$ suggest that the NaF PDT improves the absorber homogeneity while the sequential NaF+RbF PDT reduces it again. While this effect might be real, the differences in the QFLS spread are too low to allow a conclusive verification.

The white bars in Fig. 5.14 show selected values from literature where spatially-resolved PL was measured for similar resolutions on absorbers that were the state of the art several years ago. More specifically, the bar labelled **A** represents a value of 5.5 meV that is published in

the separate studies [162] and [238]. Incidentally, the absorbers investigated in the latter study [238] are the "predecessors" of samples H1 and H2 (i.e. they were grown in the same laboratory under similar conditions). The white bar labelled **B** represents a value of 7.6 meV from the study [209]. From the standard deviation of the quasi-Fermi level splitting, it is evident that the newest generation of state-of-the-art CIGS absorbers show a significantly better homogeneity, independent of the post-deposition treatment involved. On the topic of old records, Gütay *et al.* have shown in the study [238] that the spatial variation $\Delta\mu$ is highly dependent on the excitation density. This is investigated for the case of absorber H1 but no such dependence could be identified. The details of these measurements are presented in appendix D.13.

However, it has to be mentioned that the conclusion above is only valid for the spatially-resolved investigations in the microscopic regime. Similar experiments in the sub-microscopic regime (with resolutions of approximately 200 nm) have already been done in the study [233], where a standard deviation of 7.6 meV was found. While this value is identical to the literature data listed above, the results from the study do not refute the possibility of stronger inhomogeneities on an even smaller scale. In addition, spectrally-resolved measurements on sub-microscopic scale on absorbers that underwent different PDTs have so far not been conducted. Thus, it might be possible that the microscopic resolution used in the experiments presented in this thesis is not sufficient to resolve the influence of alkali atoms on spatially-distributed inhomogeneities. This sentiment is vindicated by the very recent study of Avancini *et al.* [242] done on absorbers very similar to the low-temperature absorbers in this thesis. The study reveals strong inhomogeneities in the GGI ratio (increase of up to 0.10) in the notch region but confined to lateral stretches of approximately 100 nm. These compositional inhomogeneities strongly correlate with structural voids in the absorber crystal that are possibly a by-product of the specific state-of-the-art CIGS growth procedure. It is argued that these voids are potentially also present in high-temperature absorbers where, as a consequence, similar compositional

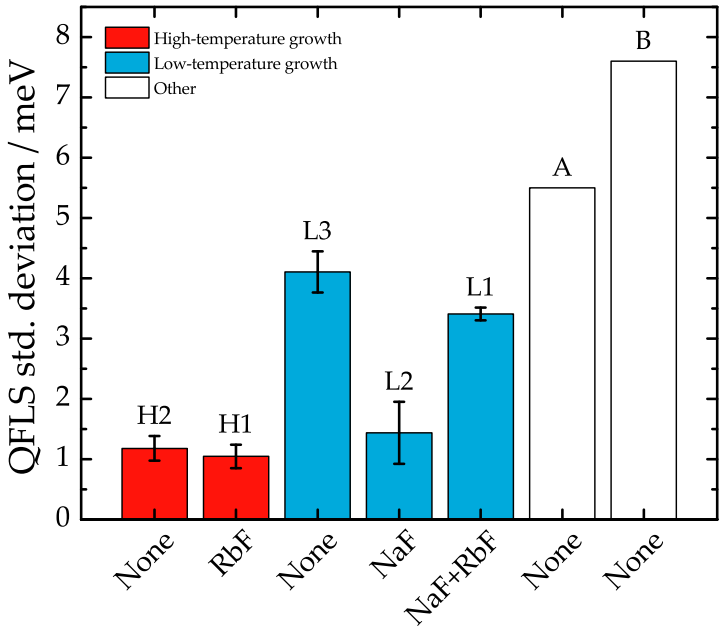

FIGURE 5.14: Bar plot showing the standard deviation of the QFLS $\Delta\mu$ for the high temperature (red bars) and low-temperature (blue bars) absorbers in dependence of their received post-deposition treatment. The values represent averages evaluated over three different scans for H1 and H2, and four different scans for L1, L2, and L3. The error bars are the standard deviations of the results between the different scans. The white bars represent the values as presented in several older studies and are detailed in the main text.

inhomogeneities on the sub-microscopic level are expected.

5.5 Summary

The radiative band-to-band recombination at room temperature in state-of-the-art CIGS absorbers can be described by Planck's generalized law of radiation. From the high-energy slope of the measured photoluminescence spectra, the quasi-Fermi level splitting $\Delta\mu$ can be extracted. Since interference fringes do not affect the high-energy slope of the PL spectra, the measurements can be intensity-calibrated which allows for the determination of the exact values of $\Delta\mu$. However, to ensure the correct determination of $\Delta\mu$, special attention must be devoted to the fitting procedure and quality of the measured PL. In this thesis, it was shown that the $\Delta\mu$ can reliably be extracted under the appropriate circumstances.

The quasi-Fermi level splitting can be used as a measure of optoelectronic quality and constitutes thus an adequate candidate to gauge the influence of alkali atoms on the CIGS absorbers. In this thesis, a comparison of $\Delta\mu$ on bare and CdS-covered absorbers revealed an improvement of the surface and bulk properties of the absorbers whenever alkali atoms are involved. The observed effects, which are generally identified as a decrease of harmful non-radiative recombination, are stronger for heavier alkali atoms (Rb) than for lighter ones (Na). Additionally, in this regard, both low-temperature and high-temperature absorbers react identically to the treatment with alkali atoms. The results of this thesis thus show that the alkali PDT does not only positively affect the surface but also the bulk of the absorber. As the quasi-Fermi level splitting presents an upper limit for the open-circuit voltage V_{OC}, the comparison between $\Delta\mu$ of the CdS-covered CIGS absorbers and V_{OC} of their corresponding finished devices is able to uncover potential losses that occur during solar cell fabrication. For the high-temperature absorbers as well as for the low-temperature ones, the difference $\Delta\mu - V_{OC}$ is measured to be very low overall, indicating minimal losses during device fabrication (however, this observation is not valid for absorber L3 that did not receive a post-deposition treatment).

Covering the absorbers with several layers of polystyrene beads eliminates the interference fringes and enables the characterization of the low-energy slope. From the interference-free PL spectra, the absorption coefficient $\alpha(E)$ can be extracted. This thesis has shown that $\alpha(E)$ extends exponentially into the band gap, indicating that Urbach-type band tails are present in state-of-the-art CIGS absorbers. An in-depth characterization of these band tails reveals that the Urbach energy E_U relates to the optoelectronic losses in the absorbers. Additionally, the results show that the alkali atoms reduce E_U and thus the band tails. Consequently, these results underline that the beneficial effects of the alkali elements can predominantly be found in the bulk of the CIGS absorber and are ultimately reflected in $\Delta\mu$ and E_U.

By conducting spatially-resolved photoluminescence measurements, it is possible to reveal local inhomogeneities, such as alloy disorder or defect distributions, that are influenced by the alkali atoms and correlate to the observed macroscopic $\Delta\mu$ and E_U values. Spatial scans with approximately one micrometer resolution are conducted on both high-temperature and low-temperature samples sets. The results in this thesis reveal that the absorbers exhibit very tiny spatial variations in the quasi-Fermi level splitting, independently of the alkali post-deposition treatments involved. It is thus concluded, at least on a microscopic scale, that the alkali atoms do not lead to a reduction of inhomogeneities which could explain the larger $\Delta\mu$ and lower E_U values. However, the results do not refute the possibility of these inhomogeneities occurring on a sub-micrometer scale, which are undetectable by the experimental setup used in this thesis.

6 Investigation of photoluminescence at low temperatures

In the previous chapter 5, the influence of the alkali atoms on selected optoelectronic quantities of the CIGS absorbers were investigated. It was found that the alkali post-deposition treatment improves both the absorber surface as well as its bulk properties by reducing non-radiative recombination and thus increasing the quasi-Fermi level splitting $\Delta\mu$. This increase in $\Delta\mu$ ultimately translates to an increase of the open-circuit voltage V_{OC} in the finished solar cell devices. Furthermore, an analysis of the band tails in state-of-the-art CIGS absorbers revealed a strong correlation, but not necessarily a causality, between Urbach energy E_U and $\Delta\mu$. Thus, it was argued that the beneficial effects of the alkali atoms act on both the mechanism that is responsible for the non-radiative recombination processes as well as on the mechanism that governs the band tails. While both these mechanisms could well be of different nature, it is also possible that they could be one and the same.

To further investigate the underlying mechanisms that cause the beneficial effects of the alkali atoms, photoluminescence experiments at low temperatures can be employed. One cause of non-radiative recombination processes can be recombination via deep-level defects inside the band gap (cf. section 2.5.2). By reducing the temperature to values as low as 10 K, the capture/emission of charge carriers into/from deep-level trap states is reduced such that the overall radiative recombination is increased. Furthermore, it can be argued that a reduction in temperature leads to a reduced charge carrier mobility such that the probability of charge carriers recombining from non-radiative recombination spots is reduced. Both these effects lead to higher radiative signals from deep-level trap states. This then enables the investigation of the effects of the alkali atoms on deep-level defects and find out whether an alkali-induced decrease in defect density is responsible for the increase in $\Delta\mu$ and V_{OC}. The investigation of deep defects in low-temperature PL experiments is tackled in the first section 6.1. The measured PL spectra do not reveal any presence of deep-level defects, even in the untreated absorbers that show the largest V_{OC} deficit. Thus, deep-level defects in state-of-the-art CIGS are either absent or only present in low concentrations. The section is based on the results published in ref. [243].

The occurrence of band tails in Cu-poor CIGS absorbers is a direct consequence of disorder. One option is the non-uniform distribution of charged impurities, either on an intra- or intergrain level or at the grain boundaries, which causes the valence and conduction band edges to be modulated and extend into the band gap. At low temperatures, these electrostatic potential fluctuations are visible to a significantly greater extent than at room temperature (where their effect is still debated). It is possible that the alkali atoms act as passivation agents, neutralizing the charged impurities and thus lead to reduced electrostatic potential fluctuations. If this were the case, the effects should be observable in the measured PL spectra at low temperatures. The investigation of electrostatic potential fluctuations and their response to the alkali atom infusion is subject of section 6.2. The results of extensive temperature- and excitation dependent PL measurements suggest, through qualitative trends between the different samples, that the alkali post-deposition treatment indeed reduces the effect of the electrostatic potential fluctuations. In addition, it is found that this reduction is stronger for heavier alkali metals. This section extends the content what will be published in ref. [207].

6.1 Deep-level defects

The topic of deep defects was first mentioned when introducing the defect model in section 2.2.2 and is slightly expanded in the following. In literature, at the time of writing, only a single study exists where a deep-level defect 0.8 eV above the valence band was reportedly measured via photoluminescence in Cu-poor CIGS [50]. However, a closer look at this study reveals that the main PL transition at low temperatures is much narrower than at room temperature. This is in stark contrast to what is usually observed in Cu-poor CIGS (cf. e.g. [171] or section 6.2). This observation may question the validity of generalizing the results from the study [50]. While the observation of a deep defect in photoluminescence spectra is thus rare, in transient photocapacitance spectra a comparable defect has been presented in several studies [51]–[54], [244]. However, some of these studies were done on absorbers that do not necessarily reflect the current state-of-the-art.

In Cu-rich CIGS absorbers, the presence of a 0.8 eV defect has successfully been confirmed in in-house photoluminescence measurements [41] and is thought to be one of the main reasons for the low V_{OC} extracted from Cu-rich devices [42], [49]. As the origin of the deep defect, the Cu_{In} antisite in the (-1/-2) double charged state is suggested [38]. The presence of this point defect has been experimentally verified via neutron powder diffraction in both Cu-poor and Cu-rich composition [245] (which does not necessarily mean that is it electronically active).

In terms of the alkali post-deposition treatment, theoretical models do not predict the formation of a deep defect involving the alkali atoms [141], such that deep-level defects in CIGS are, if present, of intrinsic nature. However, this does not exclude the possibility of the foreign alkali atoms passivating the intrinsic defects. In this context, defect spectroscopy at low temperatures is performed on the absorbers H1, H2, L1, L2, and L3 using the extended photoluminescence setup (cf. section 3.1). Due to the large background signal from the surrounding thermal black body radiation of the laboratory, high excitation densities are used and only CdS-covered absorbers are investigated. The choice for the latter is vindicated by the aim of detecting defects within the band gap. By contrast, on bare absorbers, the multitude of surface defects (due to air degradation [70]) lead to non-radiative recombination which reduces the density of charge carriers that can ultimately recombine via the deep-level defects and thus reduces any potential signal.

As an example, the photoluminescence spectra recorded at 10 K of samples H2 and L3 are shown in Fig. 6.1A and Fig. 6.1B, respectively. The spectra are represented as signal strength (in arbitrary units) in dependence of the wavelength i.e. they are shown as raw data (cf. section 3.1.1). This form of representation is chosen as the spectral calibration leads to additional artificial signals that seem to allude to the presence of deep defects. The spectral calibration for the extended setup and the InAs photovoltaic diode detector is shown and discussed in detail in appendix E.1 while the influence of the spectral calibration on the PL spectrum of sample H2 is shown in appendix E.2.

Both spectra in Fig. 6.1 show a broad peak around 1200 nm and a background signal in the whole near-infrared range. The broad peak is the well-known radiative recombination that is measured at low temperatures in Cu-poor absorbers [26]. The peak exhibits some features (several shoulders in the case of H2 and even a double-peak structure in the case of L3) which are due to interference effects. As such, the main peak in Fig. 6.1 is of no direct interest for the detection of deep defects. However, to verify the validity of the PL spectra measured with the extended setup and the InAs detector, the same samples are also measured with the conventional setup and the InGaAs camera. The recorded spectra around the main PL peak are identical and shown in appendix E.3. The insets in Fig. 6.1 show the excitation flux densities used to measure the spectra. As the InAs detector has a relatively low sensitivity, using high excitation flux densities is mandatory to measure reasonable signals. However, if the incident

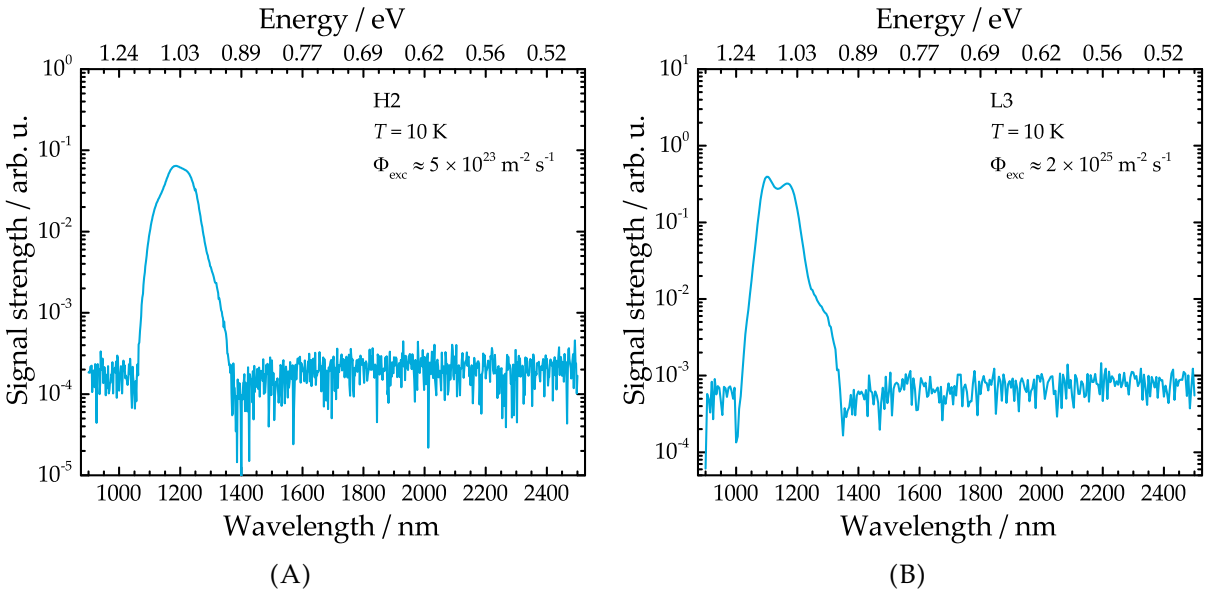

FIGURE 6.1: PL spectra measured with the extended setup at a temperature of 10 K on absorbers **(A)** H2 and **(B)** L3. The measurements were done at the excitation flux density Φ_{exc} indicated in the top-right corner of the graphs. Due to the low emitted signal of sample L3, the excitation flux density had to be increased. The spectra are displayed in the semi-logarithmic scale to better visualize the signal strength of the main transition and the absence of signals in the near-infrared range.

photon flux density reaches too large values, the photons heat up the absorber and influence the measured spectra in various ways. To that end, the effect of the excitation flux density on the measured spectrum is briefly discussed in appendix E.4 with the result being that it is better to use lower excitation flux densities than higher ones, even if this leads to an overall reduced signal strength.

The spectra in Fig. 6.1 are represented semi-logarithmically to demonstrate that it is possible to measure the main transition over several orders of magnitude of signal strength (i.e. the main PL transition carries several orders of magnitude larger signal strength than the background). For all the samples measured in the extended setup with the InAs detector, no deep-level defects beyond the main transition could be detected. The remaining PL spectra measured on the absorbers H2, L1, and L2 are shown in Fig. E.5 in appendix E.5. From these measurements, it can thus be concluded that deep-level defects, if present, exhibit very low densities such that the corresponding recombination process is several orders of magnitude more unlikely than the main transition. However, one has to be careful when drawing ulterior conclusions based on these results. For example, in Fig. 6.1A, the signal of the main peak transition is roughly three orders of magnitude larger than the background signal. This does not necessarily mean that the deep-level defect density of states is only three orders of magnitude lower than the density of states corresponding to the radiative transition (i.e. the defect DOS could be much lower).

In addition to photoluminescence, thermal admittance spectroscopy (TAS) measurements were also performed on the corresponding finished solar cell devices. The results suggest that the measured features in TAS are more likely related to an electronic transport barrier caused by the window/buffer stack rather than defect levels within the band gap [243]. Thus, neither photoluminescence nor TAS could identify deep-level defects in the present state-of-the-art CIGS absorbers, even if no alkali PDT is applied.

6.2 Electrostatic potential fluctuations

The concept of electrostatic potential fluctuations was introduced in section 2.7.4 where the model of Shklovskij and Efros was introduced [168]. It was mentioned that there exist various approaches to quantify the amplitude of the electrostatic potential fluctuations [48], [246], [247]. However, due to the limitations imposed by some of these approaches, for the samples that are presently investigated in this thesis only the evolution of the peak energy with varying temperatures and excitation densities is studied. This latter approach does not allow for the quantification of the absolute value of the fluctuation amplitude but allows for a qualitative comparison between different samples.

Before being able to analyse the temperature- and excitation dependence of the measured PL spectra however, it is mandatory to ensure that the interference effects are not perturbing the spectra. In section 4.4.4, it was shown that the polystyrene surface layer is able to completely eliminate the interference fringes from the spectra when measured at room temperature. Additional measurements at lower temperatures, presented in section 4.4.5, yielded similar results. However, due to the strange shape of the PL spectra at low temperatures, especially in the low-temperature absorbers L1, L2, and L3, the influence of interference effects needs to be investigated further.

6.2.1 Revisiting interference effects

To visualize the detrimental effects of interference fringes, Fig. 6.2A shows the PL spectra of the CdS-covered absorber L2 measured at different temperatures. In this representation, it is unclear what exactly is happening to the PL spectra when the temperature is decreased from 280 K to 20 K. Knowing that there is only a single radiative transition at room temperature, the data would suggest that this transition simply experiences a redshift with decreasing temperatures. Due to the temperature-static interference fringes, various spectral regions change in dominance such that the exact energy of the transition is not identifiable. Thus, it is impossible

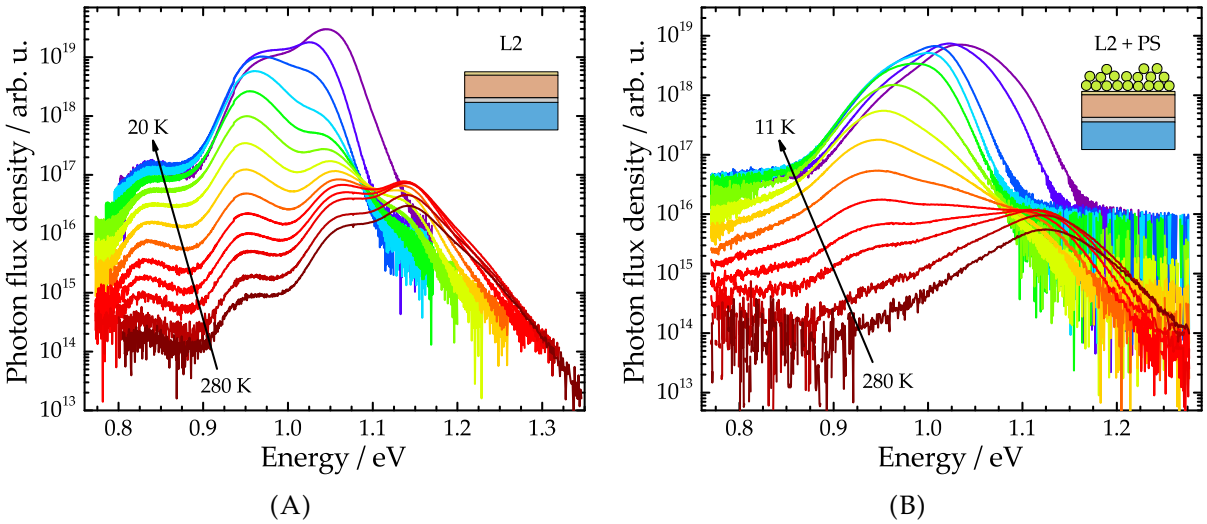

FIGURE 6.2: **(A)** PL spectra of the CdS-covered absorber L2 measured at various temperatures under a constant excitation flux density. The semi-logarithmic representation is used to better visualize the features of the spectra. Without the presence of a scattering surface layer, the absorber exhibits strong interference fringes that overlay the PL spectra and impede any information extraction. The sample stack (ignoring the SiO_x and $MoSe_2$ layers) is displayed in the top-right corner. **(B)** PL spectra measured on the same absorber after the application of several polystyrene layers. Due to the removal of the interference fringes, actual distinct features become visible.

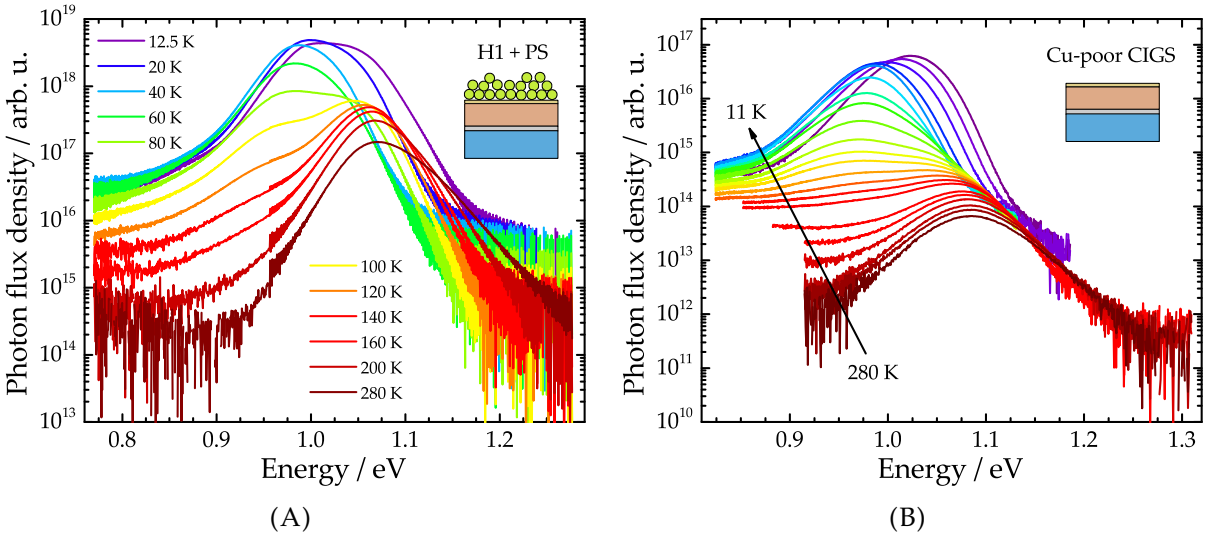

FIGURE 6.3: **(A)** PL spectra of the PS- and CdS-covered absorber H1 measured at various temperatures under a constant excitation flux density. The sample stack is displayed in the top-right corner. **(B)** PL spectra of an in-house Cu-poor CIGS absorber measured at various temperatures under a constant excitation flux density. The absorber was grown and measured by Dr. Finn Babbe.

to say whether only a single radiative transition is occurring (as seen in e.g. [170], [246]) or if a double-peak feature is manifesting (as seen in e.g. [48], [248]). Consequently, no insight can be gained from this measurement.

After eliminating the interference fringes through the deposition of the polystyrene scattering layer however, actual distinct features become visible in the PL spectra of the L2 absorber in Fig. 6.2B. While there is only a single radiative transition close to room temperature, already identified as the band-to-band recombination in chapter 5, a second transition at lower energies emerges at lower temperatures. This low-energy transition increases in dominance with decreasing temperatures and experiences first a redshift with decreasing temperatures and, at even lower temperatures, a blueshift. Furthermore, the two spectra measured at the lowest temperatures (11 K and 20 K in this case) show a peculiar behaviour as they broaden and are strongly blueshifted compared to the other spectra.

The occurrence of two distinct peaks at various temperatures is not exclusive to the absorber L2 but is also seen in the absorbers H1, H2, L1, and L3. For example, Fig. 6.3A shows the temperature-dependent PL spectra measured on the PS- and CdS-covered H1 absorber. Additionally, Fig. 6.3B shows the temperature-dependent PL spectra measured on a Cu-poor CIGS absorber that was grown in-house[1]. Both absorbers in Fig. 6.3 show thus the same behaviour as the L2 absorber in Fig. 6.2B. Furthermore, the fact that the PL spectrum of in-house CIGS absorber is clearly devoid of any interference fringes (possibly due to a considerably rougher surface) and shows a similar behaviour regarding the spectral- and temperature dependence, definitely proves that the features observable in the temperature-dependent PL spectra of the state-of-the-art CIGS absorbers are real and not the result of interference fringes.

While the above graphs suggest that the observed spectral and temperature-dependent behaviour of the PL spectrum is real, a lingering influence of interference effects cannot yet be

[1]The CGI ratio of this sample amounts to approximately 0.88. No solar cell devices were fabricated from this absorber. However, neighbouring growth processes from the same day resulted in solar cell devices with efficiencies up to 17 % (without ARC). The absorber did not receive any PDT but was grown on soda-lime glass at elevated temperatures which explains these relatively high efficiencies. The sample was grown by Dr. Finn Babbe.

dismissed. In this context, appendix E.6 shows and discusses some selected PL spectra at different temperatures along with the reflectance of absorbers L2, H1, and HS. From these measurements, it can safely be concluded that the high-temperature absorbers H1 and H2 are completely devoid of interference fringes. The same cannot be said with certainty about the low-temperature absorbers, even if it appears very likely that no interference fringes are present. As such, the results from the low-temperature absorbers are to be handled with caution.

The occurrence of both a low- and a high-energy radiative transition in Figs. 6.2B and 6.3 is a phenomenon that is already known from various studies such as e.g. [48], [248], [249]. In these studies, it could be shown that the low-energy transition as well as its temperature dependence are heavily correlated to the amplitude of the electrostatic potential fluctuations: the larger the amplitude, the more pronounced the energy shifts of the transitions with varying temperature. Furthermore, as an increase in excitation density leads to an increased density of charge carriers that screen the electrostatic potential, the fluctuations are reduced and the energy shifts are weakened. In the following, starting with the high-temperature absorbers, the energies of the PL peaks are analysed with respect to both the temperature and the excitation flux density.

6.2.2 Case of high-temperature absorbers

In the previous section it was determined that both high-temperature absorbers H1 and H2 are devoid of interference fringes when coated by several layers of polystyrene beads. However, the PS beads prevent the exact knowledge of the incident and absorbed excitation flux density as they reflect part of the incoming laser illumination. In addition, the emitted photoluminescence is also partly scattered such that a reduced fraction is collected by the detector cameras. As the layers of the PS beads cannot be deposited identically (due to the deposition process), it could be rightly argued that the samples were all measured under different, unknown excitation flux densities. To circumvent this problem, after the extensive photoluminescence measurements at various temperatures, the absorbers are measured under a fixed excitation flux density at room temperature. Afterwards, the PS beads are washed off with deionized water and the absorbers are measured again under the same conditions. The removal of the PS beads leads to the resurgence of the interference fringes. However, as the high-energy slope is not affected (cf. section 4.4.4), the PL spectra measured before and after PS removal can be scaled to a common value on said slope. The numerical scaling factor can then be used to gauge the "scattering/reflecting strength" of the PS beads and can be multiplied by the original incident excitation flux density Φ_{exc} to yield a so-called intensity scaling factor $R(\Phi_{\mathrm{exc}})$. This factor can then be used to compare the different absorbers between each other: the closer the values of $R(\Phi_{\mathrm{exc}})$ between two samples, the closer the incident photon flux density that they absorbed. Technically, the values of $R(\Phi_{\mathrm{exc}})$ are in Watts (W). For simplicity, however, the units are omitted in the following.

In the following, to not confuse the labels of the samples with the temperatures used in the PL experiments, the H1 and H2 absorbers are referred to as "H absorbers" (instead of the usual "high-temperature absorbers"). The analysis procedure for the temperature- and excitation-dependent spectra is described in the following with the example of absorber H1. As can be seen in Fig. 6.3A, the absorber is measured from 280 K to 12.5 K at eleven distinct temperatures. At each temperature, the excitation flux density is varied over several orders of magnitude. Depending on the temperature or the excitation flux density, either one or two peaks are visible. At temperatures close to room temperature, the band-to-band transition is measured and is characterized by a single peak. Decreasing the temperature leads to the emergence of a second, low-energy peak which can only be properly distinguished at the measured temperature of

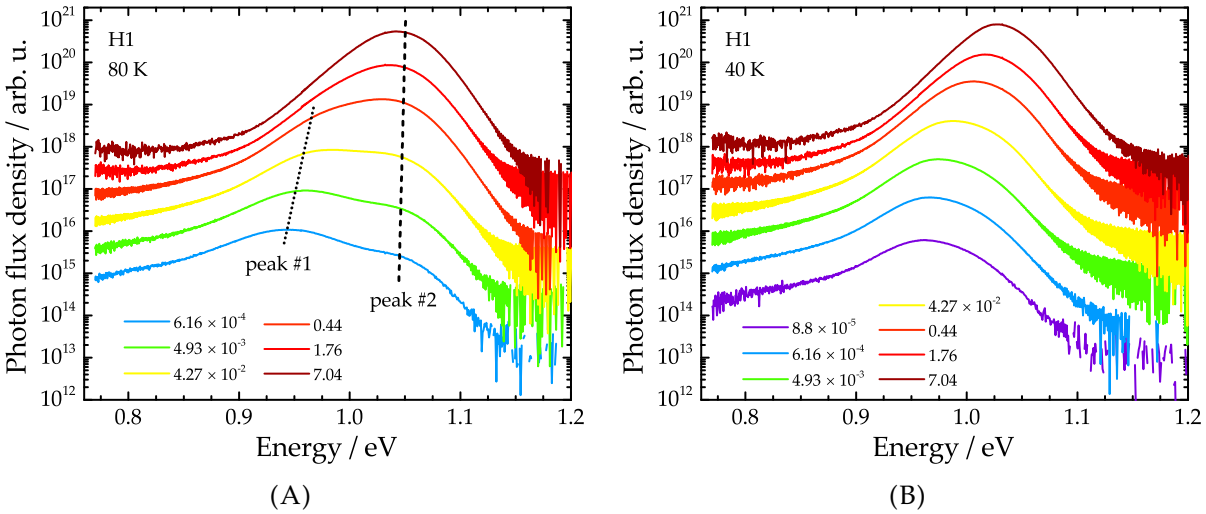

FIGURE 6.4: **(A)** PL spectra of sample H1 measured at 80 K under various excitation densities. The excitation flux densities are illustrated by the different colors and the indicated values correspond to the intensity scaling factor $R(\Phi_{exc})$ introduced in the main text. The PL spectra show two peaks: a low-energy peak #1 (dotted line) and a high-energy peak #2 (dashed line). **(B)** PL spectra of sample H1 measured at 40 K under various excitation flux densities. Due to a lower temperature (and thus increased radiative recombination rate), the measurement at an additional, lower excitation flux density is facilitated compared to e.g. a temperature of 80 K.

120 K and below. As an example, Fig. 6.4A shows the PL spectra measured at 80 K under various excitation flux densities. At the lowest excitation flux density, a clear double-peak structure can be identified with the low-energy transition (labelled peak #1) dominating the spectrum. Increasing the excitation flux density leads to a strong blueshift of the low-energy peak while the high-energy peak (labelled peak #2) shifts only slightly but increases strongly in intensity. Thus, at large excitation flux densities, the PL spectrum is dominated by the high-energy peak while the low-energy peak manifests itself as a tailing.

Below and including measured temperatures of 60 K, the low-energy peak is the only radiative transition that is observable. Fig. 6.4B displays the PL spectra measured at 40 K, showing clearly that the high-energy peak has either vanished or is completely dominated by the low-energy peak. Across the whole excitation flux density range, only one single peak, exhibiting a strong blueshift, is ever observable at this temperature. At the lowest temperatures of 20 K and 12.5 K, the spectra show a slightly different behaviour compared to the higher temperatures. The excitation-dependent PL spectra at these temperatures are shown in appendix E.7.

To analyse the energy shifts of the various peaks with both varying temperature and excitation flux density, the PL spectrum can be fitted by any number of Gaussians to extract the exact energy of the peaks. While it is possible to use other probability distribution functions such as a Voigt or Lorentzian profile, the Gaussian profile is chosen as it offers a more simplistic approach (mainly due to a reduced amount of fitting parameters). Here it needs to be mentioned that the Gaussian profile does not necessarily mirror the exact physics of the radiative transitions but is only chosen to access the peak energy. The fitting routine needs to be handled with great care as the PL spectra sometimes cannot be fitted unambiguously. Fig. 6.5A illustrates the case of a relatively straightforward fitting procedure as only a single peak is observable. However, this peak exhibits a clearly visible tailing towards low-energies. This tailing can be accounted for by fitting a second Gaussian. Doing so, however, does not significantly alter the energy of the main peak as it so strongly dominates the whole spectrum. Fig. 6.5B illustrates a more challenging fitting case: two peaks are clearly visible with the low-energy peak showing a clear

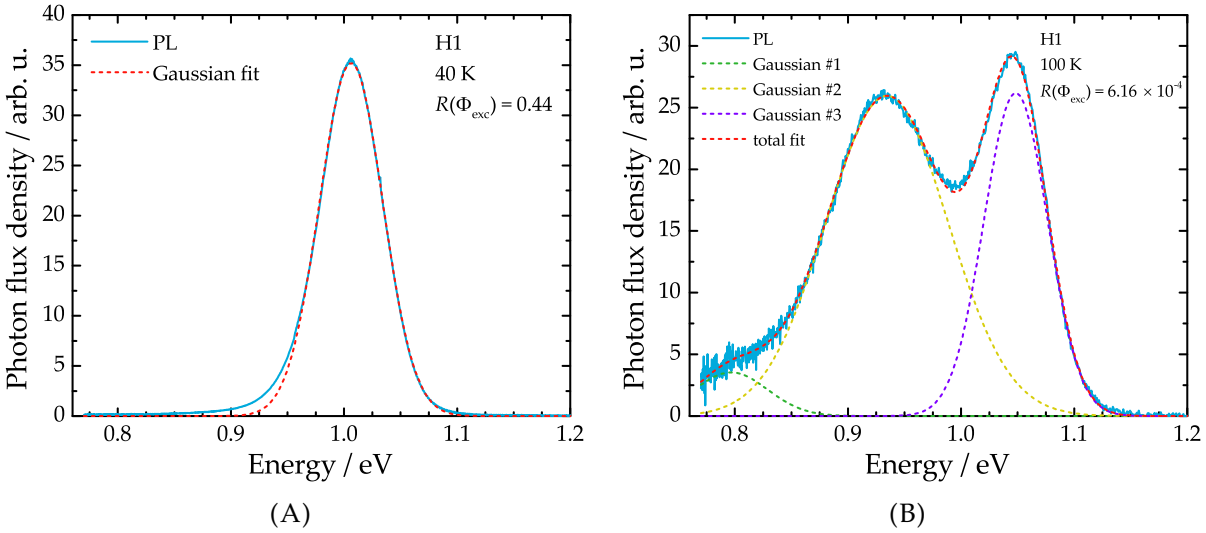

FIGURE 6.5: **(A)** PL spectrum (blue curve) measured at 40 K and under an excitation flux density of $R(\Phi_{exc}) = 0.44$ (corresponds to the orange spectrum in Fig. 6.4B). The radiative transition is of single-peak nature and can be relatively well approximated by a Gaussian (red dashed curve). The low-energy tailing of the peak can be approximated by a second Gaussian but doing so does not alter the energy of the main peak in any significant way. **(B)** PL spectrum (blue curve) measured at 100 K under a very low excitation flux density of $R(\Phi_{exc}) = 6.16 \cdot 10^{-4}$. The spectrum can be well described by a sum of three different Gaussians where Gaussians #2 (yellow dashed curve) and #3 (purple dashed curve) describe the radiative transitions and Gaussian #1 (green dashed curve) describes the tailing. The latter can be omitted without changing the energies of the two peaks in any significant way.

tailing. As was the case for Fig. 6.5A, however, fitting the tailing with a Gaussian only alters the energies of the two other peaks by a maximum of 1 - 2 meV which is deemed not significant.

The peak energies, extracted from the multiple PL spectra, are plotted against temperature for the various excitation densities in Fig. 6.6. The filled circles represent the energies of the low-energy peak while the open circles represent the energies of the high-energy peak. The excitation flux densities are visualized by the different colors and allocated at the bottom-right of the graph. For low excitation flux densities, the low-energy peaks show a redshift with increasing temperatures, up to a certain point after which a blueshift is observed. For high excitation flux densities, the redshift vanishes and the low-energy peak either remains relatively constant or shows a slight blueshift. The high-energy peak shows a steady blueshift with increasing temperature and only a weak excitation dependence. The radiative transition peaks in the sample H1 thus show a complex dependence on both the temperature and the excitation flux density.

Some of these dependencies have already been observed in literature, also in other materials. The occurrence of a low-energy peak showing a redshift with increasing temperatures has e.g. been reported in Cu(In,Ga)Se_2 [171], [248], Cu(In,Ga)(S_xSe_{1-x})$_2$ [170], impurity-doped GaAs [250], [251], Cu_2ZnSnS_4 [252], [253], $CuInTe_2$ [254], $CuGaSe_2$ [48], [246], [255], and $CuInSe_2$ [48]. Furthermore, in some of these studies, the reduction of the redshift with increasing excitation [48], [170], [171], [246], [255] as well as the blueshift of the low-energy peak beyond a certain temperature [48], [170], [246], [253], [254] have also been reported. However, in most studies only a single peak is observed over the whole measured temperature range. Only Dirnstorfer *et al.* [171], Krustok *et al.* [248], Romero *et al.* [249], and Larsen [48] report on the presence of two distinct peaks. Incidentally, three of these studies deal with Cu(In,Ga)Se_2 while the other study deals with its ternary $CuGaSe_2$. In the following, the observed behaviour of both the low- and high-energy peaks is attempted to be described with the model that was

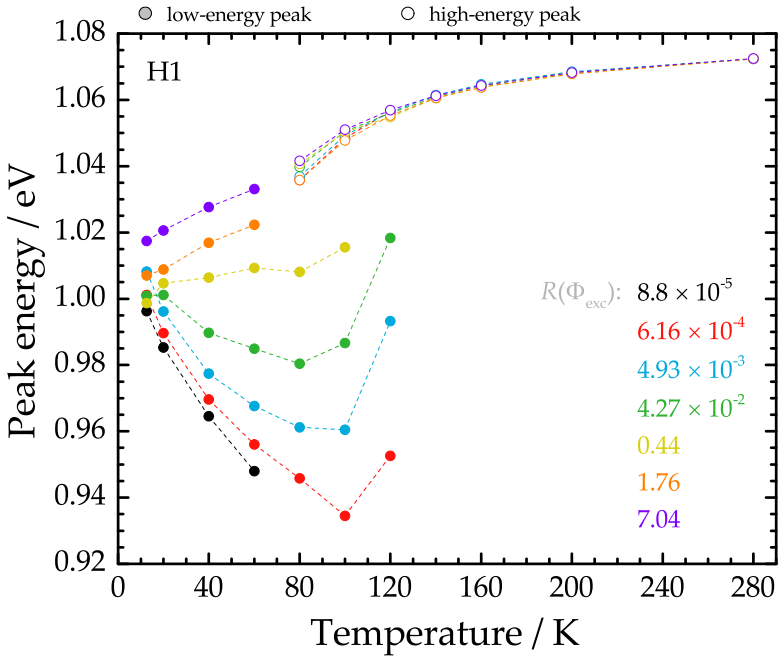

FIGURE 6.6: Energy of the radiative transitions measured in the PL spectra of sample H1 at different temperatures and excitation flux densities. The filled circles represent the low-energy peak while the open circles represent the high-energy peak. The peak energies measured under different excitation flux densities are visualized by the different colors and allocated according to the legend in the bottom-right corner.

introduced in section 2.7.4.

To initiate the description, the model is reillustrated in Fig. 6.7A showing the energy band diagram of a compensated CIGS absorber at low temperatures and under low excitation densities (cf. Fig. 2.18B in section 2.7.4). While no distinct defect transitions can be observed in Cu-poor CIGS compared to their Cu-rich counterparts, it can be assumed that the dominant donor-acceptor-pair (DA) transition is the so-called DA1 [163] which involves the shallow donor In_{Cu} and shallow acceptor V_{Cu} (cf. section 2.2.2). Thus, only a single acceptor band, also influenced by the electrostatic potential, is depicted above the valence band. At low temperatures and low excitations, the radiative recombination occurs because electrons in localized conduction band valleys recombine with holes that are localized on acceptor states. As was argued in section 2.7.4, this transition identifies as the free-to-bound transition that is related to the DA1 transition. Since this transition involves defect states, it is labelled as "DT" in the following. As the charge carriers lack sufficient thermal energy, the potential valleys are not all filled equally which prevents the definition of a single quasi-Fermi level. Instead, the occupation of the charge carriers is described by local quasi-Fermi levels [170]. Increasing the temperature leads to a higher thermal energy for the charge carriers such that they can overcome local potential barriers and diffuse into states of minimal energy, such as deep and strongly localized potential valleys (illustrated by the dark red arrows in Fig. 6.7A). Due to the increased transport and interaction between different valleys (i.e. occupation of the deep potential valleys), a single quasi-Fermi level can be established and the radiative transition shows in average a redshift. The higher the temperature, the larger the occupation and the stronger the transition redshift.

Upon reaching a certain temperature, labelled in the following T_{min}, the DT transition energy reaches its maximum redshift. Increasing the temperature beyond T_{min} leads to the remaining non-compensated acceptor states becoming ionized. The resulting free charge carriers, also gaining in mobility due to the increase in temperature, screen the charged impurities

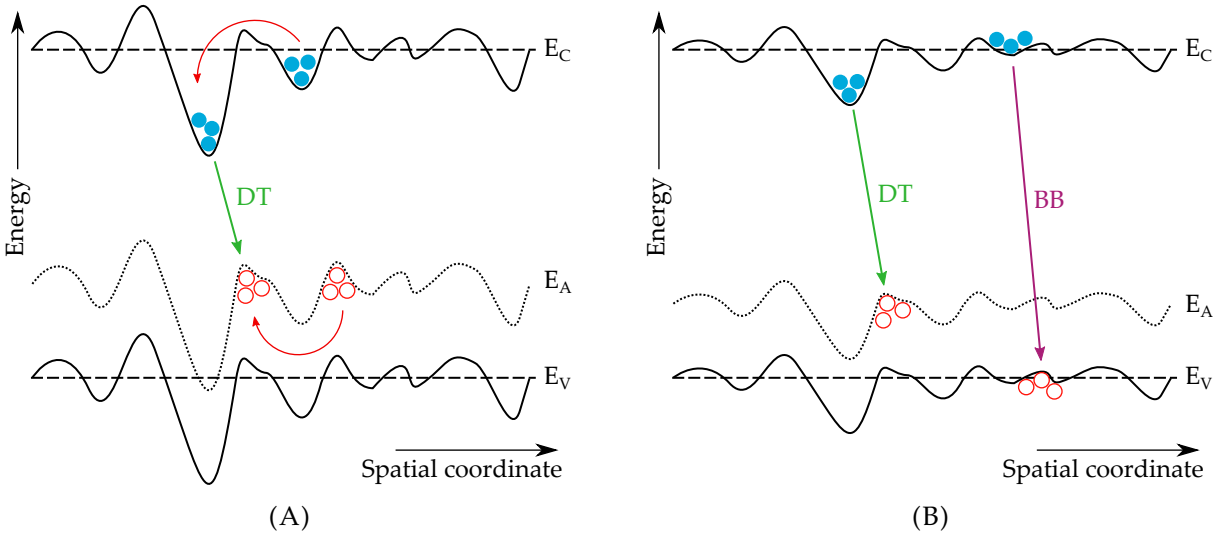

FIGURE 6.7: Schematic illustration of the energy band diagram of Cu-poor CIGS. The conduction band E_C and valence band E_V in the uncompensated case are depicted by dashed lines. Due to the presence of a locally non-homogeneous distribution of charged impurities, the band edges and acceptor levels E_A are modulated (solid and dotted lines). **(A)** At low temperatures and low excitation flux densities, a defect-related (DT - green arrow) transition is occurring between electrons (blue circles) and holes (red hollow circles). Increasing the temperature leads to a re-distribution of charge carriers into potential valleys with minimal energy states (red arrows). **(B)** Increasing the temperature and/or the excitation flux density leads to a flattening of the band edges and acceptor levels which, in turn, leads to a blueshift of the DT transition. In addition, the band-to-band transition, emitting photons of higher energies, starts occurring.

and thus reduce the electrostatic potential leading to a flattening of the bands. This situation is depicted in Fig. 6.7B which clearly demonstrates that a flattening of the bands leads to a blueshift of the DT emission. A further increase of the temperature leads to a thermal emptying of all acceptor states, significantly reducing the probability of the radiative defect-related transition occurring. As a result, the PL spectra are dominated by the band-to-band (BB) transition. Increasing the temperature up to room temperature leads to an increased density of thermally excited charge carriers, possessing large temperature-induced mobilities, which participate in the screening of the potential. This leads again to a band flattening and thus to the observed blueshift of the high-energy peak.

In addition to the influence of the temperature on the radiative transitions and the electrostatic potential, the excitation flux density also plays a major role. Increasing the excitation flux density always leads to an increased density of excited charge carriers. The situation in Fig. 6.7B can also be interpreted as a band flattening due to an increased excitation flux density from illumination. An increase of excited charge carriers can induce three mechanism that can lead to a blueshift of the radiative transition [216]. Firstly, the excited electrons and holes may neutralize the ionized donor and acceptor states, eliminating the Coulomb potential that they exert. Secondly, the excited charge carriers occupy the states in the potential valleys leading to an increased portion of higher occupied energy states (i.e. an increase in the electron quasi-Fermi level) participating in the recombination activity. Lastly, the excited free charge carriers also screen the electrostatic potential (if they possess a sufficiently large mobility). These three mechanism lead to a flattening of the bands and to a blueshift of the observed transitions.

While the model is able to describe the behaviour of the radiative transition with varying temperatures and excitation densities in Fig. 6.6 reasonably well, some aspects need to be discussed in more detail. Following the description above, it is evident that the low-energy peak is

strongly linked to the fluctuations of the bands and defect level. The high-energy peak, also influenced by the electrostatic potential fluctuations and initially identifiable at 80 K, shows only a minor blueshift with increasing excitation flux densities at temperatures below and including 120 K. Above 120 K, the dependence on the excitation flux density vanishes. This indicates a reduced influence of electrostatic potential fluctuations at high temperatures. However, the high-energy peak still shows a blueshift with increasing temperatures which constitutes a behaviour that is in contrast to the expected band gap shrinkage [25]. Consequently, a remaining influence of electrostatic potential fluctuations may still be lingering at room temperature. In this regard, it is interesting to note that other photoluminescence measurements on the same sample H1, where larger excitation densities were used (not shown here), do not show an influence on peak shape and transition energy at room temperature. It can thus be concluded that the electrostatic potential fluctuations are, if present, very weak at room temperature. The blueshift of the high-energy peak with increasing temperature thus needs to be explained by another temperature-dependent potential fluctuation mechanism (maybe even involving small band gap fluctuations). The present measurements do not allow for any further insight on this matter.

Compared to the high-energy peak, the low-energy peak shows a very strong dependence on the excitation flux density. At sufficiently large excitation flux densities, the initial redshift with increasing temperatures vanishes. This can easily be explained by the reduction of the electrostatic potential fluctuations and thus the flattening of the band edges. Without deep potential valleys, the charge carriers cannot accumulate in states with minimal energy which prevents a redshift. Spinning this argument further, an increase in temperature should then yield more charge carriers which reduce the potentials further and initiate a blueshift. This behaviour is indeed observed for the three highest excitation flux densities in Fig. 6.6. Given that the blueshift of the peak energy with increasing excitation flux densities is also temperature-dependent, it appears that the reduction of the electrostatic potential is facilitated when charge carriers with larger thermal energy and thus larger mobilities are present. These observations suggest that the redshift itself is also heavily linked to the amplitude of the fluctuations. In several studies such as e.g. [48], [170], a direct correlation between the degree of compensation and the redshift is reported: the stronger the compensation, the stronger the redshift and the higher T_{min}. However, this observation only holds true for sets of samples that show strong variations in their CGI ratio. For sets of samples that show similar CGI ratios (within 0.1), no discernible variation in redshift strength or T_{min} could be observed (case of $CuGaSe_2$) [48], [246].

A suitable quantity to gauge the strength of the electrostatic potential fluctuations, based on the present model, would be to look at the blueshift of the low-energy peak beyond T_{min}. The reasoning being that the excited charge carrier kinetics at temperatures below T_{min} are too dependent on the thermal energy. Above T_{min}, however, the free carriers contain enough thermal energy to overcome the vast majority of the potential barriers and thus participate in the recombination activity involving the lowest energy states (as well as some portion participating in the BB transition). At the highest excitation flux densities, the low-energy peak is not even observable at intermediate temperatures (i.e. between 80 K and 150 K) because the band edges are flattened so much that the BB transition dominates and is observed.

Finally, based on the present model, three behaviour characteristics that qualitatively describe the strength of the electrostatic potential fluctuations can be identified. Firstly, the blueshift of the low-energy peak beyond T_{min}, secondly the presence of the low-energy peak in dependence of the temperature and the excitation flux density, and thirdly, the blueshift of the high-energy peak intermediate temperatures (i.e. between 80 K and 150 K) with increasing excitation flux densities.

Since the present model along with the experimental conditions under which the absorber was measured (most notably the presence of the polystyrene surface layers) prevents the extraction of tangible quantities that describe the amplitude of the electrostatic potential fluctuations, qualitative trends between similar samples need to be investigated. To this end, the temperature- and excitation-dependent PL measurements were repeated on the H2 absorber. The energetic shifts of the peaks are plotted in Fig. 6.8 and exhibit a slightly different behaviour compared to the H1 absorber.

The high-energy peak shows a strong blueshift under the influence of increasing excitation flux densities at intermediate temperatures (between 80 K and 150 K) in the H2 sample. At 80 K, the low-energy peak dominates the spectrum across all excitation flux densities. Additionally, when measured under the two highest excitation flux densities, the high-energy peak is not discernible any more. This does not necessarily mean that the BB transition vanished altogether but that the DT transition is simply completely dominating the spectrum. As an example, the PL spectra measured under the lowest and highest excitation flux density at 80 K are shown in appendix E.8. At the temperature of 100 K, only the highest excitation flux density does not yield a discernible high-energy peak. According to the model in Fig. 6.7, these observations suggest that a strong electrostatic potential remains even at intermediate temperatures such that an increase of the excitation flux density leads to two effects: an increase of excited charge carriers that still diffuse into the potential valleys such that the DT transition is the dominant one, and a strong screening such that a blueshift of both DT and BB transitions is observed.

In the following, based on the three characteristics that qualitatively describe the strength of the electrostatic potential fluctuations mentioned above, the differences between absorbers H1

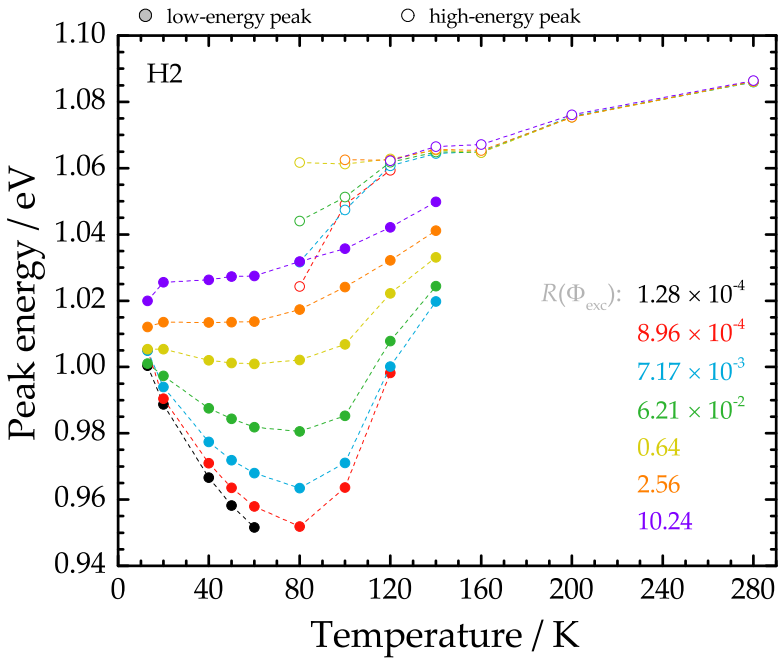

FIGURE 6.8: Energy of the radiative transitions measured in the PL spectra of sample H2 at different temperatures and excitation flux densities. The filled circles represent the low-energy peak while the open circles represent the high-energy peak. The peak energies measured under different excitation flux densities are visualized by the different colors and allocated according to the legend in the bottom-right corner. The excitation flux densities used to measure this sample are larger by approx. 30 % compared to the ones used to measure H1. This difference is attributed to slightly different polystyrene layers. Since only qualitative trends are analysed, the exact excitation flux density is of no importance.

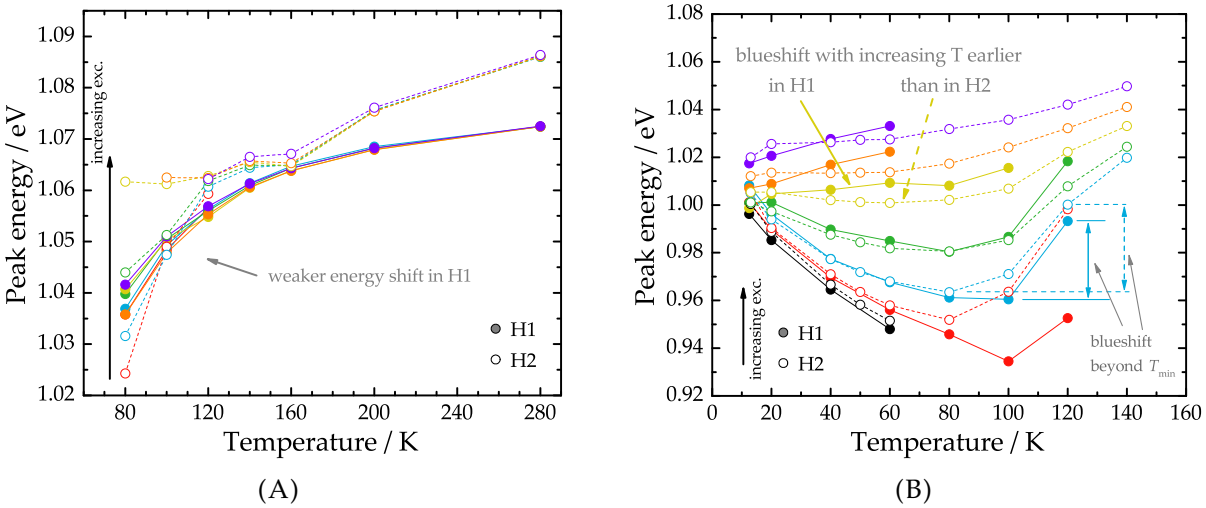

FIGURE 6.9: **(A)** Energy of the radiative high-energy transition with varying temperatures and excitation flux densities. The filled circles represent the high-energy peak of the H1 absorber while the open circles represent the high-energy peak of the H2 absorber. The color code is identical to the one in Figs. 6.6 and 6.8 and indicates that data points with the same colour have been measured under very similar excitation flux densities. **(B)** Energy of the radiative low-energy transition with varying temperatures and excitation flux densities. The characteristics of the peak shift, highlighted by the arrows and text, are explained in the main text.

and H2 are discussed. For a better comparison, Fig. 6.9A shows the different behaviour of the high-energy peak between absorbers H1 and H2 while Fig. 6.9B shows their low-energy peak.

In a first instance, Fig. 6.9A shows that the high-energy peak of absorber H2 is more susceptible to changes in the excitation flux density between 80 K and 160 K. This is expressed in the strong blueshift with increasing excitation flux densities at fixed temperatures. In contrast, the high-energy peak of absorber H1 reacts only weakly to increases in the excitation flux density. Thus, based on the behaviour of the high-energy peak, it can be concluded that the electrostatic potential fluctuations are stronger in the H2 than in the H1 absorber.

In a second instance, Fig. 6.9B reveals that the low-energy peak is visible across the whole excitation range at low and intermediate temperatures in the H2 absorber. This is in contrast to the H1 absorber where the low-energy peak is only visible at very low temperatures across all excitation flux densities. More specifically, at the excitation flux density represented by the yellow color and annotated with arrows (cf. $R(\Phi_{exc}) = 0.44$ for H1 in Fig. 6.6 and slightly larger $R(\Phi_{exc}) = 0.64$ for H2 in Fig. 6.8), the H1 absorber shows a blueshift with increasing temperatures while absorber H2 still shows a slight redshift until T_{min}. This would indicate that a lower excitation flux density in the H1 absorber is sufficient to flatten the band edges while a slightly higher excitation flux density is not able to do the same in the H2 absorber.

In a third and final instance, the blueshift of the low-energy peak in Fig. 6.9B with increasing temperature beyond T_{min} is analysed. The blueshift is evaluated from T_{min} to 120 K where both absorbers still exhibit the low-energy peak for the three lowest excitation flux densities (exemplary shown for the blue data points in Fig. 6.9B). Across the three excitation flux densities, the blueshift averages 30 meV in the case of the H1 absorber and 36 meV in the case of the H2 absorber. Hence, a stronger blueshift beyond T_{min} indicates the presence of stronger electrostatic potential fluctuations in the H2 absorber.

Thus, based on these three observed characteristics, it can be argued that the electrostatic potential fluctuations are stronger in the H2 than in the H1 absorber. Out of the three characteristics, the strongest case can be built by only considering the low-energy peak. Since the low-energy

peak is undeniably linked to the electrostatic potential fluctuations, its presence over a greater temperature and excitation range in the H2 sample already strongly hints at a higher degree of compensation. Since both H1 and H2 samples share nearly identical elemental compositions (cf. Table 3.1 in section 3.3), the weaker electrostatic potential fluctuations in the H1 absorber can be attributed to the influence of the RbF post-deposition treatment.

Before turning the attention to the low-temperature absorbers L1, L2, and L3, the subjectivity of the fitting processes needs to briefly addressed. When discussing Fig. 6.4, it was shown that the PL spectra of absorber H1 exhibit a two-peak structure at a temperature of 80 K and low excitation densities. Upon an increase in excitation density, it was concluded that only the low-energy peak shows a strong blueshift while the high-energy peak shifts only slightly. Under the largest excitation densities at this temperature, the low-energy peak is completely dominated by the high-energy peak and therefore could not be fitted. This, however, does not mean that the DT transition completely vanished. At a lower temperature of 40 K, the PL spectra of the same absorber does not reveal a high-energy peak, independent of the excitation densities used. Again, the low-energy peak completely dominates the spectra but a very small high-energy peak could still be present. This shows that the fitting process can be quite ambiguous at times and that only the peaks that are clearly visible can reliably be fitted.

To complement this argument, Fig. E.10 in the appendix E.9 shows the PL spectra measured at 140 K under varying excitation densities for both the H1 and H2 absorbers. While the graph clearly shows that the PL spectra of sample H2 exhibit a low-energy peak, there is only a small bump in the H1 sample. It is unclear if this bump represents a distinct peak or just a very strong tailing. Ultimately, it was chosen to not fit this bump as no reasonable description of the overall spectrum could be achieved. While the overall conclusion and interpretation of this section remains unaffected, this example shows the occasional ambiguity of the fitting process and the consequences it can have.

6.2.3 Case of low-temperature absorbers

Compared to the H absorbers, the L absorbers (for clarity, in the following the low-temperature absorbers are labelled "L absorbers") show a different behaviour when measuring the PL for varying temperatures and excitation flux densities. As an example, Fig. 6.10A shows the excitation-dependent PL spectra of absorber L1 at 40 K. At low excitation flux densities, sample L1 behaves identically to sample H1 in Fig. 6.4B i.e. the PL spectra exhibit a single peak (labelled peak #1). However, upon increasing the excitation flux density, a second peak at higher energies becomes visible (labelled peak #2). This high-energy peak quickly dominates the spectrum such that the low-energy peak cannot reliably be fitted. While the occurrence of a double-peak feature is also observed in the H absorbers, higher temperatures are necessary (e.g. 80 K for H1 - see Fig. 6.4A). In the L absorbers, the double-peak feature is observed at low and intermediate temperatures (20 K - 100 K). Furthermore, and very importantly, the high-energy peak does not translate to the band-to-band recombination at higher temperatures (which it does in the H absorbers). It can thus be concluded that the two radiative transitions in the L absorbers at low and intermediate temperatures are related to defect transitions.

As the high-energy peak in the L absorbers dominates the spectra across a larger excitation range, the low-energy peak cannot be used for the characterization of the electrostatic potential fluctuations. In fact, it is unclear whether the low-energy peak is even present at large excitation flux densities or if it transforms into a strong tailing. As an example, Fig. 6.10B shows the PL spectrum of absorber L1 measured at 40 K and with an scaled excitation flux density of $5.43 \cdot 10^{-2}$. Under this form, the spectrum can be fitted by two Gaussians: one accounting for the low-energy peak (or strong tailing) and one accounting the high-energy peak i.e. the actual

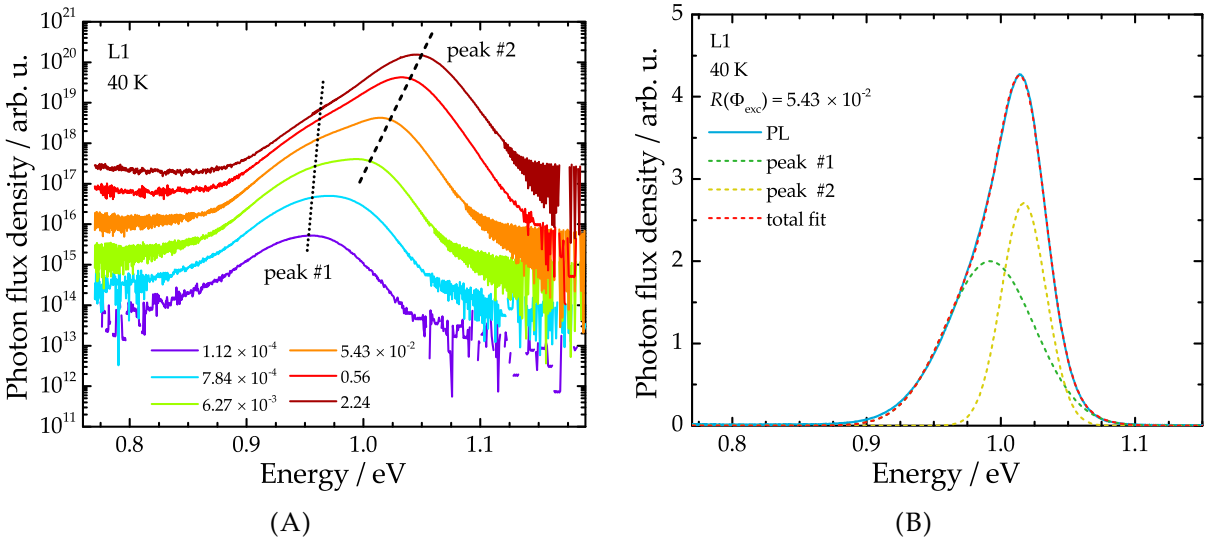

FIGURE 6.10: **(A)** PL spectra measured at 40 K and under varying excitation flux densities on the absorber L1. Depending on the excitation flux density, the spectra show a double-peak feature. At low excitations, a single low-energy peak (peak #1 - dotted line) is visible while for higher excitations, an additional, high-energy peak (peak #2 - dashed line) appears. **(B)** PL spectrum of absorber L1 measured at 40 K and under the excitation density ratio of $5.43 \cdot 10^{-2}$ (corresponds to the orange spectrum in Fig. 6.10A). Under this excitation flux density, the high-energy pears clearly dominates the PL spectrum and can reliably be fitted (yellow dashed line). The low-energy peak, however, can only be estimated since it appears as a strong tailing. As such, it can still approximated by a broad Gaussian (green dashed line) such that the overall fit (red dashed line) describes the measured spectrum reasonably well.

radiative transition. Due to the strong dominance of the high-energy peak in all absorbers L1, L2, and L3, its evolution with temperature and excitation flux density serves as a gauging quality for the strength of the electrostatic potential fluctuations. Here it needs to be mentioned that the high-energy peak in the L absorbers does not represent the same transition as in the H absorbers. Hence, the term "high-energy peak" should only be considered the same when comparing within the H and L absorber sample sets.

Extracting the high-energy peak energy versus the different temperatures yields the graph in Fig. 6.11. The lack of data points, compared to the H absorbers, is immediately evident. This lack of data points is both due to the experimental parameters sometimes not wisely chosen (smaller range of excitation flux densities used when measuring the L2 absorbers e.g.) and due to the physics occurring in the absorbers (high-energy peak only visible for higher excitation flux densities - see e.g. Fig. 6.10A). Additionally, Fig. 6.11 shows no data points at temperatures below 20 K and above 100 K. The lack of data points for these temperatures is due to the occurrence of three peaks over a slightly broader spectral range. As an example, the PL spectra recorded at 11 K for absorber L1 and at 120 K for absorber L3 are showcased in appendix E.10. While it is possible to fit the peaks with three different Gaussians, doing so in a narrow spectral width yields several possible total fits but with a variety of parameter sets[2]. As such, it is not possible to reliably extract the various peak energies and the choice to only use the data points where the peaks are clearly visible and can reliably be fitted is ultimately taken. While the amount of data points is thus considerably lower in the L absorbers compared to the H absorbers, they are nonetheless sufficient to allow for the observation of a trend.

[2]Here it needs to be mentioned that the situation is different to e.g. Fig. 6.5B where three Gaussians were also used to fit the spectrum. In Fig. 6.5B, one Gaussian fit is used solely for the purpose of accounting for the strong tailing at low energies. As such, the parameter set can be severely restricted for this specific Gaussian. When fitting distinct peaks, however, the same cannot be done.

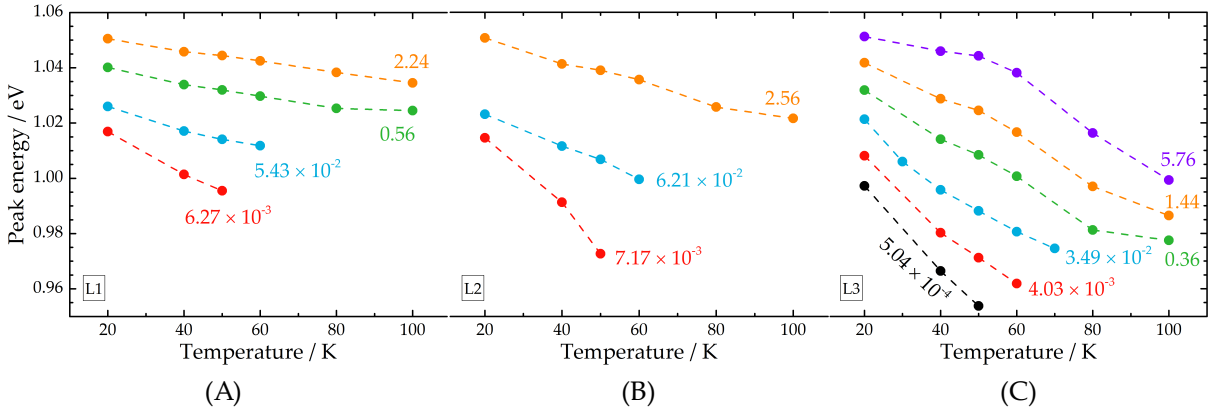

FIGURE 6.11: Energy of the "high-energy" radiative transition measured in the PL spectra at different temperatures and excitation flux densities in the absorbers **(A)** L1, **(B)** L2, and **(C)** L3. The data points with the same colour share a similar intensity scaling factor $R(\Phi_{exc})$ and can thus reliably be compared between each other. The value of $R(\Phi_{exc})$ is indicated next to the data points.

As can be seen in Fig. 6.11, in all three absorbers L1, L2, and L3, the high-energy peak only shows a redshift with increasing temperatures up to 100 K. This is in contrast to the H absorbers that showed a blueshift beyond the temperature T_{min}, which was generally below 100 K. As was already mentioned when discussing the H absorbers, T_{min} is correlated to the degree of compensation in the semiconductor. Since the L absorbers show a lower CGI ratio (cf. Table 3.1 in section 3.3), they are more compensated and it may thus be possible that T_{min} lies beyond 100 K. Since the complicated structure of the PL spectra at higher temperatures prevents the reliable extraction of peak energies, this assumption cannot be verified. Given the different behaviour of the L absorbers compared to the H absorbers, only one of the three model characteristics to describe electrostatic potential fluctuations can be used here: the evolution of the peak energy with temperature and excitation flux density.

Looking at the different colors in Fig. 6.11, with the same colors representing similar intensity scaling factors that can be compared between different samples, a clear trend can be made out. The high-energy peak of absorber L3 shows a strong redshift across a wide range of excitation flux densities. Increasing the excitation flux density only leads to a small weakening of the redshift, indicating that the excitation flux densities are not large enough to reduce the electrostatic potential and flatten the bands. In contrast, the high-energy peak of absorber L2 shows a considerably weaker redshift under its largest excitation flux density. Finally, the high-energy peak of absorber L1 shows an even weaker redshift at even lower excitation flux densities than the absorber L2. It can thus be concluded that lower excitation flux densities are necessary to flatten the fluctuating band edges in the L1 absorber than in the L2 absorber. These results suggest that the alkali post-deposition treatment reduces the electrostatic potential fluctuations and that this reduction is stronger if heavier alkalis are involved.

While the low-energy and high-energy peaks could be assigned to specific transitions in the model illustrated in Fig. 6.7 for the absorbers H1 and H2, the same cannot be done for the L absorbers. The characterization of the various possible defect-related transitions in Cu-poor CIGS absorbers and their dependence to the degree of compensation is an extremely complicated research topic and not the primary focus of this thesis. However, the behaviour presented in Fig. 6.11 proves that the high-energy peak in the L absorbers is related to electrostatic potential fluctuation, no matter the exact defect transition involved. Finally, it needs to be mentioned that the behaviour in Fig. 6.7 could also be explained by band gap fluctuations. However, to clearly distinguish between electrostatic and band gap fluctuations, the width of the peaks needs to be analysed [216]. Such an analysis is more reliable when only solitary peaks are witnessed in the

PL spectra and thus cannot be done for the measurements in this thesis.

At the end of section 6.2.2, the ambiguity and subjectivity of the fitting procedure was mentioned in the case of the H absorbers. For the L absorbers, whose measured PL spectra show a more complicated peak structure, this issue is even more crucial. Thus, here it needs to be mentioned that the fitting procedure was kept as consistent as possible while remaining within the limits of what makes sense (e.g. assigning a distinct peak to a strong tailing is assuming, rather than determining, the peak energy and is thus avoided).

Finally the same conclusion in both H and L absorbers is reached: a reduction of the electrostatic potential fluctuations in absorbers treated with heavier alkali post-deposition treatments. Regarding the exact mechanism that leads to this reduction, one could envision that the extrinsic alkali atoms compensate/neutralize the charged impurities that are present in Cu-poor CIGS by forming a Alk_{Cu} defect species. The idea for this suggestion is taken from recent theoretical calculations by Malitckaya *et al.* that suggest that the formation of neutral Alk_{Cu} point defects is energetically the most favourable of all point alkali-related point defect species [141]. However, it needs to be mentioned that the same calculations also reveal a higher formation energy when heavier alkali atoms are involved. The discussion about the influence of the alkali atoms on the electrostatic potential fluctuations is continued in section 7.2.

6.2.4 Comparison to other studies

Only sparse information about electrostatic potential fluctuations in state-of-the-art CIGS absorbers is available. At the time of writing, only three studies, revolving around the effects of the potassium fluoride treatment, were published. In one study by Jensen *et al.*, photoluminescence experiments at low temperatures were conducted on Cu-poor CIGS absorbers grown on Na-containing substrates [147]. The samples were divided into two sets: one set that received a KF PDT and one set that remained untreated. While the study concludes the results by stating that the KF PDT leads to a reduction of electrostatic potential fluctuations, the interpretation of the results is ambiguous. Specifically, the authors decided to fit the low-energy slope of the measured PL spectra to extract the amplitude of the fluctuations. However, the PL spectra that are presented in the study strongly resemble spectra that are riddled with interference fringes: even at room temperature several peaks and shoulders are visible. Consequently, it is fair to say that this study does not deliver a convincing argument in terms of electrostatic potential fluctuations and alkali PDT.

A more recent study by Guthrey *et al.* presents cathodoluminescence (CL) spectrum imaging measurements on Cu-poor CIGS grown on SLG and having undergone various PDTs (None, NaF, KF, and a combined NaF+KF) [256]. The results do not only show that the fluctuation amplitude is reduced in the treated absorbers, but also that the fluctuations show a certain spatial inhomogeneity on the sub-micron scale. However, the study does not reveal a clear difference between NaF and KF PDT and offers no insight on the fluctuation amplitude in the sample that received a combined NaF+KF PDT. The extraction of fluctuation amplitude was also done by fitting the low-energy slope. However, in this case the measured CL spectra are clearly devoid of any interference fringes, making these results much more trustworthy than the ones from Jensen *et al.*.

Finally, Jiang *et al.* performed kelvin probe force microscopy and scanning spreading resistance microscopy on CIGS absorber without and with KF PDT [257]. These surface sensitive measurement techniques reveal a reduced electrostatic potential at the grain boundaries on the surface after applying the KF PDT [257].

While the studies mentioned above use different experimental techniques, all claim that the

alkali post-deposition treatment reduces the electrostatic potential fluctuations. As an underlying mechanism, Guthrey *et al.* suggest a compensation effect: the alkali atoms occupy the copper vacancies V_{Cu} as well as reduce the In_{Cu} antisites [256].

6.3 Summary

From photoluminescence measurements conducted on state-of-the-art CIGS absorbers at room temperature in the previous chapter 5, it was found that the alkali post-deposition treatment leads to an increase of the optoelectronic quality of the absorbers by reducing the non-radiative recombination. In addition, investigations of the sub band gap emission, more specifically the band tails, have revealed a reduced density of states extending into the band gap in absorbers that received an alkali PDT.

A prominent cause of non-radiative recombination is the presence of deep-level defects within the band gap of the semiconductor. By reducing the temperature of the absorber, the radiative recombination rate from possible defect states is increased. Thus, if deep-level defects were present in a significant concentration, they would act as radiative recombination centers in photoluminescence experiments at low temperatures. To detect the radiative signals from potential deep-level defects, photoluminescence measurements at 10 K are conducted in the extended setup that allows for the detection of signals up to wavelengths of 2400 nm (i.e. transitions of 0.5 eV). The measured PL spectra in this thesis do not reveal any presence of deep-level defects in the state-of-the-art CIGS absorbers, independent of the alkali post-deposition treatment. These results do not suggest that one can categorically deny the presence of any deep-level defects but suggest only that, if deep-level defects are present, their concentration is low.

A possible origin of band tails are fluctuating band edges that are due to a non-equally distributed partition of charged impurities or due to ionized impurities at the grain boundaries. These electrostatic potential fluctuations can severely influence the measured PL spectra at low temperatures. While there are various models in literature that attempt to describe charge carrier dynamics and recombination in the presence of the fluctuating band edges, no consensus has currently been found. However, it is possible to qualitatively gauge the amplitude of the fluctuations by performing temperature- and excitation-dependent photoluminescence measurements and investigating the energy of the radiative transitions. The measured PL spectra of the high-temperature absorbers H1 and H2 reveal a defect-related radiative transition at low temperatures and the band-to-band transition at intermediate and high temperatures. Between the samples, both the defect-related and band-to-band transition appear to be more severely affected by the temperature and excitation flux density changes in the H2 than in the H1 absorber. These results suggest that the electrostatic potential fluctuations are larger in the non-treated H2 absorber than in the H1 absorber that received a RbF PDT.

Compared to the high-temperature absorbers, the PL spectra of the low-temperature absorbers show a slightly different behaviour: depending on the temperature and excitation flux density, two defect-related transitions and one band-to-band transition can be observed. To avoid the potential falsification of extracted information due to a conflicted fitting process, only the dominant defect-related transition is investigated in detail. Between the absorbers L1, L2, and L3, this transition appears to be most severely affected in the absorber that did not receive any PDT and the least affected in the absorber that received a sequential NaF+RbF PDT. Thus, the same conclusion as in the high-temperature absorbers is reached: the alkali PDT leads to a reduction of the electrostatic potential fluctuations and this reduction is stronger for heavier alkalis.

The experimental results agree with other experimental studies which suggest the compensation of V_{Cu} acceptors and reduction of In_{Cu} donors through the alkali atoms to be the underlying mechanism of the electrostatic potential fluctuation reduction. The implications of reduced electrostatic potential fluctuations at low temperatures for the performance of solar cell devices at room temperature are not immediately evident and are the subject of the following chapter 7.

7 What limits the voltage in $Cu(In,Ga)Se_2$ solar cells?

In the three preceding chapters, various optoelectronic aspects of state-of-the-art CIGS absorbers were tackled and the influence of the alkali post-deposition treatment could be identified in terms of measured quantities. More specifically, photoluminescence measurements at room temperature revealed an increase in the quasi-Fermi level splitting $\Delta\mu$ in both CdS-covered and bare CIGS absorber that received an alkali treatment. This increase in the QFLS, and ultimately V_{OC}, was identified to be due to a reduced rate of non-radiative recombination. Additional PL experiments at room temperature, enabling the analysis of band tails, revealed a reduced Urbach energy E_U in absorbers that underwent an alkali PDT. Following these results, an empirical correlation between the quasi-Fermi level splitting deficit and Urbach energy was established. The results of the room temperature PL measurements suggest that the alkali PDT, while also altering the surface, predominantly affects the bulk CIGS material.

Photoluminescence measurements conducted at low temperatures enable the investigation of deep-level trap states as well as the influence of electrostatic potential fluctuations on the emitted spectra. While no deep-level defects could optically be detected with the experimental setup used in the framework of this thesis, a reduction of the fluctuation amplitude of the band edges with alkali PDT could be observed.

In this chapter, the various results are tied together and explanations are suggested. The chapter is divided into three main sections. The first section 7.1 compares the state-of-the-art CIGS absorbers and solar cells to the best devices from the crystalline silicon (c-Si) and gallium arsenide (GaAs) technology. The comparison is done in terms of Urbach energy, external radiative efficiency, and open-circuit voltage losses and reveals that the best CIGS devices exhibit very similar optoelectronic qualities compared to c-Si but are still very far off from GaAs. Some of the results in this section are to be published in ref. [207].

The second section 7.2 attempts the description of the influence of the alkali post-deposition treatment on the CIGS solar cells. The description is based both on published results from literature and on the experimental results attained in the framework of this thesis. It is suggested that the NaF PDT consists predominantly of a bulk effect increasing the hole carrier concentration which leads to a larger quasi-Fermi level splitting. The heavier RbF PDT alters both the surface and the bulk of the CIGS absorber through a reduction of the non-radiative recombination, as well as possible changes in the doping.

Based on its preceding sections, the final section 7.3 discusses remaining open questions revolving around the voltage losses in CIGS solar cells. The content of this section is heavily inspired by literature results and is thus to be viewed as an open discussion rather than an attempt at finding solutions to the remaining open questions. The section focusses on the limiting mechanisms that are closely linked to the experimental results of this thesis: potential fluctuations, deep-level defects, structural defects, and photon recycling.

7.1 Cu(In,Ga)Se$_2$ solar cells: State of the Art

7.1.1 Revisiting band tails

In section 5.3, from the photoluminescence measured on the CdS-covered CIGS absorbers, the absorption coefficient $\alpha(E)$ and ultimately the Urbach energy E_U could be extracted. By plotting the energetic quasi-Fermi level splitting deficit $E_{PL} - \Delta\mu$ against the Urbach energy in Fig. 5.9, an empirical correlation between optoelectronic losses, band tails and the alkali PDT could be established. However, the data were not sufficient to identify a specific mechanism responsible for the reduction of band tails with heavier alkali PDT. In the following, Fig. 5.9 is extended by considering the open-circuit voltage deficit $E_g - qV_{OC}$ of the finished solar cell devices (while still considering the measured E_U of the absorbers). This way, additional data points from literature can be included.

Fig. 7.1 shows the updated version of the graph where 3 new data points are added in the form of the black open diamond-shaped symbols, representing a CuInSe$_2$, a crystalline silicon c-Si, and a GaAs sample. The absorber of the CuInSe$_2$ sample was measured in the framework of this thesis and its solar cell parameters can be reviewed in Table 3.2 of section 3.3. The open-circuit voltage V_{OC} values used for the c-Si and GaAs samples are taken from the respective champion devices from ref. [9]. In terms of the Urbach energies, the lowest published values are taken from ref. [217] for GaAs and from ref. [219] for c-Si. These values are usually measured on crystals that are not necessarily used for photovoltaic applications. The selection of these literature data is inspired by the recent study from Jean *et al.* [224]. Alternative values can be found in the older study by de Wolf *et al.* [223]. The inclusion of the GaAs solar cell serves as a point of reference since it represents the material with the smallest V_{OC} deficit of all single-junction solar cells to date [9], [258]. Crystalline silicon is also included because it is the current photovoltaic market leader (see e.g. ref. [259]), which CIGS needs to rival in order to engage in serious competition between both technologies.

Due to the V_{OC} deficit being defined by the band gap energy of the material, E_g is a crucial parameter in Fig. 7.1. For both c-Si and GaAs, typical literature values for the band gap energy (1.12 eV for c-Si and 1.42 eV for GaAs) are taken [18]. For the remaining samples, the band gap energies are displayed in Table 3.2 of section 3.3 and their determination is discussed in appendix B.2.

The V_{OC} deficit of the CIGS solar cells that are treated in the framework of this thesis show the same trend in Fig. 7.1 as in Fig. 5.9 where the energetic quasi-Fermi level splitting deficit $E_{PL} - \Delta\mu$ is plotted. This observation is a consequence of the small differences between the QFLS of the absorbers and the V_{OC} of their corresponding finished solar cell devices, which were presented in section 5.2. Only the low-temperature solar cells LN1 and LN2 show a larger difference in their measured V_{OC} compared to their quasi-Fermi level splitting $\Delta\mu$. This difference was already mentioned and discussed in appendix D.4. Interestingly, the inclusion of the CuInSe$_2$ solar cell does not break the trend imposed by the CIGS absorbers. Its seamless fit into the trend can be explained by its high performance (i.e. power conversion efficiency of 18.4 %) primarily due to its band gap gradient towards the back that prevents non-radiative recombination at the back contact [111].

Looking at the overall trend of the data points in Fig. 7.1, and using GaAs as the reference point, the data suggest that voltage losses in state-of-the-art CIGS absorbers are caused by the band tails. Only c-Si and the low-temperature CIGS sample L3 deviate from the trend. This discrepancy could be explained by the presence of an additional voltage loss mechanism in the case of sample L3 as its V_{OC} deficit is considerably larger than predicted by the trend. Similarly, in the case of c-Si, the discrepancy might be explained by a different loss altogether as it shows a similar V_{OC} deficit as CIGS but a lower Urbach energy. The voltage loss of sample L3 is

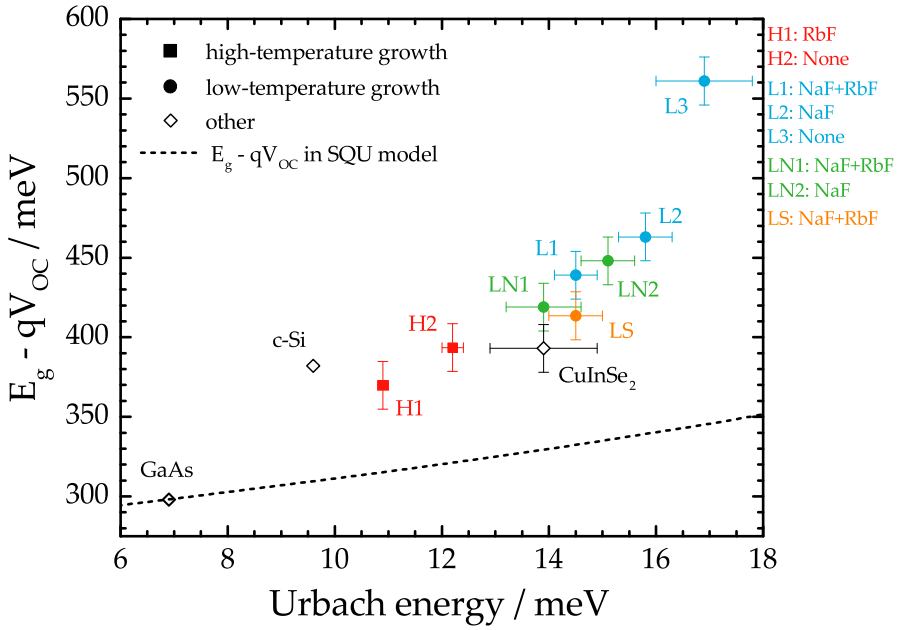

FIGURE 7.1: Open-circuit voltage deficit $E_g - qV_{OC}$ in dependence of the Urbach energy E_U for solar cell devices grown under high- (squares) and low temperatures (circles). The color code refers to solar cells that were grown under the same conditions but received different post-deposition treatments. Also included are data from literature for GaAs and c-Si (open diamonds) and from a $CuInSe_2$ sample (the E_U was measured on the absorber in the in-house setup, see appendix F.1, while the V_{OC} was measured by Thomas Feurer from Empa who also created the device). The allocation of error bars on the Urbach energy values follows the principle laid out in section 5.3.1 while an uncertainty of 15 meV is estimated for the V_{OC} deficit. The black dashed line represents the voltage losses in the Shockley-Queisser limit but adjusted for Urbach-type sub band gap absorption and emission. It is scaled to the GaAs V_{OC} deficit since GaAs is considered as reference.

discussed in more detail in section 7.2, while c-Si is discussed at the end of section 7.1.3. Band tails can contribute to voltage losses through both radiative and non-radiative recombination. These effects were briefly introduced in section 5.3 and will be elaborated in the following.

Dictated by the principle of detailed balance, states that lead to absorption processes also lead to emission processes when in thermal equilibrium. Hence, an increase in absorption due to band tails also leads to an increase in emission of thermal radiation from these states. An increase in thermal radiative emission from sub band gap states leads to an increase in the reverse saturation current density j_0 in eq. (2.22), which ultimately leads to a decrease of the open-circuit voltage V_{OC} via eq. (2.13). This voltage loss is purely of radiative nature and can be simulated by modifying the Shockley-Queisser limit to adjust for the increased absorption and emission through sub band gap states. The exact details of the modified, hereby labelled SQU, model are elaborated in appendix F.2. The open-circuit voltage deficit predicted by the SQU model is visualized by the black dashed line in Fig. 7.1 and, while non-negligible, shows that the radiative voltage loss through band tails is much too small to account for the real measured V_{OC} deficit.

In addition to radiative recombination, sub band gap states can also promote non-radiative recombination processes. As was shown in section 2.5.2, the non-radiative recombination rate can be described by the Shockley-Read-Hall equation which states that the probability of non-radiative transitions increases the deeper the trap states are situated within the band gap. In contrast, trap states that are close to the band edges only promote improbable non-radiative recombination events such that the V_{OC} is only strongly decreased if very large defect densities are present. By using the one-dimensional numerical simulation tool SCAPS [260], [261], the

voltage loss through non-radiative recombination of band tails with varying Urbach energies can be simulated. The details of the simulation are provided in appendix F.3. The simulations reveal that non-radiative recombination through tail states leads to an even smaller reduction of the V_{OC} compared to radiative recombination. Thus, based on these simulations, one might argue that band tails do not promote any significant non-radiative recombination processes. However, at the time of writing, it is not entirely clear how SCAPS handles band tails in detail. As is discussed in more detail in appendix F.3, increasing the Urbach energy from 10 meV to 15 meV at an energy of 100 meV below the band gap leads to an increase in the density of states of approximately a factor of 30. In SCAPS, such a change in the density of states can be simulated by placing an acceptor defect at 100 meV below the conduction band and increasing its density by a factor of 30. Under these conditions, the V_{OC} loss through non-radiative recombination would amount to 80 mV i.e. a severe decrease in the open-circuit voltage.

It can thus be concluded that radiative recombination processes through band tails certainly do not explain the measured voltage losses in state-of-the-art CIGS solar cells as the involved Urbach energies are too low. Given the ambiguities revolving around non-radiative recombination through tail states, it remains unclear whether band tails are detrimental or not but the possibility of them representing a strong limiting mechanism for the voltage in CIGS needs to be entertained.

Fig. 7.1 cleary shows that the alkali PDT leads to a reduction of both the voltage losses and the Urbach energy in the CIGS samples. While it is not yet entirely clear if there exists a causality between both reductions, it is certain that the alkali PDT reduces the band tails. To not encumber the presentation and discussion of the remaining experimental data, suggestions about the exact influence of the alkali PDT are given in the later section 7.2.

Finally, it needs to be mentioned that the insertion of crystalline silicon in Fig. 7.1 is not unambiguous as it is an indirect semiconductor whose absorption edge fundamentally differs from direct semiconductors. Its inclusion, however, also serves another purpose: to show that the voltage losses in the best c-Si devices are comparable to the ones in state-of-the-art CIGS devices. This point is consolidated in the following two sections.

7.1.2 External radiative efficiency

In the previous section, the open-circuit voltage deficit $E_g - qV_{OC}$ for state-of-the-art CIGS solar cells was shown. The voltage losses in these solar cells have several origins (and are quantified in the subsequent section 7.1.3) but the largest contribution stems from non-radiative recombination. The loss ΔV_{OC}^{nrad} in open-circuit voltage due to non-radiative recombination is strongly linked to the external radiative efficiency η_{ext} that can be measured in photoluminescence measurements.

The external radiative efficiency η_{ext}, in terms of photoluminescence, of an absorber is defined as

$$\eta_{ext} = \frac{Y_{PL}}{\Phi_{inc}}, \tag{7.1}$$

where Y_{PL} is the emitted photon flux density that is measured in PL experiments and described by Planck's generalized law (5.1) and Φ_{inc} is the incident photon flux density. In intensity-calibrated photoluminescence experiments, Φ_{inc} is calibrated to equal the AM1.5 photon flux density above the band gap energy of the material. Alternatively, in terms of electroluminescence, the external radiative efficiency, labelled sometimes as external luminescence quantum efficiency Q_{ext}^{lum}, of a solar cell is defined as [262]

$$Q_{ext}^{lum}(V) = \frac{J_{em}(V)}{J_{inj}(V)}, \tag{7.2}$$

where $J_{em}(V)$ is the bias-dependent emission current due to radiative recombination and $J_{inj}(V)$ is the bias-dependent injected current in the dark. The injection current J_{inj} itself can be seen as the sum of the radiative and non-radiative recombination currents [263]. Based on Rau's reciprocity principle [262], the external radiative efficiency η_{ext} measured in photoluminescence experiments (under AM1.5 conditions) equals the external luminescence quantum efficiency Q_{ext}^{lum} under conditions of open circuit and ideal charge carrier collection. The connection between the optoelectronic and electrooptical capacities of a semiconductor material can thus be summarized as

$$\eta_{ext} = Q_{ext}^{lum}(V_{OC}). \tag{7.3}$$

The direct link between the measured V_{OC} and the external luminescence quantum efficiency Q_{ext}^{lum} was first discussed by Shockley and Queisser [76] and later mathematically described by Ross [264]. It is described as [262], [264]

$$V_{OC} = V_{OC}^{rad} + \frac{k_B T}{q} \ln\left(Q_{ext}^{lum}\right) = V_{OC}^{rad} - \Delta V_{OC}^{nrad}. \tag{7.4}$$

Here V_{OC}^{rad} is the open-circuit voltage in the radiative limit i.e. the situation where only radiative recombination is occurring. It needs to be mentioned that in the earlier discussions by Shockley and Queisser [76] as well as Ross [264], the mobility of electrons and holes was considered infinite. The impact of non-ideal carrier collection, through finite mobilities is correctly considered only through Rau's reciprocity relation [262]. The relation (7.4), describing the non-radiative voltage losses ΔV_{OC}^{nrad} based on the measured external luminescence quantum efficiency in solar cells is of fundamental nature and can thus be used across various different solar cell technologies [263], [265]–[274].

If the differences between V_{OC}^{rad} and the open-circuit voltage in the Shockley-Queisser limit V_{OC}^{SQ} are sufficiently small (which they are in the case of CIGS e.g. - see the following section 7.1.3), it is possible to approximate $V_{OC}^{rad} \approx V_{OC}^{SQ}$. Thus, eq. (7.4) can be rearranged to

$$q\left(V_{OC}^{SQ} - V_{OC}\right) = -k_B T \ln\left(Q_{ext}^{lum}\right), \tag{7.5}$$

where the left-hand side now describes the V_{OC} deficit, due to non-radiative recombination, with respect to the SQ limit in solar cells. Eq. (7.5) can easily be transferred to the case of photoluminescence measurements on absorbers by substituting the V_{OC} by the quasi-Fermi level splitting $\Delta\mu$ and the external luminescence quantum efficiency Q_{ext}^{lum} by the external radiative efficiency η_{ext}:

$$qV_{OC}^{SQ} - \Delta\mu = -k_B T \ln(\eta_{ext}). \tag{7.6}$$

Fig. 7.2 shows the non-radiative energy loss, i.e. the left-hand side expressions of equations (7.5) and (7.6), in dependence of the external radiative efficiency η_{ext} for different solar cell materials. The open symbols represent the non-radiative energy loss $q(V_{OC}^{SQ} - V_{OC})$ measured on the finished solar cell devices while the full symbols represent the non-radiative energy loss $qV_{OC}^{SQ} - \Delta\mu$ measured on the absorbers. For all measured samples, the external radiative efficiency η_{ext} is taken from PL. The square symbols represent the state-of-the-art CIGS (and the CuInSe$_2$) samples that are treated in this thesis, distinguishable through the familiar color code (cf. Fig. 7.1). The other symbols represent other samples and materials (specified in the caption and annotated in the graph). Also included in the graph are selected data from literature, represented by the star symbols, that are entirely plotted through eq. (7.5) as no corresponding PL data are available. The Q_{ext}^{lum} of the literature samples is extracted from their external quantum efficiency (EQE) spectra via Green's application [275] of Rau's reciprocity

relation [262]:

$$Q_{\mathrm{ext}}^{\mathrm{lum}} = j_{\mathrm{SC}}^{-1} \frac{2\pi q}{h^3 c^2} \exp\left(\frac{qV_{\mathrm{OC}}}{k_{\mathrm{B}}T}\right) \int \frac{EQE(E)\, E^2\, \mathrm{d}E}{\exp\left(E/k_{\mathrm{B}}T\right) - 1}, \tag{7.7}$$

where $EQE(E)$ is the external quantum efficiency. The method is described and illustrated in detail in appendix F.4. The data from literature represent champion devices and thus act as reference points[1]. However, it needs to be mentioned that the EQE spectra of all 4 literature devices were digitized. Thus, as laid out in appendix F.4, the extracted $Q_{\mathrm{ext}}^{\mathrm{lum}}$ can carry a significant error (but which is difficult to gauge).

As the open-circuit voltage in the SQ limit is needed for eqs. (7.5) and (7.6), the band gap energy is necessary (cf. section 2.4). For the samples treated in this thesis (square symbols), the band gap values are taken from Table 3.1 in section 3.3. For the Cu-rich $CuInS_2$ (diamond symbols), Cu-rich CIGS (triangle symbols), and Cu-poor CIGS (circle symbols), the measured energy of the main PL transition is taken as band gap energy. For the literature data (star symbols), the band gap energies are taken from the respective references.

The grey dashed line does not represent a fit to the data but rather the behaviour that one expects from either expressions (7.5) or (7.6) with a fixed negative slope of $k_{\mathrm{B}}T = 25.5\,\mathrm{meV}$. The fact that the different solar cell technologies, whose external radiative efficiency is measured

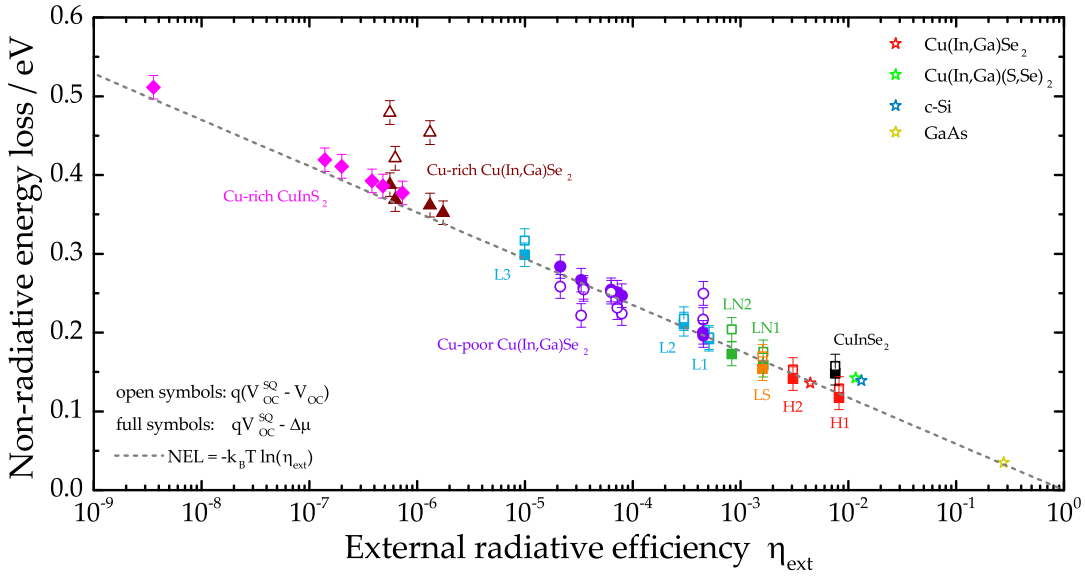

FIGURE 7.2: Non-radiative energy loss of various absorbers and solar cells in dependence of their external radiative efficiency. The open symbols represent the non-radiative loss with respect to the open-circuit voltage (7.5) of the solar cell while the full symbols represent the non-radiative loss with respect to the quasi-Fermi level splitting (7.6) of the absorber. The non-square-shaped data points represent samples that were grown and measured in-house: Cu-rich $CuInS_2$ (magenta diamonds - data provided by Alberto Lomuscio), Cu-rich CIGS (brown triangles - data provided by Dr. Finn Babbe), and Cu-poor CIGS (violet circles - data provided by Dr. Finn Babbe). The square-shaped symbols represent the samples investigated in this thesis. The star-shaped symbols represent selected solar cell data points from literature for $Cu(In,Ga)Se_2$ (red - 22.6 % champion device - data provided by Dr. Philip Jackson from ZSW), $Cu(In,Ga)(S,Se)_2$ (green - former 22.9 % champion device - data from refs. [9], [16]), c-Si (blue - 26.7 % champion device - data from ref. [276]), and GaAs (yellow - 28.8 % champion device - data from ref. [277]). The allocation of the error bars is explained in the main text. The grey dashed line represents the trend predicted by either eqs. (7.5) or (7.6) with a fixed a slope of $-k_{\mathrm{B}}T = -25.5\,\mathrm{meV}$.

[1]There are two literature data points for CIGS devices: the sample labelled $Cu(In,Ga)Se_2$ which was included because it shares a similar growth process as samples H1 and H2, and sample labelled $Cu(In,Ga)(S,Se)_2$ as it represents the CIGS device with the highest efficiency whose data are publicly available.

across 8 orders of magnitude, exhibit data points that are situated close to the dashed line, proves the fundamental validity of eq. (7.4). However, this is only the case if the band-to-band transition is present in the measured luminescence spectra [278]. Interestingly, the V_{OC} is severely limited due to the presence of deep-level defects in both Cu-rich $CuInS_2$ [279] and Cu-rich CIGS [49] absorbers and solar cells. Yet, by determining the η_{ext} only from the PL band-to-band transition, the data points still follow eq. (7.4), even if the radiative deep-level transition is the dominant one. Furthermore, for both Cu-rich $CuInS_2$ and Cu-rich CIGS, the V_{OC} measured on the solar cells is significantly lower than the $\Delta\mu$ measured on the absorbers. This can clearly be seen from the open-symbol data points of Cu-rich CIGS (the V_{OC}-related values of the Cu-rich $CuInS_2$ devices are not shown as they lie at y-values of 0.7 eV to 1 eV). This discrepancy is due to interface losses in the finished solar cell devices [49], [279].

In contrast, the Cu-poor CIGS solar cells do not exhibit such strong interface losses and can thus be found on the dashed line, bar some scatter of the purple data points. Generally, the deviation of the data points around the expected trend can be explained by different factors such as the non-precise determination of the band gap energy E_g (which is necessary to calculate V_{OC}^{SQ}), the approximation $V_{OC}^{rad} \approx V_{OC}^{SQ}$, and measurement incertitudes. To weaken the extent of these factors, an estimated uncertainty of 15 meV is attributed to the the measured data points.

Looking at the data points of the state-of-the-art CIGS absorbers and devices treated in the framework of this thesis, it comes as no surprise that the samples follow the same trend as in Fig. 7.1 since the open-circuit voltage deficit $E_g - V_{OC}$ and the non-radiative energy loss represent almost the same quantity. Comparing the state-of-the-art CIGS absorbers to the literature data, one finds that the CIGS champion device (red star) is supposedly of inferior quality compared to the H1 sample. This discrepancy could be explained by the fact that η_{ext} of the CIGS champion device is determined from the digitized EQE data whereas η_{ext} of the H1 sample is won from PL measurements. Assuming that the digitized EQE spectrum is as precise as possible, the extraction of Q_{ext}^{lum} is achieved through the usage of the measured V_{OC} (see appendix F.4). Since the V_{OC} is typically inferior to the $\Delta\mu$, the external radiative efficiency from EQE is, in most cases, inferior to the external radiative efficiency measured through PL on the absorbers. However, it also needs to be mentioned that is it also very likely that H1 is just a very good sample that naturally shows a high external radiative efficiency and thus large $\Delta\mu$ and V_{OC}. This latter sentiment seems to be vindicated as the difference in power conversion efficiency between C1 and H1 is most probably due to differences in the j_{SC} (37.8 mA/cm^2 for C1 [15] vs. 36.4 mA/cm^2 for H1) and fill factor (80.6 % for C1 [15] vs. 77.6 % for H1).

Finally, both the champion $Cu(In,Ga)(S,Se)_2$ and c-Si devices exhibit the largest external radiative efficiency amongst all the measured absorbers and solar cells (above 1 %). GaAs reigns supreme and significantly ahead of all other PV technologies.

There are two major conclusions that can be drawn from the multitude of experimental results summarized in Fig. 7.2. The first conclusion is that determining the external radiative efficiency through photoluminescence proves a fast, reliable and thus excellent method to quantify the non-radiative energy losses in CIGS absorbers. The second conclusion is that, while GaAs continues to remain the elusive champion in terms of minimal non-radiative losses, the state-of-the-art CIGS absorbers and solar cells, having undergone alkali post-deposition treatments, show similar non-radiative losses compared to the best c-Si device, even though their power conversion efficiencies are miles apart. The differences between the best CIGS and c-Si devices are detailed in the following section.

Finally, it needs to be mentioned that not only the external radiative efficiency is important, but that also the internal radiative efficiency plays a crucial role. The relationship between internal and external radiative efficiency in the case of CIGS is derived in detail in appendix F.5

and can be summarized by the numerical value of 0.021. This means that from the photons that are created inside the absorber, only 2.1 % may exit and contribute to the external radiative efficiency. The potential implications of this very weak photon out-coupling are discussed in the last section 7.3.

7.1.3 Quantified voltage losses

The previous section 7.1.2 focussed on the determination of the voltage loss due to non-radiative recombination that can conveniently be measured through intensity-calibrated photoluminescence or external quantum efficiency measurements. However, the non-radiative recombination voltage loss $\Delta V_{\mathrm{OC}}^{\mathrm{nrad}}$ is not the only loss mechanism that pushes the measured open-circuit voltage V_{OC} below its theoretical Shockley-Queisser limit $V_{\mathrm{OC}}^{\mathrm{SQ}}$. Specifically, there are two additional losses: the short-circuit voltage loss $\Delta V_{\mathrm{OC}}^{\mathrm{SC}}$ and the radiative voltage loss $\Delta V_{\mathrm{OC}}^{\mathrm{rad}}$ [278]. The short-circuit voltage loss $\Delta V_{\mathrm{OC}}^{\mathrm{SC}}$ describes the loss that stems from the difference between the real measured short-circuit current density and its SQ limit. While this difference is obviously the main origin of the solar cell performance loss due to insufficient current extraction, its influence on the V_{OC} is usually very minor. The radiative voltage loss $\Delta V_{\mathrm{OC}}^{\mathrm{rad}}$ originates from incomplete absorption as well as from the increase in saturation current density j_0 due to radiative emission through states below the band gap energy. In state-of-the-art CIGS, where the Urbach energy is relatively low (cf. Fig. 7.1), the radiative voltage loss is also quite low. The various loss terms can be summarized in the following expression [278]:

$$V_{\mathrm{OC}} = V_{\mathrm{OC}}^{\mathrm{SQ}} - \Delta V_{\mathrm{OC}}^{\mathrm{SC}} - \Delta V_{\mathrm{OC}}^{\mathrm{rad}} - \Delta V_{\mathrm{OC}}^{\mathrm{nrad}}. \tag{7.8}$$

Recently, Rau *et al.* presented a novel approach to compute and allocate quantitative values to these voltage losses [278]. The approach is based on a generalization of the Shockley-Queisser model through the determination of a so-called photovoltaic band gap energy $E_{\mathrm{g}}^{\mathrm{PV}}$ from experimentally-measured external quantum efficiency spectra. While $E_{\mathrm{g}}^{\mathrm{PV}}$ does not represent the real band gap energy of the material, its forte lies with the fact that it quantifies the external photovoltaic properties of the device and can thus be used in comparative studies of different solar cell technologies. By using $E_{\mathrm{g}}^{\mathrm{PV}}$, the $V_{\mathrm{OC}}^{\mathrm{SQ}}$ is the SQ limit can thus be calculated. The short-circuit voltage loss $\Delta V_{\mathrm{OC}}^{\mathrm{SC}}$ is then extracted by comparing the real measured j_{SC} to the $j_{\mathrm{SC}}^{\mathrm{SQ}}$ in the SQ limit. Furthermore, in conjunction with Rau's reciprocity relation [262], the measured external quantum efficiency can be used to calculate the $V_{\mathrm{OC}}^{\mathrm{rad}}$ in the radiative limit. Finally, the difference between $V_{\mathrm{OC}}^{\mathrm{rad}}$ and real measured V_{OC} yields the non-radiative voltage loss $\Delta V_{\mathrm{OC}}^{\mathrm{nrad}}$. A more detailed description of the generalized SQ model along with the exact mathematical expression for the various voltage losses in eq. (7.8) are provided in appendix F.6. The calculated voltage losses are summarized in Fig. 7.3. To provide a better frame for comparison, the literature data shown in Fig. 7.2 are also included.

The first observation is that the photovoltaic band gap energy $E_{\mathrm{g}}^{\mathrm{PV}}$ (solid horizontal bars) differs from the band gap energies E_{g} listed in Table 3.1 of section 3.3 (dashed horizontal bars). The reason for this difference is the method of band gap determination. $E_{\mathrm{g}}^{\mathrm{PV}}$ is determined from the external quantum efficiency and thus from a combination of absorption as well as carrier collection properties of the device. By contrast, the band gap energies E_{g} listed in Table 3.1 are primarily determined from the gallium concentration in the compositional notch region of the absorber (cf. section B.2).

From the green bars, it can be seen that short-circuit voltage loss $\Delta V_{\mathrm{OC}}^{\mathrm{SC}}$ is very small across all samples. This loss is smallest in the c-Si and GaAs devices, which is not surprising since their measured short-circuit current densities are very close to the ideal values [258]. Among the CIGS devices, the short-circuit loss term is smallest in the champion devices C1 and C2.

However, this difference can be attributed to the presence of an anti-reflective coating on the champion devices which is absent on the devices measured in this thesis.

The radiative voltage loss ΔV_{OC}^{rad}, represented by the blue bars, is similar across all solar cells, including c-Si. Only GaAs shows an extremely small radiative voltage loss because of its very sharp optical absorption edge, which is also represented by its typically low Urbach energy (cf. Fig. 7.1). Between the different CIGS samples, no clear differences in the ΔV_{OC}^{rad} can be distinguished. This is in contrast to the clear differences in Urbach energies in Fig. 7.1. It can thus be argued that the low-energy portion of the measured EQE spectra is too imprecise to detect discrepancies in the radiative emission between different samples. Nonetheless, it is very interesting to observe that the radiative voltage loss in CIGS and c-Si is similar even though its origin differs. In c-Si, the radiative loss is due to indirect nature of the band gap and thus weak light absorption. By contrast, in CIGS the radiative loss is due to a combination of emission through sub band gap states as well as weak absorption due to a narrow band gap notch.

Looking at the combined short-circuit and radiative voltage loss $\Delta V_{OC}^{SC} + \Delta V_{OC}^{rad}$, one can conclude that it is relatively small compared to both the measured V_{OC} and the non-radiative voltage loss ΔV_{OC}^{nrad}. Thus, the assumption $V_{OC}^{rad} \approx V_{OC}^{SQ}$, taken in the previous section 7.1.2, can be considered valid.

Concerning the open-circuit voltage loss due to non-radiative recombination ΔV_{OC}^{nrad}, the data represented in Fig. 7.3 offer only limited additional information compared to Fig. 7.2. However, Fig. 7.3 now allows a direct comparison of the performance-limiting non-radiative voltage

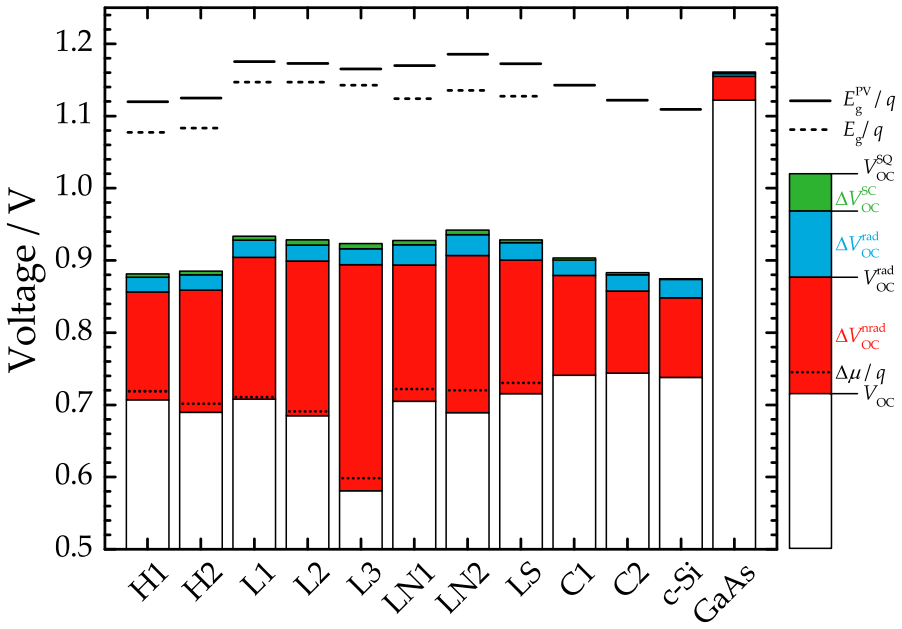

FIGURE 7.3: Open-circuit voltage losses ΔV_{OC}^{nrad} due to non-radiative recombination (red), ΔV_{OC}^{rad} due to radiative recombination from states below the band edges (blue), and ΔV_{OC}^{SC} due to the mismatch between real and ideal short-circuit current density (green) for the samples investigated in this thesis as well as selected literature data. Also shown is the measured open-circuit voltage V_{OC} on the solar cells (white), the measured quasi-Fermi level splitting $\Delta\mu$ on the CdS-covered absorber (dotted horizontal bars), the photovoltaic band gap energy E_g^{PV} (solid horizontal bars), and the mainly compositionally-determined band gap energy E_g from Table 3.1. The literature data are the same that are included in Fig. 7.2 i.e. the Cu(In,Ga)Se$_2$ champion device (C1), the Cu(In,Ga)(S,Se)$_2$ champion device (C2) [9], [16], the champion c-Si device [276], and the champion GaAs device [277]. The E_g^{PV} for GaAs amounts to 1.42 eV and is not shown here. Furthermore, since no EQE data are available, sample CuInSe$_2$ is missing.

loss across different samples consistently determined by the same method. In numbers, the best CIGS devices show a non-radiative voltage loss ΔV_{OC}^{nrad} that reads 149 meV for sample H1, 138 meV for sample C1, and 113 meV for sample C2[2]. The latter shows an almost identical non-radiative voltage loss compared to the 110 meV measured on the c-Si device. The non-radiative voltage loss in the best GaAs device reads 33 meV.

The summary of the various voltage losses of CIGS devices and the insightful comparison to the best available PV technologies in c-Si and GaAs leads to important conclusion and opens up the way to potential new strategies for device improvement. The following very brief discussion focusses around the best devices shown in Fig. 7.3 i.e. C2, c-Si, and GaAs. Between the best CIGS and c-Si device, the voltage losses, independent of their origin, are identical. However, the corresponding power conversion efficiencies are very far apart: 22.9 % for CIGS and 26.7 % for Si [9]. Thus, this huge difference in performance stems from other losses, most notably in the short-circuit current density j_{SC} (38.8 mA/cm^2 for C2 vs. 42.7 mA/cm^2 for c-Si [9]) and the fill factor FF (79.5 % for C2 vs. 84.9 % for c-Si [9]), keeping in mind that both samples have a similar band gap energy. Decades of intensive research on silicon-based solar cells have led to sophisticated designs that offer a plethora of advantages. For example, even though c-Si exhibits a low absorption coefficient due to its indirect semiconductor nature, this deficiency is overcome through the implementation of optimized surface designs that guarantee both a minimized surface reflection as well as enhanced light trapping capabilities [258]. Furthermore, an interdigitated back-contact design offers other additional benefits such as reduced grid shading as well as reduced series resistance [258]. All these concepts, which are chiefly responsible for the large short-circuit current density and fill factor in c-Si, are missing from the CIGS cell architecture. However, research in this domain is well under way as new strategies are proposed and tested. One such strategy is the thinning of the CdS buffer layer down to 10 nm to reduce the parasitic UV absorption and thus generate a larger j_{SC}. As a thinner CdS layer causes detrimental interface recombination, a high-resistive (HR) passivation layer needs to be used. A promising candidate for this HR layer is TiO_2, which has already been implemented and shown to successfully increase the j_{SC} [280]. Another strategy is the inclusion of a back-contact reflector to improve light absorption in the near-infrared. Very recently, experiments culminating in the deposition of a thinner than 100 nm Al layer on top of the molybdenum back contact have yielded promising results in the form of a j_{SC} increase of 0.3 - 0.7 mA/cm^2 [281]. These strategies to improve j_{SC} are only two in a list of multiple possible design solutions and adaptations. Since the improvement of the short-circuit current density is not the main topic of this thesis, the following discussions and sections will revolve around the voltage improvement only.

The comparison of the voltage losses between C2 and c-Si offers another interesting conclusion. As was already mentioned, the radiative loss term ΔV_{OC}^{rad} in both materials is of the same magnitude but of different origin. The same can be said about the non-radiative loss term ΔV_{OC}^{nrad}: in state-of-the-art c-Si solar cells, the extracted open-circuit voltage is fundamentally limited through Auger recombination due to high doping concentrations [282]–[286] such that further voltage improvements potentially require a paradigm shift in design architecture. In contrast, the quest for the identification of the V_{OC}-limiting mechanisms in CIGS is still ongoing. However, as can be seen in the results that have been presented in this thesis and their comparison to sample C2 in Fig. 7.3, improvements in the V_{OC} are likely still possible in the case of CIGS.

[2]The ΔV_{OC}^{nrad} loss between H1 and C1 is slightly different in Fig. 7.3 compared to Fig. 7.2. This is due to the fact that in the latter mostly the measured quantities of the H1 absorber are shown, while in the former the solar cell quantities are shown. As already discussed in Fig. F.4A, the H1 solar cells are expected to show slight discrepancies compared to the absorbers as the growth process is slightly inhomogeneous.

Since the largest loss in V_{OC} in CIGS is due to non-radiative recombination, the largest portion of effort should be allocated to identifying the origins of non-radiative recombination.

7.1.4 Summary

The comparison of CIGS with the highest-performing solar cell technologies of crystalline silicon and gallium arsenide paints a telling picture of the current status of the Cu(In,Ga)Se_2 thin-film technology.

The CIGS samples measured in the framework of this thesis show a clear empirical correlation between the open-circuit voltage deficit $E_g - qV_{OC}$ measured on the solar cells and the Urbach energy E_U measured on the absorbers. This correlation suggests that band tails are responsible for the voltage losses in state-of-the-art CIGS absorbers. While literature data of GaAs and measured data of $CuInSe_2$ seamlessly fit into the trend purported by the CIGS samples, literature data of c-Si shows a slight deviation. Using GaAs as a reference point, it was shown that radiative recombination through tail states leads to voltage losses that are much too small compared to the real measured losses. Attempts to simulate the voltage losses through non-radiative recombination processes did not yield conclusive results. As such, the possibility of the band tails limiting the V_{OC} in state-of-the-art CIGS absorbers through non-radiative recombination remains a possibility.

Through intensity-calibrated photoluminescence measurements it is possible to extract the external radiative efficiency η_{ext} from semiconductor absorbers across several orders of magnitude. With η_{ext} being linked to the non-radiative recombination loss in the open-circuit voltage ΔV_{OC}^{nrad} through fundamental thermodynamic concepts, PL proves an excellent method to gauge the optoelectronic quality of absorbers. A comparison of different solar cell technologies reveals that the best CIGS and c-Si devices exhibit comparable non-radiative voltage losses with GaAs being the best technology by a significant margin.

From external quantum efficiency measurements, it is possible to divide the voltage losses, with respect to the SQ limit, in solar cells into their three origins: loss due to short-circuit current mismatch, loss due to radiative recombination from states below the band gap, and loss due to non-radiative recombination. A comparison between the best CIGS devices measured in the framework of this thesis and c-Si demonstrates that both technologies exhibit very similar voltage losses even if the origins of these losses are different. These results update the general perception of CIGS that currently exists in literature and indicate that improvements in the V_{OC} through the reduction of non-radiative recombination are likely still possible.

To suggest strategies for the improvement of CIGS performance, the mechanisms behind the recent increase in V_{OC} need to be understood. Thus, the following section 7.2 attempts to explain the influence of the alkali atoms on the optoelectronic performance of CIGS devices. The description is based on the results that were achieved in the framework of this thesis and the vast information from literature. Based on the contents from the following section, the last section briefly tackles a number of remaining open questions about the origin of non-radiative recombination voltage losses in state-of-the-art CIGS.

7.2 Influence of alkali elements on the optoelectronic quality of CIGS

The description of the influence of alkali elements on the optoelectronic performance of the CIGS devices needs to account for the main alkali-related findings of this thesis:

- The quasi-Fermi level splitting $\Delta\mu$ is increased in absorbers that contain sodium compared to absorbers that do not. Furthermore, adding the heavier alkali element rubidium in a post-deposition treatment leads to an additional increase in $\Delta\mu$. The increase in $\Delta\mu$ is attributed to an optoelectronic improvement of both the absorber surface and the bulk through the reduction of non-radiative recombination.
- The band tails, expressed by the Urbach energy E_U, are reduced in absorbers that received an alkali treatment. Similarly to the increase in $\Delta\mu$, the decrease in E_U is more pronounced whenever the heavier alkali Rb is involved but can also already be observed in absorbers where only Na is added.
- The electrostatic potential fluctuations, measured through PL at low temperatures, are reduced in absorbers that underwent an alkali PDT. Similarly to the quasi-Fermi level splitting $\Delta\mu$ and the Urbach energy E_U, the fluctuations are less severe when heavier alkalis are involved.

A general overview of the alkali post-deposition treatment from literature was given in section 2.6.3 with appendices A.4 and A.5 offering a more focussed overview concerning changes in doping and open-circuit voltage. Due to the large amount of (sometimes conflicting) results from literature, it is impossible to account for every single reported observation. Thus, in the following, preference is given to recent studies which present observations that best describe the experimental results of this thesis. Additionally, only the results on the high-temperature samples H1 and H2, as well as on the low-temperature samples L1, L2, and L3 are discussed because only these samples were fully measured in the framework of this thesis (i.e. only for these samples the results listed above were gathered).

7.2.1 Influence of NaF

The measurements on the samples L2 and L3 in this thesis have shown that the treatment of the CIGS absorber with NaF leads to an increase in the quasi-Fermi level splitting $\Delta\mu$ (cf. section 5.2.1) (which ultimately translates to an increase in the open-circuit voltage V_{OC} in the finished solar cell device). In addition, the absorber treatment with NaF leads to reduced electrostatic potential fluctuations at low temperatures (cf. section 6.2.3) and reduced band tails at room temperature (cf. section 5.3).

It is reported in literature that Na, upon introduction into the CIGS absorber, diffuses into the grains and along the grain boundaries [121], [122]. Whether through promoting the formation of V_{Cu} acceptors [128] or reducing the In_{Cu} donors due to the formation of Na_{Cu} antisites [127], Na increases the net hole carrier concentration p_0 [130]. Since the formation of the sodium-containing compound $NaInSe_2$ is rather unlikely [141], and since Na neither passivates the grain boundaries [287] nor the surface [215], it is likely that the increase in hole carrier concentration is the chief benefit of the sodium injection. More specifically, there exists strong experimental evidence that the increase in doping alone is sufficient to invoke the beneficial increase in the open-circuit voltage V_{OC} [130], [131].

Thus, based on the observations from literature, it appears possible that the main effect of Na is an increase of the hole charge carrier concentration p_0 inside the CIGS absorber. The increase in p_0 leads to a shift of the hole quasi-Fermi level towards the valence band while the minority

charge carrier quasi-Fermi level remains constant. Hence, an increase in p-type doping leads to an increase in the quasi-Fermi level splitting as long as the overall recombination processes are dominated by non-radiative processes. A more detailed description of the influence of doping on $\Delta\mu$ is provided in the appendix F.7. Unfortunately, the increase in hole carrier concentration with NaF could not be checked for the present samples L2 and L3 as the doping concentration of sample L3 has not been measured. However, samples L2 and L3 were fabricated in the same laboratory as the solar cells discussed in ref. [130] where an increase in V_{OC} of 116 mV is attributed to the increase in hole carrier concentration following the NaF PDT (see also Table A.2 in appendix A.5). The difference of 93 meV (104 mV) in the $\Delta\mu$ (V_{OC}) that is measured between samples L3 and L2 in this thesis (cf. Fig. 5.5) is very similar to the value reported in literature. It can thus be argued that the beneficial doping effect of Na is also present in the absorber L2 of this thesis. The lack of adequate p-type doping in the L3 absorber explains its high $\Delta\mu$- and V_{OC} deficit in Figs. 5.9 and 7.1.

An increase in hole density from sample L3 to L2, either through a reduction of donors N_D, increase in acceptors N_A, or both, leads to a reduced degree of compensation N_D/N_A which, in turn, leads to reduced electrostatic potential fluctuations that were measured in section 6.2.3. Likely origins of electrostatic potential fluctuations are inter- and intragrain fluctuations in the doping concentration [231], [288], [289] and/or band bending at the grain boundaries [172]. With the presence of Na having a negligible effect on the band bending at grain boundaries [287], a more likely cause of reduced electrostatic potential fluctuations is the reduction of doping inhomogeneities through a re-organization of charged impurities via the formation of neutralizing Na_{Cu} defects or of additional copper vacancies V_{Cu}. The measured reduction of the electrostatic potential is a likely cause for the decrease of the band tails from absorber L3 to L2 in Fig 5.9.

Finally, based on the findings reported in literature and the measurements done in the framework of this thesis, it can be concluded that the NaF PDT leads to an increase in the hole carrier concentration of the CIGS absorber. This bulk effect improves the absorber quality through an increase in the quasi-Fermi level splitting which ultimately translates into an increase in the open-circuit voltage of the solar cell.

7.2.2 Influence of sodium and RbF

The measurements on the samples H1, H2, L1, and L2 in this thesis have shown that the treatment of the CIGS absorber with RbF leads to an additional increase in the quasi-Fermi level splitting $\Delta\mu$ (cf. section 5.2.1). In addition, the absorber treatment with RbF leads to reduced electrostatic potential fluctuations at low temperatures (cf. section 6.2) and reduced band tails at room temperature (cf. section 5.3).

In literature, it is reported that when injecting rubidium into the CIGS absorber that already contains sodium, Rb diffuses along the grain boundaries [152], [154], [155], pushing the Na into the grains [154] and onto the surface where it is washed away [156]. Hence, while the concentration of Na inside the grains increases [154], its overall concentration inside the whole absorber decreases [156], [157]. The injection of rubidium into the absorber either leads to an increase or a decrease in p-type doping [156]. In the case of an increase in p-type doping, the measured V_{OC} is expected to increase. However, contrary to the case of the solitary NaF PDT, so far it has not been reported yet that the change in doping alone can explain the increase in the measured V_{OC} (see Table A.2 in appendix A.5 for a listing of literature results). Due to the segregation of Rb and accompanying Cu depletion as well as In and Se enrichment at the grain boundaries and absorber surface [140], [153], [156], the beneficial effects of the RbF PDT are also linked to the formation of the $RbInSe_2$ compound [141], [159]. Most groups argue that

the change in surface morphology [140], [156] leads to reduced non-radiative recombination at the CdS/CIGS interface [156], [158], [290]. At the grain boundaries, it is speculated that, if not through the formation of the $RbInSe_2$ compound, the accompanied Cu-depletion leads to a "passivation" and thus to a reduced non-radiative recombination [153], [157]. Finally, due to a finite amount of Rb also present within the grains [157], additional beneficial effects, even if small, cannot be excluded.

Concerning the low-temperature samples L2 and L1 investigated in the framework of this thesis, colleague Dr. Florian Werner identified their hole carrier concentrations via capacitance-voltage measurements. In this context, the L2 sample shows a hole carrier concentration of $p_0 = 8 \cdot 10^{15}\,\mathrm{cm}^{-3}$ while L1 shows a lower concentration of $p_0 = 5 \cdot 10^{15}\,\mathrm{cm}^{-3}$. Thus, in the low-temperature absorbers, the sequential NaF+RbF PDT leads to a reduction in p-type doping. The influence of the doping concentration on the quasi-Fermi level splitting can be estimated via

$$\Delta(\Delta\mu) = k_\mathrm{B}T \ln\left(\frac{p_0^{\mathrm{NaF+RbF}}}{p_0^{\mathrm{NaF}}}\right), \tag{7.9}$$

which has been derived, and is explained, in appendix F.7. The abovementioned decrease in hole carrier concentration would lead to a reduction in $\Delta\mu$ of -12 meV. However, the measured difference in $\Delta\mu$ between absorber L2 and L1 is positive and amounts to +18 meV (cf. Fig. 5.5 in section 5.2.1). Thus, contrary to the NaF PDT, the sequential NaF+RbF does not increase the performance of the CIGS solar cell by influence of the doping.

Concerning the high-temperature absorbers H1 and H2, their doping concentrations are unfortunately not available. It is thus not known if the application of the RbF PDT leads to a doping increase or decrease in the high-temperature absorbers. However, even in the event of an increase in doping, it is unlikely that this doping change alone can account for the measured increase in $\Delta\mu$ between both absorbers. The reason being, as mentioned above, that to date all reported increases in hole carrier concentration following the RbF PDT are insufficient to explain the reported measured increases in V_OC in literature (see also Table A.2 in appendix A.5).

For both low-temperature absorbers L1 and L2 and high-temperature absorbers H1 and H2, a reduction in electrostatic potential fluctuations was measured following the application of the RbF PDT in section 6.2. In the hypothetical case of an increase in doping from absorber H2 to H1, the reduction of electrostatic potential fluctuations can easily be explained in the same vein as done in the previous section 7.2.1: either a reduction of donors N_D, an increase in acceptors N_A, or both, leads to a reduced degree of compensation $N_\mathrm{D}/N_\mathrm{A}$. In the case of a decrease in doping, as is measured from sample L2 to L1, the degree of compensation $N_\mathrm{D}/N_\mathrm{A}$ can also be reduced but only if both donors N_D and acceptors N_A are reduced with the donor reduction being slightly larger.

While both an increase and a decrease in p-type doping can lead to the reduction of electrostatic potential fluctuations measured in this thesis, the doping effect is not able to explain the measured differences in $\Delta\mu$ between the absorbers following the application of the RbF PDT. The increase in $\Delta\mu$ must thus be due to a reduction of non-radiative recombination. A possible explanation can be found in the segregation preference of the Rb atoms. While it has been argued in the previous section 7.2.1 that Na does not influence the surface of the absorber, the same cannot be said for Rb. In literature, the formation of the $RbInSe_2$ compound at the CIGS surface has been advocated [140], [141], [153], [156], [159] with a possible consequence being the reduction of harmful recombination at the CdS/CIGS interface. The $\Delta\mu$ measurements on bare CIGS absorbers in section 5.2 of this thesis revealed an improved absorber surface (which

could lead to an improved CdS/CIGS interface), agreeing thus with the results and suggestions from literature. However, the same measurements also reveal an improvement of the CIGS bulk. Similar to its segregation at the surface, Rb is known to segregate primarily at the grain boundaries [153]–[155], [157]. The agglomeration at the grain boundaries indicates that the beneficial Rb-induced bulk effect acts there. As mentioned above, some studies in literature suggest that the Rb leads to a reduced recombination at the grain boundaries [153], [157]. In the following, in combination with the results presented in this thesis, the suggested explanation for the bulk effect is expanded.

The electrostatic potential fluctuations are reduced following the application of the RbF PDT. This reduction can be due to a reduced degree of compensation and/or a reduced band bending at the grain boundaries. A reduced band bending can lead to an increase in $\Delta\mu$ via two ways:

- A reduction of the driving forces of the charge carriers towards the grain boundaries which ultimately leads to reduced non-radiative recombination.
- A reduction of band tails i.e. a decrease of the Urbach energy. As was discussed in section 7.1.1, smaller band tails could lead to reduced non-radiative recombination.

Finally, based on the reports from literature and the results of this thesis, here it is suggested that the RbF affects the CIGS absorber through both a surface and a bulk effect. The surface effect manifests itself as a reduction of harmful recombination at the CdS/CIGS interface. The injection of Rb into the bulk of the CIGS leads to a change in doping as well as its segregation at the grain boundaries. While the former effect may lead to an increase in the quasi-Fermi level splitting (in the case of an increase in p-type doping, which is not always observed), the latter leads to a decrease in non-radiative recombination, either through fewer carriers recombining at the grain boundaries or through a reduction of band tails.

7.2.3 Summary

Based on the measurements on state-of-the-art CIGS absorbers in this thesis and reports from literature, a tentative suggestion concerning the influence of the alkali PDT on the CIGS absorbers can be made.

The introduction of sodium into the absorber leads to an increase in the hole carrier concentration and can thus be classified as a bulk effect. The increased hole carrier concentration leads to an increase of the quasi-Fermi level splitting in the absorbers and ultimately an increase in the open-circuit voltage in the finished solar cell device. Furthermore, Na also leads to a confirmed reduction of electrostatic potential fluctuations through a re-organization of charged impurities. However, the influence of the latter, reflected in the slight reduction in Urbach energy that accompanies the injection of Na, is weak compared to the beneficial effect of the doping increase.

The injection of the rubidium alkali atoms into the absorber either leads to a decrease (measured in the low-temperature absorbers in this thesis) or an increase (reported primarily in literature) in the hole carrier concentration. The change in doping, even in the case of an increase, cannot explain the observed overall increase in $\Delta\mu$ that follows the application of the RbF PDT. Hence, Rb also influences both the CdS/CIGS interface and the grain boundaries since it strongly segregates there, leading in both cases to reduced non-radiative recombination. At the grain boundaries, the reduction of harmful carrier recombination is achieved through a reduced band bending and thus a reduced driving force towards the grain boundaries. Alternatively, or simultaneously, the reduction of the bend bending leads to a reduction of the band tails and thus reduced non-radiative recombination of charge carriers through these tails.

7.3 Voltage losses in Cu(In,Ga)Se$_2$: open questions

While the results presented in this thesis provide new insights into the underlying mechanisms of the alkali PDT on state-of-the-art CIGS absorbers, some open questions still remain. In section 7.1.3, it was shown that the voltage losses in CIGS are very similar to the ones in c-Si. However, both technologies show a significantly worse voltage output than GaAs. Thus, in order to improve the quasi-Fermi level splitting, and ultimately the open-circuit voltage, the exact origins of the voltage losses need to be identified and remedied.

This section here does not aim to answer any questions but rather aims to briefly compile prominent remaining origins of the voltage deficit that are discussed by the community. As such, the section is heavily based on reports from literature.

7.3.1 Potential fluctuations

Potential fluctuations, whether through fluctuations in the band gap energy or through fluctuations in the electrostatic potential, lead to sub band gap states that effectively reduce the band gap energy. A reduction of the band gap energy, even in the case of purely radiative charge carrier recombination, leads to a decrease in the quasi-Fermi level splitting $\Delta\mu$ and consequently in the open-circuit voltage V_{OC}. More specifically, it can be shown that average band gap fluctuations of 100 meV (assuming a Gaussian distribution and this value to be the standard deviation of the distribution) can already lead to radiative V_{OC} losses of approximately 160 mV [106]. However, in section 7.1.3, it was shown that state-of-the-art CIGS solar cells only exhibit radiative voltage losses $\Delta V_{\mathrm{OC}}^{\mathrm{rad}}$ of 20 - 30 mV.

The measured $\Delta V_{\mathrm{OC}}^{\mathrm{rad}}$ losses can be used to gauge the amplitude of the potential fluctuations. Assuming the potential fluctuations to lead to an effective decrease in the band gap energy through radiative recombination only, their impact on the radiative open-circuit voltage $V_{\mathrm{OC}}^{\mathrm{rad}}$ can be expressed as [106], [231]

$$V_{\mathrm{OC}}^{\mathrm{rad}} = V_{\mathrm{OC}}^{\mathrm{SQ}} - \frac{\sigma_{\mathrm{g}}^2}{2qk_{\mathrm{B}}T}. \tag{7.10}$$

Here σ_{g} describes the average potential fluctuation amplitude assuming a Gaussian distribution [106][3]. By recognizing that $V_{\mathrm{OC}}^{\mathrm{SQ}} - V_{\mathrm{OC}}^{\mathrm{rad}} = \Delta V_{\mathrm{OC}}^{\mathrm{rad}}$ and rearranging, one arrives at

$$\sigma_{\mathrm{g}} = \sqrt{2qk_{\mathrm{B}}T\,\Delta V_{\mathrm{OC}}^{\mathrm{rad}}}. \tag{7.11}$$

Thus, for radiative voltage losses of 20 - 30 mV, the average potential fluctuations amount to 32 - 39 meV. At this point, it is not possible to declare which contribution to the total potential fluctuations σ_{g} stems exactly from band gap and which one from electrostatic potential fluctuations.

In the previous section 7.2, it was argued that the alkali PDT leads to reduced degree of compensation which is experimentally measured through reduced electrostatic potential fluctuations at low temperatures. As was mentioned, one origin of electrostatic potential fluctuations are spatial fluctuations in the doping concentration. In this context, Krause *et al.* measured doping fluctuations between neighbouring CIGS grains that result in estimated V_{OC} losses of 17 mV [288]. Similarly, Nicolaeva *et al.* investigated lateral inhomogeneities of both acceptor densities in the absorber layer and donor densities in the buffer/window layer with corresponding estimated V_{OC} losses of below 25 mV [289]. However, in both these studies, it is unclear if

[3] It needs to be mentioned that the band tails of the samples in this thesis follow an Urbach-type behaviour rather than a Gaussian one. However, close to the band edges, both Urbach and Gaussian lead to states within the same order of magnitude. Hence, in a first approximation, eq. (7.10) can be used.

screening effects were taken into account. In fact, the influence of electrostatic potential fluctuations due to screening effects at room temperature is still heavily debated (see e.g. ref. [231] vs. ref. [246]) and no general consensus has been reached yet.

In the scenario where electrostatic potential fluctuations (other than the ones caused by band bending) are irrelevant at room temperature, the focus can be shifted onto band gap fluctuations and investigate whether there exist some studies that present concrete values for σ_g. Here it is important to remember the results from section 5.4 that revealed negligible variations in optoelectronic quantities on a micrometer scale. Thus, if there are band gap fluctuations, they have to be present on a sub-micrometer scale. A recent study by Abou-Ras *et al.* reveals only weak compositional variations on a length scale of 10 - 100 nm resulting in correspondingly weak band gap fluctuations that would only have a negligible effect on the V_{OC} [231]. On a slightly larger length scale, Avancini *et al.* reveal lateral variations in the GGI ratio in the absorber notch region of maximal 0.1 but confined to stretches of approxiamtely 100 nm [242]. These compositional variations translate into band gap fluctuations σ_g of approximately 12 meV, which, in turn, results in a small V_{OC} reduction of only 3 mV [242]. However, these estimations ignore the impact of compositional variations on the lattice strain. More specifically, changes in the gallium content of 1 % absolute can lead to an increase of band gap fluctuations of 6 meV due to the resulting deviations of the crystal from its perfect tetragonal structure [106]. Hence, in the case of GGI variations of 0.1, strain-induced band gap fluctuations of 60 meV can theoretically be expected [242]. These values are, albeit slightly larger, in good agreement to what is estimated through the radiative voltage loss ΔV_{OC}^{rad} above.

Finally, it can be concluded that potential fluctuations are still very much present in CIGS absorbers. However their detrimental effect on the radiative open-circuit voltage, as expressed through the low values of ΔV_{OC}^{rad} in Fig. 7.3, is only minor. So far, no studies exist that explore the effects of non-radiative recombination through the band tails. It is thus possible, as indicated by the correlation between voltage deficit and Urbach energies in Fig. 7.1, that band tails heavily engage in non-radiative recombination and hence limit the $\Delta\mu$ and V_{OC} in state-of-the-art CIGS solar cells.

7.3.2 Deep-level defects

The measurement of the photoluminescence emitted across a wide spectral range at low temperatures in section 6.1 did not reveal any deep-level defects in the samples investigated in this thesis. However, as was argued, this result does not claim that one can categorically deny the presence of any deep-level trap densities, however small, in CIGS absorbers. In fact, based on photoluminescence spectroscopy alone, it is extremely challenging to gauge threshold densities that are still detectable as, for recombination processes to occur, electron and hole capture cross-sections also play a role.

To visualize the impact of small deep-level trap densities on the V_{OC}, a very simple SCAPS simulation can be employed. For the following example, the simulation parameters listed in appendix F.3 can be used with the following modifications: no Urbach tails but a single acceptor defect situated 0.6 eV above the valence band and exhibiting electron and hole capture cross sections of 10^{13} cm^2. Increasing the trap density from $5 \cdot 10^{11}$ cm^{-3} to $5 \cdot 10^{12}$ cm^{-3} leads to a loss in V_{OC} of approximately 70 mV. While these values may not necessarily represent reality, they allow to gauge the detrimental nature of deep-level traps even at concentrations considerably lower than the doping crystal defect.

In literature, there exists experimental evidence of deep-level traps states in CIGS, even if the corresponding measurements were done on samples that may not necessarily represent the current state of the art [50]–[54], [244]. The lack of any deep-level trap induced PL signal in this thesis prevented their consideration concerning the influence of the alkali PDT in the previous

section 7.2. However, if the defect model introduced in section 2.2.2 is to be believed, a deep level defect in CIGS would be the double-charged Cu_{III} antisite [38]. In this case, the theoretical calculations by Malitckaya *et al.* deem its passivation through alkali elements unlikely [141].

Finally, it can be said that the results, both in this thesis and in literature, concerning deep-level defects in CIGS are not conclusive and considerable effort should be invested in the future to bring about a clearer picture.

7.3.3 Structural defects

As no material is ever perfect, structural defects are expected to also play a role in the CIGS absorbers. There are a multitude of structural defects, depending on their definition, such as line and planar defects [172], variations in bond lengths [291], interfaces, as well as voids [242]. Covering all these topics by far surpasses the framework of this thesis which is why special focus is given to only two distinct kinds of structural defects in the following: voids and grain boundaries. The reason being that both these defects are directly related to either the samples investigated in this thesis or the presumed influence of the alkali post-deposition treatment.

Voids are structural defects of which detailed information is very sparse. Recently, Avancini *et al.* published an in-depth study of void formation and their effect on solar cell performance in a sample that very closely resembles the low-temperature sample L1 investigated in this thesis [242]. The study reveals that voids are unavoidable by-products of the multi-stage co-evaporation process used for the fabrication for state-of-the-art CIGS solar cells. However, while voids are definitely present in the low-temperature CIGS absorbers, it is yet unclear if this also always applies to high-temperature CIGS absorbers. For the specific sample investigated in the study [242], the voids are measured to be approximately 100 nm in diameter and show a lateral appearance of 0.5 - 1 void/μm^2 beneath the CIGS surface. Assuming recombination velocities at their unpassivated surfaces of 10^4 cm/s, the V_{OC} deficit through non-radiative recombination is simulated to be approximately 30 meV [242].

Assuming the hypothesis that voids are unavoidable when growing CIGS absorbers via the multi-stage process [242] to be correct, one could imagine that a different deposition process would lead to void-less absorbers. One such alternative growing process is the two-step process where Cu-In-Ga precursors are sputtered onto a Mo-coated glass substrate and then subjected to a "sulfurization after selenization" step [292]. This growing process is employed by Solar Frontier and enabled fabrication of the former Cu(In,Ga)$(S,Se)_2$ champion device (C2 in Fig. 7.3). The potential lack of voids in the C2 device might explain the lower non-radiative voltage loss ΔV_{OC}^{nrad} of 114 mV compared to the loss of 138 mV seen in the Cu(In,Ga)Se_2 (C1) champion device in Fig. 7.3. The difference of 24 mV between both devices agrees reasonably well with the simulated void-induced V_{OC} loss [242] mentioned above. However, this assumption is only valid if voids are indeed present in the high-temperature C1 device and absent in the C2 device, which is not known.

The topic of planar defects, such as grain boundaries, is very highly debated in the CIGS community. While some groups claim that grain boundaries are beneficial for charge carrier collection and thus would lead to an increase in j_{SC} (see e.g. [227]), other groups rightfully identify grain boundaries as harmful recombination centers that reduce the V_{OC} (see e.g. [172]). Recently, more and more groups publish high-quality studies on CIGS devices with efficiencies beyond 20 % and revolving around the topic of grain boundaries [153], [155], [231]. A central theme in most GB-centred publications is the passivation of defects at the grain boundaries following the injection of heavy alkali elements. However, this interpretation is still open to debate. What is certain, however, is that grain boundaries still exhibit recombination velocities

of around $5 \cdot 10^3$ cm/s, even in the best devices [288]. Consequently, one might think that a GB-free CIGS absorber layer allows the extraction of larger voltages due to lower detrimental recombination at planar defects. This thought is especially valid when considering that published device simulations predict an increase of approximately 100 mV in GB-free CIGS devices [172], [293], [294]. While polycrystalline CIGS absorber have always been the better performers, a very recent breakthrough enabled the formation of a 20 % efficient mono-crystalline CIGS solar cell device [295]. However, while this device has been treated with a sequential NaF + KF PDT, the growth process is far from optimized, as is evident from the large gallium concentration and the lack of a double band gap grading. Nonetheless, having highly-efficient mono-crystalline CIGS absorbers as a pendant to poly-crystalline ones is ideal to tackle some of the remaining open questions, such as the exact influence of GBs, that revolve around voltage losses in CIGS.

Finally, it can be concluded that structural defects still play a major role in state-of-the-art CIGS solar cells. With the difference in non-radiative voltage loss between the best CIGS and GaAs devices being around 80 mV (cf. Fig. 7.3), it appears that one possible solution to bridge this gap is to minimize the amount of grain boundaries.

7.3.4 Lack of photon recycling

In section 7.1.2 and appendix F.5, the relationship between external and internal radiative efficiency was discussed. Since the external radiative efficiency η_{ext} is linked to the non-radiative voltage losses through fundamental thermodynamic concepts [76], [264], even in the case of 100 % internal radiative efficiency η_{int}, the extracted V_{OC} is reduced when the photon out-coupling is poor. This is specifically the case in CIGS where the probability of photon out-coupling can be estimated to be 2.1 %. A simple estimation via eq. (7.4) thus predicts a V_{OC} loss of 100 mV even in the case of 100 % internal radiative efficiency i.e. no non-radiative recombination.

So far, photon recycling in CIGS has not gathered much attention since a certain η_{int} is necessary for photon out-coupling optimization schemes to become beneficial. This threshold is estimated to be at approximately 40 % internal radiative efficiency according to Kirchartz *et al.* [79], [296] (albeit this threshold value was calculated for metal-halide perovskites and may thus be different for CIGS).

In the case of CIGS, assuming an external radiative efficiency of 1 % (valid assumption for the best CIGS-related devices - see Fig. 7.2), the internal radiative efficiency is estimated to amount to an impressive 47 %. This is a value where increasing the probability of photon exiting the device may already return improvements in the V_{OC}. As was identified in appendix F.5, the main reasons for the poor photon out-coupling in CIGS are the high parasitic absorption in the Mo back contact and the low re-absorption due to the narrow band gap minimum. Research to identify and implement suitable back reflector layers, that would reduce the parasitic absorption, is currently under way [61]. Similarly, research on methods to reliably implement a wider gallium notch are also under way (see e.g. refs. [28], [297]), however, one might argue that photon re-absorption necessitates a complete paradigm shift away from the double band gap grading that is currently integral to the state-of-the-art CIGS devices.

Thus, it can be concluded that photon recycling is not yet the most pressing issue but, with ever decreasing non-radiative recombination, it will be a major performance bottleneck in the future.

8 Summary

The general aim of this thesis was to investigate the influence of the alkali post-deposition treatment (PDT) on the voltage losses in state-of-the-art Cu(In,Ga)Se_2 solar cells. To that end, in the framework of the European Commission's Sharc25 project, CIGS absorbers, having undergone different alkali PDTs, were provided. Two main sample sets were primarily investigated. The first sample set consisted of absorbers grown on an alkali-free substrate at low temperatures with a NaF solitary PDT, a sequential NaF+RbF PDT and no PDT at all. The second sample set consisted of absorbers grown on an alkali-containing substrate at high temperatures with a solitary RbF PDT and no PDT at all. The voltage losses were investigated through photoluminescence spectroscopy experiments that enabled the determination of selected optoelectronic quantities such as the quasi-Fermi level splitting, the absorption coefficient, electronic defects, and potential fluctuations. Furthermore, the voltage losses in state-of-the-art CIGS solar cells were to be compared to the dominating PV technologies c-Si (in terms of market) and GaAs (in terms of performance). The insights that could be gained from the results of this thesis are described in the following.

Conducting PL measurements on state-of-the-art Cu-poor CIGS absorbers at room temperature should yield a single broad spectral peak that describes the band-to-band transition. However, for the absorbers investigated in this thesis, a distorted PL spectrum is recorded. The distortion is manifested by the occurrence of a multiple-peak or shoulder structure that is due to interference fringes. Since the interference-induced spectral distortion limits the information that can be gained from PL measurements, a method had to be found to suppress the interference fringes. To do so, in a first the step, possible origins of these interference effects were investigated.

An important feature of state-of-the-art CIGS absorbers is the presence of a compositional double gallium gradient inducing a double-graded band gap structure. By performing PL measurements on exfoliated absorbers under different configurations in this thesis, it was found that the band-to-band transition is emitted solely from the band gap minimum inside the bulk of the absorber. The emitted photons from the band gap minimum carry thus a low energy and are only weakly re-absorbed on their way through the absorber. This weak re-absorption is one of the main reasons for the possible occurrence of interference effects in state-of-the-art CIGS absorbers. Other reasons suggested by literature reports, such as a smooth surface and an adequate film thickness, have also been confirmed through measurements in this thesis.

In the framework of this thesis, an experimental method to remove the interference fringes from the measured PL spectra at room temperature was developed. The method revolves around measuring the PL for different sample-tilting angles (i.e. by rotating the absorber around its own axis and keeping the detector fixed). In this so-called angle-resolved photoluminescence (ARPL) configuration, the emitted photons, exhibiting different phases, are collected. Since a shift in phase leads to a shift of the interference fringes, summing and averaging over the angle-resolved spectra removes the interference fringes from the spectra. Comparing the newly interference-free spectra to the interference-riddled spectra revealed that the high-energy slope of the PL spectra is not affected by the interference fringes. While it is possible to remove the interference fringes from the PL spectra at room temperature, the geometrical limitations of the experimental setup (i.e. the cryostat) do not allow for ARPL to be employed at

low temperatures. Hence, another method to remove the interference fringes had to be found. In the framework of this thesis, the deposition of an auxiliary scattering layer onto the absorber surface was conceptualized. The layer consists of polystyrene (PS) beads of approximately one micrometer diameter and can be deposited at room temperature and under atmospheric conditions. Various photoluminescence measurements under different configurations were carried out on PS-covered CIGS absorbers and confirmed its effectiveness at removing interference fringes at both room and low temperatures.

With the origin and influences of the interference fringes figured out, the attention could be turned to the actual characterization of the CIGS absorbers. To analyse the voltage losses in the absorbers, the quasi-Fermi level splitting $\Delta\mu$ is determined from PL measurements at room temperature. $\Delta\mu$ describes the electrochemical energy that is transferred from the photon to the electron following absorption and represents an upper limit for the open-circuit voltage V_{OC} that can be extracted from the finished solar cell device. To determine a $\Delta\mu$ that can be compared to the V_{OC}, the PL has to be measured under AM1.5 conditions and the measured spectrum needs to be calibrated for absolute photon flux densities. In this thesis, it was shown that $\Delta\mu$ can reliably be extracted from the high-energy slope of the PL spectrum (not affected by interference fringes) in state-of-the-art CIGS absorbers when measured under appropriate conditions.

In this thesis, the $\Delta\mu$ is measured on bare and CdS-covered CIGS absorbers that received different alkali PDTs. In the CdS-covered absorbers, an increase in the $\Delta\mu$ was measured for the absorbers that were treated with an alkali PDT compared to the ones that were not. While this increase, generally identified as a consequence of reduced non-radiative recombination, could already be measured in absorbers that received a solitary NaF PDT, the increase in $\Delta\mu$ was larger when heavier alkali atoms (i.e. Rb) were involved. The increase in $\Delta\mu$ in the CdS-covered absorbers mirrors the measured increase in V_{OC} in the solar cell devices indicating that the beneficial effect of the PDT is already present in the absorber, independent of the window layer. Prior to the measurements in this thesis, the community was of the common opinion that the effect of the alkali PDT is mainly a reduced recombination at the CdS/CIGS interface. In this thesis, however, it could be shown that the alkali PDT already improves the optoelectronic quality of the bare absorbers. Hence, the alkali atoms improve the CIGS bulk and its surface via a reduction of non-radiative recombination before any CdS deposition. This new insight shifted the action of the alkali PDT from a strongly predominant surface effect to a combined bulk and surface effect.

To investigate possible reasons for the reduction of non-radiative recombination following the application of the alkali PDT, local inhomogeneities on the microscopic scale, deep-level defects, electrostatic potential fluctuations, and band tails were investigated.

Local inhomogeneities, caused e.g. by alloy disorder or locally varying defect distributions, were accessed by measuring the PL in an experimental setup that allows for spatially-resolved scans with micrometer resolution. The measurements on the state-of-the-art CIGS absorbers in this thesis did not reveal any significant inhomogeneities on the microscopic scale, independent of the applied alkali PDT or lack thereof.

Deep-level trap states within the band gap can act as non-radiative recombination centers that limit the $\Delta\mu$ of the absorber. By measuring the PL spectra at low temperatures (10 K), the radiative recombination rate is increased, improving thus the probability that the deep defects are optically detected. The measured PL spectra of the CIGS absorbers in this thesis did not reveal the presence of deep-level defects, irrespective of the applied alkali PDT. However, this does not necessarily mean that the presence of deep-level defects in state-of-the-art CIGS absorbers can be categorically denied, only that they are potentially present only at low concentrations.

Electrostatic potential fluctuations are an intrinsic feature in Cu-poor CIGS absorbers and arise from inter- and intragrain fluctuations of charged impurities as well as from the band bending at the grain boundaries. They are measured at low temperatures where they influence the defect transitions through spectral broadening and significantly alter the transitions' response to changes in temperature and excitation flux density. The investigation of electrostatic potential fluctuations was only made possible after the removal of interference fringes via the PS scattering layer that was conceptualized in the framework of this thesis. The qualitative comparison of the PL spectra between the different absorbers in this thesis revealed a reduction of electrostatic potential fluctuations in absorbers that underwent an alkali PDT treatment. In addition, the reduction of the electrostatic potential fluctuations appears to be stronger when heavier alkalis are involved.

Band tails are harmful sub band gap states that can originate from both band gap and electrostatic potential fluctuations. The tail states are accessed through the determination of the absorption coefficient $\alpha(E)$ from the low-energy slope of the measured PL spectra at room temperature. The determination of $\alpha(E)$ thus also necessitated an interference-free spectrum. The state-of-the-art CIGS absorbers all exhibit band tails that are of Urbach type i.e. extend exponentially into the band gap. A closer investigation revealed that the "strength" of the band tails, expressed through the Urbach energy E_U, is reduced in absorbers that received an alkali PDT. In addition, the reduction is stronger whenever Rb is present compared to Na only. These results confirm the occurrence of a bulk improvement after PDT and suggest that the beneficial bulk effect dominates over the beneficial surface effect. Comparing the $\Delta\mu$ deficit (i.e. the difference between band gap energy and $\Delta\mu$) to E_U revealed an empirical correlation between both. This correlation suggests that the measured increase in $\Delta\mu$ following the application of the alkali PDT is due to a reduction of the band tails.

By considering not only the $\Delta\mu$ of the absorbers but also the V_{OC} of the corresponding solar cells, the correlation between V_{OC} deficit (e.g. $E_g - qV_{OC}$) and E_U could be extended to also include data from literature. Using GaAs, which shows the lowest E_U and V_{OC} deficit among all photovoltaic technologies, as a reference, it was shown that radiative recombination through tail states leads to voltage losses that are much too small to explain the measured V_{OC} deficit with increasing Urbach energies. Attempts to simulate the voltage losses by considering non-radiative recombination through the tail states remained inconclusive. Hence, it is still possible that the band tails are the main culprit of the voltage limitations in state-of-the-art CIGS solar cells by promoting non-radiative recombination.

Finally, to see how the state-of-the-art CIGS solar cells (and current champion devices from literature) compare to the leading PV technologies c-Si and GaAs, the voltage losses were extracted and quantified from their external quantum efficiency. Both in terms of the radiative voltage loss (mainly due to recombination through tail states) and in terms of the non-radiative voltage loss, the best CIGS solar cells behave very similarly to the champion c-Si device. These results were consolidated by the determination of the external radiative efficiency from PL measurements on the CIGS absorbers. It was thus concluded that while the best CIGS and c-Si devices exhibit very similar voltage losses, GaAs shows significantly smaller voltage losses.

Based on the insights gained in this thesis and numerous studies published in literature, a explanation for the influence of the alkali PDT in state-of-the art CIGS absorbers was tentatively suggested. This explanation attributes the influence of the NaF (or sodium originating from an alkali-containing substrate) predominantly to an increase in the hole carrier concentration and thus a bulk effect. An increase in the hole carrier concentration, without any other changes, leads to an increase in quasi-Fermi level splitting in the absorber and thus ultimately to an increase in the open-circuit voltage in the solar cell.

The beneficial effect of the heavier RbF PDT can only partly be explained by a change in doping (and only if an increase in the hole carrier concentration is observed, which is not necessarily always the case). Thus, as a consequence of the segregation of the Rb atoms at the CIGS surface and grain boundaries, the non-radiative recombination at these structural defects is reduced. At the grain boundaries, this could be achieved either through a reduction in band bending, decreasing thus the driving force towards the grain boundaries, or through a reduction in band tails over which the carriers can recombine non-radiatively.

9 Outlook

The results of this thesis are able to paint a clearer picture of the influence of the alkali elements on the recombination processes and voltage losses in state-of-the-art CIGS solar cells. However, some open questions regarding the results remain and possible approaches on how to tackle them are briefly discussed in the following. A brief discussion about remaining open questions was already provided in section 7.3 and shall not be repeated here.

One of the main results of this thesis is the insight that the alkali elements do not only improve the CIGS surface but also the bulk. While the influence of the alkali elements on the band tails suggests that the alkali improvement is predominantly occurring in the bulk, the results do not disclose how much the surface is improved. To that end, an experiment can be designed that revolves about the preparation of fresh bare CIGS absorbers having undergone different PDTs (i.e. just like the low-temperature absorbers in this thesis). Immediately after preparation, these absorbers are to be measured via photoluminescence to determine their quasi-Fermi level splitting or external radiative efficiency. Then the absorbers are to be subjected to an etching step where the surface layers are removed. After the etching step, the photoluminescence measurements are to be repeated and the results compared to the ones prior to the etching step. Depending on whether the emitted photon flux density decreases (and by how much) or remains constant, the effect of the alkali elements can be more accurately allocated to either the surface or the bulk of the absorber. Design preparations for this new experiment are under way at the time of writing.

Another main result of this thesis is the reduction of band tails with heavier alkali PDT. Comparing the reduction of the band tails to the reduced quasi-Fermi level splitting and open-circuit voltage deficit (i.e. $E_g - \Delta\mu$ and $E_g - qV_{OC}$) revealed a correlation that suggests that the reduced band tails are responsible for the lower voltage losses after alkali PDT. While it has been shown that the calculated voltage losses in case of radiative recombination are too small compared to the measured voltage losses, 1D SCAPS simulations considering non-radiative recombination remained inconclusive. It is thus important to resolve the issue with the simulation and understand exactly how band tails influence non-radiative recombination.

Due to the comparison between state-of-the-art CIGS solar cells and c-Si as well as GaAs, it was possible to update the standing of CIGS relative to the leading PV technologies. This was done by extracting the various voltage losses from the external quantum efficiency spectra of the solar cells. While it could be shown that the best CIGS devices show similar radiative and non-radiative voltage losses as c-Si, no clear differences in the radiative losses between the samples in this thesis were seen. To investigate the radiative voltage losses between the different CIGS absorbers in general (and to keep the analysis to the absorbers themselves and not revert to a full solar cell structure), a method similar to the one presented in ref. [278] could be applied where the absorptivity $a(E)$ of the absorbers is used instead of the EQE.

Even though the answering of a single question sometimes raises a thousand more, the insights that could be achieved in this thesis can be used to understand, and improve, the voltage loss in CIGS solar cells.

A Appendix of Chapter 2

A.1 The solar spectrum

As already mentioned in section 2.3.2, the solar cell power conversion efficiency depends on the illumination power. Operating solar cells are obviously using the sunlight as radiation source to create electricity. However, on Earth, the amount of sunlight depends on various external factors such as time of day or geographical position, which is why a certain standard irradiance spectrum has been introduced for solar cell testing [298]. This standard spectrum is known under the label "AM1.5 spectrum" where "AM" stands for air mass and the number 1.5 represents the path length of the sunlight through the atmosphere of the Earth. More specifically, the air mass is defined as $1/\cos(z)$ where z represents the angle between the position of the Sun in the sky and the zenith. An air mass value of 1.5 is reached for an angle z of 48.2°. These specific conditions were chosen after careful analysis of sunny sites in the United States by the National Renewable Energy Laboratory (NREL) and have shown to be a reasonable representation for illumination conditions on a clear day at mid geographical latitude. A complete list of atmospheric conditions can be found in ref. [299].

The AM1.5 irradiance spectrum is shown as the blue curve in Fig. A.1. Integrating over the whole spectrum yields the irradiance or power density of $1000\,\mathrm{W/m^2}$. It is this quantity that is inserted as P_{in} in eq. (2.15). The red curve in Fig. A.1 shows the AM0 spectrum i.e. the solar irradiance spectrum outside the Earth's atmosphere. The difference between both spectra is due to scattering and absorption processes of the solar radiation in the atmosphere.

The solar spectrum can be approximated by using some theoretical concepts. Assuming that the Sun behaves like a black body, its emitting spectral radiance can be described by Planck's law of radiation [167]

$$B(\lambda, T) = \frac{2hc^2}{\lambda^5} \frac{1}{\exp\left(\frac{hc}{\lambda k_{\mathrm{B}} T}\right) - 1}, \tag{A.1}$$

where h is Planck's constant and c is the velocity of light. The spectral radiance in the form of eq. (A.1) is in units of power (W) per unit area ($\mathrm{m^2}$) per unit solid angle (sr) and per unit wavelength (m). To calculate the spectral irradiance received from the Sun as shown in Fig. A.1, a suitable temperature and appropriate solid angle have to be selected. Most of the Sun's radiation is emitted from the photosphere (i.e. the visible region of the Sun). According to ref. [300], the effective temperature of the photosphere amounts to $T = 5772\,\mathrm{K}$. While the Sun emits radiation into the whole space, i.e. a solid angle of 4π, only a fraction is emitted into the solid angle that arrives at the Earth. The half angle θ_{s} under which the Sun can be seen from the Earth can be estimated from simple geometrics. Using $149.6 \cdot 10^9\,\mathrm{m}$ as the distance between Earth and Sun [300] and $6.957 \cdot 10^8\,\mathrm{m}$ as Sun radius [301], the half angle θ_{s} amounts to approx. 0.27°.

With the above considerations in mind, the solid angle into which the Sun emits its radiance can be calculated to be $6.79 \cdot 10^{-5}\,\mathrm{sr}$ [20] and hence, the spectral irradiance from the Sun impinging on the Earth Λ is:

$$\Lambda(\lambda) = B(\lambda, 5772\,\mathrm{K}) \cdot 6.79 \cdot 10^{-5}\,\mathrm{sr}. \tag{A.2}$$

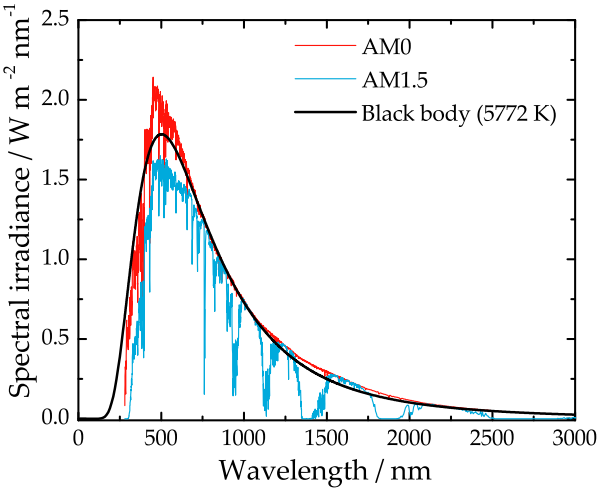

FIGURE A.1: Graph depicting the solar spectra AM0 (red curve) and AM1.5 (blue curve) as provided from the NREL [299]. The black curve shows the spectral irradiance as calculated based on Planck's law of radiation in eq. (A.2).

The black curve in Fig. A.1 shows the spectral irradiance Λ as calculated from the expression (A.2) for the spectral range in question. Despite minor discrepancies, the AM0 spectrum can reasonably well be approximated by the black body radiation taking into account the appropriate temperature and angles. The discrepancies could be explained by the varying inhomogeneities of the photosphere (see e.g. ref. [302]).

A.2 Optical and collection losses

As already briefly introduced in section 2.3.2, the optical and collection losses can be analysed by external quantum efficiency (EQE) measurements. In this context, Fig. A.2 shows the EQE spectrum of a real CIGS solar cell device. If the solar cell were an ideal device, i.e. if photon absorption and charge carrier collection were ideal, the EQE would be a rectangular unity function (black curve). However, due to losses, the real EQE (red curve) looks considerably different. Upon illumination, in a first instance, the EQE is reduced due to grid shading i.e. the metallic grid on the surface of the solar cell reflects the incoming light such that it cannot get absorbed by the cell (Fig. A.2 **a)**). In a second instance, all the light that is not reflected by the metallic grid, will then be partially reflected by the window layer (Fig. A.2 **b)**). With a bandgap energy of roughly 3.3 eV [74], the ZnO window layer also represents a parasitic absorption medium for the incoming light, reducing the photon flux that can ultimately reach the CIGS absorber even further. But not only the photons with energies above the ZnO band gap energy get absorbed, a small fraction of lower energy photons can also get absorbed in the window layer due to free carrier absorption (Fig. A.2 **c)**). Beyond the window layer, the incoming photons are also absorbed in the buffer layer. With a band gap energy of 2.4 eV, the CdS layer represents another major parasitic absorption medium (Fig. A.2 **d)**). Upon reaching the absorber, the higher energy photons are generally all absorbed while photons with energies close to the CIGS band gap energy can also be transmitted (Fig. A.2 **e)**). In addition to non-absorption in the absorber layer, it is also possible for the excited charge carriers to not be collected by the electrical contacts. Depending on the quality of the CIGS absorber, the collection length that is defined as the sum of the SCR width and diffusion length may prove to be smaller than the absorber thickness, leading to collection losses. Finally, due to states within the band gap, even photons with lower energies than the band gap energy may get absorbed (Fig. A.2 **f)**). This sub band gap absorption technically does not represent a loss in terms of j_{SC} but, as will be shown in appendix F.2, represents a clear limitation for the V_{OC}.

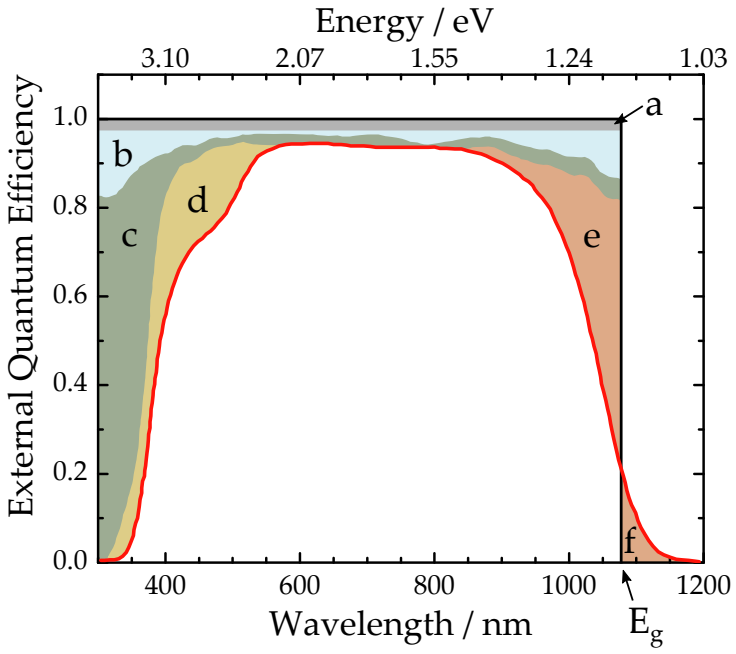

FIGURE A.2: External quantum efficiency spectrum of a real CIGS based solar cell device (red curve). The black rectangle represents the EQE of an ideal device with band gap energy E_g. The different optical and collection losses are visualised by colors, matching the colors of the different solar cell layers as shown in Fig. 2.8, and can be categorised as follows: **a)** grid shading, **b)** surface reflection, **c)** parasitic absorption in the window layer, **d)** parasitic absorption in the buffer layer, **e)** incomplete absorption and collection in the absorber, **f)** sub band gap absorption. Figure adapted from [25], [303].

While several strategies to reduce optical and collection losses already exist and can be reviewed in ref. [80], they usually consist of using alternative materials for the window and buffer layer, along with changes in absorber doping, all of which are currently not optimized and consequently lead to lower solar cell performances. The EQE curve shown in Fig. A.2 is adapted from ref. [303] and shows the optical and collection losses of a 20.4 % efficient CIGS device. Table A.1 provides a quantification of the different loss mechanism for this specific solar cell. With a band gap energy of 1.15 eV, the j_{SC} in the SQ model amounts to 42.3 mA/cm^2 and with a total of 17.1 % optical and collection losses, only a j_{SC} of 35.1 mA/cm^2 can be extracted from the device. The loss percentage of around 17 % is in line with reported values from literature [304], making it a typical optical and collection loss that can be expected in state-of-the-art CIGS solar cells.

TABLE A.1: Quantified (in percent) optical and collection loss mechanisms for a 20.4 % efficiency CIGS solar cell according to ref. [303].

Loss mechanism	Percentage / %
Grid shading	- 3.1
ZnO surface reflection	- 2.1
Parasitic absorption in ZnO	- 4.1
Parasitic absorption in CdS	- 3.3
Incomplete absorption and collection in CIGS	- 5.2
Sub band gap absorption	+ 0.7

A.3 Electrical resistance losses

Compared to ideal solar cells where the excited electrons can be extracted from the bulk material to the contacts without losses, in real devices the charge carriers encounter electric resistances. As such, a real solar cell can be described by an electric circuit as visualized in Fig. A.3 with the inclusion of parasitic shunt R_{sh} and series R_S resistances. Consequently, the total current density j_{real} is not described by eq. (2.12) but by the more extensive expression

$$j_{real} = j_0 \left[\exp\left(\frac{q(V - jR_S)}{Ak_BT} \right) - 1 \right] + \frac{V - jR_S}{R_{sh}} - j_{ph}. \tag{A.3}$$

Here A describes the diode ideality factor and is introduced in section 2.5.3. The shunt resistances are mainly a consequence of current leakage across the pn junction while series resistances originate from the material bulk resistance as well as contact (grid) resistances. Both types of resistances reduce the fill factor FF according to [81]

$$FF = FF_0 \left(1 - \frac{R_S}{R_{sh}} \right) \tag{A.4}$$

where FF_0 represents the fill factor in the ideal case. From eq. (A.4) it is clear that one wishes for an overall low series resistance R_S and an overall high shunt resistance R_{sh} for high efficiency solar cells.

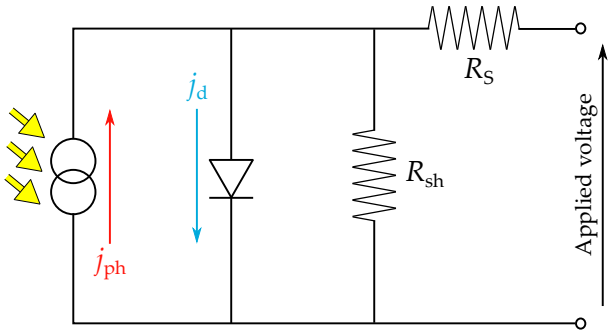

FIGURE A.3: Electrical circuit of a solar cell. Upon illumination, the solar cell generates a current density j_{ph} in the opposite direction as the diode current density j_d. The total current density j_{real} is attenuated due to the presence of parasitic shunt R_{sh} and series R_S resistances. Figure adapted from [81].

A.4 Alkali literature overview

In the following, a more refined literature overview, compared to the one in section 2.6.3, of alkali post-deposition effects on the doping concentration in CIGS is provided. This overview is given in the following and is divided into the impact of the various alkali PDTs reported in published studies.

Case of sodium

If sodium is introduced in the form of a post-deposition treatment into the CIGS absorber, it segregates at the grain boundaries (GB) while also diffusing into the grains [157]. In the case of the Na supply stemming from an alkali-containing substrate, Na exhibits the same diffusion behaviour as in the case of the PDT [118] but, due to the higher temperature during growth, it also participates in the interdiffusion of In and Ga [134]. While theoretical calculations based on DFT rule out the possibility of Na passivating defects at the GBs [287], the presence of Na inside the absorber clearly leads to an increase in p-type doping [130]. The p-type doping in Cu-poor CIGS is dictated by the indium-on-copper antisite defect In_{Cu} acting as a shallow donor and the copper vacancy V_{Cu} acting as an acceptor (cf. section 2.2.2). Due to the fact that

Cu-poor CIGS is clearly compensated (cf. section 6.2), the hole carrier density p_0 is given by the difference between the acceptor and donor densities $p_0 = N_A - N_D$. Thus, an increase in p_0 is either due to a decrease in the donor density N_D, an increase in N_A, or a combination of both. The influence of Na on these mechanisms is supported by theoretical calculations. In this context, Yuan *et al.* advocate for the formation of compensating sodium-on-copper antisites Na_{Cu} at elevated temperatures (e.g. during growth or during the PDT) followed by a rapid out-diffusion of Na leading to an overall increase of acceptors V_{Cu} [128]. By contrast, Wei *et al.* suggest the elimination of the In_{Cu} donors due to the favourable formation of electrically inactive Na_{Cu} point defects [127].

While measurements of the hole carrier densities and their direct impact on the measured solar cell parameters are sparsely available, Pianezzi *et al.* and Laemmle published useful data from their investigations of the NaF PDT on low-temperature [130] and high-temperature [131] absorbers, respectively. Their measured hole carrier densities and open-circuit voltage V_{OC} are shown in Table A.2 in appendix A.5. In the case of the low-temperature absorbers, the acceptor density rose by almost two orders of magnitude from $10^{14}\,cm^{-3}$ to $8 \cdot 10^{15}\,cm^{-3}$. The change in the open-circuit voltage ΔV_{OC} due to a change in doping can be estimated by [130]

$$\Delta V_{OC} = \frac{k_B T}{q} \ln\left(\frac{N_A^{\text{NaF PDT}}}{N_A^{\text{None}}}\right), \tag{A.5}$$

and equals $\Delta V_{OC} = 113\,mV$ in this case. This estimated increase agrees exceptionally well with the real measured increase of 116 mV from a V_{OC} of 561 mV before to a V_{OC} of 667 mV after NaF PDT [130]. Similarly, in the case of the high-temperature absorbers, the acceptor density rose from $4 \cdot 10^{14}\,cm^{-3}$ to $2.3 \cdot 10^{15}\,cm^{-3}$ after NaF PDT, indicating an estimated ΔV_{OC} increase of 45 mV. The measured increase in the open-circuit voltage equated 46 mV [131], again displaying an excellent agreement.

Case of potassium

Even though none of the samples presented in this thesis were treated with potassium, it is worth having a brief look at the data published in literature. The changes in doping and open-circuit voltage V_{OC} from solar cells grown on alkali-free substrates, extracted from three different studies [130], [139], [149], are shown in Table A.2 in appendix A.5. In all three cases, the injection of K into the absorber leads to an increase in the hole carrier concentration. As the reason for p-type conductivity, the compensation of donor-like defects is suggested [139]. In this specific case, to reduce the donor concentration, potassium must act as a K_{Cu} antisite. While Malitckaya *et al.* do not refute the possibility of the formation of K_{Cu}, they calculate a formation energy slightly above 1 eV which could render the formation unlikely [141]. By contrast, Yuan *et al.* argue that, in K-rich conditions, the formation energy is reduced, thus rendering the formation of K_{Cu} more likely [128].

Another explanation for the increase in p-type doping could be found in the formation of the $KInSe_2$ layer at the surface [39], [143] and the In-enrichment at the grain boundaries [137]. Both these effects would reduce the indium amount in the grains, thus potentially lowering the density of the In_{Cu} donors and consequently increasing the density of non-compensated acceptors V_{Cu}.

Regardless of its exact origin, the doping increase alone is not sufficient to explain the increase in V_{OC} that follows the injection of potassium alkalis. Thus, the potassium atoms must influence the absorber in other ways. An extensive review of literature results can be found in ref. [150].

Case of rubidium

Based on very sparse information currently available, the treatment of CIGS absorbers with RbF in the absence of other alkalis leads to an increase in p-type doping [157]. The formation of the compensating antisite defect Rb_{Cu} requires even higher energies than the previously-mentioned K_{Cu} defect [141] and is thus unlikely. However, the formation of the $RbInSe_2$ compound at the CdS/CIGS interface [159], as well as the In-enrichment at the GBs [152] could, as is the case for the KF PDT, explain a reduction in In_{Cu} and thus an overall increase in hole charge carriers.

In the absence of other alkalis, the RbF PDT leads to strong increase in the V_{OC} [157] that cannot be explained by the increased doping alone. Thus, both potassium and rubidium alkali atoms reduce the non-radiative recombination in CIGS solar cells not only through an increase in p-type doping but also through additional mechanisms.

Case of sodium and potassium

Sodium and potassium can be incorporated into the CIGS absorbers either via a sequential NaF + KF PDT applied to absorbers grown on alkali-free substrates, or via a KF PDT applied to absorbers grown on sodium-containing substrates. As was already mentioned in section 2.6.3, in the case where both sodium and potassium are present, the p-type doping is either increased or decreased. While an increase in p-type doping is generally observed (see ref. [150] for a list of studies reporting an increase in doping), a decrease is only reported by two groups. One of these groups is Sharc25 project partner Empa who specialise on the growth of low-temperature CIGS absorber on alkali-free substrates. In this case, the doping is measured through capacitance-voltage measurements [130]. The other group is from the National Renewable Energy Laboratory (NREL) who do not provide quantitative measurements of the doping concentration but only conclude on it based on surface-sensitive measurements on KF-treated CIGS absorbers grown on alkali-containing substrates [257], [305]. They report a decrease in the hole carrier concentration in the near-surface region, which is not necessarily indicative of the bulk doping concentration. Consequently, only Empa really measure a decrease in hole carrier concentration inside the CIGS absorber following the sequential NaF + KF PDT. Hence, it can deemed very likely that the decrease in hole carrier density is either due to the lack of alkali elements during absorber growth, the low temperatures used during the absorber growth itself, or a combination of both [114].

Table A.2 in appendix A.5 shows measured doping concentrations and V_{OC} in samples where the potassium alkali element is involved. The increase in V_{OC} that is observed following the sequential NaF + KF or the solitary KF PDT cannot be explained by the change in doping alone (not in the case of an increase in doping and especially not in the case of a decrease in doping). Thus, as was the case for the KF and RbF PDTs on alkali-free substrates, the heavier alkali elements provide additional benefits other than a change in p-type doping.

Case of sodium and rubidium

Table A.2 in appendix A.5 summarizes very recent literature results of the RbF PDT performed on CIGS grown on alkali-containing substrates. Except for the case of Heinemann *et al.* [161], the injection of Rb into the CIGS absorbers typically leads to an increase in p-type doping. However, the slight decrease in the hole carrier concentration reported in [161] can be explained by the extensive RbF doping study conducted in the same laboratory by Kodalle *et al.* [156]. The study clearly demonstrates that the doping decreases for short RbF PDT durations. Extending the RbF PDT to longer durations, in this case 10 minutes and beyond, leads to an increase in the hole carrier concentration. Given the fact that the exact duration of the

RbF PDT is not disclosed in the study by Heinemann *et al.*, and comparing the measured V_{OC} values before and after the PDT, it is likely that the RbF PDT duration was kept short which explains the decrease in p-type doping. The study by Kodalle *et al.* shows that the influence of the alkali elements is extremely sensitive to the conditions of the post-deposition treatment [156] and can be interpreted as an exclamation for the disclosure of the latter in order to clearly distinguish between the results of the numerous published studies.

Thus, it can be concluded that the sequential NaF + RbF PDT typically leads to an increase in doping. However, as is the case for the NaF + KF PDT, the low-temperature absorbers prepared by Empa seem to show an opposite reaction as they exhibit a reduced doping after treatment with heavy alkalis (cf. section 7.2.2). Consequently, it is very important to understand why the rubidium (as well as potassium) alkali element can influence the doping behaviour in different ways. A possible explanation can also be found in the study by Kodalle *et al.*, who show that small amounts of injected Rb lead to a doping decrease while larger amounts lead to a doping increase [156]. Upon introduction into the absorber, Rb diffuses along the grain boundaries, pushing the Na into the grains and onto the surface where it is washed away. Thus, while the concentration of Na inside the grains increases [154], its overall concentration inside the absorber decreases. This decrease of Na is larger the more Rb is present inside the absorber [156]. Hence, in the case of the absorber only containing sodium, the hole concentration is dictated by the concentration of V_{Cu} acceptors and In_{Cu} donors, some of which have been neutralized by the sodium via the formation of Na_{Cu}. Injecting a small amount of Rb neutralizes the doping increase set up during the sodium injection as a decrease in hole carrier concentration is observed. Upon increasing the amount of injected Rb atoms, this trend is reversed again as an increase in doping is observed. The exact mechanism of this doping change, whether through a reduction or increase of V_{Cu} or In_{Cu}, is not clear yet.

It is possible that the above explanation somehow relates to the fact why a decrease in doping is typically observed in the CIGS absorbers prepared by Empa. However, to uncover the exact mechanism requires further investigation and is not topic of this thesis.

A.5 Collection of doping changes in CIGS from literature

TABLE A.2: Open-circuit voltage V_{OC} and hole carrier concentration p_0 as published by various studies. The table is divided into 5 sections which are divided by a horizontal line. Each section describes the influence of a specific alkali element and follows the order laid out in the previous appendix A.4. Furthermore, each study represented in the table consists of a total of 3 lines, where the first line describes the optoelectronic quantities without the influence of the specific alkali PDT, the second line the impact of the specific alkali PDT, and the third line the real measured gain in V_{OC} (middle column) and the estimated gain in V_{OC} due to a change in doping (right-hand column).

Sample	V_{OC} / mV	p_0 / 10^{15} cm^{-3}
Alkali-free[a]	561	0.1
NaF[a]	677	8
Gain in V_{OC} in mV[a]	**116**	**113**
Alkali-free[b]	585	0.4
NaF[b]	631	2.3
Gain in V_{OC} in mV[b]	**46**	**45**
Alkali-free[a]	561	0.1
KF[a]	696	2
Gain in V_{OC} in mV[a]	**135**	**77**
Alkali-free[c]	533	1.16
KF[c]	644	2.04
Gain in V_{OC} in mV[c]	**111**	**15**
Alkali-free[d]	585	0.72
KF[d]	637	1.74
Gain in V_{OC} in mV[d]	**52**	**23**
Alkali-free[e]	473	0.1
RbF[e]	668	6.2
Gain in V_{OC} in mV[e]	**195**	**107**
NaF[a]	677	8
NaF + KF[a]	714	3
Gain in V_{OC} in mV[a]	**37**	**-25**
SLG[f]	581	3
SLG + KF[f]	694	6.3
Gain in V_{OC} in mV[f]	**113**	**19**
SLG[g]	652	7.7
SLG + KF[g]	720	19
Gain in V_{OC} in mV[g]	**68**	**23**
SLG[h]	666	1
SLG + RbF[h]	689	0.8
Gain in V_{OC} in mV[h]	**23**	**-6**
SLG[i]	667	6.5
SLG + RbF[i]	704	11.6
Gain in V_{OC} in mV[i]	**37**	**15**
SLG[j]	682	3.5
SLG + RbF[j]	717	6
Gain in V_{OC} in mV[j]	**35**	**14**

[a]ref. [130] [b]ref. [131] [c]ref. [139]
[d]ref. [149] [e]ref. [157] [f]ref. [146]
[g]ref. [147] [h]ref. [161] [i]ref. [54] [j]ref. [158]

B Appendix of Chapter 3

B.1 Sample structure and solar cells

In section 3.3, an overview of the different samples investigated in this thesis is given. This appendix complements that section by providing the sample structure as well as the measured solar cell parameters of each solar cell.

Fig. B.1 shows the typical geometry and allocation of 10 individual solar cells onto a single strip for the case of the high-temperature samples. The bare and CdS-covered sample strips have the same dimensions as the solar cell sample strip and are thus not explicitly visualized. The solar cell parameters measured on the **H1** and **H2** solar cells are presented in Table B.1.

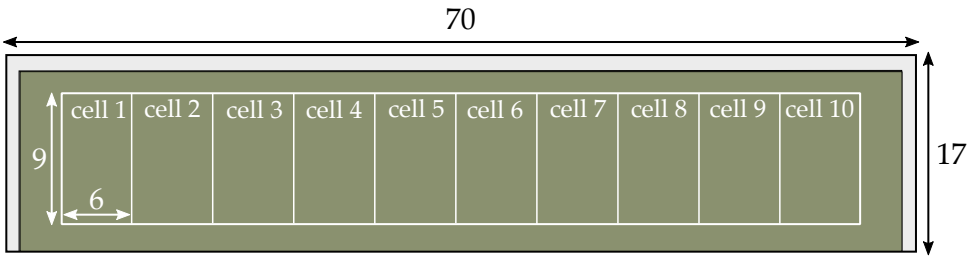

FIGURE B.1: Typical sample strip of the high-temperature samples **H1** and **H2** housing 10 individual solar cells. The indicated numbers represent the dimensions in units of mm.

Fig. B.2 shows the typical sample geometry of the low-temperature samples **L1**, **L2**, and **L3**. The upper half of the square sample strip is converted into 6 individual solar cells. One quarter of the sample strip was used for other purposes and so was not available for investigation. Of the remaining quarter, half is kept as bare absorber while the other half received a CdS layer. Table B.2 presents the corresponding measured solar cell parameters.

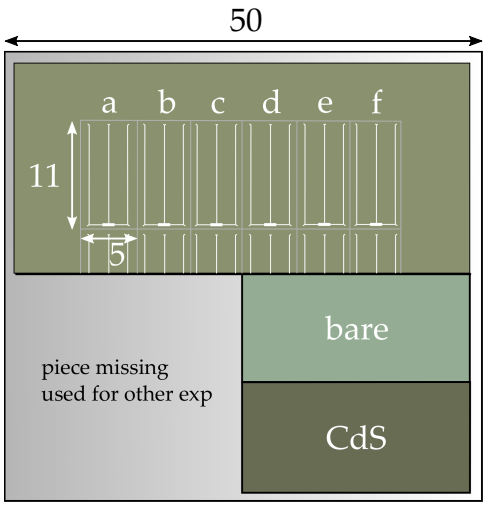

FIGURE B.2: Typical sample strip of the low-temperature samples **L1**, **L2**, and **L3**. The indicated numbers represent the dimensions in units of mm.

Fig. B.3 shows the typical sample geometry of the low-temperature samples **LN1**, **LN2**, and **LN3**. The upper half of the square sample strip is converted into 6 individual solar cells. The bottom half of the sample strip is divided into bare absorber and CdS-covered absorber. Table B.3 presents the measured electrical properties of the solar cells. Solar cells **a** of LN2 and **c** of LN3, for reason unknown, exhibit a very poor performance. It is assumed that something during the measurement went wrong. These solar cells are not considered when computing the average that is presented in Table 3.2 in section 3.3.

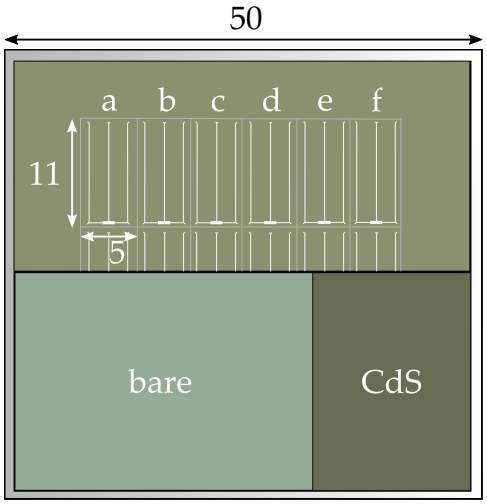

FIGURE B.3: Typical sample strip of the low-temperature samples **LN1**, **LN2**, and **LN3**. The indicated numbers represent the dimensions in units of mm.

TABLE B.1: Solar cell parameters of the high-temperature samples **H1** and **H2**. Sample H1 received a RbF PDT while sample H2 did not receive any PDT. Indicated are the short-circuit current density j_{SC}, the open-circuit voltage V_{OC}, the fill factor FF, and the power conversion efficiency η. All samples are without anti-reflective coating. The measurements of these parameters were done after growth by the project partner ZSW.

Sample	Solar cell	j_{SC} / mA cm^{-2}	V_{OC} / V	FF / %	η / %
H1	1	36.0	0.709	75.8	19.4
	2	36.1	0.713	78.4	20.2
	3	36.0	0.712	78.0	20.0
	4	36.1	0.712	78.3	20.1
	5	36.2	0.709	77.9	20.0
	6	36.3	0.708	78.1	20.1
	7	36.5	0.705	77.6	20.0
	8	36.6	0.703	77.1	19.8
	9	36.8	0.702	77.5	20.0
	10	37.0	0.699	77.5	20.0
H2	1	35.3	0.692	78.6	19.2
	2	35.2	0.690	77.7	18.9
	3	35.2	0.713	77.7	19.5
	4	35.2	0.687	76.9	18.6
	5	35.3	0.686	77.7	18.8
	6	35.6	0.687	78.1	19.1
	7	35.8	0.686	77.8	19.1
	8	36.0	0.685	77.6	19.1
	9	36.2	0.685	78.5	19.4
	10	36.6	0.684	78.1	19.5

TABLE B.2: Solar cell parameters of the low-temperature samples **L1**, **L2**, and **L3**. Sample L1 received a sequential NaF+RbF PDT, sample L2 received only a NaF PDT, and sample L3 received no PDT. Indicated are the short-circuit current density j_{SC}, the open-circuit voltage V_{OC}, the fill factor FF, and the power conversion efficiency η. All samples are without anti-reflective coating. The measurements of these parameters were done after growth by the project partner Empa.

Sample	Solar cell	j_{SC} / mA cm^{-2}	V_{OC} / V	FF / %	η / %
L1	a	33.0	0.705	77.2	18.0
	b	33.3	0.708	77.3	18.2
	c	33.3	0.708	76.5	18.1
	d	33.1	0.709	77.4	18.2
	e	32.9	0.709	77.8	18.2
	f	33.1	0.708	77.8	18.3
L2	a	31.7	0.684	77.7	16.9
	b	31.5	0.686	77.9	16.8
	c	31.0	0.686	78.1	16.6
	d	30.7	0.686	78.1	16.4
	e	30.4	0.685	78.2	16.3
	f	30.3	0.684	78.1	16.2
L3	a	31.7	0.577	72.2	13.2
	b	-	-	-	-
	c	31.4	0.581	72.3	13.2
	d	31.2	0.582	72.8	13.2
	e	31.3	0.583	73.3	13.4
	f	31.4	0.582	73.8	13.5

TABLE B.3: Solar cell parameters of the low-temperature samples **LN1**, **LN2**, and **LN3**. Sample LN1 received a sequential NaF+RbF PDT, sample LN2 received only a NaF PDT, and sample LN3 received no PDT. Indicated are the short-circuit current density j_{SC}, the open-circuit voltage V_{OC}, the fill factor FF, and the power conversion efficiency η. All samples are without anti-reflective coating. The measurements of these parameters were done after growth by the project partner Empa.

Sample	Solar cell	j_{SC} / mA cm^{-2}	V_{OC} / V	FF / %	η / %
LN1	a	33.0	0.703	76.9	17.8
	b	33.3	0.705	76.9	18.0
	c	32.8	0.706	76.4	17.7
	d	33.0	0.706	76.3	17.8
	e	32.6	0.705	77.9	17.9
	f	-	-	-	-
LN2	a	32.0	0.669	53.7	11.5
	b	32.2	0.691	75.5	16.8
	c	31.6	0.695	75.2	16.5
	d	31.8	0.692	75.8	16.7
	e	31.5	0.689	76.2	16.5
	f	31.8	0.678	74.9	16.2
LN3	a	30.7	0.569	67.7	11.8
	b	31.0	0.568	66.9	11.8
	c	34.8	0.092	21.2	0.7
	d	30.9	0.569	62.2	11.0
	e	31.0	0.569	67.2	11.9
	f	31.2	0.567	68.1	12.0

B.2 Determination of band gap energies

For some quantities that are used in this thesis, the band gap energy E_g of the CIGS absorbers/solar cells is needed. Table 3.1 in section 3.3 lists the band gap energies of the samples that are primarily investigated in this thesis. There are several methods that can be used to determine the band gap energy. A recent comparison between the different methods, based on the external quantum efficiency, can be found in ref. [306]. It is not unusual for the different methods to return slightly different values. It is thus very important, when comparing between different absorbers, to use the same method for the band gap energy determination.

For the samples investigated in this thesis, only the band gap of the $CuInSe_2$ sample was determined by using its EQE spectrum. The determination was conducted by Thomas Feurer from Empa and the method of choice was the integration of the EQE spectrum and energy determination of the inflection point [306].

For the remaining samples of this thesis where E_g is relevant, a different method was used. This method revolved around the determination of the depth-dependent composition of the CIGS absorber and can be broken down into the following steps:

- The integral GGI composition, i.e. the average GGI composition over the whole absorber thickness, is measured through X-ray fluorescence (XRF).
- The indium and gallium depth profiles are measured via secondary ion mass spectrometry (SIMS).
- The SIMS data are calibrated relative to the XRF data. This means that from the Ga and In profiles determined by SIMS the average is taken and its value is calibrated to the corresponding values received through XRF.
- After calibration, the band gap depth profile is computed from the Ga and In profiles based on the expression (2.11).
- Finally, as verification, the GGI and E_g profile is inserted into the optical model presented in ref. [28] and the EQE spectrum is simulated. The low-energy edge of the simulated EQE spectrum is then compared to the measured EQE spectrum. If the agreement between curves is insufficient, the GGI values are corrected by offsets until a good agreement is reached.

The measurement of the band gap energies following this method was carried out by Dr. Romain Carron and Enrico Avancini from Empa. In addition, the XRF and SIMS measurements were done on the solar cells. The resulting band gap profiles are displayed in Figs. B.4 and B.5. The values for E_g used throughout the thesis are from bulk band gap minimum.

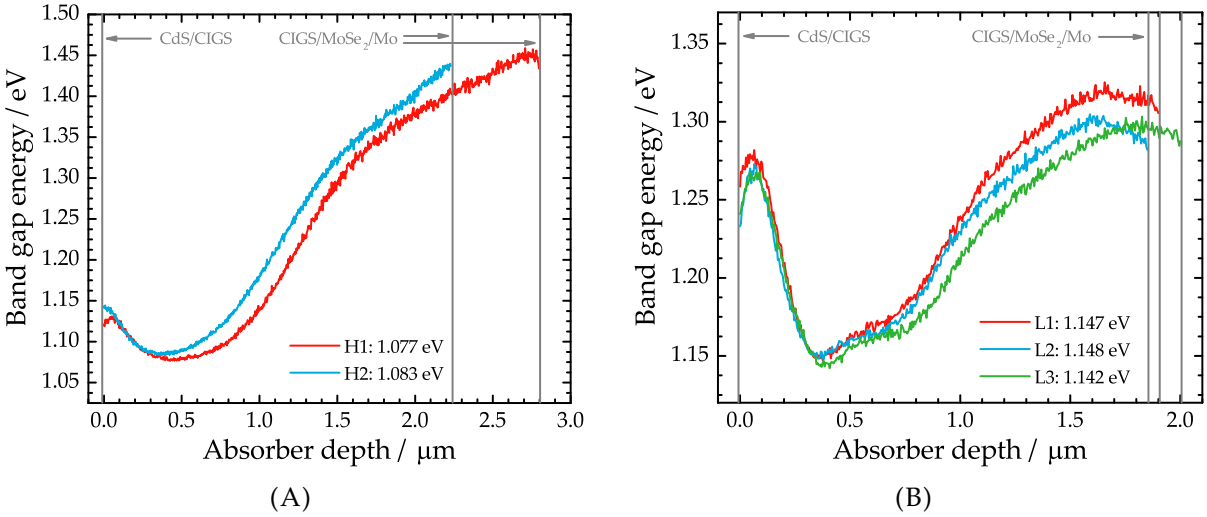

FIGURE B.4: **(A)** Band gap energy profile for sample H1 (red) and H2 (blue). The indicated values are taken from the bulk band gap minimum. **(B)** Band gap energy profile for sample L1 (red), L2 (blue), and L3 (green). The indicated values are taken from the bulk band gap minimum.

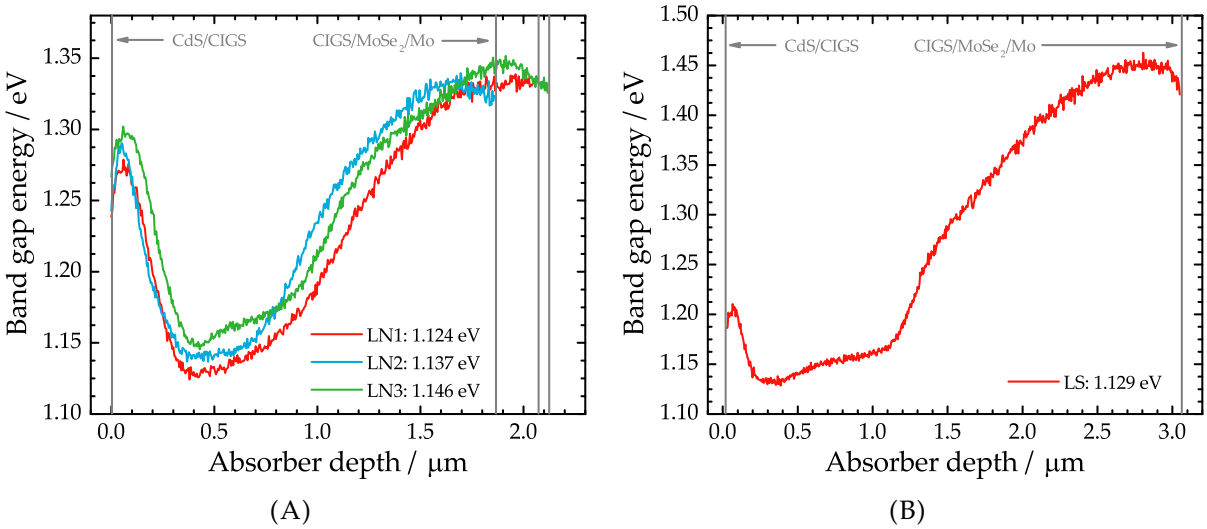

FIGURE B.5: **(A)** Band gap energy profile for sample LN1 (red), LN2 (blue), and LN3 (green). The indicated values are taken from the bulk band gap minimum. **(B)** Band gap energy profile of sample LS. The indicated value is taken from the bulk band gap minimum.

C Appendix of Chapter 4

C.1 Exfoliation experiment on a bare Cu(In,Ga)Se_2 absorber

Similarly to the experiment described in section 4.1 and shown in Fig. 4.5, an additional exfoliation experiment on the bare H1 sample was conducted. Photoluminescence was measured on the absorber in the normal (N) configuration before cutting the absorber into two pieces. One piece was exfoliated after a glue curation duration of 6 hours while the other piece was exfoliated after a long 168 hours. The results, displayed in Fig. C.1, show the same energy red-shift behaviour as seen for the other samples in section 4.1. In the present case, the energy red-shift amounts to 18 meV after a curation time of 6 hours while a reduce red-shift of 10 meV is measured after curating the glue for 168 hours.

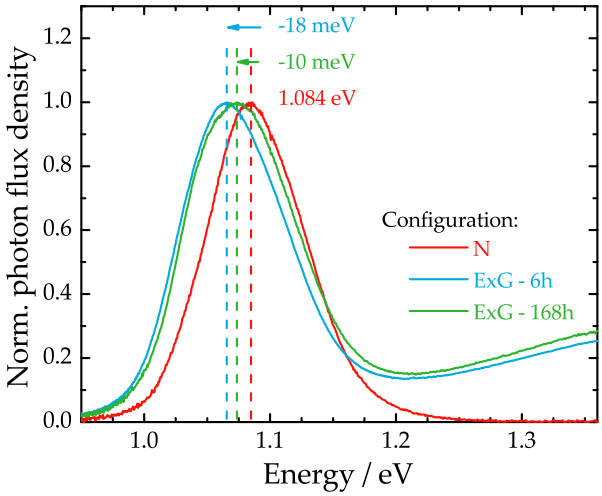

FIGURE C.1: PL spectra measured on the bare H1 absorber. The red curve shows the PL spectrum measured in the normal configuration (N) prior to exfoliation. The blue curve shows the PL spectrum measured in the (ExG) configuration on the exfoliated absorber piece after a glue curation duration of 6 hours while the green curve shows the respective spectrum after a curation time of 168 hours. Figure adapted from ref. [191].

C.2 Excitation-dependent PL on exfoliated Cu(In,Ga)Se_2

In section 4.1, the presence of a high-energy peak in exfoliated Cu(In,Ga)Se_2 absorbers is observed when the samples are measured in the (ExB) configuration (cf. Fig. 4.3). It is argued that this photoluminescence transition is due to a radiative recombination at the back of the absorber where the GGI content is considerably higher than in the band gap minimum inside the bulk. As a reason, the presence of transport barriers, which charge carriers that are excited close to the back of the absorber are not able to overcome, is suggested. Furthermore, it is suggested that only a fraction of excited charge carriers may overcome these barriers while another fraction is excited beyond the barriers, explaining the reason for the observation of the main radiative transition even in the (ExB) configuration.

To verify this assumption, PL spectra are measured in the (ExB) configuration for varying laser photon flux densities. If the diffusion-limiting mechanism is indeed a transport barrier, an increased density of excited charge carriers must eventually lead to an increased radiative recombination rate from the band gap minimum inside the bulk. Fig. C.2 displays the measured PL spectra on the CdS-covered CIGS absorbers H1 and H2. The effect of the excitation

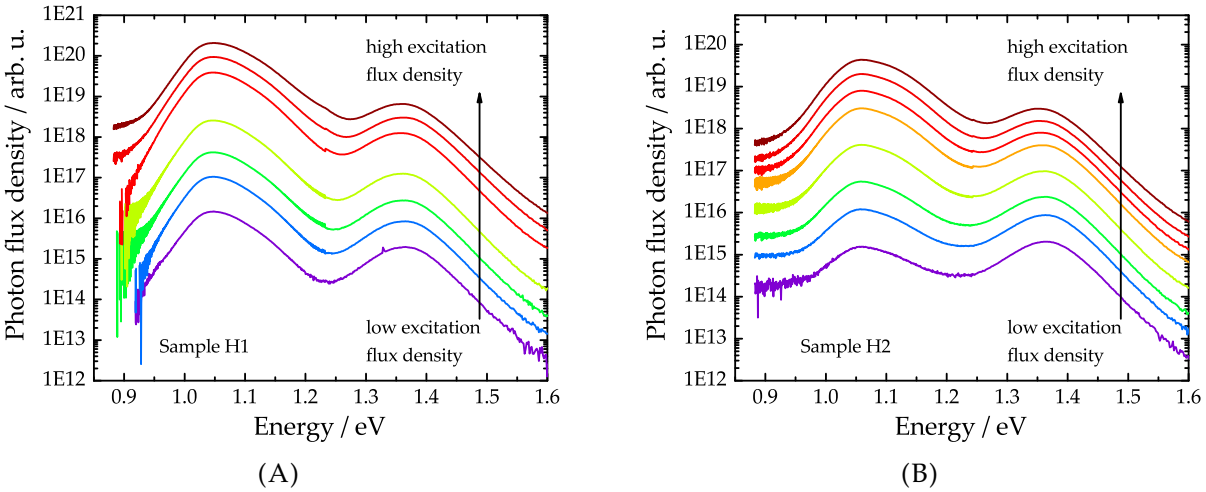

FIGURE C.2: PL spectra measured in the (ExB) configuration (cf. Fig. 4.3) for varying incoming laser light flux densities (labelled as excitation flux densities) on CdS-covered CIGS samples H1 (**A**) and H2 (**B**). As the excitation source, the 514.5 nm wavelength of the Argon ion laser was used.

dependence can very well be seen in the H2 sample where, at low excitation flux densities, the high-energy radiative transition at the back of the absorber is dominant. Increasing the excitation flux density then gradually leads to a shift in the transition dominance with the radiative transition from the band gap minimum becoming the dominant recombination. While the high-energy transition is never the dominant one in the H1 sample, the radiative recombination rate from the low-energy transition also increases at a faster rate with increasing excitation flux densities.

Thus, in both samples the radiative recombination rate from the low-energy transition increases with increasing excitation flux densities, which constitutes an additional argument for the presence of transport barriers at the back of the absorbers.

C.3 Cu(In,Ga)Se_2 penetration depth for varying excitation energies

Following photoluminescence measurements on the Cu(In,Ga)Se_2 under different configurations in section 4.1, it was concluded that the PL is originating from the band gap minimum inside the bulk. To underline this interpretation, an additional experiment with different laser excitation wavelengths was conducted. The excitation profile within the absorber, following its illumination, depends on the energy of the incoming radiation as well as on the absorption properties of the absorber. According to the law of Lambert-Beer, the spatially-dependent photon flux density $\Phi_\gamma(x)$ of the incoming radiation is given by [20]

$$\Phi_\gamma(x) = \Phi_\gamma(0)\exp\left(-\alpha x\right), \tag{C.1}$$

where $\Phi_\gamma(0)$ denotes the photon flux density at the surface of the absorber that has an absorption coefficient α. The inverse of the absorption coefficient is defined as the penetration depth $L = \alpha^{-1}$ of the incoming radiation. In the study of Alonso *et al.*, the optical functions of polycrystalline CIGS absorber with varying Ga contents were measured via spectral ellipsometry [31]. From the measured extinction coefficient κ, via the relation $\alpha = 4\pi\kappa/\lambda$, where λ is the radiation wavelength, the wavelength-dependent absorption coefficient can be extracted. Fig. C.3A shows the then calculated penetration depth in dependence of the radiation wavelength for two CIGS absorbers with different Ga content. Unfortunately, the samples under investigation in [31] did not exhibit a double gallium gradient but a more homogeneous Ga distribution

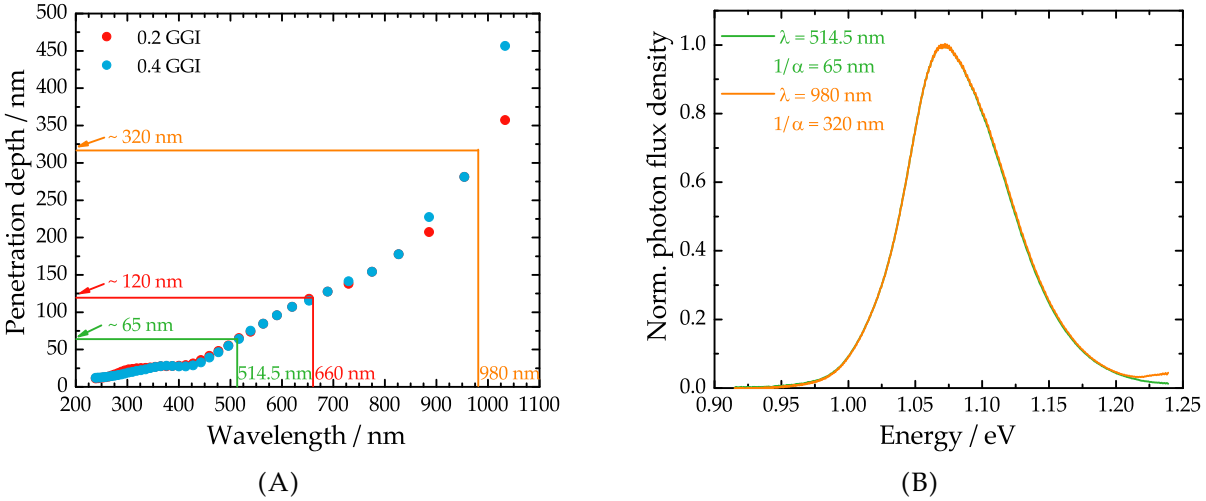

FIGURE C.3: **(A)** Penetration depth for different excitation wavelengths. The penetration depth values were extracted and calculated as described in the main text. Also indicated are the approximative values for the different laser wavelengths that are available for PL experiments in our laboratory. **(B)** PL spectra measured on sample H1 in the normal (N) configuration following the laser excitation wavelengths 514.5 nm and 980 nm.

throughout the absorber which is why the following interpretations are only approximately true. It can be seen that a laser excitation wavelength of 514.5 nm has a rather short penetration depth of around 65 nm while a laser excitation wavelength of 980 nm has a considerably larger penetration depth of 320 nm. As such, using the 514.5 nm laser line as excitation source would be more surface sensitive than the 980 nm laser line which would rather probe the bulk material. Fig. C.3B shows the PL spectra measured on the CdS-covered H1 absorber sample using the two mentioned laser excitation wavelength. Since both measured PL spectra are identical, the origin of the PL emission is expected to be originating from the band gap minimum inside the bulk.

C.4 ARPL on bare H0 and CdS-covered L1 samples

For the sake of completeness, Fig. C.4 shows the ARPL measurements on the bare H0 absorber. These results, together with the results on the CdS-covered H0 absorber in Fig. 4.10, show that it is possible to remove the interference fringes on CIGS absorbers with and without the CdS layer. The ARPL process is described and explained in detail in section 4.3.

The complete set of ARPL graphs for the CdS-covered L1 sample are provided in Fig. C.5. These graphs act as supplements to the graphs shown in Fig. 4.11.

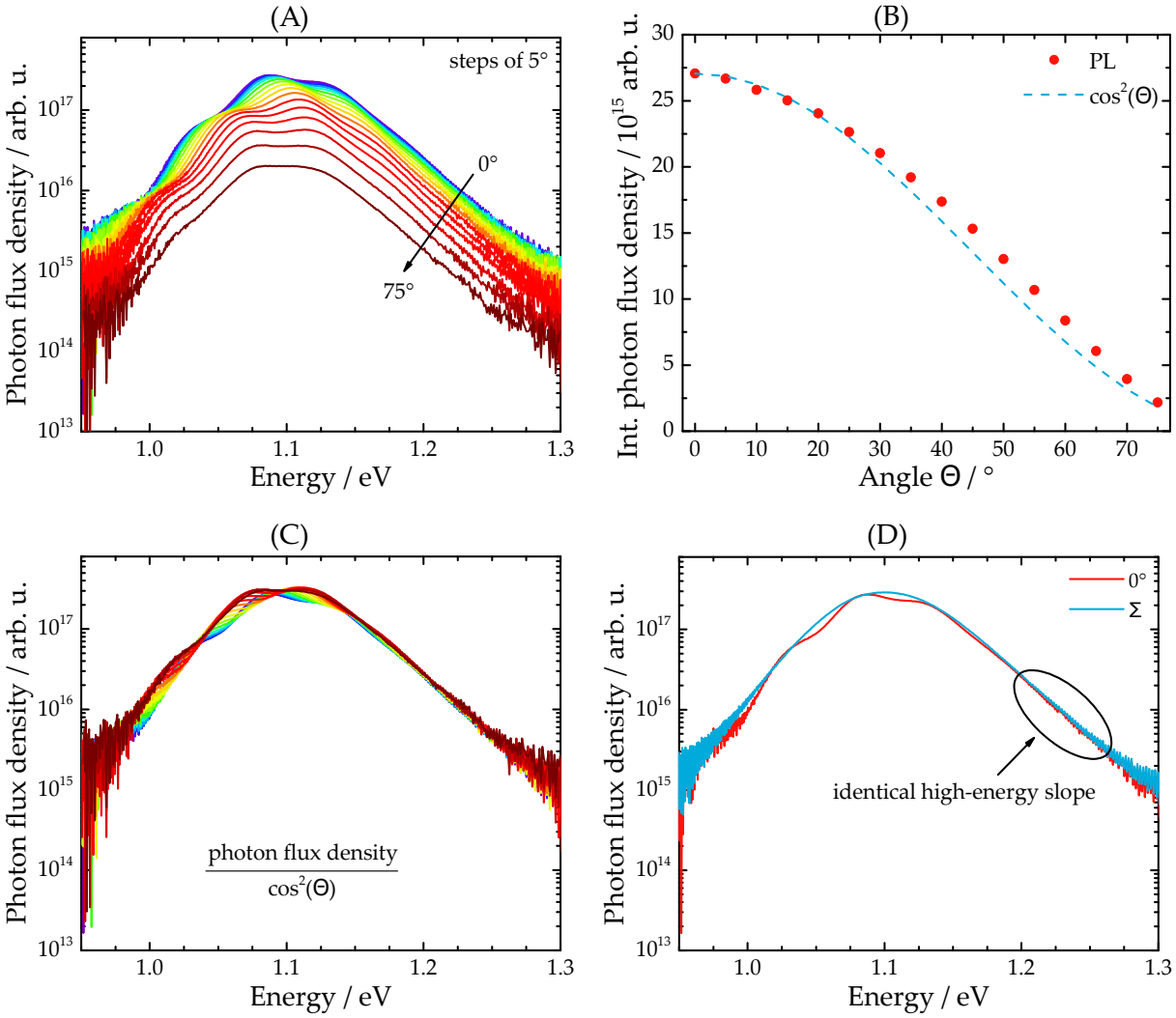

FIGURE C.4: **(A)** PL spectra measured under varying excitation/detection angles Θ, from 0° to 75° in steps of 5°. The measurements are done on the bare absorber of the H0 sample. **(B)** Integrated photon flux density of the PL spectra (red dots) plotted against the tilting angles. The decrease in photon flux density closely follows a $\cos^2$-dependence (blue dashed line). **(C)** Multiplying the various PL spectra by $\cos^{-2}(\Theta)$ leads to the curves being scaled to a similar common photon flux density. **(D)** Comparison between the PL spectrum measured at 0° (red curve) and the interference-free PL spectrum (blue curve) that results from summing and averaging over all scaled PL spectra.

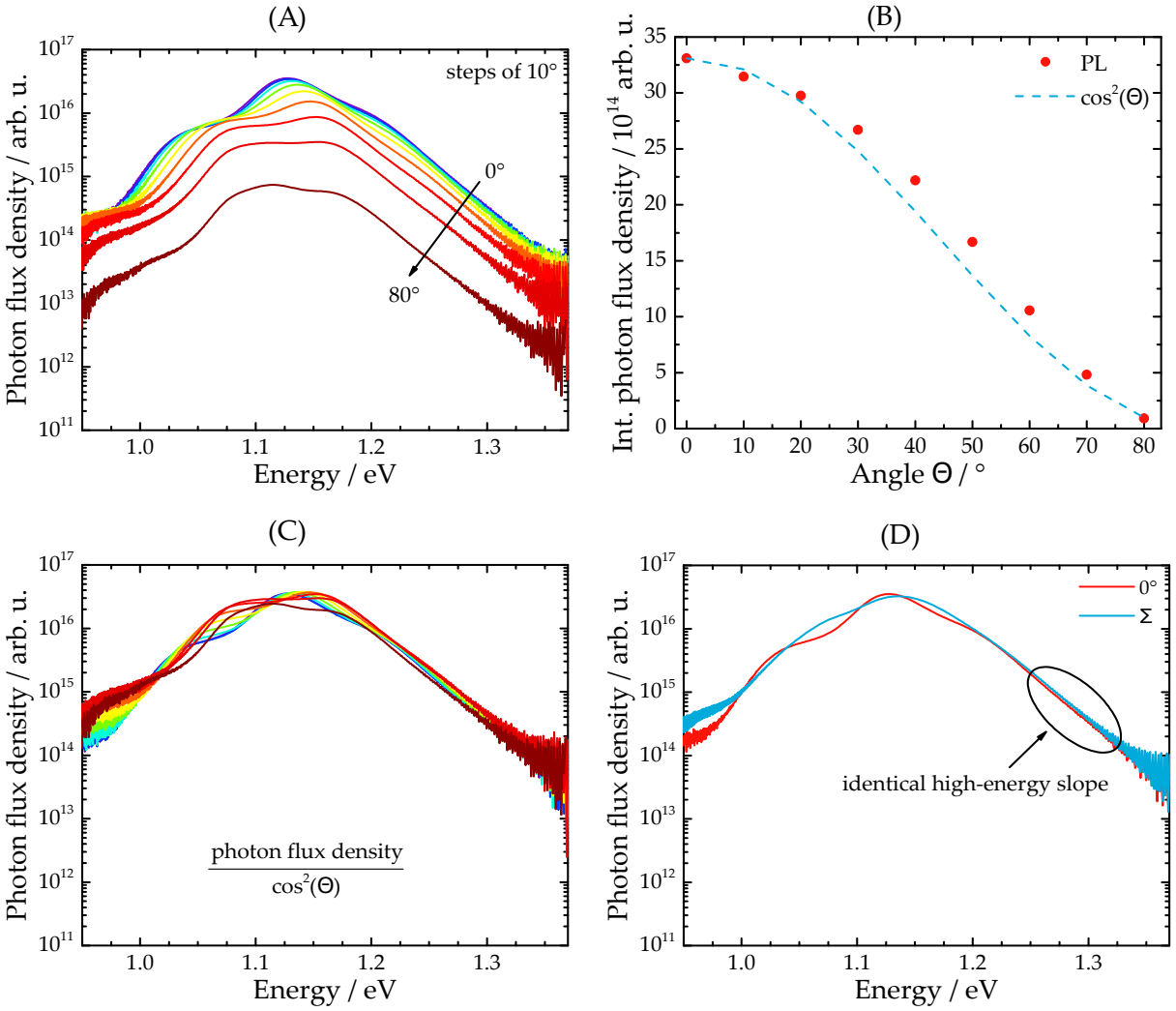

FIGURE C.5: **(A)** PL spectra measured under varying excitation/detection angles Θ, from 0° to 80° in steps of 10°. The measurements are done on the CdS-covered absorber of the L1 sample. **(B)** Integrated photon flux density of the PL spectra (red dots) plotted against the tilting angles. The decrease in photon flux density closely follows a $\cos^2$-dependence (blue dashed line). **(C)** Multiplying the various PL spectra by $\cos^{-2}(\Theta)$ leads to the curves being scaled to a similar common photon flux density. **(D)** Comparison between the PL spectrum measured at 0° (red curve) and the PL spectrum (blue curve) that results from summing and averaging over all scaled PL spectra. The slight bumps on the low-energy slope indicate that the interference fringes are not completely removed.

C.5 Additional reflectance spectra

While it is possible to remove the interference fringes from the PL spectra of both bare and CdS-covered H0 samples through ARPL, the method does not work on the L1 sample. One reason could be that the interference effects in the L1 are so much stronger than in the H0 samples, for example due to a smoother sample surface. If this were the case, then the effects of the stronger interference fringes would be observable in the reflectance spectra shown in Fig. C.6. Comparing the fluctuation amplitudes (qualitatively) between the samples, no significant difference can be spotted. The reflectance values, in all three samples, fluctuate with the same amplitude at low energies. Even if the interference fringes in the L1 sample are stronger at higher energies, the reflectance spectra alone do not explain why the ARPL method fails on the L1 absorber.

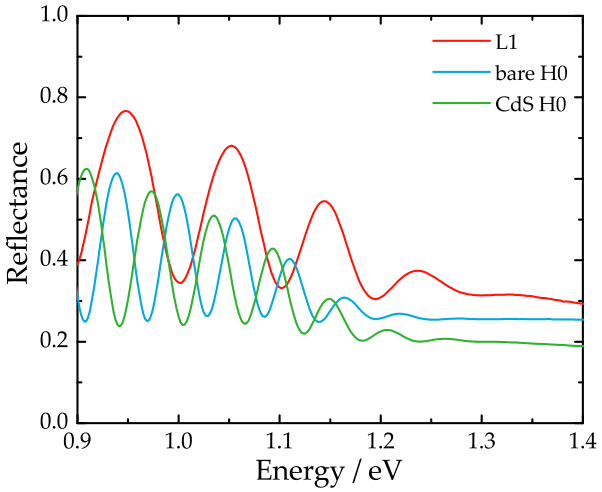

FIGURE C.6: Reflectance spectra measured on the CdS-covered L1 absorber (red curve), bare H0 absorber (blue curve) and CdS-covered H0 absorber (green curve). The differences in fluctuation periods (between H0 and L1) are due to different sample thicknesses.

C.6 Excitation-dependent PL on sample L1

Fig. C.7 shows the PL spectra of the CdS-covered L1 absorber measured at room temperature for different excitation flux densities. While the total photon flux density increases with increasing excitation, the shape of the PL spectra remains identical.

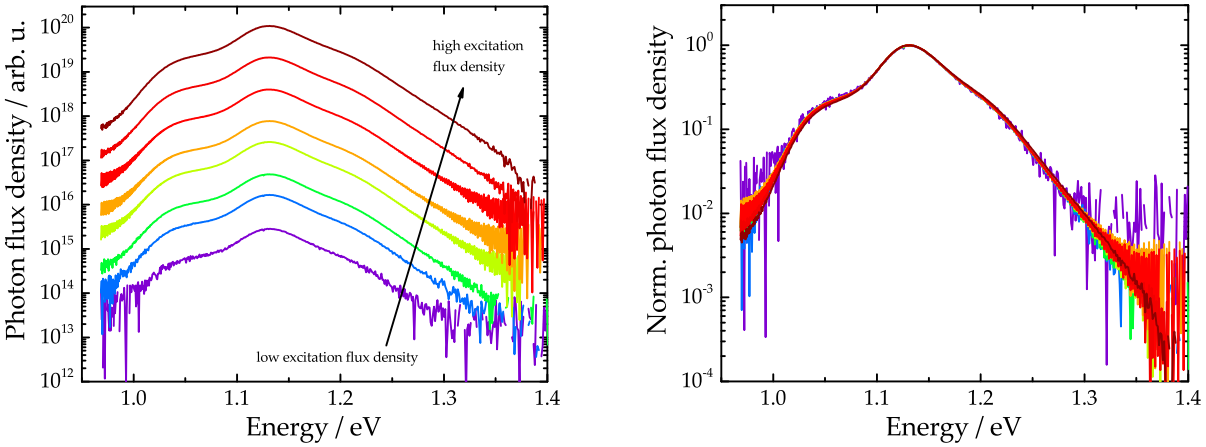

FIGURE C.7: **(A)** PL spectra of the CdS-covered L1 absorber measured at different excitation density fluxes (at least three orders of magnitude). **(B)** Normalized corresponding PL spectra to show that varying the excitation density by several orders of magnitude does not alter the spectral shape of the emitted PL.

C.7 Scanning electron microscope scan

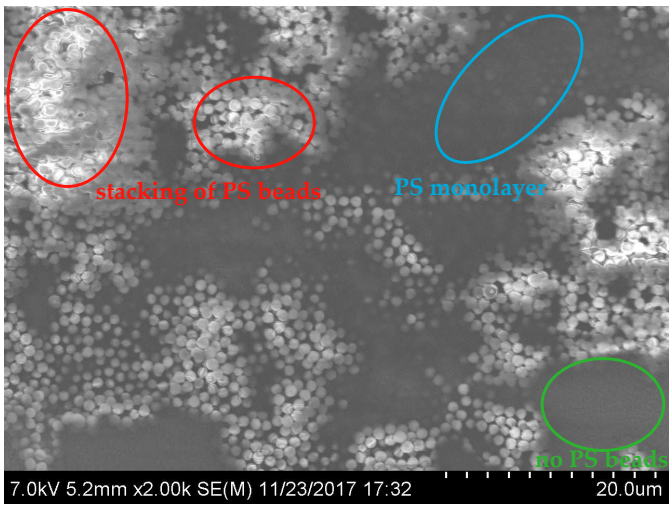

FIGURE C.8: Scanning electron microscope top-view of sample HT covered by a PS layer that resulted from three consecutive deposition processes. The scan reveals regions where the PS beads stack up to form a thick layer (highlighted in red), regions where only a monolayer is observed (highlighted in blue) and even regions where no PS beads are observed (highlighted in green). It is assumed that the strong inhomogeneity of the PS layer is due to the deposition process and cannot be controlled. However, it is also assumed that this structure is rather beneficial to the removal of interference effects. Measurement done by Daniel Siopa from the University of Luxembourg.

C.8 Reflectance of absorbers covered by polystyrene

The following graphs show the reflectance spectra measured on the samples L1, L2, L3, and H2, all having undergone the same ten-times repeated polystyrene deposition process. These are shown in addition to the corresponding reflectance graph for the H1 in Fig. 4.15B in section 4.4.2. Due to the "volatility" of the deposition process, it cannot be guaranteed that the PS layer on the samples shows the same surface morphology in all the cases. It is important to add, in order to be completely transparent when communicating the results, that there seemed to be a calibration error during the measurement of the reflectance on sample L1 without PS beads. The interference fringes are considerably larger than for the other samples L2 and L3. In addition, both the reflectance of the L1 sample with and without PS was offset to fit within the physically relevant ranges of the measured reflectance (i.e. between 0 and 1), which was

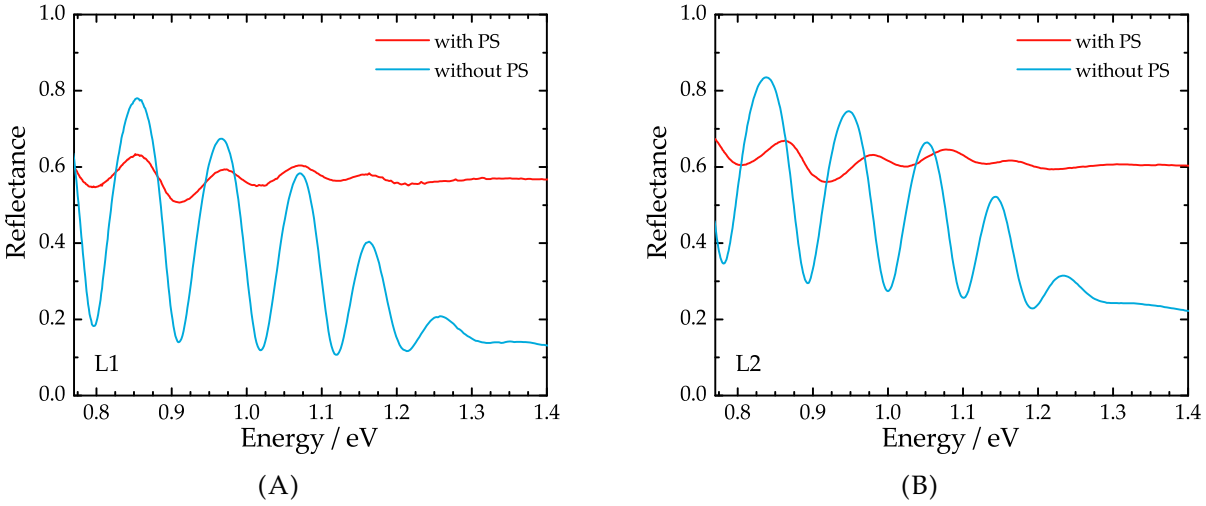

FIGURE C.9: **(A)** Reflectance spectra measured on the sample L1 after a ten-time repeated PS deposition process (red curve) and without any PS at all (blue curve). **(B)** Reflectance spectra measured on the sample L2 after a ten-time repeated PS deposition process (red curve) and without any PS at all (blue curve).

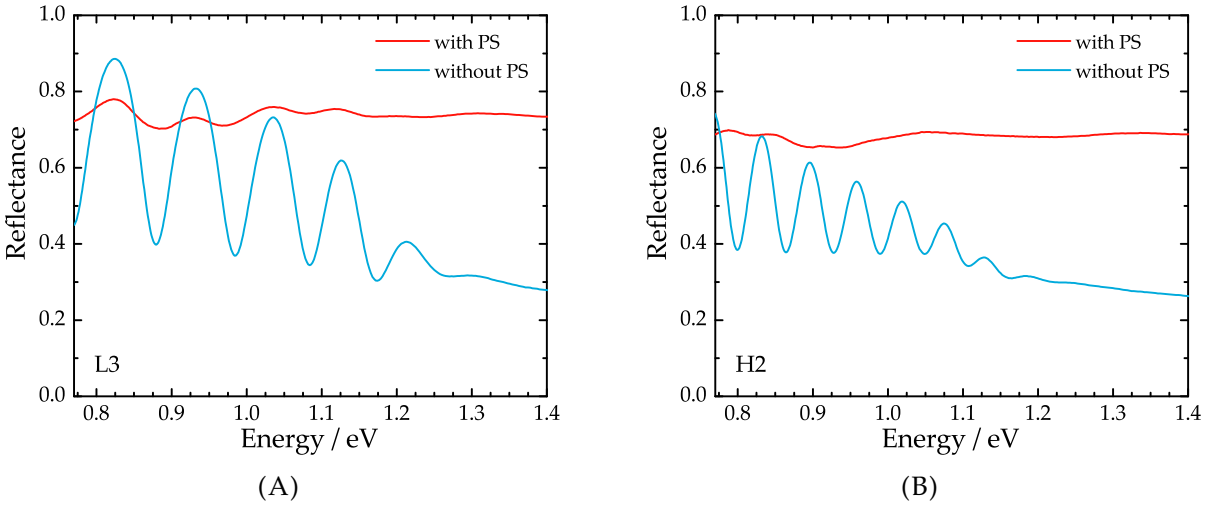

FIGURE C.10: **(A)** Reflectance spectra measured on the sample L3 after a ten-time repeated PS deposition process (red curve) and without any PS at all (blue curve). **(B)** Reflectance spectra measured on the sample H2 after a ten-time repeated PS deposition process (red curve) and without any PS at all (blue curve).

not the case in the original measurement. Nonetheless, the comparison between both spectra for the L1 sample is still valid.

C.9 Polystyrene reflectance and transmittance

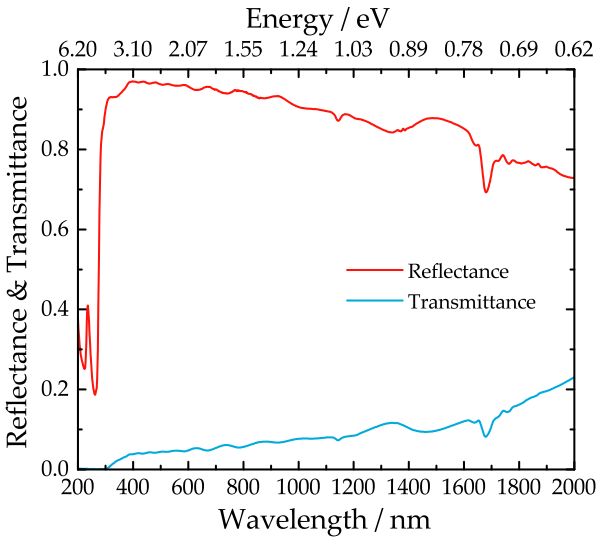

FIGURE C.11: Reflectance (red curve) and transmittance (blue curve) spectra measured on a microscopically thick PS layer deposited on a piece of conventional microscope slide glass.

C.10 ARPL in the cryostat

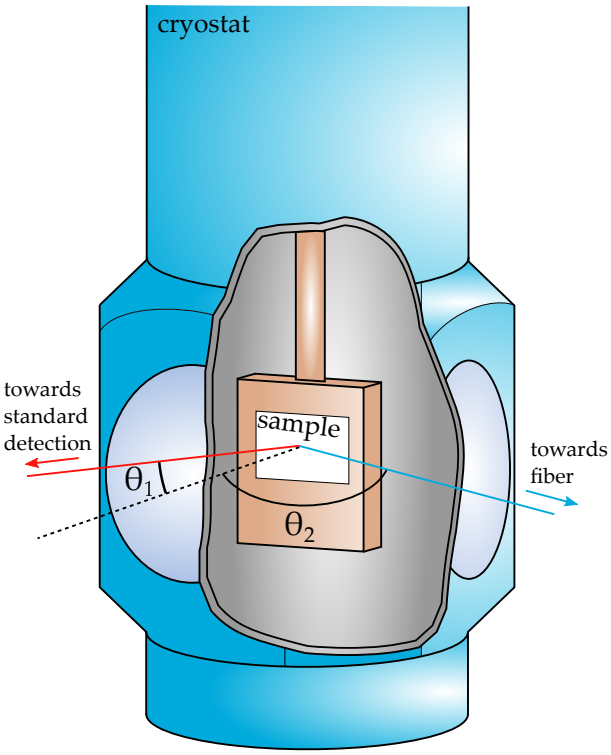

FIGURE C.12: Angle-resolved photoluminescence measurement of a sample inside the cryostat. The sample is attached to a sample rod that can be rotated. In typical measurements, the laser excitation is incident onto the sample from the same window as the emitted PL is collected. By slightly rotating the rod, the incidence angle can be slightly increased (compared to the sample surface normal) which also leads to the same rotation for the confocal detection angle θ_1. This standard detection path is illustrated by the red line. The emitted photons can also be detected at a second and larger angle θ_2 by holding a collection fiber close to the other window of the cryostat. This collection path is illustrated by the blue line. The collection efficiency along the blue line is significantly lower than along the standard red line.

C.11 ARPL on PS-covered CIGS absorbers

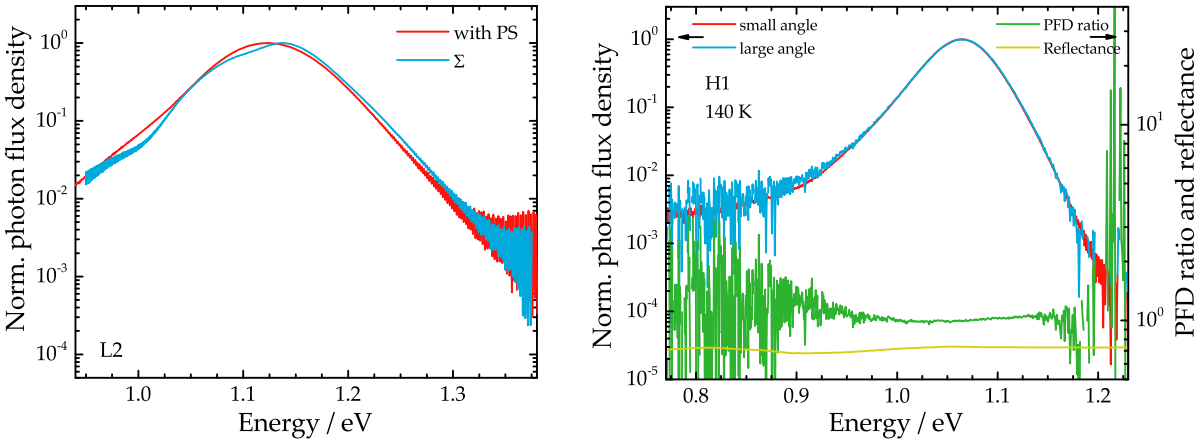

FIGURE C.13: **(A)** Normalized PL spectra measured on the CdS-covered L2 absorber after a ten-times repeated PS deposition process (red curve) and the resulting curve from angle summation through ARPL (blue curve) on the same sample without PS beads. These measurements were done at room temperature. **(B)** Normalized PL spectra measured at a small (red curve) and large (blue curve) detection angle on the CdS- and PS-covered H1 sample at 140 K. Both spectra are identical, which is reflected by the flat PFD ratio (green curve). The corresponding reflectance spectrum (yellow curve) shows no interference fringes.

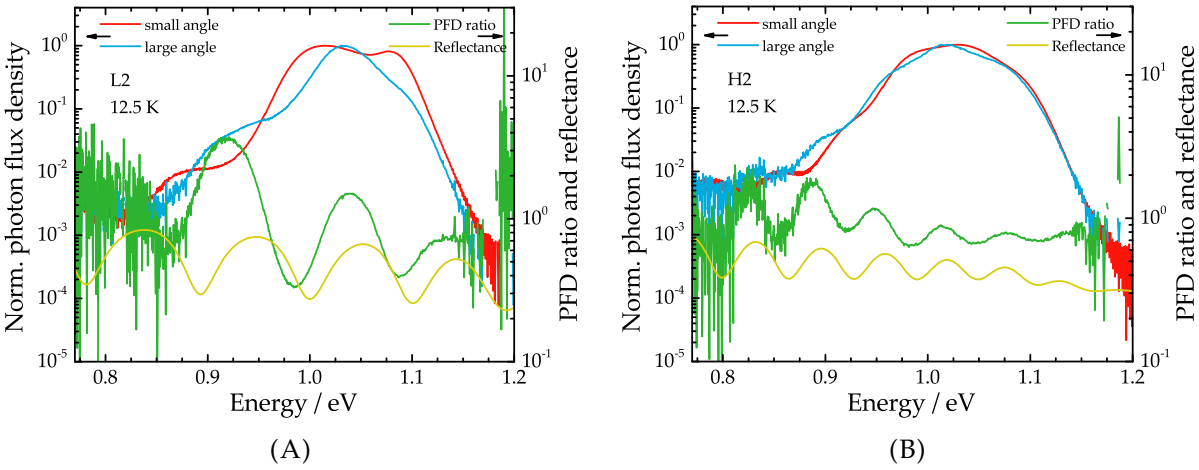

FIGURE C.14: **(A)** Normalized PL spectra measured at a small (red curve) and large (blue curve) detection angle on the CdS-covered L2 sample without PS at 12.5 K. Both spectra show significant interference fringes following a certain pattern that is extracted in PFD ratio (green curve). The corresponding reflectance spectrum (yellow curve) shows very similar fringes, although they are spectrally offset. This spectral offset is due to the PL and reflectance measurements having taken place on different absorber pieces. **(B)** Normalized PL spectra measured at a small (red curve) and large (blue curve) detection angle on the CdS-covered H2 sample without PS at 12.5 K. Both spectra show significant interference fringes following a certain pattern that is extracted in PFD ratio (green curve). The corresponding reflectance spectrum (yellow curve) shows very similar fringes, although they are spectrally offset. This spectral offset is due to the PL and reflectance measurements having taken place on different absorber pieces.

C.12 Low-energy signal at low T and large angles

In Fig. 4.18 in section 4.4.5, a bump is observed in the PL spectrum at low energies when measured at large angles. Interestingly, the signal at low energies appears at different temperatures for different samples. In the case mentioned above, the signal was present in the L2 sample already at 140 K, while at the same temperature the H1 sample does not show any such signal, as shown in Fig. C.13B in appendix C.11. Instead, for the H1 sample, a lower temperature of 100 K (Fig. 4.18B) is needed for the low-energy signal to be detected. These observations indicate that the occurrence of the low-energy signal is likely to be due to the polystyrene beads and not due to interference fringes. While the angle-resolved setup in the cryostat did not allow for a precise quantitative determination of the small and large angles used, using simple geometrics and assuming a small angle of 20° and a large angle of 70°, the optical path of the photons through the polystyrene layer is up to 3 times longer when measured under the large angle. This longer path may explain why the low-energy signal is observed when measured under the large angle if it is due to the PS beads.

Another explanation might be found when considering the background noise of the measurements. The signal detection at large angles was done by simply holding a fiber next to the cryostat window (cf. Fig. C.12 in appendix C.10), meaning that the collection of the emitted PL is not optimized (in contrast to the collection under small angles). Furthermore, measuring the photons emitted under a larger angle, as was shown in section 4.3, also leads to decrease of the photon flux density. Both these signal-decreasing mechanisms lead to a higher signal-to-noise ratio (clearly observable in the blue curves in both Fig. 4.18A and Fig. 4.18B) and might even lead to a larger background signal in general. A possible evidence for the larger background signal can be found on the high-energy slope of the PL spectra in Fig. 4.18A and Fig. 4.18B where the noisy background signal sets in at lower energies when measured under the large angle.

D Appendix of Chapter 5

D.1 Effect of various parameters on the PL spectrum

In this section, the effects of the quasi-Fermi level splitting $\Delta\mu$, of the temperature T and of the band gap energy E_g on the emitted photoluminescence spectrum are briefly described. The effects are visualized by simulating the emitted photon flux density Y_{PL} according to Planck's generalized law (5.1):

$$Y_{PL} = \frac{1}{4\pi^2\hbar^3c^2} \frac{a(E)E^2}{\exp\left(\frac{E-\Delta\mu}{k_B T}\right) - 1}. \tag{D.1}$$

The absorption spectrum $a(E)$ is simulated by assuming a Gaussian distribution of band gap energies according to Mattheis *et al.* [230] and can thus be expressed as a complementary error function

$$a(E, E_g, \sigma_g) = \frac{1}{2}\mathrm{erfc}\left(\frac{E_g - E}{\sqrt{2}\sigma_g}\right), \tag{D.2}$$

where σ_g is the standard deviation of the band gap energy distribution. While the absorptivity under this form does not describe the real measured PL spectra[1], its inclusion into Planck's generalized law leads to a well-enough description of the high-energy slope of the PL and is thus suitable to show the qualitative effects of variations in E_g, $\Delta\mu$, and T. The results of the simulations are shown in Fig. D.1 where the black arrows and descriptions indicate the change in parameters and the green arrows and descriptions visualize their main effect.

In Fig. D.1A, it can be seen that an increase in the band gap energy E_g leads to an increase in the QFLS $\Delta\mu$ if the emitted photon flux density Y_{PL} remains constant. The explanation of this effect can be found by combining equations (2.4) and (2.7):

$$n \cdot p = N_C N_V \exp\left(\frac{\Delta\mu - E_g}{k_B T}\right). \tag{D.3}$$

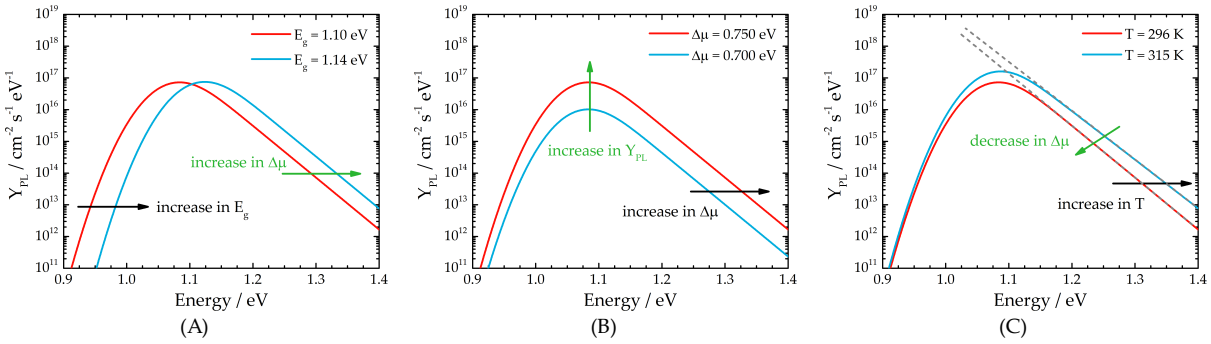

FIGURE D.1: Simulated PL spectra according to equations (D.1) and (D.2) for changes in: **(A)** band gap energy E_g, **(B)** quasi-Fermi level splitting $\Delta\mu$, **(C)** temperature T. The changes are visualized by black arrows and the resulting effects are represented by green arrows.

[1] In real measured PL spectra, the sub band gap absorption does not exhibit a Gaussian but rather an exponential behaviour - see section 5.3.

Increasing the band gap energy leads to a decrease of the intrinsic charge carriers. For the emitted photon flux density to remain constant, the quasi-Fermi level splitting has to increase. Thus, when comparing the quasi-Fermi level splitting for different samples, one needs to be careful to also consider the involved band gap energies. Increasing the band gap energy also leads to additional effects: a reduction in the portion of the AM1.5 spectrum that can be absorbed, and a reduction of thermalization losses as the involved photon energies are higher. However, these effects are much weaker than the decrease in intrinsic charge carrier densities.

Fig. D.1B shows that increasing the quasi-Fermi level splitting $\Delta\mu$ at a constant band gap energy E_g leads to an increased density of excited charge carriers and thus an increased radiative recombination rate which is measured as a higher photon flux density. The shape and energetic position of the PL spectrum is not influenced by a variation in $\Delta\mu$.

Changing the temperature T of the absorber primarily leads to a change of the high-energy slope as seen in Fig. D.1C and thus to a decrease of the quasi-Fermi level splitting $\Delta\mu$. While a change of the high-energy slope is the primary consequence of sufficiently small temperature variations, very large temperature variations lead to more significant changes in the shape of the PL spectrum.

D.2 Effect of temperature on the extraction of $\alpha(E)$

The extracted values for the quasi-Fermi level splitting $\Delta\mu$ and the temperature T are crucial for the derivation of the absorption spectrum. In Fig. 5.3, the measured PL spectrum was fitted with two different temperatures: a temperature that was left as a free parameter resulting in the value of $T_{\text{free}} = 333\,\text{K}$ and a temperature that was fixed to $T_{\text{fixed}} = 296\,\text{K}$. The derived absorptivity spectra in Fig. 5.3B showed significant differences between both fits. From these absorptivity spectra, the absorption coefficient spectra $\alpha(E)$ are derived and are shown in Fig. D.2. Not only are the $\alpha(E)$ spectra shifted with regard to each other, their shape is also different. This is underlined by the extraction of the Urbach energy E_U from the selected range, using the Levenberg-Marquardt algorithm. The function that is fitted is a modified version of eq. (5.6) (where the E_0 was omitted for simplification). To ensure a good fitting quality for the selected algorithm, the natural logarithm of $\alpha(E)$ is taken. While the fitting quality for both spectra is satisfying (see indicated R^2 value), the extracted Urbach energies show significant differences and clearly demonstrate the necessity to use a realistic value for the temperature during the fitting process.

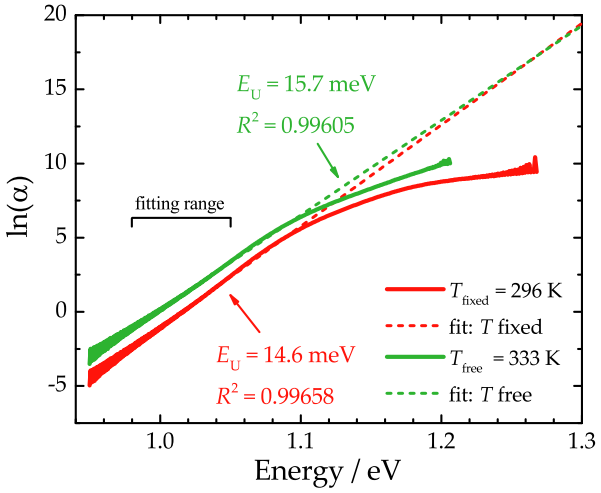

FIGURE D.2: Natural logarithm of the absorption coefficient spectra $\alpha(E)$ resulting from two different fitted temperature values. The red spectrum results from a fixed temperature of 296 K while the green spectrum results from a free temperature of 333 K. Both spectra show differences in their spectral distribution and shape. The extracted Urbach energy E_U and fitting quality R^2 (Levenberg-Marquardt) are also indicated.

D.3 Temporal evolution of $\Delta\mu$ for samples L1, L2, and L3

In section 5.2.1, the quasi-Fermi level splitting $\Delta\mu$ of samples L1, L2, and L3 was shown and discussed for both bare and CdS-covered absorbers. It was mentioned that the samples were kept in ambient atmosphere for several weeks in order to enter a stable state where air degradation of the surface ceased to occur. Measurements prior and after this situation were done and are presented in Fig. D.3 showing the measured quasi-Fermi level splitting for certain periods in time. The first data points are allocated to month 0, representing the first PL measurements on these samples. These measurements occurred a few weeks after sample preparation and a few days after the first spectrophotometric measurements (that were done to gauge the severity of interference effects). Thus, even though the samples were already exposed to air for a few days, month 0 represents the first time a laser was incident on their surface. The data set that is showed in Fig. 5.5 in section 5.2.1 is from the experiments done 1.5 months after the first measurement (as indicated in the graph).

From the temporal evolution, it is clear to see that over several months the $\Delta\mu$ of the CdS-covered absorbers (full circles) remains constant, proving the good passivation properties of the CdS layer. For the bare absorber (hollow circles), the $\Delta\mu$ decreases over time which is expected due to surface degradation [70]. However, what is not expected are the identical $\Delta\mu$ values for both the CdS-covered and bare L1 absorber (red circles) for the very first PL measurements. While the degradation of the solar cell (and absorber) properties in air have been known for years, the influence of light in the degradation dynamics has only recently been brought up by Hölscher *et al.* [307]. It is argued that the surface's exposure to air alone does not suffice for the degradation, but that ambient light of low intensity (can be as low as 0.03 suns) is needed to catalyse the degradation process. Thus the surface degradation in light/air, that the samples were exposed to for several days prior to the first PL measurements, can explain the low $\Delta\mu$ values of the bare L2 and L3 absorbers but does not fit to the high value for the bare L1 absorber.

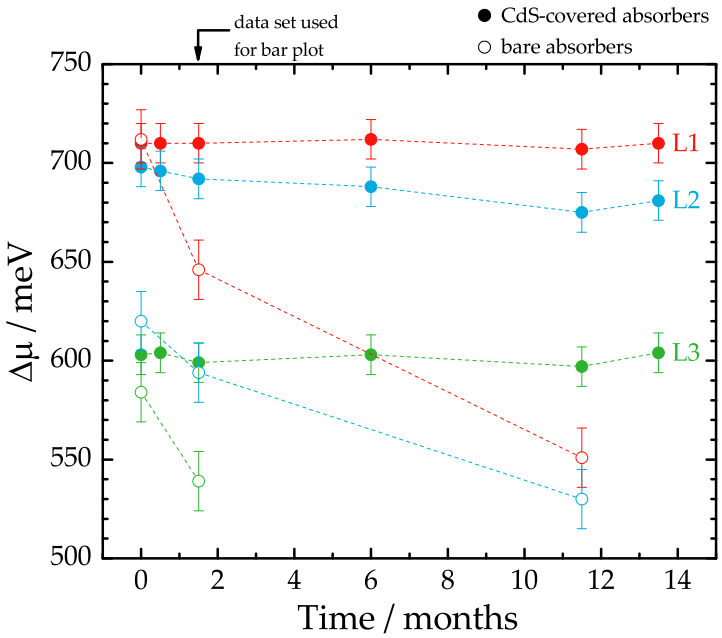

FIGURE D.3: Temporal evolution of absorber quality in terms of quasi-Fermi level splitting $\Delta\mu$ measured across several months. Measured samples consists of bare absorbers (hollow circles) and CdS-covered absorber (full circles). The red circles correspond to the L1 sample, the blue circles correspond to the L2 sample, and the green circles correspond to the L3 sample. Error bars are included and explained in section 5.2.1.

In section 2.6.3, the possibility of a thin $RbInSe_2$ surface layer was briefly introduced. Thus, it might be possible that such a surface layer passivates the absorber surface for low light intensities. Once the surface is illuminated by a laser with a certain excitation density ($\approx 85\,\mathrm{mW\,cm^{-2}}$), the degradation of the layer and the surface underneath is catalysed, just as is the case for the NaF-treated and non-treated absorbers but where the degradation already sets in at lower light intensities. This explanation only constitutes a possibility and further investigations are needed. As an example, one could think of preparing a similar sample set again and immediately after growth, enclose them inside an air- and light-tight container i.e. some kind of "dark vacuum". This "dark vacuum" is then only to be broken under controlled circumstances and the measured results are to be compared to additional samples from a control trial.

Finally the idea of human failure also needs to be entertained. Even if most care is always taken in the laboratory, humans err and so it might be possible that the measured data from the bare and CdS-covered L1 sample actually belong to the same CdS-covered sample and the labelling and sample selection were mixed up during experiments.

D.4 Quasi-Fermi level splitting of samples LN1, LN2, and LN3

The sample set LN1, LN2, and LN3 underwent similar experiments as the set L1, L2, and L3. Fig. D.4A shows the temporal evolution of the quasi-Fermi level splitting $\Delta\mu$ across several days. The data reveal that the CdS-covered absorbers of sample LN1 and LN2 show identical $\Delta\mu$ values. This is not due to an identical absorber quality as the results would *a priori* suggest, but rather due to an increased band gap energy E_g of the absorber LN2 (see Table 3.1 in section 3.3). Thus, the QFLS deficit $E_g - \Delta\mu$ would be a more accurate quantity for comparison. To be consistent with the data set of sample L1, L2, and L3, the $\Delta\mu$ is nonetheless shown as the parameter of choice. Prior to the first measurements, the samples were kept in standard atmospheric conditions for 3 days. Contrastingly to sample L1, the bare absorber of sample LN1 does not show an identical value compared to the corresponding CdS-covered absorber at the first day of measurement. This different behaviour could potentially be explained by the different absorber growth conditions (of which the exact details are unknown) and elemental composition as exemplary expressed through the gallium gradient in section B.2.

All measured $\Delta\mu$ values exhibit a constant value over the space of 10 days. Intriguingly, the values measured 9 days after the first measurement show some significant discrepancies compared to the prior values. Reasons for these discrepancies possibly include: measurement on different spots (although great care was taken to always measure on the same spots), hiccup in the calibration of the PL setup, and increase in $\Delta\mu$ due to a light-soaking effect. The first reason can carefully be discarded if a certain absorber homogeneity is assumed. The second reason is possible but an investigation of the log files did not reveal any significant hiccup (however, there might have been an undocumented hiccup as not every small step in the calibration is recorded. A short lapse in concentration is sometimes sufficient to falsify the calibration). The third reason seems likely and light-soaking effects on CIGS-based solar cells are reported in literature (see e.g. [308]). However, no such effect was seen during live scans, neither in the L1, L2, and L3 sample set nor in the LN1, LN2, and LN3 set. In addition, the measurement conditions were always the same such that a light-soaking effect would always have been observed.

Due to the discrepancies for the data points measured 9 days after the first measurement, the data set measured on day 7 is selected for graphical representation in the bar plot in Fig. D.4B. Keeping in mind that sample LN2 (NaF only PDT) has a larger band gap energy than sample LN1 (NaF + RbF PDT), the results are consistent with the interpretation of the L1, L2, and L3 sample set given in section 5.2.1. However, for this specific sample set, the difference between

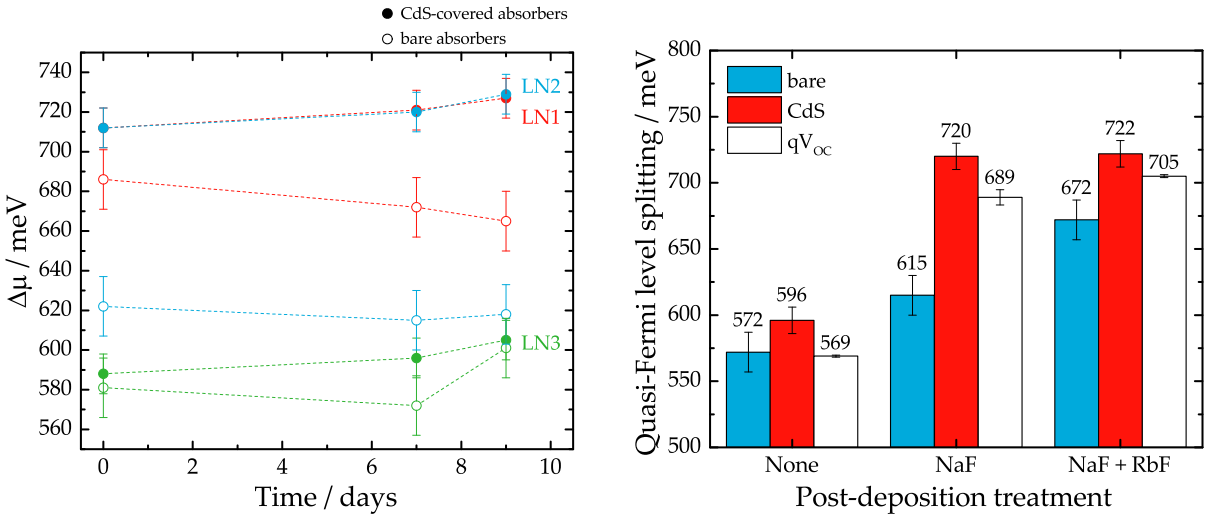

FIGURE D.4: **(A)** Temporal evolution of absorber quality in terms of quasi-Fermi level splitting $\Delta\mu$ measured across several days. Measured samples consists of bare absorbers (hollow circles) and CdS-covered absorber (full circles). The red circles correspond to the LN1 sample, the blue circles correspond to the LN2 sample, and the green circles correspond to the LN3 sample. Error bars are included and explained in section 5.2.1. **(B)** Bar plot showing the quasi-Fermi level splitting of bare (blue bars) and CdS-covered (red bars) CIGS absorbers having undergone different post-deposition treatments. For comparison, the qV_{OC} (white bars) as measured on the finished solar cell devices is also shown. The non-treated sample corresponds to sample LN3, the NaF treated sample corresponds to sample LN2 and the NaF+ RbF treated sample corresponds to sample LN1.

$\Delta\mu$ and V_{OC} is surprisingly high which is in strong contrast to the results for the other sample sets in Fig. 5.5 and Fig. 5.7. As a possible explanation for this difference, the deposition of a non-optimized window layer on these absorber, whose compositional variation differs from regular absorber, is suggested.

D.5 Collection of spatially-resolved PL spectra

Fig. D.5 shows the intensity-calibrated PL spectra that are measured spatially-dependent on the bare and CdS-covered H1 and H2 absorbers under AM1.5 illumination as presented in Fig. 5.6 in section 5.2.2.

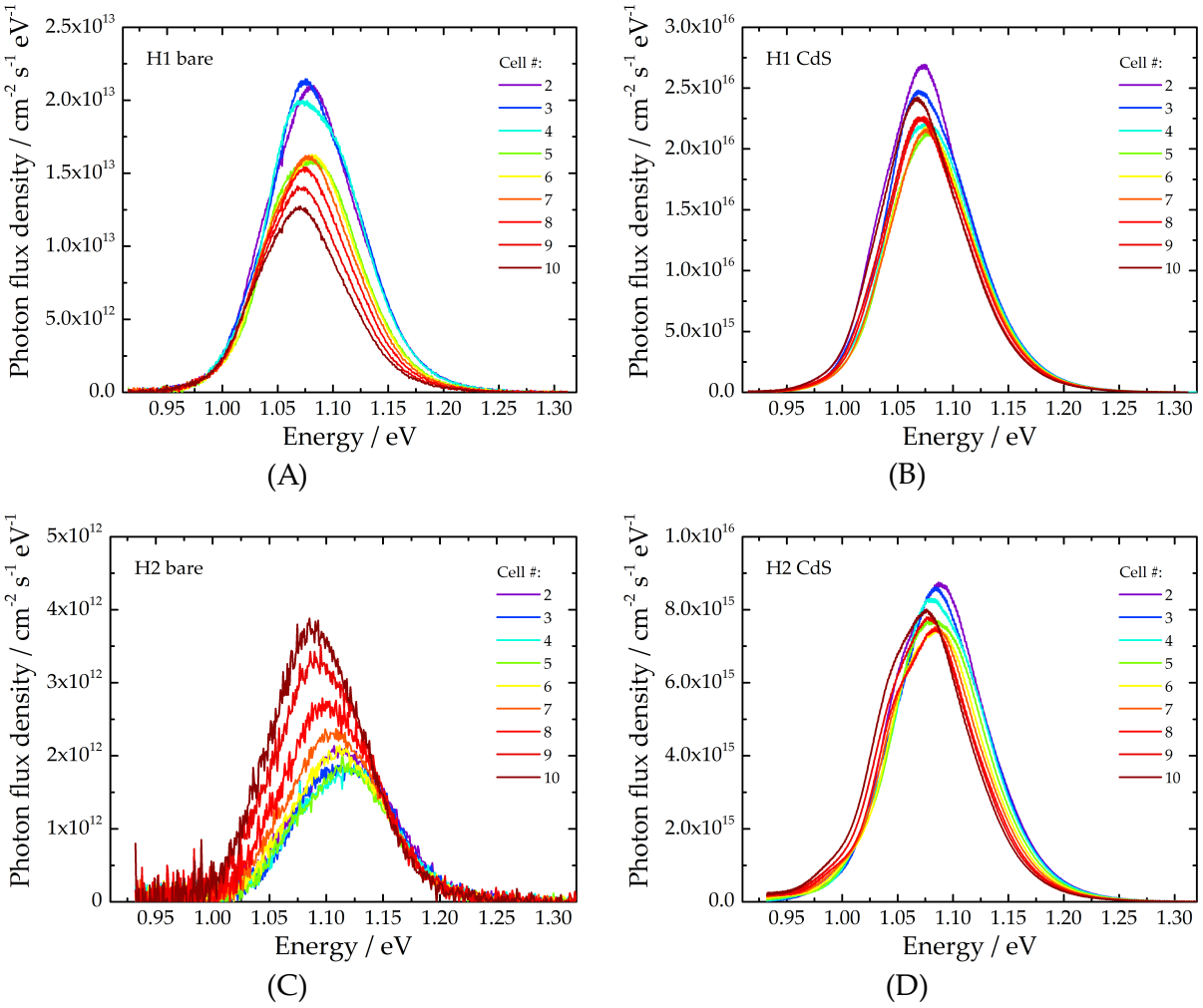

FIGURE D.5: Intensity-calibrated PL spectra measured spatially-dependent under AM1.5 illumination on the **(A)** bare H1 absorber, **(B)** CdS-covered H1 absorber, **(C)** bare H2 absorber, and **(D)** CdS-covered H2 absorber. The different colors correspond to the different cell placements on the absorber strip (as indicated by the legend) which can be reviewed in appendix B.1.

D.6 Temporal evolution of $\Delta\mu$ for samples H1 and H2

Fig. D.6 shows the temporal evolution of the quasi-Fermi level splitting $\Delta\mu$ for samples H1 and H2. Since the measurements were not always done on the same spots on the absorbers and with the absorbers showing a certain spatial variation in the band gap energy, the temporal evolution is represented as the energetic QFLS deficit $E_{PL} - \Delta\mu$. As was the case for the low-temperature sample set in section D.3, the first data points are allocated to month 0, representing the first PL measurements on these samples. These measurements occurred a few weeks after sample preparation and a few days after the first spectrophotometric measurements (that were done to gauge the severity of interference effects). Contrary to the low-temperature sample set L1, L2, and L3, the bare absorber of the RbF-treated H1 CIGS sample shows a significantly lower $\Delta\mu$ for the first measurement. This result suggests that no passivating $RbInSe_2$, whose presence was suggested on the bare L1 absorber surface, is present if the sample is grown in a high-temperature process. Consequently, one can suggest that the alkali PDT might lead to slightly different effects, depending on the sample growth conditions.

Additionally, the CdS-covered absorbers in Fig. D.6 show a slight increase of $E_{PL} - \Delta\mu$ over time. This suggests a small increasing non-radiative recombination rate potentially due to a slow degradation of the CdS buffer layer. However, the increase in $E_{PL} - \Delta\mu$ is too small to allow for further interpretations.

As was the case for the low-temperature samples, ample time was given to the bare absorbers to allow them to reside in a stable state before extensive measurements. As such, the PL measurements shown in section 5.2.2 of the bare absorbers are from month 1.5, and for the CdS-covered absorbers are from month 0.5.

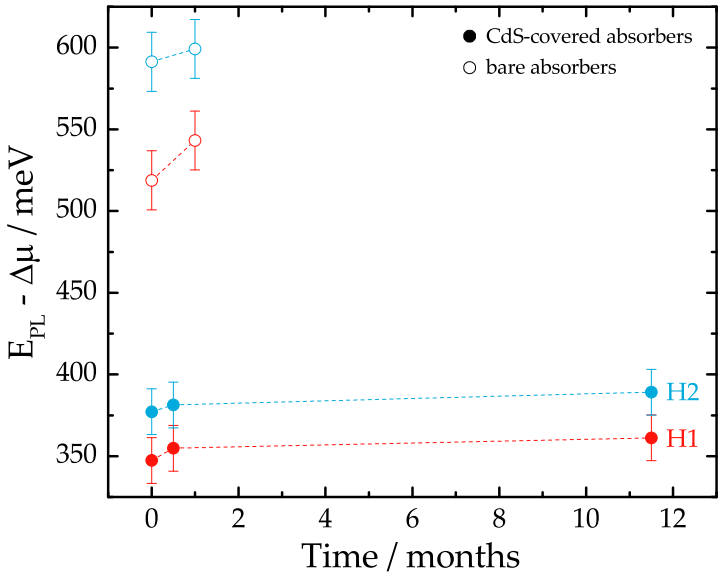

FIGURE D.6: Temporal evolution of absorber quality in terms of energetic quasi-Fermi level deficit $E_{PL} - \Delta\mu$ measured across several months. Measured samples consists of bare absorbers (hollow circles) and CdS-covered absorber (full circles). The red circles correspond to the H1 sample, while the blue circles correspond to the H2 sample. Error bars are included and explained in section 5.2.2.

D.7 Absorption coefficient spectra for various samples

In section 5.3.1, the absorption coefficient spectra of samples H1, H2, L1, L2, and L3 are shown for a narrow spectral range. In this context, Fig. D.7A shows the absorption coefficient spectra of samples L1, L2, and L3 for a broader spectral where the influence of the background signal can clearly be seen at low energies. In addition, recording the spectrum over a broad range allows the fitting across several fitting ranges. As an example, the bottom-right inset in Fig. D.7A shows the extracted Urbach energies for sample L1 for the different fitting ranges. This fitting process is done on the low-temperature samples at different excitation densities (improving only the signal-to-noise ratio - Fig. D.7 only shows the spectra recorded at the highest excitation density used in the experiments). From the extracted Urbach energies across the different fitting ranges and excitation densities, a mean value is computed and plotted in Fig. 5.9. The standard deviation forms the error bars in the same graph.

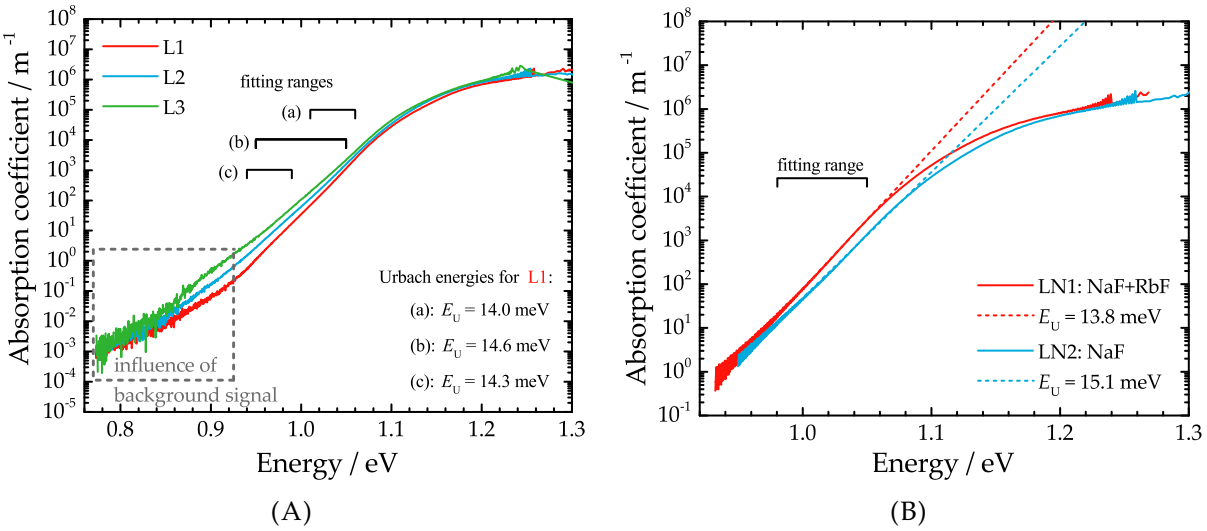

FIGURE D.7: **(A)** Absorption coefficient spectra of samples L1 (red curve), L2 (blue curve), and L3 (green curve) in semi-logarithmic representation over a broad spectral range. A fit to the data of sample L1 for the fitting ranges (a) 1.01 - 1.06 eV, (b) 0.95 - 1.05 eV, and (c) 0.94 - 0.99 eV yields the extracted Urbach energies indicated in the bottom-right corner. The grey-dashed box shows the background signal. **(B)** Absorption coefficient spectra of samples LN1 (red curve) and LN2 (blue curve) in semi-logarithmic representation. A fit (dashed lines) to the data in the indicated fitting range yields the Urbach energies as shown in the bottom-right corner.

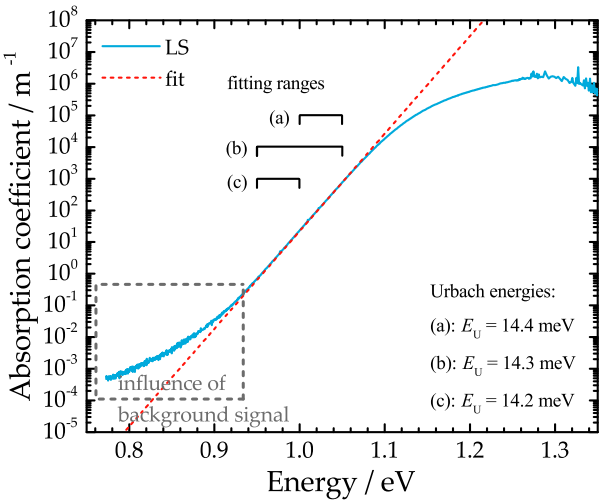

FIGURE D.8: Absorption coefficient spectrum of sample LS in semi-logarithmic representation. The fitting ranges were fixed to three different spectral intervals: (a) 1.00 - 1.05 eV, (b) 0.95 - 1.05 eV, and (c) 0.95 - 1.00 eV. The extracted Urbach energies from the fits (the fit over range (b) is shown as an example by the red dashed line) are displayed in the bottom-right corner.

Fig. D.7B shows the absorption coefficient spectra of samples samples LN1 and LN2 measured across a narrow spectral range. Also shown are the fitting range and the corresponding extracted Urbach energies. The same measurements across a wider spectral range were also done but are not shown here.

Fig. D.8 shows the absorption coefficient spectrum of sample LS for a specific excitation density measured across a broad spectral range. For this specific measured spectrum, the extracted Urbach energies are displayed in the bottom-right corner of the graph.

D.8 Other techniques for the extraction of E_U

In section 5.3.2, the extraction of the Urbach energy from data measured by techniques other than photoluminescence is discussed. In this context, Fig. D.9A shows the external quantum efficiency measured on the solar cells of samples L1, L2, and L3. Compared to the photocurrent spectroscopy data in Fig. 5.10A, the EQE data is very choppy which leads to a reduced precision for the fits. A fit in the selected range yields the Urbach energies that are displayed in the bottom-right corner of the graph. Comparing the values between the samples, it is evident that the Urbach energies extracted from EQE follow the same trend as the ones extracted from PL and PCS i.e. a reduction in samples treated with heavier alkali metals.

The extracted Urbach energies from the different measurement techniques are compared to each other in Fig. 5.10B where a clear discrepancy is observed: the Urbach energies extracted from PL are lower than the ones extracted from EQE which, in turn, are lower than the ones extracted from PCS. There a several possible reasons for this discrepancy.

One first reason would be that the PL is measured on absorbers while EQE and PCS are measured on finished solar cell devices. Thus, it could be possible that the solar cell fabrication process itself leads to stronger band tails and thus a larger Urbach energy. However, as was

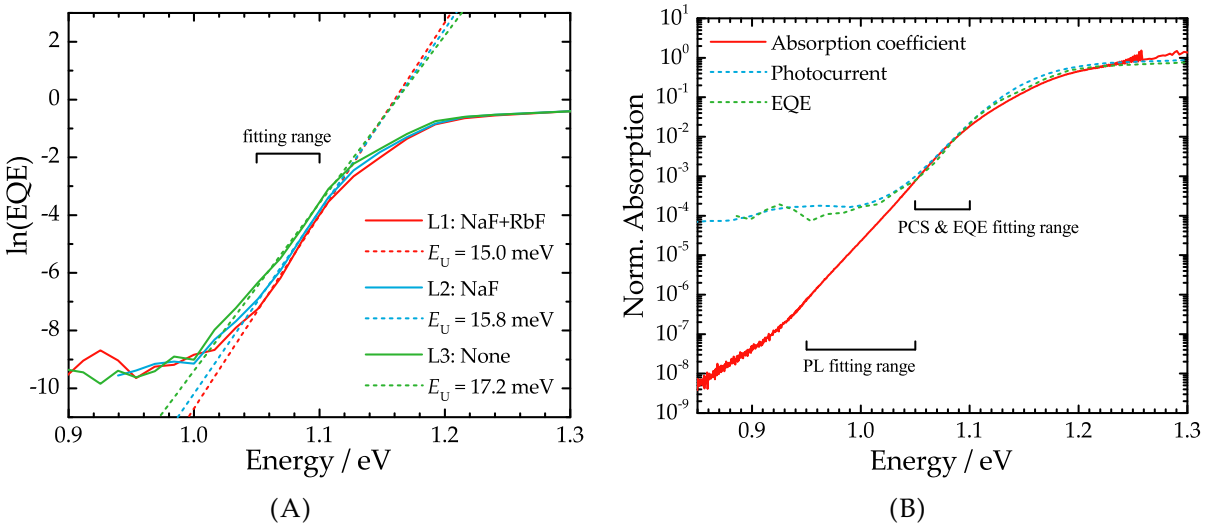

FIGURE D.9: **(A)** External quantum efficiency measured on the solar cells L1 (red cruve), L2 (blue curve), and L3 (green curve). The natural logarithm is taken to allow a greater fit precision in the indicated fitting range (1.05 - 1.10 eV). The Urbach energies extracted from the fits (dashed lines) are listed in the bottom-right corner. The EQE experiments were performed by Dr. Romain Carron from Empa. **(B)** Normalized absorption related spectra measured via different techniques on the absorber and solar cell L1. The red curve represents the absorption coefficient from PL, the blue dashed curve shows the photocurrent and the green dashed curve represents the EQE. Also indicated are the different fitting ranges used by the techniques to extract the Urbach energy. The PCS experiments were performed by Dr. Emilie Bourgeois from the University of Hasselt.

shown in Fig. 5.9, small Urbach energy increases are related (but not necessarily the cause) to large QFLS $\Delta\mu$ losses. Thus, if the Urbach energy would be increased by up to 2 meV (approximate difference between E_U from PL and PCS e.g.), a large difference (up to 40 meV) between the $\Delta\mu$ of the absorber and the qV_{OC} of the solar cell should be measured. However, this is not the case as is clearly shown in section 5.2.

A second reason could be inhomogeneities between absorber and solar cell sample pieces. This possibility can also be discarded using a similar reason as for the first possibility: both solar cell and absorber were grown on substrates in the same process but were only spatially separated. If the growth process would be so inhomogeneous as to result in so distinct differences in the Urbach energies, then the measured qV_{OC} would never be as close to the measured $\Delta\mu$ as is the case in these state-of-the-art absorbers.

A third reason would be a difference in sensitivity for the measurement of the sub band gap absorption properties between the techniques. In this context, Fig. D.9B shows the absorption coefficient, photocurrent, and external quantum efficiency measured on sample L1. The spectra are normalized at high energies for easier comparison. It is immediately evident, as was mentioned already several times, that the absorption properties can be resolved across several orders of magnitude by PL measurements. By comparison, PCS and EQE allow for the detection of a much smaller fraction of the absorption properties. This forcefully limits the fitting to a certain range, e.g. 1.05 to 1.10 eV. In the case of PL, however, 1.05 eV is already the upper limit for the fits, which can de done at energies as low as 0.95 eV. Since the band-to-band absorption process dominates at energies close to the band gap energy (1.14 eV in this case), for a reliable extraction of the Urbach energy, the fits need to be done at considerably lower energies. It can thus be argued that the fitting range of 1.05 - 1.10 eV is too high such that it is influenced by the band-to-band process. This can be verified by fitting the absorption coefficient data, derived from PL, in the same region. Doing so yields on average an Urbach energy that is larger by approximately 1 meV (not shown here). This confirms that the larger Urbach energies extracted from PCS and EQE can be explained by its forceful extraction at too high energies.

While the reasoning above explains the lower Urbach energies extracted from PL, the other two techniques also differ between themselves. However, due to the lack of information, as the measurements were not done by me, it is not possible to explain this difference. A suggestion would be a reduced influence of the background signal due to the involvement of the lock-in technique or imprecise fits due to the choppy data points in the case of EQE.

D.9 External quantum efficiency of H1 and H2

Similar to the external quantum efficiency measurements done on the low-temperature samples in appendix D.8, Fig. D.10A shows the EQE of one H1 and one H2 solar cell. A fit from 1.00 eV to 1.05 eV yields the Urbach energies indicated in the bottom-right corner. In Fig. D.10B, the extracted Urbach energies from EQE (red squares) are compared to the ones from PL (blue circles). Again the data show that, no matter the measurement technique, the band tails are weakened when the absorber is treated with alkali atoms. The differences in absolute E_U between EQE and PL can be explained with the same reasoning laid out in the above appendix D.8.

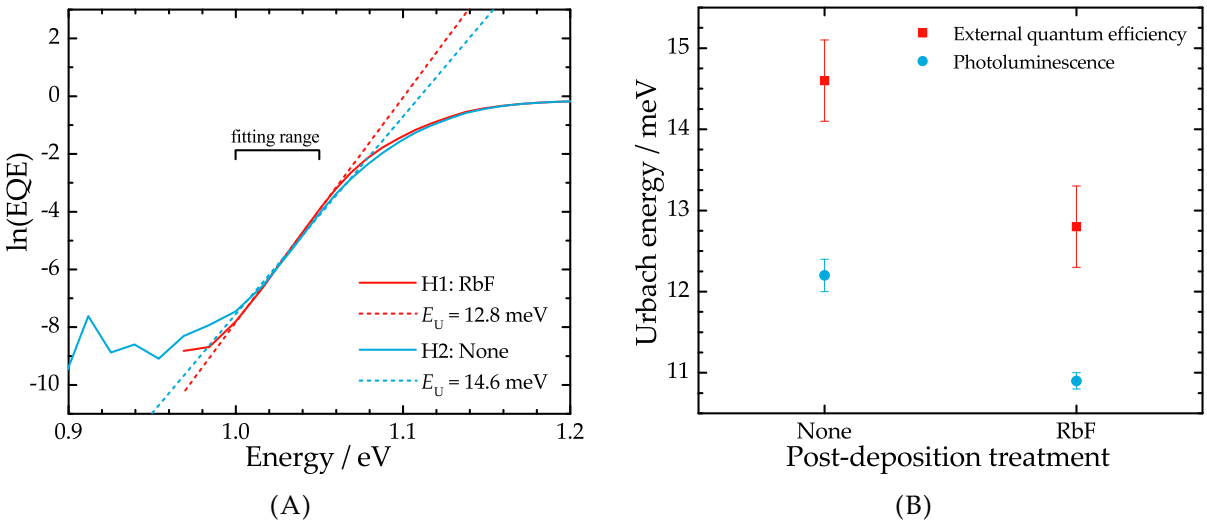

FIGURE D.10: **(A)** External quantum efficiency measured on the solar cells H1 (red curve) and H2 (blue curve). The natural logarithm is taken to allow a greater fit precision in the indicated fitting range (1.00 - 1.05 eV). The Urbach energies extracted from the fits (dashed lines) are listed in the bottom-right corner. The EQE experiments were conducted by Dr. Romain Carron from Empa. **(B)** Comparison of the extracted Urbach values for the high-temperature samples in dependence of the PDT they received after growth. The none-treated sample corresponds to sample H2 while the RbF-treated sample corresponds to sample H1. The red squares correspond to the results from EQE (error bars estimated at 0.5 eV) while the blue circles correspond to PL.

D.10 Spatially-resolved μ-PL on absorber H1

From each measured spectrum of the spatially-resolved PL scan introduced in section 5.4.1, the quasi-Fermi level splitting can be extracted. Due to a poor collection of the emitted PL signal, which is a consequence of the high resolution of the confocal optics [209], the recorded PL spectra show a large background signal and noise. These unwanted signals prevent the optimized extraction of the quasi-Fermi level splitting as laid out in section 5.1.3. Due to the high-energy slope of the PL spectrum not being spectrally resolved to larger energies, the fitting procedure yields large variations in the lattice temperature if it is kept as a free fitting parameter. This is exemplified in Fig. D.11 showing two of the 1681 PL spectra of the $41 \cdot 41\ \mu m^2$ scan of sample H1. Fitting the spectra in the indicated range (1.18 - 1.24 eV), the extracted temperatures range from a minimum of 291 K (blue curve, PL spectrum number 1007) to a maximum of 313 K (red curve, PL spectrum number 449). By eye, both spectra show a minimal discrepancy at high-energies but are otherwise identical. In addition, a logical explanation for why the temperature should vary for different spots on the absorber is lacking. It can thus be concluded that the discrepancy between the different extracted temperatures is entirely due to the fitting process being hampered by the large noise at high energies. Using a smaller

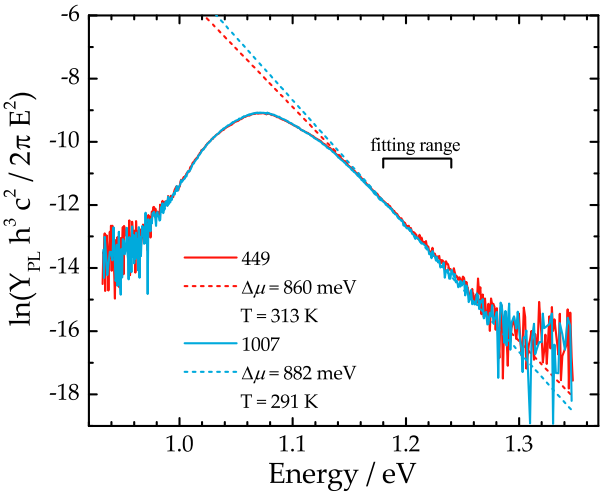

FIGURE D.11: Photoluminescence spectra recorded on pixel number 449 (red curve) and on pixel number 1007 (blue curve) of the absorber H1. By keeping the temperature T as a free parameter, the fits yield significantly different values for the temperature and the $\Delta\mu$ even though both spectra are nearly identical.

fitting range (1.20 - 1.22 eV), the extracted temperature values range from 286 K to 370 K. This even larger difference demonstrates the influence of the noise and the fitting range.

Thus, for the fits of the PL spectra of the different absorbers, the temperature is kept fixed at a value that leads to an acceptable fit. The temperatures and excitation densities used for the spectrally-resolved μ-PL experiments on all absorbers in this thesis are displayed in Table D.1. Even if these temperatures do not represent the real temperature, a variation in temperature across the absorber is excluded and the consistency of the fitting process consequently allows for the statistical evaluation of the quasi-Fermi level splitting within each sample.

The histogram in Fig. 5.12 in section 5.4.1 shows the small spatial spread of the quasi-Fermi level splitting measured on the absorber H1. For additional visualization purposes, Fig. D.12 shows all 1681 PL spectra of the $41 \cdot 41\ \mu m^2$ map, demonstrating how very similar the spectra are. Furthermore, Fig. D.13A shows two spectra exhibiting the lowest (red curve, PL spectrum number 476) and highest (blue curve, PL spectrum number 1523) $\Delta\mu$ of all the spectra. As was already indicated by the cross-correlation coefficient, the spatial variation of the quasi-Fermi level splitting is primarily due to fluctuations of the band gap energy. Fig. D.13B confirms this as it shows the shift in transition energy between the two spectra.

TABLE D.1: Rough estimations for the excitation densities used to measure the spatially-resolved photoluminescence maps on the different absorbers. Also indicated is the temperature that was used as a fixed fitting parameter to extract the quasi-Fermi level splitting for each recorded PL spectrum.

Sample	Excitation density / 10^{24} photons $m^{-2}\ s^{-1}$	Temperature / K
H1	4	310
H2	8	310
L1	12	310
L2	24	310
L3	240	340

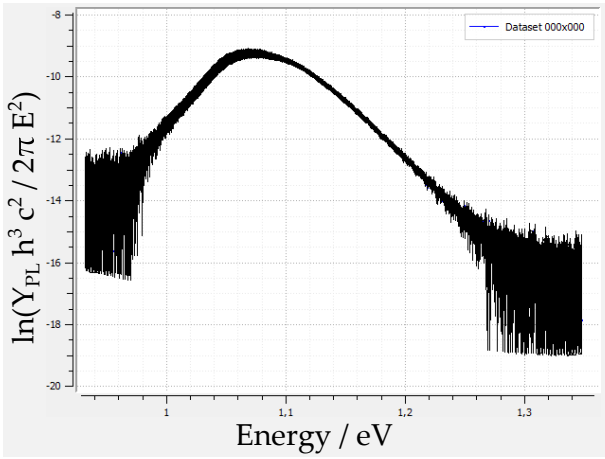

FIGURE D.12: All 1681 PL spectra that make up the $41 \cdot 41\,\mu m^2$ map of sample H1 in Fig. 5.11 in section 5.4.1.

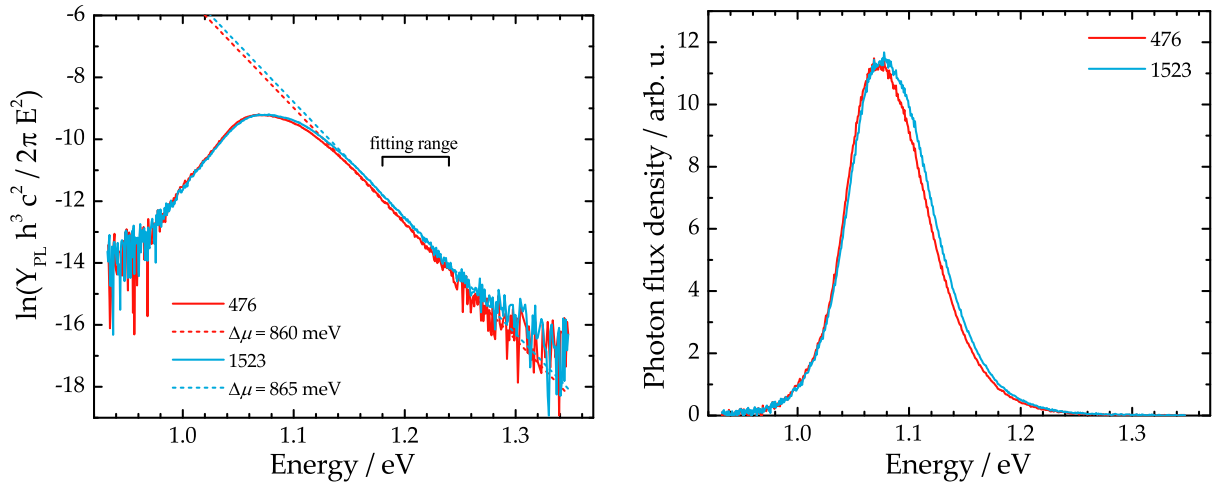

FIGURE D.13: **(A)** Photoluminescence spectra recorded on pixel number 476 (red curve) and on pixel number 1523 (blue curve) of the absorber H1. By keeping the temperature T fixed to 310 K, the fits result in $\Delta\mu = 860$ meV for the red curve and $\Delta\mu = 865$ meV for the blue curve. **(B)** In the linear representation of the PL spectra, it can clearly be seen that the difference in $\Delta\mu$ is largely due to a shift in band gap energy and not due a lower non-radiative recombination rate.

D.11 Spatially-resolved μ-PL on absorber H2

In section 5.4.1, the photon flux density, quasi-Fermi level splitting and transition energy maps of the absorber H1 are shown and discussed. The cross-correlation coefficient calculated by comparing the maps between each other indicated that the spatial variation of $\Delta\mu$ is largely due to a spatial variation of the band gap energy. Fig. D.14 shows the same maps but for the H2 absorber. The cross-correlation coefficient, as well as a straightforward judgement by eye, reveal that the spatial variation of $\Delta\mu$ is due to the unequal distribution of regions exhibiting stronger and weaker non-radiative recombination. However, the overall very low spread in $\Delta\mu$ of 1.18 meV does not allow for any further conclusion except to notice the very homogeneous nature of the H2 absorber.

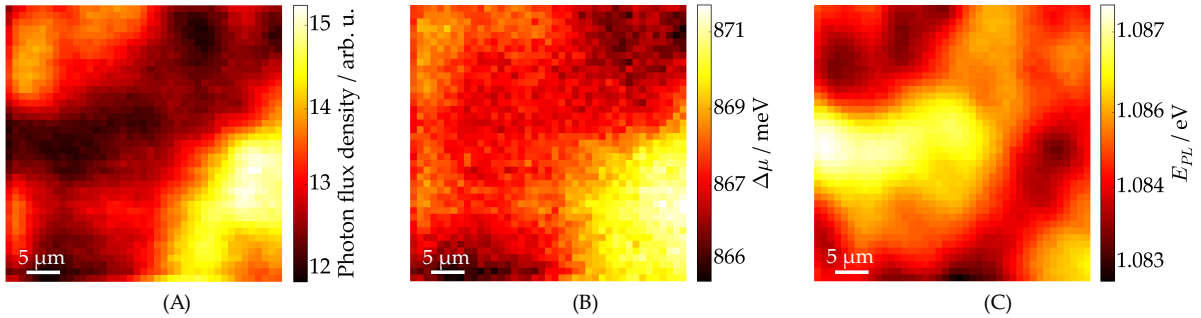

FIGURE D.14: Spatially-resolved $41 \cdot 41\,\mu m^2$ photoluminescence maps of sample H2 where each pixel represents the **(A)** integrated photon flux density Y_{PL}, **(B)** quasi-Fermi level splitting $\Delta\mu$, and **(C)** the transition energy E_{PL} of the corresponding measured spectrum.

D.12 Spatially-resolved μ-PL on absorber L1

In section 5.4.2 and Fig. 5.13, the photon flux density, quasi-Fermi level splitting and transition energy maps of absorber L1 are shown. From the statistical distribution of $\Delta\mu$, it is seen that the quasi-Fermi level splitting shows a larger spread in this low-temperature absorber compared to the high-temperature absorbers H1 and H2. For the sake of completeness, Fig. D.15 shows the PL spectra of pixel 283 (red curve) and of pixel 560 (blue curve) that both show the lowest and highest $\Delta\mu$. Furthermore, the plot reveals the difficulty of the fitting procedure on the low-temperature absorbers as the fitting range has to be narrowed as much as possible to avoid influences from interference fringes (clearly reaching up to energies of 1.25 eV) and influences from the background. The transition energy E_{PL} that is used in Fig. 5.13 is extracted from the peak around 1.1 eV.

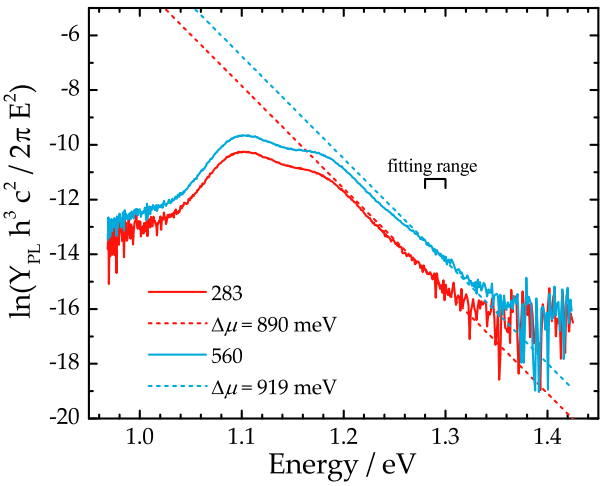

FIGURE D.15: Photoluminescence spectra recorded on pixel number 283 (red curve) and on pixel number 560 (blue curve) of the absorber L1. By keeping the temperature T fixed to 310 K, the fits result in $\Delta\mu = 890$ meV for the red curve and $\Delta\mu = 919$ meV for the blue curve.

D.13 Influence of excitation density on absorber H1

In the study [238] by Gütay *et al.*, it was shown that the spatial variation of $\Delta\mu$ is highly dependent on the excitation density. Due to the weak collection of the emitted PL, it is necessary to use high excitation densities to analyse signals that are not completely dominated by noise. To still be able to measure decent signals even at lower excitation densities, the absorbers were cooled down to a temperature of 83 K where non-radiative recombination processes are rendered more improbable. At this temperature, the standard deviation of $\Delta\mu$ doubles when measured across two orders of magnitude of excitation density. These results are then extrapolated

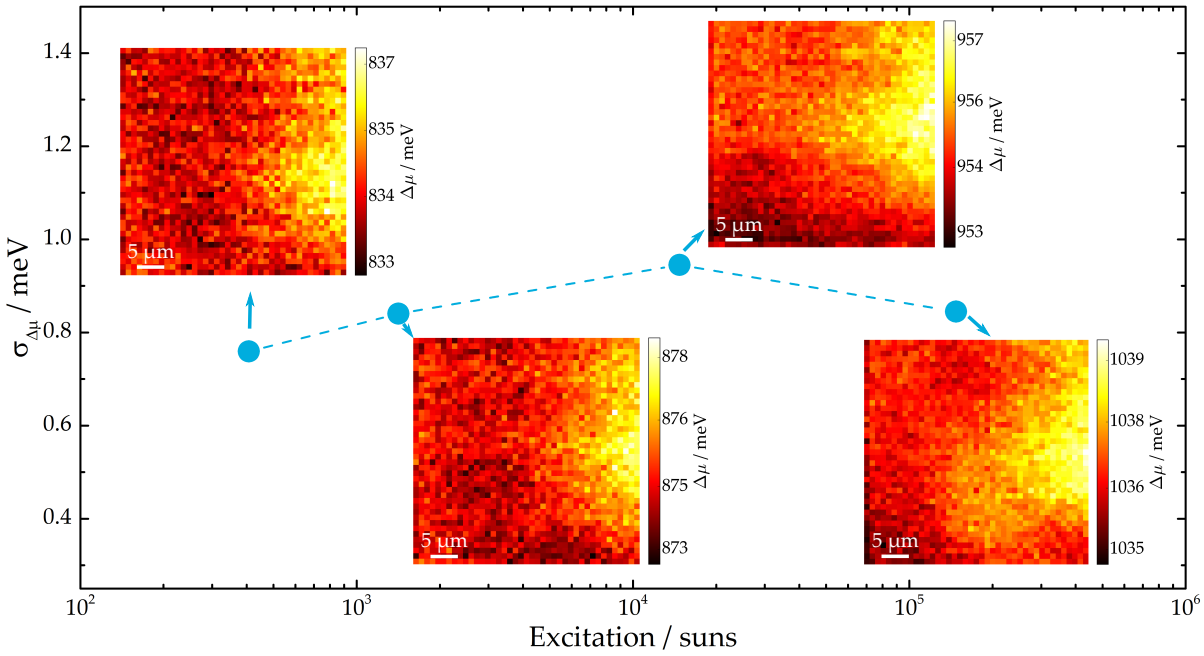

FIGURE D.16: Standard deviation of the QFLS $\sigma_{\Delta\mu}$ of sample H1 measured for different excitation densities at room temperature. Also included are the respective maps.

to room temperature where the spatial variation of $\Delta\mu$ was only measured for two distinct excitation densities that only differ by a factor of 2. Thus, the study assumes that the spatial variation of $\Delta\mu$ behaves identically at room temperature as it does at lower temperatures based on only two data points. This is a very dangerous assumption, especially considering that recombination processes at low temperatures are completely dominated by electrostatic potential fluctuations in Cu-poor CIGS absorber (cf. section 6.2). Nonetheless, to verify the claims of the study [238], the influence of the excitation density on the spatial distribution of the involved quantities is verified on absorber H1. This absorber is chosen because it emits the highest PL signal and can thus, even at room temperature, be measured with very low excitation densities. In this context, Fig. D.16 shows the standard deviation of the QFLS $\sigma_{\Delta\mu}$ for different excitation densities at room temperature. The excitation densities used are similar to the ones reported in the study [238]. The plot clearly demonstrates that the spatial variation of $\Delta\mu$ does not depend on the excitation density at room temperature (at least in the investigated excitation range). While similar measurements on the low-temperature absorbers are missing, it is assumed that they behave very similarly.

E Appendix of Chapter 6

E.1 Spectral calibration function for the InAs detector

In section 6.1, the PL spectra measured in the InAs photovoltaic diode detector at 10 K of samples H2 and L3 are shown. The spectra are presented as raw data, without background correction and spectral calibration. The general procedure of spectrally calibrating the measured PL spectra is described in section 3.1.1, with the specific procedure for the extended setup and the InAs detector being presented and discussed in the following. Fig. E.1A shows the known spectrum for calibration (red curve) as well as the measured spectrum in the extended setup of the halogen lamp (blue curve). Both spectra are normalized to enable a comparative view[1]. While the known halogen lamp spectrum is smooth, the measured spectrum shows several kinks which are either due to water vapour absorption or change of long pass (LP) filters in the double-monochromator (indicated by black arrows in the figure).

Fig. E.1B shows the calibration function (CF) spectrum (green curve) that is retrieved by dividing the known halogen lamp spectrum by the measured spectrum. Due to dispersion and losses of the collected light, the measured lamp spectrum approaches low photocurrent values

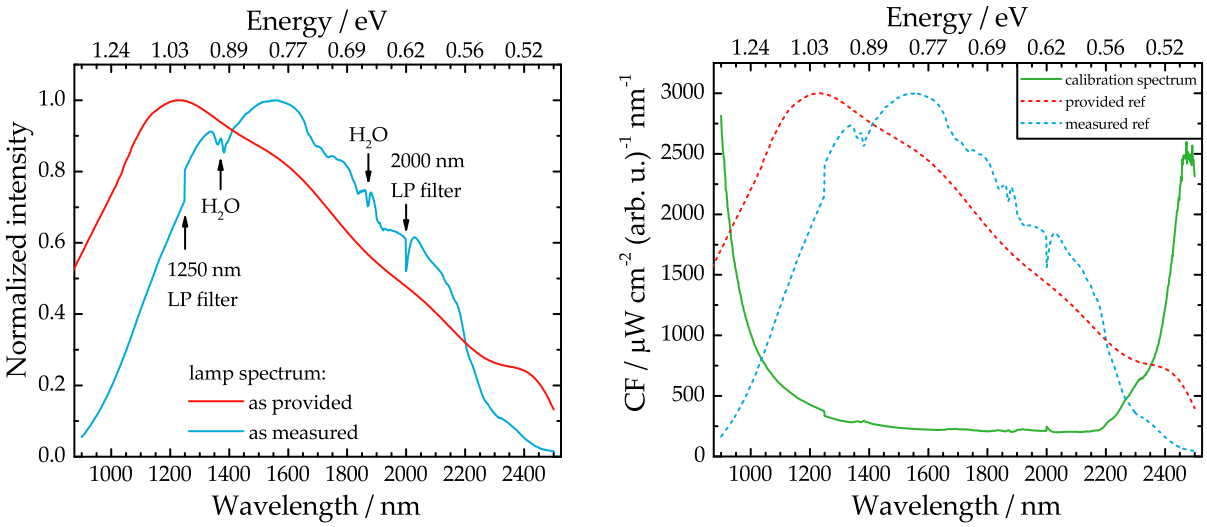

FIGURE E.1: **(A)** Normalized spectra of the halogen lamp used for spectral calibration. The red curve shows the lamp spectrum as provided by the manufacturer (in $\mu W\,cm^{-2}\,nm^{-1}$) while the blue curve shows the measured lamp spectrum (in arbitrary units). The various kinks in the measured lamp spectrum are due to water vapour absorption or filter changes and are accordingly indicated. **(B)** Calibration function spectrum (green curve) resulting from the division of the known spectrum by the measured spectrum. Both lamp spectra are scaled and represented by dashed curves to better visualize their differences and how they relate to the calibration function.

[1]For the record: the known halogen lamp spectrum is provided in $\mu W\,cm^{-2}\,nm^{-1}$ while the InAs detector measures the lamp spectrum as a photocurrent, typically in μA.

at small and large wavelengths. Consequently, the division of both spectra leads to very large values for the calibration function at small and large wavelengths.

E.2 Spectral calibration of absorbers H2's PL spectrum

The influence of the calibration spectrum on the measured sample spectra is exemplified in Fig. E.2 on the basis of absorber H2. Fig. E.2A shows the raw PL spectrum which is the same that is shown in Fig. 6.1A in section 6.1. Applying the calibration function spectrum to the raw spectrum by means of multiplication yields the spectrum in Fig. E.2B. Due to the large values of the spectral calibration spectrum at small and large wavelengths, as shown in Fig. E.1B, some artificial signals occur at these wavelengths (highlighted by the red arrows). The subsequent Jacobian conversion to switch from wavelength to energy space [173] results in a spectrum with even more artificial signals (due to the non-linearity of the Jacobian conversion) in Fig. E.2C. The reason for the occurrence of these additional signals is mainly a non-zero background signal. Consequently, it should appear logical that a spectral calibration of the

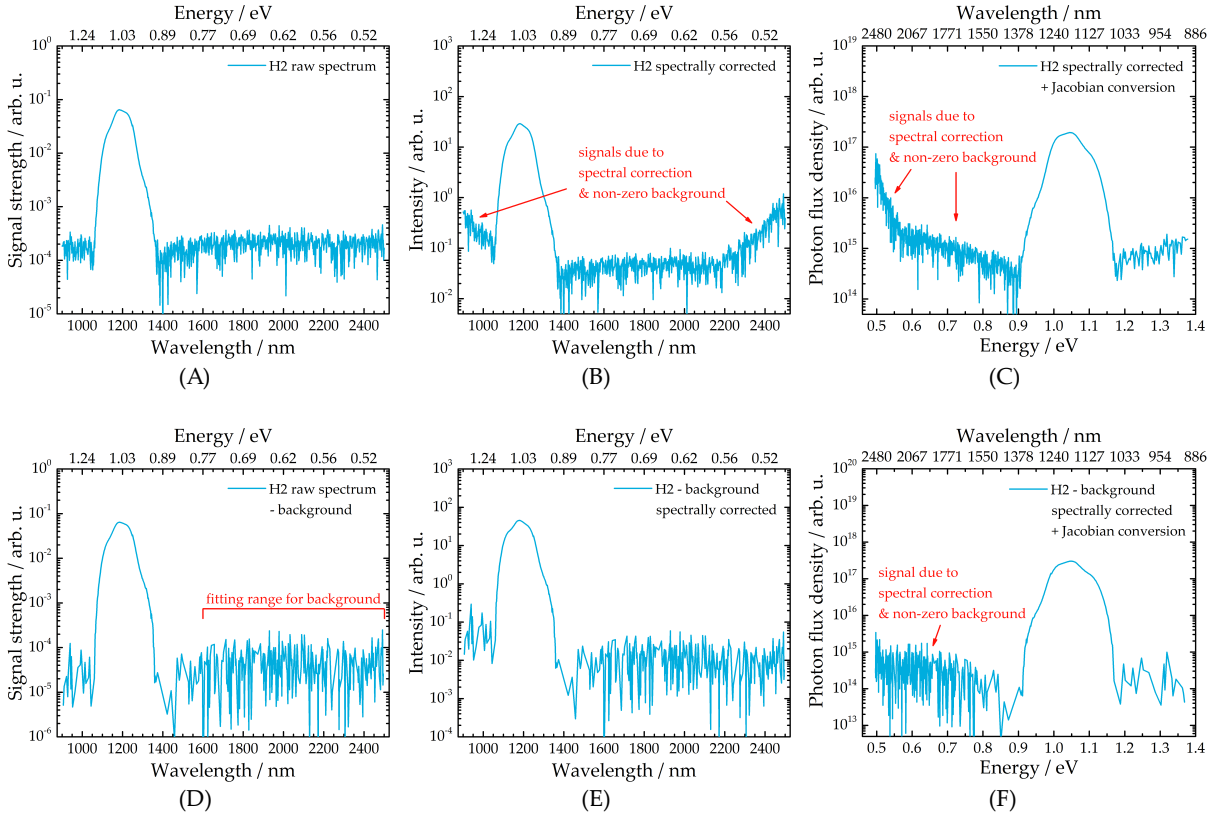

FIGURE E.2: Series of PL spectra that show the influence of the spectral calibration on absorber H2 when measured in the extended setup. For the graphs in the upper row, the background signal is not subtracted. The standard procedure of spectral calibration is to multiply the raw spectrum **(A)** with the calibration function, resulting in **(B)**. Due to a non-zero background, the spectral calibration introduces additional signals at small and large wavelengths. A subsequent Jacobian conversion from wavelength to energy space in **(C)** amplifies these artificial signals. By contrast, the lower row shows the spectrum **(D)** where the background was identified from the near-infrared signal noise and subtracted from the measured raw PL spectrum. In this case, the spectral calibration **(E)** does not lead to the occurrence of discernible artificial signals in wavelength space. However, after a Jacobian conversion to energy space **(F)**, the non-ideal background correction leads to some remaining artificial signals being observed.

measured spectrum after background subtraction should prevent the occurrence of artificial signals.

In this context, Fig. E.2D shows the raw spectrum of absorber H2 where the background signal is subtracted. The background signal is determined by fitting the measured spectrum at large wavelengths (fitting range from 1600 nm to 2500 nm in this case) by a linear function with zero slope. Since the measured spectra are displayed in semi-logarithmic representation, the data that are below or equal 0 after the background subtraction are culled, explaining the reduced amount of data points in Fig. E.2D as compared to Fig. E.2A. After applying the spectral calibration to the background-subtracted spectrum in Fig. E.2E, no additional signals are detected in the near-infrared range. The subsequent Jacobian conversion then leads to the spectrum in Fig. E.2F showing a significantly different picture than Fig. E.2C where no background subtraction was performed. However, due to the large noise in the mid-infrared range, the background subtraction, as described above, cannot be executed to such a degree where the non-linear Jacobian conversion does not introduce the semblance of artificial signals. The only remedy to this problem would be to remove all the data in the mid-infrared range. Instead of resorting to this solution, it is decided to show the spectra in their raw state where no data manipulation is done. While the representation of the raw spectrum fails to highlight the real spectral shape of the radiative transition peak, it is clearly sufficient to show the absence of distinct signals at wavelengths beyond the peak.

E.3 Comparison: extended vs. conventional setup

To verify the validity of the measurements shown above and in section 6.1, the samples are also measured in the conventional PL setup with the InGaAs CCD array. In this context, Fig. E.3 shows the spectrally calibrated PL spectrum of absorber H2 as measured in the InAs (blue curve) and in the InGaAs detector (red curve). The spectral shape of the radiative transition differs from the one presented in Fig. 6.1A and Fig. E.2 as the absorber was measured under a lower excitation density to prevent signal saturation of the InGaAs detector. Both spectra show a nearly identical radiative transition with some slight discrepancies that could be explained by the significantly poorer signal collection and thus larger noise contribution in the extended setup (InAs). It can thus be concluded that the measured spectra in the extended setup are real and that no alien signals are introduced (apart from the ones discussed in the previous section E.2).

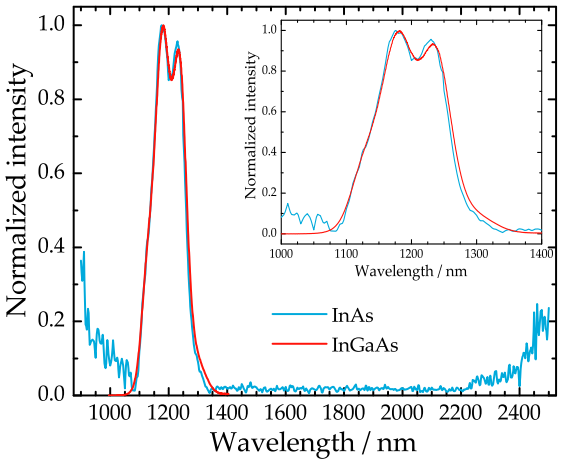

FIGURE E.3: Normalized and spectrally calibrated PL spectra of absorber H2, measured at 10 K in the extended setup (InAs detector - blue curve) and in the conventional setup (InGaAs detector - red curve). The inset shows an enlarged view of the main radiative transition and allows for an improved comparison of both spectra.

E.4 Influence of excitation density on the PL spectrum at 10 K

Due to the poor signal collection and large noise contribution to the measured PL spectra in the extended setup, large excitation densities need to be used to measure adequate signal strengths such that possible deep-level transitions are discernible from the background noise. However, when using too large excitation densities, the samples heat up and the PL spectra are distorted. This effect is shown in Fig. E.4 where the absorber H2 was measured under an excitation flux density of approximately $5 \cdot 10^{23}\,\mathrm{m}^{-2}\,\mathrm{s}^{-1}$ (red curve) and under a higher excitation flux density of approximately $2 \cdot 10^{25}\,\mathrm{m}^{-2}\,\mathrm{s}^{-1}$ (blue curve). When measured under the 40 times higher excitation flux density, the collected signal strength of the main transition almost increases twofold but also allows for the occurrence of interference fringes (indicated in black) on the low-energy slope. This leads to severe complications in the interpretation of the data as possible deep-level defects around 1550 nm (i.e. 0.8 eV) become non-discernible. Thus, in the trade-off between larger signals with its distorted PL features and lower signals with undistorted spectra, the latter is chosen.

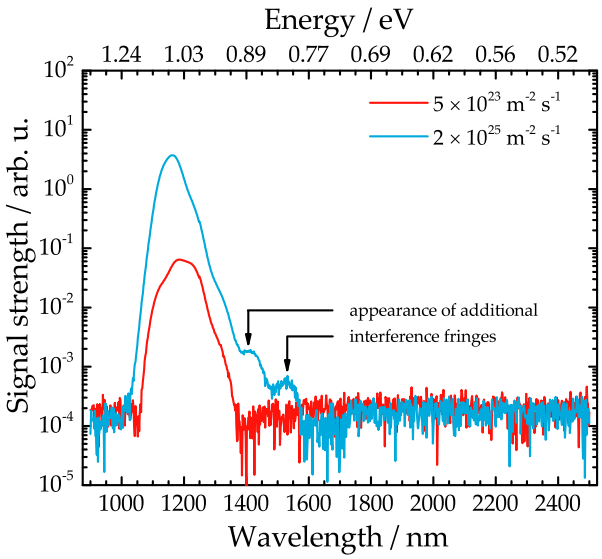

FIGURE E.4: Raw PL spectra of absorber H2 measured at 10 K in the InAs detector under a low excitation flux density (red curve) compared to a high excitation flux density (blue curve). Measuring the PL under a 40 times higher excitation flux density leads to a larger collected signal strength but also to the occurrence of interference fringes on the low-energy slope, as indicated by the black arrows.

E.5 PL spectra of samples H1, L1, L2, measured with the InAs detector

Fig. E.5 shows the PL spectra of the absorbers H1, L1, and L2 measured at 10 K with the extended setup. The recorded spectra do not hint at the presence of deep-level defects due to the absence of any signal in the near-infrared range.

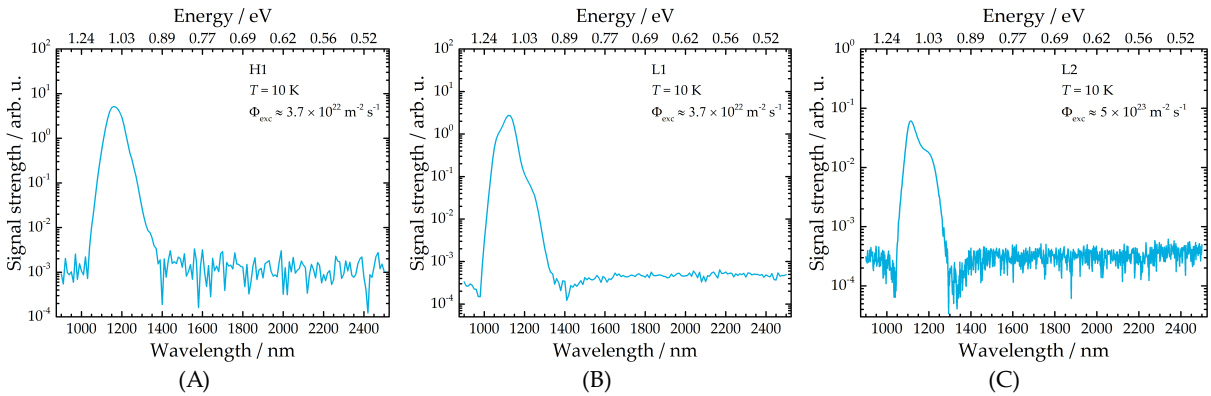

FIGURE E.5: PL spectra measured with the extended setup at a temperature of 10 K on absorbers **(A)** H1, **(B)** L1, and **(C)** L2. The measurements were done at the excitation flux density indicated in the top-right corner of the graphs. Due to the varying optoelectronic quality between the absorbers, the excitation flux density was adjusted. The spectra are displayed in the semi-logarithmic scale to better visualize the signal strength of the main transition and the absence of signals in the near-infrared range.

E.6 Low-temperature PL of HS, H1, and L2

In section 6.2.1 it is shown that the polystyrene scattering layer removes the interference fringes from the PL spectra measured at various temperatures. Doing so reveals distinct features such as an additional radiative transition at low energies. While the general behaviour of these temperature-dependent PL spectra is also seen in other interference-free samples and in literature, it is not entirely certain whether the spectra are completely interference-free. To that end, in the following, the PL spectra of three different samples are analysed and compared to the measured reflectance.

The first sample is the CdS-covered absorber HS whose surface shows a particularly high roughness (cf. Fig. 4.7 in section 4.2.1) which results in only very weak interference fringes. While these interference fringes are too weak to affect the PL spectrum at room temperature, at low temperatures however, after a redshift of the radiative emission, the weak interference fringes manifest as small bumps in the PL spectrum. This is shown, for example, in Fig. E.6A where the PL spectrum measured at 80 K is compared to the reflectance spectrum.

The second sample is the PS- and CdS-covered H1 absorber whose PL spectra at temperatures of 80 K and 40 K are shown alongside its reflectance spectrum in Fig. E.6B. While this absorber usually shows moderate interference fringes, the polystyrene layers are able to completely eliminate them which is clearly seen in the reflectance spectrum. As a consequence, the PL spectra do not show bumps that resemble the ones seen for absorber HS. It can thus be safely concluded that the interference fringes do not affect the sample H1. The same conclusion is reached for sample H2 (spectra not shown here).

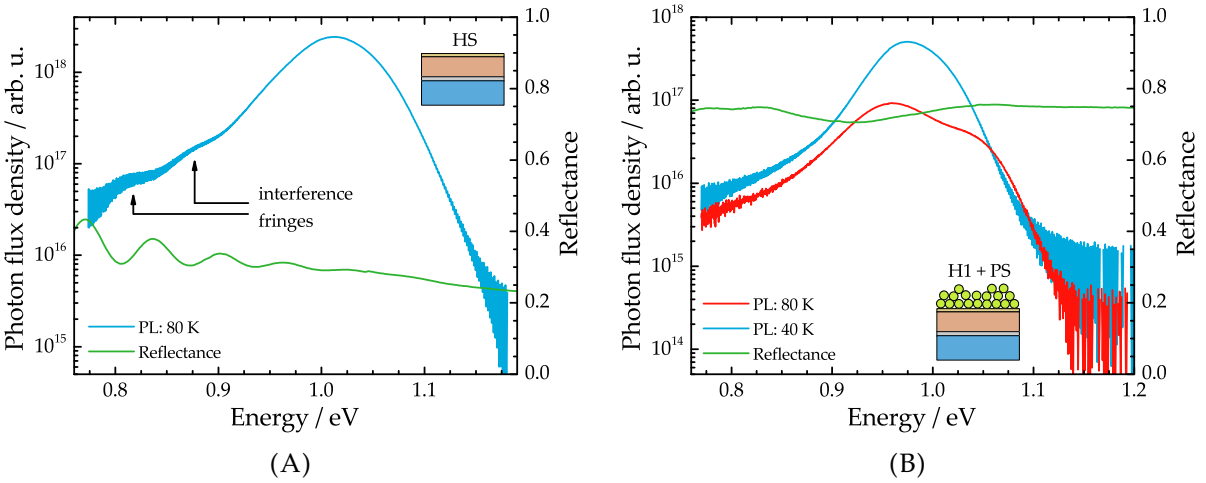

FIGURE E.6: **(A)** PL spectrum measured at 80 K (blue curve) and reflectance spectrum measured at room temperature (green curve) on the CdS-covered absorber HS. The bumps in the PL spectrum at low energies are due to interference fringes. **(B)** PL spectra measured at 80 K (blue curve) and 40 K (red curve) as well as reflectance spectrum measured at room temperature (green curve) on the PS- and CdS-covered absorber H1.

The third sample is the PS- and CdS-covered absorber L2. Fig. E.7 shows the PL spectra measured at both 140 K and 50 K as well as the reflectance spectrum. In the reflectance spectrum, some fringes are still observable. While these fringes are much weaker than the fringes that are observed without polystyrene layers (cf. Fig. C.9B in appendix C.8), they are still non-negligible and appear stronger than for the HS absorber in Fig. E.6A. Here it needs to be mentioned that the reflectance spectrum was measured after the temperature-dependent PL measurements. As such, one can think of two instances that could change the interpretation of the results: in a first instance, it is not known how the temperature affects the polystyrene beads. While the PS layers did not change appearance during and after the temperature-dependent measurements, it is still possible that their properties are changed. Thus the reflectance of the PS-covered absorber after the temperature-dependent measurement might not represent the properties prior to the measurement. Secondly, the sample has to be transferred from one laboratory to another and installed in the spectrophotometer to measure the reflectance. As such, an involuntary mechanical change to the PS layers cannot be excluded.

Looking at the PL measured at 50 K reveals no bumps in the spectrum. A similar observation is made for the PL spectrum measured at 140 K where no bumps are seen at low energies. At energies slightly above 1.0 eV, a bump can be identified but it is unclear if this bump is due to a real transition or due to interference effects. Fact is: the PL spectra at both temperatures show a very similar photon flux density (due to different excitation densities). It can thus be concluded that the emitted intensity of the PL is not important for the appearance of interference fringes (as one could expect that a higher signal leads to an improved distinction of interference effects). The PL spectrum measured at 50 K clearly makes the case of the interference fringes not affecting the PL while the spectrum measured at 140 K could argue for the influence of interference fringes. Looking at the properties that characterize the phenomenon of interference fringes in thin films, described in section 4.2, it can also be concluded that the temperature has a minimal effect on the properties of interference fringes, if at all.

Given the above insights coupled with the results from the angle-resolved measurements in section 4.4.5, it is assumed that the interference fringes do not affect the PL spectra of the low-temperature absorber L1, L2, and L3 when coated with polystyrene layers and measured at low temperatures. However, the results should still be handled with caution and interpreted with a tiny but healthy amount of scepticism.

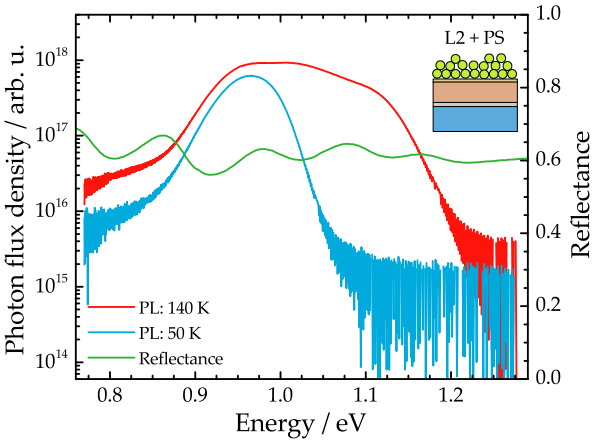

FIGURE E.7: PL spectra measured at 140 K (red curve) and 50 K (blue curve) as well as reflectance spectrum measured at room temperature (green curve) on the PS- and CdS-covered absorber L2. For the PL spectra to display similar photon flux densities, the spectra measured at different excitation densities are chosen for comparison in this case.

E.7 PL of H1 at 12.5 K and 20 K

The excitation-dependent PL spectra of sample H1 measured at temperatures of 12.5 K and 20 K are shown in Fig. E.8A and Fig. E.8B respectively. Across all excitation densities, both a low-energy and high-energy peak are visible. This is in contrast to the spectra measured at slightly higher temperatures where only one peak at low energies is ever observable (cf. Fig. 6.4B e.g.). The exact nature of the high-energy peak at very low temperatures is not exactly known but it is suspected that it relates to the slightly higher band gap at the surface of the absorber (cf. band gap grading in Fig. 4.2). Due to the low thermal energy of the excited charge carriers, the diffusion into the bulk band gap minimum is impeded such that a portion of the charge carriers recombine from the surface band gap. To verify this assumption, further investigation are needed but are not subject of this thesis.

Given the not yet disclosed nature of the high-energy peak, it was decided to concentrate on the low-energy peak. However, both peaks were fitted by separate Gaussians to ensure that the overall fit provides a satisfying description of the spectrum. Consequently, the high-energy peak energies at the temperatures 12.5 K and 20 K are not plotted in Fig. 6.6.

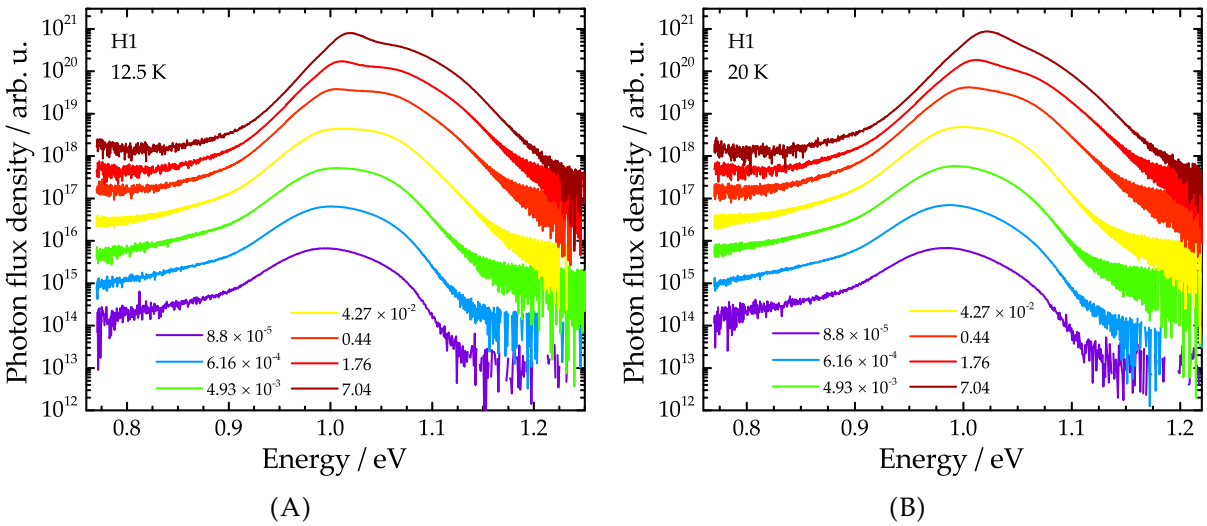

FIGURE E.8: PL spectra of sample H1 measured under various excitation densities and at a temperature of **(A)** 12.5 K and **(B)** 20 K.

E.8 PL of H2 at 80 K under different excitation densities

When describing Fig. 6.8 in section 6.2.2 it was mentioned that the high-energy peak in the PL spectra of absorber H2 at a temperature of 80 K is completely dominated by the low-energy peak at high excitation densities. To illustrate this dominance, Fig. E.9 shows the PL spectra measured under the lowest and highest excitation densities. At the lowest excitation density, the PL spectrum can be fitted with three Gaussians: one Gaussian to account for the low-energy tailing (red curve), one Gaussian to describe the low-energy peak (blue curve), and one Gaussian to describe the small high-energy peak (green curve). The accumulated fit is not shown but agrees extremely well with the measured spectrum. At the highest excitation density, a single Gaussian is sufficient to describe the low-energy peak (blue curve), demonstrating that the high-energy peak is completely negligible (if it is still there at all). Additionally, a minor tailing at lower energies is observed but is omitted in the fitting procedure.

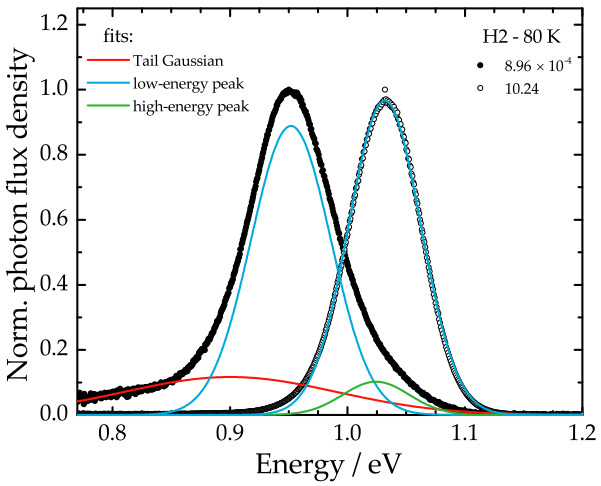

FIGURE E.9: PL spectra of absorber H2 measured at 80 K under the lowest (closed black circles) and highest excitation density (open black circles). When measured under the lowest excitation density, the PL spectrum can be fitted with three separate Gaussians. Under the highest excitation density, the PL spectrum can be described by a single Gaussian. The legend in the top left corner illustrates the functions of the fits.

E.9 PL of H1 and H2 at 140 K

The main conclusion of section 6.2.2 is that the H1 absorber shows weaker electrostatic potentials than the H2 absorber. One argument that supports this conclusion is the occurrence of the low-energy peak in the H2 absorber over a broader temperature and excitation density range. More specifically, at a temperature of 140 K, the low-energy peak in the H2 absorber is still present while it was declared that the H1 absorber does not show a low-energy peak under the same conditions. In this context, Fig. E.10 shows the excitation-dependent PL spectra of sample H1 and H2 at 140 K. Fig. E.10B undeniably shows both a low- (peak #1) and a high-energy peak (peak #2) across all five excitation densities in the H2 sample. But Fig. E.10A reveals that there is also a small bump at low energies and low excitation densities in the H1 sample. *A priori*, it is not unreasonable to also consider this bump as a low-energy peak. Alternatively, the bump can also be regarded as a strong tailing. Ultimately, it was attempted to fit the bump with a low-energy Gaussian peak but no parameter set yielded an overall satisfying description of the PL spectra. It was thus concluded that there is no low-energy peak in the H1 sample at 140 K.

This example demonstrates the occasional ambiguity of the fitting process and that different fitting attempts (or subjective views) can potentially lead to different outcomes.

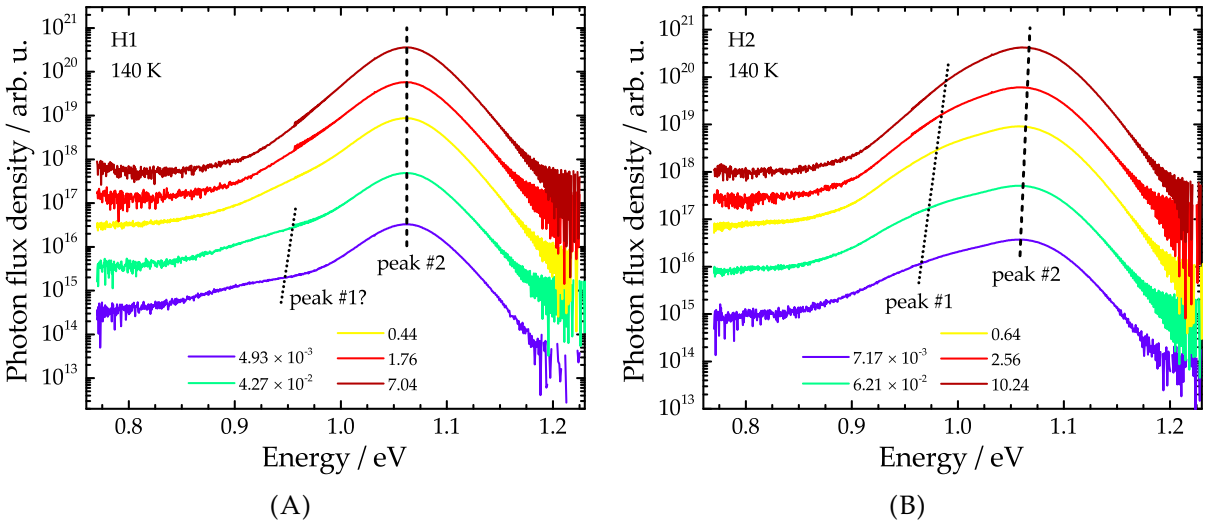

FIGURE E.10: **(A)** PL spectra of sample H1 measured at 140 K under various excitation densities. The spectra are dominated by the high-energy peak (peak #2 - dashed line). Under low excitation densities, a low-energy peak is potentially visible (peak #1 - dotted line) **(B)** PL spectra of sample H2 measured at 140 K under various excitation densities. Under all measured excitation densities, the low-energy and high-energy peaks are visible.

E.10 PL spectra of L1 and L3 at different temperatures

In Fig. 6.11 in section 6.2.3 only the high-energy peak is plotted for a relatively narrow temperature range from 20 K to 100 K. The reason being that the PL spectra measured at lower and higher temperatures show a more peculiar behaviour through the exhibition of up to three peaks. In this context, Fig. E.11A shows the PL spectra of absorber L1 measured at 11 K under varying excitation densities. The straight, dashed, and dotted lines visualize the three different peaks that appear and disappear/merge for different excitation densities. For example, under low excitation densities only peak #1 and peak #2 are visible. Under high excitation densities, peak #1 disappears (or goes over to a large tailing), peak #2 is still visible while an additional peak #3 becomes visible. Under certain excitation densities, these three peaks are visible simultaneously which makes their characterization with 3 Gaussian fits extremely challenging as a multitude of different set parameters can yield agreeable overall fits. This situation is clearly different from the situation in the high-temperature absorbers where a third Gaussian is only ever used to fit a clear low-energy tail where its fitting parameters can be severely restricted (cf. Fig. 6.5B in section 6.2.2).

The same challenging fitting situation presents itself at temperatures above 100 K. For example, Fig. E.11B shows the PL spectra of absorber L3 measured at 120 K under five different excitation densities. The presence and shifts of the three different peaks are indicated by the lines. Interestingly, peak #3 at the highest energies translates into the band-to-band transition at room temperature. This shows that the two peaks at low energies and lower temperatures (excluding the spectra at 11 K) are very likely defect related. Of these two peaks at low energies, only the high-energy peak #2 can reliably be fitted across a wider temperature and excitation range. This is why this peak energy is chosen as the plotted quantity in Fig. 6.11.

While Figs. E.11A and E.11B act only as examples, the same behaviour is observed across all three low-temperature absorbers. Looking at the PL spectra of the high-temperature absorbers in appendix E.7, a common behaviour shared between all absorbers can be recognized. At the lowest temperatures, the PL measured on both sample sets shows a high-energy peak that

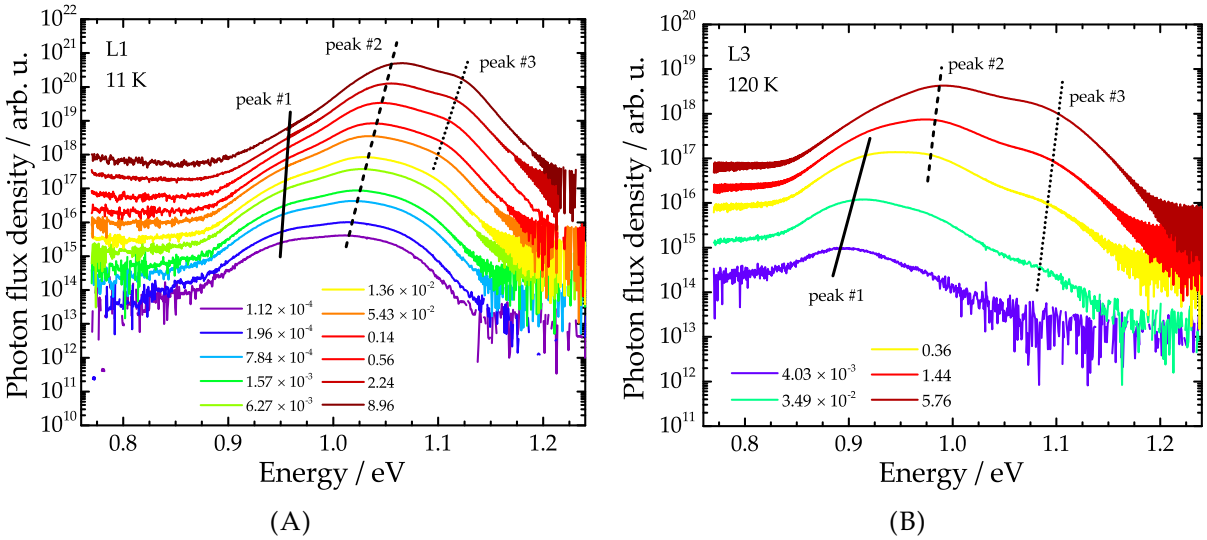

FIGURE E.11: **(A)** PL spectra of sample L1 measured at 11 K under various excitation densities. The spectra show the occurrence of three distinct peaks: a low-energy peak #1 (straight line), a high-energy peak #2 (dashed line) and a higher-energy peak #3 (dotted line). **(B)** PL spectra of sample L3 measured at 120 K under various excitation densities. The spectra show the occurrence of three distinct peaks: a low-energy peak #1 (straight line), a high-energy peak #2 (dashed line) and a higher-energy peak #3 (dotted line). The different peaks between **(A)** and **(B)** do not necessarily relate to each other.

is not seen as such at intermediate temperatures. This peak can tentatively be assigned to the recombination of the PL from the surface band gap minimum. Furthermore, while there seems to exist a single defect-related transition in the high-temperature absorbers, the two transitions seen in the low-temperature absorbers are also supposed to be defect-related. Under the assumption that this identification is correct, the low-energy peaks can then be analysed in dependence to temperature and excitation density even if their exact assignment to specific radiative transitions is not subject of this thesis.

F Appendix of Chapter 7

F.1 Absorption coefficient of $CuInSe_2$ absorber

In section 7.1.1, the V_{OC} deficit of various samples is plotted in dependence of the sample's Urbach energy. While the Urbach energies of most samples have already been presented in chapter 5 and its corresponding appendix D, Fig. F.1 shows the absorption coefficient spectrum of the $CuInSe_2$ absorber. Due to the relatively bumpy low-energy slope (interference effects can be excluded), the Urbach energy varies significantly depending on the fitting range. This leads to a rather large statistical distribution of extracted Urbach energies, which is ultimately reflected in the wide error bar attributed to this sample in Figs. 7.1 and F.3.

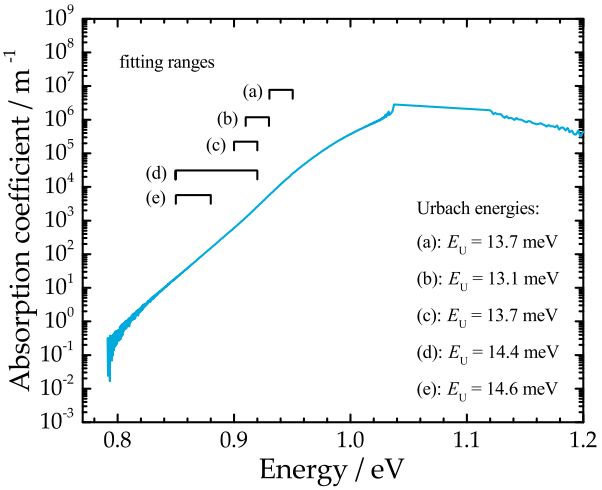

FIGURE F.1: Absorption coefficient spectra of the CdS-covered $CuInSe_2$ absorber. Visualized are 5 different fitting regions with the corresponding extracted Urbach energies indicated in the bottom-right corner.

F.2 Band tails in the Shockley-Queisser model

In Fig. 7.1 of section 7.1.1, the open-circuit voltage deficit $E_g - qV_{OC}$ is graphically visualized in dependence of the Urbach energy E_U. Next to the measured data, a modified Shockley-Queisser model for the V_{OC} deficit is shown. It serves as a proof that the radiative losses in V_{OC} with increasing E_U are much too small to account for the real measured V_{OC} losses. The simulated model will briefly be explained in the following (some of the mathematical expressions have already been derived and introduced, but, for convenience purposes, will be repeated here).

The Shockley-Queisser model was introduced in section 2.4 with one of its core assumptions being that the semiconductor exhibits a step-like absorption. By modifying this assumption, i.e. by allowing for tail states below the band gap energy to contribute to both absorption and emission, the Shockley-Queisser model can be adjusted to also include radiative losses through states that extend exponentially into the band gap. This is done by assigning the absorption

coefficient $\alpha(E)$ from eq. (5.6) to the absorption properties below the band gap energy E_g:

$$\alpha(E) = \begin{cases} \alpha_0 \exp\left(-\frac{E_0 - E}{E_U}\right), & \text{for } E < E_g \\ \alpha_0, & \text{for } E \geq E_g. \end{cases} \tag{F.1}$$

For reasons of simplification $E_0 \approx E_g$ is assumed, and to ensure that the absorptivity above E_g equals unity, α_0 is set to $10^5\,\mathrm{cm}^{-1}$. The latter is a very strong simplification as the absorptivity coefficient above the band gap is not constant but follows a square-root behaviour (cf. section 2.7.1). The absorption coefficient $\alpha(E)$ can then be inserted into the simple expression that was used for the absorptivity $a(E)$ in eq. (5.4) i.e.

$$a(E) = 1 - \mathrm{e}^{-\alpha(E)d}, \tag{F.2}$$

where the thickness d is assumed to be $2.5\,\mu$m. In the original SQ model the determination of j_{SC}^{SQ} and j_0^{SQ} was done via eqs. (2.16) and (2.18). In order to account for a non-step-like absorption, the absorptivity $a(E)$ is included in the expressions while still assuming, as postulated by the SQ model, that the carrier collection is ideal. Thus, in the Shockley-Queisser-Urbach (SQU) model, the short-circuit j_{SC}^{SQU} and saturation current density j_0^{SQU} are

$$j_{SC}^{SQU} = q \int_0^\infty a(E) \cdot \Phi_{sun}(E)\,\mathrm{d}E, \tag{F.3}$$

$$j_0^{SQU} = q \int_0^\infty a(E) \cdot \Phi_0(E, T = 296K)\,\mathrm{d}E. \tag{F.4}$$

where $\Phi_0(E, T = 296K)$ is the photon flux density emitted as thermal radiation at a temperature of 296 K from eq. (F.6). Inserting both current densities into the expression (2.13)

$$V_{OC}^{SQU} = \frac{k_B T}{q} \ln\left(\frac{j_{SC}^{SQU}}{j_0^{SQU}} + 1\right), \tag{F.5}$$

allows to calculate the open-circuit voltage V_{OC}^{SQU} in the SQU limit. Fig. F.2A shows the calculated V_{OC}^{SQU} for increasing Urbach energies E_U for three different band gap energies (left-hand y-axis). These band gap energies are chosen to roughly represent the lowest measured value (1.08 eV) and the highest measured value (1.15 eV) for the CIGS absorbers/solar cells investigated in this thesis. The band gap energy of 1.42 eV corresponds to the one of the GaAs semiconductor material. Additionally, the V_{OC}^{SQU} deficit is displayed as well (right-hand y-axis). From the simulated curves, it is clear that the band gap energy does not lead to a strong change in the V_{OC}^{SQU} deficit, neither in absolute values nor in the slope, for Urbach energies below $k_B T$ at room temperature. However, for Urbach energies larger than $k_B T$, the saturation current density j_0^{SQU} rises sharply which leads to strong losses in V_{OC}^{SQU}, even at a fixed band gap energy. The rise of the saturation current density for Urbach energies above $k_B T$ can be understood by analysing the black body (BB) radiation $\Phi_0(E)$:

$$\Phi_0(E) = \frac{2\pi}{h^3 c^2} \frac{E^2}{\exp\left(E/k_B T\right) - 1}. \tag{F.6}$$

The photon flux density from the room temperature BB radiation increases sharply with increasing energies and assumes a maximum at approximately 41 meV. At energies larger than $E \gg k_B T$, the photon flux density decays near-exponentially with $E^2 \exp\left(E/k_B T\right)$. For a semiconductor material with band gap energies above 1 eV and no band tails, the emitted photon flux density from thermal BB radiation is thus very small. However, in the case of band tails,

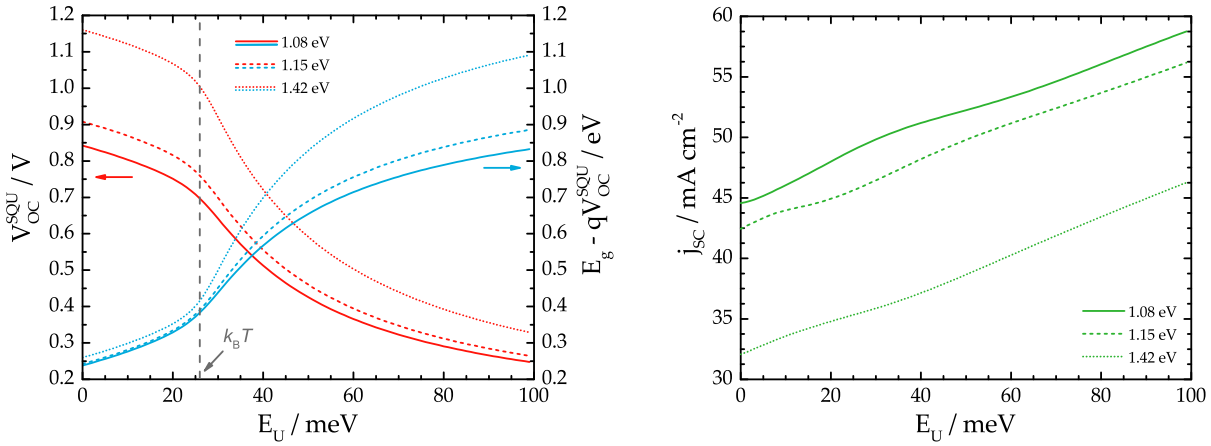

FIGURE F.2: **(A)** Open-circuit voltage V_{OC}^{SQU} (red curves and left-hand y-axis) and V_{OC}^{SQU} deficit (blue curves and right-hand y-axis) for increasing Urbach energies. The voltage is simulated via the SQU model for three different band gap energies: 1.08 eV (straight line), 1.15 eV (dashed line), and 1.42 eV (dotted line). Also included is the Urbach energy that corresponds to k_BT at room temperature (grey vertical dashed line). **(B)** Corresponding short-circuit current density j_{SC}^{SQU} in the SQU model for the three different band gaps with increasing Urbach energies.

a larger portion of thermal photons are emitted as absorption and emission below the band gap is permitted. For Urbach energies larger than k_BT, the exponential decrease of the band tails below the band gap is slower than the decrease of the photon flux density from the BB radiation which brings about the strong increase in saturation current density. A very useful visualizing of the explanation above can be found in ref. [224].

While there is a small but steady decrease of V_{OC}^{SQU} for increasing Urbach energies even below k_BT, the solar cell power conversion efficiency remains almost constant due to a steady increase of j_{SC}^{SQU}. The increase of the short-circuit current, due to states below the band gap energies that promote additional absorption, was first mentioned in appendix A.2 and is visualized in Fig. F.2B. Only above k_BT, where V_{OC}^{SQU} collapses, are strong reductions in the efficiency expected.

The model here is a very simple approach, most notably expressed in the straightforward expression for the absorptivity $a(E)$ in equation (F.2) that is derived from Lambert-Beer's law for a planar front surface and no multiple reflections within the absorber. There exist more sophisticated models that consider Lambertian light trapping with total back-surface reflection. In these models, the mathematical expression for the absorptivity becomes significantly more involved [309]–[311]. On the basis of such an absorptivity, Jean *et al.* computed the radiative losses in V_{OC} with increasing Urbach energies [224]. While a direct comparison between the simple model employed here and the more sophisticated model of Jean *et al.* reveals some differences, these are too small to be deemed significant (especially for Urbach energies below k_BT).

Due to small differences in $E_g - qV_{OC}^{SQ}$ below k_BT as seen in Fig. F.2A, the model that is included in Fig. 7.1 in section 7.1.1 is calculated using a band gap energy of 1.12 eV and scaled to the deficit of the GaAs solar cell.

Finally, it needs to be mentioned that the model used here is technically only valid for small Urbach energies i.e. $E_U < k_BT$. The fact that the model still returns mathematically valid values that are shown in Fig. F.2 is due to the strong assumptions of the model. However, since Fig. 7.1 in section 7.1.1 only deals with Urbach energies below k_BT, the interpretation and conclusion

remain correct.

F.3 Details of the SCAPS simulation

In section 7.1.1, the voltage loss due to non-radiative recombination through the band tails is simulated with the help of the numerical simulation tool SCAPS. Here, the details and values used for the simulation are provided. As sample, a standard Mo/CIGS/CdS/ZnO stack is assumed (for simplicity, the intrinsic ZnO layer is neglected). The details for the parameters that enter the simulation are provided in Table F.1. These parameters are inspired by refs. [41], [56] and consist of typical values used in such simulations. For the CIGS layer, the radiative recombination coefficient B is set to zero to only account for non-radiative recombination. Furthermore, the absorption coefficient $\alpha(E)$ is set to follow a square-root behaviour above the band gap energy E_g i.e.

$$\alpha(E) = \alpha_0 \sqrt{\frac{E - E_g}{k_B T}}. \tag{F.7}$$

The band tails are simulated by including two defects: a donor defect that acts a valence band tail, and an acceptor defect that acts a conduction band tail. Both defects share the same density $N_d = 5 \cdot 10^{12}\,\mathrm{cm}^{-3}$ and capture cross-section $\sigma_n = \sigma_p = 10^{-13}\,\mathrm{cm}^2$. These parameters are set such that the effective lifetime amounts to 200 ns, which is a reasonable value that is encountered in state-of-the-art CIGS absorbers [93]. To simplify the simulation, no graded band gap of the CIGS absorber is assumed.

In terms of operation, only the current-voltage curves are simulated as the simulation of V_{OC} is the main goal. Before increasing the Urbach energy in distinct steps, the V_{OC} of the solar

TABLE F.1: Parameters used for the ZnO, CdS, and Cu(In,Ga)Se_2 material in the SCAPS simulation. Indicated are the thickness d, the band gap energy E_g, the electron affinity χ, the relative dielectric permittivity ϵ/ϵ_0, the effective density of states of the conduction N_C and valence N_V bands, the thermal velocity of electrons and holes v_{th}, the electron μ_n and hole μ_p mobility, the donor N_D and acceptor N_A concentration, the prefactor α_0 of the absorption coefficient (F.7), the radiative recombination coefficient B, the electron σ_n and hole σ_p capture cross-section, and the defect density N_d.

	ZnO	CdS	Cu(In,Ga)Se_2
d / nm	200	30	3000
E_g / eV	3.3	2.4	1.12
χ / eV	4.45	4.2	4.5
ϵ/ϵ_0	9	10	13.6
N_C / cm^{-3}	$2.2 \cdot 10^{18}$	$2.2 \cdot 10^{18}$	$2.2 \cdot 10^{18}$
N_V / cm^{-3}	$1.8 \cdot 10^{19}$	$1.8 \cdot 10^{19}$	$1.8 \cdot 10^{19}$
v_{th} / $\mathrm{cm\,s}^{-1}$	10^7	10^7	10^7
μ_n / $\mathrm{cm}^2\,\mathrm{V}^{-1}\,\mathrm{s}^{-1}$	100	100	100
μ_p / $\mathrm{cm}^2\,\mathrm{V}^{-1}\,\mathrm{s}^{-1}$	25	25	25
N_D / cm^{-3}	10^{18}	10^{17}	0
N_A / cm^{-3}	0	0	10^{16}
α_0 / cm^{-1}	0	0	10^5
B / $\mathrm{cm}^3\,\mathrm{s}^{-1}$	0	0	0
σ_n / cm^2	-	-	10^{-13}
σ_p / cm^2	-	-	10^{-13}
N_d / cm^{-3}	-	-	$5 \cdot 10^{12}$

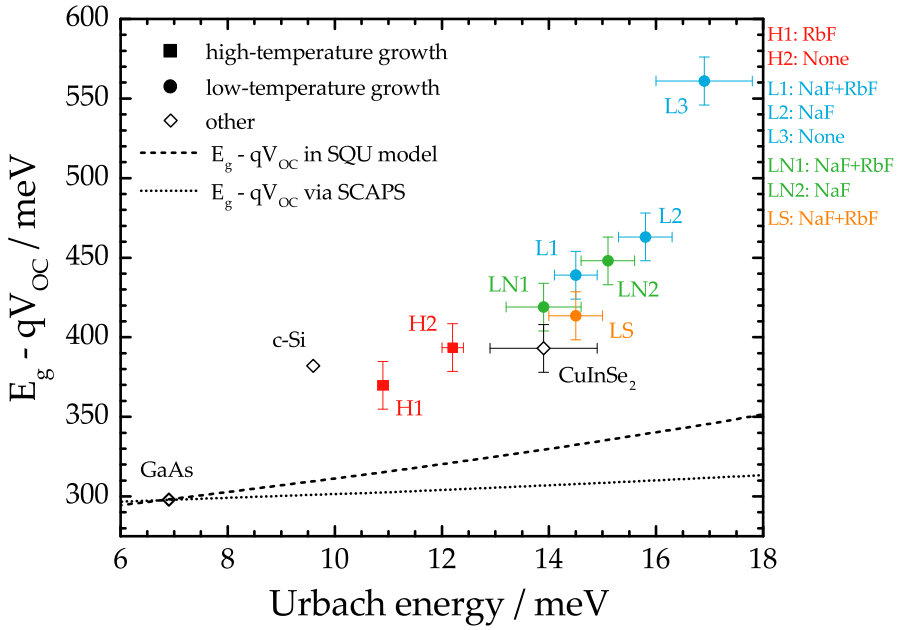

FIGURE F.3: Open-circuit voltage deficit $E_g - qV_{OC}$ in dependence of the Urbach energy E_U for solar cell devices grown under high- (squares) and low temperatures (circles). The color code refers to solar cells that were grown under the same conditions but received different post-deposition treatments. Also included are data from literature for GaAs and c-Si (open diamonds) and from a $CuInSe_2$ sample (the E_U was measured on the absorber in the in-house setup, see section F.1, while the V_{OC} was measured by Thomas Feurer from Empa who also created the device). The allocation of error bars on the Urbach energy values follows the principle laid out in section 5.3.1 while an uncertainty of 15 meV is estimated for the V_{OC} deficit. The black dashed line represents the voltage losses in the Shockley-Queisser limit but adjusted for Urbach-type sub band gap absorption and emission. The black dotted line represents the voltage losses due to non-radiative recombination of sub band gap states simulated with SCAPS. Both simulated voltage losses are scaled to the GaAs V_{OC} deficit since it is considered as the reference.

cell stack without tail influence is simulated and compared to the Shockley-Queisser limit to ensure a correct starting point.

The results of the SCAPS simulation are shown by the dotted line in Fig. F.3 and reveal no significant voltage losses following non-radiative recombination through tail states. However, it is not entirely clear how SCAPS exactly deals with the presence of band tails. This can be illustrated by a simple example. Assuming two distinct Urbach energies: $E_{U,1} = 10$ meV and $E_{U,2} = 15$ meV. With the absorption coefficient being proportional to the density of states, an increase in Urbach energy from $E_{U,1}$ to $E_{U,2}$ at 100 meV below the band gap leads to an increase in density of states of:

$$\frac{\exp\left(-0.1/E_{U,2}\right)}{\exp\left(-0.1/E_{U,1}\right)} \approx 30. \tag{F.8}$$

The influence on non-radiative recombination processes through the increase of a factor of 30 in the density of states 100 meV below the band gap can be simulated in SCAPS by placing an isolated acceptor defect 100 meV below the conduction band and varying its the density by the same factor of 30. Again, as mentioned above, the initial values (defect density, capture cross-sections) of the acceptor defect are chosen such that a minority carrier lifetime of 200 ns is calculated. After an increase of a factor of 30 in the defect density, a decrease in the V_{OC} of approximately 80 mV is simulated. While these simulated values do not necessarily represent reality, they are useful in exhibiting a different outcome to the SCAPS simulation where only band tails are considered. As of the time of writing, it is unclear why an identical increase in

the density of states through an increase in Urbach energy leads to two different outcomes.

F.4 Extracting $Q_{\mathbf{ext}}^{\mathbf{lum}}$ from EQE

Equation (7.4) in section 7.1.2 was introduced as one of Rau's reciprocity relations that links the electrical open-circuit voltage V_{OC} to the optical luminescence quantum efficiency $Q_{\mathrm{ext}}^{\mathrm{lum}}$ [262]. Under its more general form, the reciprocity relation allows to link the emitted photon flux density (optical output at V_{OC}) to the material's external quantum efficiency EQE (electrical input at j_{SC}). Under these conditions, the excess photon flux density $\phi_{\mathrm{em}}(E)$ emitted normal to the solar cell is given as [262]

$$\phi_{\mathrm{em}}(E) = \mathrm{EQE}(E)\,\Phi_0(E)\left[\exp\left(\frac{qV_{\mathrm{OC}}}{k_{\mathrm{B}}T}\right) - 1\right], \tag{F.9}$$

where $\Phi_0(E)$ is the black body radiation (F.6). Due to the application of the open-circuit bias voltage V_{OC}, the exponential term in the brackets dominates and, inserting eq. (F.6) the emitted photon flux density can be written under the form

$$\phi_{\mathrm{em}}(E) = \frac{2\pi}{h^3c^2}\,\exp\left(\frac{qV_{\mathrm{OC}}}{k_{\mathrm{B}}T}\right)\,\frac{\mathrm{EQE}(E)\,E^2}{\exp\left(E/k_{\mathrm{B}}T\right) - 1}. \tag{F.10}$$

To calculate the total emitted photon flux density, one then only needs to integrate eq. (F.10). Finally, to calculate the external luminescence quantum efficiency $Q_{\mathrm{ext}}^{\mathrm{lum}}$, the number of electron-hole pairs that are recombining inside the material has to be calculated. The number of recombining electon-hole pairs is dictated by the total absorbed incident photon flux density. Under AM1.5 conditions, the latter is just

$$\int \Phi_{\mathrm{sun}}(E)\cdot\mathrm{EQE}(E)\,\mathrm{d}E = \frac{j_{\mathrm{SC}}}{q}. \tag{F.11}$$

Thus, the external radiative efficiency can be calculated via

$$Q_{\mathrm{ext}}^{\mathrm{lum}} = j_{\mathrm{SC}}^{-1}\,\frac{2\pi q}{h^3c^2}\,\exp\left(\frac{qV_{\mathrm{OC}}}{k_{\mathrm{B}}T}\right)\int\frac{\mathrm{EQE}(E)\,E^2\,\mathrm{d}E}{\exp\left(E/k_{\mathrm{B}}T\right) - 1}. \tag{F.12}$$

Calculating the external quantum efficiency through eq. (F.12) necessitates a very clean and precise EQE spectrum. However, this is sometimes not given, especially if the data are digitized from other published sources. The validity of the approach can be verified by computing the emitted photon flux density through eq. (F.10). In fact, for $E \gg k_{\mathrm{B}}T$, the Bose-Einstein term can be approximated by a Boltzmann distribution, yielding

$$\phi_{\mathrm{em}}(E) = \frac{2\pi}{h^3c^2}\,\mathrm{EQE}(E)\,E^2\exp\left(\frac{-\left(E - qV_{\mathrm{OC}}\right)}{k_{\mathrm{B}}T}\right). \tag{F.13}$$

The emitted photon flux density in eq. (F.13) has the same form as the photon flux density given by Planck's generalized law of radiation (5.1), where the absorptivity $a(E)$ is replaced by the external quantum efficiency $\mathrm{EQE}(E)$ and the open-circuit voltage qV_{OC} by the quasi-Fermi level splitting $\Delta\mu$. This similarity is a consequence of Rau's reciprocity relations [262]. The exact conditions and limitations of Rau's reciprocity relations are not discussed here but, in the case of high-quality solar cells, they have been proven to be accurate through both experimental findings [278] and numerical simulations [312].

As an example, Fig. F.4A shows the EQE spectrum (red curve - left-hand y-axis) and the calculated emitted photon flux density $\phi_{\mathrm{em}}(E)$ (blue curve - right-hand y-axis) through eq. (F.13)

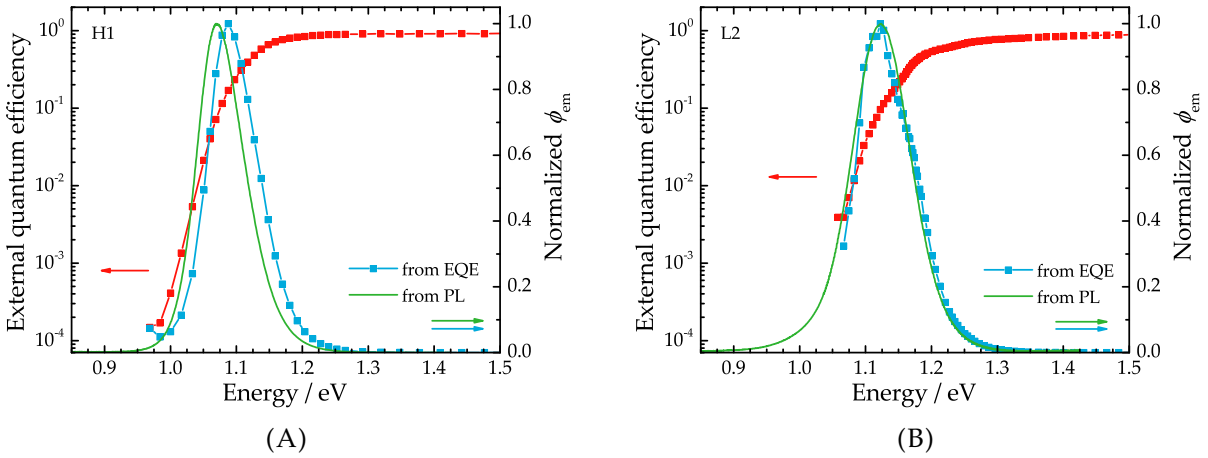

FIGURE F.4: Measured external quantum efficiency spectrum (red curve - left-hand y-axis) and calculated emitted photon flux density spectrum (blue curve - right-hand y-axis) of solar cells **(A)** H1 and **(B)** L2. Also shown are the PL spectra (green curve - right-hand y-axis) measured on the corresponding polystyrene-covered absorbers. The EQE spectra were measured and provided by Dr. Romain Carron from Empa, but, in the case of the L2 sample, did not extend to very low energies.

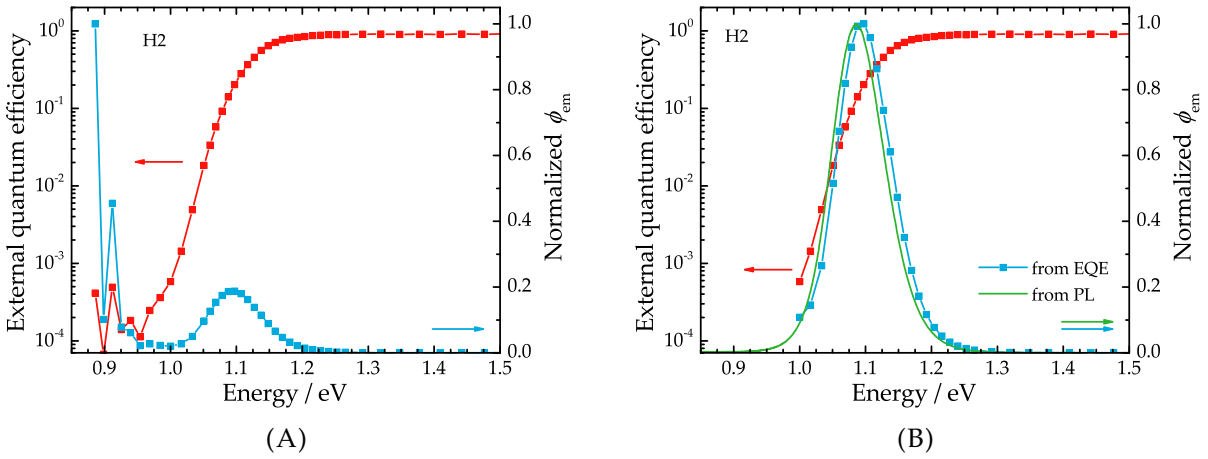

FIGURE F.5: Measured external quantum efficiency spectrum (red curve - left-hand y-axis) and calculated emitted photon flux density spectrum (blue curve - right-hand y-axis) of solar cell H2. **(A)** In the case where the EQE spectrum shows non-zero signals at low energies, the calculated emitted photon flux density is vastly overestimated. **(B)** Removing the non-zero signals from the EQE spectrum allows for a reliable determination of the photon flux density that strongly resembles the measured PL spectrum (green curve - righ-hand y-axis) of the corresponding polystyrene-covered absorber. The EQE spectra were measured and provided by Dr. Romain Carron from Empa.

of one of the solar cells of sample H1. It can be seen that the calculated photon flux density resembles the measured PL spectrum (green curve - right-hand y-axis) remarkably well. Both luminescence spectra are energetically shifted with respect to each other. This shift is considered a discrepancy in band gap energy as the EQE was measured on a solar cell while the PL was measured on an absorber. A more homogeneous sample growth process leads to less discrepancies between solar cells and absorbers, as is proven by Fig. F.4B where the calculated $\phi_{em}(E)$ spectrum is compared to the measured PL spectrum of the L2 sample.

Fig. F.5 shows the influence of the EQE spectrum on the calculated emitted photon flux density $\phi_{em}(E)$ and consequently on the external radiative efficiency. In Fig. F.5A, the measured EQE spectral exhibits non-zero signals at low energies. These signals lead to a vast overestimation of the calculated photon flux density $\phi_{em}(E)$ such that the computation of the external

radiative efficiency yields an erroneous value. To solve this issue, the non-zero data points are culled from the EQE spectrum until the calculated photon flux density spectrum resembles a broad single peak. The result of such a culling is shown in Fig. F.5B where the calculated $\phi_{\mathrm{em}}(E)$ now exhibits a strong resemblance to the measured PL spectrum (even if, as was the case for sample H1, there is a discrepancy in the band gap energies between absorber and solar cell).

F.5 Internal radiative efficiency

Equation (7.4) in section 7.1.2 describes a very important relationship between the optical and electrical properties of a solar cell. However, since the external radiation efficiency is measured *outside* whereas the open-circuit voltage is measured *inside* the solar cell, this relationship is *a priori* not intuitive. One might ask why the internal pendant to η_{ext}, the internal radiative efficiency, is not the parameter of importance here. The internal radiative efficiency η_{int} can be defined as [79]

$$\eta_{\mathrm{int}} = \frac{R_{\mathrm{rad}}}{R_{\mathrm{rad}} + R_{\mathrm{SRH}}}, \tag{F.14}$$

with R_{rad} and R_{SRH} being the radiative and non-radiative recombination rates respectively and originally introduced in eqs. (2.26) and (2.28). This definition provides a more intuitive approach to the V_{OC} that can be extracted from the solar cell as it clearly states that non-radiative recombination inside the absorber is harmful. Since, in the ideal case, the charge carriers are collected before recombining, the emitted photon flux density outside the solar cell should be irrelevant. This conundrum is solved by applying the principle of detailed balance stating that a good absorber is also a good emitter [78]. In fact, eq. (7.4) was originally derived on the basis of thermodynamics and thus clearly demonstrates that, while the internal radiative efficiency is important, the maximum solar cell efficiency can only be attained for an optimal out-coupling of photons following radiative emission inside the absorber. This statement reveals an entire new path of solar cell optimization: not only is it sufficient to minimize the non-radiative recombination rate R_{SRH}, but also the photon out-coupling needs to be maximized. The latter concept is generally labelled as "photon recycling" and is a very relevant topic in GaAs [313], [314]: due to the large difference in refractive indices between absorber material and the air outside, the escape cone of photons hitting the surface from inside the absorber only amounts to 16° [313]. Photons hitting the surface under larger angles are reflected back into the absorber and, in the absence of parasitic absorption, are re-absorbed, creating new electron-hole pairs. These pairs can then again undergo a radiative recombination with the resulting photons attempting a new escape from the material.

The relationship between external and internal radiative efficiency can be described as [296]

$$\eta_{\mathrm{ext}} = \frac{p_{\mathrm{em}}\eta_{\mathrm{int}}}{(1-\eta_{\mathrm{int}}) + (p_{\mathrm{em}} + p_{\mathrm{par}})\,\eta_{\mathrm{int}}} \tag{F.15}$$

$$= \frac{p_{\mathrm{em}}\eta_{\mathrm{int}}}{1 - p_{\text{re-abs}}\eta_{\mathrm{int}}}, \tag{F.16}$$

where p_{em} describes the probability of photonic emission through the surface, p_{par} the probability of parasitic absorption, and $p_{\text{re-abs}} = 1 - p_{\mathrm{em}} - p_{\mathrm{par}}$ the probability of photon re-absorption inside the absorber. In CIGS, due to the poor reflectivity of the Mo back contact [315] and the narrow band gap minimum inside the bulk, the parasitic absorption is maximal and the re-absorption of photons can be neglected. Thus, the relationship between external and internal radiative efficiency is simplified considerably:

$$\eta_{\mathrm{ext}} = p_{\mathrm{em}}\eta_{\mathrm{int}}. \tag{F.17}$$

The probability of photonic emission through the surface p_{em} can be estimated. In Fig. F.6, following the radiative recombination of electron-hole pairs, the number N of photons are emitted into a 4π solid angle inside the absorber. Due to the poor reflectivity of the Mo at the back mentioned above, only the number of photons N_Ω that are emitted in a solid angle Ω_{c} towards the surface can exit the absorber. This solid angle can be calculated to be

$$\Omega_{\mathrm{c}} = \int_0^{2\pi} \mathrm{d}\varphi \int_0^{\theta_{\mathrm{c}}} \sin\theta \, \mathrm{d}\theta, \tag{F.18}$$

where φ is the azimuthal angle and θ the angle between surface normal and direction of the emitted photons. The critical angle θ_{c} can be determined from Snell's law to be $\theta_{\mathrm{c}} = \sin^{-1}(1/n)$ where n is the refractive index of the absorber. Using the expansion of the Taylor series, the critical solid angle can finally be approximated to $\Omega_{\mathrm{c}} \approx \pi/n^2$. Thus, the number of photons inside the solid angle amounts to $N_\Omega = N \cdot \Omega_{\mathrm{c}}/4\pi$. Finally, the probability of photonic emission is determined by the ratio between the number of photons emitted through the surface and the number of photons emitted inside the absorber:

$$p_{\mathrm{em}} = T \frac{N_\Omega}{N} = T \frac{\pi/n^2}{4\pi} = T \frac{1}{4n^2}, \tag{F.19}$$

where T is the transmittance of the surface. Assuming normal incidence (valid assumption as θ_{c} is rather small), the transmittance T of a planar surface can be rewritten according to Fresnel's equations such that [199]

$$T = 1 - R = 1 - \left(\frac{n_{\mathrm{air}}/n - 1}{n_{\mathrm{air}}/n + 1} \right)^2, \tag{F.20}$$

where R is the inner reflection of the planar surface and n_{air} the index of refraction in air. Inserting eq. (F.20) into eq. (F.19) yields

$$p_{\mathrm{em}} = \frac{1}{n(1+n)^2}, \tag{F.21}$$

and finally, with $n \approx 3$ [31], the relationship between internal and external radiative efficiency in CIGS is established [93]:

$$\eta_{\mathrm{ext}} = 0.021 \cdot \eta_{\mathrm{int}}. \tag{F.22}$$

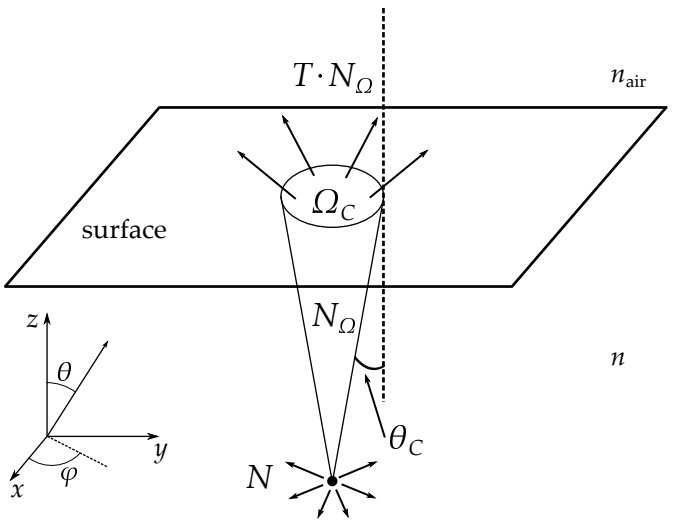

FIGURE F.6: Schematic illustration of photon emission inside the absorber following the radiative recombination of charge carriers. While the number of photons N are emitted into the solid angle 4π, only the number N_Ω of photons emitted into the solid angle Ω_{C}, limited by the critical angle θ_{C}, may exit the absorber.

Thus, under the assumptions above, only 2.1 % of the photons that are created through radiative recombination are able to exit the absorber.

F.6 Method to quantify voltage losses

In section 7.1.3, the losses to the measured open-circuit voltage V_{OC}, originating from different sources, are quantified for the various state-of-the-art CIGS, as well as for c-Si and GaAs solar cells. The method of extracting these voltages losses is based entirely on the recent work by Rau *et al.* [278] and is briefly explained below. The method can be seen as a generalization of the Shockley-Queisser model that was first introduced in section 2.4. To achieve this generalization, the fundamental idea is to determine a so-called photovoltaic band gap energy $E_{\mathrm{g}}^{\mathrm{PV}}$ from the measured external quantum efficiency (EQE) spectrum. Since the low-energy part of the EQE spectrum mimics the absorption properties of the material, a band gap energy extracted from the EQE constitutes an external property that is tightly linked to the photovoltaic performance of the device.

The determination of $E_{\mathrm{g}}^{\mathrm{PV}}$ is based on the assumption that the smeared-out (i.e. non-step-like) absorption edge of the EQE spectrum can be approximated by a distribution of band gap energies $P(E_{\mathrm{g}})$:

$$\mathrm{EQE}(E) = \int_{-\infty}^{\infty} P(E_{\mathrm{g}})\, H\left(E - E_{\mathrm{g}}\right)\, \mathrm{d}E_{\mathrm{g}}, \tag{F.23}$$

where $H(E - E_{\mathrm{g}})$ is the Heaviside function equalling 1 for $E > E_{\mathrm{g}}$ and 0 for $E < E_{\mathrm{g}}$. To be able to use the convolution theorem and to get rid of the Heaviside function, eq. (F.23) is differentiated with respect to the energy

$$\frac{\mathrm{d}}{\mathrm{d}E}\mathrm{EQE}(E) = \int_{-\infty}^{\infty} P(E_{\mathrm{g}})\, \delta(E - E_{\mathrm{g}})\, \mathrm{d}E_{\mathrm{g}} = P(E) = P(E_{\mathrm{g}}) \tag{F.24}$$

Thus, by differentiating the measured EQE spectrum, it is possible to extract the distribution of band gap energies $P(E_{\mathrm{g}})$. To determine a single photovoltaic band gap energy $E_{\mathrm{g}}^{\mathrm{PV}}$, Rau *et al.* use the following definition:

$$E_{\mathrm{g}}^{\mathrm{PV}} = \frac{\int_a^b E_{\mathrm{g}}\, P(E_{\mathrm{g}})\, \mathrm{d}E_{\mathrm{g}}}{\int_a^b P(E_{\mathrm{g}})\, \mathrm{d}E_{\mathrm{g}}}. \tag{F.25}$$

Here the integration limits a and b are chosen as the energy values of the full width at half maximum of the distribution $P(E_{\mathrm{g}})$ i.e. $a = b = P_{\mathrm{max}}(E_{\mathrm{g}})/2$. A practical example of how the photovoltaic band gap energy $E_{\mathrm{g}}^{\mathrm{PV}}$ was extracted in this thesis is given in Fig. F.7. The red circles represent the measured external quantum efficiency of sample H1. Since the measured data points are limited, the EQE spectrum is extended through the use of an one-dimension interpolation spline (blue line). This way the available data points can be increased artificially, rendering the differentiation operation much smoother. The green curve in Fig. F.7 shows the distribution of band gap energies $P(E_{\mathrm{g}})$ according to eq. (F.24). The shaded area represents the denominator in eq. (F.25) and serves to visualize the spectral region where $E_{\mathrm{g}}^{\mathrm{PV}}$ is ultimately determined from.

Both the photovoltaic band gap energy $E_{\mathrm{g}}^{\mathrm{PV}}$ and the measured external quantum efficiency EQE can then be used to calculate the various parameters that contribute to the open-circuit voltage V_{OC} in their theoretical limits i.e.:

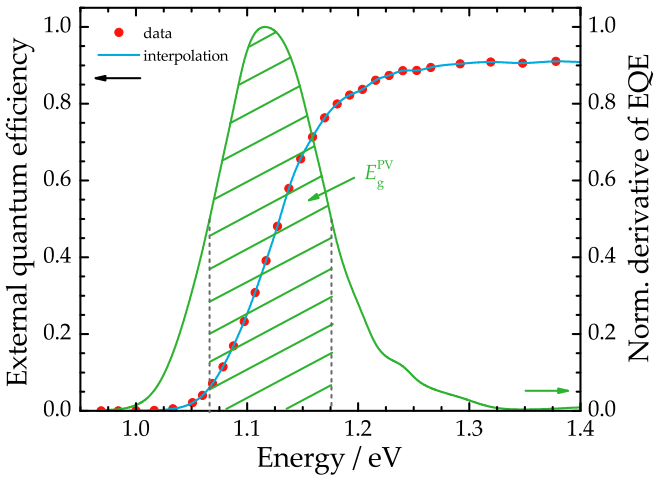

FIGURE F.7: External quantum efficiency spectrum measured on a solar cell device of sample H1 used to determine the photovoltaic band gap energy E_g^{PV}. The red circles represent the measured data points while the blue line represents the extended data as calculated through an one-dimension interpolation spline (left-hand y-axis). The green curve represents the normalized derivative of the interpolated external quantum efficiency (right-hand y-axis). The shaded area represents the spectral region used to calculate E_g^{PV} according to eq. (F.25).

$$j_{SC}^{SQ} = q \int_{E_g^{PV}}^{\infty} \Phi_{sun}(E)\, dE, \tag{F.26}$$

$$j_0^{SQ} = q \int_{E_g^{PV}}^{\infty} \Phi_0(E)\, dE, \tag{F.27}$$

$$j_{SC} = q \int_{-\infty}^{\infty} EQE(E)\, \Phi_{sun}(E)\, dE, \tag{F.28}$$

$$j_0^{rad} = q \int_{-\infty}^{\infty} EQE(E)\, \Phi_0(E)\, dE. \tag{F.29}$$

Equations (F.26) and (F.27) represent the Shockley-Queisser limits introduced in section 2.4. Eq. (F.28) does not represent a theoretical limit but rather should be equal to the short-circuit current j_{SC} measured through current-voltage experiments if the measured EQE spectrum exhibits an adequate precision. Eq. (F.29) represents the radiative limit of j_0 i.e. the saturation current density of the solar cell that is purely due to the non-step-like absorption (mostly due to band tails) without any contributions from non-radiative recombination processes.

The open-circuit voltage V_{OC}, originally defined in eq. (2.13), can be expanded (ignoring the $+1$ term and assuming $A = 1$):

$$V_{OC} = \frac{k_B T}{q} \ln\left(\frac{j_{SC}}{j_0}\right) = \frac{k_B T}{q} \ln\left(\frac{j_{SC}^{SQ}}{j_0^{SQ}} \cdot \frac{j_{SC}}{j_{SC}^{SQ}} \cdot \frac{j_0^{SQ}}{j_0^{rad}} \cdot \frac{j_0^{rad}}{j_0}\right), \tag{F.30}$$

where each of the terms in the natural logarithm now represents a distinct loss to the open-circuit voltage. They can be summarized as

$$V_{OC} = V_{OC}^{SQ} - \Delta V_{OC}^{SC} - \Delta V_{OC}^{rad} - \Delta V_{OC}^{nrad}, \tag{F.31}$$

$$V_{OC}^{SQ} = k_B T/q \cdot \ln\left(j_{SC}^{SQ}/j_0^{SQ}\right), \tag{F.32}$$

$$\Delta V_{OC}^{SC} = k_B T/q \cdot \ln\left(j_{SC}^{SQ}/j_{SC}\right), \tag{F.33}$$

$$\Delta V_{OC}^{rad} = k_B T/q \cdot \ln\left(j_0^{rad}/j_0^{SQ}\right), \tag{F.34}$$

$$\Delta V_{OC}^{nrad} = k_B T/q \cdot \ln\left(j_0/j_0^{rad}\right). \tag{F.35}$$

Eq. (F.32) represents the V_{OC} in the SQ limit i.e. the upper theoretical limit. Eq. (F.33) represents the short-circuit current voltage loss due to the difference between the theoretical SQ limit and the experimentally measured value of the short-circuit current density j_{SC}. Eq. (F.34) represents the radiative voltage loss that stems from the fact that the real absorption edge is not step-like, as assumed in the SQ model, but rather smeared-out. The non-step-like absorption edge leads to states inside the band gap which, due to radiative emission, lead to an increase in the saturation current density j_0^{rad}. Finally, the last eq. (F.35) describes the voltage loss term due to non-radiative recombination. Besides computing the ratio between the real measured saturation current density j_0 and its radiative value j_0^{rad}, the non-radiative voltage loss can also be computed with the help of the external radiative efficiency η_{ext} as in eq. (7.4):

$$\Delta V_{OC}^{nrad} = \frac{k_B T}{q} \ln\left(\eta_{ext}\right). \tag{F.36}$$

For the samples for which the external quantum efficiency spectrum is available, the various voltages losses are calculated through equations (F.32) to (F.35) after having calculated the photovoltaic band gap energy through eq. (F.25). The V_{OC} and j_{SC} are taken from the measured JV curves (cf. Table 3.2 in section 3.3). The non-radiative voltage loss is calculated through both equations (F.35) and (F.36) and is found to be identical to within 99.99 % between both equations for all samples. The external radiative efficiency η_{ext} used in eq. (F.36) is extracted from the EQE spectra according to the method described in the previous appendix F.4. Furthermore, since the quality of the measured EQE spectrum has a huge influence on the calculated values, the measured EQE spectra are prepared via the approach laid out in the previous appendix F.4, i.e. the emitted photon flux density is calculated and its shape is verified.

F.7 Influence of doping on $\Delta\mu$

In section 7.2.1, it was argued that an increase in p-type doping leads to an increase in the quasi-Fermi level splitting $\Delta\mu$ and consequently in the open-circuit voltage V_{OC}. In the following, the mechanism of this increase is briefly explained.

As was described in section 2.5.1, in the case of a p-type semiconductor and under low-injection conditions, an increase in the hole carrier concentration p_0 leads to decrease of the radiative lifetime τ_{rad} through an increase in the radiative recombination rate R_{rad} via

$$R_{rad} = B p_0 \Delta n = \frac{\Delta n}{\tau_{rad}}, \tag{F.37}$$

under the conditions of constant excitation i.e. constant minority charge carrier density Δn. The increase in radiative recombination rate is the result of an increased density of holes available for electrons from the conduction band to recombine with. In the Shockley-Queisser model i.e. in an ideal solar cell, the doping concentration is neglected because perfect charge carrier collection is assumed. This means that increasing the radiative band-to-band recombination does not matter since it is an unavoidable consequence of the principle of detailed balance. However, in real solar cells, where charge carrier collection is not perfect, this is not the case: increasing the radiative recombination leads to a decrease in the radiative lifetime which means that the excited charge carriers have less time to be extracted by the electrical contacts.

In state-of-the-art CIGS absorbers, the recombination is dominated by non-radiative recombination. As a consequence, the effective electron charge carrier lifetime τ_{eff} (cf. eq. (2.34)) is shorter than the radiative lifetime. An experimental example can be found in ref. [93] where time-resolved photoluminescence was measured on the LS absorber that also features in this

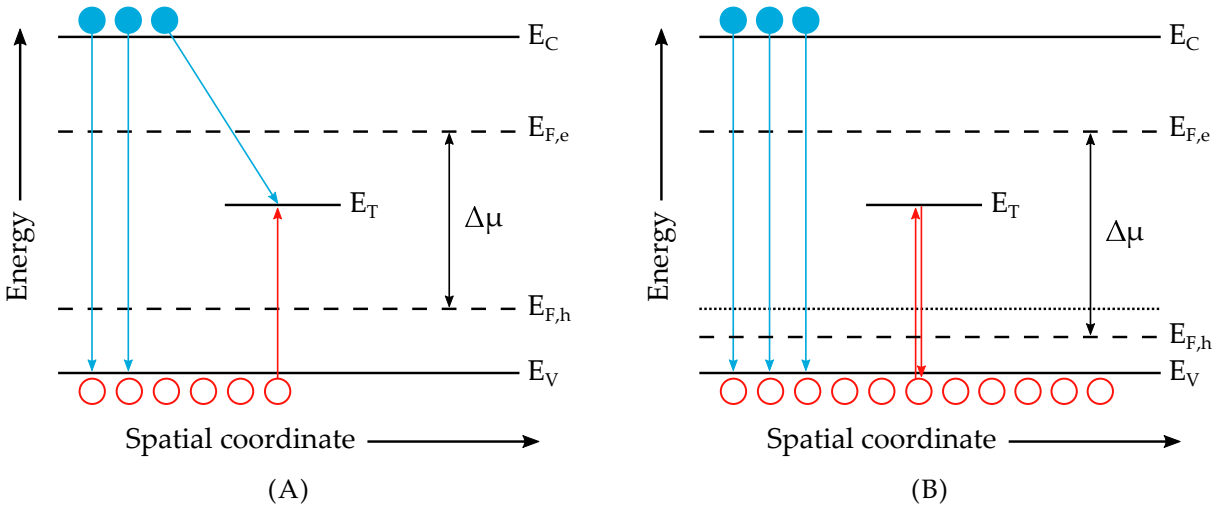

FIGURE F.8: **(A)** Schematic energy band diagram of a p-type semiconductor under low injection conditions. Some of the electrons (blue circles) in the conduction band recombine radiatively with holes (hollow red circles) in the valence band. Other electrons recombine with holes after both are captured in the deep-level defect states at E_T leading to non-radiative recombination. The latter transition is depicted as non-local only for clarity purposes and can also occur locally. **(B)** Increasing the hole carrier concentration leads to a larger probability of the radiative band-to-band transition occurring while the probability of trap-assisted non-radiative recombination remains the same.

thesis. The LS absorber, with its corresponding solar cell efficiency amounting to 19.2 %, has a measured effective lifetime τ_{eff} of 253 ns and an estimated radiative lifetime τ_{rad} of 2.6 μs. This means that, as long as the effective lifetime is dominated by non-radiative recombination processes, decreasing the radiative lifetime through an increase in p-type doping does not affect the lifetime of the minority charge carriers. Thus, under constant excitation conditions, a constant minority charge carrier lifetime leads to a constant density of excited minority carriers Δn i.e. a constant electron quasi-Fermi level $E_{F,e}$. However, the increase of the p-type doping leads to the hole quasi-Fermi level $E_{F,h}$ shifting closer to the valence band which then leads to an increase in the quasi-Fermi level splitting $\Delta\mu$.

The influence of a p-type doping increase on the charge carrier recombination dynamics is illustrated in Fig. F.8A where the non-radiative recombination process is represented by the presence of a deep-level trap at mid band gap $E_T = E_g/2$. In a p-type absorber and under low injection conditions, the density of holes in valence band $p \approx p_0$ is larger than the density of excited electrons in the conduction band Δn. Some of the electron engage in a radiative recombination with holes from the valence band. For a non-radiative recombination process to occur via the deep-level defect, both electrons and holes must be captured by the defect state. As was discussed in section 2.5.2, the capture and emission of charge carriers in defect states is self-balancing under steady state conditions.

Increasing the p-type conductivity increases the density of holes while the density of minority charge carriers remains constant if the injection conditions are not changed. Under these circumstances, the capture and emission of holes and electrons in and from the defect states does not change. However, due to more holes being available, the probability of electrons from the conduction band recombining radiatively with holes in the valence band increases. Thus, an increase in doping, as long as the non-radiative recombination process dominates the transients and lifetime, does not passivate deep-level trap states but increases the probability of radiative emission.

The change in the quasi-Fermi level splitting can be calculated with the use of eq. (2.7) i.e.

$$\Delta\mu = k_{\mathrm{B}}T \ln\left(\frac{np}{n_{\mathrm{i}}^2}\right). \tag{F.38}$$

Under the above conditions i.e. low-injection and p-type, it is that $p \approx p_0 \gg n$ such that:

$$\Delta\mu \approx k_{\mathrm{B}}T \ln\left(\frac{\Delta n \cdot p_0}{n_{\mathrm{i}}^2}\right). \tag{F.39}$$

Changing the doping, say after the application of a post-deposition treatment, and in the case of identical excitation conditions (i.e. identical Δn), the change in quasi-Fermi level splitting can be expressed through (keeping in mind that a change in hole charge carrier concentration does not change the intrinsic charge carrier concentration n_{i} - cf. section 2.1.1):

$$\Delta\mu^{\mathrm{PDT}} - \Delta\mu^{\mathrm{None}} = k_{\mathrm{B}}T \ln\left(\frac{\Delta n \cdot p_0^{\mathrm{PDT}}}{n_{\mathrm{i}}^2}\right) - k_{\mathrm{B}}T \ln\left(\frac{\Delta n \cdot p_0^{\mathrm{None}}}{n_{\mathrm{i}}^2}\right) = k_{\mathrm{B}}T \ln\left(\frac{p_0^{\mathrm{PDT}}}{p_0^{\mathrm{None}}}\right). \tag{F.40}$$

Acknowledgements

A PhD project is not something that is done easily. From the beginning to the end, there are many hardships and many obstacles to overcome. It is thus very important to have the appropriate assistance, guidance, and sometimes even a bulldozer, to overcome these barriers and (eventually) reach the end of the project. Thus, if I were the only one who would have contributed to this thesis, then it would probably be blank. For the manuscript to be present under its current form, a ton of people need to be acknowledged.

My first and foremost thanks goes to Susanne. Since I did my Bachelor thesis at the Laboratory for Photovoltaics, I knew exactly what to expect when I applied for a PhD position after completing my studies abroad. Susanne managed to create a fun and enjoyable working environment in her research group which makes it a pleasure to get up out of bed and come to work everyday. In addition, with her passion and love for the many topics she is interested in, it is very easy to stay motivated as you are swept along. She is a brilliant supervisor and one of the leading experts in her field which is why I consider myself very lucky to have had the opportunity to continue my research interests under her. But most importantly, at least to me, Susanne is one of the most reliable and fair persons I know. She is very busy and has a ton of important projects to take care of (and students to supervise!) but always finds time to give a guiding and helping hand. She is very eager to enter in discussions about complicated topics and, even if she is initially of the opposite opinion, it is possible to convince her with the right arguments (but obviously the arguments have to be good!). She is very considerate towards one's private life and knows exactly what matters and what does not. It is thus very easy to flourish under her supervision.

My second thanks goes out to Jan Lagerwall, Roland Sanctuary, Stephan Buecheler, and Thomas Kirchartz for being part of my dissertation defence committee. I would like to use the opportunity and express my heartfelt gratitude more specifically towards Roland who was there the first day I visited the University of Luxembourg for the first lectures of the Physics study programme and guided me during my studies. I am very happy that Roland is part of the beginning and end of my journey as a "student".

A big thanks goes to the whole Sharc25 consortium for being able to be part of this exciting and very interesting project. Special thanks to Benjamin Bissig, Romain Carron (especially him!), Patrick Reinhard, Enrico Avancini, Thomas Feurer, Emilie Bourgeois, Wolfram Witte, and Philip Jackson for samples, measurements and guidance!

Another huge thanks goes to Phil Dale for the initial idea with the polystyrene beads and our energy project. Without him most of the results of this thesis would not have been possible.

A very very special thanks also to the person that made me want to become a phycisist: my Secondary School teacher Claude Schmitz. Before having him as my physics teacher, I was actually really bad at physics (and I probably still am). Having him become my physics teacher was probably one of the best things to happen in my Secondary School career as he not only gave me the passion to want to do physics, but he also taught me that certain things in life are not for granted and you need to work for them. I certainly wouldn't be the person I am today if he didn't shake me up during my "more rebellious" years in Secondary School.

After Susanne comes the rest of the LPV and LEM team that I need to thank. Special thanks to Thomas Schuler for technical assistance, great music, and beer. Patricia gets a big thanks for her good mood, great organization skills and placing the never-ending orders for Helium!

Special thanks also to Alex Redinger for being my supervisor during my Bachelor Thesis and teaching me that being organized is a very great asset. A million thanks to a million of former and current group members that are too many to list but I will try anyway: João, Helene, Sergey, Marina, Valérie, Levent, Maxime, Michele, Thomas, Jan, Tobias, Sara, Erika, Conrad, Finn, David, Jessica, Hiroki, Matej, Germain, Diego, Tobias R., Hossam, Florian, Anastasiya, Florian E., Valentina, Omar, Pascal, Korra, Viba, Sudhanshu, Venky, Damilola, Nayia, Ali G., Ben, Baby Jan, Jonathan, Leo, Mohit, and Alexandre. I would also like to thank the awesome people from the Luxembourg Institute of Science and Technology that I had the pleasure to meet and befriend: David, Mads, Charlotte, Constance, Cosme, Mauro, Carlos, and Phillip.

Being able to do a PhD project in my country is something that was very important to me (since I even consider leaving my home village as "stepping abroad"). As such I was always close to my friends that are like family to me. I would like to use this opportunity to sincerely thank them for being there for me. Special thanks goes to Ben, Cédric, Vincent, Sam, and Alex.

Aside from the family that I choose to have, I also need to thank my blood-related family. Special thanks here to my parents and my brother who have always supported me and been there for me.

And, last but not least, I want to thank Isabelle with the bottom of my heart. Everybody who knows us, knows also very well who I would be without her. While we have been together for a long long time now, it never ceases to amaze me how she can put up with me. That I can can live life to the fullest is all thanks to her.

I am certain that I forgot to thank some people. If you are reading this and have not been acknowledged I sincerely apologize. But do not fret, you are in good company since I also didn't acknowledge Liverpool Football Club with which I share a deep love/hate relationship. But, in a all seriousness, if you contributed to this thesis and were not acknowledged, you are hereby now! Thanks a lot!

Scientific contributions

First author publications

M. H. Wolter, B. Bissig, P. Reinhard, S. Buecheler, P. Jackson, and S. Siebentritt, "Correcting for interference effects in the photoluminescence of Cu(In,Ga)Se_2 thin films", *Phys. Stat. Sol. C* 14(6), 1600189 (2017)

M. H. Wolter, B. Bissig, E. Avancini, R. Carron, S. Buecheler, P. Jackson, S. Siebentritt, "Influence of Sodium and Rubidium Postdeposition Treatment on the Quasi-Fermi level Splitting of Cu(In,Ga)Se_2 Thin Films", *IEEE Journal of Photovoltaics* 8(5), 1320-1325 (2018)

M. H. Wolter, D. Siopa, P. Thiele, P. Dale, E. Avancini, B. Bissig, R. Carron, S. Buecheler, and S. Siebentritt, "Applying a surface treatment to chalcopyrite thin films to eliminate interference effects", *in preparation*

M. H. Wolter, R. Carron, E. Avancini, B. Bissig, T. P. Weiss, S. Nishiwaki, T. Feurer, S. Buecheler, P. Jackson, W. Witte, E. Bourgeois, G. Degutis, and S. Siebentritt, "Influence of light and heavy alkali atoms on the band tails in Cu(In,Ga)Se_2 thin-film absorbers", *in preparation*

Co-authored publications

A. Redinger, M. Mousel, M. H. Wolter, N. Valle, and S. Siebentritt, "Influence of S/Se ratio on series resistance and on dominant recombination pathway in $Cu_2ZnSn(SSe)_4$ thin film solar cells", *Thin Solid Films* 535, 291-295 (2013)

F. Werner, M. H. Wolter, G. Sozzi, S. Di Napoli, R. Menozzi, P. Jackson, W. Witte, R. Carron, E. Avancini, T. P. Weiss, and S. Siebentritt, "Alkali treatments of Cu(In,Ga)Se_2 thin-film absorbers and their impact on transport barriers", *Progress in Photovoltaics: Research and Application* 26(11), 911-923 (2018)

T. P. Weiss, R. Carron, M. H. Wolter, J. Löckinger, E. Avancini, S. Siebentritt, S. Buecheler, and A. N. Tiwari, "Time-resolved photoluminescence on double graded Cu(In,Ga)Se_2 - impact of front surface recombination and its temperature dependence", *Science and Technology of Advanced Materials* 535, 313-323 (2019)

F. Babbe, H. Elanzeery, M. H. Wolter, K. Santhosh, and S. Siebentritt, "Experimental evidence of a third acceptor in $CuInSe_2$ and Cu(In,Ga)Se_2 absorber layers", *submitted*

D. Siopa, S. Tombolato, F. Babbe, M. H. Wolter, P. Anacleto, K. Abderrafi, S. Sadewasser, and P. Dale, "Cu(In,Ga)Se_2-based micro solar cells via electrochemical selective area deposition for concentrator photovoltaics application", *submitted*

C. Spindler, F. Babbe, M. H. Wolter, K. Santhosh, P. Hilgert, F. Werner, and S. Siebentritt, "Electronic Defects in Cu(In,Ga)Se_2 - towards a comprehensive model", *submitted*

S. Siebentritt, F. Werner, M. H. Wolter, E. Avancini, M. Bär, E. Bourgeois, S. Buecheler, R. Carron, P. Jackson, T. Kunze, M. Malitckaya, R. Manaligod, R. Menozzi, N. Nicoara, M. Puska, M. Raghuwanshi, S. Sadewasser, G. Sozzi, A. Vilalta-Clemente, and A. N. Tiwari, "Heavy alkali treatment of chalcopyrite solar cells: surface versus bulk effects", *in preparation*

Conference contributions

M. H. Wolter, P. Reinhard, B. Bissig, S. Buecheler, P. Jackson, and S. Siebentritt, "Correcting for interference effects in Cu(In,Ga)Se_2-based thin films", *20^{th} International Conference on Ternary and Multinary Compounds*, Halle (Saale), Germany, 2016, poster presentation

M. H. Wolter, B. Bissig, E. Avancini, R. Carron, S. Buecheler, and S. Siebentritt, "Influence of sodium and rubidium post-deposition treatment on the quasi-Fermi level splitting of Cu(In,Ga)Se_2 thin films", *44^{th} IEEE Photovoltaic Specialist Conference*, Washington D.C., United States of America, 2017, oral presentation

M. H. Wolter, B. Bissig, P. Reinhard, E. Avancini, R. Carron, S. Buecheler, W. Witte, P. Jackson, and S. Siebentritt, "Influence of interference effects and alkali post-deposition treatment on the quasi-Fermi level splitting of Cu(In,Ga)Se_2 thin films", *Nanotechnology and Next Generation High Efficiency Photovoltaics International School and Workshop*, Palma de Mallorca, Spain, 2017, oral presentation

M. H. Wolter, F. Werner, B. Bissig, E. Avancini, T. Weiss, R. Carron, S. Buecheler, P. Jackson, W. Witte, G. Sozzi, S. Di Napoli, R. Menozzi, and S. Siebentritt, "Defects, barriers and quasi-Fermi level splitting in high efficiency Cu(In,Ga)Se_2 solar cells", *1^{st} public Sharc25 project workshop*, Stuttgart, Germany, 2017, oral presentation

M. H. Wolter, D. Siopa, P. Dale, B. Bissig, E. Avancini, R. Carron, S. Buecheler, P. Jackson, D. Hariskos, W. Witte, and S. Siebentritt, "Removing interference effects in photoluminescence of Cu(In,Ga)Se_2 thin films to investigate potential fluctuations", *European Materials Research Society Spring Meeting*, Strasbourg, France, 2018, oral presentation

Bibliography

[1] United Nations. (2018). Secretary-General's press encounter on climate change, [Online]. Available: https://www.un.org/sg/en/content/sg/press-encounter/2018-03-29/secretary-generals-press-encounter-climate-change-qa (visited on 04/12/2019) (cit. on p. 3).

[2] Intergovernmental Panel on Climate Change. (2018). Global Warming of 1.5 degree C, [Online]. Available: https://www.ipcc.ch/sr15/ (visited on 04/12/2019) (cit. on p. 3).

[3] International Energy Agency. (). World Energy Balances 2018: Overview, [Online]. Available: https://webstore.iea.org/world-energy-balances-2018 (visited on 04/12/2019) (cit. on p. 3).

[4] P. Gerland, A. E. Raftery, H. Ev ikova, N. Li, D. Gu, T. Spoorenberg, L. Alkema, B. K. Fosdick, J. Chunn, N. Lalic, G. Bay, T. Buettner, G. K. Heilig, and J. Wilmoth, "World population stabilization unlikely this century", *Science*, vol. 346, no. 6206, pp. 234–237, 2014 (cit. on p. 3).

[5] BP. (2019). BP Statistical Review of World Energy, [Online]. Available: https://www.bp.com/content/dam/bp/business-sites/en/global/corporate/pdfs/energy-economics/statistical-review/bp-stats-review-2018-full-report.pdf (visited on 04/12/2019) (cit. on p. 3).

[6] CIGS-PV. (2019). CIGS White Paper 2019, [Online]. Available: https://cigs-pv.net/wortpresse/wp-content/uploads/2019/04/CIGS_White_Paper_2019_online.pdf (visited on 04/12/2019) (cit. on p. 3).

[7] European Commission. (2018). Statement/18/4155, [Online]. Available: http://europa.eu/rapid/press-release_STATEMENT-18-4155_en.htm (visited on 04/12/2019) (cit. on p. 3).

[8] Solar Frontier press release. (2019). Solar Frontier Achieves World Record Thin-Film Solar Cell Efficiency of 23.35%, 2019-01-17, [Online]. Available: http://www.solar-frontier.com/eng/news/2019/0117_press.html (visited on 04/02/2019) (cit. on pp. 3, 26, 32).

[9] M. A. Green, Y. Hishikawa, E. D. Dunlop, D. H. Levi, J. Hohl-Ebinger, and A. W. Ho-Baillie, "Solar cell efficiency tables (version 52)", *Progress in Photovoltaics: Research and Applications*, vol. 26, no. 7, pp. 427–436, 2018 (cit. on pp. 3, 14, 15, 26, 128, 132, 135, 136).

[10] National Renewable Energy Laboratory. (2019). Best Research-Cell Efficiency Chart, [Online]. Available: https://www.nrel.gov/pv/cell-efficiency.html (visited on 04/12/2019) (cit. on p. 3).

[11] Sharc25 Consortium. (2015). Super high efficiency Cu(In,Ga)Se2 thin-film solar cells approaching 25%, [Online]. Available: http://www.sharc25.eu (visited on 04/12/2019) (cit. on p. 3).

[12] A. Chirilă, P. Reinhard, F. Pianezzi, P. Bloesch, A. R. Uhl, C. Fella, L. Kranz, D. Keller, C. Gretener, H. Hagendorfer, D. Jaeger, R. Erni, S. Nishiwaki, S. Buecheler, and A. N. Tiwari, "Potassium-induced surface modification of Cu(In,Ga)Se2 thin films for high-efficiency solar cells", *Nature Materials*, vol. 12, no. 12, pp. 1107–1111, 2013 (cit. on pp. 3, 4, 15, 18, 32, 34, 35).

[13] P. Jackson, D. Hariskos, E. Lotter, S. Paetel, R. Wuerz, R. Menner, W. Wischmann, and M. Powalla, "New world record efficiency for Cu(In,Ga)Se2 thin-film solar cells beyond 20%", *Progress in Photovoltaics: Research and Applications*, vol. 19, no. 7, pp. 894–897, 2011 (cit. on pp. 3, 31).

[14] D. Rudmann, A. F. da Cunha, M. Kaelin, F. Kurdesau, H. Zogg, A. N. Tiwari, and G. Bilger, "Efficiency enhancement of Cu(In,Ga)Se2 solar cells due to post-deposition Na incorporation", *Applied Physics Letters*, vol. 84, no. 7, pp. 1129–1131, 2004 (cit. on pp. 4, 32).

[15] P. Jackson, R. Wuerz, D. Hariskos, E. Lotter, W. Witte, and M. Powalla, "Effects of heavy alkali elements in Cu(In,Ga)Se 2 solar cells with efficiencies up to 22.6%", *physica status solidi (RRL) - Rapid Research Letters*, vol. 10, no. 8, pp. 583–586, 2016 (cit. on pp. 4, 15, 20, 32, 34, 36, 53, 133).

[16] T. Kato, J.-L. Wu, Y. Hirai, H. Sugimoto, and V. Bermudez, "Record Efficiency for Thin-Film Polycrystalline Solar Cells Up to 22.9% Achieved by Cs-Treated Cu(In,Ga)(Se,S) 2", *IEEE Journal of Photovoltaics*, vol. 9, no. 1, pp. 325–330, 2019 (cit. on pp. 4, 20, 32, 132, 135).

[17] S. Hunklinger, *Festkörperphysik*. De Gruyter Oldenbourg, 2011 (cit. on p. 7).

[18] S. M. Sze and K. K. Ng, *Physics of Semiconductor Devices*. New Jersey: John Wiley & Sons, Inc., 2007 (cit. on pp. 7, 12, 29, 128).

[19] D. A. Neamen, *Semiconductor Physics and Devices*, 4th Editio. McGraw-Hill, 2011 (cit. on pp. 7, 12).

[20] P. Würfel, *Physics of Solar Cells*. Wiley-VCH Verlag GmbH & Co. KGaA, 2005 (cit. on pp. 12, 37, 42, 84, 85, 95, 153, 170).

[21] W. Shockley, "The Theory of p-n Junctions in Semiconductors and p-n Junction Transistors", *Bell System Technical Journal*, vol. 28, no. 3, pp. 435–489, 1949 (cit. on p. 12).

[22] J. L. Shay and J. H. Wernick, *Ternary Chalcopyrite Semiconductors: Growth, Electronic Properties, and Applications*. Pergamon Press Oxford, 1975 (cit. on p. 13).

[23] S. Schorr and G. Geandier, "In-situ investigation of the temperature dependent structural phase transition in CuInSe2 by synchrotron radiation", *Crystal Research and Technology*, vol. 41, no. 5, pp. 450–457, 2006 (cit. on p. 13).

[24] T. Tinoco, C. Rincón, M. Quintero, and G. S. Pérez, "Phase Diagram and Optical Energy Gaps for CuIn_{y}Ga_{1-y}Se2 Alloys", *Physica Status Solidi (a)*, vol. 124, no. 2, pp. 427–434, 1991 (cit. on p. 13).

[25] W. N. Shafarman and L. Stolt, "Cu(InGa)Se2 Solar Cells", in *Handbook of Photovoltaic Science and Engineering*, A. Luque and S. Hegedus, Eds., John Wiley & Sons Ltd, England, 2003 (cit. on pp. 14, 18, 19, 117, 155).

[26] S. Siebentritt, L. Gütay, D. Regesch, Y. Aida, and V. Deprédurand, "Why do we make Cu(In,Ga)Se2 solar cells non-stoichiometric?", *Solar Energy Materials and Solar Cells*, vol. 119, pp. 18–25, 2013 (cit. on pp. 14, 43, 57, 108).

[27] T. Gödecke, T. Haalboom, and F. Ernst, "Phase equilibiria of Cu-In-Se III. The In2Se3-Cu2Se subsystem", *Zeitschrift für Metallkunde*, vol. 91, pp. 651–662, 2000 (cit. on p. 14).

[28] R. Carron, E. Avancini, T. Feurer, B. Bissig, P. A. Losio, R. Figi, C. Schreiner, M. Bürki, E. Bourgeois, Z. Remes, M. Nesladek, S. Buecheler, and A. N. Tiwari, "Refractive indices of layers and optical simulations of Cu(In,Ga)Se 2 solar cells", *Science and Technology of Advanced Materials*, vol. 19, no. 1, pp. 396–410, 2018 (cit. on pp. 14, 82, 145, 166).

[29] A. Klein, "Energy band alignment in chalcogenide thin film solar cells from photoelectron spectroscopy", *Journal of Physics: Condensed Matter*, vol. 27, no. 13, p. 134 201, 2015 (cit. on pp. 14, 15).

[30] P. D. Paulson, R. W. Birkmire, and W. N. Shafarman, "Optical characterization of CuIn1-xGaxSe2 alloy thin films by spectroscopic ellipsometry", *Journal of Applied Physics*, vol. 94, no. 2, pp. 879–888, 2003 (cit. on p. 14).

[31] M. Alonso, M. Garriga, C. Durante Rincón, E. Hernández, and M. León, "Optical functions of chalcopyrite CuGa x In 1-x Se 2 alloys", *Applied Physics A: Materials Science & Processing*, vol. 74, no. 5, pp. 659–664, 2002 (cit. on pp. 14, 82, 170, 215).

[32] H. J. Queisser, "Defects in Semiconductors: Some Fatal, Some Vital", *Science*, vol. 281, no. 5379, pp. 945–950, 1998 (cit. on p. 15).

[33] J. Heyd, G. E. Scuseria, and M. Ernzerhof, "Hybrid functionals based on a screened Coulomb potential", *The Journal of Chemical Physics*, vol. 118, no. 18, pp. 8207–8215, 2003 (cit. on p. 16).

[34] J. Bekaert, R. Saniz, B. Partoens, and D. Lamoen, "Native point defects in CuIn 1-x Ga x Se 2 : hybrid density functional calculations predict the origin of p- and n-type conductivity", *Phys. Chem. Chem. Phys.*, vol. 16, no. 40, pp. 22 299–22 308, 2014 (cit. on p. 16).

[35] B. Huang, S. Chen, H.-X. Deng, L.-W. Wang, M. A. Contreras, R. Noufi, and S.-H. Wei, "Origin of Reduced Efficiency in Cu(In,Ga)Se$_2$ Solar Cells With High Ga Concentration: Alloy Solubility Versus Intrinsic Defects", *IEEE Journal of Photovoltaics*, vol. 4, no. 1, pp. 477–482, 2014 (cit. on p. 16).

[36] L. E. Oikkonen, M. G. Ganchenkova, A. P. Seitsonen, and R. M. Nieminen, "Formation, migration, and clustering of point defects in CuInSe 2 from first principles", *Journal of Physics: Condensed Matter*, vol. 26, no. 34, p. 345 501, 2014 (cit. on p. 16).

[37] Y. S. Yee, B. Magyari-Köpe, Y. Nishi, S. F. Bent, and B. M. Clemens, "Deep recombination centers in Cu2ZnSnS4 revealed by screened-exchange hybrid density functional theory", *Physical Review B*, vol. 92, no. 19, p. 195 201, 2015 (cit. on p. 16).

[38] J. Pohl and K. Albe, "Intrinsic point defects in CuInSe2 and CuGaSe2 as seen via screened-exchange hybrid density functional theory", *Physical Review B*, vol. 87, no. 24, p. 245 203, 2013 (cit. on pp. 16, 17, 108, 144).

[39] M. Malitckaya, H.-P. Komsa, V. Havu, and M. J. Puska, "First-Principles Modeling of Point Defects and Complexes in Thin-Film Solar-Cell Absorber CuInSe 2", *Advanced Electronic Materials*, vol. 3, no. 6, p. 1 600 353, 2017 (cit. on pp. 16, 157).

[40] R. Saniz, J. Bekaert, B. Partoens, and D. Lamoen, "Structural and electronic properties of defects at grain boundaries in CuInSe 2", *Physical Chemistry Chemical Physics*, vol. 19, no. 22, pp. 14 770–14 780, 2017 (cit. on p. 16).

[41] C. Spindler, "Optical Detection of Deep Defects in Cu(In,Ga)Se2", PhD thesis, 2018, http://hdl.handle.net/10993/37016 (cit. on pp. 16–18, 27, 41, 47–49, 108, 210).

[42] C. Spindler, F. Babbe, M. H. Wolter, K. Santhosh, P. Hilgert, F. Werner, and S. Siebentritt, "Electronic Defects in Cu(In,Ga)Se2 - towards a comprehensive model", *submitted*, (cit. on pp. 16, 17, 41, 108).

[43] N. Rega, S. Siebentritt, J. Albert, S. Nishiwaki, A. Zajogin, M. Lux-Steiner, R. Kniese, and M. Romero, "Excitonic luminescence of Cu(In,Ga)Se2", *Thin Solid Films*, vol. 480-481, pp. 286–290, 2005 (cit. on pp. 16, 17).

[44] S. Siebentritt, M. Igalson, C. Persson, and S. Lany, "The electronic structure of chalcopyrites-bands, point defects and grain boundaries", *Progress in Photovoltaics: Research and Applications*, vol. 18, no. 6, pp. 390–410, 2010 (cit. on p. 16).

[45] S. Siebentritt and U. Rau, *Shallow Defects in the Wide Gap Chalcopyrite*. Springer-Verlag Berlin Heidelberg, 2006 (cit. on pp. 16, 39, 43–45).

[46] F. Babbe, H. Elanzeery, M. H. Wolter, K. Santhosh, and S. Siebentritt, "Experimental evidence of a third acceptor in CuInSe2 and Cu(In,Ga)Se2 absorber layers", *submitted*, (cit. on pp. 17, 100).

[47] S. Siebentritt, I. Beckers, T. Riemann, J. Christen, A. Hoffmann, and M. Dworzak, "Reconciliation of luminescence and Hall measurements on the ternary semiconductor CuGaSe2", *Applied Physics Letters*, vol. 86, no. 9, p. 091 909, 2005 (cit. on p. 17).

[48] J. K. Larsen, "Inhomogeneities in Epitaxial Chalcopyrites studied by Photoluminescence", PhD thesis, University of Luxembourg, 2011, http://hdl.handle.net/10993/15580 (cit. on pp. 17, 44, 45, 51, 52, 100, 101, 110–112, 114, 117).

[49] F. Babbe, "Optical Analysis of Efficiency Limitations of Cu(In,Ga)Se2 grown under Copper Excess", PhD thesis, 2019, http://hdl.handle.net/10993/38677 (cit. on pp. 17, 27, 41, 86, 108, 133).

[50] L. M. Mansfield, D. Kuciauskas, P. Dippo, J. V. Li, K. Bowers, B. To, C. DeHart, and K. Ramanathan, "Optoelectronic Investigation of Sb-Doped Cu(In,Ga)Se 2", *IEEE Journal of Photovoltaics*, vol. 5, no. 6, pp. 1769–1774, 2015 (cit. on pp. 17, 108, 143).

[51] J. T. Heath, J. D. Cohen, W. N. Shafarman, D. X. Liao, and A. A. Rockett, "Effect of Ga content on defect states in CuIn 1-x Ga x Se 2 photovoltaic devices", *Applied Physics Letters*, vol. 80, no. 24, pp. 4540–4542, 2002 (cit. on pp. 17, 108, 143).

[52] X. Hu, T. Sakurai, A. Yamada, S. Ishizuka, S. Niki, and K. Akimoto, "Investigation of the relative density of deep defects in Cu(In,Ga)Se 2 thin films dependent on Ga content by transient photocapacitance method", *Japanese Journal of Applied Physics*, vol. 53, no. 6, p. 068 008, 2014 (cit. on pp. 17, 108, 143).

[53] T. Sakurai, H Uehigashi, M. Islam, T Miyazaki, K Akimoto, S Ishizuka, K Sakurai, A Yamada, K Matsubara, and S Niki, "Study on deep defects in Cu(In,Ga)Se2 solar cells by photocapacitance spectroscopy", in *2008 33rd IEEE Photovolatic Specialists Conference*, IEEE, 2008, pp. 1–4 (cit. on pp. 17, 108, 143).

[54] S. Karki, P. Paul, G. Rajan, B. Belfore, D. Poudel, A. Rockett, E. Danilov, F. Castellano, A. Arehart, and S. Marsillac, "Analysis of Recombination Mechanisms in RbF-Treated CIGS Solar Cells", *IEEE Journal of Photovoltaics*, vol. 9, no. 1, pp. 313–318, 2019 (cit. on pp. 17, 108, 143, 160).

[55] C. Spindler, D. Regesch, and S. Siebentritt, "Revisiting radiative deep-level transitions in CuGaSe 2 by photoluminescence", *Applied Physics Letters*, vol. 109, no. 3, p. 032 105, 2016 (cit. on p. 18).

[56] R. Scheer and H.-W. Schock, *Chalcogenide Photovoltaics*. WILEY-VCH Verlag, 2011 (cit. on pp. 18–20, 27–29, 31, 33, 210).

[57] J. Hedstrom, H. Ohlsen, M. Bodegard, A. Kylner, L. Stolt, D. Hariskos, M. Ruckh, and H.-W. Schock, "ZnO/CdS/Cu(In,Ga)Se/sub 2/ thin film solar cells with improved performance", in *Conference Record of the Twenty Third IEEE Photovoltaic Specialists Conference - 1993 (Cat. No.93CH3283-9)*, IEEE, 1993, pp. 364–371 (cit. on pp. 18, 32, 33).

[58] F. Kessler and D. Rudmann, "Technological aspects of flexible CIGS solar cells and modules", *Solar Energy*, vol. 77, no. 6, pp. 685–695, 2004 (cit. on p. 18).

[59] P. Reinhard, A. Chirila, P. Blosch, F. Pianezzi, S. Nishiwaki, S. Buecheler, and A. N. Tiwari, "Review of Progress Toward 20% Efficiency Flexible CIGS Solar Cells and Manufacturing Issues of Solar Modules", *IEEE Journal of Photovoltaics*, vol. 3, no. 1, pp. 572–580, 2013 (cit. on p. 18).

[60] A. Chirilă, S. Buecheler, F. Pianezzi, P. Bloesch, C. Gretener, A. R. Uhl, C. Fella, L. Kranz, J. Perrenoud, S. Seyrling, R. Verma, S. Nishiwaki, Y. E. Romanyuk, G. Bilger, and A. N. Tiwari, "Highly efficient Cu(In,Ga)Se2 solar cells grown on flexible polymer films", *Nature Materials*, vol. 10, no. 11, pp. 857–861, 2011 (cit. on pp. 18, 19, 31–33).

[61] B. Bissig, "Micro- and macroscopic characterization of recombination losses in high efficiency Cu(In,Ga)Se2 thin film solar cells", PhD thesis, ETH Zurich, 2018 (cit. on pp. 19, 145).

[62] S. Nishiwaki, N. Kohara, T. Negami, and T. Wada, "MoSe 2 layer formation at Cu(In,Ga)Se 2/Mo Interfaces in High Efficiency Cu(In1- xGa x)Se 2 Solar Cells", *Japanese Journal of Applied Physics*, vol. 37, no. Part 2, No. 1A/B, pp. L71–L73, 1998 (cit. on p. 19).

[63] T. Wada, N. Kohara, S. Nishiwaki, and T. Negami, "Characterization of the Cu(In,Ga)Se2/Mo interface in CIGS solar cells", *Thin Solid Films*, vol. 387, no. 1-2, pp. 118–122, 2001 (cit. on p. 19).

[64] N. Kohara, S. Nishiwaki, Y. Hashimoto, T. Negami, and T. Wada, "Electrical properties of the Cu(In,Ga)Se2/ MoSe2/Mo structure", *Solar Energy Materials and Solar Cells*, vol. 67, no. 1-4, pp. 209–215, 2001 (cit. on p. 19).

[65] D. Abou-Ras, G. Kostorz, D. Bremaud, M. Kälin, F. Kurdesau, A. Tiwari, and M. Döbeli, "Formation and characterisation of MoSe2 for Cu(In,Ga)Se2 based solar cells", *Thin Solid Films*, vol. 480-481, pp. 433–438, 2005 (cit. on p. 19).

[66] P. Reinhard, S. Buecheler, and A. Tiwari, "Technological status of Cu(In,Ga)(Se,S)2-based photovoltaics", *Solar Energy Materials and Solar Cells*, vol. 119, pp. 287–290, 2013 (cit. on p. 19).

[67] T. Feurer, P. Reinhard, E. Avancini, B. Bissig, J. Löckinger, P. Fuchs, R. Carron, T. P. Weiss, J. Perrenoud, S. Stutterheim, S. Buecheler, and A. N. Tiwari, "Progress in thin film CIGS photovoltaics - Research and development, manufacturing, and applications", *Progress in Photovoltaics: Research and Applications*, vol. 25, no. 7, pp. 645–667, 2017 (cit. on pp. 19, 20).

[68] M. A. Contreras, M. J. Romero, B. To, F Hasoon, R Noufi, S Ward, and K Ramanathan, "Optimization of CBD CdS process in high-efficiency Cu(In,Ga)Se2-based solar cells", *Thin Solid Films*, vol. 403-404, pp. 204–211, 2002 (cit. on pp. 19, 35).

[69] D. Schmid, M. Ruckh, and H. Schock, "Photoemission studies on Cu(In, Ga)Se2 thin films and related binary selenides", *Applied Surface Science*, vol. 103, no. 4, pp. 409–429, 1996 (cit. on p. 19).

[70] D. Regesch, L. Gütay, J. K. Larsen, V. Deprédurand, D. Tanaka, Y. Aida, and S. Siebentritt, "Degradation and passivation of CuInSe2", *Applied Physics Letters*, vol. 101, no. 11, 2012 (cit. on pp. 19, 90, 108, 183).

[71] T. M. Friedlmeier, P. Jackson, A. Bauer, D. Hariskos, O. Kiowski, R. Menner, R. Wuerz, and M. Powalla, "High-efficiency Cu(In,Ga)Se 2 solar cells", *Thin Solid Films*, vol. 633, pp. 13–17, 2017 (cit. on pp. 19, 20, 32, 33, 53).

[72] W. Witte, S. Spiering, and D. Hariskos, "Substitution of the CdS buffer layer in CIGS thin-film solar cells", *Vakuum in Forschung und Praxis*, vol. 26, no. 1, pp. 23–27, 2014 (cit. on p. 19).

[73] N. Naghavi, D. Abou-Ras, N. Allsop, N. Barreau, S. Bücheler, A. Ennaoui, C.-H. Fischer, C. Guillen, D. Hariskos, J. Herrero, R. Klenk, K. Kushiya, D. Lincot, R. Menner, T. Nakada, C. Platzer-Björkman, S. Spiering, A. Tiwari, and T. Törndahl, "Buffer layers and transparent conducting oxides for chalcopyrite Cu(In,Ga)(S,Se)2 based thin film photovoltaics: present status and current developments", *Progress in Photovoltaics: Research and Applications*, vol. 18, no. 6, pp. 411–433, 2010 (cit. on p. 20).

[74] V Srikant and D. R. Clarke, "On the optical band gap of zinc oxide", *Journal of Applied Physics*, vol. 83, no. 10, pp. 5447–5451, 1998 (cit. on pp. 20, 154).

[75] J. Nelson, *The Physics of Solar Cells*. Imperial College Press, London, 2003 (cit. on p. 21).

[76] W. Shockley and H. J. Queisser, "Detailed Balance Limit of Efficiency of p-n Junction Solar Cells", *Journal of Applied Physics*, vol. 32, no. 3, pp. 510–519, 1961 (cit. on pp. 23, 131, 145).

[77] P. W. Bridgman, "Note on the Principle of Detailed Balancing", *Physical Review*, vol. 31, no. 1, pp. 101–102, 1928 (cit. on p. 23).

[78] G Kirchhoff, "Ueber das Verhältniss zwischen dem Emissionsvermögen und dem Absorptionsvermögen der Körper für Wärme und Licht", *Annalen der Physik und Chemie*, vol. 185, no. 2, pp. 275–301, 1860 (cit. on pp. 23, 214).

[79] T. Kirchartz and U. Rau, "What Makes a Good Solar Cell?", *Advanced Energy Materials*, vol. 1703385, p. 1 703 385, 2018 (cit. on pp. 23, 145, 214).

[80] S. Siebentritt, "What limits the efficiency of chalcopyrite solar cells?", *Solar Energy Materials and Solar Cells*, vol. 95, no. 6, pp. 1471–1476, 2011 (cit. on pp. 23, 30, 31, 155).

[81] M. A. Green, *Solar Cells: Operating Principles, Technology and System Applications*. Englewood Cliffs, New Jersey: Prentice-Hall Inc., 1982 (cit. on pp. 24, 156).

[82] L. C. Hirst and N. J. Ekins-Daukes, "Fundamental losses in solar cells", *Progress in Photovoltaics: Research and Applications*, vol. 19, no. 3, pp. 286–293, 2011 (cit. on p. 25).

[83] T. Markvart, "Solar cell as a heat engine: energy-entropy analysis of photovoltaic conversion", *physica status solidi (a)*, vol. 205, no. 12, pp. 2752–2756, 2008 (cit. on p. 25).

[84] A. De Vos and H. Pauwels, "On the thermodynamic limit of photovoltaic energy conversion", *Applied physics*, vol. 25, no. 2, pp. 119–125, 1981 (cit. on p. 25).

[85] U. Rau, U. W. Paetzold, and T. Kirchartz, "Thermodynamics of light management in photovoltaic devices", *Physical Review B*, vol. 90, no. 3, p. 035 211, 2014 (cit. on p. 25).

[86] F. Dimroth, M. Grave, P. Beutel, U. Fiedeler, C. Karcher, T. N. D. Tibbits, E. Oliva, G. Siefer, M. Schachtner, A. Wekkeli, A. W. Bett, R. Krause, M. Piccin, N. Blanc, C. Drazek, E. Guiot, B. Ghyselen, T. Salvetat, A. Tauzin, T. Signamarcheix, A. Dobrich, T. Hannappel, and K. Schwarzburg, "Wafer bonded four-junction GaInP/GaAs//GaInAsP/GaInAs concentrator solar cells with 44.7% efficiency", *Progress in Photovoltaics: Research and Applications*, vol. 22, no. 3, pp. 277–282, 2014 (cit. on p. 26).

[87] E. D. Kosten, J. H. Atwater, J. Parsons, A. Polman, and H. A. Atwater, "Highly efficient GaAs solar cells by limiting light emission angle", *Light: Science & Applications*, vol. 2, no. 1, e45–e45, 2013 (cit. on p. 26).

[88] F. Dimroth and S. Kurtz, "High-Efficiency Multijunction Solar Cells", *MRS Bulletin*, vol. 32, no. 03, pp. 230–235, 2007 (cit. on p. 26).

[89] L. Kranz, A. Abate, T. Feurer, F. Fu, E. Avancini, J. Löckinger, P. Reinhard, S. M. Zakeeruddin, M. Grätzel, S. Buecheler, and A. N. Tiwari, "High-Efficiency Polycrystalline Thin Film Tandem Solar Cells", *The Journal of Physical Chemistry Letters*, vol. 6, no. 14, pp. 2676–2681, 2015 (cit. on p. 26).

[90] M. C. Hanna, Z. Lu, and A. J. Nozik, "Hot carrier solar cells", in *AIP Conference Proceedings*, vol. 309, AIP, 1997, pp. 309–316 (cit. on p. 26).

[91] D. König, K. Casalenuovo, Y. Takeda, G. Conibeer, J. Guillemoles, R. Patterson, L. Huang, and M. Green, "Hot carrier solar cells: Principles, materials and design", *Physica E: Low-dimensional Systems and Nanostructures*, vol. 42, no. 10, pp. 2862–2866, 2010 (cit. on p. 26).

[92] J. I. Pankove, *Optical processes in semiconductors*. Dover Publications, New York, 1971 (cit. on pp. 27, 42, 85, 94, 95).

[93] T. P. Weiss, R. Carron, M. H. Wolter, J. Löckinger, E. Avancini, S. Siebentritt, S. Buecheler, and A. N. Tiwari, "Time-resolved photoluminescence on double graded Cu(In,Ga)Se 2 – Impact of front surface recombination and its temperature dependence", *Science and Technology of Advanced Materials*, vol. 20, no. 1, pp. 313–323, 2019 (cit. on pp. 28, 54, 88, 210, 215, 218).

[94] W. K. Metzger, I. L. Repins, and M. A. Contreras, "Long lifetimes in high-efficiency Cu(In,Ga)Se2 solar cells", *Applied Physics Letters*, vol. 93, no. 2, p. 022 110, 2008 (cit. on p. 28).

[95] A. Redinger, S. Levcenko, C. J. Hages, D. Greiner, C. A. Kaufmann, and T. Unold, "Time resolved photoluminescence on Cu(In, Ga)Se 2 absorbers: Distinguishing degradation and trap states", *Applied Physics Letters*, vol. 110, no. 12, p. 122 104, 2017 (cit. on p. 28).

[96] M. Maiberg, T. Hölscher, S. Zahedi-Azad, W. Fränzel, and R. Scheer, "Investigation of long lifetimes in Cu(In,Ga)Se 2 by time-resolved photoluminescence", *Applied Physics Letters*, vol. 107, no. 12, p. 122 104, 2015 (cit. on p. 28).

[97] J. Chantana, D. Hironiwa, T. Watanabe, S. Teraji, K. Kawamura, and T. Minemoto, "Investigation of Cu(In,Ga)Se 2 absorber by time-resolved photoluminescence for improvement of its photovoltaic performance", *Solar Energy Materials and Solar Cells*, vol. 130, pp. 567–572, 2014 (cit. on p. 28).

[98] W. Shockley and W. T. Read, "Statistics of the Recombinations of Holes and Electrons", *Physical Review*, vol. 87, no. 5, pp. 835–842, 1952 (cit. on p. 28).

[99] R. N. Hall, "Electron-Hole Recombination in Germanium", *Physical Review*, vol. 87, no. 2, pp. 387–387, 1952 (cit. on p. 28).

[100] C.-t. Sah, R. Noyce, and W. Shockley, "Carrier Generation and Recombination in P-N Junctions and P-N Junction Characteristics", *Proceedings of the IRE*, vol. 45, no. 9, pp. 1228–1243, 1957 (cit. on p. 28).

[101] U. Rau, K. Taretto, and S. Siebentritt, "Grain boundaries in Cu(In, Ga)(Se, S)2 thin-film solar cells", *Applied Physics A*, vol. 96, no. 1, pp. 221–234, 2009 (cit. on p. 29).

[102] U Rau, A Jasenek, H. Schock, F Engelhardt, and T. Meyer, "Electronic loss mechanisms in chalcopyrite based heterojunction solar cells", *Thin Solid Films*, vol. 361-362, pp. 298–302, 2000 (cit. on p. 30).

[103] I. Hengel, A. Neisser, R. Klenk, and M. Lux-Steiner, "Current transport in CuInS2:Ga/Cds/Zno – solar cells", *Thin Solid Films*, vol. 361-362, pp. 458–462, 2000 (cit. on p. 30).

[104] U. Rau and H. Schock, "Electronic properties of Cu(In,Ga)Se 2 heterojunction solar cells-recent achievements, current understanding, and future challenges", *Applied Physics A: Materials Science & Processing*, vol. 69, no. 2, pp. 131–147, 1999 (cit. on p. 30).

[105] U. Rau and J. H. Werner, "Radiative efficiency limits of solar cells with lateral band-gap fluctuations", *Applied Physics Letters*, vol. 84, no. 19, pp. 3735–3737, 2004 (cit. on pp. 31, 94, 95).

[106] J. H. Werner, J. Mattheis, and U. Rau, "Efficiency limitations of polycrystalline thin film solar cells: case of Cu(In,Ga)Se2", *Thin Solid Films*, vol. 480-481, pp. 399–409, 2005 (cit. on pp. 31, 94, 95, 142, 143).

[107] J. L. Shay, S. Wagner, and H. M. Kasper, "Efficient CuInSe 2 /CdS solar cells", *Applied Physics Letters*, vol. 27, no. 2, pp. 89–90, 1975 (cit. on p. 31).

[108] A. M. Gabor, J. R. Tuttle, D. S. Albin, M. A. Contreras, R. Noufi, and A. M. Hermann, "High-efficiency CuIn x Ga 1- x Se 2 solar cells made from (In x ,Ga 1- x) 2 Se 3 precursor films", *Applied Physics Letters*, vol. 65, no. 2, pp. 198–200, 1994 (cit. on p. 31).

[109] P. Jackson, D. Hariskos, R. Wuerz, O. Kiowski, A. Bauer, T. M. Friedlmeier, and M. Powalla, "Properties of Cu(In,Ga)Se 2 solar cells with new record efficiencies up to 21.7%", *physica status solidi (RRL) - Rapid Research Letters*, vol. 9, no. 1, pp. 28–31, 2015 (cit. on p. 32).

[110] O. Lundberg, M. Edoff, and L. Stolt, "The effect of Ga-grading in CIGS thin film solar cells", *Thin Solid Films*, vol. 480-481, pp. 520–525, 2005 (cit. on p. 33).

[111] T. Feurer, B. Bissig, T. P. Weiss, R. Carron, E. Avancini, J. Löckinger, S. Buecheler, and A. N. Tiwari, "Single-graded CIGS with narrow bandgap for tandem solar cells", *Science and Technology of Advanced Materials*, vol. 19, no. 1, pp. 263–270, 2018 (cit. on pp. 33, 54, 128).

[112] T. Nakada, "Invited Paper: CIGS-based thin film solar cells and modules: Unique material properties", *Electronic Materials Letters*, vol. 8, no. 2, pp. 179–185, 2012 (cit. on p. 33).

[113] W. Witte, D. Abou-Ras, K. Albe, G. H. Bauer, F. Bertram, C. Boit, R. Brüggemann, J. Christen, J. Dietrich, A. Eicke, D. Hariskos, M. Maiberg, R. Mainz, M. Meessen, M. Müller, O. Neumann, T. Orgis, S. Paetel, J. Pohl, H. Rodriguez-Alvarez, R. Scheer, H.-W. Schock, T. Unold, A. Weber, and M. Powalla, "Gallium gradients in Cu(In,Ga)Se 2 thin-film solar cells", *Progress in Photovoltaics: Research and Applications*, vol. 23, no. 6, pp. 717–733, 2015 (cit. on p. 33).

[114] P. Reinhard, B. Bissig, F. Pianezzi, E. Avancini, H. Hagendorfer, D. Keller, P. Fuchs, M. Döbeli, C. Vigo, P. Crivelli, S. Nishiwaki, S. Buecheler, and A. N. Tiwari, "Features of KF and NaF Postdeposition Treatments of Cu(In,Ga)Se 2 Absorbers for High Efficiency Thin Film Solar Cells", *Chemistry of Materials*, vol. 27, no. 16, pp. 5755–5764, 2015 (cit. on pp. 34, 35, 158).

[115] M Lammer, U Klemm, and M Powalla, "Sodium co-evaporation for low temperature Cu(In,Ga)Se2 deposition", *Thin Solid Films*, vol. 387, no. 1-2, pp. 33–36, 2001 (cit. on p. 33).

[116] E. Cadel, N. Barreau, J. Kessler, and P. Pareige, "Atom probe study of sodium distribution in polycrystalline Cu(In,Ga)Se2 thin film", *Acta Materialia*, vol. 58, no. 7, pp. 2634–2637, 2010 (cit. on p. 34).

[117] O. Cojocaru-Mirédin, P.-P. Choi, D. Abou-Ras, S. S. Schmidt, R. Caballero, and D. Raabe, "Characterization of Grain Boundaries in Cu(In,Ga)Se2 Films Using Atom-Probe Tomography", *IEEE Journal of Photovoltaics*, vol. 1, no. 2, pp. 207–212, 2011 (cit. on p. 34).

[118] P.-P. Choi, O. Cojocaru-Mirédin, R. Wuerz, and D. Raabe, "Comparative atom probe study of Cu(In,Ga)Se2 thin-film solar cells deposited on soda-lime glass and mild steel substrates", *Journal of Applied Physics*, vol. 110, no. 12, p. 124 513, 2011 (cit. on pp. 34, 35, 156).

[119] D. Abou-Ras, S. S. Schmidt, R. Caballero, T. Unold, H.-W. Schock, C. T. Koch, B. Schaffer, M. Schaffer, P.-P. Choi, and O. Cojocaru-Mirédin, "Confined and Chemically Flexible Grain Boundaries in Polycrystalline Compound Semiconductors", *Advanced Energy Materials*, vol. 2, no. 8, pp. 992–998, 2012 (cit. on p. 34).

[120] J. Keller, R. Schlesiger, I. Riedel, J. Parisi, G. Schmitz, A. Avellan, and T. Dalibor, "Grain boundary investigations on sulfurized Cu(In,Ga)(S,Se)2 solar cells using atom probe tomography", *Solar Energy Materials and Solar Cells*, vol. 117, pp. 592–598, 2013 (cit. on p. 34).

[121] O. Cojocaru-Mirédin, T. Schwarz, P.-P. Choi, M. Herbig, R. Wuerz, and D. Raabe, "Atom Probe Tomography Studies on the Cu(In,Ga)Se2 Grain Boundaries", *Journal of Visualized Experiments*, no. 74, pp. 1–8, 2013 (cit. on pp. 34, 35, 138).

[122] A. Laemmle, R. Wuerz, T. Schwarz, O. Cojocaru-Mirédin, P.-P. Choi, and M. Powalla, "Investigation of the diffusion behavior of sodium in Cu(In,Ga)Se2 layers", *Journal of Applied Physics*, vol. 115, no. 15, p. 154 501, 2014 (cit. on pp. 34, 35, 138).

[123] R. V. Forest, E. Eser, B. E. McCandless, J. G. Chen, and R. W. Birkmire, "Reversibility of (Ag,Cu)(In,Ga)Se2 electrical properties with the addition and removal of Na: Role of grain boundaries", *Journal of Applied Physics*, vol. 117, no. 11, p. 115 102, 2015 (cit. on p. 34).

[124] D. W. Niles, K. Ramanathan, F. Hasoon, R. Noufi, B. J. Tielsch, and J. E. Fulghum, "Na impurity chemistry in photovoltaic CIGS thin films: Investigation with x-ray photoelectron spectroscopy", *Journal of Vacuum Science & Technology A: Vacuum, Surfaces, and Films*, vol. 15, no. 6, pp. 3044–3049, 1997 (cit. on p. 34).

[125] L. E. Oikkonen, M. G. Ganchenkova, A. P. Seitsonen, and R. M. Nieminen, "Effect of sodium incorporation into CuInSe 2 from first principles", *Journal of Applied Physics*, vol. 114, no. 8, p. 083 503, 2013 (cit. on p. 34).

[126] L. Kronik, D. Cahen, and H. W. Schock, "Effects of Sodium on Polycrystalline Cu(In,Ga)Se2 and Its Solar Cell Performance", *Advanced Materials*, vol. 10, no. 1, pp. 31–36, 1998 (cit. on p. 34).

[127] S.-H. Wei, S. B. Zhang, and A. Zunger, "Effects of Na on the electrical and structural properties of CuInSe2", *Journal of Applied Physics*, vol. 85, no. 10, pp. 7214–7218, 1999 (cit. on pp. 34, 138, 157).

[128] Z.-K. Yuan, S. Chen, Y. Xie, J.-S. Park, H. Xiang, X.-G. Gong, and S.-H. Wei, "Na-Diffusion Enhanced p-type Conductivity in Cu(In,Ga)Se2 : A New Mechanism for Efficient Doping in Semiconductors", *Advanced Energy Materials*, vol. 6, no. 24, p. 1 601 191, 2016 (cit. on pp. 34, 138, 157).

[129] T. Nakada, D. Iga, H. Ohbo, and A. Kunioka, "Effects of Sodium on C u (I n , G a) S e 2 -Based Thin Films and Solar Cells", *Japanese Journal of Applied Physics*, vol. 36, no. Part 1, No. 2, pp. 732–737, 1997 (cit. on p. 34).

[130] F. Pianezzi, P. Reinhard, A. Chirilă, B. Bissig, S. Nishiwaki, S. Buecheler, and A. N. Tiwari, "Unveiling the effects of post-deposition treatment with different alkaline elements on the electronic properties of CIGS thin film solar cells", *Physical Chemistry Chemical Physics*, vol. 16, no. 19, p. 8843, 2014 (cit. on pp. 34–36, 138, 139, 156–158, 160).

[131] A. Laemmle, "Investigation of the sodium (potassium) diffusion in Cu(In,Ga)Se2 solar cells", PhD thesis, Karlsruhe Institute of Technology, 2015 (cit. on pp. 34, 138, 157, 160).

[132] D. J. Schroeder and A. A. Rockett, "Electronic effects of sodium in epitaxial CuIn1-xGaxSe2", *Journal of Applied Physics*, vol. 82, no. 10, pp. 4982–4985, 1997 (cit. on p. 35).

[133] K. Timmo, M. Altosaar, J. Raudoja, E. Mellikov, T. Varema, M. Danilson, and M. Grossberg, "The effect of sodium doping to CuInSe2 monograin powder properties", *Thin Solid Films*, vol. 515, no. 15, pp. 5887–5890, 2007 (cit. on p. 35).

[134] D. Colombara, F. Werner, T. Schwarz, I. Cañero Infante, Y. Fleming, N. Valle, C. Spindler, E. Vacchieri, G. Rey, M. Guennou, M. Bouttemy, A. G. Manjón, I. Peral Alonso, M. Melchiorre, B. El Adib, B. Gault, D. Raabe, P. J. Dale, and S. Siebentritt, "Sodium enhances indium-gallium interdiffusion in copper indium gallium diselenide photovoltaic absorbers", *Nature Communications*, vol. 9, no. 1, p. 826, 2018 (cit. on pp. 35, 156).

[135] A. Rockett, "The effect of Na in polycrystalline and epitaxial single-crystal CuIn1-xGaxSe2", *Thin Solid Films*, vol. 480-481, pp. 2–7, 2005 (cit. on p. 35).

[136] P. Salomé, H. Rodriguez-Alvarez, and S. Sadewasser, "Incorporation of alkali metals in chalcogenide solar cells", *Solar Energy Materials and Solar Cells*, vol. 143, pp. 9–20, 2015 (cit. on p. 35).

[137] A. Stokes, M. Al-Jassim, D. Diercks, and B. Gorman, "Alkali segregation and matrix concentrations in thin film Cu(In,Ga)Se2 at targeted interfaces characterized in 3-D at the nanoscale", in *2015 IEEE 42nd Photovoltaic Specialist Conference (PVSC)*, IEEE, 2015, pp. 1–4 (cit. on pp. 35, 157).

[138] A. Stokes, M. Al-Jassim, and B. Gorman, "Semi-statistical Atom Probe Tomography Analysis of Thin Film Grain Boundaries", *Microscopy and Microanalysis*, vol. 22, no. S3, pp. 644–645, 2016 (cit. on p. 35).

[139] A. Laemmle, R. Wuerz, and M. Powalla, "Efficiency enhancement of Cu(In,Ga)Se 2 thin-film solar cells by a post-deposition treatment with potassium fluoride", *physica status solidi (RRL) - Rapid Research Letters*, vol. 7, no. 9, pp. 631–634, 2013 (cit. on pp. 35, 157, 160).

[140] E. Avancini, R. Carron, T. P. Weiss, C. Andres, M. Bürki, C. Schreiner, R. Figi, Y. E. Romanyuk, S. Buecheler, and A. N. Tiwari, "Effects of Rubidium Fluoride and Potassium Fluoride Postdeposition Treatments on Cu(In,Ga)Se2 Thin Films and Solar Cell Performance", *Chemistry of Materials*, vol. 29, no. 22, pp. 9695–9704, 2017 (cit. on pp. 35, 36, 91, 139, 140).

[141] M. Malitckaya, H.-P. Komsa, V. Havu, and M. J. Puska, "Effect of Alkali Metal Atom Doping on the CuInSe 2 -Based Solar Cell Absorber", *The Journal of Physical Chemistry C*, vol. 121, no. 29, pp. 15 516–15 528, 2017 (cit. on pp. 35, 36, 108, 123, 138–140, 144, 157, 158).

[142] P. Pistor, D. Greiner, C. A. Kaufmann, S. Brunken, M. Gorgoi, A. Steigert, W. Calvet, I. Lauermann, R. Klenk, T. Unold, and M.-C. Lux-Steiner, "Experimental indication for band gap widening of chalcopyrite solar cell absorbers after potassium fluoride treatment", *Applied Physics Letters*, vol. 105, no. 6, p. 063 901, 2014 (cit. on p. 35).

[143] E. Handick, P. Reinhard, J.-H. Alsmeier, L. Köhler, F. Pianezzi, S. Krause, M. Gorgoi, E. Ikenaga, N. Koch, R. G. Wilks, S. Buecheler, A. N. Tiwari, and M. Bär, "Potassium Postdeposition Treatment-Induced Band Gap Widening at Cu(In,Ga)Se 2 Surfaces – Reason for Performance Leap?", *ACS Applied Materials & Interfaces*, vol. 7, no. 49, pp. 27 414–27 420, 2015 (cit. on pp. 35, 157).

[144] T. M. Friedlmeier, P. Jackson, A. Bauer, D. Hariskos, O. Kiowski, R. Wuerz, and M. Powalla, "Improved Photocurrent in Cu(In,Ga)Se 2 Solar Cells: From 20.8% to 21.7% Efficiency with CdS Buffer and 21.0% Cd-Free", *IEEE Journal of Photovoltaics*, vol. 5, no. 5, pp. 1487–1491, 2015 (cit. on p. 35).

[145] H. Elanzeery, F. Babbe, M. Melchiorre, A. Zelenina, and S. Siebentritt, "Potassium Fluoride Ex Situ Treatment on Both Cu-Rich and Cu-Poor CuInSe2 Thin Film Solar Cells", *IEEE Journal of Photovoltaics*, vol. 7, no. 2, pp. 684–689, 2017 (cit. on p. 35).

[146] I. Khatri, H. Fukai, H. Yamaguchi, M. Sugiyama, and T. Nakada, "Effect of potassium fluoride post-deposition treatment on Cu(In,Ga)Se 2 thin films and solar cells fabricated onto sodalime glass substrates", *Solar Energy Materials and Solar Cells*, vol. 155, pp. 280–287, 2016 (cit. on pp. 35, 36, 160).

[147] S. A. Jensen, S. Glynn, A. Kanevce, P. Dippo, J. V. Li, D. H. Levi, and D. Kuciauskas, "Beneficial effect of post-deposition treatment in high-efficiency Cu(In,Ga)Se2 solar cells through reduced potential fluctuations", *Journal of Applied Physics*, vol. 120, no. 6, p. 063 106, 2016 (cit. on pp. 35, 58, 123, 160).

[148] D. Shin, J. Kim, T. Gershon, R. Mankad, M. Hopstaken, S. Guha, B. T. Ahn, and B. Shin, "Effects of the incorporation of alkali elements on Cu(In,Ga)Se 2 thin film solar cells", *Solar Energy Materials and Solar Cells*, vol. 157, pp. 695–702, 2016 (cit. on p. 35).

[149] A. Laemmle, R. Wuerz, and M. Powalla, "Investigation of the effect of potassium on Cu(In,Ga)Se 2 layers and solar cells", *Thin Solid Films*, vol. 582, pp. 27–30, 2015 (cit. on pp. 35, 157, 160).

[150] C. P. Muzzillo, "Review of grain interior, grain boundary, and interface effects of K in CIGS solar cells: Mechanisms for performance enhancement", *Solar Energy Materials and Solar Cells*, vol. 172, pp. 18–24, 2017 (cit. on pp. 36, 157, 158).

[151] J.-L. Wu, Y. Hirai, T. Kato, H. Sugimoto, and V. Bermudez, "New World Record Efficiency up to 22.9% for Cu(In,Ga)(S,Se)2 Thin-Film Solar Cells", *7th World Conference on Photovoltaic Energy Conversion (WCPEC-7)*, (cit. on p. 36).

[152] P. Schöppe, S. Schönherr, R. Wuerz, W. Wisniewski, G. Martínez-Criado, M. Ritzer, K. Ritter, C. Ronning, and C. S. Schnohr, "Rubidium segregation at random grain boundaries in Cu(In,Ga)Se2 absorbers", *Nano Energy*, vol. 42, no. August, pp. 307–313, 2017 (cit. on pp. 36, 139, 158).

[153] P. Schöppe, S. Schönherr, P. Jackson, R. Wuerz, W. Wisniewski, M. Ritzer, M. Zapf, A. Johannes, C. S. Schnohr, and C. Ronning, "Overall Distribution of Rubidium in Highly Efficient Cu(In,Ga)Se 2 Solar Cells", *ACS Applied Materials & Interfaces*, vol. 10, no. 47, pp. 40 592–40 598, 2018 (cit. on pp. 36, 139–141, 144).

[154] A. Vilalta-Clemente, M. Raghuwanshi, S. Duguay, C. Castro, E. Cadel, P. Pareige, P. Jackson, R. Wuerz, D. Hariskos, and W. Witte, "Rubidium distribution at atomic scale in high efficient Cu(In,Ga)Se 2 thin-film solar cells", *Applied Physics Letters*, vol. 112, no. 10, p. 103 105, 2018 (cit. on pp. 36, 91, 139, 141, 159).

[155] M. Raghuwanshi, A. Vilalta-Clemente, C. Castro, S. Duguay, E. Cadel, P. Jackson, D. Hariskos, W. Witte, and P. Pareige, "Influence of RbF post deposition treatment on heterojunction and grain boundaries in high efficient (21.1%) Cu(In,Ga)Se2 solar cells", *Nano Energy*, vol. 60, pp. 103–110, 2019 (cit. on pp. 36, 139, 141, 144).

[156] T. Kodalle, M. D. Heinemann, D. Greiner, H. A. Yetkin, M. Klupsch, C. Li, P. A. van Aken, I. Lauermann, R. Schlatmann, and C. A. Kaufmann, "Elucidating the Mechanism of an RbF Post Deposition Treatment in CIGS Thin Film Solar Cells", *Solar RRL*, vol. 2, no. 9, p. 1 800 156, 2018 (cit. on pp. 36, 139, 140, 158, 159).

[157] R. Wuerz, W. Hempel, and P. Jackson, "Diffusion of Rb in polycrystalline Cu(In,Ga)Se 2 layers and effect of Rb on solar cell parameters of Cu(In,Ga)Se 2 thin-film solar cells", *Journal of Applied Physics*, vol. 124, no. 16, p. 165 305, 2018 (cit. on pp. 36, 139–141, 156, 158, 160).

[158] S. Ishizuka, N. Taguchi, J. Nishinaga, Y. Kamikawa, S. Tanaka, and H. Shibata, "Group III elemental composition dependence of RbF postdeposition treatment effects on Cu(In,Ga)Se2 thin films and solar cells", *Journal of Physical Chemistry C*, vol. 122, no. 7, pp. 3809–3817, 2018 (cit. on pp. 36, 140, 160).

[159] N. Taguchi, S. Tanaka, and S. Ishizuka, "Direct insights into RbInSe 2 formation at Cu(In,Ga)Se 2 thin film surface with RbF postdeposition treatment", *Applied Physics Letters*, vol. 113, no. 11, p. 113 903, 2018 (cit. on pp. 36, 139, 140, 158).

[160] N. Nicoara, T. Kunze, P. Jackson, D. Hariskos, R. F. Duarte, R. G. Wilks, W. Witte, M. Bär, and S. Sadewasser, "Evidence for Chemical and Electronic Nonuniformities in the Formation of the Interface of RbF-Treated Cu(In,Ga)Se 2 with CdS", *ACS Applied Materials & Interfaces*, vol. 9, no. 50, pp. 44 173–44 180, 2017 (cit. on p. 36).

[161] M. D. Heinemann, T. Kodalle, C. Hages, M. Klupsch, D. Greiner, L. Korte, S. Levcenco, T. Unold, R. Schlatmann, and C. A. Kaufmann, "Evaluation of recombination losses in thin film solar cells using an LED sun simulator - the effect of RbF post-deposition on CIGS solar cells", *EPJ Photovoltaics*, vol. 9, p. 9, 2018 (cit. on pp. 36, 158, 160).

[162] T. Unold and L. Gütay, "Photoluminescence Analysis of Thin-Film Solar Cells", in *Advanced Characterization Techniques for Thin Film Solar Cells*, Weinheim, Germany: Wiley-VCH Verlag GmbH & Co. KGaA, 2011, pp. 151–175 (cit. on pp. 39, 44, 82–85, 104).

[163] S. Siebentritt, N. Rega, A. Zajogin, and M. C. Lux-Steiner, "Do we really need another PL study of CuInSe2?", *physica status solidi (c)*, vol. 1, no. 9, pp. 2304–2310, 2004 (cit. on pp. 41, 43, 96, 115).

[164] P Wurfel, "The chemical potential of radiation", *Journal of Physics C: Solid State Physics*, vol. 15, no. 18, pp. 3967–3985, 1982 (cit. on pp. 42, 82).

[165] H. Barry Bebb and E. W. Williams, "Transport and Optical Phenomena", in *Semiconductors and Semimetals Vol. 8*, R. K. Willardson and A. C. Beer, Eds., Academic Press, New-York, 1972 (cit. on p. 42).

[166] G. Rey, C. Spindler, F. Babbe, W. Rachad, S. Siebentritt, M. Nuys, R. Carius, S. Li, and C. Platzer-Björkman, "Absorption Coefficient of a Semiconductor Thin Film from Photoluminescence", *Physical Review Applied*, vol. 9, no. 6, p. 064 008, 2018 (cit. on pp. 42, 82, 85–87, 95).

[167] M. Planck, *The theory of heat radiation*. P. Blakinston's Son & Co., 1914 (cit. on pp. 43, 153).

[168] B. I. Shklovskij and A. L. Efros, *Electronic Properties of Doped Semiconductors*. Springer-Verlag Berlin, 1984 (cit. on pp. 43, 45, 110).

[169] A. Bauknecht, S. Siebentritt, J. Albert, and M. C. Lux-Steiner, "Radiative recombination via intrinsic defects in CuxGaySe2", *Journal of Applied Physics*, vol. 89, no. 8, pp. 4391–4400, 2001 (cit. on pp. 43, 45).

[170] S. A. Schumacher, J. R. Botha, and V. Alberts, "Photoluminescence study of potential fluctuations in thin layers of Cu(In0.75Ga0.25)(SySe1-y)2", *Journal of Applied Physics*, vol. 99, no. 6, p. 063 508, 2006 (cit. on pp. 45, 111, 114, 115, 117).

[171] I Dirnstorfer, M. Wagner, D. M. Hofmann, M. D. Lampert, F Karg, and B. K. Meyer, "Characterization of CuIn(Ga)Se2 Thin Films", *physica status solidi (a)*, vol. 168, no. 1, pp. 163–175, 1998 (cit. on pp. 45, 96, 108, 114).

[172] D. Abou-Ras, S. S. Schmidt, N. Schäfer, J. Kavalakkatt, T. Rissom, T. Unold, R. Mainz, A. Weber, T. Kirchartz, E. Simsek Sanli, P. A. van Aken, Q. M. Ramasse, H.-J. Kleebe, D. Azulay, I. Balberg, O. Millo, O. Cojocaru-Mirédin, D. Barragan-Yani, K. Albe, J. Haarstrich, and C. Ronning, "Compositional and electrical properties of line and planar defects in Cu(In,Ga)Se 2 thin films for solar cells - a review", *physica status solidi (RRL) - Rapid Research Letters*, vol. 10, no. 5, pp. 363–375, 2016 (cit. on pp. 45, 139, 144, 145).

[173] J. Mooney and P. Kambhampati, "Get the basics right: Jacobian conversion of wavelength and energy scales for quantitative analysis of emission spectra", *Journal of Physical Chemistry Letters*, vol. 4, no. 19, pp. 3316–3318, 2013 (cit. on pp. 50, 198).

[174] R. Kniese, M. Powalla, and U. Rau, "Evaluation of electron beam induced current profiles of Cu(In,Ga)Se2 solar cells with different Ga-contents", *Thin Solid Films*, vol. 517, no. 7, pp. 2357–2359, 2009 (cit. on p. 52).

[175] R. Djemour, M. Mousel, A. Redinger, L. Gütay, A. Crossay, D. Colombara, P. J. Dale, and S. Siebentritt, "Detecting ZnSe secondary phase in Cu 2 ZnSnSe 4 by room temperature photoluminescence", *Applied Physics Letters*, vol. 102, no. 22, p. 222 108, 2013 (cit. on p. 57).

[176] T Weber, H Stolz, W. V. D. Osten, M Heuken, and K Heime, "Fabry-Perot oscillations in epitaxial ZnSe layers", *Semiconductor Science and Technology*, vol. 10, no. 8, pp. 1113–1116, 1995 (cit. on pp. 57, 65).

[177] L. Zeković and V. Urošević, "The role of interference in the electroluminescence of thin anodic oxide films", *Thin Solid Films*, vol. 78, no. 3, pp. 279–286, 1981 (cit. on pp. 57, 58).

[178] L. Zeković, B. Jovanić, L. Ristovski, G. Davidović-Ristovski, and V. Urošević, "Investigation of the porosity of thin Anodic Al2O3 films by interference of photoluminescence radiation", *Thin Solid Films*, vol. 157, no. 1, pp. 59–68, 1988 (cit. on p. 57).

[179] F. Lin, N. Xiang, X. C. Wang, J. Arokiaraj, W. Liu, and S. J. Chua, "Suppression of Interference-Induced Reflectivity Fluctuations in GaN-Based Semiconductor Saturable Absorber Mirror", *Journal of The Electrochemical Society*, vol. 155, no. 5, H307, 2008 (cit. on p. 57).

[180] E. Namvar and M. Fattahi, "Interference effects on the photoluminescence spectrum of GaN/InxGa1-xN single quantum well structures", *Journal of Luminescence*, vol. 128, no. 1, pp. 155–160, 2008 (cit. on p. 57).

[181] J. K. Larsen, S.-Y. Li, J. J. S. Scragg, Y Ren, C. Hägglund, M. D. Heinemann, S. Kretzschmar, T. Unold, and C. Platzer-Björkman, "Interference effects in photoluminescence spectra of Cu 2 ZnSnS 4 and Cu(In,Ga)Se 2 thin films", *Journal of Applied Physics*, vol. 118, no. 3, p. 035 307, 2015 (cit. on pp. 57, 64–67, 72).

[182] R. Djemour, A. Redinger, M. Mousel, L. Gütay, and S. Siebentritt, "Multiple phases of Cu 2 ZnSnSe 4 detected by room temperature photoluminescence", *Journal of Applied Physics*, vol. 116, no. 7, p. 073 509, 2014 (cit. on p. 57).

[183] ——, "Erratum: "Multiple phases of Cu 2 ZnSnSe 4 detected by room temperature photoluminescence" [J. Appl. Phys. 116 , 073509 (2014)]", *Journal of Applied Physics*, vol. 118, no. 8, p. 089 902, 2015 (cit. on p. 57).

[184] K. Tanaka, T. Shinji, and H. Uchiki, "Photoluminescence from Cu2ZnSnS4 thin films with different compositions fabricated by a sputtering-sulfurization method", *Solar Energy Materials and Solar Cells*, vol. 126, pp. 143–148, 2014 (cit. on p. 58).

[185] L. Van Puyvelde, J. Lauwaert, P. Smet, S. Khelifi, T. Ericson, J. Scragg, D. Poelman, R. Van Deun, C. Platzer-Björkman, and H. Vrielinck, "Photoluminescence investigation of Cu 2 ZnSnS 4 thin film solar cells", *Thin Solid Films*, vol. 582, pp. 146–150, 2015 (cit. on p. 58).

[186] R. T. Holm, S. W. McKnight, E. D. Palik, and W Lukosz, "Interference effects in luminescence studies of thin films", *Applied Optics*, vol. 21, no. 14, p. 2512, 1982 (cit. on pp. 58, 65).

[187] M. Moldovan, T. H. Myers, and N. C. Giles, "Investigation of donor-acceptor pair luminescence from ZnSe:N epilayers", *Journal of Applied Physics*, vol. 84, no. 10, pp. 5743–5749, 1998 (cit. on p. 58).

[188] M. Ramírez-López, Y. L. Casallas-Moreno, M. Pérez-Caro, A. Escobosa-Echevarria, S. Gallardo-Hernández, J. Huerta-Ruelas, and M. Lopez-Lopez, "Study of interference effects on the photoluminescence of AlGaN/GaN quantum wells", *physica status solidi (c)*, vol. 12, no. 4-5, pp. 365–368, 2015 (cit. on p. 58).

[189] M. Wełna, R. Kudrawiec, J. Misiewicz, M. Yano, K. Koike, and S. Sasa, "Contactless electroreflectance spectroscopy of ZnO/ZnMgO quantum wells: Optical transitions and Fabry-Perot features", *physica status solidi (a)*, vol. 212, no. 4, pp. 780–784, 2015 (cit. on p. 58).

[190] C. Krämmer, C. Huber, A. Redinger, D. Sperber, G. Rey, S. Siebentritt, H. Kalt, and M. Hetterich, "Diffuse electroreflectance of thin-film solar cells: Suppression of interference-related lineshape distortions", *Applied Physics Letters*, vol. 107, no. 22, p. 222 104, 2015 (cit. on p. 58).

[191] M. H. Wolter, B. Bissig, E. Avancini, R. Carron, S. Buecheler, P. Jackson, and S. Siebentritt, "Influence of Sodium and Rubidium Postdeposition Treatment on the Quasi-Fermi Level Splitting of Cu(In,Ga)Se 2 Thin Films", *IEEE Journal of Photovoltaics*, vol. 8, no. 5, pp. 1320–1325, 2018 (cit. on pp. 58, 60–62, 81, 90, 169).

[192] M. H. Wolter, B. Bissig, P. Reinhard, S. Buecheler, P. Jackson, and S. Siebentritt, "Correcting for interference effects in the photoluminescence of Cu(In,Ga)Se2 thin films", *Physica Status Solidi (C) Current Topics in Solid State Physics*, vol. 14, no. 6, pp. 2–5, 2017 (cit. on p. 58).

[193] M. H. Wolter, D. Siopa, P. Thiele, P. Dale, E. Avancini, B. Bissig, R. Carron, S. Buecheler, and S. Siebentritt, "Applying a surface treatment to chalcopyrite thin films to eliminate interference effects", *in preparation*, (cit. on p. 58).

[194] M. Powalla, P. Jackson, W. Witte, D. Hariskos, S. Paetel, C. Tschamber, and W. Wischmann, "High-efficiency Cu(In,Ga)Se2 cells and modules", *Solar Energy Materials and Solar Cells*, vol. 119, pp. 51–58, 2013 (cit. on p. 63).

[195] K. Ramanathan, M. A. Contreras, C. L. Perkins, S. Asher, F. S. Hasoon, J. Keane, D. Young, M. Romero, W. Metzger, R. Noufi, J. Ward, and A. Duda, "Properties of 19.2% efficiency ZnO/CdS/CuInGaSe2 thin-film solar cells", *Progress in Photovoltaics: Research and Applications*, vol. 11, no. 4, pp. 225–230, 2003 (cit. on p. 63).

[196] G. Bauer, S. Heise, S. Knabe, O. Neumann, R. Brüggemann, D. Hariskos, and W. Witte, "Depth dependent optoelectronic properties of Cu(In,Ga)Se2 with lateral resolution in the micron/submicron scale from luminescence studies", *Energy Procedia*, vol. 10, pp. 208–212, 2011 (cit. on p. 63).

[197] J. Haarstrich, H. Metzner, C. Ronning, A. Undisz, T. Rissom, C. Kaufmann, and H. Schock, "Luminescence properties of Ga-graded Cu(In,Ga)Se2 thin films", *Thin Solid Films*, vol. 520, no. 9, pp. 3657–3662, 2012 (cit. on p. 63).

[198] G. R. Fowles, *Introduction to modern optics*, 2nd Ed. Holt, Rinehart, and Winston, 1975 (cit. on p. 63).

[199] F. Pedrotti and L. Pedrotti, *Introduction to Optics*, 2nd Ed. Prentice-Hall Inc., 1993 (cit. on pp. 63, 215).

[200] N. Naghavi, F. Mollica, J. Goffard, J. Posada, A. Duchatelet, M. Jubault, F. Donsanti, A. Cattoni, S. Collin, P. Grand, J. Greffet, and D. Lincot, "Ultrathin Cu(In,Ga)Se 2 based solar cells", *Thin Solid Films*, vol. 633, pp. 55–60, 2017 (cit. on p. 67).

[201] O. Poncelet, R. Kotipalli, B. Vermang, A. Macleod, L. A. Francis, and D. Flandre, "Optimisation of rear reflectance in ultra-thin CIGS solar cells towards >20% efficiency", *Solar Energy*, vol. 146, pp. 443–452, 2017 (cit. on p. 67).

[202] Merck. (2018). Polystyrene Latex Beads, [Online]. Available: `https://www.sigmaaldrich.com/catalog/product/sigma/lb11?lang=fr{\&}region=LU` (visited on 10/23/2018) (cit. on p. 74).

[203] H. Van Gorp, P. Walke, A. M. Bragança, J. Greenwood, O. Ivasenko, B. E. Hirsch, and S. De Feyter, "Self-Assembled Polystyrene Beads for Templated Covalent Functionalization of Graphitic Substrates Using Diazonium Chemistry", *ACS Applied Materials & Interfaces*, vol. 10, no. 14, pp. 12 005–12 012, 2018 (cit. on p. 74).

[204] J. Rybczynski, U. Ebels, and M. Giersig, "Large-scale, 2D arrays of magnetic nanoparticles", *Colloids and Surfaces A: Physicochemical and Engineering Aspects*, vol. 219, no. 1-3, pp. 1–6, 2003 (cit. on p. 74).

[205] S. J. Hudak, K. Haber, G. Sando, L. H. Kidder, and E. N. Lewis, "Practical Limits of Spatial Resolution in Diffuse Reflectance NIR Chemical Imaging", *NIR news*, vol. 18, no. 6, pp. 6–8, 2007 (cit. on pp. 76, 77).

[206] Y. J. Cho, K. S. Yook, and J. Y. Lee, "Cool and warm hybrid white organic light-emitting diode with blue delayed fluorescent emitter both as blue emitter and triplet host", *Scientific Reports*, vol. 5, no. 1, p. 7859, 2015 (cit. on pp. 76, 77).

[207] M. H. Wolter, R. Carron, E. Avancini, B. Bissig, T. P. Weiss, S. Nishiwaki, T. Feurer, S. Buecheler, P. Jackson, W. Witte, E. Bourgeois, G. Degutis, and S. Siebentritt, "Influence of light and heavy alkali atoms on the band tails of Cu(In,Ga)Se2 thin-film absorbers", *in preparation*, 2019 (cit. on pp. 81, 107, 127).

[208] G. Bauer, R. Brüggemann, S. Tardon, S. Vignoli, and R. Kniese, "Quasi-Fermi level splitting and identification of recombination losses from room temperature luminescence in Cu(In1-xGax)Se2 thin films versus optical band gap", *Thin Solid Films*, vol. 480-481, pp. 410–414, 2005 (cit. on pp. 82, 83).

[209] L. Gutay and G. H. Bauer, "Non-uniformities of opto-electronic properties in Cu(In,Ga)Se2 thin films and their influence on cell performance studied with confocal photoluminescence", in *2009 34th IEEE Photovoltaic Specialists Conference (PVSC)*, IEEE, 2009, pp. 000 874–000 877 (cit. on pp. 82, 84, 85, 100, 104, 191).

[210] F. Urbach, "The Long-Wavelength Edge of Photographic Sensitivity and of the Electronic Absorption of Solids", *Physical Review*, vol. 92, no. 5, pp. 1324–1324, 1953 (cit. on p. 85).

[211] C. F. Klingshirn, *Semiconductor Optics*, Fourth Edi. Springer-Verlag Berlin Heidelberg, 2012 (cit. on p. 85).

[212] A. Redinger, S. Kretzschmar, and T. Unold, "Quantitative PL imaging of Thin Film Solar Cells - Potential and Pitfalls", *in preparation*, 2019 (cit. on p. 86).

[213] W. H. Press, S. A. Teukolsky, W. T. Vetterling, and B. P. Flannery, *Numerical Recipes: The Art of Scientific Computing*, Third Edit. Cambridge University Press, 2007 (cit. on p. 86).

[214] J. K. Katahara and H. W. Hillhouse, "Quasi-Fermi level splitting and sub-bandgap absorptivity from semiconductor photoluminescence", *Journal of Applied Physics*, vol. 116, no. 17, p. 173 504, 2014 (cit. on pp. 87, 94).

[215] S. Bröker, D. Kück, A. Timmer, I. Lauermann, B. Ümsür, D. Greiner, C. A. Kaufmann, and H. Mönig, "Correlating the Local Defect-Level Density with the Macroscopic Composition and Energetics of Chalcopyrite Thin-Film Surfaces", *ACS Applied Materials & Interfaces*, vol. 7, no. 23, pp. 13 062–13 072, 2015 (cit. on pp. 91, 138).

[216] G Rey, G Larramona, S Bourdais, C Choné, B Delatouche, A Jacob, G Dennler, and S Siebentritt, "On the origin of band-tails in kesterite", *Solar Energy Materials and Solar Cells*, vol. 179, no. October 2017, pp. 142–151, 2018 (cit. on pp. 94, 95, 116, 122).

[217] M. D. Sturge, "Optical Absorption of Gallium Arsenide between 0.6 and 2.75 eV", *Physical Review*, vol. 127, no. 3, pp. 768–773, 1962 (cit. on pp. 94, 128).

[218] S. R. Johnson and T. Tiedje, "Temperature dependence of the Urbach edge in GaAs", *Journal of Applied Physics*, vol. 78, no. 9, pp. 5609–5613, 1995 (cit. on p. 94).

[219] G. Cody, "Urbach edge of crystalline and amorphous silicon: a personal review", *Journal of Non-Crystalline Solids*, vol. 141, no. C, pp. 3–15, 1992 (cit. on pp. 94, 128).

[220] G. D. Cody, T Tiedje, B Abeles, T. D. Moustakas, B Brooks, and Y Goldstein, "Disorder and the optical absorption edge of hydrogenated amorphous silicon", *Le Journal de Physique Colloques*, vol. 42, no. C4, pp. C4–301–C4–304, 1981 (cit. on p. 94).

[221] A. E. Rakhshani, "Heterojunction properties of electrodeposited CdTe/CdS solar cells", *Journal of Applied Physics*, vol. 90, no. 8, pp. 4265–4271, 2001 (cit. on p. 94).

[222] W. Zhang, M. Saliba, D. T. Moore, S. K. Pathak, M. T. Hörantner, T. Stergiopoulos, S. D. Stranks, G. E. Eperon, J. A. Alexander-Webber, A. Abate, A. Sadhanala, S. Yao, Y. Chen, R. H. Friend, L. A. Estroff, U. Wiesner, and H. J. Snaith, "Ultrasmooth organic–inorganic perovskite thin-film formation and crystallization for efficient planar heterojunction solar cells", *Nature Communications*, vol. 6, no. 1, p. 6142, 2015 (cit. on p. 94).

[223] S. De Wolf, J. Holovsky, S.-J. Moon, P. Löper, B. Niesen, M. Ledinsky, F.-J. Haug, J.-H. Yum, and C. Ballif, "Organometallic Halide Perovskites: Sharp Optical Absorption Edge and Its Relation to Photovoltaic Performance", *The Journal of Physical Chemistry Letters*, vol. 5, no. 6, pp. 1035–1039, 2014 (cit. on pp. 94, 98, 128).

[224] J. Jean, T. S. Mahony, D. Bozyigit, M. Sponseller, J. Holovský, M. G. Bawendi, and V. Bulović, "Radiative Efficiency Limit with Band Tailing Exceeds 30% for Quantum Dot Solar Cells", *ACS Energy Letters*, vol. 2, no. 11, pp. 2616–2624, 2017 (cit. on pp. 94, 128, 209).

[225] S. John, C. Soukoulis, M. H. Cohen, and E. N. Economou, "Theory of Electron Band Tails and the Urbach Optical-Absorption Edge", *Physical Review Letters*, vol. 57, no. 14, pp. 1777–1780, 1986 (cit. on p. 94).

[226] L. Gütay, D. Regesch, J. K. Larsen, Y. Aida, V. Depredurand, A. Redinger, S. Caneva, S. Schorr, C. Stephan, J. Vidal, S. Botti, and S. Siebentritt, "Feedback mechanism for the stability of the band gap of CuInSe2", *Physical Review B*, vol. 86, no. 4, p. 045 216, 2012 (cit. on p. 94).

[227] M. Raghuwanshi, B. Thöner, P. Soni, M. Wuttig, R. Wuerz, and O. Cojocaru-Mirédin, "Evidence of Enhanced Carrier Collection in Cu(In,Ga)Se2 Grain Boundaries: Correlation with Microstructure", *ACS Applied Materials & Interfaces*, vol. 10, no. 17, pp. 14 759–14 766, 2018 (cit. on pp. 94, 144).

[228] S. Sadewasser, T. Glatzel, S. Schuler, S. Nishiwaki, R. Kaigawa, and M. Lux-Steiner, "Kelvin probe force microscopy for the nano scale characterization of chalcopyrite solar cell materials and devices", *Thin Solid Films*, vol. 431-432, no. 03, pp. 257–261, 2003 (cit. on p. 94).

[229] R. Baier, J. Lehmann, S. Lehmann, T. Rissom, C. Alexander Kaufmann, A. Schwarzmann, Y. Rosenwaks, M. C. Lux-Steiner, and S. Sadewasser, "Electronic properties of grain boundaries in Cu(In,Ga)Se2 thin films with various Ga-contents", *Solar Energy Materials and Solar Cells*, vol. 103, pp. 86–92, 2012 (cit. on p. 94).

[230] J. Mattheis, U. Rau, and J. H. Werner, "Light absorption and emission in semiconductors with band gap fluctuations—A study on Cu(In,Ga)Se2 thin films", *Journal of Applied Physics*, vol. 101, no. 11, p. 113 519, 2007 (cit. on pp. 95, 181).

[231] D. Abou-Ras, N. Schäfer, C. J. Hages, S. Levcenko, J. Márquez, and T. Unold, "Inhomogeneities in Cu(In,Ga)Se 2 Thin Films for Solar Cells: Band-Gap Versus Potential Fluctuations", *Solar RRL*, vol. 2, no. 1, p. 1 700 199, 2018 (cit. on pp. 95, 139, 142–144).

[232] E. Bourgeois, E. Londero, K. Buczak, J. Hruby, M. Gulka, Y. Balasubramaniam, G. Wachter, J. Stursa, K. Dobes, F. Aumayr, M. Trupke, A. Gali, and M. Nesladek, "Enhanced photoelectric detection of NV magnetic resonances in diamond under dual-beam excitation", *Physical Review B*, vol. 95, no. 4, p. 041 402, 2017 (cit. on p. 98).

[233] L. Gütay, C. Lienau, and G. H. Bauer, "Subgrain size inhomogeneities in the luminescence spectra of thin film chalcopyrites", *Applied Physics Letters*, vol. 97, no. 5, p. 052 110, 2010 (cit. on pp. 100, 104).

[234] L. Guetay, "Konfokale Photolumineszenz von Cu (In , Ga) Se 2", PhD thesis, University of Oldenburg, 2008 (cit. on p. 100).

[235] L. Gütay and G. Bauer, "Spectrally resolved photoluminescence studies on Cu(In,Ga)Se2 solar cells with lateral submicron resolution", *Thin Solid Films*, vol. 515, no. 15, pp. 6212–6216, 2007 (cit. on p. 100).

[236] J. K. Larsen, L. Gütay, Y. Aida, and S. Siebentritt, "Spatial variations of optoelectronic properties in single crystalline CuGaSe2 thin films studied by photoluminescence", *Thin Solid Films*, vol. 519, no. 21, pp. 7332–7336, 2011 (cit. on p. 100).

[237] J. K. Larsen, L. Gütay, and S. Siebentritt, "Influence of secondary phase CuxSe on the optoelectronic quality of chalcopyrite thin films", *Applied Physics Letters*, vol. 98, no. 20, p. 201 910, 2011 (cit. on p. 100).

[238] L. Gütay and G. Bauer, "Local fluctuations of absorber properties of Cu(In,Ga)Se2 by sub-micron resolved PL towards real life conditions", *Thin Solid Films*, vol. 517, no. 7, pp. 2222–2225, 2009 (cit. on pp. 100, 104, 194, 195).

[239] ——, "Lateral variations of optoelectronic quality of Cu(In1–xGax)Se2 in the submicron-scale", *Thin Solid Films*, vol. 487, no. 1-2, pp. 8–13, 2005 (cit. on p. 100).

[240] G. H. Bauer and L. Gütay, "Analyses of Local Open Circuit Voltages in Polycrystalline Cu(In,Ga)Se2 Thin Film Solar Cell Absorbers on the Micrometer Scale by Confocal Luminescence", *CHIMIA International Journal for Chemistry*, vol. 61, no. 12, pp. 801–805, 2007 (cit. on p. 100).

[241] R. E. Walpole, R. H. Myers, S. L. Myers, and K. Ye, *Probability and statistics for engineers and scientists*. Prentice Hall Upper Saddle River, 2002 (cit. on p. 101).

[242] E. Avancini, D. Keller, R. Carron, Y. Arroyo-Rojas Dasilva, R. Erni, A. Priebe, S. Di Napoli, M. Carrisi, G. Sozzi, R. Menozzi, F. Fu, S. Buecheler, and A. N. Tiwari, "Voids and compositional inhomogeneities in Cu(In,Ga)Se 2 thin films: evolution during growth and impact on solar cell performance", *Science and Technology of Advanced Materials*, vol. 19, no. 1, pp. 871–882, 2018 (cit. on pp. 104, 143, 144).

[243] F. Werner, M. H. Wolter, S. Siebentritt, G. Sozzi, S. Di Napoli, R. Menozzi, P. Jackson, W. Witte, R. Carron, E. Avancini, T. P. Weiss, and S. Buecheler, "Alkali treatments of Cu(In,Ga)Se 2 thin-film absorbers and their impact on transport barriers", *Progress in Photovoltaics: Research and Applications*, vol. 26, no. 11, pp. 911–923, 2018 (cit. on pp. 107, 109).

[244] X. Hu, T. Sakurai, A. Yamada, S. Ishizuka, S. Niki, and K. Akimoto, "Investigation of deep-level defects in Cu(In,Ga)Se 2 thin films by a steady-state photocapacitance method", *Journal of Applied Physics*, vol. 116, no. 16, p. 163 703, 2014 (cit. on pp. 108, 143).

[245] C. Stephan, S. Schorr, M. Tovar, and H.-W. Schock, "Comprehensive insights into point defect and defect cluster formation in CuInSe2", *Applied Physics Letters*, vol. 98, no. 9, p. 091 906, 2011 (cit. on p. 108).

[246] J. K. Larsen, K. Burger, L. Gütay, and S. Siebentritt, "Temperature dependence of potential fluctuations in chalcopyrites", in *2011 37th IEEE Photovoltaic Specialists Conference*, IEEE, 2011, pp. 000 396–000 401 (cit. on pp. 110, 111, 114, 117, 143).

[247] S. Siebentritt, N. Papathanasiou, and M. Lux-Steiner, "Potential fluctuations in compensated chalcopyrites", *Physica B: Condensed Matter*, vol. 376-377, no. 1, pp. 831–833, 2006 (cit. on p. 110).

[248] J. Krustok, H. Collan, M. Yakushev, and K. Hjelt, "The Role of Spatial Potential Fluctuations in the Shape of the PL Bands of Multinary Semiconductor Compounds", *Physica Scripta*, vol. T79, no. 1, p. 179, 1999 (cit. on pp. 111, 112, 114).

[249] M. J. Romero, H. Du, G. Teeter, Y. Yan, and M. M. Al-Jassim, "Comparative study of the luminescence and intrinsic point defects in the kesterite Cu2ZnSnS4 and chalcopyrite Cu(In,Ga)Se2", *Physical Review B*, vol. 84, no. 16, p. 165 324, 2011 (cit. on pp. 112, 114).

[250] P. W. Yu, "Excitation-dependent emission in Mg-, Be-, Cd-, and Zn-implanted GaAs", *Journal of Applied Physics*, vol. 48, no. 12, pp. 5043–5051, 1977 (cit. on p. 114).

[251] S. H. Park and B. D. Choe, "Interimpurity transitions in heavily doped semiconductors", *Journal of Applied Physics*, vol. 68, no. 11, pp. 5916–5918, 1990 (cit. on p. 114).

[252] J. P. Leitão, N. M. Santos, P. a. Fernandes, P. M. P. Salomé, A. F. da Cunha, J. C. González, G. M. Ribeiro, and F. M. Matinaga, "Photoluminescence and electrical study of fluctuating potentials in Cu2ZnSnS4-based thin films", *Physical Review B*, vol. 84, no. 2, p. 024 120, 2011 (cit. on p. 114).

[253] J. P. Teixeira, R. A. Sousa, M. G. Sousa, a. F. da Cunha, P. a. Fernandes, P. M. P. Salomé, and J. P. Leitão, "Radiative transitions in highly doped and compensated chalcopyrites and kesterites: The case of Cu2ZnSnS4", *Physical Review B*, vol. 90, no. 23, p. 235 202, 2014 (cit. on p. 114).

[254] A. Jagomägi, J. Krustok, J. Raudoja, M. Grossberg, M. Danilson, and M. Yakushev, "Photoluminescence studies of heavily doped CuInTe2 crystals", *Physica B: Condensed Matter*, vol. 337, no. 1-4, pp. 369–374, 2003 (cit. on p. 114).

[255] J Krustok, J Raudoja, M Yakushev, R. D. Pilkington, and H. Collan, "On the Shape of the Close-to-Band-Edge Photoluminescent Emission Spectrum in Compensated CuGaSe2", *physica status solidi (a)*, vol. 173, no. 2, pp. 483–490, 1999 (cit. on p. 114).

[256] H. Guthrey, J. Moseley, J. Nishinaga, H. Shibata, H. Takahashi, and M. Al-Jassim, "Spatially Resolved Recombination Analysis of CuIn x Ga 1-x Se 2 Absorbers With Alkali Postdeposition Treatments", *IEEE Journal of Photovoltaics*, vol. 8, no. 6, pp. 1833–1840, 2018 (cit. on pp. 123, 124).

[257] C.-S. Jiang, B. To, S. Glynn, H. Mahabaduge, T. Barnes, and M. Al-Jassim, "Recent progress in nanoelectrical characterizations of CdTe and Cu(In,Ga)Se2", in *2017 IEEE 44th Photovoltaic Specialist Conference (PVSC)*, IEEE, 2017, pp. 1–6 (cit. on pp. 123, 158).

[258] A. Polman, M. Knight, E. C. Garnett, B. Ehrler, and W. C. Sinke, "Photovoltaic materials: Present efficiencies and future challenges", *Science*, vol. 352, no. 6283, aad4424–aad4424, 2016 (cit. on pp. 128, 134, 136).

[259] Fraunhofer Institute for Solar Energy Systems. (2018). Photovoltaics Report, [Online]. Available: `https://www.ise.fraunhofer.de/content/dam/ise/de/documents/publications/studies/Photovoltaics-Report.pdf` (visited on 03/15/2019) (cit. on p. 128).

[260] M. Burgelman, P. Nollet, and S. Degrave, "Modelling polycrystalline semiconductor solar cells", *Thin Solid Films*, vol. 361-362, pp. 527–532, 2000 (cit. on p. 129).

[261] M. Burgelman, K. Decock, S. Khelifi, and A. Abass, "Advanced electrical simulation of thin film solar cells", *Thin Solid Films*, vol. 535, pp. 296–301, 2013 (cit. on p. 129).

[262] U. Rau, "Reciprocity relation between photovoltaic quantum efficiency and electroluminescent emission of solar cells", *Physical Review B*, vol. 76, no. 8, p. 085 303, 2007 (cit. on pp. 130–132, 134, 212).

[263] T. Kirchartz, L. Krückemeier, and E. L. Unger, "Research Update: Recombination and open-circuit voltage in lead-halide perovskites", *APL Materials*, vol. 6, no. 10, p. 100 702, 2018 (cit. on p. 131).

[264] R. T. Ross, "Some Thermodynamics of Photochemical Systems", *The Journal of Chemical Physics*, vol. 46, no. 12, pp. 4590–4593, 1967 (cit. on pp. 131, 145).

[265] J. Yao, T. Kirchartz, M. S. Vezie, M. A. Faist, W. Gong, Z. He, H. Wu, J. Troughton, T. Watson, D. Bryant, and J. Nelson, "Quantifying Losses in Open-Circuit Voltage in Solution-Processable Solar Cells", *Physical Review Applied*, vol. 4, no. 1, p. 014 020, 2015 (cit. on p. 131).

[266] M. Yamaguchi, H. Yamada, Y. Katsumata, K.-H. Lee, K. Araki, and N. Kojima, "Efficiency potential and recent activities of high-efficiency solar cells", *Journal of Materials Research*, vol. 32, no. 18, pp. 3445–3457, 2017 (cit. on p. 131).

[267] T. Kirchartz and U. Rau, "Electroluminescence analysis of high efficiency Cu(In,Ga)Se2 solar cells", *Journal of Applied Physics*, vol. 102, no. 10, p. 104 510, 2007 (cit. on p. 131).

[268] T. Kirchartz, A. Helbig, W. Reetz, M. Reuter, J. H. Werner, and U. Rau, "Reciprocity between electroluminescence and quantum efficiency used for the characterization of silicon solar cells", *Progress in Photovoltaics: Research and Applications*, vol. 17, no. 6, pp. 394–402, 2009 (cit. on p. 131).

[269] W. Tress, N. Marinova, O. Inganäs, M. K. Nazeeruddin, S. M. Zakeeruddin, and M. Graetzel, "Predicting the Open-Circuit Voltage of CH 3 NH 3 PbI 3 Perovskite Solar Cells Using Electroluminescence and Photovoltaic Quantum Efficiency Spectra: the Role of Radiative and Non-Radiative Recombination", *Advanced Energy Materials*, vol. 5, no. 3, p. 1 400 812, 2015 (cit. on p. 131).

[270] K. Tvingstedt, O. Malinkiewicz, A. Baumann, C. Deibel, H. J. Snaith, V. Dyakonov, and H. J. Bolink, "Radiative efficiency of lead iodide based perovskite solar cells", *Scientific Reports*, vol. 4, no. 1, p. 6071, 2015 (cit. on p. 131).

[271] K. Vandewal, K. Tvingstedt, A. Gadisa, O. Inganäs, and J. V. Manca, "On the origin of the open-circuit voltage of polymer–fullerene solar cells", *Nature Materials*, vol. 8, no. 11, pp. 904–909, 2009 (cit. on p. 131).

[272] D. Baran, M. S. Vezie, N. Gasparini, F. Deledalle, J. Yao, B. C. Schroeder, H. Bronstein, T. Ameri, T. Kirchartz, I. McCulloch, J. Nelson, and C. J. Brabec, "Role of Polymer Fractionation in Energetic Losses and Charge Carrier Lifetimes of Polymer: Fullerene Solar Cells", *The Journal of Physical Chemistry C*, vol. 119, no. 34, pp. 19 668–19 673, 2015 (cit. on p. 131).

[273] D. Baran, T. Kirchartz, S. Wheeler, S. Dimitrov, M. Abdelsamie, J. Gorman, R. S. Ashraf, S. Holliday, A. Wadsworth, N. Gasparini, P. Kaienburg, H. Yan, A. Amassian, C. J. Brabec, J. R. Durrant, and I. McCulloch, "Reduced voltage losses yield 10% efficient fullerene free organic solar cells with >1 V open circuit voltages", *Energy & Environmental Science*, vol. 9, no. 12, pp. 3783–3793, 2016 (cit. on p. 131).

[274] W. Zhao, D. Qian, S. Zhang, S. Li, O. Inganäs, F. Gao, and J. Hou, "Fullerene-Free Polymer Solar Cells with over 11% Efficiency and Excellent Thermal Stability", *Advanced Materials*, vol. 28, no. 23, pp. 4734–4739, 2016 (cit. on p. 131).

[275] M. A. Green, "Radiative efficiency of state-of-the-art photovoltaic cells", *Progress in Photovoltaics: Research and Applications*, vol. 20, no. 4, pp. 472–476, 2012 (cit. on p. 131).

[276] M. A. Green, Y. Hishikawa, W. Warta, E. D. Dunlop, D. H. Levi, J. Hohl-Ebinger, and A. W. Ho-Baillie, "Solar cell efficiency tables (version 50)", *Progress in Photovoltaics: Research and Applications*, vol. 25, no. 7, pp. 668–676, 2017 (cit. on pp. 132, 135).

[277] M. A. Green, K. Emery, Y. Hishikawa, W. Warta, and E. D. Dunlop, "Solar cell efficiency tables (version 40)", *Progress in Photovoltaics: Research and Applications*, vol. 20, no. 5, pp. 606–614, 2012 (cit. on pp. 132, 135).

[278] U. Rau, B. Blank, T. C. Müller, and T. Kirchartz, "Efficiency Potential of Photovoltaic Materials and Devices Unveiled by Detailed-Balance Analysis", *Physical Review Applied*, vol. 7, no. 4, p. 044 016, 2017 (cit. on pp. 133, 134, 151, 212, 216).

[279] A. Lomuscio, T. Schwarz, B. Gault, M. Melchiorre, D. Raabe, and S. Siebentritt, "Quasi Fermi level splitting of Cu-poor and Cu-rich CuInS2 absorber layers", *submitted to Physical Review Applied*, 2019 (cit. on p. 133).

[280] J. Löckinger, S. Nishiwaki, T. P. Weiss, B. Bissig, Y. E. Romanyuk, S. Buecheler, and A. N. Tiwari, "TiO2 as intermediate buffer layer in Cu(In,Ga)Se2 solar cells", *Solar Energy Materials and Solar Cells*, vol. 174, no. September 2017, pp. 397–404, 2018 (cit. on p. 136).

[281] B. Bissig, R. Carron, L. Greuter, S. Nishiwaki, E. Avancini, C. Andres, T. Feurer, S. Buecheler, and A. N. Tiwari, "Novel back contact reflector for high efficiency and double-graded Cu(In,Ga)Se 2 thin-film solar cells", *Progress in Photovoltaics: Research and Applications*, vol. 26, no. 11, pp. 894–900, 2018 (cit. on p. 136).

[282] T. Trupke, J. Zhao, A. Wang, R. Corkish, and M. A. Green, "Very efficient light emission from bulk crystalline silicon", *Applied Physics Letters*, vol. 82, no. 18, pp. 2996–2998, 2003 (cit. on p. 136).

[283] E. Yablonovitch and T. Gmitter, "Auger recombination in silicon at l o w carrier densities", *Applied Physics Letters*, vol. 49, no. 10, pp. 587–589, 1986 (cit. on p. 136).

[284] T. Tiedje, E. Yablonovitch, G. Cody, and B. Brooks, "Limiting efficiency of silicon solar cells", *IEEE Transactions on Electron Devices*, vol. 31, no. 5, pp. 711–716, 1984 (cit. on p. 136).

[285] A. Richter, S. W. Glunz, F. Werner, J. Schmidt, and A. Cuevas, "Improved quantitative description of Auger recombination in crystalline silicon", *Physical Review B*, vol. 86, no. 16, p. 165 202, 2012 (cit. on p. 136).

[286] A. Richter, M. Hermle, and S. W. Glunz, "Reassessment of the Limiting Efficiency for Crystalline Silicon Solar Cells", *IEEE Journal of Photovoltaics*, vol. 3, no. 4, pp. 1184–1191, 2013 (cit. on p. 136).

[287] D. Barragan-Yani and K. Albe, "Influence of Na and Ga on the electrical properties of perfect 60 dislocations in Cu(In, Ga)Se 2 thin-film photovoltaic absorbers", *Journal of Applied Physics*, vol. 123, no. 16, p. 165 705, 2018 (cit. on pp. 138, 139, 156).

[288] M. Krause, A. Nikolaeva, P. Jackson, D. Hariskos, W. Witte, and D. Abou-Ras, "Microscopic materials properties of a high-efficiency Cu(In,Ga)Se2 solar cell - a case study", in *2018 IEEE 7th World Conference on Photovoltaic Energy Conversion (WCPEC) (A Joint Conference of 45th IEEE PVSC, 28th PVSEC & 34th EU PVSEC)*, IEEE, 2018, pp. 3873–3874 (cit. on pp. 139, 142, 145).

[289] A. Nikolaeva, M. Krause, J. Marquez, C. Hages, S. Levcenko, T. Unold, W. Witte, D. Hariskos, and D. Abou-Ras, "Fluctuations in net doping and lifetime in Cu(In,Ga)Se2 solar cells", in *2018 IEEE 7th World Conference on Photovoltaic Energy Conversion (WCPEC) (A Joint Conference of 45th IEEE PVSC, 28th PVSEC & 34th EU PVSEC)*, IEEE, 2018, pp. 2512–2514 (cit. on pp. 139, 142).

[290] D. Hauschild, D. Kreikemeyer-Lorenzo, P. Jackson, T. M. Friedlmeier, D. Hariskos, F. Reinert, M. Powalla, C. Heske, and L. Weinhardt, "Impact of a RbF Postdeposition Treatment on the Electronic Structure of the CdS/Cu(In,Ga)Se 2 Heterojunction in High-Efficiency Thin-Film Solar Cells", *ACS Energy Letters*, vol. 2, no. 10, pp. 2383–2387, 2017 (cit. on p. 140).

[291] C. S. Schnohr, S. Eckner, P. Schöppe, E. Haubold, F. D'Acapito, D. Greiner, and C. A. Kaufmann, "Reversible correlation between subnanoscale structure and Cu content in co-evaporated Cu(In,Ga)Se2 thin films", *Acta Materialia*, vol. 153, pp. 8–14, 2018 (cit. on p. 144).

[292] T. Kato, "Cu(In,Ga)(Se,S)2 solar cell research in Solar Frontier: Progress and current status", *Japanese Journal of Applied Physics*, vol. 56, no. 4S, 04CA02, 2017 (cit. on p. 144).

[293] M. Gloeckler, J. R. Sites, and W. K. Metzger, "Grain-boundary recombination in Cu(In,Ga)Se2 solar cells", *Journal of Applied Physics*, vol. 98, no. 11, p. 113 704, 2005 (cit. on p. 145).

[294] K. Taretto and U. Rau, "Numerical simulation of carrier collection and recombination at grain boundaries in Cu(In,Ga)Se2 solar cells", *Journal of Applied Physics*, vol. 103, no. 9, p. 094 523, 2008 (cit. on p. 145).

[295] J. Nishinaga, T. Nagai, T. Sugaya, H. Shibata, and S. Niki, "Single-crystal Cu(In,Ga)Se 2 solar cells grown on GaAs substrates", *Applied Physics Express*, vol. 11, no. 8, p. 082 302, 2018 (cit. on p. 145).

[296] T. Kirchartz, F. Staub, and U. Rau, "Impact of Photon Recycling on the Open-Circuit Voltage of Metal Halide Perovskite Solar Cells", *ACS Energy Letters*, vol. 1, no. 4, pp. 731–739, 2016 (cit. on pp. 145, 214).

[297] E. Avancini, R. Carron, B. Bissig, P. Reinhard, R. Menozzi, G. Sozzi, S. Di Napoli, T. Feurer, S. Nishiwaki, S. Buecheler, and A. N. Tiwari, "Impact of compositional grading and overall Cu deficiency on the near-infrared response in Cu(In, Ga)Se2 solar cells", *Progress in Photovoltaics: Research and Applications*, vol. 25, no. 3, pp. 233–241, 2017 (cit. on p. 145).

[298] C. Gueymard, D. Myers, and K. Emery, "Proposed reference irradiance spectra for solar energy systems testing", *Solar Energy*, vol. 73, no. 6, pp. 443–467, 2002 (cit. on p. 153).

[299] National Renewable Energy Laboratory. (2018). Reference Air Mass 1.5 Spectra, [Online]. Available: `https://www.nrel.gov/grid/solar-resource/spectra-am1.5.html` (visited on 08/08/2018) (cit. on pp. 153, 154).

[300] D. R. Williams. (2018). Sun Fact Sheet, [Online]. Available: `https://nssdc.gsfc.nasa.gov/planetary/factsheet/sunfact.html` (visited on 08/08/2018) (cit. on p. 153).

[301] E. E. Mamajek, A. Prsa, G. Torres, P. Harmanec, M. Asplund, P. D. Bennett, N. Capitaine, J. Christensen-Dalsgaard, E. Depagne, W. M. Folkner, M. Haberreiter, S. Hekker, J. L. Hilton, V. Kostov, D. W. Kurtz, J. Laskar, B. D. Mason, E. F. Milone, M. M. Montgomery, M. T. Richards, J. Schou, and S. G. Stewart, "IAU 2015 Resolution B3 on Recommended Nominal Conversion Constants for Selected Solar and Planetary Properties", pp. 1–6, 2015 (cit. on p. 153).

[302] J. W. Evans and R. Michard, "Observational Study of Macroscopic Inhomogeneities in the Solar Atmosphere. III. Vertical Oscillatory Motions in the Solar Photosphere.", *Astrophysical Journal*, vol. 136, pp. 493–506, 1962 (cit. on p. 154).

[303] F. H. Pianezzi, "Electronic transport and doping mechanisms in Cu(In,Ga)Se2 thin film solar cells", PhD thesis, ETH Zürich, 2014 (cit. on p. 155).

[304] L. Kosyachenko, X Mathew, P. Paulson, V. Lytvynenko, and O. Maslyanchuk, "Optical and recombination losses in thin-film Cu(In,Ga)Se 2 solar cells", *Solar Energy Materials and Solar Cells*, vol. 130, pp. 291–302, 2014 (cit. on p. 155).

[305] J. A. Aguiar, A. Stokes, C.-S. Jiang, T. Aoki, P. G. Kotula, M. K. Patel, B. Gorman, and M. Al-Jassim, "Revealing Surface Modifications of Potassium-Fluoride-Treated Cu(In,Ga)Se 2 : A Study of Material Structure, Chemistry, and Photovoltaic Performance", *Advanced Materials Interfaces*, vol. 3, no. 17, p. 1 600 013, 2016 (cit. on p. 158).

[306] R. Carron, C. Andres, E. Avancini, T. Feurer, S. Nishiwaki, S. Pisoni, F. Fu, M. Lingg, Y. E. Romanyuk, S. Buecheler, and A. N. Tiwari, "Bandgap of thin film solar cell absorbers: A comparison of various determination methods", *Thin Solid Films*, vol. 669, no. July 2018, pp. 482–486, 2019 (cit. on p. 166).

[307] T. Hölscher, T. Schneider, M. Maiberg, and R. Scheer, "Critical role of air-light exposure on co-evaporated Cu(In,Ga)Se 2 solar cells", *Japanese Journal of Applied Physics*, vol. 57, no. 8S3, 08RC07, 2018 (cit. on p. 183).

[308] T. C. M. Müller, T. M. H. Tran, B. E. Pieters, A. Gerber, R. Carius, and U. Rau, "Effect of light soaking on the electro- and photoluminescence of Cu(In,Ga)Se 2 solar cells", *Applied Physics Letters*, vol. 103, no. 18, p. 183 504, 2013 (cit. on p. 184).

[309] M. A. Green, "Lambertian light trapping in textured solar cells and light-emitting diodes: analytical solutions", *Progress in Photovoltaics: Research and Applications*, vol. 10, no. 4, pp. 235–241, 2002 (cit. on p. 209).

[310] C. Ulbrich, S. Fahr, J. Üpping, M. Peters, T. Kirchartz, C. Rockstuhl, R. Wehrspohn, A. Gombert, F. Lederer, and U. Rau, "Directional selectivity and ultra-light-trapping in solar cells", *physica status solidi (a)*, vol. 205, no. 12, pp. 2831–2843, 2008 (cit. on p. 209).

[311] T. Kirchartz, K. Seino, J.-M. Wagner, U. Rau, and F. Bechstedt, "Efficiency limits of Si/SiO2 quantum well solar cells from first-principles calculations", *Journal of Applied Physics*, vol. 105, no. 10, p. 104 511, 2009 (cit. on p. 209).

[312] X. Wang and M. S. Lundstrom, "On the Use of Rau's Reciprocity to Deduce External Radiative Efficiency in Solar Cells", *IEEE Journal of Photovoltaics*, vol. 3, no. 4, pp. 1348–1353, 2013 (cit. on p. 212).

[313] I. Schnitzer, E. Yablonovitch, C. Caneau, and T. J. Gmitter, "Ultrahigh spontaneous emission quantum efficiency, 99.7% internally and 72% externally, from AlGaAs/GaAs/AlGaAs double heterostructures", *Applied Physics Letters*, vol. 62, no. 2, pp. 131–133, 1993 (cit. on p. 214).

[314] O. D. Miller, E. Yablonovitch, and S. R. Kurtz, "Strong Internal and External Luminescence as Solar Cells Approach the Shockley–Queisser Limit", *IEEE Journal of Photovoltaics*, vol. 2, no. 3, pp. 303–311, 2012 (cit. on p. 214).

[315] N. Dahan, Z. Jehl, T. Hildebrandt, J.-J. Greffet, J.-F. Guillemoles, D. Lincot, and N. Naghavi, "Optical approaches to improve the photocurrent generation in Cu(In,Ga)Se 2 solar cells with absorber thicknesses down to 0.5 μ m", *Journal of Applied Physics*, vol. 112, no. 9, p. 094 902, 2012 (cit. on p. 214).